



TECHNICAL REPORT 0-6936-1
TxDOT PROJECT NUMBER 0-6036

Development of Semi-integral Bridge Abutment Details for Texas Conditions

Jorge Zornberg
Behdad Mofarraj
Todd Helwig
Jakob Walter

December 2023
Published January 2025

<https://library.ctr.utexas.edu/ctr-publications/0-6936-1.pdf>



Technical Report Documentation Page

1. Report No. FHWA/TX-24/0-6936-1		2. Government Accession No.		3. Recipient's Catalog No.	
4. Title and Subtitle Development of Semi-integral Bridge Abutment Details for Texas Conditions				5. Report Date Submitted: June 2023	
				6. Performing Organization Code	
7. Author(s) Jorge Zornberg, PhD, PE (ORCID: 0000-0002-6307-1047) Behdad Mofarraj, PhD (ORCID: 0000-0002-2861-3912) Todd Helwig, PhD Jakob Walter, PE				8. Performing Organization Report No. 0-6936-1	
9. Performing Organization Name and Address Center for Transportation Research The University of Texas at Austin 3925 W. Braker Lane, 4 th Floor Austin, TX 78759				10. Work Unit No. (TRAIS)	
				11. Contract or Grant No. 0-6936	
12. Sponsoring Agency Name and Address Texas Department of Transportation Research and Technology Implementation Division 125 E. 11 th Street Austin, TX 78701				13. Type of Report and Period Covered Technical Report August 2016 – August 2023	
				14. Sponsoring Agency Code	
15. Supplementary Notes Project performed in cooperation with the Texas Department of Transportation and the Federal Highway Administration.					
16. Abstract Semi-integral bridges constitute a promising alternative to conventional TxDOT bridges because they eliminate the need for deck expansion joints, which may significantly reduce bridge maintenance costs and potentially result in significant savings over the bridge service life. Adopting semi-integral bridges is particularly relevant to Districts with comparatively cold winters (e.g., Amarillo), where the use of deicing salts has resulted in significant joint maintenance problems. However, the elimination of expansion joints requires careful consideration because of the soil-structure interaction between the bridge structure and abutment backfill caused by the bridge's daily and seasonal thermal expansion/contraction. In this research, the data collected from the monitoring of two pilot semi-integral bridges in Texas, USA, are presented and evaluated. In this study, the effect of daily and seasonal temperature changes on the displacement of various bridge components, changes in abutment earth pressure, foundation interaction, ratcheting, backfill settlement, etc., have been successfully captured. Among the findings are increased backfill lateral earth pressure due to ratcheting, continuous settlement of the backfill, loss of vertical support for the approach slabs, asymmetric expansion/contraction of the bridge, and slight displacement of the bridge superstructure toward one end of the bridge. In addition, it was found that the thermal expansion/contraction of the bridge deck results in cyclic lateral loading of the abutment caps and the bridge foundations despite a lack of rigid connection between the foundations and the superstructure.					
17. Key Words Semi-integral, bridge, integral, soil-structure interaction, instrumentation, monitoring, ratcheting, abutment, settlement, earth pressure, deep foundation				18. Distribution Statement No restrictions. This document is available to the public through the National Technical Information Service, Alexandria, Virginia 22312; www.ntis.gov.	
19. Security Classif. (of report) Unclassified	20. Security Classif. (of this page) Unclassified	21. No. of pages TBD [Total count excl. cover]		22. Price	



**THE UNIVERSITY OF TEXAS AT AUSTIN
CENTER FOR TRANSPORTATION RESEARCH**

Development of Semi-integral Bridge Abutment Details for Texas Conditions

Jorge Zornberg, PhD, PE
Behdad Mofarraj, PhD
Todd Helwig, PhD, PE
Jakob Walter, PE

CTR Technical Report:	0-6936-1
Report Date:	Submitted: June 2023
Project:	0-6936
Project Title:	Development of Integral/Semi-integral Abutments for Texas Bridges
Sponsoring Agency:	Texas Department of Transportation
Performing Agency:	Center for Transportation Research at The University of Texas at Austin

Project performed in cooperation with the Texas Department of Transportation and the Federal Highway Administration.

Center for Transportation Research
The University of Texas at Austin
3925 W. Braker Lane, 4th floor
Austin, TX 78759

<http://ctr.utexas.edu/>

Disclaimers

Author's Disclaimer: The contents of this report reflect the views of the authors, who are responsible for the facts and the accuracy of the data presented herein. The contents do not necessarily reflect the official view or policies of the Federal Highway Administration or the Texas Department of Transportation (TxDOT). This report does not constitute a standard, specification, or regulation.

Patent Disclaimer: There was no invention or discovery conceived or first actually reduced to practice in the course of or under this contract, including any art, method, process, machine manufacture, design,, or composition of matter, or any new useful improvement thereof, or any variety of plant, which is or may be patentable under the patent laws of the United States of America or any foreign country.

Engineering Disclaimer

NOT INTENDED FOR CONSTRUCTION, BIDDING, OR PERMIT PURPOSES.

Project Engineer: Jorge G. Zornberg, Ph.D., P.E.
Professional Engineer License State and Number: California No. C 056325
P.E. Designation: Research Supervisor

Acknowledgments

The research team is thankful for the significant input provided by TxDOT's PMC throughout the development of this research project, initially under the leadership of Mr. Mike Hyzak, and subsequently under the direction of Dr. Niyi Arowojolu. The continued, skillful support by TxDOT's Project Manager Jade Adediwura is also gratefully acknowledged. All findings and opinions presented in this report are solely from the research team.

Table of Contents

Chapter 1. Assessment of the Current Practice.....	30
1.1. Introduction to the Assessment of the Current Practice.....	30
1.2. Overview of the Current Practice	30
1.3. Types of Bridges	31
1.3.1. Conventional Bridge	31
1.3.2. Semi-Integral Abutment Bridge (SIAB).....	32
1.3.3. Integral Abutment Bridge (IAB).....	33
1.3.4. Geosynthetic Reinforced Soil – Integral Bridge System (GRS-IBS) .	34
1.3.5. Portal Frame Bridge.....	35
1.4. Current Practice in the United States	36
1.4.1. IAB.....	36
1.4.2. Foundation Types.....	37
1.4.3. Backfill Material	39
1.4.4. Approach Slabs	41
1.4.5. Girder/Beam Design	43
1.5. SIAB	44
1.5.1. Foundation Types.....	44
1.5.2. Backfill Material	45
1.5.3. Approach Slabs	46
1.5.4. Girder/Beam Design	46
1.5.5. Integral Bridge General Design Criteria	46
1.6. Current Practice in Europe.....	47
1.6.1. IAB & SIAB	49
1.7. Current Practice in Asia	52
1.7.1. The Japanese Approach	52
1.7.2. Korean Integral Bridges.....	54
Chapter 2. Assessment of the Current State of the Practice in Texas.....	56
2.1. Existing Integral/Semi-integral Abutment Bridges in Texas.....	56
2.1.1. El Paso County IAB.....	56
2.1.2. Mack Creek Bridge.....	57
2.1.3. Fannin County SIAB.....	58
2.1.4. El Paso County SIAB.....	60
2.2. Field Data of IAB/SIAB in Texas.....	61

2.2.1. El Paso County IAB Field Data	61
2.2.2. Mack Creek Bridge Field Data	62
2.2.3. Fannin County SIAB Field Data.....	63
2.2.4. El Paso County SIAB Field Data.....	63
Chapter 3. Survey of State DOTs and Texas Districts.....	64
3.1. Introduction to the Surveys.....	64
3.1.1. Survey of State DOTs	64
3.1.2. Survey of TxDOT Districts.....	64
3.2. Development of State DOT Survey	64
3.2.1. Phase 1 Questionnaire.....	65
3.2.2. Phase 2 Questionnaire.....	65
3.3. Development of Texas District Survey.....	66
3.4. Distribution and Response Rate.....	66
3.4.1. State DOT Survey	66
3.4.2. Texas District Survey.....	67
3.5 Analysis of Responses	68
3.4.3. State DOT Survey	68
3.4.4. Texas District Survey.....	80
Chapter 4. Field Condition Assessments of Selected Texas Bridges	85
4.1. Introduction to Field Condition Assessments	85
4.2. Bridges Inspected.....	85
4.2.1. Description of El Paso County IAB.....	86
4.2.2. Description of Mack Creek SIAB.....	88
4.3. Survey Results	88
4.3.1. Survey of Anthony IAB.....	88
4.3.2. Survey of Mack Creek SIAB	93
4.4. Material Characterization.....	105
4.5. Conclusion to Field Condition Assessments.....	111
Chapter 5. Identification of Relevant Parameters and Quantification of the Range of their Representative Values	113
5.1. Introduction to Identification of Relevant Parameters for Numerical Simulations	113
5.2. Baseline Structure Identification.....	113
5.3. Subsoil Characteristics.....	113
5.4. Material Properties.....	114

5.4.1. Mack Creek Parameters	114
5.4.2. China Creek Parameters.....	116
5.5. Load/Displacement Characteristics	117
5.6. Conclusion to Identification of Relevant Parameters for Numerical Simulations	117
Chapter 6. Experimental Component.....	119
6.1. Background Information.....	119
6.2. Instrumentation	122
6.3. Scope of the Experimental Program	123
6.4. Experimental Results	124
6.4.1. Initial Baseline Configuration.....	124
6.4.2. Movements Away from Soil Mass (Active)	131
6.4.3. Movements into Soil Mass (Passive).....	136
6.4.4. Coarse Soil-Wall Interface.....	141
6.4.5. Wrap-Around Geotextile Reinforcement.....	147
6.4.6. Compressible Inclusion.....	152
6.5. Analysis of Experimental Results.....	157
6.6. Digital Image Correlation	161
6.7. Conclusions of the Experimental Component	163
Chapter 7. Field Monitoring of Mack Creek Semi-integral Bridge.....	165
7.1. Introduction to Mack Creek Bridge Field Monitoring.....	165
7.2. Field Monitoring of Mack Creek SIAB.....	165
7.2.1. Initial Instrumentation Plan (Summer 2017)	165
7.2.2. Additional Instrumentation of Mack Creek SIAB (Winter 2020)	174
7.3. Analysis of the Performance of Mack Creek Bridge	189
7.4. Conclusions on Field Monitoring of Mack Creek SIAB	192
Chapter 8. Field Monitoring of China Creek Semi-integral Bridge	194
8.1. Initial Conditions of China Creek Bridge	194
8.2. Instrumentation Plan for China Creek SIAB	197
8.2.1. Logger Equipment	198
8.2.2. Logger Programming.....	216
8.2.3. Construction Sequence of China Creek Bridge Replacement	219
8.3. Analysis of the Performance of China Creek Bridge.....	262
8.3.1. Analysis of the Data from the Monitoring System	262
8.3.2. Analysis of the Data from Field Survey Campaigns	281

8.4. Conclusions on Field Monitoring of China Creek SIAB.....	289
Chapter 9. Analysis Of Soil-structure Interaction Data From China Creek Semi-integral Bridge	291
9.1. Introduction to the Analysis of China Creek SIAB Soil-structure Interaction Data.....	291
9.2. Bridge Description	292
9.3. Instrumentation Description.....	293
9.4. Thermal Expansion and Contraction of the Bridge	295
9.5. Lateral Earth Pressures on Abutment Walls	303
9.6. Abutment Backfill Settlements	309
9.7. Conclusions on the Analysis of China Creek SIAB Soil-structure Interaction Data.....	311
Chapter 10. Analysis of Foundation Monitoring Data from China Creek Semi-integral Bridge	314
10.1. Introduction to the Analysis of China Creek SIAB Foundation Monitoring Data	314
10.2. Description of China Creek Bridge.....	315
10.2.1. Geotechnical Characterization of the Foundation Soil	316
10.3. Instrumentation Overview	316
10.4. Instrumentation Data.....	317
10.5. Analysis of Drilled Shaft Behavior.....	321
10.6. Conclusions to the Analysis of China Creek SIAB Foundation Monitoring Data	326
Chapter 11. Compilation of Design Concepts, Limitations and Details.....	328
11.1. Introduction to the Compilation of Design Concepts, Limitations and Details	328
11.2. Design Recommendations	328
11.2.1. Backfill Placement/Protection	328
11.2.2. Rigorous Quality Control.....	331
11.2.3. Foundation Design	334
11.2.4. Season of Completion	336
11.2.5. Surface Runoff Management	337
11.2.6. Approach Pavement Design.....	337
11.3. Proposed Semi-integral Bridge Abutment Details.....	337
11.3.1. Woven Geotextile Fabric	338
11.3.2. Select Rockfill.....	340

11.3.3. Compressible Inclusion.....	341
11.3.4. Filter Fabric.....	342
11.3.5. Wingwalls	342
11.3.6. Approach Slab Bond Breaker	342
11.3.7. Foundation Design	343
11.3.8. Thermal Movements	343
11.3.9. Abutment Earth Pressures.....	343
Appendix A. Relevant Information on the Survey of State DOTs and Texas Districts	345
A.1: Phase 1 Questionnaire of State DOT Survey	346
A.2: Phase 2 Questionnaire of State DOT Survey	348
A.3: TxDOT District Survey.....	355
Introduction.....	355
Glossary of Terms.....	355
A.4: MnDOT IAB/SIAB Design Details	361
A.5: Oklahoma DOT CLSM Backfilling Specifications	396
A.6: PennDOT Approach Slab Details	399
Appendix B. Numerical Simulation and Parametric Evaluation of Integral/Semi- Integral Bridges Considering Representative Ranges of Relevant Parameters ..	434
B.1: Introduction to the Numerical Simulations	434
B.2: Finite Element Model of Mack Creek Bridge.....	434
B.3: Description of the Finite Element Model of Mack Creek Bridge.....	434
B.4: Mack Creek Bridge Finite Element Model Results	440
B.5: Preliminary Sensitivity Analyses	444
B.5.1: Choice of Displacement Amplitudes and Number of Cycles	444
B.5.2: Influence of Lateral Displacement Amplitude	447
B.5.3: Numerical Simulation Considering the Alternative Approach for Modeling the Abutment-cap System	455
B.5.4: Numerical Simulation Considering the New Numerical Model	460
B.5.4.1: New Geometry Description.....	460
B.5.4.2: New Geometry Results	462
B.5.5: Analysis of the Daily Cyclic Response.....	464
B.6: Temperature Distribution Within the Deck Section.....	501
B.6.1: General Formulation of Heat Flow in Concrete.....	501
B.7: Conclusion to the Numerical Simulations.....	505

References	508
------------------	-----

List of Tables

Table 1.1: General design limits of IAB/SIAB (adapted from Maruri and Petro, 2005)	46
Table 1.2: Highlights of European IAB/SIAB design criteria (adapted from White, 2007)	48
Table 1.3: Examples of PFB girder to abutment corner connections and load transfer mechanisms (Iwasaki et al., 2011).....	53
Table 2.1: Integral/semi-integral abutment bridges in Texas	56
Table 2.2: Compilation of bridge condition ratings for known IAB and SIAB in Texas	61
Table 3.1: States responding to phase 1 and 2 DOT questionnaires.....	67
Table 3.2: List of districts responding to TxDOT internal survey.....	68
Table 3.3: Initial DOT responses regarding the number of IAB/SIAB in inventory and required backfill material	71
Table 3.4: State DOT phase 2 questionnaire responses of IAB/SIAB history and general design factors	74
Table 3.5: State DOT phase 2 questionnaire responses regarding IAB design	75
Table 3.6: State DOT phase 2 questionnaire responses regarding SIAB design ..	77
Table 3.7: State DOT phase 2 questionnaire responses regarding IAB/SIAB construction.....	79
Table 4.1: Secant friction angle and overall MC failure envelope based on CD triaxial tests on Mack Creek backfill material	109
Table 4.2: Best fit parameters used in modeling Mack Creek backfill soil using Hardening Soil model of Plaxis	110
Table 5.1: Soil parameters used in the preliminary numerical model	115
Table 5.2: Structural parameters used in the preliminary numerical model	115
Table 5.3: Soil parameters used in the calibration of the preliminary numerical model.....	116
Table 5.4: Structural parameters used in the calibration of the preliminary numerical model.....	116
Table 6.1: Values of soil settlement and heave based on image correlation for baseline test.....	129
Table 6.2: Values of soil settlement and heave based on image correlation for active movements test	134

Table 6.3: Values of soil settlement and heave based on image correlation for passive movements test.....	139
Table 6.4: Values of soil settlement and heave based on image correlation for coarse interface test.....	145
Table 6.5: Values of soil settlement and heave based on image correlation for wrap-around geotextile test.....	150
Table 6.6: Values of soil settlement and heave based on image correlation for geofoam inclusion test (extent of soil settlement measured from steel wall, not the edge of geofoam sheeting)	155
Table 8.1: Specifications for model 4815 pressure cell (geokon.com).....	204
Table 8.2: Specifications for model 4435 soil extensometer (geokon.com).....	205
Table 8.3: Specifications for model 4420 crackmeter (geokon.com)	210
Table 8.4: Specifications for model 6160 MEMS tiltmeter (geokon.com)	212
Table 8.5: Specifications for SAAV static measurements (measurand.com).....	212
Table 8.6: Dielectric constant for some materials commonly encountered in construction settings.....	284

List of Figures

Figure 1.1: Diagram of conventional bridge structure.....	31
Figure 1.2: Modified example of semi-integral abutment detail (Husain and Bagnariol, 1999)	33
Figure 1.3: Modified example of integral abutment detail (PennDOT, 2007)	34
Figure 1.4: General design layout of GRS-IBS (Adams et al., 2011)	35
Figure 1.5: Example of a portal frame bridge: (a) profile view; (b) superstructure cross section; and (c) steel girder end detail (Iwasaki et al. 2011)	36
Figure 1.6: Kii Bridge layout and instrumentation details: (a) plan view; and (b) profile view (Ooi et al., 2010).....	38
Figure 1.7: Integral abutment backfill requirements across the United States (Maruri and Petro, 2005).....	39
Figure 1.8: Relationship between abutment wall movement and earth pressure (Clough and Duncan, 1991).....	40
Figure 1.9: Lateral earth pressure distribution on integral abutment backwall: (a) stub abutment on piles; (b) stub abutment on shallow foundation; and (c) full height wall abutment (Oesterle and Tabatabai, 2014)	41
Figure 1.10: New York State DOT detail for integral abutments with steel girders	42
Figure 1.11: Development of subsidence zone beneath approach slab of integral abutment (Horvath, 2005).....	43
Figure 1.12: SIAB abutment and foundation detail (Burke, 2009).....	45
Figure 1.13: Integral abutment founded on a spread footing, as used in the United Kingdom (White, 2007)	49
Figure 1.14: Evolution of Swiss IAB approach slab connections (Dreier et al., 2011)	50
Figure 1.15: Longitudinal displacements at the surface of IAB with moving transition slab (Burdet et al., 2015).....	51
Figure 1.16: 3D rendering of VFT-WIB®: (a) bridge deck/girder system; and (b) end detail (Petzek et al., 2015).....	51
Figure 1.17: Evolution of bridge structures in Japan (Tatsuoka et al., 2009).....	52
Figure 1.18: Approach slab example of Japanese PFB (adapted from Iwasaki et al., 2011)	54
Figure 1.19: Two tested abutment-pile connections by Ahn et al. (2011).....	54
Figure 2.1: El Paso County IAB roadway (looking west)	57

Figure 2.2: El Paso County IAB (southeast corner of bridge looking northwest)	57
Figure 2.3: Mack Creek Bridge roadway (looking east).....	58
Figure 2.4: Mack Creek Bridge abutment view (looking east).....	58
Figure 2.5: Fannin County SIAB roadway-to-bridge-deck transition (from north end looking southwest)	59
Figure 2.6: Fannin County SIAB profile view (looking northwest).....	59
Figure 2.7: El Paso County SIAB roadway-to-bridge-deck transition (from west end looking northeast).....	60
Figure 2.8: El Paso County SIAB profile view (from east end looking southwest)	60
Figure 3.1: Initial DOT questionnaire responses regarding IAB design: (a) allowance of IAB; (b) superstructures designed with IAB; and (c) substructures designed with IAB	69
Figure 3.2: Initial DOT questionnaire responses regarding SIAB design: (a) allowance of SIAB; (b) superstructures designed with SIAB; and (c) substructures designed with SIAB	70
Figure 3.3: TxDOT District questionnaire responses regarding bridge maintenance: (a) joint maintenance interval; (b) problems driving maintenance; and (c) traffic effect of maintenance	81
Figure 3.4: TxDOT District questionnaire responses regarding bridge approaches: (a) use of approach slabs; (b) standards used for approach slabs; and (c) preferred approach to roadway joint for IAB/SIAB	82
Figure 3.5: TxDOT District questionnaire responses regarding IAB/SIAB pros & cons: (a) IAB/SIAB concerns; and (b) IAB/SIAB potential benefits	84
Figure 4.1: Plan and profile as-built drawing of Anthony IAB	87
Figure 4.2: Photograph of Anthony IAB taken at southwest corner of bridge facing east/northeast.....	87
Figure 4.3: Photograph of Mack Creek Bridge taken on north approach facing south.....	88
Figure 4.4: Photograph of survey points (orange dots) on Anthony IAB east abutment face	89
Figure 4.5: Photograph of survey points (orange dots) on Anthony IAB west transition from roadway to approach slab and approach slab to bridge deck	89
Figure 4.6: Summer and winter surveys of west transitions from: (a) roadway to approach slab; and (b) approach slab to bridge deck.....	91
Figure 4.7: Summer and winter surveys of east transitions from: (a) roadway to approach slab; and (b) approach slab to bridge deck.....	92

Figure 4.8: Photograph of west transition from approach road (left) to approach slab (right) on Anthony IAB	93
Figure 4.9: Survey points of bridge approach road to deck transitions during August 2017 and December 2017 for: (a) east approach; and (b) west approach	95
Figure 4.10: Photograph of bump at the end of Mack Creek Bridge and survey points on east approach centerline	95
Figure 4.11: Cracking at the approach slab-bridge deck connection: (a) 12/7/17; and (b) 4/10/18.....	96
Figure 4.12: Repaved approach slabs of Mack Creek Bridge (orange dots are survey points).....	97
Figure 4.13: Differential settlement revealed by the difference in height of guardrails between approach slab and bridge deck.....	97
Figure 4.14: Differential settlement between guardrails constructed on top of the deck and south approach slab (November 2019).....	98
Figure 4.15: Use of clayey natural soil as base material for asphalt pavement in approach slabs	100
Figure 4.16: Traces of water on the northern abutment cap under the bridge deck	101
Figure 4.17: Water gathered under the box girders (view from south abutment).....	101
Figure 4.18: Water droplets gathered underneath the girders	102
Figure 4.19: Settlement of concrete placed behind wingwalls (southwest wingwall)	103
Figure 4.20: Loss of fill placed behind wingwalls due to erosion (left image shows an overhead view of the gap between sheetpile and pile cap)	104
Figure 4.21: Void caused by erosion of fill under shoulder of southern approach	104
Figure 4.22: Damage to earth pressure cell cables due to unanticipated settlement of concrete.....	105
Figure 4.23: Triaxial setup used to measure shear strength of Mack Creek soil	106
Figure 4.24: Triaxial test results for Mack Creek backfill soil (stress-strain curves)	107
Figure 4.25: Triaxial test results for Mack Creek soil (volumetric strain data)..	107
Figure 4.26: Triaxial specimen at failure (9 psi effective confinement).....	108
Figure 4.27: Mohr circles at failure for the triaxial tests performed on Mack Creek backfill with Mohr-Coulomb failure envelope of $\tau = 1.5 + \sigma \tan(37^\circ)$	109
Figure 4.28: Comparison of simulated triaxial results from hardening soil models with actual triaxial tests performed in the laboratory (stress-strain curves)	110

Figure 4.29: Comparison of simulated triaxial results from hardening soil models with actual triaxial tests performed in the laboratory (volumetric strain curves)	111
Figure 5.1: 28th day compressive strength test results for concrete used in the west abutment drilled shaft, phase I.....	117
Figure 6.1: Schematic of typical integral bridge abutment.....	119
Figure 6.2: Experimental testing equipment: (a) profile view schematic; and (b) photo taken prior to first conducted test	121
Figure 6.3: Grain size distribution of soil used in experimental testing program	122
Figure 6.4: Time-history of lateral force for the baseline test	125
Figure 6.5: Time-history of wall rotation for the baseline test (Note: the mobilized passive and active force per Rankine theory)	126
Figure 6.6: Full-frame photo of completed final cycle of baseline test.....	126
Figure 6.7: Photos from top viewing window of soil box during baseline test: (a) at beginning of test; and after (b) cycle 1.5; (c) cycle 1.10; (d) cycle 2.5; (e) cycle 2.10; (f) cycle 3.5; and (g) cycle 3.10	128
Figure 6.8: Pressure cell locations and lateral earth pressure distribution on stiffened steel wall for most forward position rotated into soil mass during: (a) first set of 10 cycles; (b) second set of 10 cycles; and (c) third set of 10 cycles of baseline test.....	130
Figure 6.9: Time-history of lateral force for the active movements test	132
Figure 6.10: Time-history of wall rotation for active movements test (Note: the mobilized passive and active force per Rankine theory)	132
Figure 6.11: Photos from top viewing window of soil box during active movements test: (a) at beginning of test; and after (b) cycle 1.5; (c) cycle 1.10; (d) cycle 2.5; (e) cycle 2.10; (f) cycle 3.5; and (g) cycle 3.10.....	133
Figure 6.12: Pressure cell locations and lateral earth pressure distribution on stiffened steel wall for most forward position rotated into soil mass during: (a) first set of 12 cycles; (b) second set of 11 cycles; and (c) third set of 10 cycles of active movements test	135
Figure 6.13: Time-history of lateral force for passive movements test	136
Figure 6.14: Time-history of wall rotation for passive movements test (Note: the mobilized passive and active force per Rankine theory)	137
Figure 6.15: Photos from top viewing window of soil box during passive movements test: (a) at beginning of test; and after (b) cycle 1.5; (c) cycle 1.10; (d) cycle 2.5; (e) cycle 2.10; (f) cycle 3.5; and (g) cycle 3.10.....	138
Figure 6.16: Pressure cell locations and lateral earth pressure distribution on stiffened steel wall for most forward position rotated into soil mass during: (a) first set of 10 cycles; (b) second set of 10 cycles; and (c) third set of 10 cycles of passive movements test.....	140

Figure 6.17: Time-history of lateral force for coarse interface test	142
Figure 6.18: Time-history of wall rotation for coarse interface test (Note: the mobilized passive and active force per Rankine theory)	142
Figure 6.19: Photos from top viewing window of soil box during coarse interface test: (a) at beginning of test; and after (b) cycle 1.5; (c) cycle 1.10; (d) cycle 2.5; (e) cycle 2.10; (f) cycle 3.5; and (g) cycle 3.10	144
Figure 6.20: Pressure cell locations and lateral earth pressure distribution on stiffened steel wall for most forward position rotated into soil mass during: (a) first set of 10 cycles; (b) second set of 10 cycles; and (c) third set of 10 cycles of coarse interface test.....	146
Figure 6.21: Time-history of lateral force for wrap-around geotextile test	148
Figure 6.22: Time-history of wall rotation for wrap-around geotextile test (Note: the mobilized passive and active force per Rankine theory)	148
Figure 6.23: Photos from top viewing window of soil box during wrap-around geotextile test: (a) at beginning of test; and after (b) cycle 1.5; (c) cycle 1.10; (d) cycle 2.5; (e) cycle 2.10; (f) cycle 3.5; and (g) cycle 3.10.....	150
Figure 6.24: Pressure cell locations and lateral earth pressure distribution on stiffened steel wall for most forward position rotated into soil mass during: (a) first set of 10 cycles; (b) second set of 10 cycles; and (c) third set of 10 cycles of wrap-around geotextile test.....	151
Figure 6.25: Time-history of lateral force for geofoam inclusion test.....	153
Figure 6.26: Time-history of wall rotation for geofoam inclusion test (Note: the mobilized passive and active force per Rankine theory)	153
Figure 6.27: Photos from top viewing window of soil box during geofoam inclusion test: (a) at beginning of test; and after (b) cycle 1.5; (c) cycle 1.10; (d) cycle 2.5; (e) cycle 2.10; (f) cycle 3.5; and (g) cycle 3.10.....	154
Figure 6.28: Pressure cell locations and lateral earth pressure distribution on stiffened steel wall for most forward position rotated into soil mass during: (a) first set of 10 cycles; (b) second set of 10 cycles; and (c) third set of 10 cycles of geofoam inclusion test	156
Figure 6.29: Unit weight and number of standard deviations from the mean for each testing configuration	157
Figure 6.30: Comparison of all configurations relative to baseline for: a) soil settlement; and b) extent of settlement beyond rotating wall	158
Figure 6.31: Comparison of all configurations relative to baseline for: a) maximum heave; and b) extent of heave beyond settlement region	159
Figure 6.32: Comparison of all configurations' increase in lateral earth pressure from minimum to maximum measured in: a) first series of rotations; b) second series of rotations; and c) third series of rotations	161
Figure 6.33: Side view of experimental setup (baseline test)	162

Figure 6.34: Vertical settlement contour plots for baseline test	163
Figure 7.1: Location of installed pressure cells and data loggers	166
Figure 7.2: Average pressure reading of two contact pressure cells on Mack Creek Bridge south abutment and average temperature reading of two data loggers beneath bridge.....	169
Figure 7.3: Average pressure reading of two contact pressure cells on Mack Creek Bridge north abutment and average temperature reading of two data loggers beneath bridge.....	170
Figure 7.4: Pressure reading of control contact pressure cell on Mack Creek Bridge north wingwall and average temperature reading of two data loggers beneath bridge.....	171
Figure 7.5: Average and daily fluctuations of pressure behind south abutment backwall	171
Figure 7.6: Average and daily fluctuations of pressure behind the north abutment backwall	172
Figure 7.7: Site profile for Mack Creek Bridge.....	172
Figure 7.8: Average and daily fluctuations of ambient temperature as recorded by data loggers beneath the bridge.....	172
Figure 7.9: Temperature variations in mounted pressure cells as compared with ambient temperature.....	173
Figure 7.10: Assembly of sensor and logger equipment for temporary additional instrumentation of Mack Creek SIAB	174
Figure 7.11: Enclosure assembled for additional monitoring of Mack Creek SIAB	175
Figure 7.12: Testing of equipment on rooftop of Civil Engineering Department at UT Austin.....	176
Figure 7.13: Flow chart of the Python program developed for data collection, processing and visualization	177
Figure 7.14: New messages received from data logger	178
Figure 7.15: Archived messages post-processing by Python.....	178
Figure 7.16: Example output of file management algorithm developed in Python	179
Figure 7.17: Example output of plotting program developed in Python	180
Figure 7.18: Equipment installed on Mack Creek SIAB in January 2020	181
Figure 7.19: Closeup of equipment installed on south abutment: (a) logger equipment and laser distance meter; and (b) crackmeter installed between backwall and pile cap + loggerbox	181

Figure 7.20: Closeup of equipment installed on north abutment, laser target and crackmeter installed between backwall and pile cap: (a) view from behind; and (b) top view.....	182
Figure 7.21: Closeup of pole-mounted equipment on south abutment, which includes solar panel, ClimaVue50, SI-111SS and lightning protection device: (a) installation of SI-111SS for measuring deck surface temperatures; and (b) closeup of SI-111SS.....	182
Figure 7.22: Mack Creek Bridge deck length change.....	183
Figure 7.23: Histogram of daily changes in bridge length.....	184
Figure 7.24: (a) Deck surface temperature; (b) ambient air temperature; and (c) solar irradiance at Mack Creek Bridge	185
Figure 7.25: Histogram of daily deck surface temperature changes.....	186
Figure 7.26: Histogram of daily ambient temperature changes.....	186
Figure 7.27: Illustration showing lateral deformation at abutment caps due to interaction between deck and abutment caps.....	187
Figure 7.28: Relative displacement between pile caps and abutment backwalls as recorded by crackmeters	188
Figure 7.29: Changes in relative humidity of ambient air at Mack Creek.....	189
Figure 7.30: Daily ambient temperature change vs daily earth pressure change at south abutment wall (November and July 2018)	190
Figure 7.31: (a) South abutment average earth pressure percentage increase vs average ambient air temperature during identified periods of sustained earth pressure increase; and (b) south abutment average earth pressure vs average ambient air temperature during identified periods of sustained earth pressure increase	191
Figure 8.1: Swallow nests under China Creek Bridge.....	194
Figure 8.2: High water level in China Creek after a precipitation event in August 2018.....	195
Figure 8.3: Corroded bents under China Creek Bridge to be replaced.....	196
Figure 8.4: Seepage of water through deck joints.....	196
Figure 8.5: Cracked edge of pavement at end of the approach slab due to backfill settlement	197
Figure 8.6: Logger equipment in NEMA enclosure	200
Figure 8.7: External Geokon model 8032 multiplexer (geokon.com)	200
Figure 8.8: CR6 data logger (campbellsci.com)	201
Figure 8.9: RF401 radio (campbellsci.com)	201
Figure 8.10: CELL205 cellular modem (campbellsci.com)	201

Figure 8.11: GK-404 handheld VW readout device (geokon.com).....	202
Figure 8.12: Model 4815 earth pressure cell (geokon.com)	203
Figure 8.13: Suggested installation procedure for earth pressure cells (geokon.com)	203
Figure 8.14: Proposed installation location of pressure cells and soil extensometers on east abutment.....	204
Figure 8.15: Model 4435 soil extensometer (geokon.com)	205
Figure 8.16: Model 4430 deformation meter (geokon.com).....	206
Figure 8.17: Model 4200 concrete embedment strain gauge (geokon.com).....	207
Figure 8.18: Model 4200L concrete embedment strain gauge	208
Figure 8.19: Example installation location for strain gauges, tiltmeters and crackmeters (west side of China Creek Bridge)	208
Figure 8.20: Model 4151 miniature strain gauge (geokon.com)	209
Figure 8.21: Model 4420 crackmeter (geokon.com)	210
Figure 8.22: Model 6160 MEMS tiltmeter (geokon.com).....	211
Figure 8.23: SAAV array on reel prior to installation (measurand.com)	213
Figure 8.24: Schematics for installation of SAAV in an inclinometer casing (measurand.com).....	213
Figure 8.25: ClimaVue50 sensor (campbellsci.com).....	214
Figure 8.26: SI-111SS infrared radiometer (campbellsci.com)	214
Figure 8.27: OptoNCDT ILR 1181-30 laser distance meter.....	215
Figure 8.28: General scheme of a CRBasic program	216
Figure 8.29: Variable declarations in CRBasic.....	217
Figure 8.30: Example data table definition in CRBasic	217
Figure 8.31: Main body of a CRBasic program.....	218
Figure 8.32: Scan loop example in CRBasic	219
Figure 8.33: SlowSequence example in a CRBasic program	219
Figure 8.34: First half of old China Creek Bridge demolition.....	220
Figure 8.35: Installation of soil nail wall as temporary support for active roadway crossing the undemolished half of China Creek Bridge (Picture provided by Samuel Groves).....	220
Figure 8.36: Drill bit exiting hole to dump excavated soil	222
Figure 8.37: Soil cuttings collected during drilling operations in November 2019	223
Figure 8.38: Casing used for top 20 ft of drilled shafts	223

Figure 8.39: Gray shale covered with powdery red dirt recovered from a depth of 30 ft	224
Figure 8.40: Heap of soil excavated from drilled shaft (Note broken shale pieces on top (25 ft and below) and wetter/plastic material removed beforehand)	224
Figure 8.41: Lowering of rebar cage.....	225
Figure 8.42: Propping rebar cage to keep it off the bottom of the hole before concrete pouring.....	225
Figure 8.43: Forming of abutment backwalls after placement of girders and precast panels, March 2020 (east abutment).....	226
Figure 8.44: Top view of earth pressure cell (GK-4810) installed on inside of form on west abutment backwall, March 2020 (photographer standing on one precast panel placed on deck)	227
Figure 8.45: Finished surface of east abutment backwall with pressure cell (GK-4810) installed between two girders on left, March 2020	228
Figure 8.46: GK-4200L as installed on the deck, perpendicular to the direction of the bridge, March 2020	229
Figure 8.47: A pair of GK-4200 strain gauges installed on the deck during phase 1 of construction	229
Figure 8.48: Different colored tape represents binary values to help identify sensor	230
Figure 8.49: (a) Strain gauge cables were routed underneath the bridge through a small gap between foam boards; and (b) coiled strain gauge (red) and earth pressure cell (blue) wires	230
Figure 8.50: Predrilled block of wood used to help keep track of cables coming from embedded strain gauges	231
Figure 8.51: Concrete placement on deck, phase I, March 2020.....	232
Figure 8.52: Finished deck surface, phase I, March 2020	232
Figure 8.53: Covered deck surface after concrete placement, phase I, March 2020	233
Figure 8.54: Five-ft PVC conduits transported to China Creek Bridge to house SAAV sensors in drilled shafts (conduits pictured have been assembled into 10-ft sections using PVC cement and couplers).....	234
Figure 8.55: PVC conduits assembled into 40-ft sections using additional couplers and joint reinforcement	234
Figure 8.56: Reinforcement of PVC conduit joints: (a) threaded couplers + heavy duty PVC cement; and (b) compression couplers + flexible couplers + hose clamps	235

Figure 8.57: Attachment of 40-ft PVC conduit to rebar cage: (a) heavy duty zipties used on either side of joints; and (b) combination of steel hose clamps and heavy duty zipties used at each middle section	236
Figure 8.58: Assembled PVC conduits attached to drilled shafts to serve as SAAV housing.....	236
Figure 8.59: Strain gauges attached to long rebars of drilled shafts	236
Figure 8.60: Instrumented rebar cage intended for China Creek Bridge east-center drilled shaft, phase 2	237
Figure 8.61: Installation of east abutment instrumented drilled shaft: (a) lift and transportation to drilled shaft location of rebar cage using a front loader; (b) rebar cage raised from the top using a crane (note the extent of curvature on the rebar cage and PVC conduit); (c) lowering of rebar cage into the hole; and (d) final placement of rebar cage before concrete is poured.....	239
Figure 8.62: (a) Concrete being pumped into drilled shaft; and (b) final orientation of instrumented shaft and sensors	239
Figure 8.63: Formwork for construction of pile caps and wingwalls	240
Figure 8.64: (a) West abutment cap pressure cell (before formwork completion); and (b) east abutment pressure cell (after formwork completion).....	241
Figure 8.65: (a) Pouring concrete for abutment cap with a concrete tremie (west abutment); and (b) completion of abutment cap surface (notice SAAV conduit sticking out between two girder pedestals).....	242
Figure 8.66: Installation of earth pressure cells on wingwall forms to measure backfill pressure acting on wingwalls.....	243
Figure 8.67: SAAV installation in east abutment center drilled shaft	244
Figure 8.68: SAAV verification tool screen (green light indicates successful installation)	244
Figure 8.69: Capped SAAV conduit on east abutment.....	245
Figure 8.70: Miniature strain gauge next to drill guide used for installation on side of bottom flange of bridge girder.....	246
Figure 8.71: Installation of miniature strain gauges on bridge girder: (a) epoxied strain gauge; and (b) strain gauge installation (cables are routed along top flange)	246
Figure 8.72: Mounted miniature strain gauges on bottom flange of middle girder	247
Figure 8.73: Location of three pairs of concrete-embedded strain gauges on east abutment backwall	247
Figure 8.74: Pair of earth pressure cells mounted on back of form intended for west abutment backwall.....	248
Figure 8.75: Placement of precast concrete panels on deck	248

Figure 8.76: Phase 2 deck concrete placement	249
Figure 8.77: Instrumented concrete sample cylinders	250
Figure 8.78: Installation of VW displacement transducers to be used as backfill settlement sensors: (a) hole excavation using auger; and (b) vertical sensor placement in hole	251
Figure 8.79: Settlement sensor installation locations: (a) west abutment; and (b) east abutment	252
Figure 8.80: Soil extensometer installation in backfill: (a) west abutment; and (b) east abutment	253
Figure 8.81: Stainless steel plates attached to top flange of settlement sensors .	254
Figure 8.82: Crackmeter installed for measuring relative displacement between approach slab and sleeper slab.....	254
Figure 8.83: Crackmeter installed for measuring relative displacement between approach slab and wingwall.....	255
Figure 8.84: Crackmeter installed for measuring relative displacement between abutment cap and abutment backwall + tiltmeter installed on abutment backwall	255
Figure 8.85: Piezometer measuring water pressure in backfill, prior to installation (sensor is fully inserted and sealed on the back to prevent water infiltration from creekside in case of flooding)	256
Figure 8.86: Creekside piezometer installed on abutment cap	256
Figure 8.87: Superstrut mounted on southwest wingwall; infrared radiometer is pointed toward deck surface to measure surface temperature	257
Figure 8.88: Solar panel mounted on south railing of east end of China Creek Bridge.....	258
Figure 8.89: China Creek Bridge construction completed and opened to traffic on July 31, 2020.....	258
Figure 8.90: Upside-down installation of logger enclosures mounted to bottom of deck; to prevent water damage to housed equipment, all cord grip holes need to be as close to lid as possible	259
Figure 8.91: Wiring of the east side data logger station, equipped with a laser distance meter (fun fact: the battery-operated fan pictured was our best defense against the late-July heat and creekside mosquito swarm while wiring the loggers)	260
Figure 8.92: PVC pipes to protect cables routed on top of abutment caps.....	261
Figure 8.93: Deck length change measured by laser distance meter	263
Figure 8.94: Comparison of laser distance meter and deck strain gauges for measuring deck length change	263

Figure 8.95: Deck length change calculated using embedded strain gauge data	264
Figure 8.96: Temperature data collected from China Creek SIAB (missing deck surface temperature data is due to rodent activity)	265
Figure 8.97: Internal deck temperature vs deck strain	266
Figure 8.98: Ambient air temperature vs deck strain	267
Figure 8.99: Joint movement as recorded by crackmeters installed between approach slab and sleeper slab	268
Figure 8.100: Relative displacement between abutment caps and backwalls	269
Figure 8.101: Total cap/backwall crackmeter readings vs total deck length change	269
Figure 8.102: Relative displacement between top of wingwall and approach slab	270
Figure 8.103: East abutment backfill settlement	270
Figure 8.104: West abutment backfill settlement	271
Figure 8.105: Difference between average strains recorded at opposite ends of each approach slab	272
Figure 8.106: West abutment earth pressure cell measurements	273
Figure 8.107: East abutment earth pressure cell measurements (note: 1 kPa = 0.000145038 psi)	273
Figure 8.108: Piezometer readings	274
Figure 8.109: Abutment wall tiltmeter readings (+ denotes tilt toward creek)	274
Figure 8.110: Scatter plot of strains at the top of the deck vs strains at the bottom of the girder at 15 and 30 ft from west abutment wall	275
Figure 8.111: Deformation profile snapshots of drilled shafts: (a) east abutment; and (b) west abutment (positive deformation is toward center of bridge/creek)	277
Figure 8.112: Abutment cap displacement records: (a) east abutment; and (b) west abutment	278
Figure 8.113: West abutment drilled shaft profiles: (a) foundation profile; (b) deflection profile; (c) curvature profile; and (d) moment profile (shape array data captured at 7:30 pm on December 5, 2020)	279
Figure 8.114: Schematic of a deflected drilled shaft	279
Figure 8.115: Instrumented west drilled shaft's maximum moment and abutment cap displacement data (Note: positive displacement signifies drilled shafts bending toward center of bridge)	281
Figure 8.116: West approach expansion joint appears to be intact and undamaged (photograph taken by Samuel Groves, TXDOT, on February 22, 2021)	282
Figure 8.117: China Creek Bridge GPR survey locations (August 2021)	283

Figure 8.118: Raw GPR data recorded during survey #3 at northeast approach slab, perpendicular to the roadway direction	284
Figure 8.119: Application of Time Zero Adjustment to raw GPR data.....	285
Figure 8.120: Migration processing of GPR data	286
Figure 8.121: Deconvolution processing of GPR data	286
Figure 8.122: Processed GPR profile of section #3 on NE approach slab	287
Figure 8.123: Processed GPR profile for section 25: (a) unannotated; and (b) annotated.....	288
Figure 9.1: Schematic of China Creek SIAB and location of installed sensors .	293
Figure 9.2: Instrumentation and backfilling of China Creek Bridge west abutment; top right inset shows a close-up of steel plate attached to top of settlement sensors after backfill placement.....	295
Figure 9.3: Ambient air temperature time-history data collected from China Creek Bridge site	296
Figure 9.4: Time-history of changes in bridge length measured using girder-mounted strain gauges compared to foundation shape array and abutment cap crackmeter measurements	297
Figure 9.5: Coefficient of Thermal Expansion (CTE) calculation based on deck strain gauges.....	298
Figure 9.6: Time-history of east and west abutment wall displacement relative to their original positions at completion of construction	298
Figure 9.7: Diagram showing Neutral Thermal Expansion Point (NTEP) and effective expansion length for each abutment wall.....	300
Figure 9.8: Time-history of NTEP distance from east abutment wall, normalized to total length of bridge.....	301
Figure 9.9: Time-history of change in bridge midpoint position relative to time of construction (positive values indicate that midpoint has moved eastward).....	301
Figure 9.10: Semi-integral bridge abutment resistance model: (a) diagram showing elements that resist thermal expansion/contraction of an SIAB; and (b) hypothetical force-displacement diagram of resisting elements (positive 'x' signifies abutment wall displacement toward backfill)	303
Figure 9.11: Time-history of lateral earth pressures recorded in: (a) east abutment; and (b) west abutment	304
Figure 9.12: Time-history plot of ratio between thermal expansion of deck slab right above girder's top flange relative to bottom of girder (girder top-to-bottom thermal expansion ratio)	306
Figure 9.13: Time-history plot of lateral thrust force acting on abutment walls estimated from EPC readings.....	307

Figure 9.14: Measured stress – strain behavior for abutment backfills at abutment wall mid-depth: (a) east abutment; and (b) west abutment (Note: positive strain values indicate backfill compression)	309
Figure 9.15: Time-history of settlement data collected from four backfill settlement sensors, calculated relative to start of monitoring (10/22/2020)	310
Figure 9.16: East backfill settlement and wall displacement during a 10-day period in October 2021	310
Figure 10.1: Schematic of China Creek SIAB and installed sensors (EPC: Earth Pressure Cell)	315
Figure 10.2: Shape array installation: (a) installation of drilled shaft rebar cage fitted with a shape array casing; and (b) installation of shape array inside casing after abutment caps were formed	317
Figure 10.3: Time-history of ambient air temperature data collected using on-site weather station	318
Figure 10.4: Time-history of changes in deck length (deck thermal expansion/contraction)	318
Figure 10.5: Time-history of change in expansion joint width between abutment caps and abutment walls measured by crackmeters	319
Figure 10.6: Time-history of abutment cap displacement data measured by drilled shaft shape arrays	320
Figure 10.7: Sketch of changes in abutment area in response to bridge thermal expansion/contraction:(a) initial position; (b) bridge expansion; and (c) bridge contraction	321
Figure 10.8: West abutment drilled shaft profiles on two different dates: (a) subsurface profile; (b) lateral deflection profile; (c) curvature profile; and (d) flexural moment profile	322
Figure 10.9: Maximum bending moment acting on drilled shafts (positive bending moments indicate bending toward bridge center as sketched in Figure 10.7)	323
Figure 10.10: Time-history of changes in east abutment cap position and expansion joint width (arrows indicate abutment cap general displacement direction during highlighted periods)	325
Figure 10.11: Sketch of cyclic p-y behavior of foundation soil in different conditions: (a) period of average daily temperature increase; (b) period of average temperature decrease; and (c) period of no change in average daily temperature	326
Figure 11.1: Backfill material flowing behind wingwall	329
Figure 11.2: Buckling of wooden forms retaining the backfill placed during phase 1 on the west end of the bridge	330
Figure 11.3: Sandy/clayey soil excavated from the site was used as base material for the approach roadway	332

Figure 11.4: No separation between base material and backfill material	332
Figure 11.5: According to drawings, a perforated drainage pipe was planned to pass through the wingwall (west abutment view, phase 2).....	333
Figure 11.6: Approach slab drawings and construction details mistakenly overlooked during bridge construction	334
Figure 11.7: Example SIAB design by OHDOT	336
Figure 11.8: Proposed abutment detail for future TxDOT bridges.....	338
Figure B.55: Vertical displacements at the top of the backfill-abutment interface for daily cycles	472
Figure B.79: Shadings of deviatoric strains (in %) in the backfill accumulated after 50 cycles of δ_h/h equal to: (a) 1 mm; (b) 2 mm; (c) 3 mm; (d) 4 mm; and (e) 5 mm	493

Chapter 1. Assessment of the Current Practice

1.1. Introduction to the Assessment of the Current Practice

Semi-integral bridges constitute a promising alternative to conventional TxDOT bridges because they eliminate the need for deck expansion joints, which may significantly reduce bridge maintenance costs and potentially result in significant savings over the bridge service life. Adopting semi-integral bridges is particularly relevant to Districts with comparatively cold winters (e.g., Amarillo), where the use of deicing salts has resulted in significant joint maintenance problems. However, the elimination of expansion joints requires careful consideration because of the soil-structure interaction between the bridge structure and abutment backfill caused by the bridge's daily and seasonal thermal expansion/contraction.

This study includes an initial comprehensive evaluation of the state-of-the-practice in the US regarding the adoption of integral and semi-integral bridges. It also involved a large-scale experimental study focusing on the effect of cyclic movements on the potential buildup of lateral earth pressures acting on the backwalls of a semi-integral bridge. In addition, a numerical evaluation was conducted to understand the variables governing the performance of these types of bridge structures. However, the most relevant aspect of this study involved the design of a monitoring system, its installation, and its subsequent operation for two pilot semi-integral bridges in Texas. These comprehensive field monitoring projects allowed evaluation of the effect of daily and seasonal temperature changes on the displacement of various bridge components, of the changes in abutment earth pressure, of unexpected outcomes regarding foundation interaction, on the buildup of lateral earth pressures against the bridge backwalls (ratcheting), and on the evolution of backfill settlements.

1.2. Overview of the Current Practice

The primary objective of this project is to develop a set of design details to implement Integral/Semi-Integral Abutment Bridge (IAB/SIAB) technology in Texas conditions. In conjunction with these design details, a pilot short course is to be developed to share the design procedures identified with associated bridge engineers.

An important focus of this project is on the elimination of expansion joints in bridges and the corresponding thermal expansion expected, and how this changes foundation performance and soil-structure interaction beneath and behind the abutments.

As part of the assessment of the current practice through existing literature, different types of IAB/SIAB were identified and differentiated from conventional bridge structures in the State of

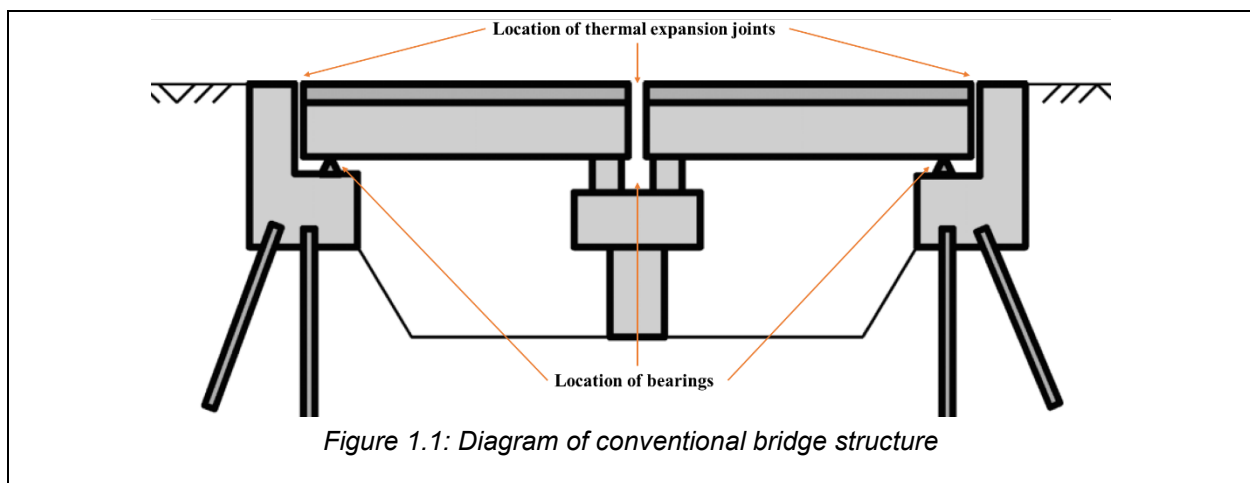
Texas. Specific practices regarding IAB/SIAB from different countries of interest were also identified.

1.3. Types of Bridges

The bridge types described have been reported in the literature by researchers working within the field of soil-structure interaction for bridges. While the precise definition of some of these structures is not identical across all countries or regions, this report uses what is considered the most common definition.

1.3.1. Conventional Bridge

The conventional bridge structure involves a system in which the loads of the superstructure are supported by girders placed upon bearings that separate superstructures from abutments and substructures. Additionally, thermal expansion joints are installed between the superstructure and abutment and, in some cases, at intermediate piers (Olson et al., 2013). Figure 1.1 depicts a generalized form of a conventional bridge. The figure shows that the girders of the bridge superstructure are isolated from other parts of the bridge structure.



Advantages attributed to conventional bridge design include:

- Only vertical loads from the superstructure are transferred to the abutment and substructure
- Secondary loads from expansion and contraction due to temperature changes are prevented by thermal expansion joints
- Significant experience has already been gained regarding construction of these types of bridges

Despite these apparent benefits, a number of disadvantages to the conventional bridge system have been identified (e.g. Arsoy et al. (1999), Abendroth and Grimann (2005), Hassiotis et al. (2006), Laman and Kim (2009)). The reported disadvantages of constructing conventional bridges are:

- Bearings and thermal expansion joints add initial material cost to bridge construction
- Thermal expansion joints are particularly susceptible to deterioration and damage from environmental conditions, de-icing efforts and traffic
- Foreign objects can fill expansion joint voids, causing blockage and resulting in loads upon the superstructure for which it was not originally designed
- Bearings are easily susceptible to corrosion, and difficult and costly to replace

This type of bridge construction has been very common throughout the United States. Further discussion of the current state of the practice for bridges in the United States is provided in Section 1.4.

1.3.2. Semi-Integral Abutment Bridge (SIAB)

An SIAB differs from a conventional bridge in that it does not include thermal expansion joints. To be considered an SIAB, expansion joints at all locations along the bridge deck, as well as at the deck-abutment interface and abutment-approach road/slab interface must be eliminated. While the deck and approach are integrally constructed, the superstructure and substructure are not. These types of bridges are most commonly constructed on rigid foundations and can consist of either single or multiple spans (Husain and Bagnariol, 1999). In the case of a single span bridge, the structure may be referred to as an SIAB as no intermediate joints exist. SIAB may also refer to a bridge in which thermal expansion joints are installed at intermediate piers, but not at bridge abutments. A design detail example of this abutment type from the Ontario Semi-Integral Abutment Bridge Manual is shown in Figure 1.2.

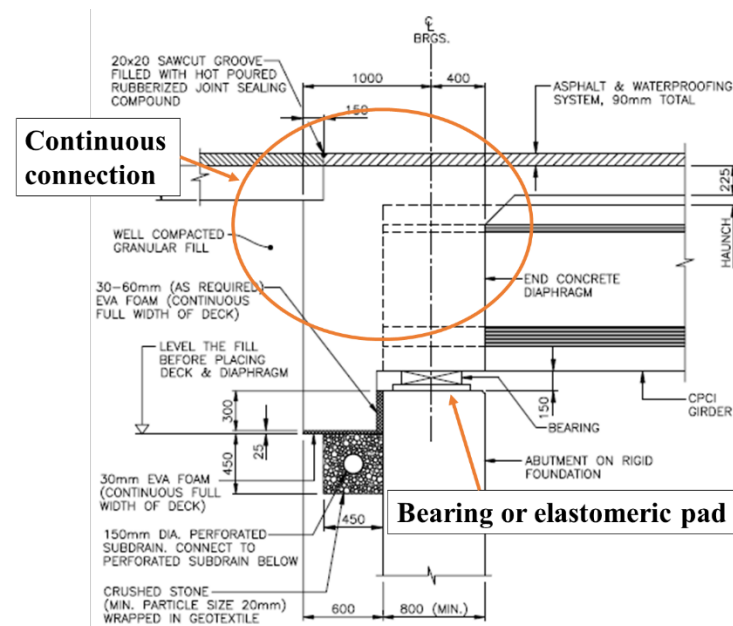


Figure 1.2: Modified example of semi-integral abutment detail (Husain and Bagnariol, 1999)

The benefits derived from SIAB are solely a result of the removal of thermal expansion joints. By eliminating these elements, bridges are no longer susceptible to improperly functioning joints that may lock up or deteriorate due to salting or de-icing chemicals in the winter (Shreedhar and Hosur, 2014; Kunin and Alampalli, 2000). Another leading cause driving the removal of thermal expansion joints in bridge design is the cost associated with manufacture, installation and maintenance. It has become widely accepted that reducing the number of expansion joints in a bridge directly reduces cost and required maintenance over the bridge lifetime (Mistry, 2005; White, 2007; Burke, 2009; Kirupakaran et al. 2012). Furthermore, bridges lacking expansion joints have been found to exhibit improved ride quality, reduced noise and greater resistance to damage from heavy vehicles (Oesterle and Tabatabai, 2014).

1.3.3. Integral Abutment Bridge (IAB)

IAB is an advanced form of SIAB. Both IAB and SIAB have no thermal expansion joints between the bridge superstructure and approach road/slab and at intermediate piers, if applicable. However, in IAB bearings and elastomeric pads isolating the superstructure from the substructure are absent, which results in a connection between the bridge deck, girders, abutment wall, and foundations. The rigid connection is a moment-resisting type in which expansion and contraction of the superstructure will result in bending of deep foundation piles if used. A design detail example from the Pennsylvania Department of Transportation of an integral abutment is shown in Figure 1.3.

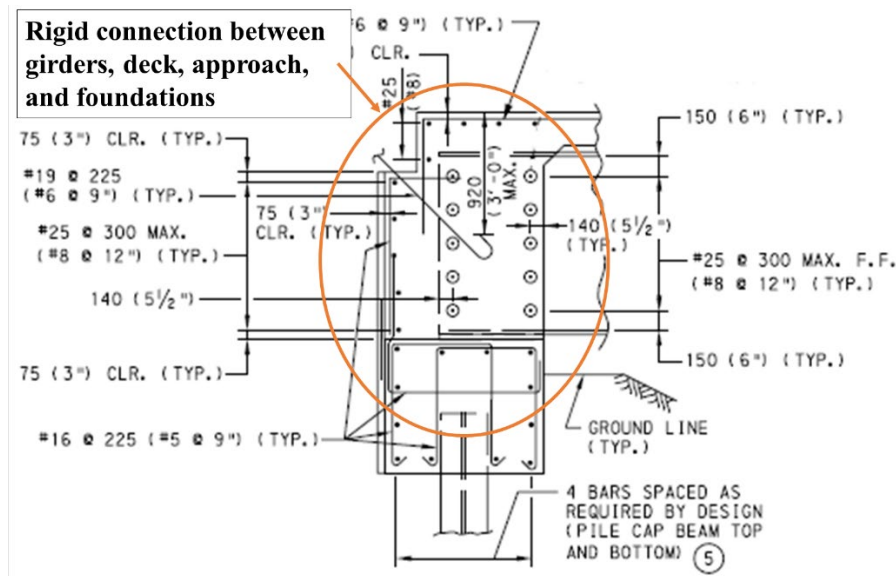


Figure 1.3: Modified example of integral abutment detail (PennDOT, 2007)

The integral abutment design eliminates both expansion joints and bearings, which further reduces construction and maintenance cost when compared to SIAB (Arsoy et al. 1999; Hassiotis et al., 2006; Huffaker, 2013). However, the fully integral abutment concept does introduce the issue of lateral movement-inducing forces upon the substructure during expansion and contraction of the superstructure due to daily and seasonal temperature gradients. The extent, relative severity and proper analysis of these movements have been investigated by many researchers such as Kim and Laman (2010), Frosch and Lovell (2011), and Rhodes and Cakebread (2014).

1.3.4. Geosynthetic Reinforced Soil – Integral Bridge System (GRS-IBS)

An additional bridge type that has been constructed in the United States and that utilizes a form of integral abutments is GRS-IBS. This system includes a Reinforced Soil Foundation (RSF), which is composed of compacted granular fill material encapsulated by a geotextile fabric. Additionally, the RSF increases the bearing width and capacity of the GRS abutment and prevents water from infiltrating underneath the GRS mass. RSFs are an alternative to deep foundations for loose granular soils, soft fine-grained soils and organic soils. The abutment is constructed using alternating layers of compacted fill and closely spaced geosynthetic reinforcement at a typical spacing of 12 inches or less. The final bridge girders are placed directly on the soil mass abutment without any joints or Cast-In-Place (CIP) concrete. Finally, the approach is integrated into the bridge superstructure by placing GRS layers that attach to the end of the bridge beams (Adams et al. 2011). A schematic of a GRS-IBS abutment layout, as proposed by the US Federal Highway Administration in the interim implementation guide by Adams et al. (2011), is shown in Figure 1.4.

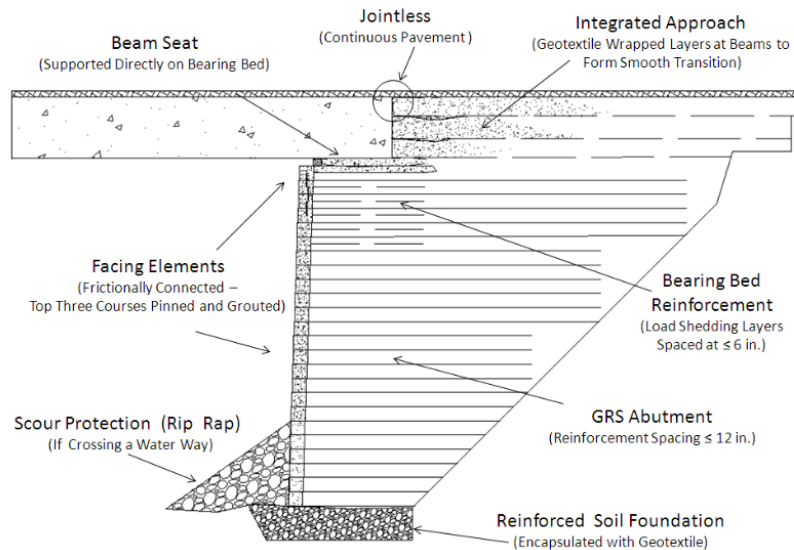


Figure 1.4: General design layout of GRS-IBS (Adams et al., 2011)

The use of GRS-IBS throughout the United States has been increasing. This system does not include the use of a shallow foundation to support the bridge load over the geosynthetic-reinforced soil structure, which had been previously implemented (e.g. Zornberg et al. 2001, Abu-hejleh et al. 2002).

1.3.5. Portal Frame Bridge

A fourth type of integral abutment bridge is the portal frame bridge. These structures are especially common in Japan, but have also been constructed in many European countries. Portal frame bridges are similar to IAB in that a rigid, moment-resisting connection exists between the superstructure and abutment. However, the major difference is in the substructure: portal frame bridges are most commonly supported by shallow foundations. Backfill material can vary and geosynthetic-reinforced soil behind the abutment backwalls is common for portal frame bridge structures. The current state-of-the-art practice for portal frame bridges is discussed in detail by Iwasaki et al. (2011), and Figure 1.5 presents an example of the details for a steel I-beam girder portal frame bridge. The bridge is 149.28 ft in length, 42.49 ft in width and 45.28 ft in height from the base of the shallow foundation to the top of the bridge deck. This type of bridge structure offers simple and elegant solutions for single-span passages, and advantages similar to those of IAB. However, they do have length maximums in various countries across the world that typically do not exceed 656.17 ft.

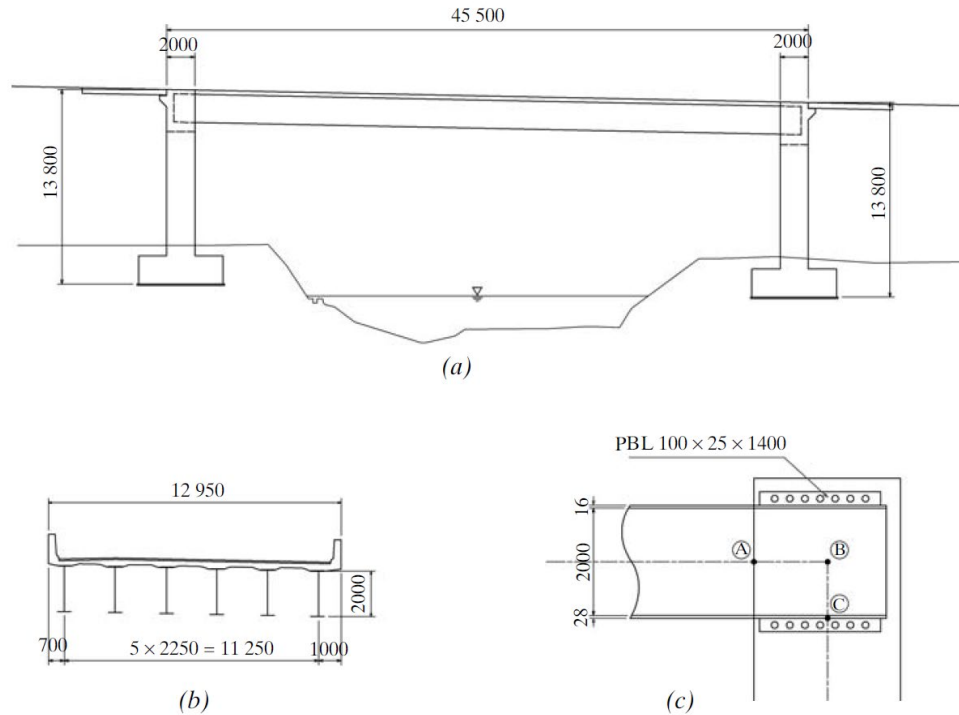


Figure 1.5: Example of a portal frame bridge: (a) profile view; (b) superstructure cross section; and (c) steel girder end detail (Iwasaki et al. 2011)

1.4. Current Practice in the United States

The following sections focus on the current state of the practice of IAB and SIAB in the United States. Reports prepared by various State DOTs are the main basis for the evaluation presented herein. In addition, design standards and research published in journals and conferences are also included. In an extensive and reasonably recent survey into the use of IAB/SIAB in the United States, conducted by White (2007), it was identified that over 9,000 integral and over 4,000 SIAB currently exist within the US. This study evaluated several different factors involved in the design of jointless bridges, which will be revisited in later sections of this chapter. A survey conducted prior to White (2007), with comparatively more detailed information related to the use and design of IAB in the US, can be found in the proceedings of the FHWA conference on Integral Abutments and Jointless Bridges (IAJB). Maruri and Petro (2005) found that Missouri and Tennessee have the highest number of IAB/SIAB, with over 4,000 and 2,000, respectively. Additional states with over 1,000 IAB/SIAB include Illinois, Iowa, Kansas and Washington.

1.4.1. IAB

Many agencies throughout the United States specify different standards for various aspects of IAB. This is a result of the extensive experience of numerous state DOTs, with the first IAB being constructed in 1938 near Eureka, Ohio (Burke, 2009). The four components of IAB that most commonly differ from those of conventional bridge structures are foundation type,

abutment backfill material, approach slabs and girder design. Consequently, these bridge components were evaluated in the most recent literature to determine the most prevalent design details within the US, and the reasons, if any, for their respective differences from conventional bridges.

1.4.2. Foundation Types

Steel bearing piles are the most common foundation type for integral abutments and typically consist of H-sections (Maruri and Petro, 2005). Furthermore, according to a survey conducted by Maruri and Petro (2005), a small majority of states using steel bearing piles require their orientation to allow for bending about the weak axis when subjected to lateral loads from bridge expansion and contraction. However, the lack of continuity on this topic suggests it is an aspect of integral abutments that warrants further research.

Research reported by Oesterle and Tabatabai (2014) found that regardless of the foundation type used, the vertical load capacity decreased as lateral displacement increased. The greatest allowance for lateral displacement in steel H-piles occurred when oriented for bending about the stiff axis in a low stiffness soil due to the high ratio of pile-to-soil stiffness. Other foundation types discussed by Oesterle and Tabatabai (2014) include pre-stressed concrete piles and concrete-filled pipe piles. Pre-stressed concrete piles were found to provide very high displacement capacity, but cracking and spalling of the element would likely be severe and detrimental to the serviceability of the structure. Conversely, the concrete-filled pipe piles also demonstrated high displacement capacity, with improved performance after many cycles of lateral loading – this is referred to as having “stable loops.”

Other foundation types used for integral abutments identified by Maruri and Petro (2005) include friction piles, spread footings and, in rare cases (Nevada and Hawaii), drilled shafts. One well-documented case of an IAB built on drilled shaft foundations is the Kii Bridge on the island of Oahu, Hawaii. Ooi et al. (2010) presented instrumentation and observation results of the abutment movements, lateral earth pressure, strain, axial load and moment in the drilled shafts. An overview of the bridge and instrumentation layout can be seen in Figure 1.6.

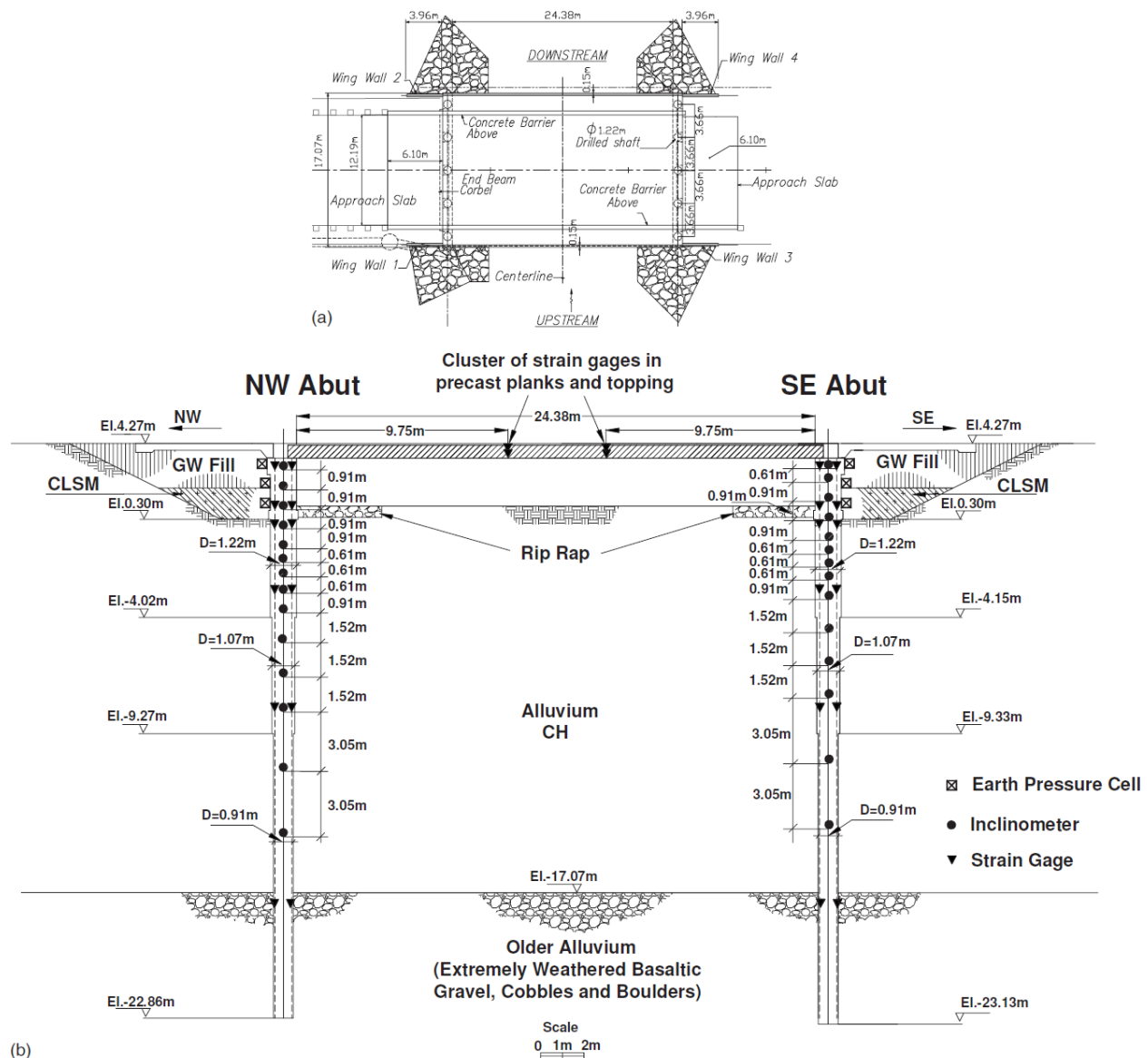


Figure 1.6: Kii Bridge layout and instrumentation details: (a) plan view; and (b) profile view (Ooi et al., 2010)

Over a 45-month observation period, Ooi et al. (2010) found the use of drilled shafts in this location to be suitable. Long-term abutment movements were governed by concrete creep and shrinkage, as opposed to thermal effects, due to the low temperature gradients in tropical climates. Furthermore, the most significant deformation in the drilled shafts was caused by excavation and backfilling.

While the precise foundation type to be used may vary by state, deep foundations are undoubtedly the most common type paired with integral abutments. In his book, *Integral & Semi-Integral Bridges*, Burke (2009) compiled the typical design considerations from engineers implementing integral abutments. The highlights of this list include:

- Each abutment foundation should consist of a single row of slender vertical piles
- Only pile types able to tolerate significant distortion without failure should be used
- Orienting the weak axis of H-piles normal to the direction of flexure is preferred
- Place piles in pre-bored holes and backfilling with granular material
- Limit the length of the integral structure to minimize pile flexure
- Limit the skew angle of the structure

1.4.3. Backfill Material

A second commonly disputed design aspect for integral abutments is the proper backfill material to be placed, as this can have a major effect on the performance of the structure throughout its lifetime. It is a common requirement that backfill material be compacted, but some state DOTs adopt different approaches to reduce the effects of long-term temperature gradients on integral abutments. The information in Figure 1.7 below is compiled from a survey conducted by Maruri and Petro (2005) regarding integral abutment backfill requirements.

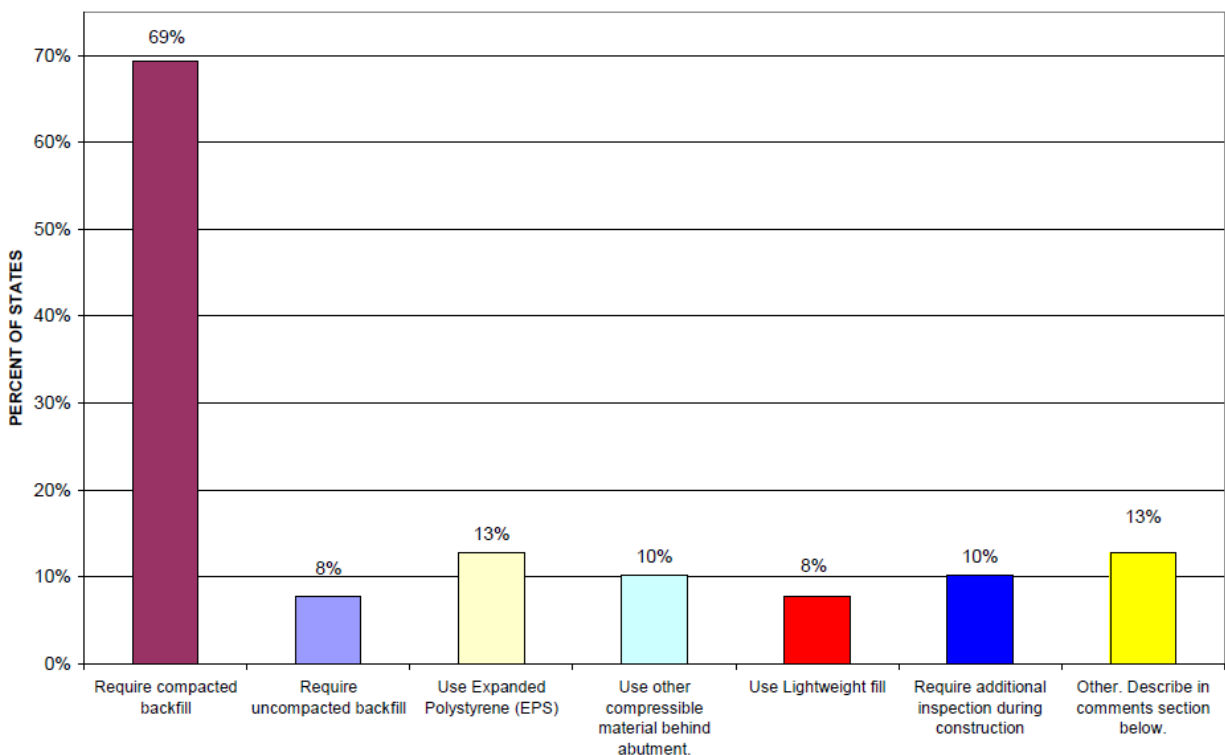


Figure 1.7: Integral abutment backfill requirements across the United States (Maruri and Petro, 2005)

A more recent survey conducted by White (2007) found similar statistics regarding the number of states requiring compacted backfill. However, it was also discovered that 23% of respondents require a compressible material immediately behind the abutment stem to reduce the magnitude of soil pressure that would be generated on the abutment backwall. White (2007) also established that 59% of respondents account for the full passive earth pressure upon integral abutment backwalls, while the remaining respondents account for at rest, active and, in some cases, no specific lateral earth pressure. The previously cited study on the Kii Bridge in Hawaii found that with a well-graded gravel fill over a controlled, low-strength material in native soil of highly plastic clay, earth pressures reduced to active or less in the long-term (Ooi et al, 2010).

The study conducted by Oesterle and Tabatabai (2014) resulted in lateral earth pressure distribution recommendations on integral abutment backwalls when backfilled with a granular material. The earth pressure coefficients used in these formulations are based on the chart presented in Clough and Duncan (1991), shown in Figure 1.8.

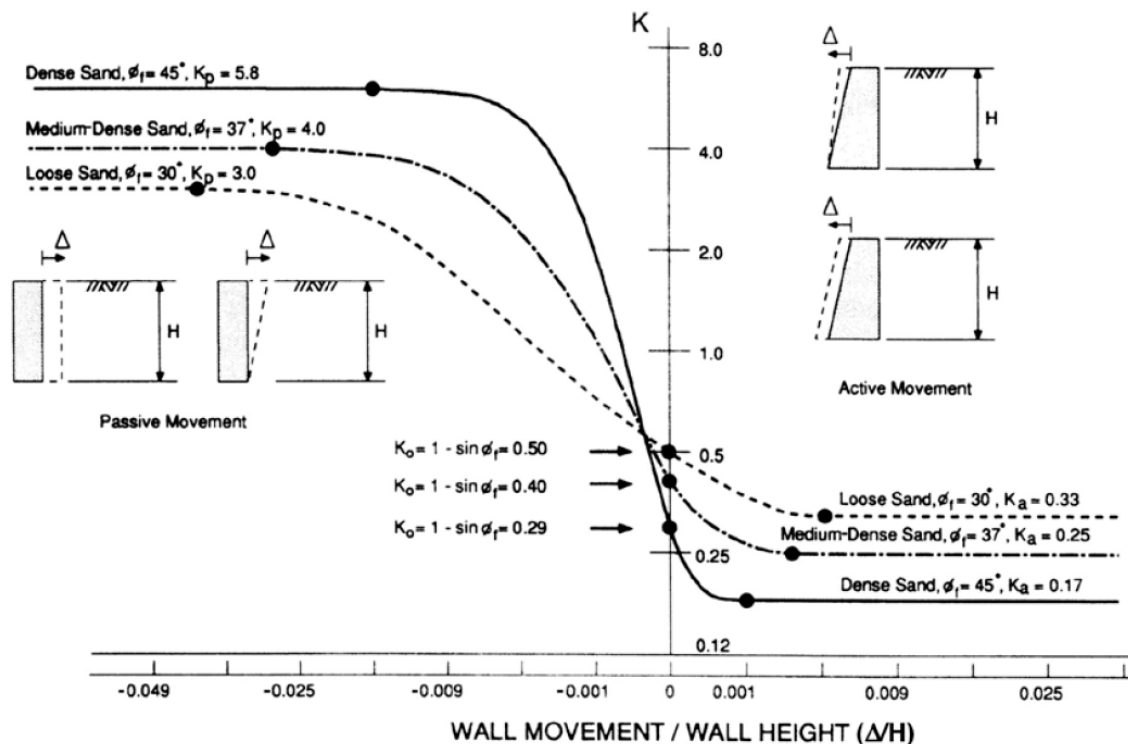


Figure 1.8: Relationship between abutment wall movement and earth pressure (Clough and Duncan, 1991)

Using the chart in Figure 1.8 to determine lateral earth pressure coefficients of a granular backfill material, Figure 1.9 could be used to determine a realistic, long-term abutment lateral earth pressure distribution. The values shown in brackets with asterisks in Figure 1.9(a) and Figure 1.9(b) indicate a resultant force of the triangular distribution.

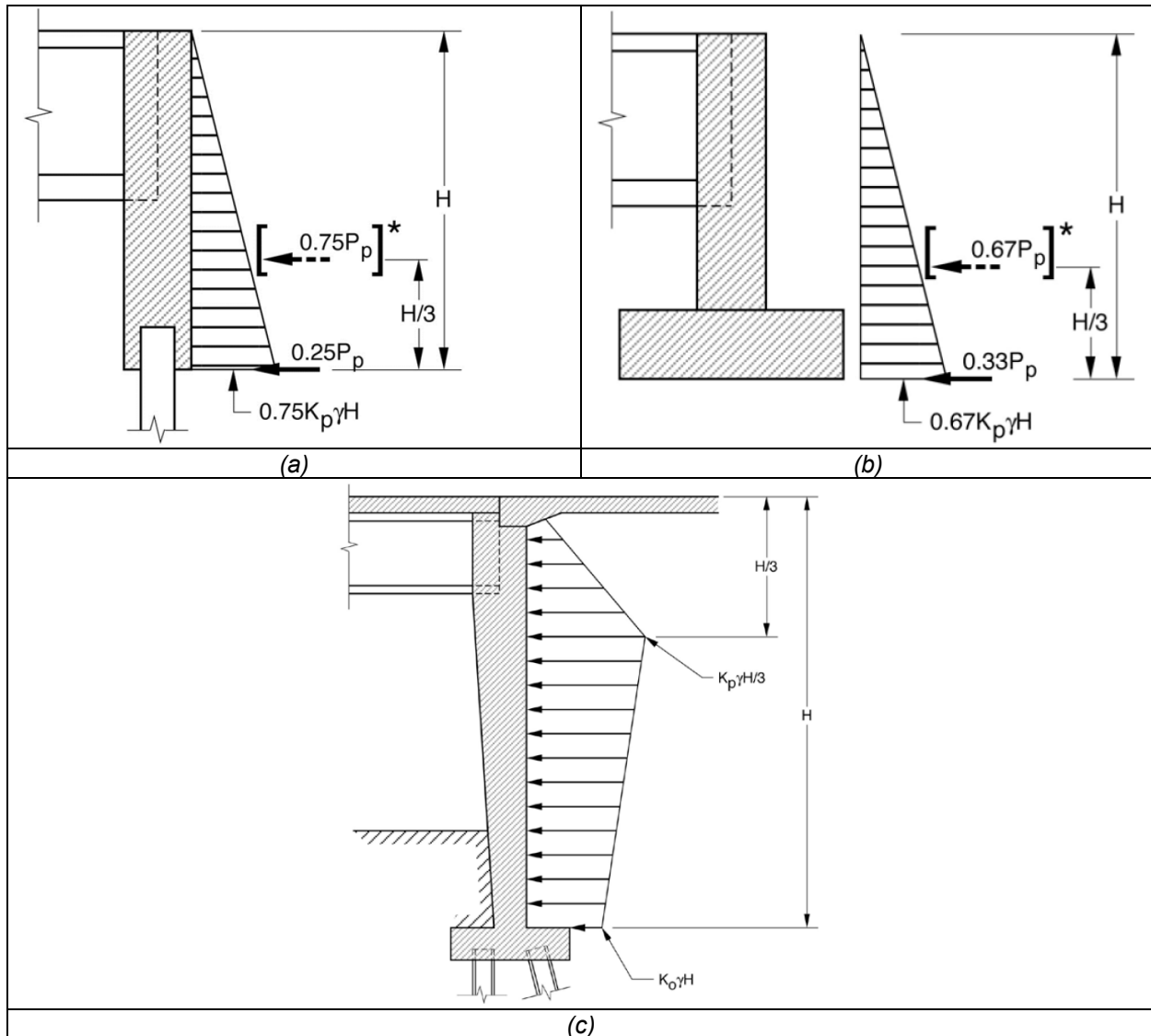


Figure 1.9: Lateral earth pressure distribution on integral abutment backwall: (a) stub abutment on piles; (b) stub abutment on shallow foundation; and (c) full height wall abutment (Oesterle and Tabatabai, 2014)

While some states may require controlled low strength material, expanded polystyrene, or some form of man-made material for backfilling, the consensus is that if a soil material is to be used, a well graded, granular material should be chosen. This type of material is both easy to compact in narrow spaces and provides adequate drainage around the abutment. Well graded material is also desired as it provides more significant interlocking of particles when compared to a poorly graded material (Arockiasamy et al., 2004).

1.4.4. Approach Slabs

The use of reinforced concrete approach slabs is typical for integral abutments and most take a form similar to that of the New York State DOT detail shown in Figure 1.10. In this detail, the

integral nature of the girders, deck and approach slab is represented by the reinforcement steel that connects them, and the girder cast directly into the pile cap/abutment.

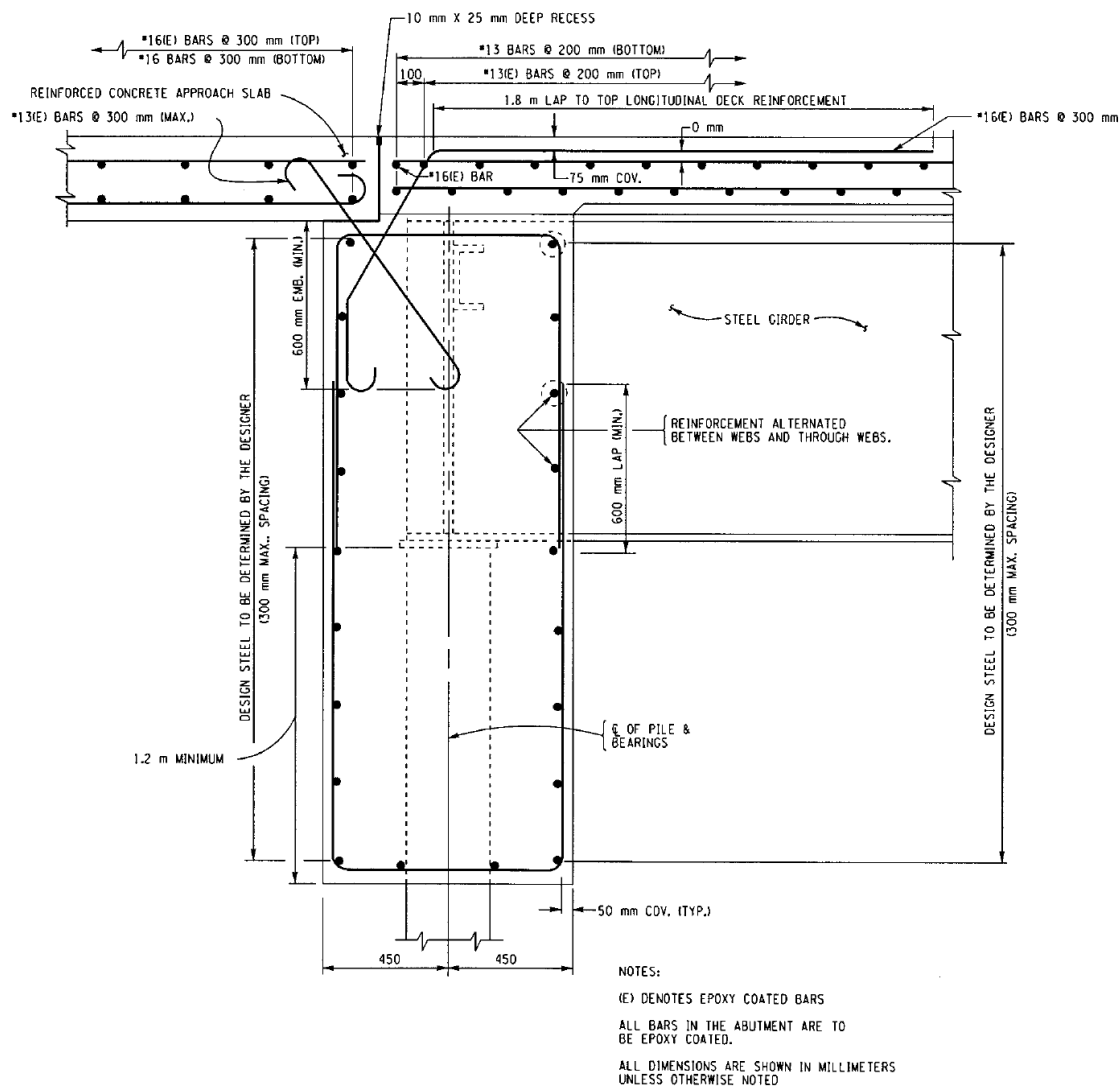


Figure 1.10: New York State DOT detail for integral abutments with steel girders

Kunin and Alampalli (2000) discuss the nuances of different approach slab details. The two most common details include: (1) reinforcing steel connecting the approach slab to the abutment corbel or lip (as shown in Figure 1.10), or with longitudinal steel connecting the bridge deck directly to the approach slab; and (2) resting the approach slab on the abutment corbel or lip without any connecting steel. The use of reinforcement steel to rigidly connect elements is slightly more common, but both methods perform satisfactorily across the United States and Canada.

An issue related to the approach slabs of integral abutments that has gained increasing attention in the 21st century is the subsidence zone that may develop below approach slabs in the region

near the abutment backwall. Horvath (2005) discusses the development of this subsidence zone and relates it to the soil-wedge slumping that occurs behind the abutment during contraction periods in winter months. Figure 1.11 illustrates the location in which these zones develop relative to bridge abutments and approach slabs. A notable feature of Figure 1.11 is the inward long-term abutment position. This difference between the long-term position and original construction position is a result of increasing lateral earth pressure upon the abutment with cyclic displacements from seasonal temperature fluctuations. “Ratcheting” is the commonly used term for this behavior and is discussed by Civjan et al. (2013), Fartaria (2010), Rhodes and Cakebread (2014), Peng-fei and Ling-wei (2015), and numerous others.

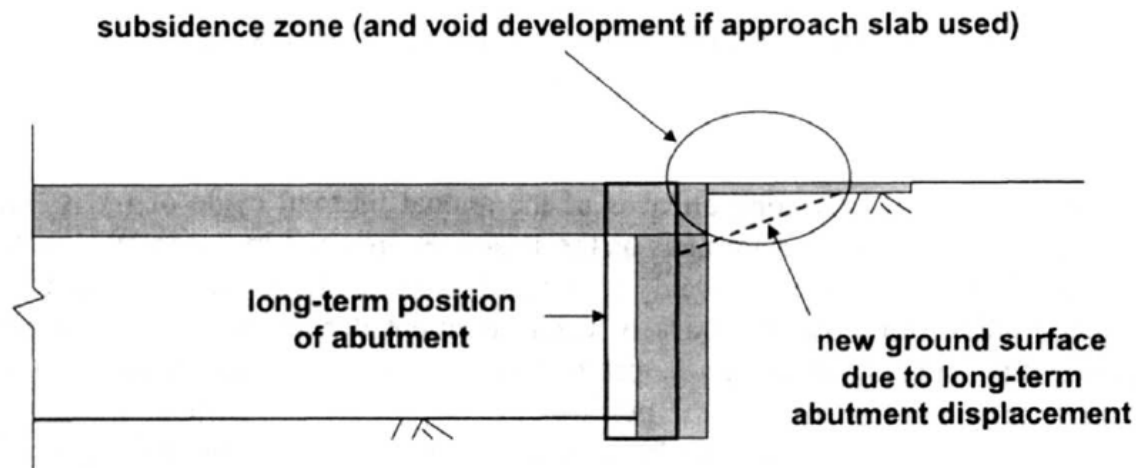


Figure 1.11: Development of subsidence zone beneath approach slab of integral abutment (Horvath, 2005)

The investigation of subsidence zones has gained recent attention because of its prevalence and relatively quick development as compared to the buildup of lateral earth pressures behind abutments (ratcheting). Reid et al. (1998) referenced a survey in which every one of the 140 IABs studied in South Dakota had developed such a subsidence zone, ranging in depth from 0.5 to 14 inches and extended up to 10 feet behind the abutment backwall.

Efforts to remediate the ratcheting effect and subsidence zone development have led to design details that include compressible inclusions between abutment backwalls and soil backfill for integral abutments. At the time of his survey, White (2007) reported that 23% of states in the US used such a compressible material within the backfill of integral abutments. Other remediation techniques being researched include geosynthetic-reinforced backfill, large quantities of geofoam in backfilling and controlled low strength material.

1.4.5. Girder/Beam Design

The type of superstructure used for the design of an IAB bears less importance when compared to foundation types, or approach and abutment details. Both steel and concrete girders have been used across the United States in IAB design with only slight differences in performance.

Hassiotis et al. (2006) reported that both girder types have been used for long-span IAB. However, the following observations were made of 30 steel and 54 pre-stressed concrete superstructures:

- All bridge types experienced some minor deck and approach slab cracking
- Performance was poorer for bridges with a skew greater than 30 degrees
- Greater span lengths lead to overall poorer deck and/or approach slab performance
- Minor backfill settlement beneath approach slabs was more common with concrete IAB

While both concrete and steel superstructures are entirely viable for IAB, the appropriate thermal loading conditions, which will differ based on the material used, should be meticulously determined. Since IAB behavior depends heavily on the bridge temperature throughout seasonal fluctuations (Hassiotis et al., 2006), the most accurate methods of determining temperature distributions should be implemented. In a report prepared for TxDOT, Chen et al. (2009) addressed the thermal loads associated with steel bridges for Texas conditions and provided the most recent design guidelines for such considerations. Until similar research is conducted on concrete bridges for Texas conditions, the AASHTO LRFD Bridge Design Specifications provides the most accurate means for estimating bridge temperatures.

1.5. SIAB

Shortly after IABs were implemented in the United States, the concept of SIAB emerged. Chapter 9 of Burke (2009) discusses this development in detail and establishes that over half of state DOTs had constructed an SIAB prior to the year 2000. Statements identifying the most significant benefits and limitations of SIAB from the states most heavily adopting the technology are also provided. Overall, SIAB are researched less than other types of IAB. In the United States, the number of SIAB in service is less than half that of IAB in service (Maruri and Petro, 2005).

1.5.1. Foundation Types

The foundation systems most commonly implemented for SIAB are similar to those for conventional bridge structures. Figure 1.12 depicts detail of an SIAB abutment, foundation, and integral superstructure and approach components.

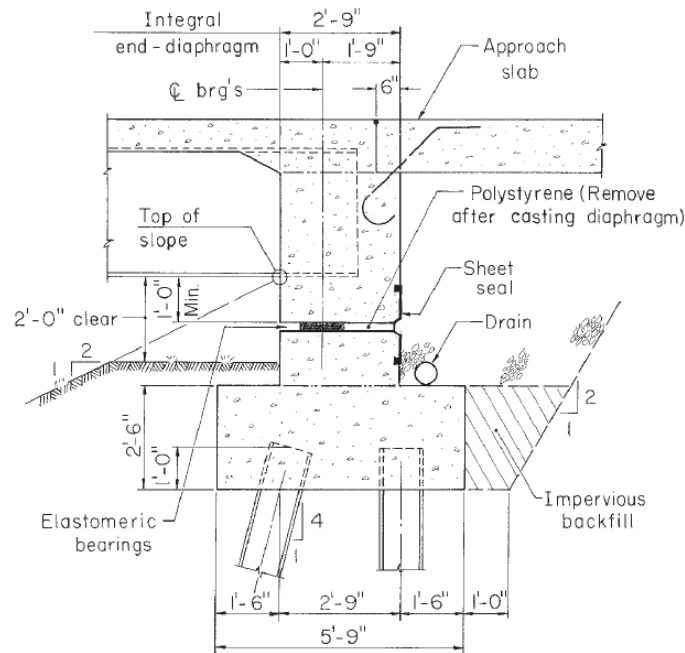


Figure 1.12: SIAB abutment and foundation detail (Burke, 2009)

Burke (2009) accompanies this detail in the textbook by endorsing the use of spread footings on bedrock, two or more rows of piles, and pedestals-to-bedrock with SIAB. However, implementing foundations such as footings on compressible subsoils, a single row of flexible piles, etc. is not recommended, and so the foundation systems for SIAB and IAB differ. Because of the inclusion of a bearing between the superstructure and substructure of SIAB, foundation types are often not specified by state DOTs within the United States, as interaction between the two components will be minimal (White, 2007).

1.5.2. Backfill Material

Because of the similarities in abutment backwall soil-structure interaction between SIAB and IAB, the backfill requirements for both bridge types are typically the same throughout the United States. Consequently, many researchers discuss backfill material requirements without differentiating between IAB and SIAB. In his textbook, Burke (2009) discusses the specifics of backfilling SIAB, and highlights the importance of developing a system in which the abutment backwall and soil interact compositely to support both the superstructure of the bridge and approach slab. A final recommendation for the backfill material is to ensure it is protected from erosion. Diverting any water away from the backfill and providing protection with full-width approach slabs are key design details mentioned by Burke (2009).

1.5.3. Approach Slabs

As with the backfill material requirements for IAB and SIAB, only minor differences between the approach slabs for the two bridge types are cited. Since SIAB was developed to prevent the lateral loading of deep foundations that exists with IAB, the interaction with the approach slab remains the same, regardless of the presence of a bearing between the superstructure and abutment.

1.5.4. Girder/Beam Design

Just as with IAB, the type of girder or beam used in SIAB design should be carefully considered so that proper thermal loads are analyzed. However, in contrast to conventional bridge structures, there are no restrictions regarding the type of girder or beam that could feasibly be used for SIAB.

1.5.5. Integral Bridge General Design Criteria

In an effort to compile easily referenced information regarding the design criteria of IAB/SIAB in the United States, Table 1.1 presents the maximum span, length, skew, and curvature for steel and pre-stressed concrete IAB/SIAB. It should also be noted that in the survey conducted by Maruri and Petro (2005), the sections of IAB/SIAB reported to have caused the most problems were the approach slabs. Specifically, the settlement and cracking thereof were identified as the number 1 and 2 most common issues, respectively.

Table 1.1: General design limits of IAB/SIAB (adapted from Maruri and Petro, 2005)

Prestressed Concrete Girders	Range	Steel Girders	Range
<u>Maximum Span</u>		<u>Maximum Span</u>	
IAB	60 - 200 ft	IAB	65 - 300 ft
SIAB	90 - 200 ft	SIAB	65 - 200 ft
<u>Total Length</u>		<u>Total Length</u>	
IAB	150 - 1175 ft	IAB	150 - 650 ft
SIAB	90 - 3280 ft	SIAB	90 - 500 ft
<u>Maximum Skew</u>		<u>Maximum Skew</u>	
IAB	15 - 70 deg	IAB	15 - 70 deg
SIAB	20 - 45 deg	SIAB	30 - 40 deg
<u>Maximum Curvature</u>		<u>Maximum Curvature</u>	
IAB	0 - 10 deg	IAB	0 - 10 deg
SIAB	0 - 10 deg	SIAB	0 - 10 deg

Additional highlights of the survey conducted by Maruri and Petro (2005), which is the most recent survey of IAB/SIAB design in the United States, are:

- The two forces most accounted for in the design of IAB/SIAB are temperature and passive earth pressure upon the abutments

- The most common pile orientation for IAB is with the weak axis parallel to the centerline of the bridge
- The most common earth pressure used in design is full passive, with active as the least common
- The force most often used to determine the capacity of the piles is bending due to expansion/contraction of the superstructure
- The most common backfill requirement is compacted granular fill

1.6. Current Practice in Europe

Outside the United States, the implementation of integral abutment technology is prevalent in England, Finland, Germany, Ireland and Sweden, all of which construct IAB, with Germany as the only country not to construct SIAB, per the survey conducted by White (2007). Other countries, such as France and Italy, have also begun adopting the technology to a lesser extent, but lack the substantial experience of the previously mentioned countries.

Table 1.2 highlights the key design criteria studied for IAB and SIAB in European countries by White (2007). While it is clear the design philosophy of IAB/SIAB throughout European countries differs, there is a history of successful implementation across the continent. In 2006 the International Workshop on IABs was held in Sweden, during which researchers from eight different European countries discussed their design, construction and maintenance practices for IAB, and also confirmed plans for continued use of these structures (White et al., 2010).

While implementation of IAB/SIAB has been rising in Europe since the 1990s, the most common applications are associated with railway bridges. Railway companies in both Germany and Austria have released design guidelines for IAB structures, while non-railway IAB guidelines are still commonly at the designer's discretion (Pak et al., 2017).

Table 1.2: Highlights of European IAB/SIAB design criteria (adapted from White, 2007)

Design Criteria	England	Finland	Germany	Ireland	Sweden
<u>Use IAB?</u>	Yes	Yes	Yes	Yes	Yes
Maximum Skew Angle	30+	30	None	30+	None
Steel Pile Foundations?	Yes	Yes	Rarely	yes	Yes
Steel Pipe Pile with Reinforced Concrete?	Rarely	No	Rarely	Yes	Yes
Reinforced Concrete Pile Foundations?	Yes	Rarely	Yes	Yes	No
Prestressed Pile Foundations?	Rarely	No	No	Rarely	Yes
Spread Footing Foundations?	Yes	No	Yes	Yes	Yes
Active, Passive, or Other Soil Pressure Assumed?	Other	Span Dependent	Passive	Other	Span Dependent
Approach Slabs Recommended?	No	Yes	Yes	No	Varies
Wingwalls Permitted to be Cast Rigid with Abutment Stem?	Yes	Yes	Yes	Yes	Yes
<u>Use SIAB?</u>	Yes	Yes	No	Yes	Yes
Maximum Skew Angle	30+	30	-	30+	None
Steel Pile Foundations?	Yes	Yes	-	Yes	Yes
Steel Pipe Pile with Reinforced Concrete?	Rarely	No	-	Yes	Yes
Reinforced Concrete Pile Foundations?	Yes	Rarely	-	Yes	-
Prestressed Pile Foundations?	Rarely	No	-	Rarely	Yes
Spread Footing Foundations?	Yes	Yes	-	Yes	Yes
Active, Passive, or Other Soil Pressure Assumed?	Other	Span Dependent	-	Other	Span Dependent
Approach Slabs Recommended?	No	Yes	-	No	Varies
Wingwalls Permitted to be Cast Rigid with Abutment Stem?	Yes	Yes	-	Yes	Yes

1.6.1. IAB & SIAB

1.6.1.1. Foundation Types

The most common foundation type used for IAB in Europe, per White et al. (2010), are large diameter steel pipe piles filled with reinforced concrete. A major difference in foundation selection, as compared to the United States, is the limited use of steel H-piles. There is no agreement in Europe regarding whether a stiff or flexible foundation element is best used with IAB. England, Ireland and Sweden install sleeves around deep foundation elements to allow greater freedom in bending, while Finland typically constructs very stiff concrete filled pipe piles with diameters up to 3.94 ft. Furthermore, the United Kingdom allows for construction of IAB upon shallow foundations, which is not typically permitted by DOTs in the United States. A typical detail of this foundation type is shown in Figure 1.13.

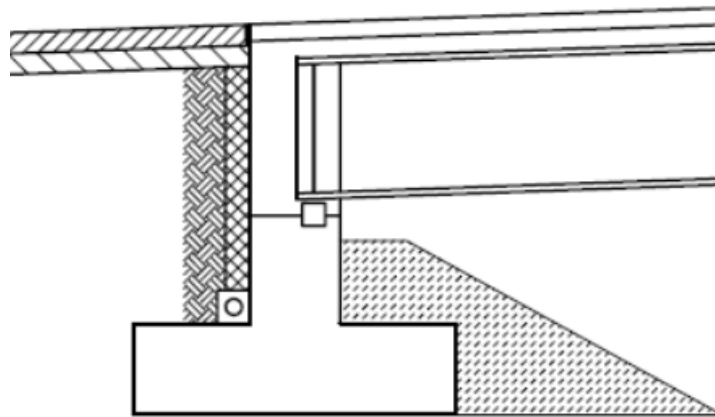


Figure 1.13: Integral abutment founded on a spread footing, as used in the United Kingdom (White, 2007)

1.6.1.2. Backfill Material

Backfilling requirements for European IAB are documented and agreed upon even less than those in the United States. The most common backfill requirement is well-compacted sand or gravel, with even backfilling on both sides of the abutment specified in some cases. Additionally, unlike the United States, no European countries require installation of an elastic compressible material behind the abutment backwall (White et al., 2010). Estimation of earth pressures upon the abutments and associated design typically take into account a mobilized earth pressure force. Considerations for such a design load are discussed by Pak et al. (2017).

1.6.1.3. Approach Slabs

Switzerland is the leading European country conducting research on the performance of approach slabs for IAB and SIAB. Figure 1.14 depicts the evolution of the approach slabs used in Switzerland, with (a) being an early rendition and (c) being the most commonly recommended detail to date. The study conducted by Dreier et al. (2011), in which the details shown in Figure

1.14 were described, was expanded upon by Burdet et al. (2015) with an experimental component to investigate these moving, buried transition slabs. Figure 1.15 depicts how the buried approach slab, with a fully rigid connection to the abutment backwall, will rigidly move with the expansion and contraction of the IAB and distribute surface movements across the length of the slab. This is in contrast to the sharp displacement transitions generated from details shown in Figure 1.14(a) and Figure 1.14(b). The detail of Figure 1.14(a) and Figure 1.15 includes granular backfill below and above the approach slab, with asphaltic pavement as the uppermost layer on top of the slab. Furthermore, the approach slab can be protected with a waterproofing membrane, and the smooth interface with the soil that this would generate on the top surface of the approach slab was shown to prevent pavement cracking in the experiment conducted by Burdet et al. (2015).

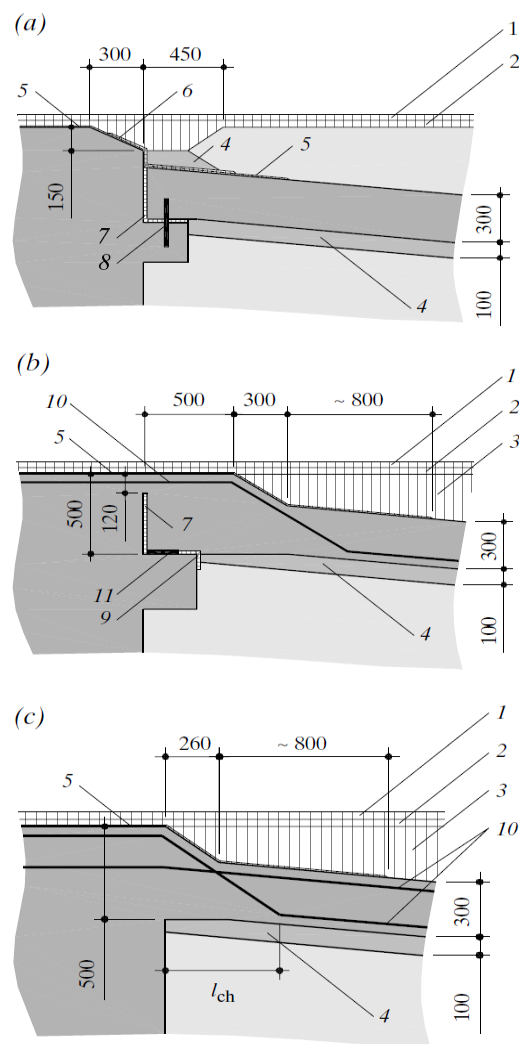


Figure 1.14: Evolution of Swiss IAB approach slab connections (Dreier et al., 2011)

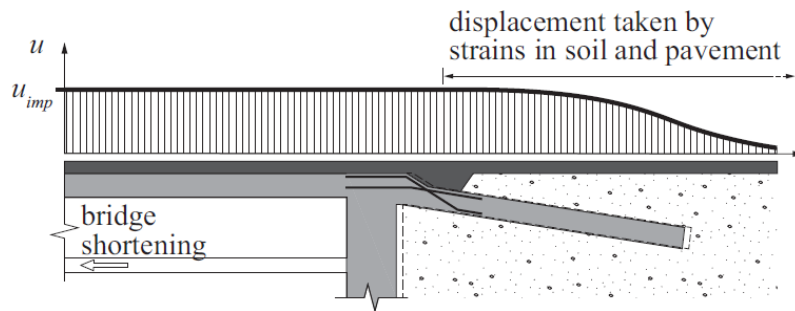


Figure 1.15: Longitudinal displacements at the surface of IAB with moving transition slab (Burdet et al., 2015)

1.6.1.4. Girder/Beam Design

Similar to United States design standards, a variety of girder types may be used on IAB and SIAB in Europe. Precast/pre-stressed concrete beams are the dominate type of superstructure, and steel and cast-in-place concrete beams are permitted, but less frequently implemented (White et al., 2010). A unique type of bridge superstructure that has emerged in the European market within the past five years is the “prefabricated composite beam – filler beam,” commonly referred to as VFT-WIB® from the German name. This composite bridge structure is being constructed in conjunction with integral abutments in Romania, Germany and Poland. The benefits of this structure type, specifically as applied to a newly constructed bridge in Romania following construction of the first VFT-WIB® case study bridge in Germany in 2008, have been discussed in Petzek et al. (2015). A schematic of the girder and concrete deck system for the VFT-WIB® bridge, along with the end portion cast into the concrete abutments is shown in Figure 1.16.

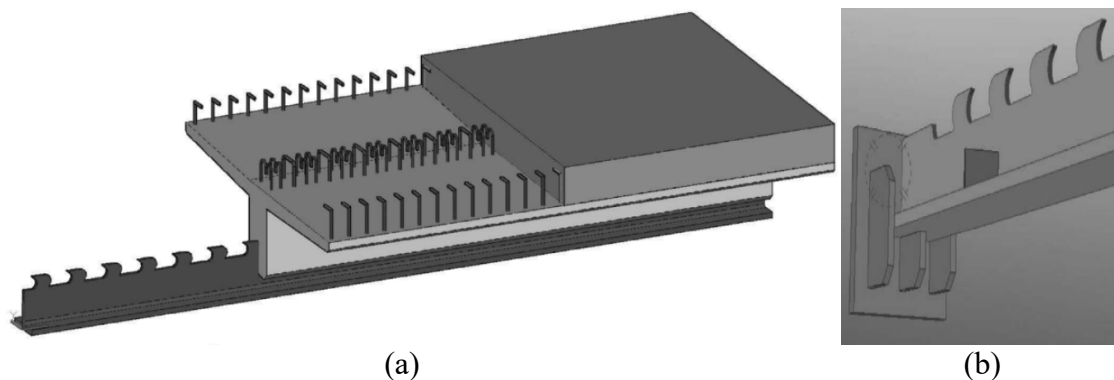


Figure 1.16: 3D rendering of VFT-WIB®: (a) bridge deck/girder system; and (b) end detail (Petezek et al., 2015)

Petezek et al. (2015) highlight the advantages of the VFT-WIB® integral abutment bridge design with the following points:

- Elimination of bearings and expansion joints reduce maintenance and increase riding performance
- Construction is fast and simple with precast and preformed members
- Cost and material usage is minimized with the advantages of composite behavior
- Slender and aesthetically pleasing profiles can be achieved

1.7. Current Practice in Asia

1.7.1. The Japanese Approach

The leading authority on IAB among Asian countries is Japan. Significant research has been conducted by Tatsuoka et al. (2009, 2012) and Muñoz et al. (2012) that included cyclic lateral load testing on the four evolutions of bridge structures shown in Figure 1.17. These studies found that geosynthetic layers in the backfill of an integrated bridge structure would reduce the settlement of soil beneath the approach region by 50% and, in some cases, more. Furthermore, connecting these reinforcement layers with the abutment backwalls would nearly eliminate any surface settlements. Such research has led to the first construction of a GRS IAB in 2011 after previous heavy use of the GRS RW and integral concepts. In Japan, the experience has been that a GRS IAB is less costly when compared to a comparable box girder or GRS RW bridge (Watanabe, 2011).

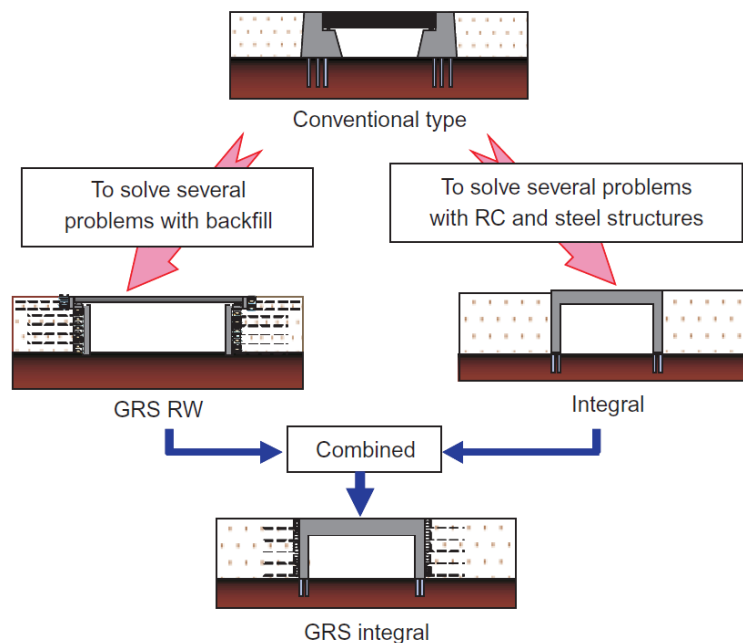
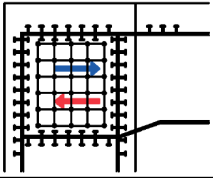
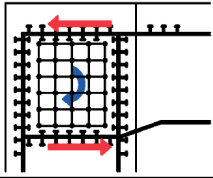
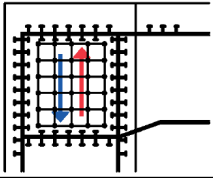
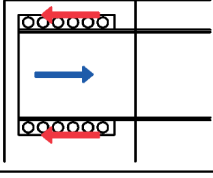
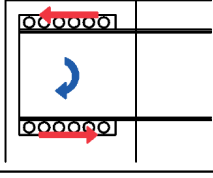
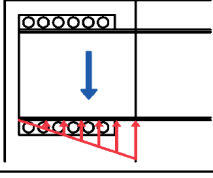
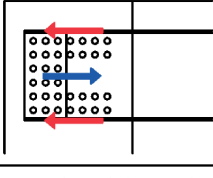
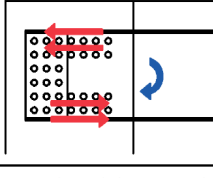
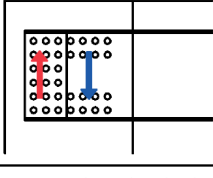


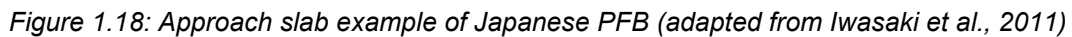
Figure 1.17: Evolution of bridge structures in Japan (Tatsuoka et al., 2009)

While GRS integral structures make up a substantial portion of railway bridge construction in Japan, highway bridges are now primarily constructed as Portal Frame Bridges (PFB). Since 1995, PFB have been used almost exclusively for highway bridges and are deemed acceptable for spans up to 656.17 ft (Iwasaki et al., 2011). While these structures are labeled differently than IAB, they still consist of a rigid, moment-resisting connection between the superstructure and abutments, even though this may take many different forms, as shown in Table 1.3.

Table 1.3: Examples of PFB girder to abutment corner connections and load transfer mechanisms (Iwasaki et al., 2011)

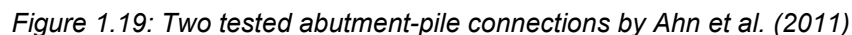
Bridge name	Transmission mechanism of corner forces at the girder-abutment connection		
	Axial force	Bending moment	Shearing force
Ofukishi river bridge			
	Studs on web	Studs on flange	Studs on web
Nakataharuki river bridge			
	Perforated steel plates (PSP)	Perforated steel plates (PSP)	Bearing force of concrete
Shimotani ike bridge			
	Perforated steel flange plates	Perforated steel flanges and web	Perforated steel web plate

In addition to unique superstructure-abutment connection details, the Japanese have also developed approach slabs that differ from both the United States and European practice. Figure 1.18 depicts the approach slab detail of a PFB constructed in 2000. The slab is set below the asphaltic pavement to smoothly distribute strains in the backfill, as opposed to passing them onto the pavement. Also included are shear keys in the upper face that prevent sharp increases of horizontal tensile stress in the pavement above. Finally, the slab is tapered at the end to prevent large surface displacements due to expansive and contractive movements of the bridge that are realized most prominently at the end of the approach slab.



Other Asian countries have limited experience with IAB/SIAB as defined in United States literature. Starossek (2009) compiled a report on the Shin Chon Bridge in South Korea, which is 3,477.7 ft in length with individual spans up to 557.74. This structure was claimed to be semi-integral, but upon further review this claim was based on the lack of thermal expansion joints and bearings at intermediate piers. The structure did, in fact, have thermal expansion joints at the end abutments and was isolated from the approaching roadway, which does not meet the US criteria for semi-integral. Cases such as these highlight the inconsistency in terminology and practice of IAB/SIAB across the world.

Research has been conducted by Ahn et al. (2011) on the integral H-pile-to-concrete-abutment-joint stiffness and strength. Figure 1.19(a) depicts a rendering of the weakest connection tested, while Figure 1.19(b) depicts the strongest. This research also revealed that, when loaded, rotation about the abutment-pile interface was realized, which would suggest that the displacement of the abutment in the field would have a greater rotational component than translational.



Despite limited field applications of integral abutments in Korea, research interest is growing and the results that may be achieved going forward should be monitored for further performance predictions.

Chapter 2. Assessment of the Current State of the Practice in Texas

2.1. Existing Integral/Semi-integral Abutment Bridges in Texas

Throughout discussions with the Texas Department of Transportation (TxDOT) Bridge Division, several structures were identified as having either integral or semi-integral bridge abutments. Currently, there is one in-service Integral Abutment Bridge (IAB) and one in-service Semi-Integral Abutment Bridge (SIAB). Two additional structures, built nearly 20 years ago or more, were identified as having semi-integral abutment characteristics, and these were also investigated by the University of Texas at Austin. In the following sections, bridges in the State of Texas identified as relevant to the current study are described. Table 2.1 below provides a summary of the bridges considered.

Table 2.1: Integral/semi-integral abutment bridges in Texas

Common Name	Abutment Type	Superstructure Type	TxDOT District	Nearest Town	Total Length	Year Built
El Paso County IAB	Integral	Continuous Deck, Steel Plate Girder - Multiple	El Paso	Anthony, TX	222	1998
Mack Creek Bridge	Semi-Integral	Simple Span Deck, Prestressed Concrete Box Girder - Single	Tyler	Palestine, TX	68	2017
Fannin County SIAB	Semi-Integral/Conventional	Simple Span Deck, Prestressed Concrete Girder - Multiple	Paris	Randolph, TX	222	1998
El Paso County SIAB	Semi-Integral	Simple Span Deck, Prestressed Concrete Girder - Multiple	El Paso	Fabens, TX	245	1960

2.1.1. El Paso County IAB

This bridge is located in Anthony, Texas and has been identified as the sole IAB in the State of Texas. This bridge has a continuous deck and steel plate girder superstructure with integral abutments. The structure was built in 1998 with five lanes, at a total width of 80 feet and total length of 222 feet. The length of the bridge is divided equally into two spans and has no skew. The Average Annual Daily Traffic (AADT) was last evaluated in 2013 at 32,530 Vehicles Per Day (VPD). A photograph of the bridge roadway facing west is shown in Figure 2.1 and a profile view is shown in Figure 2.2.



Figure 2.1: El Paso County IAB roadway (looking west)



Figure 2.2: El Paso County IAB (southeast corner of bridge looking northwest)

The subsurface soils underlying the El Paso County IAB are primarily moist compacted sand with some areas of dry sand and silty sand. The H-pile foundations of the bridge are located entirely within the regions of moist sand found at the exploratory boreholes.

2.1.2. Mack Creek Bridge

This bridge is located outside the town of Palestine, Texas and was recently constructed over Mack Creek. This structure is a continuous deck, simple-span, pre-stressed concrete box-girder bridge with semi-integral abutments. Construction of this structure was completed in August 2017, with one lane in each direction, at a total width of 26 feet and total length of 68.42 feet. The AADT for the bridge replaced by Mack Creek Bridge was evaluated in 2015 at 510 VPD. Photographs of the bridge roadway and one of the abutments are shown in Figure 2.3 and Figure 2.4, respectively.



Figure 2.3: Mack Creek Bridge roadway (looking east)



Figure 2.4: Mack Creek Bridge abutment view (looking east)

The subsurface soils at Mack Creek Bridge site include a relatively shallow layer of silty sand underlain by significant layers of lean to sandy/silty clay. The sheet-pile foundations are located primarily within this clay layer, which extends to a depth beyond the exploratory boreholes.

2.1.3. Fannin County SIAB

This bridge is located in the town of Randolph, Texas. The structure is a simple-span deck, pre-stressed concrete-girder bridge with abutments that have both semi-integral and conventional

characteristics. This structure was built in 1998 with two lanes, at a total width of 46 feet and total length of 222 feet. The length of the bridge is divided into three separate spans, the largest of which is 110 feet long. The bridge has no skew and the AADT in 2008 was 1,800 VPD. Photographs from atop and below the bridge are shown in Figure 2.5 and Figure 2.6, respectively.



Figure 2.5: Fannin County SIAB roadway-to-bridge-deck transition (from north end looking southwest)



Figure 2.6: Fannin County SIAB profile view (looking northwest)

The soils at the Fannin County SIAB site include a relatively shallow clay layer underlain by a shale deposit that extends beyond the depth of the exploratory boreholes. The north and south ramps leading up to the bridge deck were constructed of imported fill. Drilled shaft foundations support the bridge at the abutments and piers. The foundations at the abutments are located partly in the fill layer and partly in the clay/shale deposit. The piers are exposed and the drilled shafts that extend into the clay/shale are equal in length to the exposed regions.

2.1.4. El Paso County SIAB

This structure is located in Fabens, Texas. The structure is a simple-span deck, pre-stressed concrete-girder bridge with semi-integral abutments similar to those at Mack Creek Bridge. The structure was built in 1960 with two lanes, a total width of 29.2 feet and total length of 245 feet. The bridge length is divided into four spans, with a maximum individual span length of 65 feet, and was constructed with no skew. AADT was last measured in 2013 at 23,270 VPD. Figure 2.7 and Figure 2.8 depict the roadway-to-bridge-deck transition and a profile view of the bridge, respectively.



Figure 2.7: El Paso County SIAB roadway-to-bridge-deck transition (from west end looking northeast)



Figure 2.8: El Paso County SIAB profile view (from east end looking southwest)

The soils at the El Paso County SIAB consist of shallow deposits of sand and silty clay underlain by relatively dense sand extending the entire depth of the exploratory boreholes. The abutments

are founded on arrays of deep foundations into the dense sand with some fill near the approach roads, while the intermediate piers are supported by shallow foundations.

2.2. Field Data of IAB/SIAB in Texas

Site visits to all four of the previously mentioned bridges have been conducted. Prior to these site visits, significant effort was made to collect performance data related to these bridges, including contact with the Austin TxDOT Bridge Division as well as representatives from each bridge's respective district office. This preliminary investigation yielded the most recent bridge inspection reports for the El Paso County IAB and Fannin County SIAB. Furthermore, past reports for the El Paso County SIAB were not available from the El Paso District Office.

Table 2.2 includes the most recent bridge condition ratings for the bridges discussed in Section 2.1. The scoring system ranges from 0, corresponding to a component damaged beyond repair, to 9, representing excellent condition.

Table 2.2: Compilation of bridge condition ratings for known IAB and SIAB in Texas

Bridge Condition Ratings (0 to 9 scale with 9 = excellent)					
Common Name	Deck	Superstructure	Substructure	Structural Evaluation	Roadway Approach
El Paso County IAB	7	8	7	7	6
Mack Creek Bridge	-	-	-	-	-
Fannin County SIAB	7	8	6	6	7
El Paso County SIAB	6	5	5	5	6

Data for specific bridges that will be or is currently being collected is described in the subsequent sections.

2.2.1. El Paso County IAB Field Data

The collection of performance data included:

- Conduct survey of bridge abutments for lateral displacement observations
- Conduct survey of road-approach-to-bridge-deck transition to evaluate the development of any “bump at the end of the bridge” or settlements in the pavement or superstructure
- Photograph any signs of distress on the bridge structure or road approach
- Document and quantify the development of any cracks present in the bridge structure or approaching roadway

2.2.2. Mack Creek Bridge Field Data

Because of the unique opportunity provided by the construction of Mack Creek Bridge, a more comprehensive field monitoring program was established. The following list includes tasks completed in an effort to collect robust performance data of an SIAB in Texas conditions.

(6/23/17) Site visit to Mack Creek Bridge

- Meet with TxDOT construction personnel to discuss logistics of field instrumentation plan
- View bridge construction to assess need for any changes to field instrumentation plan
- Photograph current construction stage at bridge and for planning purposes
- Conduct survey of bridge abutments for baseline comparison with surveys after backfilling

(7/3/17) Site visit to Mack Creek Bridge

- Install two pressure cells on abutment backwalls on each side of bridge (four total)
- Install one pressure cell in a location not expected to be affected by cyclic bridge movements for baseline pressure comparison
- Mount two four-channel data loggers on bridge underside to receive output from pressure cells and measure ambient air temperature
- Collect pressure cell readings taken during installation procedure to verify cells are working properly and begin long-term reading schedule

(7/13/17) Site visit to Mack Creek Bridge

- Observe and aid in backfilling of abutment backwalls to ensure no damage is done to pressure cells and that necessary sand layer is place against pressure cell faces
- Conduct survey of bridge abutments to determine effect of backfilling on structure
- Collect data recorded since previous site visit to view daily cycles and compare ambient temperature measurements to nearby weather station
 - o Continue long-term reading schedule

(8/18/17) Site visit to Mack Creek Bridge

- Collect data recorded since previous site visit to ensure pressure cells and data loggers continue working properly and for data analysis
 - o Continue long-term reading schedule
- Install lithium batteries in data loggers to facilitate operation up to one year without replacement
- Conduct survey of bridge abutments for final constructed status
- Photograph final completed stage of bridge

A minimum of two site visits per year (once during summer and once during winter months) were completed to continue data collection and field condition surveys.

2.2.3. Fannin County SIAB Field Data

The collection of performance data included:

- Conduct survey of bridge abutments for lateral displacement observations
- Conduct survey of road-approach-to-bridge-deck transition to evaluate the development of any “bump at the end of the bridge” or settlements in the pavement or superstructure
- Photograph any signs of distress on the bridge structure or road approach
- Document and quantify the development of any cracks present in the bridge structure or approaching roadway

2.2.4. El Paso County SIAB Field Data

An inspection of this bridge to verify its semi-integral characteristics was conducted in summer conditions. The bridge was found to have the necessary semi-integral characteristic of having the girders cast into the backwall of the abutment. Furthermore, the bearing pads between the girders and pile cap were partially embedded into the abutment, which may or may not have been the design intention.

The initial inspection of the El Paso County SIAB was simple and consisted of visual identification of any structural deficiencies and photographs of the structure. Since the bridge passes over Interstate 10, which is relatively busy near the town of Fabens, additional traffic control would have been required for a more thorough inspection.

Chapter 3. Survey of State DOTs and Texas Districts

3.1. Introduction to the Surveys

In this chapter, the survey results collected from State Departments of Transportation and different districts within the State of Texas regarding the use of Integral Abutment Bridges (IAB) and Semi-Integral Abutment Bridges (SIAB) are presented.

3.1.1. Survey of State DOTs

The development and collection of responses to a survey related to the use of IAB and SIAB across the United States was distributed to US State DOTs in two phases.

The first phase included a short online questionnaire, the primary goal of which was to obtain contact information at each State DOT of an individual who would be likely to complete the entire survey. The questionnaire also inquired about the general use of IAB/SIAB by the DOT and the soil conditions common to the regions in which they are used.

Phase two of the survey included a longer questionnaire in spreadsheet format that requested greater detail about the history, design construction, and limitations of IAB/SIAB at each DOT. The goal of this second survey was to obtain enough information from DOTs across the United States to determine the primary advantages of IAB/SIAB and their potential applicability in Texas conditions. Additional inquiries were also made at each DOT for any available design guidelines related to IAB/SIAB.

3.1.2. Survey of TxDOT Districts

In addition to the survey of US State DOTs, a second survey was developed for TxDOT Districts. This survey was conducted in an online single-phase format that included a questionnaire, the length of which was between that of the State DOT survey phase 1 and 2 questionnaires. The purpose of the TxDOT District survey was twofold. The primary purpose was to identify any IAB/SIAB of which the research team may have been unaware, while the secondary purpose was to evaluate the likelihood of a given district to adopt the new IAB/SIAB technology. Additionally, the questionnaire sought to identify characteristics of the various districts along with design practices and common maintenance issues of bridges constructed throughout the state.

3.2. Development of State DOT Survey

The State DOT survey was divided into two phases, an approach that proved useful on prior experiences of research team members with surveys of DOTs. Specifically, this approach was proven successful with TxDOT Project 0-5812, in which a single-page document provided

answers to basic but important initial questions and also established a contact at many of the agencies to which the survey was sent. A similar format was selected for this project, but rather than a survey in Word document format, an online survey was created for ease of use by respondents. The second phase follow-up survey was then disseminated as an Excel file due to the in-depth nature of the questionnaire.

3.2.1. Phase 1 Questionnaire

The phase 1 questionnaire sent to US DOTs is shown in Appendix A.1: Phase 1 Questionnaire of State DOT Survey. Questions 1 through 10 are revised versions of some of the most important questions from phase 2. These 10 questions aimed to obtain an initial response regarding what agencies use IAB/SIAB. Additionally, this phase should have identified any special cases that may be of interest related to bridge superstructures, foundations and/or backfill materials. The final three questions sought to obtain enough information to establish contact with a specific individual likely to respond to a larger questionnaire, thus increasing the number of responses to the entire survey. Phase 2 Questionnaire

The phase 2 questionnaire addressed aspects of IAB/SIAB such as history, design construction and maintenance. This portion of the survey was intended to obtain in-depth information helpful to the project team from those DOTs that responded to phase 1. The full phase 2 questionnaire can be found in Appendix A.2: Phase 2 Questionnaire of State DOT Survey.

During the development of the phase 2 questionnaire, significant attention was devoted to the project work plan, which contains “preliminary questions for the US Survey.” The questions were complemented with the Survey of Integral Abutment Bridge Design Criteria by White (2007), which was deemed useful due to the comparisons he was able to draw between responses he received from around the world on the application of IAB and SIAB. Furthermore, the report by Maruri & Petro (2005) was reviewed to ensure all major categories for the comparison of integral/semi-integral abutments were included in the development of the phase 2 questionnaire. The analysis of survey responses by Maruri & Petro (2005) provided an excellent framework for the analysis of responses received by the TxDOT Project 0-6936 research team.

The goals of the phase 2 questionnaire were as follows:

- To increase understanding of the soil conditions in which IAB and SIAB are most beneficial.
- To determine the structural components (superstructure type, foundation type, etc.) that are best used in conjunction with IAB and SIAB.
- To understand what project requirements and/or constraints lead to the selection of an IAB/SIAB as opposed to a conventional bridge.

- To establish contacts with State DOTs that have had strong success with IAB and SIAB.
- To establish contacts with State DOTs that have had failures with IAB and SIAB (if applicable).
- To gain further understanding of how IAB and SIAB will change design procedures if adopted into use by TxDOT bridge engineers.
- To compile the current limitations of IAB and SIAB that are not applicable to conventional bridges.

3.3. Development of Texas District Survey

The internal TxDOT District survey was developed to include all questions originally identified in the project's work plan, as well as other topics considered relevant by the performing and receiving agencies since the project commenced. The goal of this survey was to collect design and construction practices for bridges across the State of Texas, identify any unknown IAB/SIAB structures, and assess the willingness for additional construction of IAB/SIAB in the state. Accordingly, the survey began with an introduction of relevant terms, focused mostly on bridge practices in the respective district (super/sub-structure types, approach slab details, etc.), and then sought opinions regarding the pros and cons of IAB/SIAB within the district. The full survey disseminated to the 25 TxDOT Districts is provided in Appendix A.3: TxDOT District Survey

Similar to the initial questionnaire of State DOTs, the TxDOT District survey was distributed to participants in an online format with multiple choice and essay format questions. Districts that identified use of IAB/SIAB were contacted by the research team for follow-up discussions regarding the performance of and experience with IAB/SIAB technology.

3.4. Distribution and Response Rate

All online surveys were distributed by TxDOT via pre-existing email lists, with the research team drafting the email messages accompanying the links provided to the online surveys. Any follow-up contact, including distribution of the State DOT phase 2 questionnaire, was carried out by the research team.

3.4.1. State DOT Survey

Responses to the phase 1 State DOT online survey were received from 25 of 50 states, corresponding to a 50% response rate. Table 3.1 lists the states that submitted phase 1 and 2 questionnaire responses. It should also be noted that responses were received from two different individuals associated with the Florida and New Hampshire DOTs.

Table 3.1: States responding to phase 1 and 2 DOT questionnaires

Respondent #	State Represented	Responded to Phase 1	Responded to Phase 2
1	Alabama	Yes	
2	Alaska	Yes	
3	Arkansas	Yes	
4	California	Yes	
5	Delaware	Yes	Yes
6	Florida	Yes	
7	Georgia	Yes	
8	Indiana	Yes	Yes
9	Kansas	Yes	
10	Maryland	Yes	
11	Minnesota	Yes	Yes
12	Mississippi	Yes	
13	Missouri	Yes	Yes
14	Montana	Yes	Yes
15	Nebraska	Yes	Yes
16	New Hampshire	Yes	Yes
17	New Mexico	Yes	
18	Ohio	Yes	Yes
19	Oklahoma	Yes	Yes
20	Pennsylvania	Yes	Yes
21	South Dakota	Yes	Yes
22	Tennessee	Yes	
23	Vermont	Yes	
24	Virginia	Yes	
25	Wisconsin	Yes	

3.4.2. Texas District Survey

Of the 25 TxDOT Districts, responses to the online survey were received from 19, corresponding to a response rate of 76%. Table 3.2 lists the TxDOT Districts that responded to the survey. It should also be noted that responses were received from three different individuals from the Houston District and two different individuals from the Yoakum District.

Table 3.2: List of districts responding to TxDOT internal survey

Respondent #	District Represented
1	Amarillo
2	Atlanta
3	Beaumont
4	Brownwood
5	Bryan
6	Childress
7	Corpus Christi
8	Dallas
9	El Paso
10	Fort Worth
11	Houston
12	Odessa
13	Paris
14	Pharr
15	San Angelo
16	Tyler
17	Waco
18	Wichita Falls
19	Yoakum

3.5 Analysis of Responses

Questionnaire responses received from State DOTs and Texas Districts have been compiled to analyze the use of IAB/SIAB across the United States and the feasibility/benefit of such technology in Texas. The following sections include figures depicting the questionnaire results as well as a discussion of the data's relevance.

3.4.3. State DOT Survey

3.4.3.1. Phase 1 Responses

The phase 1 State DOT questionnaire investigated general use of IAB/SIAB throughout the United States. Figure 3.1 and Figure 3.2 illustrate the use of this technology among responding states. These figures also show the prevalence of common superstructure and substructure types with IAB/SIAB technology. The initial responses indicated that steel H-piles and precast concrete are by far the most common foundation and superstructure types, respectively. Additionally, drilled shaft foundations were reported as the second most common foundation type for SIAB, which is of interest to TxDOT.

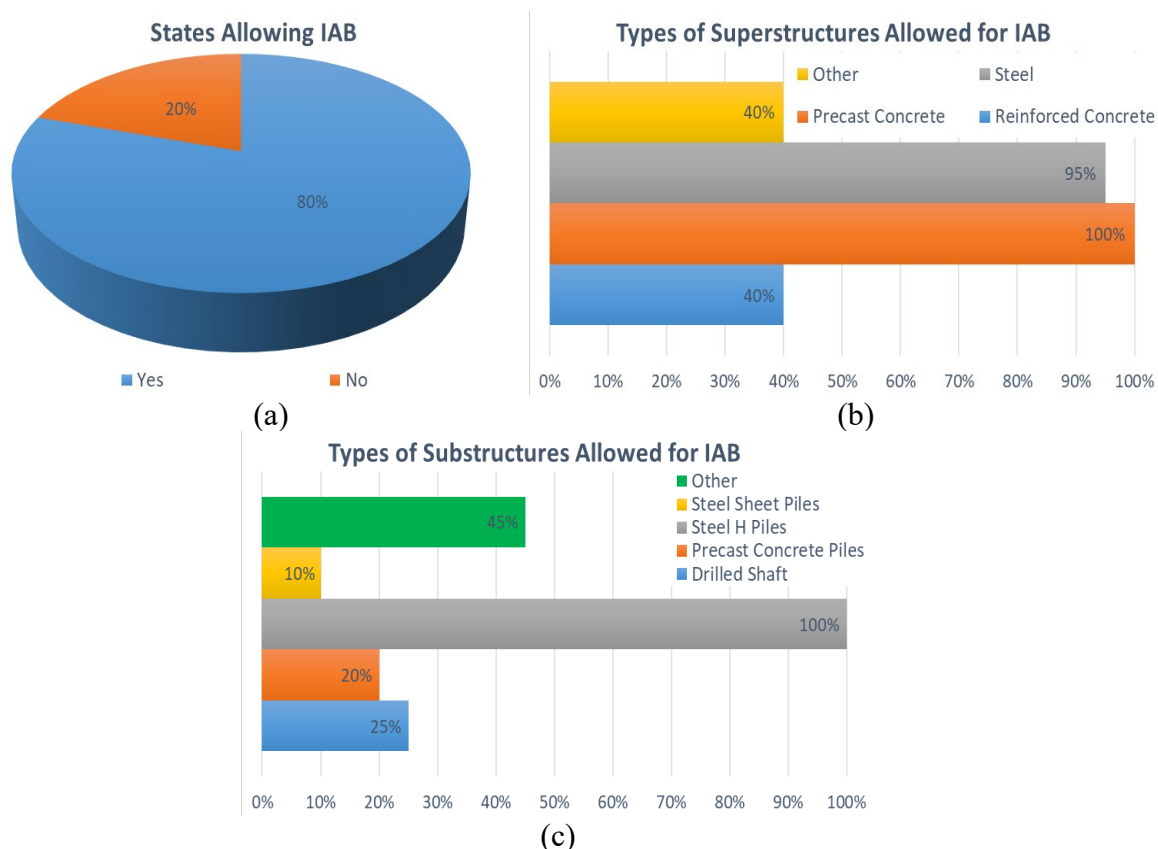
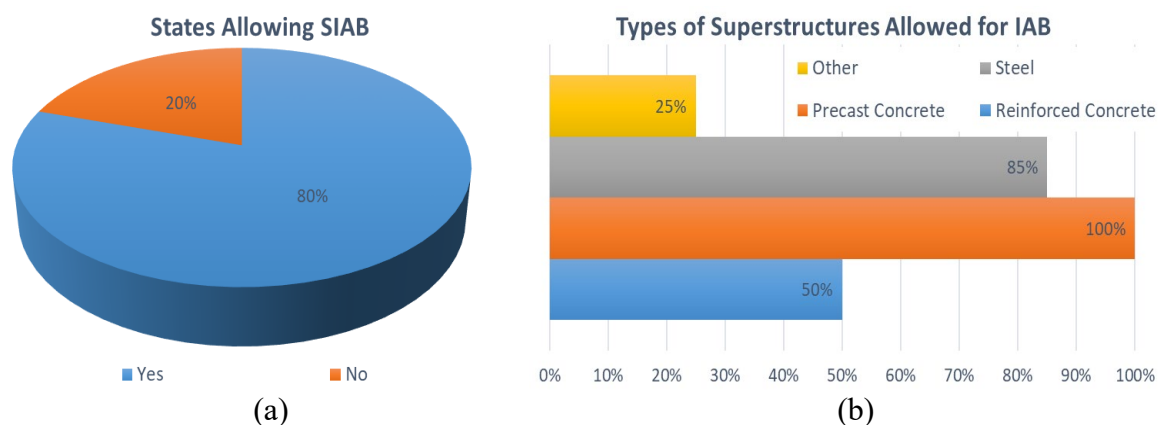


Figure 3.1: Initial DOT questionnaire responses regarding IAB design: (a) allowance of IAB; (b) superstructures designed with IAB; and (c) substructures designed with IAB



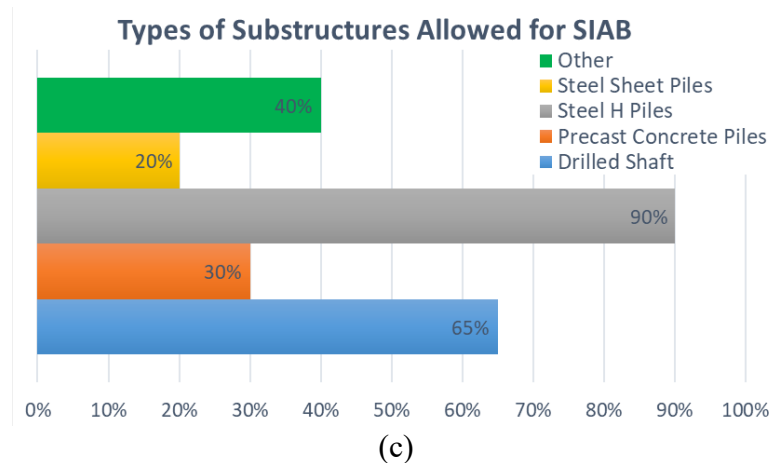


Figure 3.2: Initial DOT questionnaire responses regarding SIAB design: (a) allowance of SIAB; (b) superstructures designed with SIAB; and (c) substructures designed with SIAB

Because of the diversity in response format to questions regarding the number of IAB/SIAB structures in inventory for a given DOT and type of backfill material required, responses thereto have been compiled in tabular format. Table 3.3 details the initial responses and, in most cases, includes the exact wording used by respondents. Of the states that construct IAB and/or SIAB, the predominant backfill type is undoubtedly a granular free-draining material. While some states indicated the required use of additional compressible materials or a drainage feature, these were most often not specified. Some responses indicated that no backfill requirements are in place. However, with the exception of Missouri IAB, this is only the case for states with a small inventory of IAB/SIAB.

Table 3.3: Initial DOT responses regarding number of IAB/SIAB in inventory and required backfill material

Responding State	# of IAB	Backfill for IAB	# of SIAB	Backfill for SIAB
Virginia	All since 2007	Expanded polystyrene	1/3 of jointless bridge inventory	Expanded polystyrene
Kansas	More than 50	In-situ soil	More than 15	Select soil
Alabama	<i>Does not construct IAB</i>		18	Nothing special
Florida	<i>Does not construct IAB or SIAB</i>			
New Hampshire	4	Granular soil	3	Granular soil
Delaware	1	Structural backfill borrow, type C	50	Structural backfill borrow, type C
Mississippi	<i>Does not construct IAB or SIAB</i>			
Wisconsin	105	Clean, compacted backfill, type A	<i>Does not construct SIAB</i>	
Missouri	More than 1000	No requirements	2	No requirements
California	15-20% of all bridges	Structural backfill, 95% compaction	unavailable	Structural backfill, 95% compaction
Tennessee	Thousands	2' of #57 stone aggregate & select backfill behind	<i>Does not construct SIAB</i>	
Oklahoma	491	Controlled low strength material (CLSM)	<i>Does not construct SIAB</i>	
Maryland	<i>Does not construct IAB</i>		85-100	#57 stone aggregate
Indiana	Many	Course aggregate with perforated drain pipe	Several	Course aggregate with perforated drain pipe
New Mexico	About 100	A-1a, and sometimes flowable fill	About 100	A-1a, compacted to 95% (1-1/2" max.)
South Dakota	About 800	Free draining granular soil	About a dozen	Free draining granular soil
Georgia	<i>Does not construct IAB or SIAB</i>			
Nebraska	Constructed since 1975	Granular soil	Constructed since 1975	Granular soil
Minnesota	About 90	Modified 10% MNDOT, spec. 3149.2B4	More than 6	Modified 10% MNDOT, spec. 3149.2B4
Montana	About 5% of all bridges	Crushed, well graded sand or gravel; sometimes EPS foam	About 95% of all bridges	Crushed, well graded sand or gravel; sometimes EPS foam
Arkansas	Est. 30-40	Unclassified soil	None yet	Unclassified soil
Ohio	998	2' of porous soil	1332	2' of porous soil
Vermont	75-100	select graded free-draining soil and some geofoam	15-20	select graded free-draining soil and some geofoam
Alaska	<i>Does not construct IAB, but has many</i>		About 10% of all bridges	95% compaction for 50' behind end of bridge
Pennsylvania	About 1500	AASHTO #3, 5, or 57 coarse aggregate (open-graded)	Less than 100	AASHTO #3, 5, or 57 coarse aggregate (open-graded)

To create a personalized follow-up questionnaire, all information on State DOT practices acquired from phase 1 was prefilled into the phase 2 questionnaire for each specific state. These personalized forms were then distributed to the states that agreed to follow-up communications on the phase 1 questionnaire. Correspondence during this stage of the survey was solely with the individual phase 1 respondent who provided contact information in the response section.

3.4.3.2. Phase 2 Responses

Of the states that responded to the phase 1 questionnaire, 23 of the 25 agreed to follow-up communications. Of those that indicated a willingness to respond further, 11 State DOTs provided some form of response to the phase 2 questionnaire. The following paragraphs discuss additional details of each State DOT response beyond the questionnaire answers. Table 3.4, Table 3.5, Table 3.6 and Table 3.7, shown in a subsequent part of this section, summarize all questionnaire responses.

Delaware

Although the State of Delaware indicated a willingness to respond further, additional responses to the phase 2 questionnaire were not provided. However, the DelDOT Bridge Design Manual was forwarded by Barry Benton and can be found at the following link: http://www.deldot.gov/Publications/manuals/bridge_design/. Within this document, integral and semi-integral abutments are discussed in section 107.4.1.

Indiana

INDOT provided answers to the phase 2 questionnaire, but did not submit any additional guidelines, manuals or other supporting documents.

Minnesota

In addition to phase 2 questionnaire responses, MnDOT provided design details of IAB and SIAB abutments, approaches and an overall design guidance document. These documents are included in Appendix A.4: MnDOT IAB/SIAB Design Details.

Missouri

MoDOT provided answers to the phase 2 questionnaire, but did not submit any additional guidelines, manuals or other supporting documents.

Montana

MDT provided answers to the phase 2 questionnaire, but did not submit any additional guidelines, manuals or other supporting documents.

Nebraska

NDOT provided answers to the phase 2 questionnaire, but did not submit any additional guidelines, manuals or other supporting documents.

New Hampshire

NHDOT provided phase 2 questionnaire responses, as well as a link to the State's Bridge Design Manual, given here: <https://www.nh.gov/dot/org/projectdevelopment/bridgedesign/manual.htm>.

Chapter 6 is particularly relevant to TxDOT Project 0-6936, as it details all substructure components including, but not limited to, integral abutments, semi-integral abutments and approach slabs.

Ohio

The Ohio DOT provided answers to the phase 2 questionnaire, but did not submit any additional guidelines, manuals or other supporting documents.

Oklahoma

The Oklahoma DOT provided responses to the phase 2 questionnaire, as well as information regarding the Controlled Low Strength Material (CLSM) used for backfilling integral and semi-integral abutments. Appendix A.5: Oklahoma DOT CLSM Backfilling Specifications provides a brief overview of the CLSM material that was reported to provide better performance with IAB/SIAB and corresponding approach slabs when used as a backfill material. The complete Oklahoma DOT specifications document can be found at the following link:

http://www.odot.org/c_manuals/specbook/oe_ss_2009.pdf.

Pennsylvania

In addition to a very thorough response to the phase 2 questionnaire, PennDOT included bridge approach slab details and a design spreadsheet used for IAB in the state. The approach slab details are included in Appendix A.6: PennDOT Approach Slab Details, and the design spreadsheet will be disseminated to TxDOT as an Excel file so that it may be explored and potentially utilized for future design. The design spreadsheet can also be found at the following link:

<http://www.penndot.gov/ProjectAndPrograms/Bridges/Documents/Plans%20and%20Specifications%20Documents/IntegralAbutmentDesign/IntegralAbutment.xlsm>.

South Dakota

SDDOT provided answers to the phase 2 questionnaire, but did not submit any additional guidelines, manuals or other supporting documents.

Table 3.4: State DOT phase 2 questionnaire responses of IAB/SIAB history and general design factors

	Indiana	Minnesota	Missouri	Montana	Nebraska	New Hampshire	Ohio	Oklahoma	Pennsylvania	South Dakota
First IAB	1989	-	1970	-	1970	1992	1935	1977	Late 1990s	1970s
IAB Quantity	-	-	3000	-	-	12	998	500	>1500	888
First SIAB	1994	2007	2000	-	1969	Unknown	1968	-	Early 2010s	Unknown
SIAB Quantity	-	-	10	-	-	2	1332	None	<100	Unknown
Why Start IAB/SIAB?	Eliminate expansion joints that poorly protected substructure and beam ends from moisture	Reduce deterioration of super and substructures at bridge ends; simplicity and cost effectiveness	Prevent degradation of joints and bearings from salt water in winter and reduce bridge costs	Elimination of joints and bearings	Remove leaky joints over supports, which resulted in lots of repairs	Remove expansion joints away from bearing seat	To get rid of leaking expansion joints	Joints leak and led to corrosion on beam ends, pier caps, columns, abutment seats, and paint failures	Removal of joints to prevent corrosion and accelerate construction	Elimination of deck joints
Poorly Performing IAB/SIAB	None	-	10		Not many	Not known	Few	None	<50	None
Problems with IAB/SIAB	1) Approach slab settlement; 2) Pavement ledge failures; 3) Diaphragm cracking in the bent face due to beam rotation	-	Long bridges, or those with really rocky backfill had abutment spalling issues	Cracking around cantilever wingwalls	Details for large skew, stand anchors along wing walls, predrilling for piles, pile orientation, compaction and friction under approach	Bump at end of sleeper slab	End of approach slab settlement	Bump at end of the bridge, approach slab settlement, water infiltration, and wing wall movements	Leakage at the deck and end diaphragms water proofing membrane detail	-
Problem Solutions	1) Compaction; 2) changed connection to longitudinal bar assembly embedded into bridge deck	-	Some converted to SIAB and others being monitored		Improved details	Underdrain added in free draining material	New approach slab standard drawing	Controlled Low Strength Material has resulted in better performance	Provide physical attachment of membrane to abutment to prevent soil from getting behind membrane	-
Common Foundation Soils	Clay and sand	-	Mostly clay and rock	All types	-	Granular, sand, clay, and rock	Glacial till and associated deposits	Foundations typically to bedrock	Rock: limestone, sandstone, shale, and siltstoe	Glacial till or shales
Design Temperature Range	0 to 120 deg F	-30 to 120 deg F	-30 to 120 deg F	-	Per AASHTO	-	-	0 to 120 deg F	-	-
Design Load Impact on Selection	Most cost effective structure selected from design load analysis	No impact	No impact	No impact	No impact	HL-93 applied and best bridge selected to carry live load	No impact	More load results in greater wing wall movements and moisture	No impact	No impact
AADT Impact on Selection	-	No impact	No impact	No impact	No impact	Importance Load Modifier	No impact	No impact	No impact	No impact

Table 3.5: State DOT phase 2 questionnaire responses regarding IAB design

	Indiana	Minnesota	Missouri	Montana	Nebraska	New Hampshire	Ohio	Oklahoma	Pennsylvania	South Dakota
Are Pile Foundations Required	Yes	Yes	Yes	Yes	Yes	Yes	-	Yes	Yes	Yes
Steel Piles?	Steel H & pipe piles	Steel H piles & shell with concrete fill	Steel H piles & pipe piles with concrete fill	Steel H & sheet piles	Steel H & pipe piles	Steel H piles	Steel H & CIP piles	Steel H piles	Steel H, pipe, and monotube piles	Steel H piles
Minimum Pile Length Below Abutment Stem	25 ft	-	15 ft	-	-	Sufficient to resist loads	25 ft	15 ft	15 ft	10 ft
Orientation of Foundations	Strong axis parallel to roadway centerline	Weak axis bending	Strong axis parallel to roadway centerline	Weak axis in longitudinal direction	Varies	Varies	Web parallel to centerline of bearing	Weak axis bending	Weak axis parallel to beam orientation	Weak axis bending
Precast Concrete Piles?	No	No	No	No	No	Yes	No	No	No	No
Drilled Shaft Foundations?	No	No	No	No	No	Yes	No	No	No	Not at abutments
Are Bending Forces in Piles Accounted For?	No	No, but length kept short to avoid flexure issues	On bridges over 200 ft long with AASHTO LRFD	Yes, with analysis	Pile soil interaction using P-Delta analysis	Yes, design with elastic or inelastic approach	No	No	Yes, with bending moment tolerance xlsx	Yes, maximum structure length reduces displacement
Required Backfill Material	End bent structural fill	Select granular (Spec 3149.2B4)	Soil or rock	-	Select granular compacted to 95%	Granular: 100% 6", 25-70% #4, 0-12% #200; compacted every 8"	2 ft porous backfill and item 203 granular embankment	CLSM, which does not require compaction	Open graded with walk behind vibrator to compact	Free draining with embankment compacted to 97% dry density
Even Fill Required Front & Back of Substructure?	No	-	No	No	-	No	No	No	No	No
Compressible Inclusion Required?	Yes	No	No	No	-	No	Yes	No	Yes	No
Approach Slabs Required?	Yes, 12" RC at 20' length	Yes	Yes, RC or asphalt, 20' length	No	Yes	Yes	Yes	Yes, RC 13" thick and 30' long	Yes	Yes, simple span CIP
Earth Pressure Designed For	Neglected	Full passive	-	At rest	-	Full passive	Full passive	n/a with CLSM	Full passive	Full passive
Wingwalls cast Rigid with abutment stem?	Yes	Yes	Yes	Yes	No, stand alone cantilever	Yes	Yes, with straight wingwall	Yes	Yes	Yes
Foundation Soil Impact on Design	Decides end bearing or friction piles	-	None	Effects abutment stiffness	Must isolate foundation from fill embankment soil; no IAB over water	Effects pile design	Effects length of piles	n/a with CLSM	Determine friction or end bearing piles; pipe or H sections respectively	Determines length of piles; prebore first 10 ft

	Indiana	Minnesota	Missouri	Montana	Nebraska	New Hampshire	Ohio	Oklahoma	Pennsylvania	South Dakota
Bridge interface with pavement	Terminal joint with concrete pavement	Joint at end of approach slab	Sleeper slab beneath approach and roadway	-	Special details for asphalt and concrete	Expansion through sleeper slab at end of approach	Expansion joint at end of approach slab	Joint is provided for concrete pavement	Strip seal expansion joint at end of approach slab for large movements	Accommodated at the far end of approach slabs
Design Tools Used	LEAP Bridge program, design manual details, empirical	Bridge design manual	-	Computer models	Follow standards, analyze otherwise	Mathcadd	Hand calculation	Limiting length of 300 ft controls design	IAB spreadsheet, design manual part 4, design standards BD-667, etc.	-
Beam Ends Considered...	Simply supported	Simply supported	-	Continuous	Simply Supported	Fully fixed	Pinned	Simply supported	Fully fixed	Simply supported
Use Steel Beams?	Yes	Yes	Yes	Yes	Yes	Yes	Yes	Yes	Yes	Yes
Individual Span Limit	-	-	-	-	250 ft	150 ft	None	-	150 ft	No limit
Overall Span Limit	1000 ft	100 to 300 ft depending on skew	500 ft	-	800 ft	300 ft	400 ft	300 ft	390 ft	350 ft
Maximum Skew	60 deg	45 deg	45 deg	-	50 deg	20 deg	30 deg	No limit	30 deg	30 deg
Maximum Roadway Grade	-	-	-	-	8 ft	5%	No limit	-	5%	no limit
Maximum Bridge Width	-	-	-	-	No limit	No limit	No limit	-	-	no limit
Use RC Beams?	No	No	Yes	Yes	Yes	No	No	No	No	No
Individual Span Limit	-	-	-	-	No limit	n/a	n/a	n/a	n/a	n/a
Overall Span Limit	n/a	n/a	600 ft	-	No limit	n/a	n/a	n/a	n/a	n/a
Maximum Skew	n/a	n/a	45 deg	-	50 deg	n/a	n/a	n/a	n/a	n/a
Maximum Roadway Grade	-	-	-	-	8 ft	n/a	n/a	n/a	n/a	n/a
Maximum Bridge Width	-	-	-	-	No limit	n/a	n/a	n/a	n/a	n/a
Use PC Beams?	Yes	Yes	Yes	Yes	Yes	Yes	Yes	Yes	Yes	Yes
Individual Span Limit	-	-	-	-	190 ft	150 ft	No limit	-	120 ft	No limit
Overall Span Limit	1000 ft	100 to 300 ft depending on skew	600 ft	-	No limit	600 ft	400 ft	300 ft +	590 ft	700 ft
Maximum Skew	60 deg	45 deg	45 deg	-	50 deg	20 deg	30 deg	No limit	30 deg	30 deg
Maximum Roadway Grade	-	-	-	-	8 ft	5%	No limit	-	5%	No limit
Maximum Bridge Width	-	-	-	-	No limit	None	No limit	-	-	No limit
Account for Creep/Shrinkage of RC/PC Beams?	Yes	No	No	-	No	Yes	Yes	No	No	No

Table 3.6: State DOT phase 2 questionnaire responses regarding SIAB design

	Indiana	Minnesota	Missouri	Montana	Nebraska	New Hampshire	Ohio	Oklahoma	Pennsylvania	South Dakota
Are Pile Foundations Required	Yes	No	No	No	Yes	No	No	n/a	No	Typically, Yes
Steel Piles?	Steel H piles	Steel H piles & shell with concrete fill	Steel H piles & pipe piles with concrete fill	Steel H & sheet piles	Steel H & sheet piles	Steel H piles	Steel H piles	n/a	Steel H & pipe piles	Steel H piles
Minimum Pile Length Below Abutment Stem	25 ft	-	15 ft	-	-	Sufficient to resist loads	25 ft	n/a	15 ft	10 ft
Orientation of Foundations	Weak axis parallel to roadway centerline	Strong axis bending	Weak axis parallel to roadway centerline	Varies	Strong axis bending	Varies	Flange parallel to centerline of bearing	n/a	Strong axis parallel to beam orientation	Varies
Precast Concrete Piles?	No	No	Yes	No	Yes	No	No	n/a	No	No
Drilled Shaft Foundations?	No	Yes	Yes	Yes	Yes	Yes	Yes	n/a	No	Not at abutments
Are Bending Forces in Piles Accounted For?	No	Yes	No	Loads transferred through bearings	Yes, 10 kip maximum	Yes, design with elastic or inelastic approach	No	n/a	Yes	Varies
Required Backfill Material	End bent structural fill	Select granular (Spec 3149.2B4)	Soil or rock	-	Granular backfill	Granular: 100% 6", 25-70% #4, 0-12% #200; compacted every 8"	2 ft porous backfill and item 203 granular embankment	n/a	Open graded with walk behind vibrator to compact	Free draining with embankment compacted to 97% dry density
Even Fill Required Front & Back of Substructure?	No	No	No	No	No	No	No	n/a	No	No
Compressible Inclusion Required?	Yes	No	No	No	No	No	Yes	n/a	Yes	No
Approach Slabs Required?	Yes, 12" RC at 20' length	Yes	Yes, RC or asphalt, 20' length	No	Yes	Yes	Yes	n/a	Yes	Yes, simple span CIP
Earth Pressure Designed For	Neglected	Full passive	-	At rest	Full passive	Full passive	Full passive	n/a	Full passive	Full passive
Wingwalls cast Rigid with abutment stem?	Yes	Yes	-	No, cast with backwall	Yes	Yes	Yes, with straight wingwall	n/a	Yes	Varies
Foundation Soil Impact on Design	Decides end bearing or friction piles	-	None	Will affect stiffness model of bridge	None	Effects pile design	Effects length of piles	n/a	SIAB can be used when bedrock is too close to surface for piles	-

	Indiana	Minnesota	Missouri	Montana	Nebraska	New Hampshire	Ohio	Oklahoma	Pennsylvania	South Dakota
Bridge interface with pavement	Terminal joint with concrete pavement	Joint at end of approach slab	-	-	Special details for asphalt and concrete	Expansion through sleeper slab at end of approach	Expansion joint at end of approach slab	n/a	Accounted for in design limits to minimize thermal movements	Accommodated at the far end of approach slabs
Design Tools Used	LEAP Bridge program, design manual details, empirical	Spreadsheet and bridge design manual	-	Computer model	Follow standards, analyze otherwise	Mathcadd	Hand calculation	n/a	IAB spreadsheet, design manual part 4, design standards BD-667, etc. with engineer modifications	-
Beam Ends Considered...	Simply supported	Simply supported	-	simply supported	Simply supported	Simply supported	Simply supported	n/a	Yes	Simply supported
Use Steel Beams?	Yes	Yes	No	Yes	Yes	Yes	Yes	n/a	Yes	Yes
Individual Span Limit	-	-	-	-	No limit	150 ft	No limit	n/a	110 ft	No limit
Overall Span Limit	None	220 to 300 ft depending on skew	n/a	-	No limit	300 ft	400 ft	n/a	110 ft	350 ft
Maximum Skew	None	30 deg	n/a	-	No limit	20 deg	No limit	n/a	30 deg	30 deg
Maximum Roadway Grade	-	-	-	-	No limit	5%	No limit	n/a	5%	No limit
Maximum Bridge Width	-	-	-	-	No limit	No limit	No limit	n/a	-	No limit
Use RC Beams?	No	No	Yes	Yes	Yes	No	No	n/a	No	No
Individual Span Limit	-	-	-	-	No limit	n/a	n/a	n/a	n/a	n/a
Overall Span Limit	-	-	-	-	No limit	n/a	n/a	n/a	n/a	n/a
Maximum Skew	-	-	-	-	No limit	n/a	n/a	n/a	n/a	n/a
Maximum Roadway Grade	-	-	-	-	No limit	n/a	n/a	n/a	n/a	n/a
Maximum Bridge Width	-	-	-	-	No limit	n/a	n/a	n/a	n/a	n/a
Use PC Beams?	Yes	Yes	Yes	Yes	Yes	Yes	Yes	n/a	Yes	Yes
Individual Span Limit	-	-	-	-	No limit	150 ft	No limit	n/a	110 ft	No limit
Overall Span Limit	None	220 to 300 ft depending on skew	-	-	-	600 ft	400 ft	n/a	110 ft	700 ft
Maximum Skew	None	30 deg	-	-	-	20 deg	No limit	n/a	30 deg	30 deg
Maximum Roadway Grade	-	-	-	-	No limit	5%	No limit	n/a	5%	No limit
Maximum Bridge Width	-	-	-	-	No limit	None	No limit	n/a	-	No limit
Account for Creep/Shrinkage of PC Beams?	Yes	No	No	No	No	Yes	Yes	n/a	No	No

Table 3.7: State DOT phase 2 questionnaire responses regarding IAB/SIAB construction

	Indiana	Minnesota	Missouri	Montana	Nebraska	New Hampshire	Ohio	Oklahoma	Pennsylvania	South Dakota
Equipment Used	Contractor's option	-	Crane with pile driver, backhoe, concrete truck	Same as conventional	Typical equipment	Typical bridge construction equipment	-	Pile driving equipment	Standard construction equipment	Conventional bridge construction equipment
Construction Time Difference	-	-	-	-	Not much	Don't have information	-	Unaware of any difference	-	Little, if any
Embankment Material	Borrow	Existing material	-	-	No special requirement	Granular backfill	-	CLSM	AASHTO No. 1, 3, 5, or 57 coarse aggregate	Free draining material
Filling Material	Aggregate	Select granular (Spec 3149.2B4)	-	-	No special requirement	Granular backfill	-	CLSM	AASHTO No. 1, 3, 5, or 57 coarse aggregate	Free draining material
Maintenance Interval	Almost never	-	None required for IAB, flushing gaps and openings every 10 yrs for SIAB	-	Filling gap between slope protection and abutment, loss of backfill, preserving drainage and preventing rusting of piles near streams	Don't have information	-	Approach slab settlement with varying intervals	-	Routine maintenance only

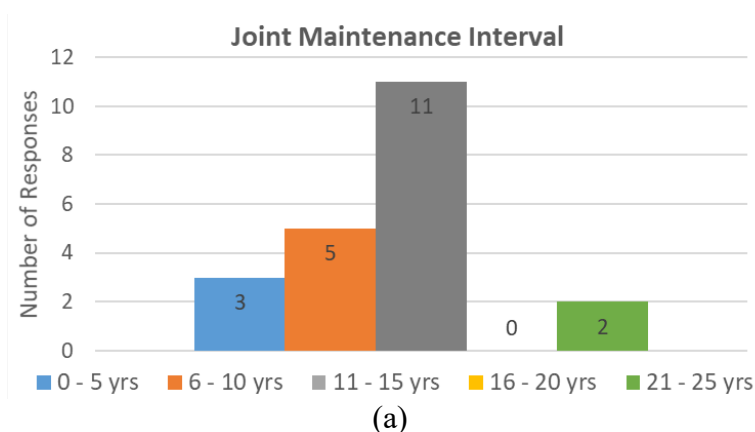
3.4.4. Texas District Survey

The survey of TxDOT Districts sought a better understanding of maintenance issues associated with bridges across the state, the current use and practices for approach slabs, and general thoughts regarding integral and semi-integral abutments.

Figure 3.3 depicts the responses related to bridge maintenance across the TxDOT Districts. Histograms of typical reoccurrence intervals for joint maintenance and the effect of maintenance on traffic are provided in Figure 3.3(a) and Figure 3.3(c), respectively. Percentages of districts responding to the problems that typically result in maintenance are shown as a pie chart in Figure 3.3(b), as more than one option shown in the legend could be chosen in the survey. From the data provided in this section of the survey, an average thermal expansion joint maintenance interval of 11 years, three months was calculated, which could result in six to nine maintenance projects on a bridge solely for expansion joints over its lifetime.

The single most common item leading to maintenance of conventional bridge structures typically constructed in Texas was deck problems, followed closely by embankment stability issues. Four of the respondents indicating “other” identified joint failure as a major maintenance issue, but the most common “other” reason by far was issues related to scour that often undermine the abutment area. Two respondents also mentioned vehicle impacts as an issue requiring frequent maintenance.

Regarding the effect of bridge maintenance on traffic, most districts identified a moderate to minimal effect. Those indicating “other” referred to the severity as dependent on the type of problem, with a consensus that issues on the deck and nearby riding surface were more severe. This suggests that maintenance associated with thermal expansion joints (which occurs approximately every 11 to 12 years) likely has the largest effect on traffic as compared to other bridge maintenance activities.



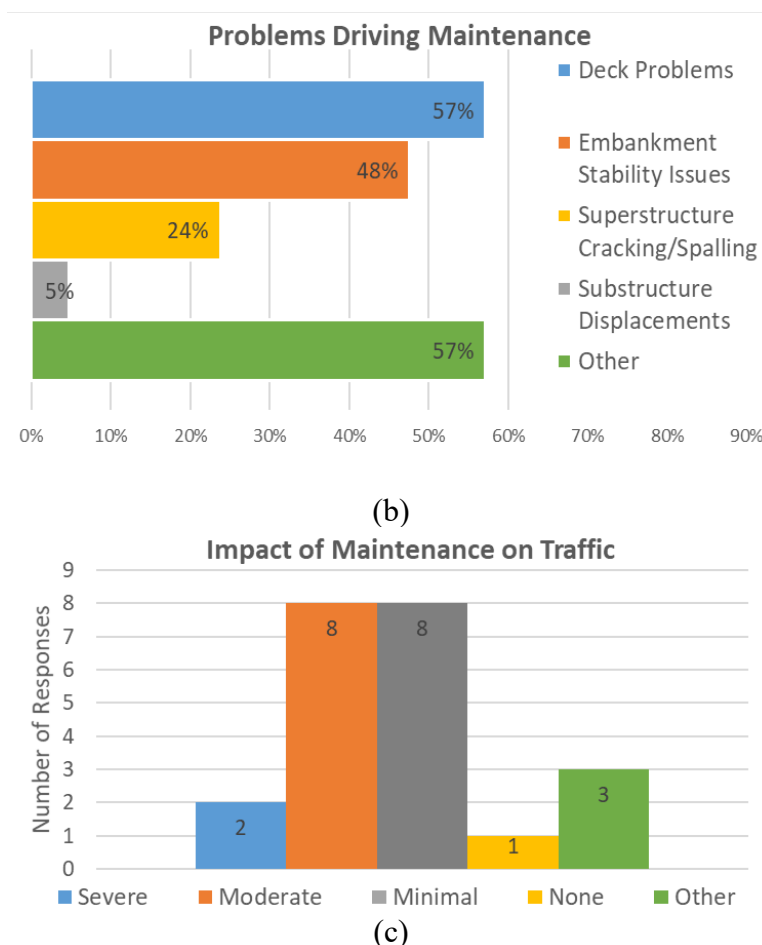


Figure 3.3: TxDOT District questionnaire responses regarding bridge maintenance: (a) joint maintenance interval; (b) problems driving maintenance; and (c) traffic effect of maintenance

The current use of approach slabs and standards used for design were of significant interest to TxDOT prior to dissemination of the Texas District survey, and thus multiple questions on this topic were added. Figure 3.4 illustrates responses to (a) the types of bridges that are designed with approach slabs, (b) the standards used for approach slab design, and (c) the type of joint preferred for construction of an approach-slab-to-roadway-transition on an IAB/SIAB. It was established that approach slabs are used in nearly all districts when designing an on-system bridge, but only about 29% of districts use them for off-system bridges. The districts that do not or selectively used approach slabs are Corpus Christi and Pharr, respectively, which are the two most southern districts. Furthermore, most districts used the statewide approach slab standards, but the following districts had modifications:

- Childress
- Atlanta
- Houston
- Dallas

Three of these four districts reside in the northern portion of the state. Regarding selection of the most effective joint type for an IAB/SIAB approach-slab-to-roadway-transition, twice as many districts selected the backer rod with silicone seal type as compared to the wide flange pavement terminal joint. Those indicating “other” attributed this answer to a lack of information on selecting the type of joint necessary for such a structure in an unknown project site.

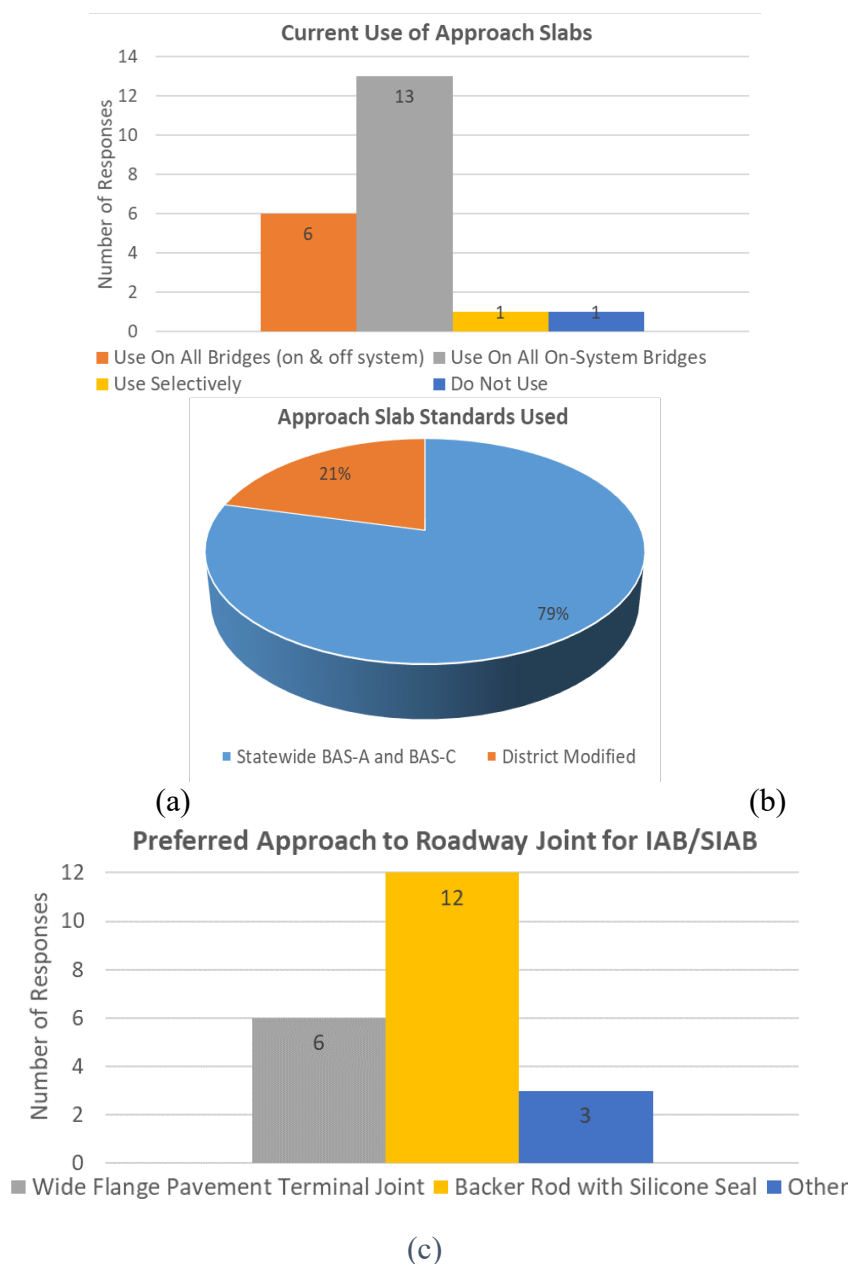
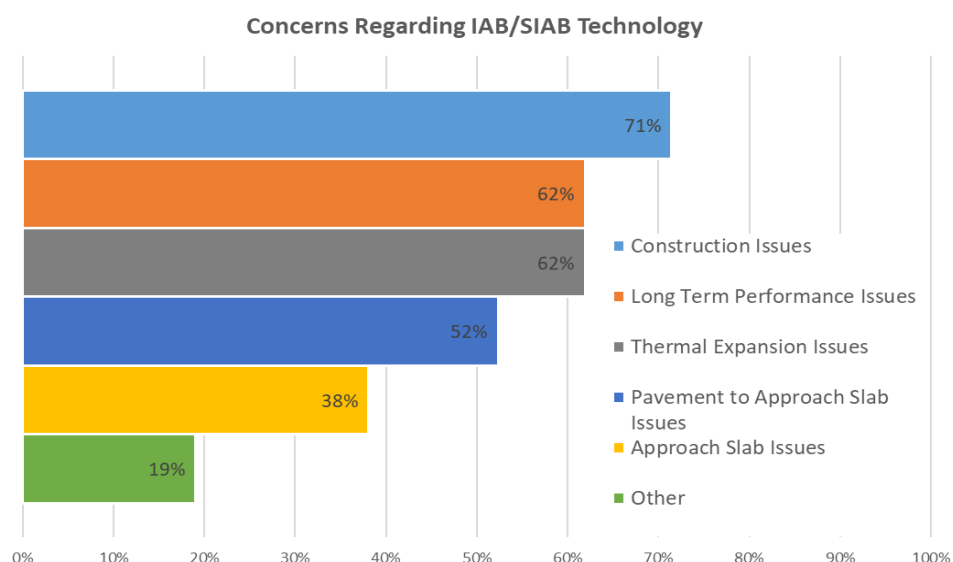


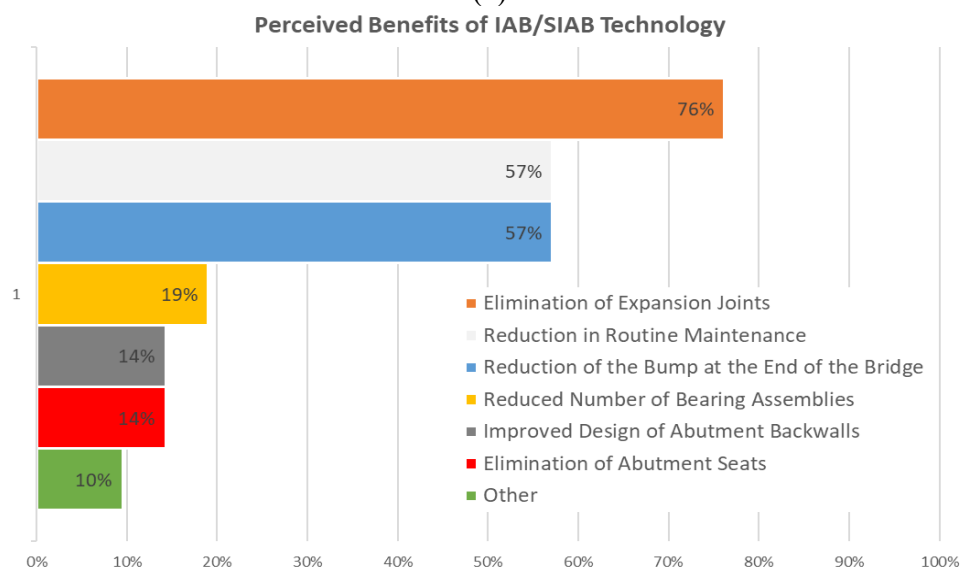
Figure 3.4: TxDOT District questionnaire responses regarding bridge approaches: (a) use of approach slabs; (b) standards used for approach slabs; and (c) preferred approach to roadway joint for IAB/SIAB

After reading an overview of IAB/SIAB (glossary of terms) and the perceived benefits of such structures (question 9) in the survey (Appendix A.3: TxDOT District Survey), district

representatives were asked about additional concerns or benefits he/she may foresee regarding this technology. Concerns were relatively wide-ranging among the different options provided, of which multiple could be selected, as shown in Figure 3.5(a). Representatives that selected “other” identified such issues as contractor weariness and a lack of familiarity for inspectors with the structure type. Additionally, it was reported that some IAB/SIAB in the Dallas District were required to be replaced with conventional structures due to poor performance. Regarding perceived benefits of IAB/SIAB technology, as shown in Figure 3.5(b), the majority of respondents selected the elimination of expansion joints, with over half selecting reduction of the bump at the end of the bridge and routine maintenance. Those who indicated “other” did not want to extrapolate benefits of the technology that are currently unknown in the State of Texas.



(a)



(b)

Figure 3.5: TxDOT District questionnaire responses regarding IAB/SIAB pros & cons: (a) IAB/SIAB concerns; and (b) IAB/SIAB potential benefits

All districts, excluding one of the three Houston District respondents, indicated a willingness to consider adopting IAB/SIAB technology. This response confirms interest and possible implementation of such structures in the State of Texas from a design perspective.

Chapter 4. Field Condition Assessments of Selected Texas Bridges

4.1. Introduction to Field Condition Assessments

Several bridge projects were selected for detailed documentation as case studies to provide an illustration for the ultimate design and detail recommendations compiled as part of this project. The applicability of common structure and substructure types in Texas is assessed, as well as a cost comparison between the selection of Integral/Semi-Integral Bridges (IAB/SIAB) and conventional bridge structures.

4.2. Bridges Inspected

Project 0-6936 required identification and field visits to a minimum of two bridges deemed relevant to the project objectives. The following bridges were selected for assessment:

- Anthony Road Bridge, near El Paso, TX (FM-1905 at I-10), a fully integral bridge
- Mack Creek Bridge, near Palestine, TX, an SIAB
- China Creek Bridge, near Wichita Falls, TX, an SIAB

These bridges were identified based on their diversity of structural, environmental and site characteristics in the following categories:

- Structural system
- Bridge type (includes integral and conventional bridge types)
- Foundation soil type
- Service age
- Maintenance frequency
- Weather conditions

Measurements and observations collected at each field condition assessment include, but are not limited to, the following:

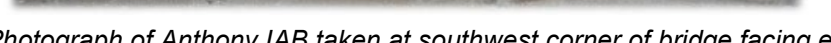
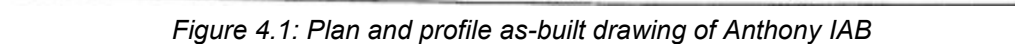
- Total station surveys of bridge abutments to determine batter and lateral movements
- Measurements to assess the “bump at the end of the bridge”

- Condition of abutment backwalls, beams, bearings and joints when applicable
- Evaluation of distress on all visible parts of the structure
- Approach pavement and bridge deck evaluation

4.2.1. Description of El Paso County IAB

The only IAB known to exist in the State of Texas is the Anthony IAB, carrying Antonio Street (FM 1905) over Interstate 10, in Anthony, TX. The Anthony IAB is a 222-ft-span, continuous steel plate girder bridge with integral abutments.

The abutments are each supported by a single row of eight driven steel H-piles, while the single interior pier is supported by 24 steel H-piles in a three-row configuration. The soil at the bridge site can be categorized as silty to coarse sand. Bridge construction was completed in May 1997. An excerpt from the as-built drawings of the bridge, including plan and profile, are provided in Figure 4.1. Additionally, a photograph of the bridge from an August 2017 visit is shown in Figure 4.2. In these figures, the fully integral nature of the abutment is demonstrated with callouts to specific details.



4.2.2. Description of Mack Creek SIAB

Concurrent with research activities, TxDOT constructed an SIAB outside Palestine, TX. This bridge carries County Road 2133 over Mack Creek and is thus commonly referred to as Mack Creek Bridge. Mack Creek Bridge measures 68.5 ft in length and 26.2 ft in overall width. The structure is a single-span, pre-stressed concrete box beam girder bridge supported by driven steel sheet pile foundations. The soil at the bridge site can generally be categorized as silty sand underlain by lean clay. Bridge construction was completed in July 2017. A photo of the bridge taken in August 2017 is shown in Figure 4.3.



Figure 4.3: Photograph of Mack Creek Bridge taken on north approach facing south

4.3. Survey Results

4.3.1. Survey of Anthony IAB

The fully integral bridge located in Anthony, TX (Anthony IAB) was surveyed using a non-prism total station on two different visits, characterized by different environmental conditions. The first survey was conducted on August 24, 2017 and the second was conducted on January 11, 2018. During the time of the first survey, the temperature ranged from 70° F to 76° F, while during the time of the second survey the temperature ranged from 50° F to 55° F. The temperatures during these two surveys in August and January represented cooler than average and warmer than average temperatures for the time of year respectively. Survey efforts on these days included shooting points on the face of the east and west facing abutments, as well as shooting points on the roadway/bridge deck along transitions from roadway to approach slab and approach slab to bridge deck. A close-up photograph of one of the steel girders set into the abutment (fully integral connection) and the survey point array is shown in Figure 4.4.



Figure 4.4: Photograph of survey points (orange dots) on Anthony IAB east abutment face

Figure 4.5 shows a photograph of the riding surface/deck of the Anthony IAB. During field visits, the turn-around lane was closed for observation and surveying activities, facilitating surveys of the transitions from the approach road to approach slab and approach slab to bridge deck. Figure 4.5 shows one alignment of survey points for this survey procedure.



Figure 4.5: Photograph of survey points (orange dots) on Anthony IAB west transition from roadway to approach slab and approach slab to bridge deck

Summaries of the bridge transition surveys conducted in the summer (August 2017) and winter (January 2018) are shown in Figure 4.6 and Figure 4.7, which show plots of the survey points identified in Figure 4.5 on the west transition area and mirrored points on the east transition area in Figure 4.4, respectively. The x-axis of these plots identifies the distance either east or west from the point of transition (indicated as 0 inches), with east in the positive direction and west in the negative direction. In each profile, the more distant west point surveyed was considered to be at a relative elevation of zero for simple visualization of the profile. It can be observed in these figures, and confirmed with visual observation of the bridge deck on site, that the riding surface slopes to the west with a more drastic slope along the west transition zone when compared to the east transition zone. This sloping profile in conjunction with the placement of traffic lights near the transition zones of the bridge led to a traffic loading that caused observed deterioration of the transition from the approaching road to approach slab on the west side of the bridge. A photograph of this distress in the primary traffic lanes is provided in Figure 4.8, with less deterioration in the turn-around lane, where surveys were conducted, likely because vehicles in the turn-around lane are not required to come to a stop. As a result, the surveyed profiles in Figure 4.6 do not illustrate this poor approach condition. Furthermore, the profiles shown in Figure 4.6 and Figure 4.7 do not show meaningful changes from summer to winter. It is possible that the bridge reached a steady-state condition since going into service over 20 years before these surveys were conducted. It is also possible that changes on the riding surface of reinforced concrete approach slabs are minimal due to integral abutment behavior.

Surveys of the bridge abutments detected that a very slight change in bridge length occurred between the August 2017 and January 2018 visits. This change in length was not consistent across the abutment faces, however, with some regions exhibiting contraction (as expected from summer to winter) and others expansion. This variation, from about 0.26 inches of contraction and 0.10 inches of expansion, indicates that the change in length between these two visits was within the range of surveying accuracy. The anticipated expansion of this steel girder bridge, with a 20°F change in temperature and using a thermal expansion coefficient of $6.0 \times 10^{-6}/^{\circ}\text{F}$ (Lafave et al., 2017), is 0.32 inches.

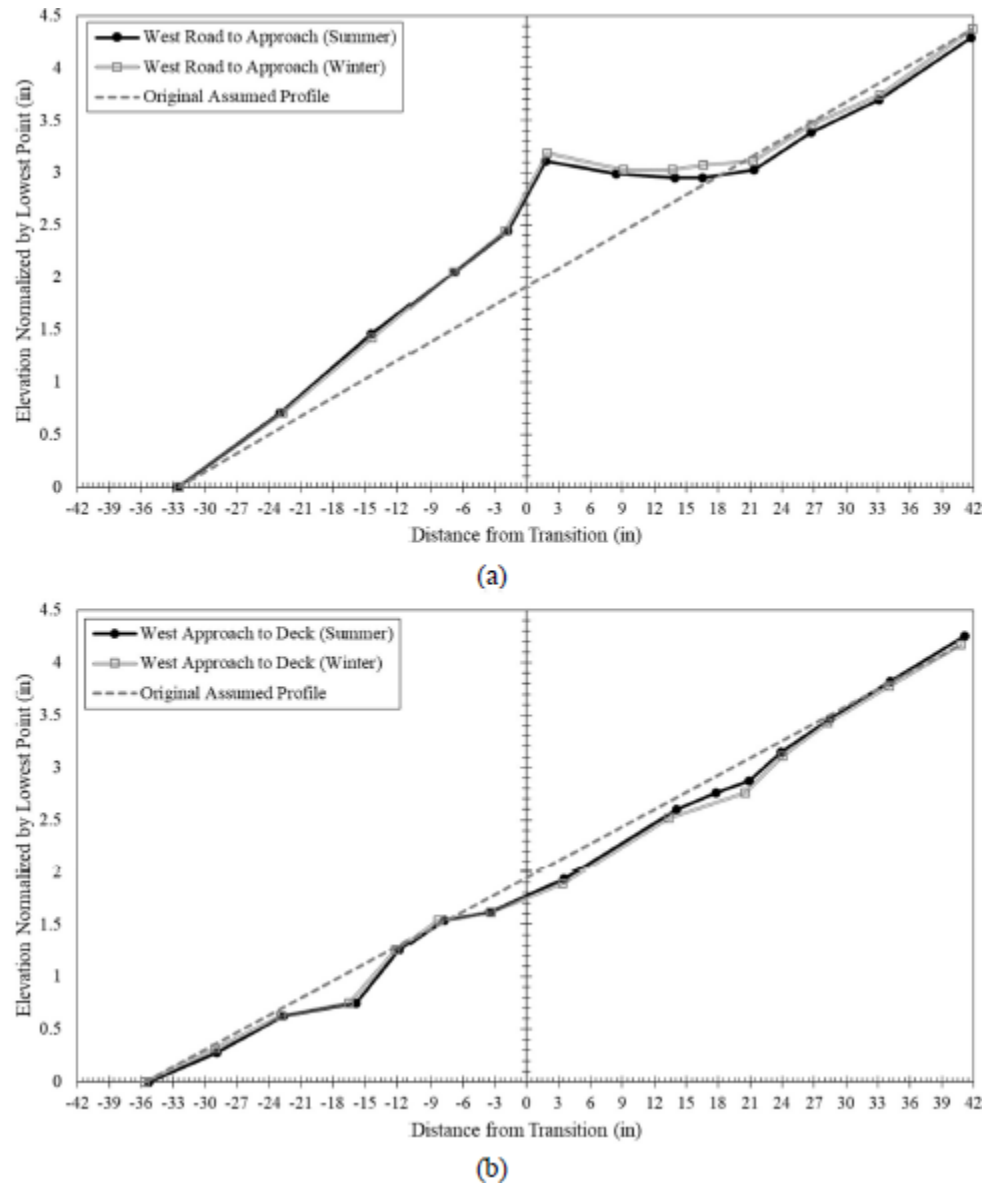
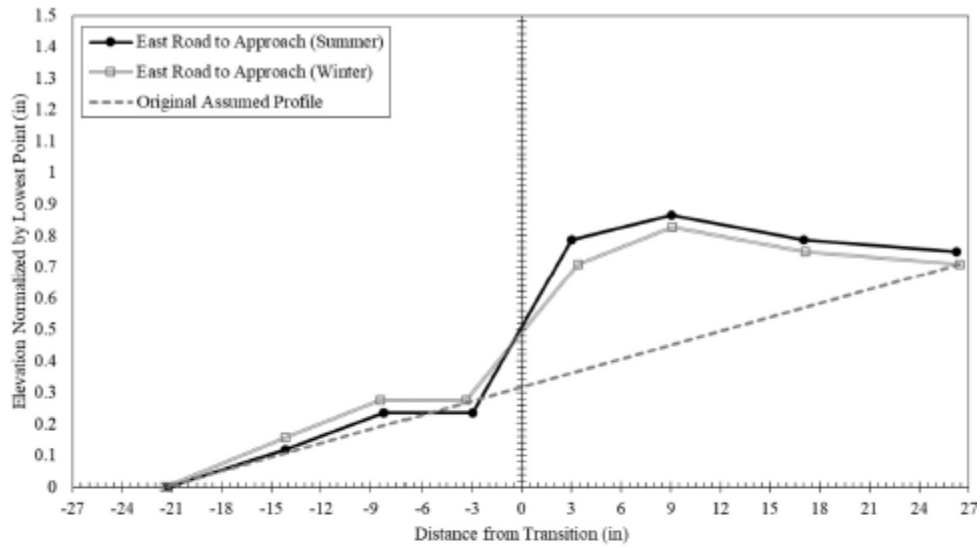
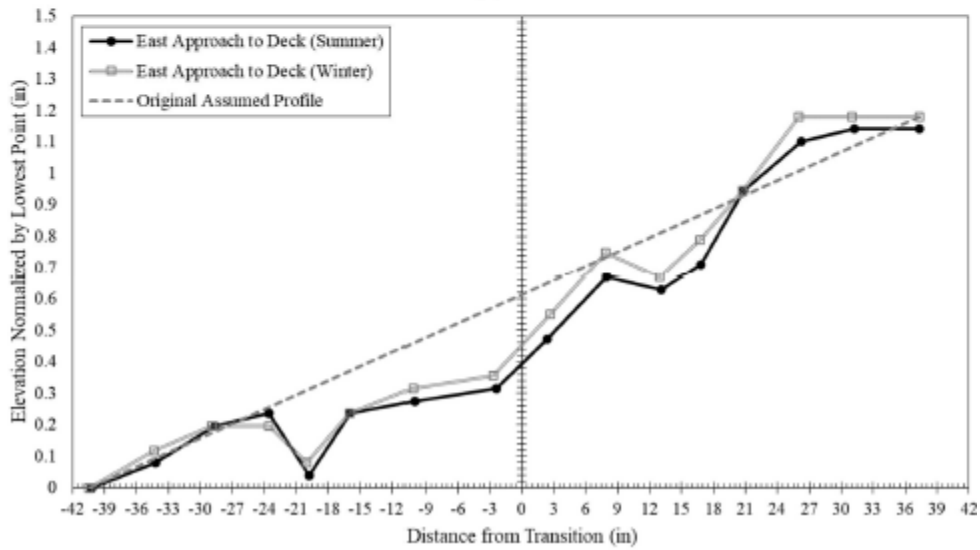


Figure 4.6: Summer and winter surveys of west transitions from: (a) roadway to approach slab; and (b) approach slab to bridge deck



(a)



(b)

Figure 4.7: Summer and winter surveys of east transitions from: (a) roadway to approach slab; and (b) approach slab to bridge deck



Figure 4.8: Photograph of west transition from approach road (left) to approach slab (right) on Anthony IAB

Since the surveys of the Anthony IAB did not show significant movements from temperature changes due to the integral performance of the structure, it was determined that the integral nature of the bridge did not result in any adverse effects.

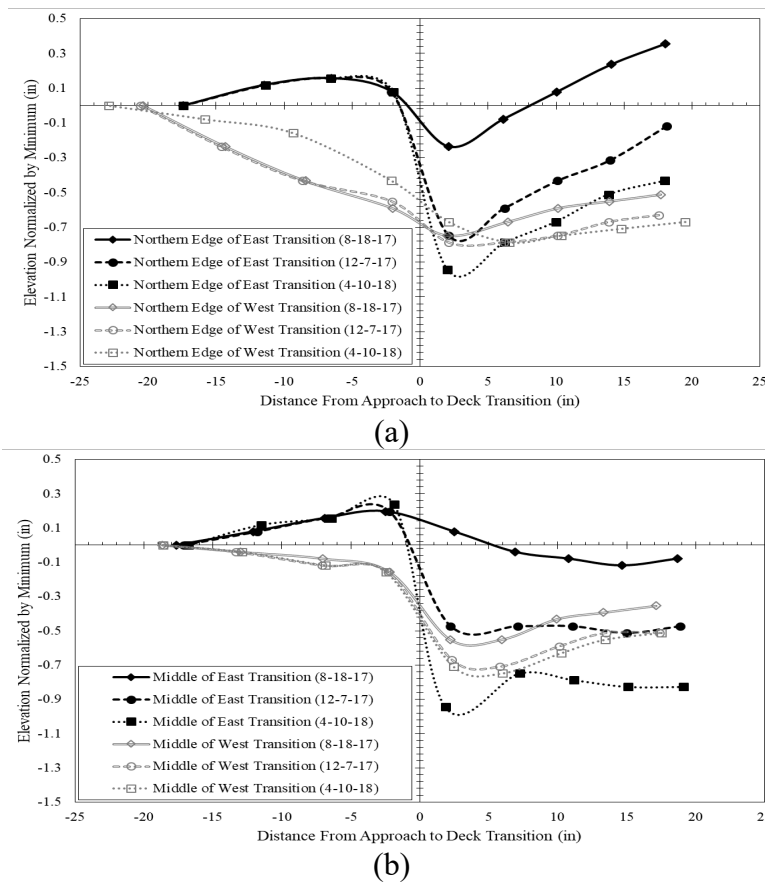
As Figure 4.8 shows, damage developed at the transition from the approach road to approach slab on the western transition, but this is primarily attributed to traffic loading. Overall, the construction of an IAB in this location allowed for the elimination of maintenance on thermal expansion joints and bridge bearings, which would have been necessary per the responses of the TxDOT District survey. Considering this cost savings, the use of an IAB structure in this location should be considered a success for TxDOT.

4.3.2. Survey of Mack Creek SIAB

Surveys of the approach-roadway-to-bridge-deck transition were conducted in three different locations on both the north and south approach-road-to-deck transition. Figure 4.9 depicts three plots of surveys conducted on profiles at the eastern edge, centerline and western edge of the transition zones from approach road to bridge deck. For each profile, the recorded point closest to the middle of the bridge was marked as an elevation of 0 inches for simple visualization and comparison of relative movement of profiles. Surveys were conducted on four different dates: August 18, 2017 (one month after construction completion); December 7, 2017; April 10, 2018; and October 16, 2018. By comparing the surveys on these three dates at any single location, a

bump at the end of the bridge can be observed on both sides that is gradually developing. This has been visually confirmed at the site and is quantified in Figure 4.10. In some cases, such as the centerline of the eastern transition (Figure 4.10), this bump development has also led to cracking of the approach road asphalt at the road-bridge deck interface (Figure 4.11). The cracking of the approach slab seen in Figure 4.11, which developed in a short four-month period from December 2017 to April 2018, led to maintenance performed at an unknown date before October 2018.

During the fourth visit, it was observed that the approach roadways had been repaved (Figure 4.12) near the abutment due to excessive settlement and the surveys conducted on this visit were consequently not compared with previously gathered data.



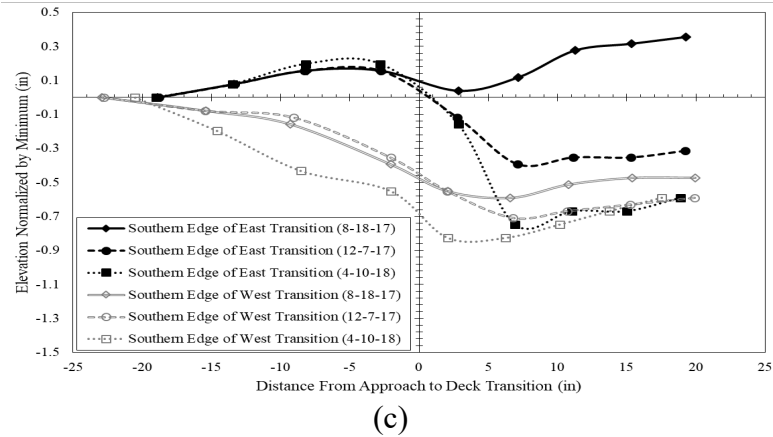


Figure 4.9: Survey points of bridge approach road to deck transitions during August 2017 and December 2017 for: (a) east approach; and (b) west approach

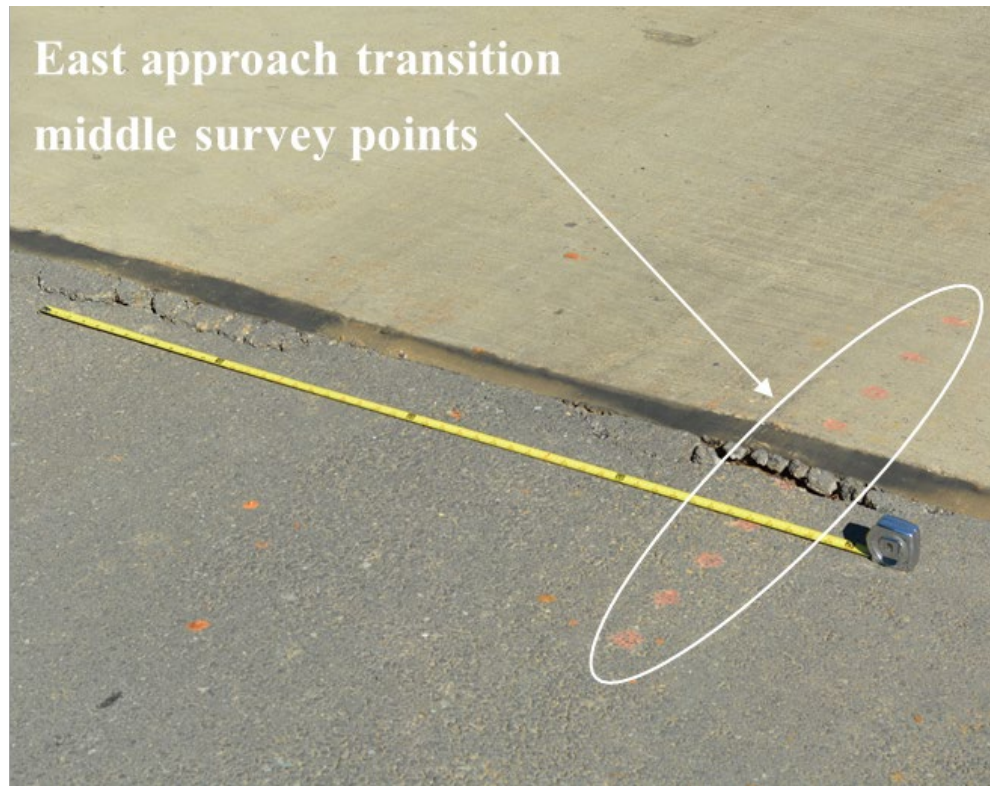


Figure 4.10: Photograph of bump at the end of Mack Creek Bridge and survey points on east approach centerline



(a)



(b)

Figure 4.11: Cracking at the approach slab-bridge deck connection: (a) 12/7/17; and (b) 4/10/18



Figure 4.12: Repaved approach slabs of Mack Creek Bridge (orange dots are survey points)

Since the original benchmarks for measuring differential settlement at the ends of the bridge were repaved, it was decided to monitor the difference in the elevation of guardrails at the ends of the bridge (Figure 4.13) as a measure for differential settlement.



Figure 4.13: Differential settlement revealed by the difference in height of guardrails between approach slab and bridge deck

The approximate differential settlement between guardrails was measured using a tape measure (Figure 4.14) and showed differential settlements of 1.5 – 2.0 inches on the north side and 3.25 – 3.5 inches on the south side. However, these numbers cannot be treated as true differential settlement between the backfill and bridge deck since the guardrails may not have been constructed flush to each other. Moreover, settlement near the edges are expected to be higher compared to the middle sections due to the presence of smaller confinement pressures. However, these numbers show that there is a difference in settlement between the two abutments and displacement on the south side is very significant.

Regarding the repaved approach slab, no significant bump or crack was detected in the repaved pavement portion since maintenance was done in fall 2018. This observation, combined with the rapid settlement observed over the first year since completion of construction, further supports the theory that the observed initial differential settlement must have been primarily due to migration of fines and not cyclic lateral expansion/contraction of the bridge.



Figure 4.14: Differential settlement between guardrails constructed on top of the deck and south approach slab (November 2019)

On average, across the three survey locations at each approach transition, the bump at the end of the bridge as of the April 10, 2018 survey was 1.076 in and 0.787 in on the east and west approaches, respectively. This differential settlement is unfavorable to the performance of the bridge. While the semi-integral nature of the structure may be attributed to the case of such excessive settlements of the backfill below the approach road, other construction issues may also

be at fault. After backfilling the semi-integral backwalls with select crushed rock backfill, native clayey soil was placed on top of the backfill prior to paving the asphalt approach road. Additionally, poor compaction techniques for the select backfill were implemented during construction and as a result, the approach road settlement may only be caused by consolidation of the soil beneath it (Figure 4.15). It is possible that the clayey soil gets compacted or pushed through the granular backfill over time as rain water seeps through the pavement cracks and cars pass over it, causing the approach road to settle continuously until most of the clayey material has settled. However, another foreseeable problem is that once this material mixes with the granular backfill, it could make the backfill weak, causing it to experience larger deformations by lowering its shear strength and stiffness. Therefore, it is strongly recommended to control and protect the backfill, especially near the abutments, to prevent excessive deformations that would require road maintenance in the short- and long-term.

Also anticipated is an average outward movement of the pile heads, which was recorded to be 0.21 inches between December and April. The anticipated amount of contraction between the hottest measured temperature (98°F) and coldest measured temperature (18°F) using a thermal expansion coefficient of $4.53 \times 10^{-6}/^{\circ}\text{F}$ is 0.30 inches, which puts the measurements within expected bounds. Movements toward the middle of the bridge of this magnitude would allow backfill soil to sluff down along the SIAB backwalls similar to what was observed in the experimental program.

Evidence that the settlements may be a result of the semi-integral nature of the bridge does exist however. Surveys of the underside of the bridge were compared across the three survey dates (8/18/2017, 12/7/2017 and 4/10/2018) where points were captured on the driven sheet piles, pile cap, and bridge girders. Movements at the head of the piles just beneath the pile cap showed an average inward movement of 0.34 inches from August to December, which is logical as average temperatures decreased during this timeframe. This shows that although the abutment is not integrally connected to the pile caps in SIAB, in cases where the bridge is constructed in summer, lateral forces on pile caps due to contraction of the bridge in winter can be expected. The magnitude of this force is expected to be directly proportional to the length of the bridge and changes in temperature from summer to winter. However, it may be reasonable to expect that this effect would be diminished if the bridge deck were completed in colder months; this would cause expansion of the bridge as the temperature rises and contraction back to its approximate original length. This scenario would likely lead to generation of larger backfill pressures against the abutment wall because it will primarily induce passive movements into the backfill soil.



Figure 4.15: Use of clayey natural soil as base material for asphalt pavement in approach slabs

During a visit to Mack Creek Bridge in November 2019, the presence of water on abutment caps and the bottom of girders on both sides of the bridge across the entire width of the bridge was detected. At this point, it is hard to explain how water made it to these locations since there are no expansion joints at the ends of this bridge that would protect the cap and bearings from the detrimental effects of surficial waters. In general, the southern side of the bridge appeared “wetter” compared to the northern side.

As can be seen in Figure 4.16, the northern abutment cap appears wet. Moreover, Figure 4.17 shows water droplets gathering underneath the box girders near the southern side from the abutment to the middle of the bridge. These water droplets are generally located near small gaps in between the adjacent girders. However, it is hard to imagine this water has flown from the surface of the bridge since the deck is made of concrete and there are no major cracks apparent on the deck. In Figure 4.18, a closer view of these water droplets is shown. According to weather records, 0.11 inches of rain was recorded the previous night at a Palestine, TX weather station, which may have caused water runoff to find its way to the top of the pile caps. However, it is hard to imagine how runoff could have found its way to the bottom, and especially the middle, of the girders. Additionally, it is hard to imagine what could have caused water droplets to only gather near the edges of the box girders and not in the middle of each girder.

As one of the advantages of omitting expansion joints between bridge deck and approach slab is to stop water runoff from causing damage to the bearing pads, future designs should be modified to stop water runoff (which could also carry harmful chemicals such as deicing salts) from

flowing to the pile cap by adjusting the geometry of abutment elements while considering the topography of the area. This will help with maximizing the benefits of SIAB/IAB structures in comparison with conventional bridge design.



Figure 4.16: Traces of water on the northern abutment cap under the bridge deck



Figure 4.17: Water gathered under the box girders (view from south abutment)



Figure 4.18: Water droplets gathered underneath the girders

In January 2020, a new set of sensors that were originally intended for China Creek were installed on Mack Creek Bridge to help gather complementary information about the behavior and performance of this bridge. During this installation, the research team discovered signs of excessive settlement of the concrete placed behind the wingwalls of both abutments and both sides (Figure 4.19). According to the drawings, this concrete is not structural (unreinforced) and was placed there to seal the surface of the fine-grained soil placed as backfill behind the sheetpile sections used for the wingwalls.

It is evident from the documented construction activities that the soil placed behind the wingwalls is the same material originally excavated from the site and therefore is a mixture of silty sands and sandy clays, which is not protected against erosion due to water infiltration after a rain event. Further inspection of gaps between the sheetpiles and pile cap (as is evident in **Error! Reference source not found.**) confirms the suspicion that these fines were eroded over time, creating large voids underneath the concrete, causing settlement and cracking.

Although this damage may not threaten the safety of the structure (as these are non-load bearing/structural components), it does lead to major cosmetic damage and the erosion damage may cause damage to the approach shoulders, requiring expensive maintenance in the future, especially in more high-profile locations.

In the case of this research project, it was discovered that the settlement of the concrete above the sheetpiles led to severe damage to the buried earth pressure cell cables as they were originally

routed through the now-eroded fill. As more settlement of the concrete occurred, these cables were dragged down and subsequently damaged, cutting off connection with the data logger (Figure 4.22). Although the sensors were not lost, it was necessary to free the cables and reroute them back to the data logger to continue collecting earth pressure data.

The observation program of Mack Creek Bridge via total station surveys, pressure cells and temperature recordings provided an excellent baseline SIAB in the State of Texas with which to assess performance.



Figure 4.19: Settlement of concrete placed behind wingwalls (southwest wingwall)



Figure 4.20: Loss of fill placed behind wingwalls due to erosion (left image shows an overhead view of the gap between sheetpile and pile cap)



Figure 4.21: Void caused by erosion of fill under shoulder of southern approach



Figure 4.22: Damage to earth pressure cell cables due to unanticipated settlement of concrete

4.4. Material Characterization

As part of the efforts to understand the performance of the SIAB over Mack Creek, a large quantity of the backfill material was collected during backfilling operations and brought back to the geotechnical laboratories at the University of Texas at Austin for subsequent testing and characterization. This material can be seen in Figure 4.15 and was used in the field. This aggregate was identified as D-Rock by the contractors of the project. The gravel particles are industrially produced by crushing larger pieces of rock and are not a naturally occurring aggregate.

To characterize this material in terms of strength and also with the goal to use the results in subsequent numerical modeling of the structure, a series of consolidated drained triaxial tests were performed. Among different modes of triaxial testing, consolidated drained testing was chosen as the most appropriate mode to understand field performance since the material being tested is made of large and relatively clean aggregates (high hydraulic conductivity) and loading rate is very small (small level of displacement over the course of a day).

Due to the fact that the grains of this soil can be as big as 0.5 inches, a triaxial cell larger than 3 inches in diameter is needed (ASTM D7181-11). For this purpose, a 6 inch-diameter triaxial cell was assembled to accommodate the testing program. A picture of the triaxial setup can be seen in Figure 4.23. This triaxial setup provided 1.5” total stroke (~10% axial strain) and 2,000 lbs (~72 psi) load capacity.



Figure 4.23: Triaxial setup used to measure shear strength of Mack Creek soil

Due to high angularity of the aggregates, compaction efforts had to be minimized to prevent membrane puncture (which occurred twice in this testing program) and therefore the results presented are for lightly compacted material.

To run a successful CD triaxial test, it must be ensured that the specimen is fully saturated so that the volume of outflow/inflow is equal to changes in pore volume and also to be able to sustain a constant pore and cell pressure during shearing as the specimen undergoes volume change. To this end, the specimen in each test was backpressure saturated to 60-70 psi followed by a final B-value check. The calculated B-value for each specimen was 0.94 and it was found that a higher B-value was not obtainable due to stiffness of the crushed rock aggregates themselves.

After backpressure saturation was completed, the shearing stage was started. Overall, three triaxial tests at effective confining pressures of 6, 9 and 12 psi were conducted to define the Mohr-Coulomb failure envelope and stiffness parameters. The stress-strain curve for these tests is shown in Figure 4.24 and the axial strain-volumetric strain curve is shown in Figure 4.25.

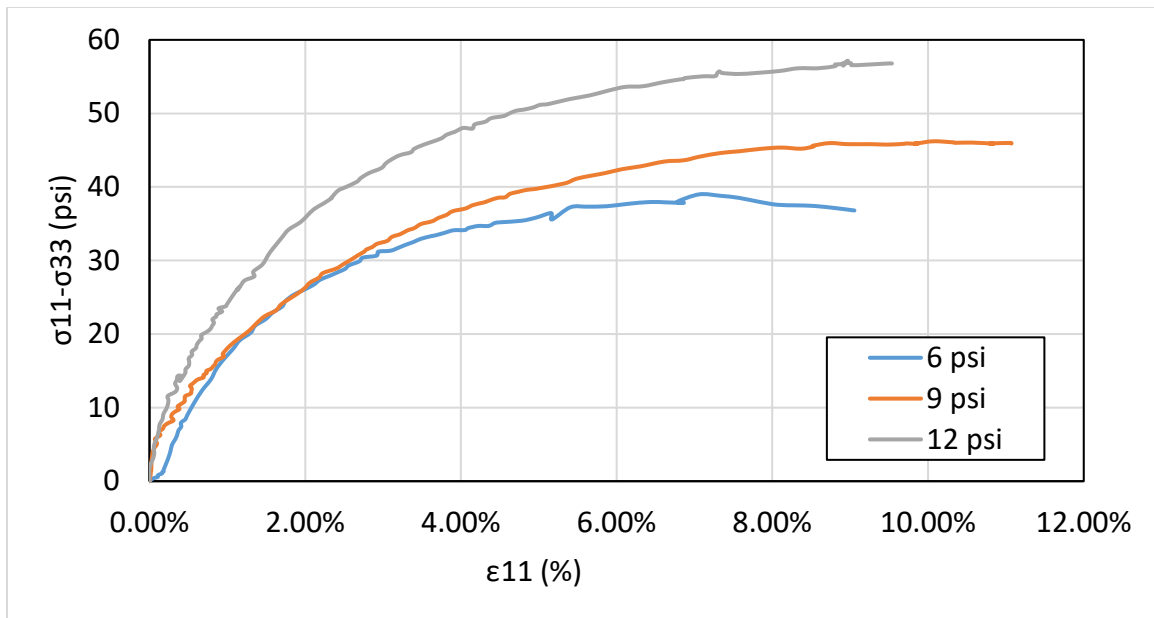


Figure 4.24: Triaxial test results for Mack Creek backfill soil (stress-strain curves)

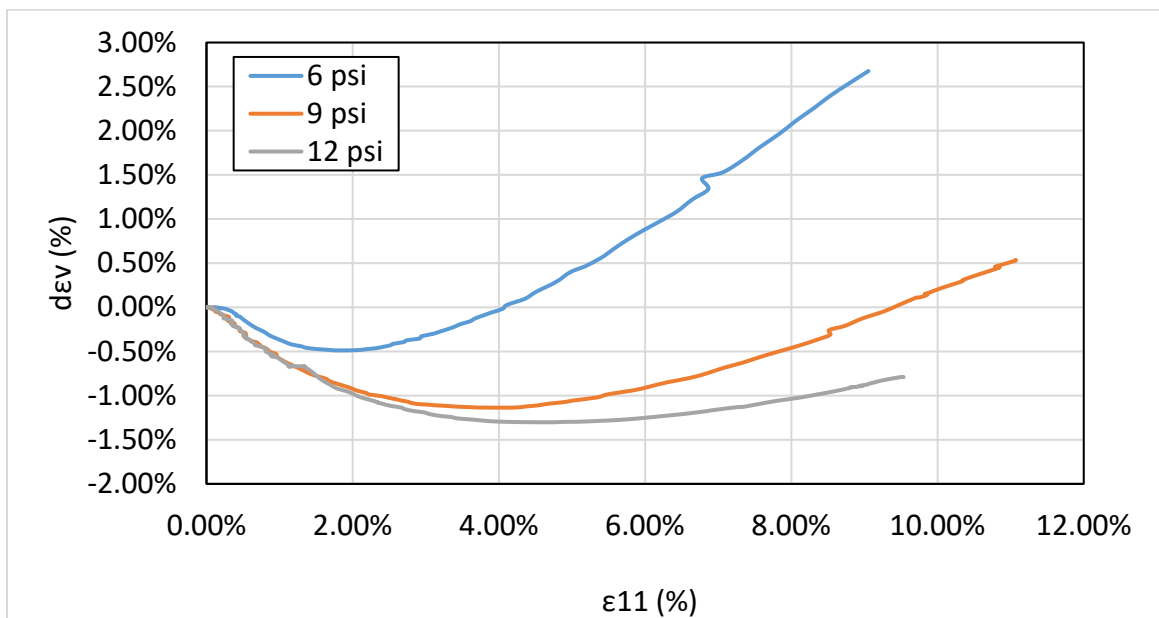


Figure 4.25: Triaxial test results for Mack Creek soil (volumetric strain data)

This material exhibited dilative behavior, despite being very lightly compacted, which is most likely due to the high degree of angularity of these particles. Inspection of the specimen after the cell was drained showed that no clear shear failure plane was observable with the naked eye and the samples appeared to experience a bulging failure, as is typical in granular materials. Figure 4.26 displays a picture of the post-shearing specimen.



Figure 4.26: Triaxial specimen at failure (9 psi effective confinement)

To obtain the Mohr-Coulomb failure envelope for this soil, Mohr circles of each specimen at the time of failure were drawn together in Figure 4.27. Moreover, the secant friction angles for each test were also calculated. These parameters are summarized in Table 4.1. As can be seen, the best fit linear Mohr-Coulomb failure envelope requires an apparent cohesion intercept of 1.5 psi, which is close to the expected zero cohesion intercept and may be due to slight local density/gradation variations between the samples.

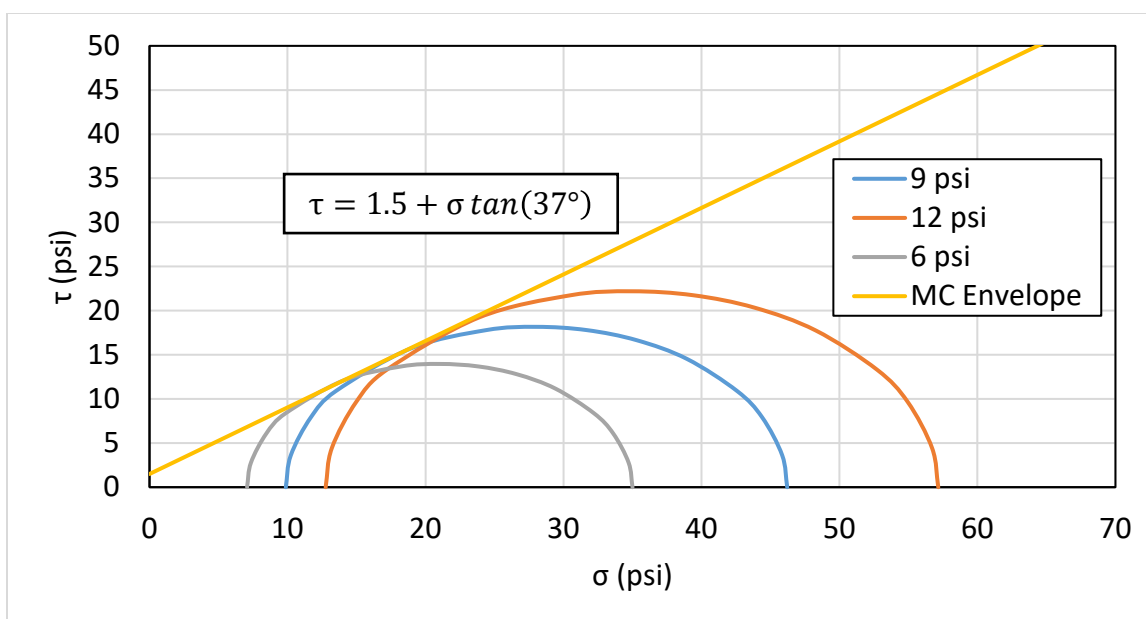


Figure 4.27: Mohr circles at failure for the triaxial tests performed on Mack Creek backfill with Mohr-Coulomb failure envelope of $\tau = 1.5 + \sigma \tan(37^\circ)$

To utilize the test results for subsequent numerical analysis, a parameter fitting using a hardening soil model as defined in Plaxis 2016 Material Models Manual was performed.

Therefore, the hardening soil model parameters that provided an optimal match to the laboratory tests were found. In the fitting process, more weight was given to 9- and 12-psi tests as the 6-psi specimen had a slightly higher density, also indicated by the behavior shown in Figure 4.25. As demonstrated by Figure 4.28 and Figure 4.29, a hardening soil model can do a decent job in capturing the behavior of this material in triaxial testing simulations. However, a good match in triaxial conditions still does not guarantee a good match in field behavior, as the soil in the field is under different stress conditions (plane strain) than in a triaxial cell and further adjustments will be needed.

Table 4.1: Secant friction angle and overall MC failure envelope based on CD triaxial tests on Mack Creek backfill material

Effective confinement (psi)	Cohesion intercept (psi)	Angle of friction
6	0	48
9	0	45
12	0	42.5
Overall	4.7	36

The best fit parameters for modeling the Mack Creek soil using the Hardening Soil Model offered in Plaxis were found through an optimization process using a combination of Excel programming and a Plaxis Soil Test module. The results are summarized in Table 4.2. The

Hardening Soil fit uses a higher angle of friction and slightly lower apparent cohesion intercept than the classic Mohr Coulomb model due to the fact that in the hardening soil model, ultimate shear strength is a factor (R_f) of what is predicted by Mohr-Coulomb parameters and the soil will reach a shear strength that is below that predicted without using this factor.

Table 4.2: Best fit parameters used in modeling Mack Creek backfill soil using Hardening Soil model of Plaxis

Parameter	Unit	Value
E_{50}^{ref}	Psi	1400
E_{oed}^{ref}	Psi	500
E_{ur}^{ref}	Psi	3500
Power (m)	-	1
ν'_{ur}	-	0.1
K_0^{nc}	-	0.3374
P_{ref}	Psi	9
c'_{ref}	Psi	1.6
ϕ'	Degree	41.5
ψ'	Degree	9.5
R_f	-	0.89

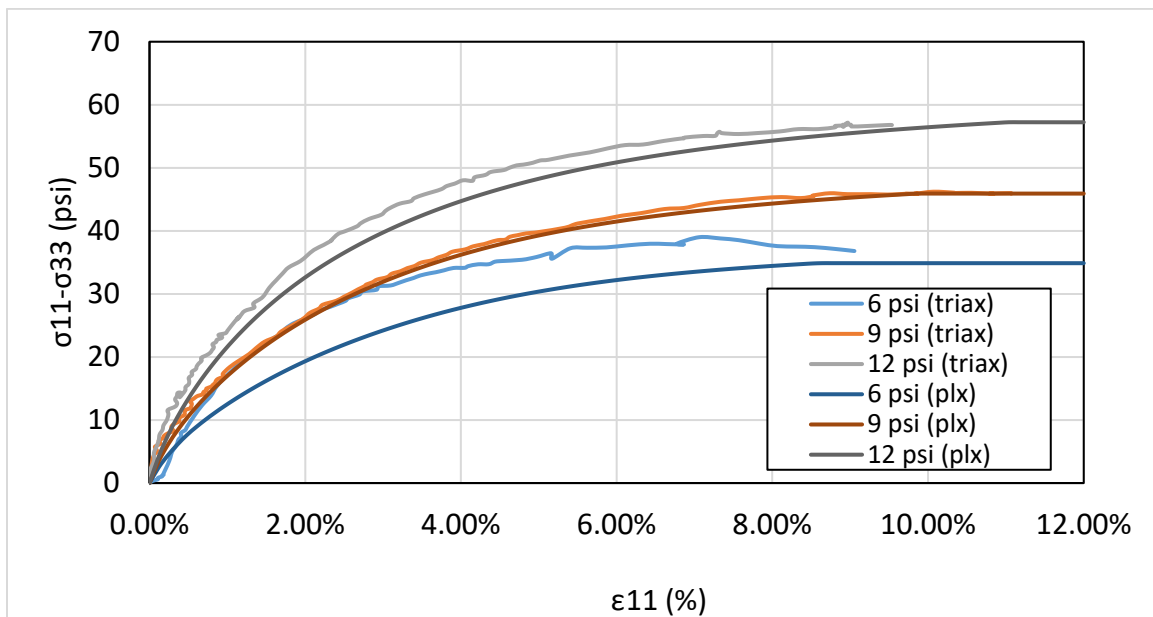


Figure 4.28: Comparison of simulated triaxial results from hardening soil models with actual triaxial tests performed in the laboratory (stress-strain curves)

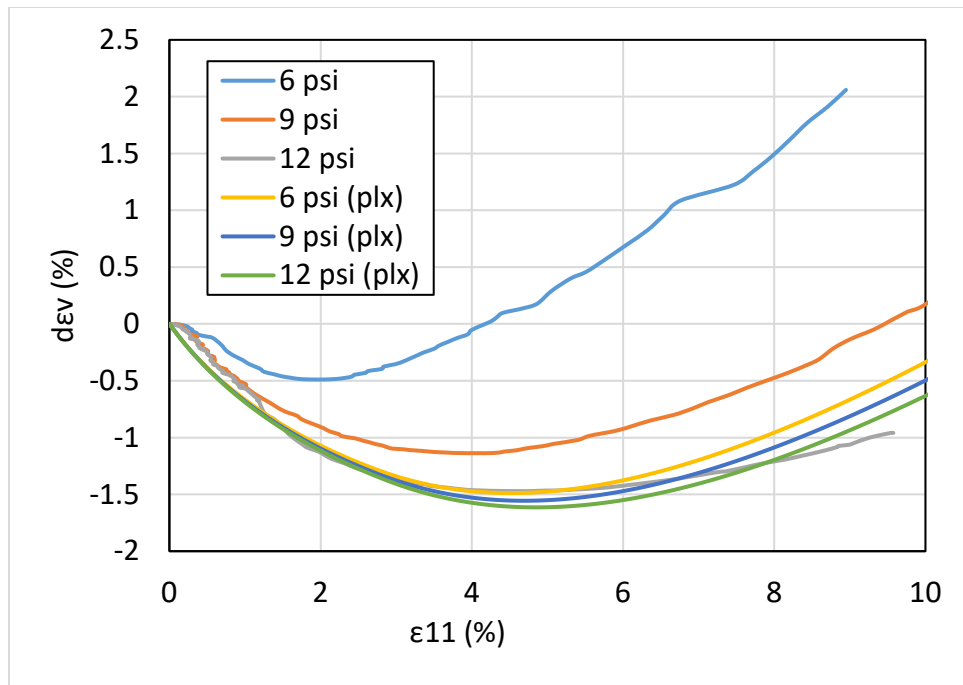


Figure 4.29: Comparison of simulated triaxial results from hardening soil models with actual triaxial tests performed in the laboratory (volumetric strain curves)

4.5. Conclusion to Field Condition Assessments

Although the Integral Abutment Bridge (IAB) near El Paso, TX has not been monitored since construction, it appears to be performing very well with very little damage observed near the approach slabs or on the structural components of the bridge. It therefore seems to be a promising bridge technology for the State of Texas.

On the other hand, the survey results from Mack Creek Semi-Integral Abutment Bridge (SIAB) revealed significant issues had developed in the short time since construction, including cracks in the approach slab, excessive settlement of the backfill and the appearance of a bump at the end of the road. Although the semi-integral nature of the bridge can be identified as one cause of these issues, another major reason for the damages observed thus far is the accidental use of clayey natural soil as base material for the approach pavement. Therefore, an important lesson learned from this project is to maintain close control of the material used in the backfill, especially if cyclic abutment movements are expected.

In November 2019, the presence of water on abutment caps and the bottom of box girders was detected, despite the lack of expansion joints in this bridge. While it is not clear how water found its way to the bottom of the box girders in the middle of the bridge, it is important to closely monitor this issue to understand how water could have found its way there. It would be beneficial to adjust the design/geometry of abutment elements so this does not happen to protect

bearing pads and abutment caps from chemicals carried by water runoff that could harm their long-term integrity.

The soil used as backfill at Mack Creek Bridge appears to be highly angular and behave as a dilative material, even under the higher confinement expected in the field. As for subsequent numerical simulations, the hardening soil model, which is the most sophisticated material model available in Plaxis, was chosen to represent this material. The hardening soil model parameters for this soil were obtained after a thorough optimization process, resulting in a good starting point for future simulations. To better model the behavior of the backfill soil, corrections would need to be made to the failure envelope and stiffness parameters to account for differences between triaxial and plane strain states of stresses and strains.

Chapter 5. Identification of Relevant Parameters and Quantification of the Range of their Representative Values

5.1. Introduction to Identification of Relevant Parameters for Numerical Simulations

The goal of this component of the study is to identify relevant parameters necessary for subsequent numerical simulation, including those needed in Texas soils, foundation details, superstructure types, substructure types and approach pavement designs. The ultimate goal is to assess the sensitivity of these parameters particularly relevant to potential projects in Texas.

5.2. Baseline Structure Identification

Mack Creek Semi-Integral Abutment Bridge (SIAB) was chosen as the baseline structure because it has been instrumented and closely monitored from the beginning of this project and sufficient information is available regarding the details of this structure through the drawings provided by TxDOT prior to construction. In addition, the soil profile data close to both abutments was obtained via Texas Cone Penetrometer (TCP) and USCS classifications of these soils are known, which would help establish an initial baseline model. The ambient temperature and abutment pressures have also been recorded every hour of each day since the beginning of the project, which would help calibrate the model to match the field response as best as possible.

5.3. Subsoil Characteristics

The site investigation included a TCP test carried out near the construction location of each abutment. The TCP test is the prospection method used by TxDOT and was developed in cooperation with the Materials & Tests and Equipment & Procurement Divisions (Palla et al., 2008). This prospection method is a dynamic field penetration test and determines penetration resistance of a cone that can be used to evaluate the soil relative density or consistency, and load bearing capacity of geomaterials encountered during geotechnical investigation (Moghaddam, 2016).

The TCP test procedure is standardized by TxDOT and documented as TxDOT Designation: Tex-132-E – Test Procedure for Texas Cone Penetration. This procedure consists of dropping, from a 0.6-m drop height, a 755-N hammer to drive a 76-mm diameter penetrometer cone attached to a 60-mm drill stem in soil or rock. The penetration is performed in three separate increments, and the first increment is completed after 12 blows or 0.15 m, whichever happens first. The result consists of the sum of the number of blows needed to achieve second and third 0.15-m increments of cone penetration. In hard materials, including rocks, after the first

increment is completed, the cone is driven 100 blows, and the penetration values for the first and second 50 blows are recorded. Further details about the TCP test can be found in TxDOT (1999).

According to the results of the TCP tests, it was possible to identify that the subsoil is composed of a 21.3-ft-thick silty sand layer over a sandy clay layer near the north abutment, while an 8.2-ft-thick clayey sand layer followed by a sand clay layer was found near the south abutment. At the time of the ground prospection, the phreatic level was located at a depth of 15.91 ft. Further details on the results of the TCP tests can be found in TxDOT (2016).

5.4. Material Properties

5.4.1. Mack Creek Parameters

The stress-strain behavior of the soil materials was represented by the Hardening Soil hyperbolic constitutive model. The Hardening Soil model is an elastoplastic type of advanced hyperbolic model, based on the Plasticity Theory, for simulating the behavior of different types of soils, both soft and stiff soils, which include soil dilatancy and introduce a yield cap. In this constitutive model, irreversible strains due to primary deviatoric loading are modeled through shear hardening while irreversible plastic strains due to primary compression in oedometer loading and isotropic loading are modeled through compression hardening. The stress-strain behavior of the structural materials was represented by the linear elastic constitutive model. The linear elastic model represents Hooke's law of isotropic linear elasticity for simulating the behavior of stiff structures in the soil, such as concrete elements or plates. Further details about the constitutive models can be found in Brinkgreve, Kumarswamy and Swolfs (2016).

Due to the limited subsurface survey performed at the site and the absence of laboratory tests on natural soil, soil parameters were obtained based on the results of the two TCP tests and the technical literature. Available correlations between the N_{TCP} resistance number and drained and undrained shear strength parameters were used (Lawson et al., 2018; TxDOT, 2018; Vasudevan, 2005; Vipulanandan et al., 2008). Also, information from different sources in the technical literature on design parameters for typical soil types were consulted (Bowles, 1997; Kulhawy and Mayne, 1990; Mesri, 1975; Poulos and Davis, 1974; Stroud and Butler, 1975; Tomlinson, 1993). Different sources were also consulted to define the parameters of the structural materials due to the absence of laboratory data (AASHTO, 2012; Abdel-Fattah et al., 2017; Cai and Ross, 2010; Caristo et al., 2018; Gerdau, 2019; Mahendran, 1996; Peric et al., 2016; Roylance, 2008; Suchsland and Woodson, 1987; TxDOT, 2016; Zheng and Fox, 2017). Table 5.1 and Table 5.2 show the material parameters used in the preliminary numerical model.

Table 5.1: Soil parameters used in the preliminary numerical model

Parameters	Unit	Material			
		M1	M2	M3	M4
Unsaturated unit weight	γ_{unsat} kN/m ³	19	17	17	20
Saturated unit weight	γ_{sat} kN/m ³	22	20	20	23
Secant stiffness in standard drained triaxial test	E_{50}^{ref} MPa	60	40	32	32
Tangent stiffness for primary oedometer loading	E_{oed}^{ref} MPa	60	40	32	32
Unloading/loading stiffness	E_{ur}^{ref} MPa	180	120	96	96
Undrained shear strength at reference level	$S_{u,ref}$ kPa	210	-	-	-
Effective cohesion	c'_{ref} kPa	-	15	15	1
Effective friction angle	ϕ' °	-	31.5	31.5	40

Table 5.2: Structural parameters used in the preliminary numerical model

Parameters	Unit	M5	M6	Material	
				Sheet pile foundation	Sheet pile anchor
Unsaturated unit weight	γ_{unsat} kN/m ³	25	10	-	-
Young's modulus	E GPa	30	4	-	-
Poisson's ratio	ν -	0.2	0.2	0.3	-
Normal stiffness (Foundation)	EA kN/m	-	-	3.163E6	-
Flexural rigidity	EI kNm ² /m	-	-	73.27E3	-
Weight	w kN/m/m	-	-	1.182	-
Normal stiffness (anchor)	EA kN	-	-	-	69.31E3

The material M1 represents the sandy clay, M2 represents the silty sand, M3 represents the same material as M2 after backfilling, M4 represents the gravel, M5 represents the reinforced concrete and M6 represents a fiberboard material used to fill the space between the abutment and pile cap. Power for stress-level dependency of stiffness with a value of 0.5 was adopted as suggested by many researchers (Duncan and Chang, 1970; Janbu, 1963; Lade and Nelson, 1987; Schanz and Vermeer, 1998). Undrained conditions were assumed for the sandy clay while drained conditions were assumed for the silty sand and the gravel. Non-porous conditions were assumed for the reinforced concrete and the fiberboard material. These conditions were chosen based on material type and were adopted to validate the baseline numerical model. The soil parameters were associated to a reference stress for stiffnesses (p_{ref}) equal to 14.5 psi, which is the default value of the software (Brinkgreve, Kumarswamy and Swolfs 2016).

An alternative approach to the preliminary numerical model was proposed by considering the influence of the elastomeric bearing pad. The stress-strain behavior of the bearing pad was modeled as linear elastic and the material properties were assigned based on AASHTO LRFD Bridge Design Specifications (2012). The values for the bearing pad parameters were unit weight (γ) equal to 15 kN/m³, Young's modulus (E) equal to 3 MPa and Poisson's ratio (ν) equal to 0.5.

The soil and structural parameters used in the alternative approach were the same as those used in the preliminary numerical model.

Due to high computational costs and the results using the alternative approach, some alterations in the soil and structural parameters of the preliminary numerical model were made to try a better match between field and numerical data. Table 5.3 and Table 5.4 show the soil and structural parameters used in the calibration of the preliminary numerical model.

Table 5.3: Soil parameters used in the calibration of the preliminary numerical model

Parameter	Unit	Sandy clay	Silty sand	Gravel
Unsaturated unit weight (γ_{unsat})	kN/m ³	19	17	20
Saturated unit weight (γ_{sat})	kN/m ³	22	20	23
Secant stiffness in standard drained triaxial test (E_{50}^{ref})	MPa	60	40	30
Tangent stiffness for primary oedometer loading ($E_{\text{oed}}^{\text{ref}}$)	MPa	60	40	30
Unloading/loading stiffness ($E_{\text{ur}}^{\text{ref}}$)	MPa	180	120	90
Undrained shear strength at reference level ($S_{\text{u,ref}}$)	kPa	210	-	-
Effective cohesion (c'_{ref})	kPa	-	15	1
Effective friction angle (ϕ')	°	-	31.5	40

Table 5.4: Structural parameters used in the calibration of the preliminary numerical model

Parameter	Unit	M5	M6	Foundation	Anchor
Unit weight (γ)	kN/m ³	25	10	-	-
Young's modulus (E)	GPa	30	4	-	-
Poisson's ratio (ν)	-	0.2	0.2	0.3	-
Normal stiffness (EA) – Plate	kN/m	-	-	3.163×10^6	-
Flexural rigidity (EI)	kNm ² /m	-	-	7.33×10^4	-
Weight (w)	kN/m/m	-	-	1.18	-
Normal stiffness (EA) – Anchor	kN	-	-	-	2.99×10^6
Out-of-plane spacing (L_{spacing})	m	-	-	-	2.62

5.4.2. China Creek Parameters

As construction of different components of China Creek Bridge took place, the research team collected different pieces of information to help with subsequent numerical modeling of the bridge. These efforts included collecting soil samples from the field during the installation of drilled shafts as well as documenting the strength properties of the concrete placed in different parts of the structure, as tested and reported by the Wichita Falls TXDOT Office. These records facilitated understanding the extent of variability in construction as well as aided with modeling the interaction between different components of the bridge. An example concrete cylinder test result for the 28th day strength is shown in Figure 5.1. Once construction was completed and all test results were obtained, the research team generated appropriate material models, which considered the effect of reinforcing steel and informed the model used for numerical simulations.

In addition, the research team coordinated a soil sampling campaign at China Creek with TXDOT to create sophisticated soil models for the subsequent numerical analysis. This data was potentially very important as the data gathered from Mack Creek Bridge suggested possible interaction between the backwall and pile caps.

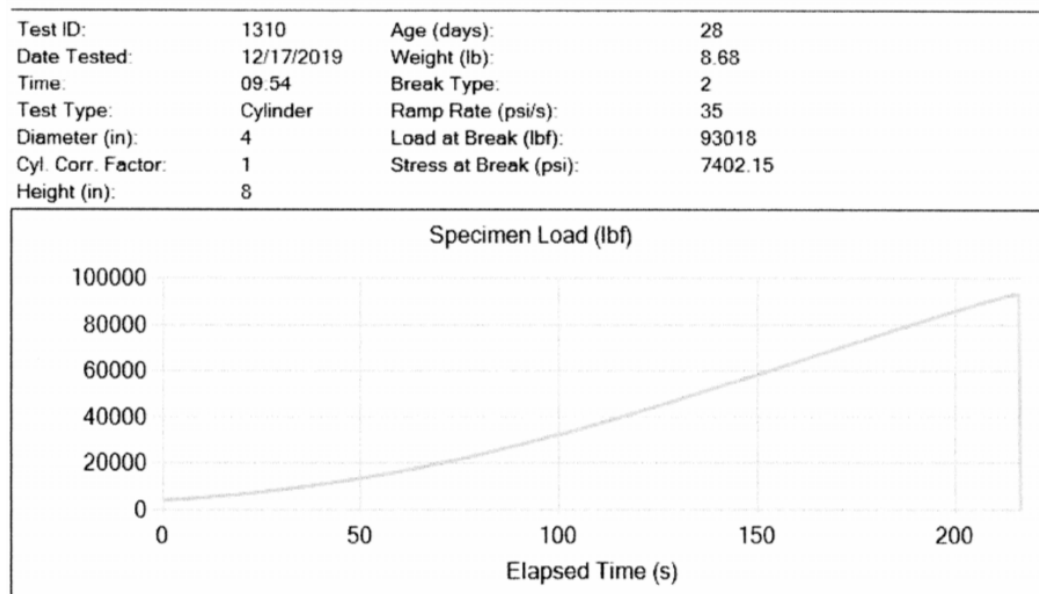


Figure 5.1: 28th day compressive strength test results for concrete used in the west abutment drilled shaft, phase I

5.5. Load/Displacement Characteristics

Through the inspection of displacement data collected using the new equipment installed at Mack Creek, there is high likelihood that there are cyclical lateral displacements/forces imposed on the pile caps due to thermal contraction and shrinkage of the bridge deck. This is an important matter because it highlights the need to check for the lateral load resistance capacity of the foundation for SIAB structures. The magnitude of the imposed displacements/forces at the pile cap will be dependent on the span length, concrete mix design and environmental variables such as temperature extremes, daily changes in temperature and even relative humidity (shrinkage). Better understanding of the extent of these effects in SIAB structures through numerical simulations and collection of more field data, is expected to help inform the future designs.

5.6. Conclusion to Identification of Relevant Parameters for Numerical Simulations

A baseline was established for subsequent numerical modeling of the bridge structures modeled to understand the effect of various components that play a role in the performance of SIAB/IAB structures in Texas. To improve the results of numerical simulations, the research team has constructed an alternative geometry to understand the effect of the elastomeric bearing pad and

reach a better match with the field data. Due to the high computational costs, some alterations in the preliminary numerical model were made to find a better match between field and numerical data. A good baseline model was developed using the information obtained from Mack Creek SIAB. The numerical analysis is presented in Appendix B. Numerical Simulation and Parametric Evaluation of Integral/Semi-Integral Bridges Considering Representative Ranges of Relevant Parameters of this report.

In addition, an evaluation of the data collected from the sensors installed at Mack Creek Bridge pointed to more details regarding the interaction between abutment backwalls and pile caps due to temperature changes and possible shrinkage of the concrete over time. As a result, these parameters will also be considered in a subsequent numerical analysis to better understand the extent of their effects on the performance of SIAB/IAB structures.

Chapter 6. Experimental Component

6.1. Background Information

Integral and Semi-Integral Bridge Abutments (IAB and SIAB, respectively) consist of a structure that is attached to the bridge superstructure by a rigid, moment-resisting connection. The abutment component involves a backwall that is in direct contact with a retained soil (typically a granular backfill) and thus interacts with this retained soil. The interaction is in part driven by thermal expansion and contraction of the bridge superstructure, which causes the connected backwall to move into and away from the retained soil respectively. These movements are repeated over many cycles of high and low temperatures throughout a bridge design lifetime and can result in lateral earth pressure ratcheting. Figure 6.1 presents a schematic of a typical integral bridge abutment with the backwall that may develop lateral earth pressure ratcheting labeled. Because IAB structures are supported by deep foundations, the expansion and contraction of the superstructure will typically result in a rotational movement of the abutment backwall. As such, the goal of developing an experimental setup to investigate the behavior of a rotating wall supporting a retained granular soil mass was established.

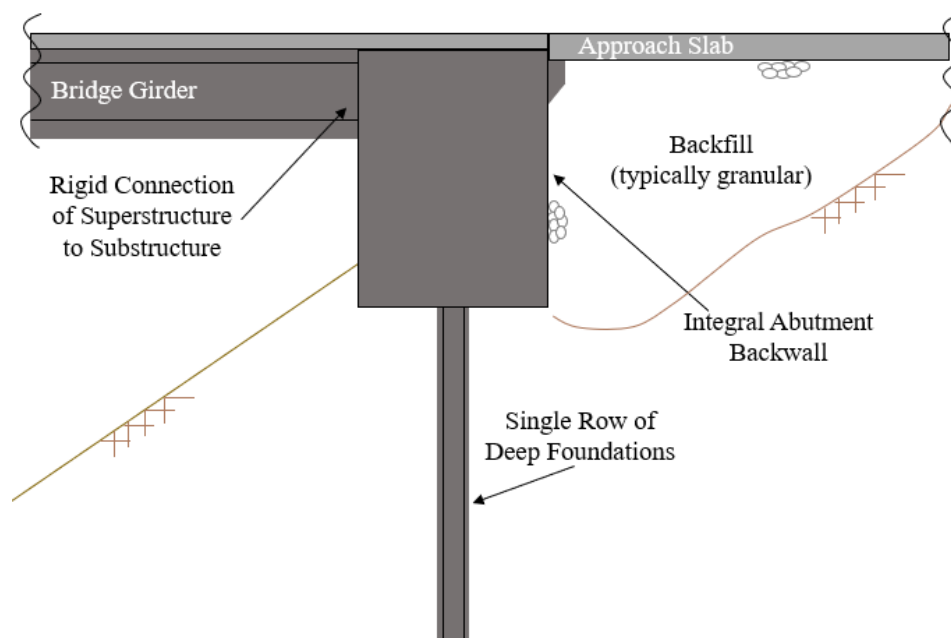


Figure 6.1: Schematic of typical integral bridge abutment

An experimental setup was conceived and implemented to investigate the magnitude and potential increase of lateral earth pressures due to ratcheting and soil settlement in an IAB subjected to repeated loading due to temperature-induced displacement. The features of this experimental setup were as follows:

- Involved a large quantity of gravelly soil to be representative of the granular backfill typical of an integral bridge abutment
- Establish a connection of a wall to allow for repeated rotation of the wall into and away from the retained gravelly soil
- Measure total load required to mobilize the moveable wall at all degrees of rotation
- Monitor lateral earth pressure acting upon the wall in multiple locations along the height.
- Record displacement of individual soil particles within the soil mass near the interface of the soil and rotating wall
- Capture digital images of a transparent side of the soil container oriented perpendicular to the rotating walls movement

By realizing the aforementioned features with experimental testing equipment, a data set was collected capable of assessing relevant aspects related to the behavior of retained soil near an integral bridge abutment or similar structure.

Figure 6.2 presents both a schematic and photo of the testing equipment setup prior to the first repeated loading test. The interior of the box with a transparent side measures 60 in long, 30 in wide and 48 in tall. The stiffened wall capable of rotating around hinges near the bottom of the box was placed with a flat face in contact with the soil a total of 6 inches from the interior boundary of the box. This configuration allowed for the stiffened wall to rotate a total of 3 in (3.87 degrees) backward before encountering the interior wall of the box behind it. The rotation of the wall was driven by a 12-in-diameter pneumatic actuator, which was connected to the wall by means of a pinned connection and a load cell between the connecting elements and piston extruding from within the actuator. The wall could rotate about two hinges welded to the bottom of the stiffened wall, which were fixed to a base frame that rests on the bottom of the soil box. This base frame consisted of four steel bars that extended to all sidewalls of the box and was restrained both by these walls and the soil placed on top of it. The base frame and hinge setup created a space of approximately 4.5 in from the bottom of the box and the base of the stiffened wall – some of which was filled by the hinges and a 1-in bar that composes part of the base frame immediately below the stiffened wall.

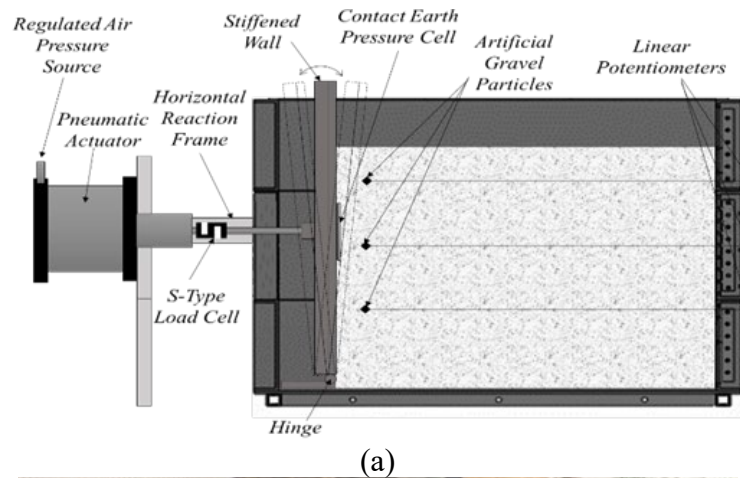


Figure 6.2: Experimental testing equipment: (a) profile view schematic; and (b) photo taken prior to first conducted test

The soil mass within the box was a rounded pea gravel that conformed to the AASHTO #8 gradation, as shown in Figure 6.3. This soil is described in the USCS system as a clean, poorly graded gravel (GP). Additionally, at all times during testing and configuration preparation, a dry condition of the soil was maintained.

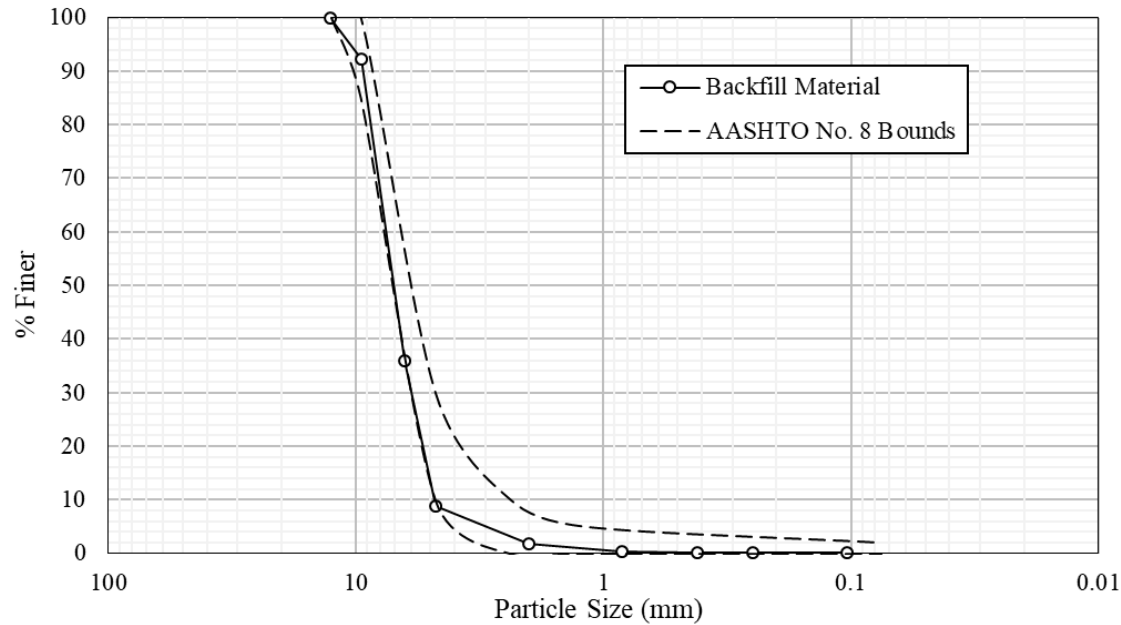


Figure 6.3: Grain size distribution of soil used in experimental testing program

6.2. Instrumentation

Relevant variables in the tested models were instrumented to provide insight into the performance of the retained soil during testing. The instrumentation plan included a load cell, four pressure cells, string potentiometers (actual number varied with test configuration), artificial soil particles, and capturing of digital images. This extensive instrumentation plan aimed at obtaining information on the force required to mobilize the stiffened wall throughout testing, the exact displacement of the wall, and movements within and at the boundaries of the retained soil could be tracked. Furthermore, the pressure distribution acting upon the wall as a result of the degree of rotation of the wall and number of past cycles could be determined at any stage of testing.

The load cell connected to the piston of the pneumatic actuator is an Omega LCCA S-beam load cell with a capacity of 20,000 lbs. The load cell was calibrated after being connected to the actuator piston and stiffened steel wall. The stiffened wall was braced in place with large diameter rods reacting against the opposing side of the soil box. In this configuration, air pressure was added to the pneumatic actuator and the force applied to the load cell was calculated based on the input force and actuator dimension. With these known variables, the force exerted on the S-beam load cell was calculated and a calibration factor was determined by comparing readings up to an input pressure of 100 psi, which corresponded to a force on the load cell of 11,310 lbs.

Two different types of pressure cells were mounted to the stiffened steel wall to determine the lateral earth pressure distribution on the structure during testing. The primary pressure cell

mounted near the center of the wall was a Geokon model 4810 vibrating wire contact pressure cell. This cell has a circular measuring surface of 9 in diameter and a stem that houses the vibrating wire transducer and temperature sensor. The stiffened wall was designed to accommodate this sensor with holes drilled for mounting the cell on the center of the wall with the midpoint of the sensing surface at a height of 28.25 in from the bottom of the soil box. The capacity of the model 4810 pressure cell is 50.76 psi, and a calibration factor was provided by the manufacturer, which was confirmed to be accurate through laboratory testing with an air pressure bladder. The supporting pressure cells mounted to the stiffened steel wall are Kyowa BEC-A soil pressure transducers. The sensing surface of the BEC-A pressure transducers are circular with a diameter of 0.91 in. The capacity of these transducers is 72.52 psi, and calibration factors were determined experimentally by use of an air pressure bladder up to an input pressure of 50 psi.

Artificial soil particles were attached to the ends of wires connected to string potentiometers that extended through the openings on the backside wall of the soil box. These particles are made of a hard-plastic material with approximately the same size and shape as the AASHTO #8 median grain size. The particles were then connected to the string potentiometers with a wire cable that was shielded in the retained soil by a firm PVC-coated metal tube with an inner diameter of 0.125 in. The configuration of artificial soil particle to connection wire and string potentiometer allows for measurement of displacements in a horizontal direction at discrete locations in the retained soil mass. The rear side of the soil box, opposite the rotating wall, was constructed with a series of narrow openings to allow for string potentiometers to pass through the wall and connect to the wires of the artificial soil particles in the retained soil mass. String potentiometers were mounted to an additional bracket on the outside of the soil box. The string potentiometers used for this purpose are UniMeasure LX-PA series with a 2.8 in range. One additional string potentiometer was used to track the movements of the rotating steel wall and was also connected to this opposing side wall of the soil box. The string potentiometer used to track the steel wall rotations was of the LX-PA series, but with a 15 in range.

Digital images of the transparent side of the soil box were captured with a tripod mounted, Nikon D5200 camera with an AF-S Nikkor 18-55 mm lens. The camera was set to autofocus and a zoom of zero for the first image captured. For all subsequent images captured, the same focus, zoom, and positional settings of the first image were retained for uniformity across all photographs.

6.3. Scope of the Experimental Program

The experimental program was intended to investigate the effect of repeated displacement cycles of an earth retaining structure into and away from a dry, granular soil mass. The rotating steel wall created for the laboratory experiment is representative of a section of an integral abutment backwall. As such, the scope of the testing configurations was to determine expected backfill

behavior at the interface of an integral bridge abutment as it relates to pressure upon the backwall and soil mass deformation. Testing was conducted to establish first a baseline condition in which the stiffened wall moves into and away from the retained soil mass. Two additional tests were conducted to evaluate how the soil would perform in the case of an IAB completed in the summer (movements away from the soil mass and back to vertical only) and in the winter (movements into the soil mass and back to vertical only). An additional test was conducted to understand soil-abutment interaction and performance with a coarse interface to simulate a rough material such as concrete as opposed to steel.

The last two tests of the experimental program sought to evaluate the possibility of remediating adverse effects of integral abutments upon the retained soil by use of either geosynthetics or a compressible inclusion. These tests included a wrap-around geosynthetic reinforcement and a geofoam layer between the wall and soil respectively. The degrees of rotation and direction of movement for these two tests was expected to be equivalent to those imposed in the first baseline and coarse interface tests. Thus, any improved soil mass behavior can easily be compared relative to the baseline condition of either a smooth or rough surface wall. The test configuration with geosynthetic reinforcement included multiple layers of a wrap-around geotextile, while the configuration with a compressible inclusion included a specified thickness of geofoam adhered to the wall prior to soil backfilling and after attaching soil pressure cells.

6.4. Experimental Results

6.4.1. Initial Baseline Configuration

The initial baseline configuration consisted of an unreinforced soil mass in the soil box, filled to a total height of 40 inches as measured from the base of the box. The soil in this configuration was filled and compacted to a unit weight of 106.60 pcf. Cycles of movements of the stiffened steel wall were imposed with the following targets:

- 10 cycles of 0.64° rotation (corresponding to 0.5 in of wall displacement at the top of the soil box) into the soil followed by 0.64° rotation away from the soil, and then returned to neutral vertical position
- 10 cycles of 0.96° (corresponding to 0.75 in of wall displacement at the top of the soil box) rotation into the soil followed by 0.96° rotation away from the soil, and then returned to neutral vertical position
- 10 cycles of 1.28° rotation (corresponding to 1.0 in of wall displacement at the top of the soil box) into the soil followed by 1.28° rotation away from the soil, and then returned to neutral vertical position

Data from the baseline test is presented in Figure 6.4 through Figure 6.8. These plots include presentation of force measured at the 20,000-lb load cell and rotation throughout testing. Also marked on the plot of rotation versus time during testing are the periods during which active earth pressure and lateral earth pressure thrust were achieved according to traditional Rankine theory. In these two plots (Figure 6.4 and Figure 6.5), three distinct cycling magnitude series can be observed. In the final set of 10 cycles, the target rotation of 1.28° into the soil mass was not able to be achieved in all cycles. This was because of earth pressure ratcheting, which was demonstrated by an equal force input (as observed in the final eight cycles of Figure 6.4) that yielded a smaller degree of rotation with each cycle (Figure 6.5). Earth pressure ratcheting was manifested in this way during the third series of 10 cycles because the maximum possible load was applied in each attempt to reach the desired rotation angle. Maximum applicable load was governed by available input air pressure to the pneumatic actuator, which was 100 psi in the laboratory where testing was conducted.

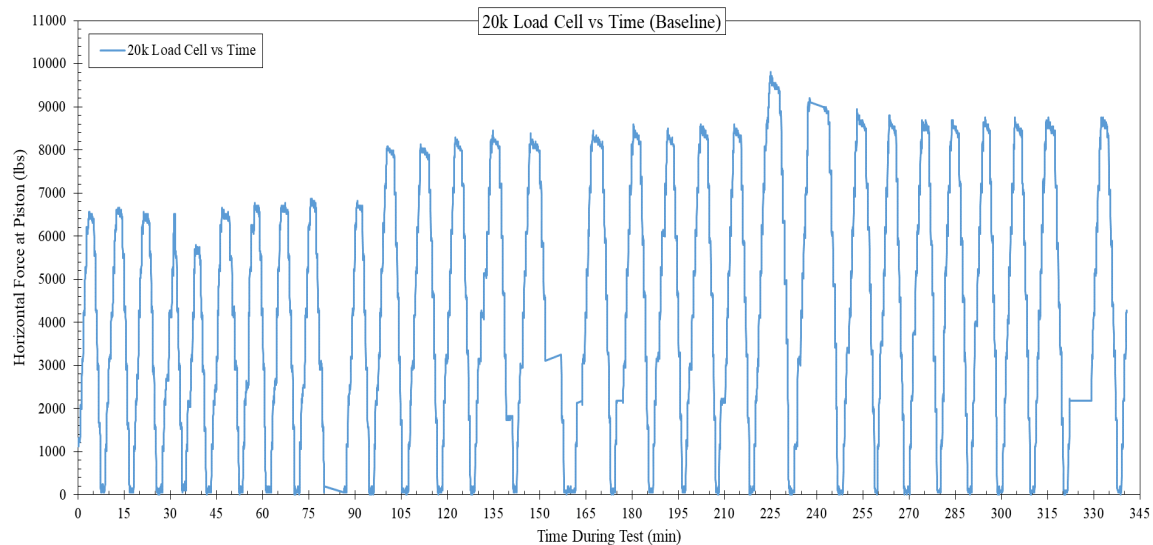


Figure 6.4: Time-history of lateral force for the baseline test

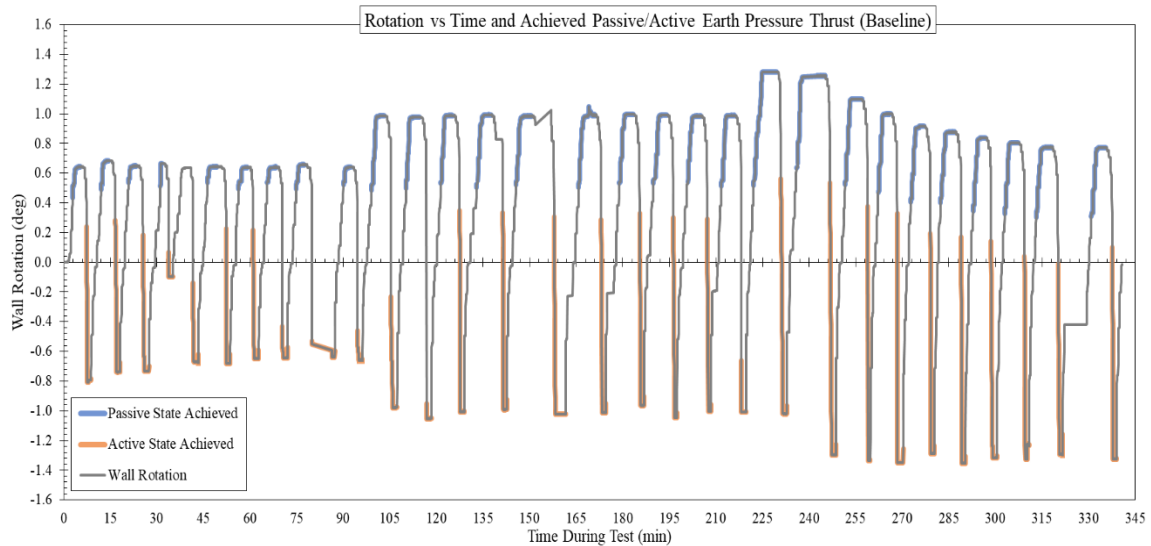


Figure 6.5: Time-history of wall rotation for the baseline test (Note: the mobilized passive and active force per Rankine theory)

Digital images captured during the testing were used to track the movement of the soil surface throughout cycling. Figure 6.6 is an example of one such image that was captured at the end of the baseline configuration test. In this image, the three distinct “windows” of the transparent side of the soil box can be observed. For the analysis of the top soil surface, the top “window” was of particular relevance.



Figure 6.6: Full-frame photo of completed final cycle of baseline test

Figure 6.7 presents a set of seven images focused on the top “window” of the soil test box through which the movement of the initial soil surface has been tracked. The image set includes the very first photo captured, along with subsequent images of the end of each 5th and 10th cycle within each of the three cyclic amplitudes. In addition to this visual representation of the soil surface progression, Table 6.1 presents final values of soil settlement and heave at the end of the

baseline test. These images and values provide a basis of comparison for subsequent tests of different configurations relative to the baseline.



(a)



(b)



(c)



(d)



(e)



(f)



(g)

Figure 6.7: Photos from top viewing window of soil box during baseline test: (a) at beginning of test; and after (b) cycle 1.5; (c) cycle 1.10; (d) cycle 2.5; (e) cycle 2.10; (f) cycle 3.5; and (g) cycle 3.10

Table 6.1: Values of soil settlement and heave based on image correlation for baseline test

Maximum Depth of Soil Settlement	Extent of Soil Settlement Beyond Steel Wall	Maximum Height of Soil Heaving	Extent of Soil Heaving Beyond Steel Wall
<i>(in)</i>	<i>(in)</i>	<i>(in)</i>	<i>(in)</i>
5.245	17.851	0.727	26.047

In addition to the forces required to mobilize the wall and soil displacements, the maximum pressure distribution acting on the stiffened wall was desired for each cycle. This was found to be at every point wherein the wall reached the most forward movement into the soil during the respective cycle. These pressure distributions along with the locations at which Pressure Cells (PC) were mounted are presented in Figure 6.8. It can be observed that in general, as the cycles continue, the pressure acting upon the wall increases. In the case of the largest rotation series however, the trend is opposite. This is a result of the ratcheting shown previously in Figure 6.5 that prevents displacements to the same degree of rotation with subsequent cycling beyond the second in this series.

For each lateral pressure distribution, pressure was plotted to a value of 0 at the top of the soil surface (40 in). For the bottom of the pressure distribution, the value of at-rest lateral earth pressure as calculated from the soil density and effective friction angle was used from the point of hinge rotation to the bottom of the box (3.5 in to 0 in). This method was used consistently for all lateral earth pressure distribution plots shown for all testing configurations.

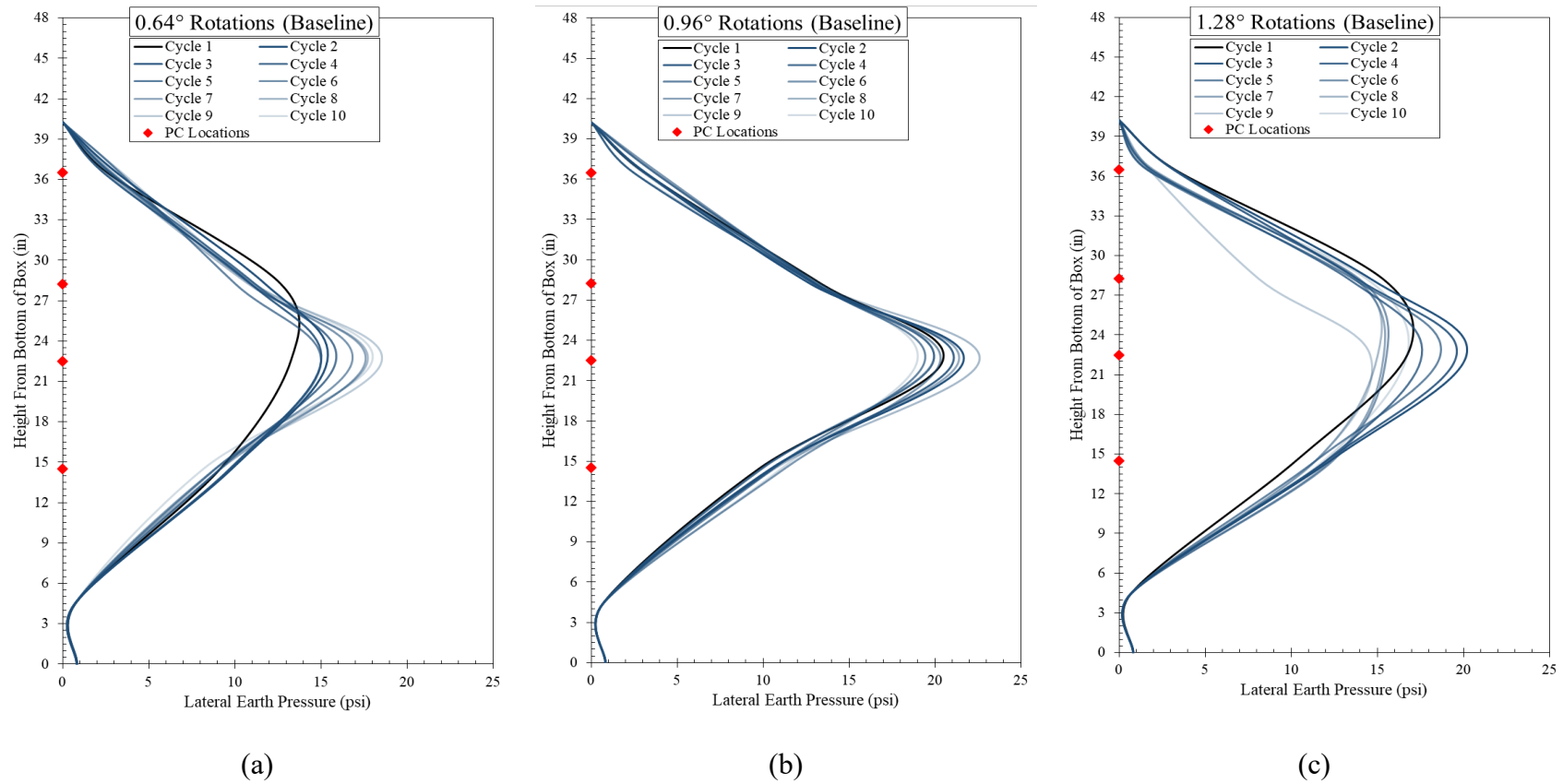


Figure 6.8: Pressure cell locations and lateral earth pressure distribution on stiffened steel wall for most forward position rotated into soil mass during: (a) first set of 10 cycles; (b) second set of 10 cycles; and (c) third set of 10 cycles of baseline test

6.4.2. Movements Away from Soil Mass (Active)

The second test conducted also consisted of an unreinforced soil mass filled in the soil box to a total height of 40 inches as measured from the base box. The soil in this configuration was filled and compacted to a unit weight of 107.15 pcf. Cycles of repeated movements of the stiffened steel wall were imposed with the following targets:

- 10 cycles of 0.64° rotation away from the soil, and then returned to neutral vertical position
- 10 cycles of 1.28° rotation away from the soil, and then returned to neutral vertical position
- 10 cycles of 1.92° rotation away from the soil, and then returned to neutral vertical position

Data from the active movements configuration are presented in Figure 6.8 through Figure 6.12. These plots show force measured by the load cell and rotation throughout testing. Also marked on the plot of rotation versus time during testing are the periods during which active earth pressure and lateral earth pressure thrust was achieved according to traditional Rankine theory. In these two plots (Figure 6.9 and Figure 6.10), three distinct cycling magnitude series can be observed. The first cycle in each of the first two magnitude series rotated farther away from the soil than desired. This was the result of an operator error, and additional cycles were added to the first to magnitude series to provide at least 10 consistent cycles in each series. Earth pressure ratcheting is not as apparent in this testing configuration compared to the baseline, but in Figure 6.10 it can be seen that as the wall rotates farther away from the soil, a passive state is achieved sooner when the wall is returned to the original vertical position. Following these two plots, the same series of seven images are presented in Figure 6.11 of the top “window” of the transparent soil side as in the baseline case. Following the images is Table 6.2, which includes values of soil settlement and heaving at the end of the test. It can be observed that the amount of soil settlement and heaving achieved is less than that compared to the baseline case. The extent of these settlements and heaving however are very similar to those of the baseline case.

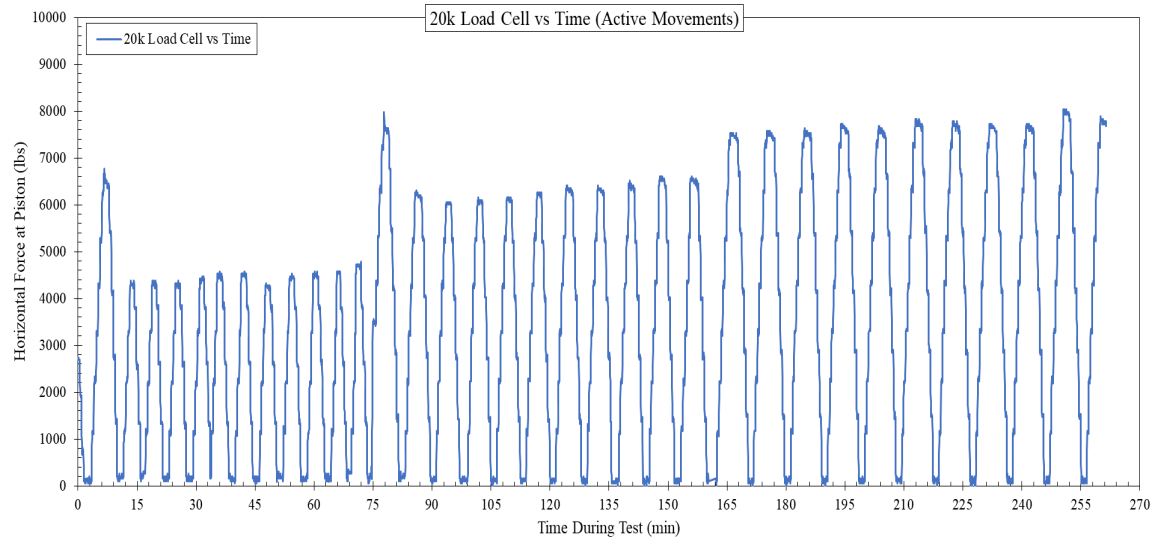


Figure 6.9: Time-history of lateral force for the active movements test

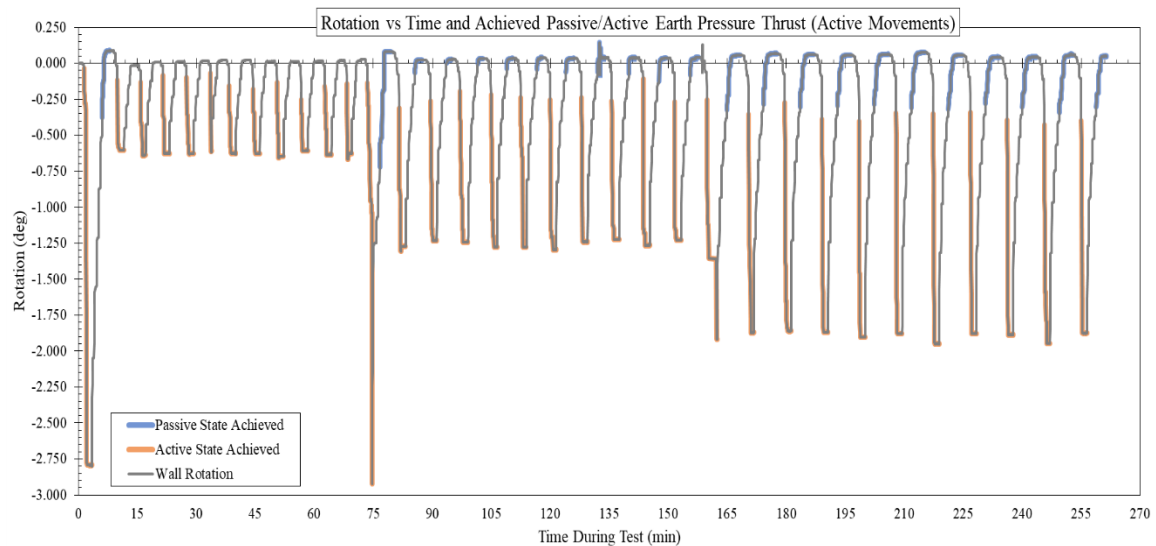


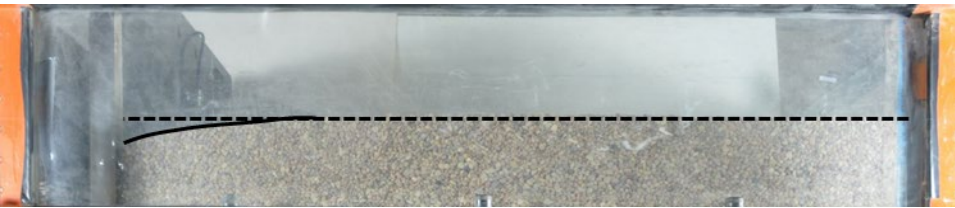
Figure 6.10: Time-history of wall rotation for active movements test (Note: the mobilized passive and active force per Rankine theory)



(a)



(b)



(c)



(d)



(e)



(f)



(g)

Figure 6.11: Photos from top viewing window of soil box during active movements test: (a) at beginning of test; and after (b) cycle 1.5; (c) cycle 1.10; (d) cycle 2.5; (e) cycle 2.10; (f) cycle 3.5; and (g) cycle 3.10

Table 6.2: Values of soil settlement and heave based on image correlation for active movements test

Maximum Depth of Soil Settlement	Extent of Soil Settlement Beyond Steel Wall	Maximum Height of Soil Heaving	Extent of Soil Heaving Beyond Steel Wall
<i>(in)</i>	<i>(in)</i>	<i>(in)</i>	<i>(in)</i>
4.304	16.129	0.689	27.505

In addition to the forces required to mobilize the wall and soil displacements, the maximum pressure distribution acting upon the stiffened wall was desired for each cycle. This was found to be at every point in which the wall reached the most forward movement into the soil during the respective cycle (vertical in this configuration). These pressure distributions along with the locations at which PCs were mounted are presented in Figure 6.12. Except for the first two cycles in each of the first two rotation series, it can be observed that in general, as the cycles continue, the pressure acting upon the wall increases. This trend is more apparent in this active movements test configuration than the baseline case. Furthermore, different locations of the PCs on the stiffened wall reveal that lateral earth pressures near the hinge location at the bottom of the wall (3.5 in from the bottom marked as height of 0 in) approach the original K_0 distribution. This is expected as soil below the point of hinge rotation experiences little to no disturbance throughout a test.

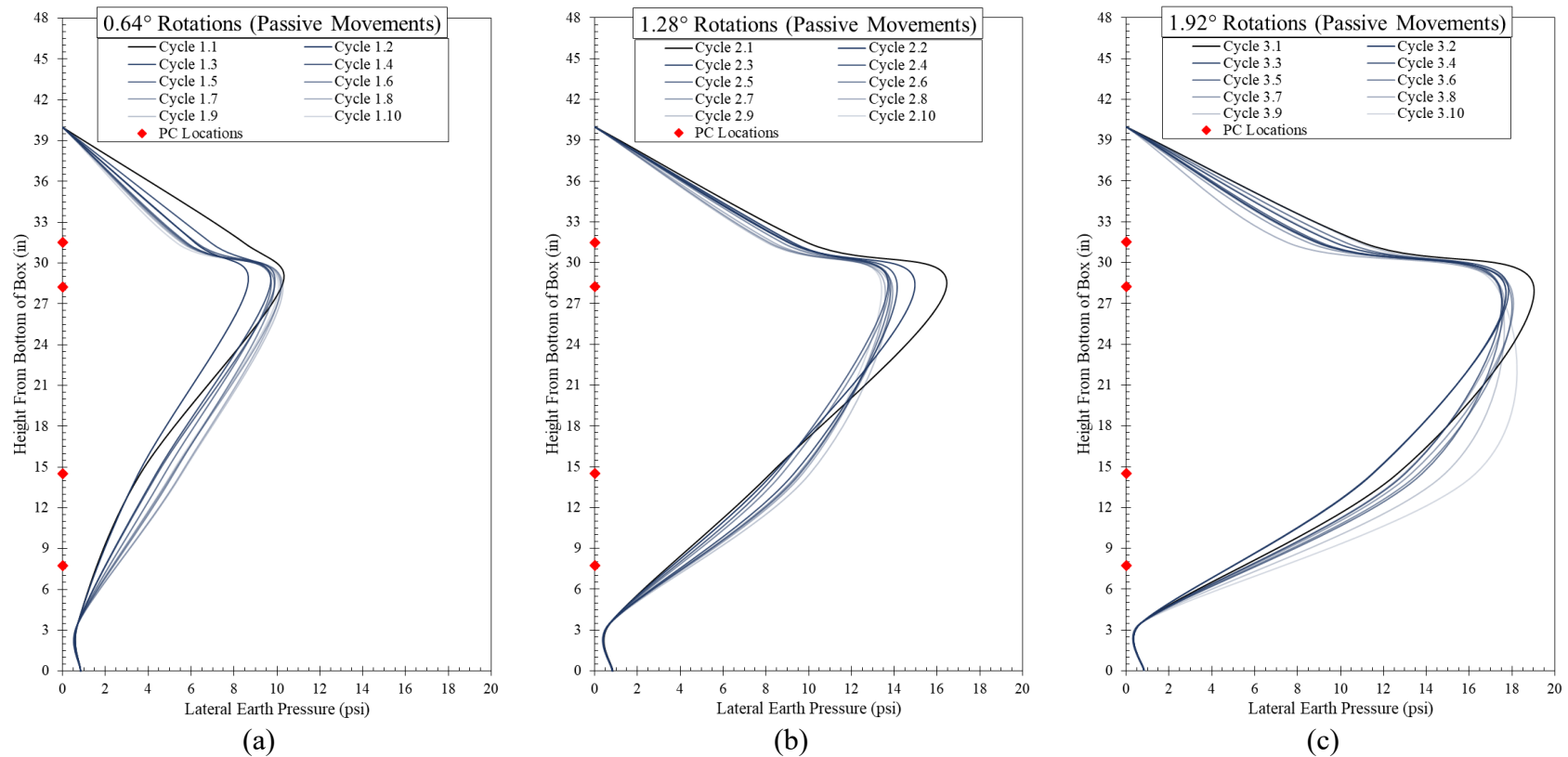


Figure 6.12: Pressure cell locations and lateral earth pressure distribution on stiffened steel wall for most forward position rotated into soil mass during: (a) first set of 12 cycles; (b) second set of 11 cycles; and (c) third set of 10 cycles of active movements test

6.4.3. Movements into Soil Mass (Passive)

The third test conducted consisted of an unreinforced soil mass filled in the soil box to a total height of 40 inches as measured from the base of the box. The soil in this configuration was filled and compacted to a unit weight of 102.15 pcf. Cycles of repeated movements of the stiffened steel wall were imposed with the following targets:

- 10 cycles of 0.64° rotation into the soil, and then returned to neutral vertical position
- 10 cycles of 1.28° rotation into the soil, and then returned to neutral vertical position
- 10 cycles of 1.92° rotation into the soil, and then returned to neutral vertical position

Data from the passive movements configuration are presented in Figure 6.13 through Figure 6.16. These plots include presentation of force measured by the load cell and rotation throughout testing. Also marked on the plot of rotation versus time during testing is the periods during which active earth pressure and lateral earth pressure thrust was achieved according to traditional Rankine theory. In these two plots (Figure 6.13 and Figure 6.14), the three distinct cycling magnitude series can easily be observed. It should be noted that a crash of the data acquisition system occurred between the eighth and ninth cycles of the first and second series of rotations, which resulted in an apparent drift of the linear potentiometer measuring wall movement and establishment of a different zero value corresponding to the wall being in a vertical position. This is particularly noticeable after the second crash, but this crash did not significantly affect the data and trends.

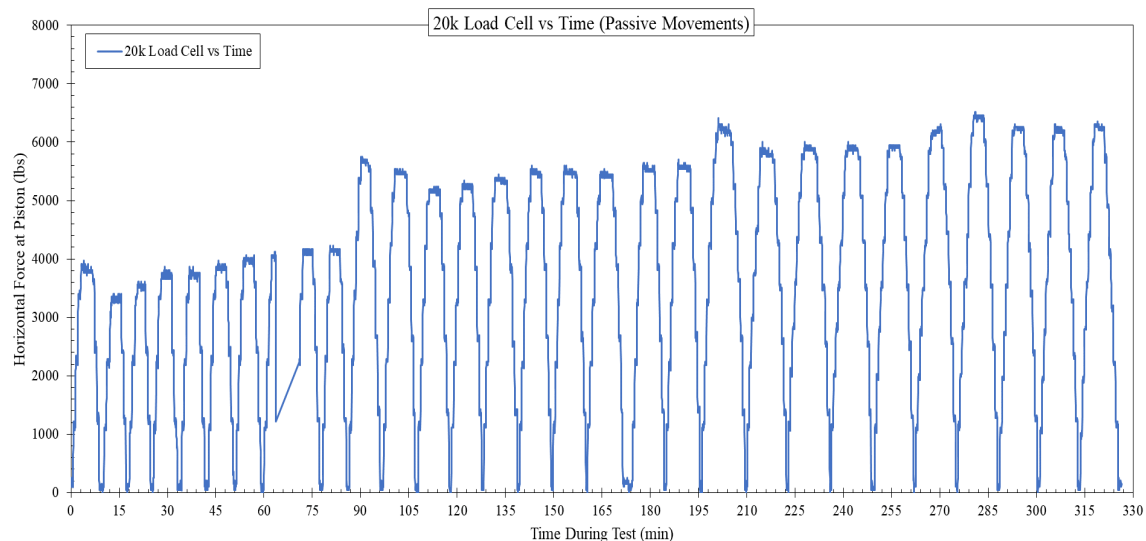


Figure 6.13: Time-history of lateral force for passive movements test

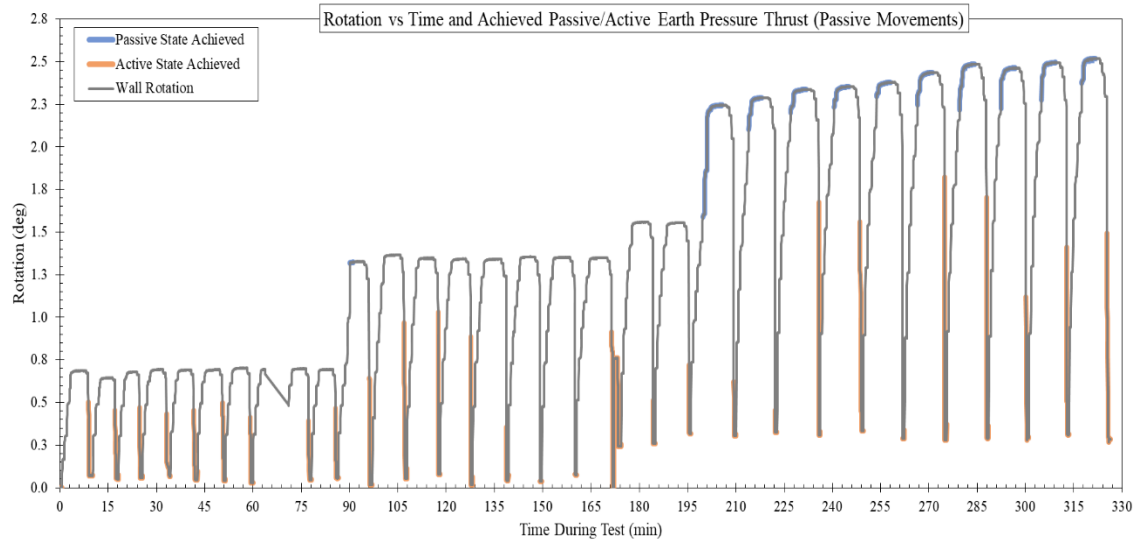


Figure 6.14: Time-history of wall rotation for passive movements test (Note: the mobilized passive and active force per Rankine theory)

Figure 6.19 presents the seven-image set focused on the top “window” of the soil test box for the passive movements test. These images in conjunction with summary values presented in Table 6.3 indicated that soil movements in the passive and active movement configurations are quite similar. Of the values reported, the most significant difference is the reduction in heaving during the passive movements test compared to the active movements. In both cases however, soil movement was less than the baseline test configuration, which is expected because of the rotations being in only a single direction.



(a)



(b)



(c)



(d)



(e)



(f)



(g)

Figure 6.15: Photos from top viewing window of soil box during passive movements test: (a) at beginning of test; and after (b) cycle 1.5; (c) cycle 1.10; (d) cycle 2.5; (e) cycle 2.10; (f) cycle 3.5; and (g) cycle 3.10

Table 6.3: Values of soil settlement and heave based on image correlation for passive movements test

Maximum Depth of Soil Settlement	Extent of Soil Settlement Beyond Steel Wall	Maximum Height of Soil Heaving	Extent of Soil Heaving Beyond Steel Wall
<i>(in)</i>	<i>(in)</i>	<i>(in)</i>	<i>(in)</i>
4.480	15.665	0.527	24.947

In addition to the forces required to mobilize the wall and soil displacements, the maximum pressure distribution acting upon the stiffened wall was desired for each cycle. This was found to be at every point in which the wall reached the most forward movement into the soil during the respective cycle. These pressure distributions along with the locations at which PCs were mounted are presented in Figure 6.16. Again, like the active movements test, the first movement in each series produces the highest pressures because of a greater force being required to mobilize the wall to this degree of rotation (Figure 6.13). Subsequently however, as the cycles continue, the pressure acting upon the wall increases. This trend is most apparent in the third of the displacement series.

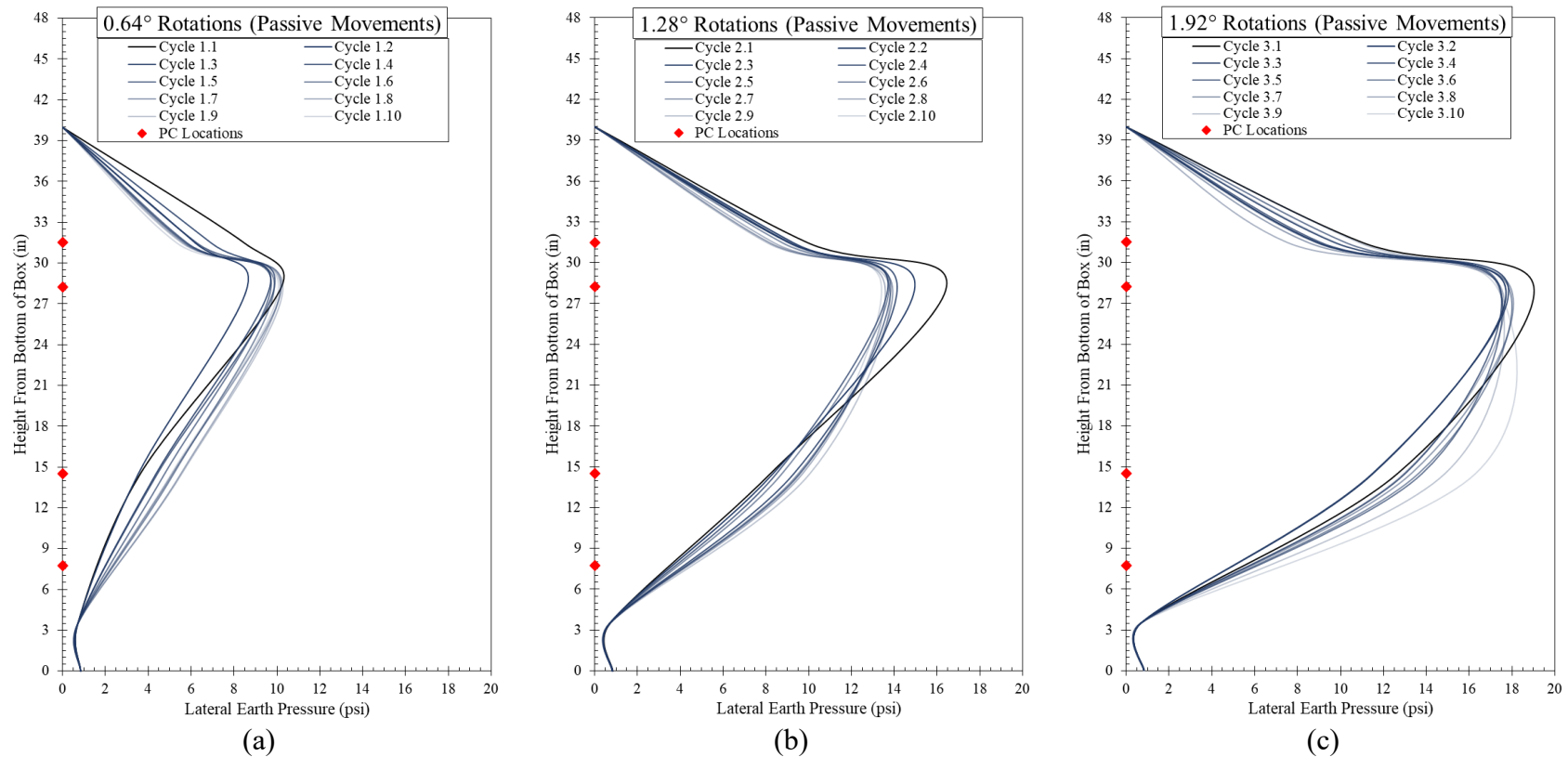


Figure 6.16: Pressure cell locations and lateral earth pressure distribution on stiffened steel wall for most forward position rotated into soil mass during: (a) first set of 10 cycles; (b) second set of 10 cycles; and (c) third set of 10 cycles of passive movements test

6.4.4. Coarse Soil-Wall Interface

The fourth test conducted consisted of an unreinforced soil mass filled in the soil box to a total height of 40 inches as measured from the base of the box. In this test, however, the side of the stiffened steel wall in contact with the retained soil had 16-grit, paint-coated sandpaper adhered to the surface. The soil in this configuration was filled and compacted to a unit weight of 107.49 pcf. Cycles of movements of the stiffened steel wall were imposed with the following targets:

- 10 cycles of 0.64° rotation into the soil followed by 0.64° rotation away from the soil, and then returned to neutral vertical position
- 10 cycles of 0.96° rotation into the soil followed by 0.96° rotation away from the soil, and then returned to neutral vertical position
- 10 cycles of 1.28° rotation into the soil followed by 1.28° rotation away from the soil, and then returned to neutral vertical position

Data from the coarse soil-wall interface configuration is presented in Figure 6.17 through Figure 6.20. These plots include presentation of force measured by the 20,000-lb load cell and rotation throughout testing. Also marked on the plot of rotation versus time during testing are the periods during which active earth pressure and lateral earth pressure thrust was achieved according to traditional Rankine theory. In these two plots (Figure 6.17 and Figure 6.18), the three distinct cycling magnitude series can easily be observed. It is also apparent that significant variability in the degree of rotation achieved in the third series of movements is present. This is despite a relatively consistent achieved load for each cycle in this final series of movements. This again is evidence of earth pressure ratcheting, which appears to be exacerbated by the coarse interface.

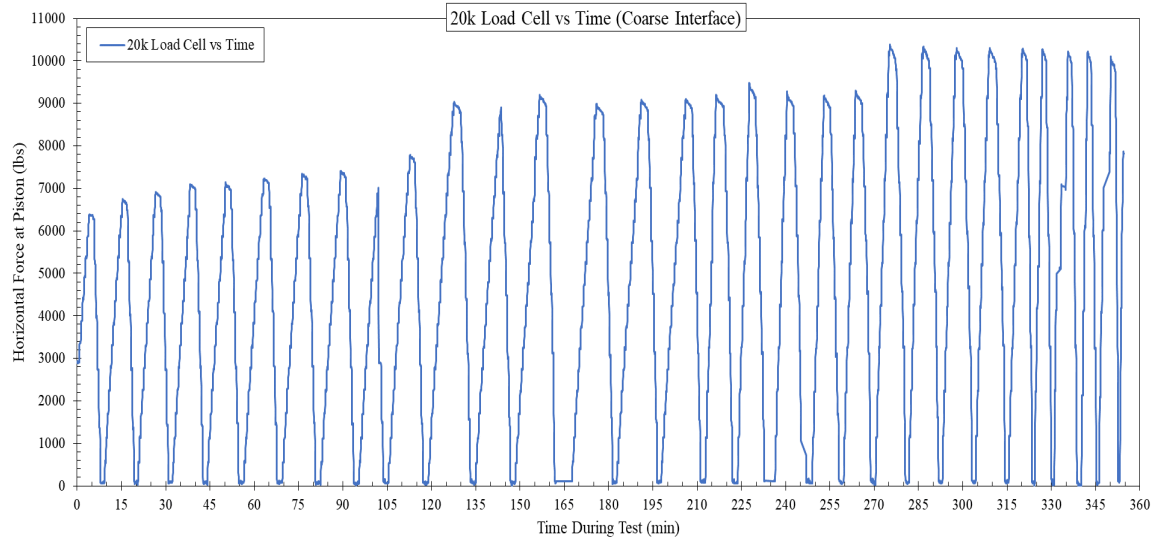


Figure 6.17: Time-history of lateral force for coarse interface test

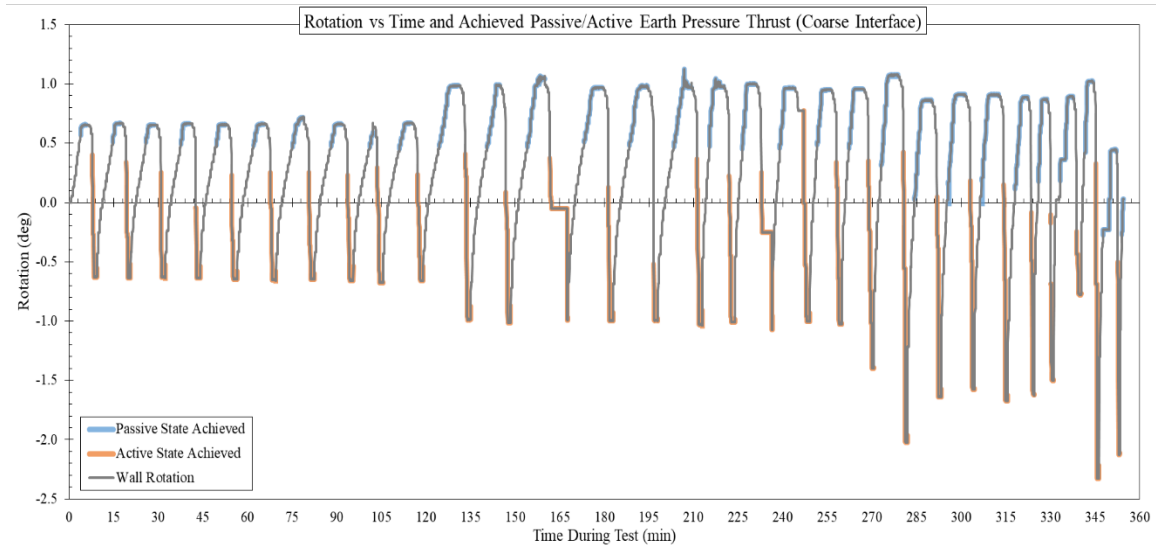


Figure 6.18: Time-history of wall rotation for coarse interface test (Note: the mobilized passive and active force per Rankine theory)

Also exacerbated by the coarse soil-wall interface is the movement of soil particles at the surface by the movements of the stiffened steel wall. This is observed and quantified in Figure 6.19 and Table 6.4, respectively. With the coarse interface, the wall had a greater influence on the movement of the soil in contact with it as more friction is present at this interface when compared to the smooth steel wall. This results in a depth of settlement greater than the height of the viewable field in the top “window” of the soil box, as well as heaving more than in previous tests. These findings suggest that an interface that allows more relatively movement between the soil particles and retaining wall performs better when subjected to repeated loaded compared to one with a coarse interface.

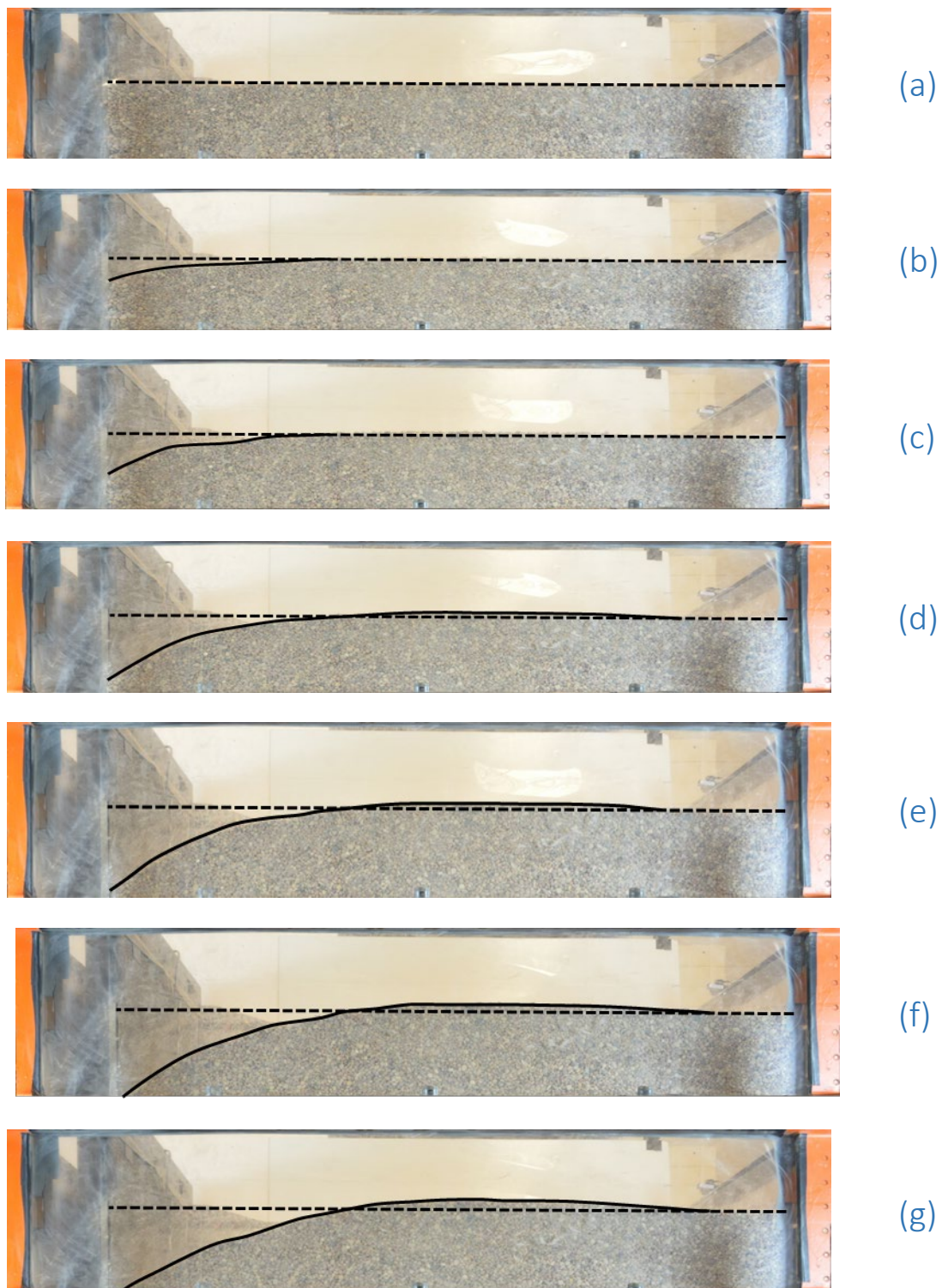


Figure 6.19: Photos from top viewing window of soil box during coarse interface test: (a) at beginning of test; and after (b) cycle 1.5; (c) cycle 1.10; (d) cycle 2.5; (e) cycle 2.10; (f) cycle 3.5; and (g) cycle 3.10

Table 6.4: Values of soil settlement and heave based on image correlation for coarse interface test

Maximum Depth of Soil Settlement	Extent of Soil Settlement Beyond Steel Wall	Maximum Height of Soil Heaving	Extent of Soil Heaving Beyond Steel Wall
<i>(in)</i>	<i>(in)</i>	<i>(in)</i>	<i>(in)</i>
> 7.0	18.700	0.873	26.949

In addition to the forces required to mobilize the wall and soil displacements, the maximum pressure distribution acting upon the stiffened wall was desired for each cycle. This was found to be at every point in which the wall reached the most forward movement into the soil during the respective cycle. These pressure distributions along with the locations at which PCs were mounted are presented in Figure 6.20. The general trend of increasing lateral earth pressure with increased number of cycles persists as it did in the baseline case. The value of lateral earth pressure is much greater in this testing sequence compared to the baseline however. Furthermore, the pressure at the center of the wall, relative to the retained soil height, is a much more pronounced extreme when compared to the previous testing configurations.

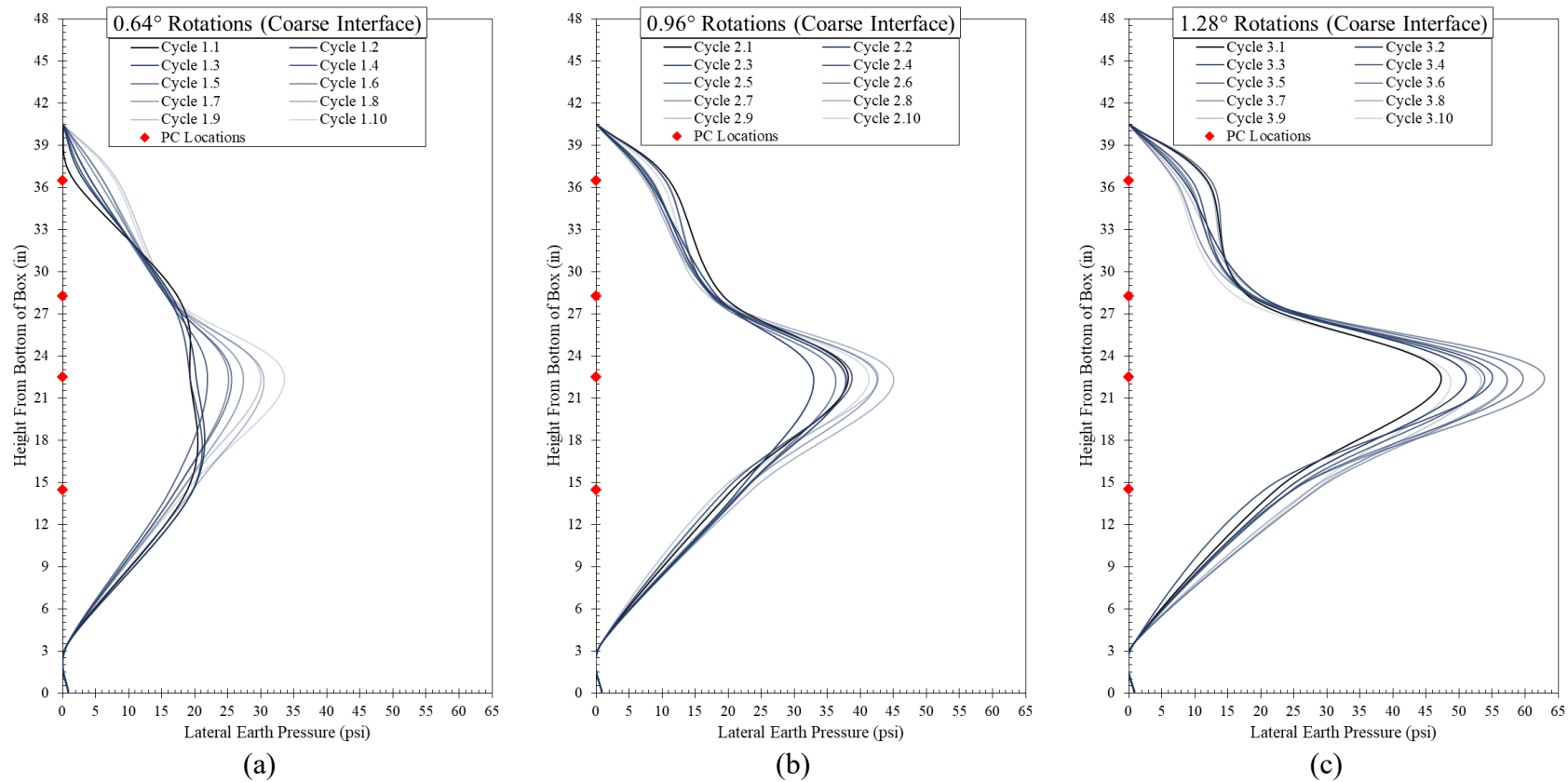


Figure 6.20: Pressure cell locations and lateral earth pressure distribution on stiffened steel wall for most forward position rotated into soil mass during: (a) first set of 10 cycles; (b) second set of 10 cycles; and (c) third set of 10 cycles of coarse interface test

6.4.5. Wrap-Around Geotextile Reinforcement

The fifth test conducted consisted of a geotextile wrap-around reinforced soil mass filled in the soil box to a total height of 40 inches as measured from the base of the box. The geotextile used was Mirafi HP570 and was oriented with the direction of loading in the cross-machine direction of the geotextile. Three wrap-around geotextile layers were constructed with a primary reinforcement length of 22 inches and a secondary reinforcement length of 8 inches. The height of each layer was 12 in, which overlaid an initial 4 in of placed soil. The soil in this configuration was filled and compacted to a unit weight of 109.66 pcf. Cycles of movements of the stiffened steel wall were imposed with the following targets:

- 10 cycles of 0.64° rotation into the soil followed by 0.64° rotation away from the soil, and returned to neutral vertical position
- 10 cycles of 0.96° rotation into the soil followed by 0.96° rotation away from the soil, and then returned to neutral vertical position
- 10 cycles of 1.28° rotation into the soil followed by 1.28° rotation away from the soil, and then returned to neutral vertical position

Data from the wrap-around geotextile reinforcement configuration is presented in Figure 6.21 through Figure 6.24. These plots include presentation of force measured by the 20,000-lb load cell and rotation throughout testing. Also marked on the plot of rotation versus time during testing are the periods during which active earth pressure and lateral earth pressure thrust were achieved according to traditional Rankine theory. In these two plots (Figure 6.21 and Figure 6.22), three distinct cycling magnitude series can be observed. Although the geotextile reinforcement was intended to reduce the extent of lateral earth pressure ratcheting with cycling, the effects of this are still observed – particularly in the first and third loading series. Similar to the baseline case, an increasing amount of applied load was required to achieve the same degree of rotation in the first series of 0.64° rotations. Additionally, when cycling to the highest magnitude of load in the third series (as limited by the pneumatic actuator cylinder diameter and available input building pressure), a decreasing degree of rotation was achieved in each subsequent cycle. These direct observations of earth pressure ratcheting may reduce the efficacy of wrap-around geotextile reinforcements to prevent such behavior in this testing configuration. However, the length of the secondary reinforcement was likely too short and thus the supportive wrap-around facing desired was not achieved.

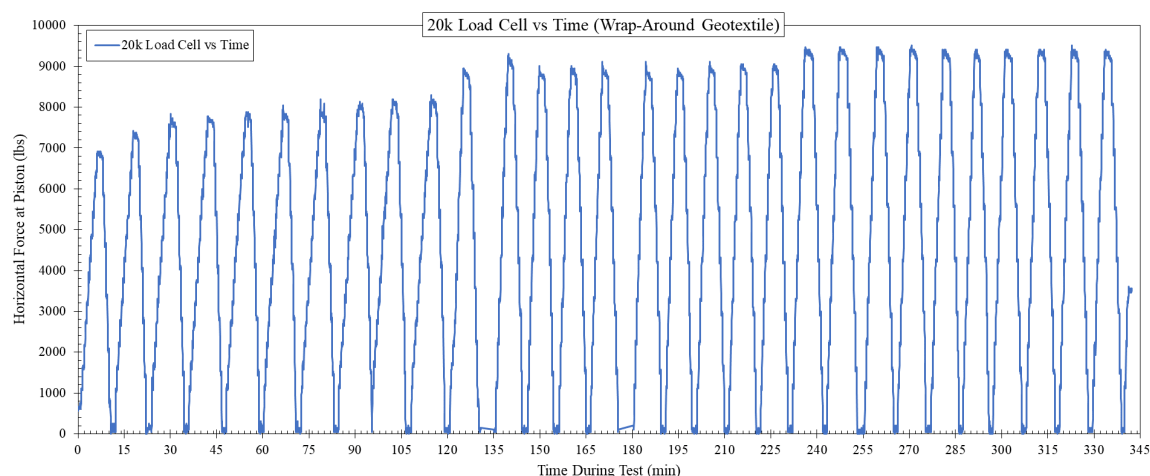


Figure 6.21: Time-history of lateral force for wrap-around geotextile test

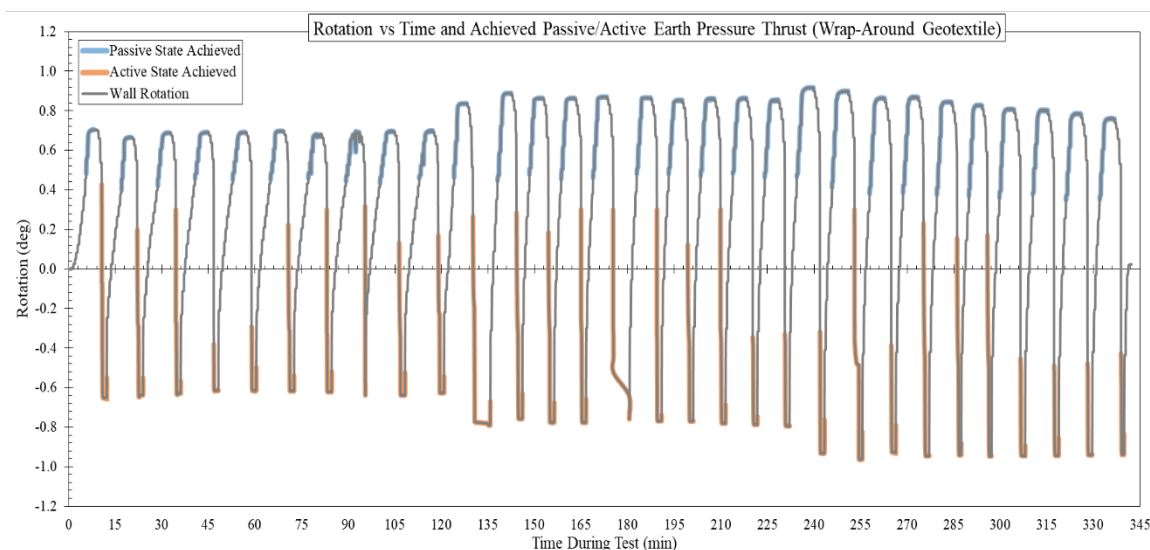


Figure 6.22: Time-history of wall rotation for wrap-around geotextile test (Note: the mobilized passive and active force per Rankine theory)

The images of the top soil box “window” provided in Figure 6.23 demonstrate how the wrap-around geotextile reinforcement with a short secondary reinforcement length was ineffective in preventing excessive movements near the soil-wall interface. This poor performance may be improved by extending the length of secondary reinforcement in the wrap-around design. The precise values of soil settlement and heave are tabulated in Table 6.5, which shows that soil heaving was increased in this configuration, and settlement was reduced relative to the baseline configuration. This improvement in soil settlement further suggests that an improved wrap-around design may result in more significant benefits to the soil mass performance. The ratio of primary and secondary reinforcement length was based on what would be used for a typical wrap-around MSE wall. The results of the testing configuration suggest that a geotechnical structure such as an MSE wall cannot be scaled down for the purposes of this test.



(a)



(b)



(c)



(d)



(e)



(f)



(g)

Figure 6.23: Photos from top viewing window of soil box during wrap-around geotextile test: (a) at beginning of test; and after (b) cycle 1.5; (c) cycle 1.10; (d) cycle 2.5; (e) cycle 2.10; (f) cycle 3.5; and (g) cycle 3.10

Table 6.5: Values of soil settlement and heave based on image correlation for wrap-around geotextile test

Maximum Depth of Soil Settlement	Extent of Soil Settlement Beyond Steel Wall	Maximum Height of Soil Heaving	Extent of Soil Heaving Beyond Steel Wall
<i>(in)</i>	<i>(in)</i>	<i>(in)</i>	<i>(in)</i>
5.066	11.682	1.098	35.638

In addition to the forces required to mobilize the wall and soil displacements, the maximum pressure distribution acting upon the stiffened wall was desired for each cycle. This was found to be at every point in which the wall reached the most forward movement into the soil during the respective cycle. These pressure distributions along with the locations at which PCs were mounted are presented in Figure 6.24. As would be expected from Figure 6.21 and Figure 6.22, increases in lateral earth pressure do occur with cycling. Again, like the coarse interface test, the pressure maximums are located at mid-height and are quite exaggerated relative to the baseline case. This configuration is like the results of the coarse interface test in that a material with greater friction than steel is between the stiffened wall and retained soil. Thus, it is not surprising that again, lateral earth pressures are overall greater than those observed in the baseline configuration.

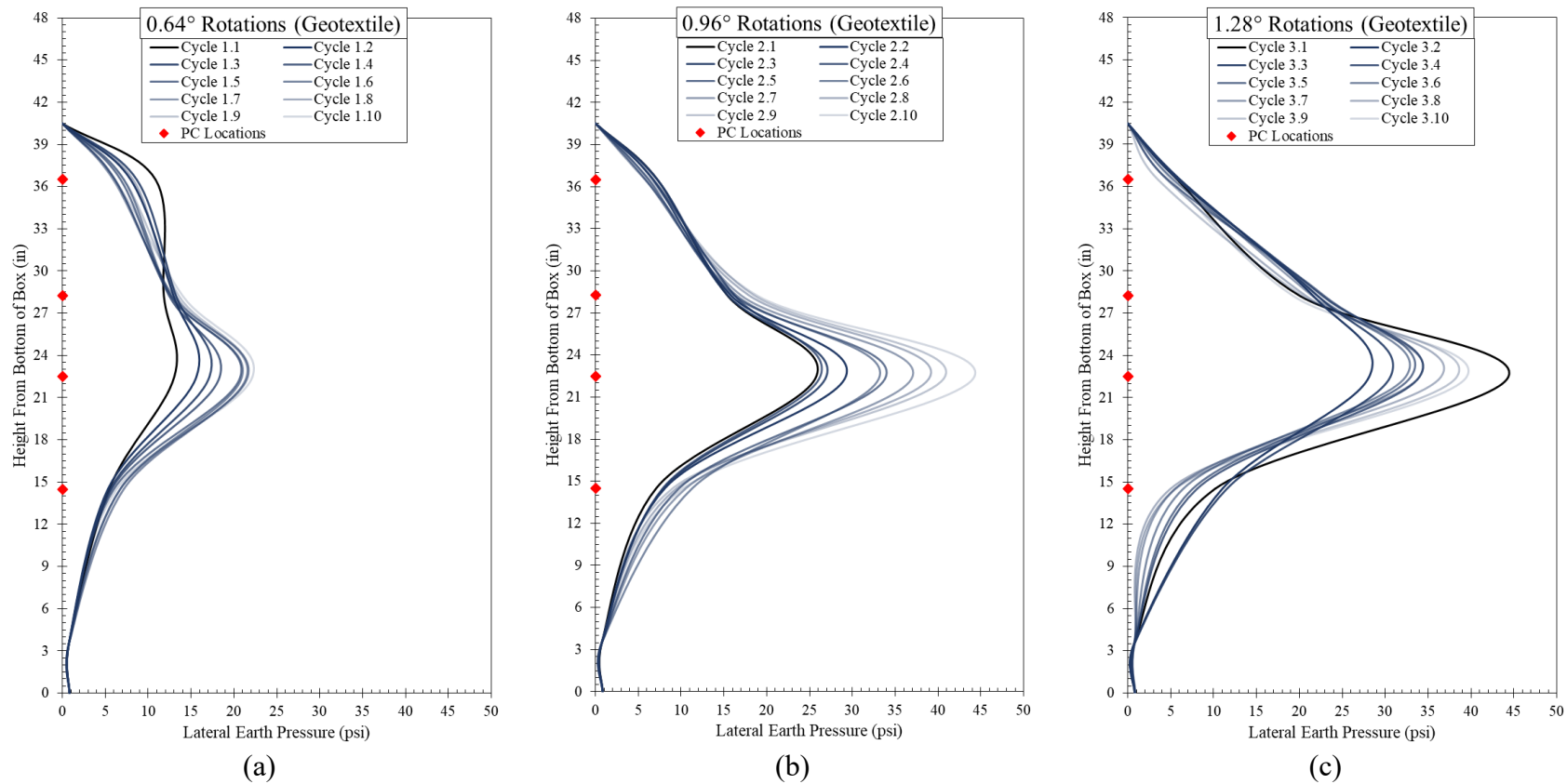


Figure 6.24: Pressure cell locations and lateral earth pressure distribution on stiffened steel wall for most forward position rotated into soil mass during: (a) first set of 10 cycles; (b) second set of 10 cycles; and (c) third set of 10 cycles of wrap-around geotextile test

6.4.6. Compressible Inclusion

The sixth and final test conducted consisted of an unreinforced soil mass filled in the soil box to a total height of 40 inches as measured from the base of the box. In this test, the side of the stiffened steel wall in contact with the retained soil had 2 inches of EPS 15 geofoam adhered to the surface. This particular geofoam has a density of 0.9 pcf, and was delivered in 1-in sheets. The first layer adhered to the wall was scored in the location of PCs to prevent loading of the cells beyond that from the lateral earth pressure of the retained soil. The second layer of full thickness 1-in geofoam in all locations of the wall was adhered to the first layer of geofoam to create an overall 2-in-thick layer between the stiffened wall and retained soil. The soil in this configuration was filled and compacted to a unit weight of 107.84 pcf. Cycles of movements of the stiffened steel wall were imposed with the following targets:

- 10 cycles of 0.64° rotation into the soil followed by 0.64° rotation away from the soil, and then returned to neutral vertical position
- 10 cycles of 0.96° rotation into the soil followed by 0.96° rotation away from the soil, and then returned to neutral vertical position
- 10 cycles of 1.28° rotation into the soil followed by 1.28° rotation away from the soil, and then returned to neutral vertical position

Data from the compressible inclusion configuration is presented in Figure 6.25 through Figure 6.28. These plots include presentation of force measured by the 20,000-lb load cell and rotation throughout testing. Also marked on the plot of rotation versus time during testing are the periods during which active earth pressure and lateral earth pressure thrust were achieved according to traditional Rankine theory. In these two plots (Figure 6.25 and Figure 6.26), three distinct cycling magnitude series can be observed, and only slight evidence of earth pressure ratcheting is existent in the third series of movements. Additionally, the magnitude of force required to achieve the target displacements was less than those of any configurations involving movements into and away from the soil mass.

The images of the top soil box “window” are provided for the geofoam inclusion configuration in Figure 6.27. The geofoam did not reduce the amount of soil settlement but did significantly reduce the amount of heave generated from movements into the soil mass. This is due to the compressibility of the material, which is free to deform during periods of high lateral earth pressure acting upon it. As a result, the geofoam compressed and densified throughout testing as opposed to soil heaving occurring. The precise values of soil settlement and heave are tabulated in Table 6.6, where soil settlement was similar to past configurations, but heaving was reduced.

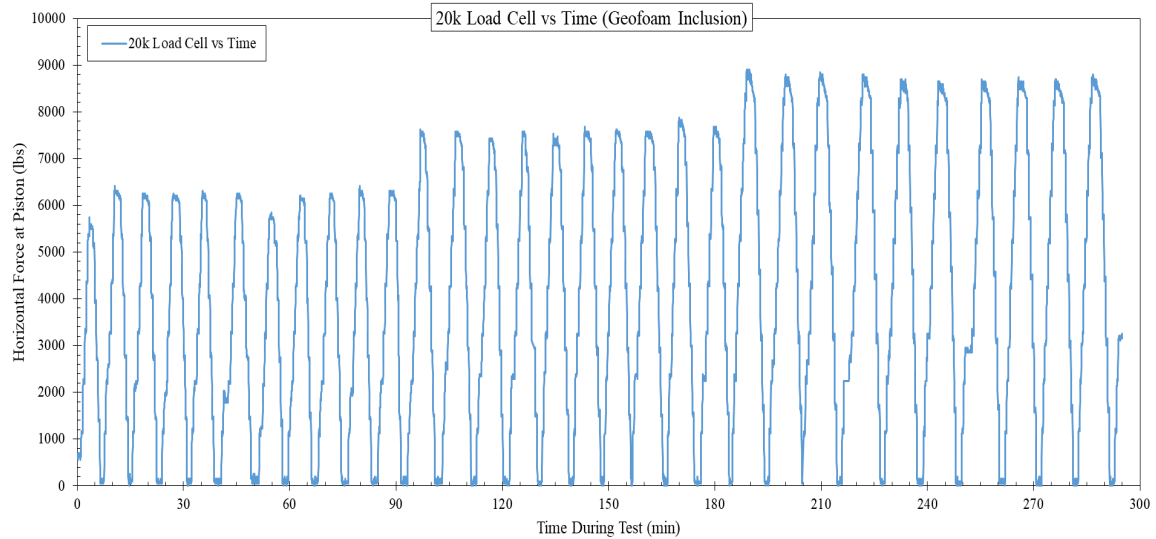


Figure 6.25: Time-history of lateral force for geofoam inclusion test

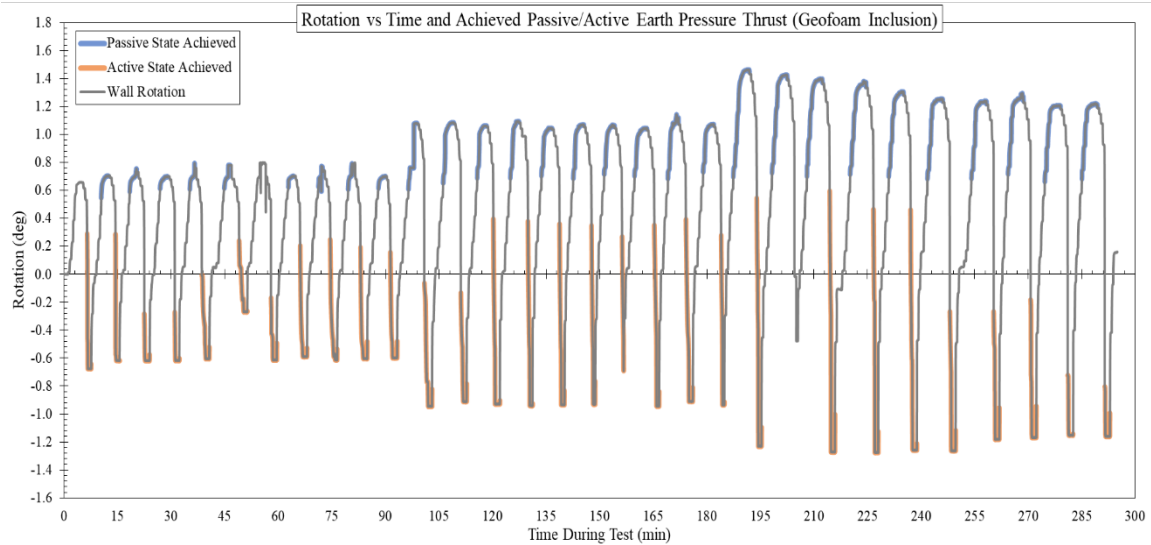


Figure 6.26: Time-history of wall rotation for geofoam inclusion test (Note: the mobilized passive and active force per Rankine theory)



(a)



(b)



(c)



(d)



(e)



(f)



(g)

Figure 6.27: Photos from top viewing window of soil box during geofoam inclusion test: (a) at beginning of test; and after (b) cycle 1.5; (c) cycle 1.10; (d) cycle 2.5; (e) cycle 2.10; (f) cycle 3.5; and (g) cycle 3.10

Table 6.6: Values of soil settlement and heave based on image correlation for geofoam inclusion test (extent of soil settlement measured from steel wall, not the edge of geofoam sheeting)

Maximum Depth of Soil Settlement	Extent of Soil Settlement Beyond Steel Wall	Maximum Height of Soil Heaving	Extent of Soil Heaving Beyond Steel Wall
<i>(in)</i>	<i>(in)</i>	<i>(in)</i>	<i>(in)</i>
5.723	19.356	0.520	20.377

In addition to the forces required to mobilize the wall and soil displacements, a pressure distribution acting upon the stiffened wall was developed at every point of the most forward movement of the wall into the soil during each cycle. These pressure distributions along with the locations at which PCs were mounted are presented in Figure 6.28. In the case of the geofoam inclusion, it is observed that increases in lateral earth pressure with cycling is greatly reduced. These increases could be considered negligible in the first two series of movements and increases potentially worth considering in design are isolated to the mid-height of the wall in the third series of movements. In viewing photos of the testing during the third series of cycles, it is apparent that the geofoam is significantly compressed at mid-height by this time, which would behave more like a rigid wall than a compressible inclusion. Considering this, it is logical that lateral earth pressure increases occur at mid-height during the third series of cycles.

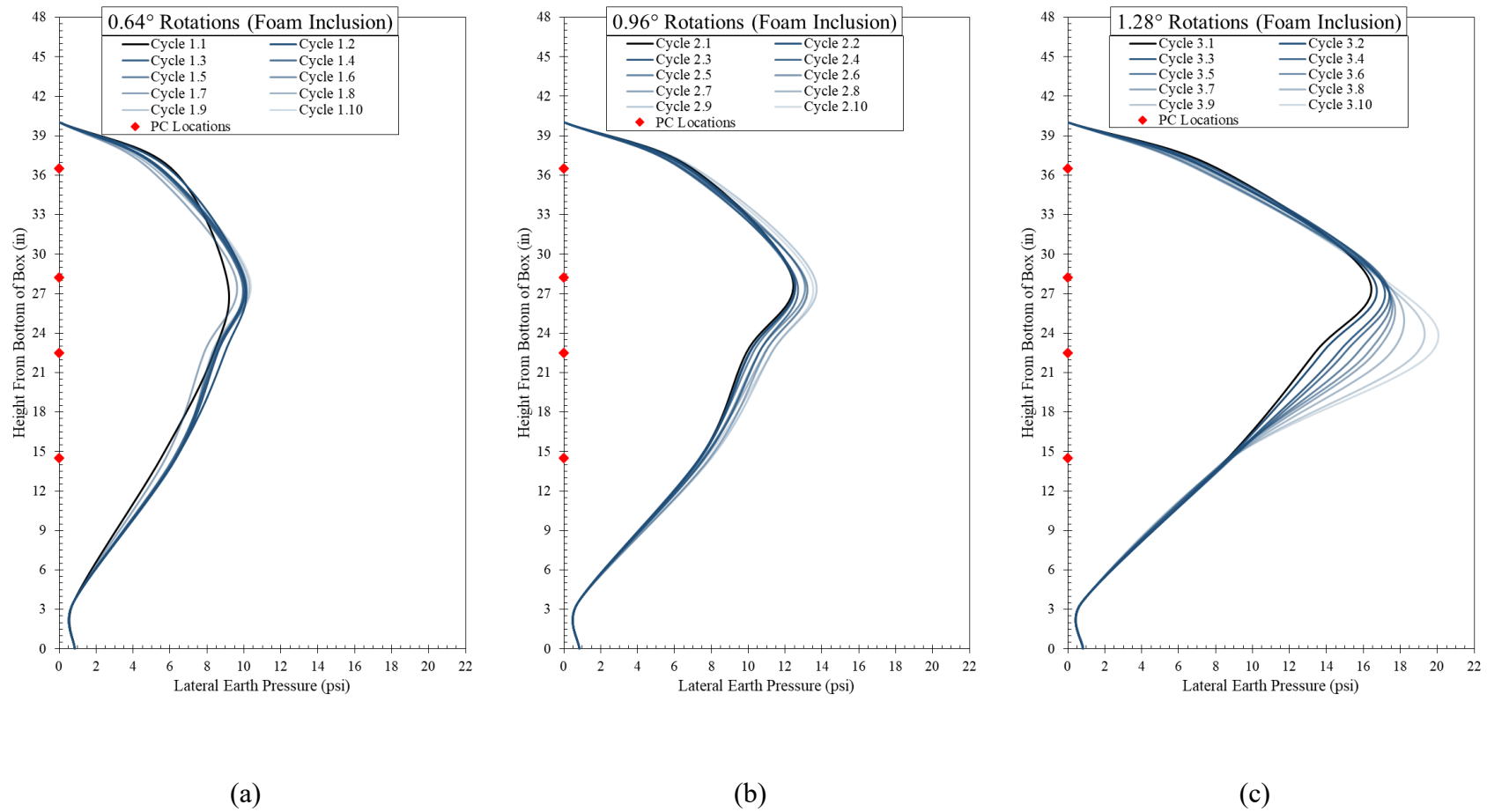


Figure 6.28: Pressure cell locations and lateral earth pressure distribution on stiffened steel wall for most forward position rotated into soil mass during: (a) first set of 10 cycles; (b) second set of 10 cycles; and (c) third set of 10 cycles of geofoam inclusion test

6.5. Analysis of Experimental Results

With the compilation of experimental test results presented in Section 6.4, a comparison of the results across testing configurations was made possible. This comparison primarily focused on the measured soil settlement and heaving from digital images, and the change in lateral earth pressures during cycling. In the case of retained soil movements, the displacements are quantified against the baseline case, while increases in lateral earth pressure throughout cycling are presented for each test. Another factor considered from the preparation process of each test configuration is the unit weight achieved in the filled box prior to testing.

Figure 6.29 shows the unit weight of the compacted poorly graded gravel in each testing configuration and how the value compares to the average via standard deviation. This plot demonstrates that four of the six tests were within $\pm 0.5\sigma$ (standard deviations) from the mean prepared unit weight of soil in the test box. Those tests that do not fall within a close range to the average are the wrap-around geotextile configuration, and the passive movements configuration. In the case of the wrap-around geotextile, the prepared unit weight is much higher than other configurations. This is likely because smaller height lifts were placed in preparing the test to allow for placement of the geotextile where desired. This coupled with an attempt to install the geotextile in a snug manner with tension in the material would have resulted in more compaction effort during this test setup compared to the other configurations. The passive movements test, which represents the loosest configuration, does not have a known reasoning for its large difference from the average unit weight prior to testing. It is likely that larger lifts however were placed, and thus less compaction effort was introduced to the soil box during filling. This being considered, it is expected that the testing configuration that consisted of movements into the soil mass only would yield a potentially noticeably different response when compared to the other tests with a higher unit weight.

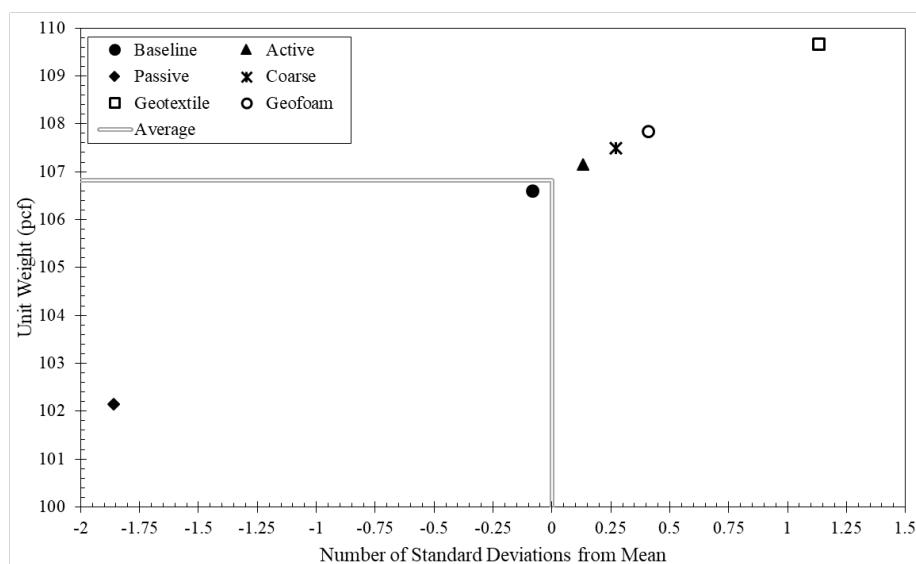


Figure 6.29: Unit weight and number of standard deviations from the mean for each testing configuration

Figure 6.30 presents the comparison of soil settlement values for each testing configuration as they compare to the baseline configuration. Positive percentages represent an increase in the measured value, while negative percentages represent a decrease in either settlement or extent relative to the baseline configuration. It is observed that both the active only and passive only movement tests as well as the geotextile reinforcement test resulted in less settlement by both measures (Figure 6.30a and Figure 6.30b). Having the opposite effect by both measures is the coarse interface and geofoam testing configuration. The common feature of these two tests, which showed an adverse effect on the settlement and extent of settlement beyond the rotating wall, was that only interface properties of the steel wall were changed. Adjusting the steel-gravel interface to something with greater friction in general causes more settlement at the soil-wall interface. This was particularly notable in the measure of maximum settlement with the coarse interface, which was the worst performer in this category. The best performer regarding the extent of settlement beyond the rotating wall was the wrap-around geotextile reinforced configuration. In this test, the maximum settlement was very close to that of the baseline, but the original soil height remained at the closest position relative to the wall when compared to all other configurations. This would result in the least amount of gap between an approach slab and backfill material, and as such would retain the integrity of the approach slab for an integral abutment the best when compared to the other testing configurations. It makes sense that both the active only and passive only movements yielded lower values of settlement and settlement extent, since the difference between the maximum and minimum degrees of rotation in these tests were only about 75% of the rotations in all other configurations. Even with this reduced amount of rotation, however, these tests still resulted in a larger extent of soil settlement relative to the geotextile configuration.

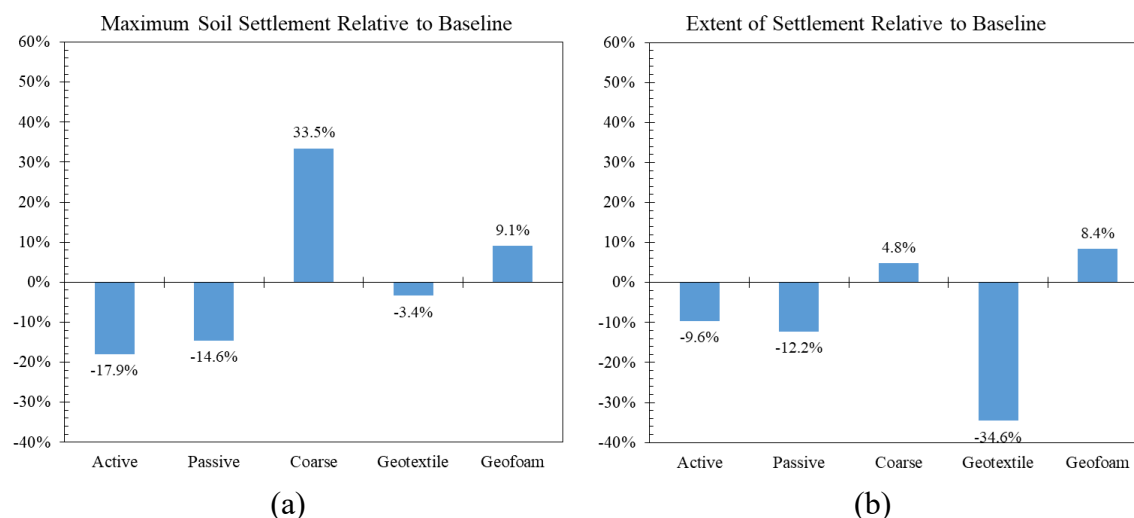


Figure 6.30: Comparison of all configurations relative to baseline for: a) soil settlement; and b) extent of settlement beyond rotating wall

Figure 6.31 illustrates the amount of heave and the extent of the heaved region behind the settled soil area in the testing box relative to the baseline configuration. Again, positive percentages

represent increased values (poorer performance) and negative values represent a decrease in heave (better performance) with respect to the baseline test. Less clear trends are observed in this measurement of performance, which may be due to the fact that heaving values were an order of magnitude less in height than settlement. As such, small changes in the amount of heave can have a considerable effect on the percentage difference relative to the baseline configuration. Two consistent observations related to the maximum heave (Figure 6.31a) and extent of heaving (Figure 6.31b) is that the wrap-around geotextile configuration performed the worst with the most heave and largest extent, while the geofoam configuration performed the best with the least heave and smallest extent. While the geofoam configuration allowed for a large amount of soil settlement, the compressibility of the material prevented movements into the soil mass from disturbing soil particles at a great distance from the stiffened steel wall. Consistent across both measures of heaving is the fact that the coarse interface test also performed worse compared to the baseline. This further supports that idea that a smooth interface is preferred for a geotechnical structure supporting backfill subjected to repeated loading.

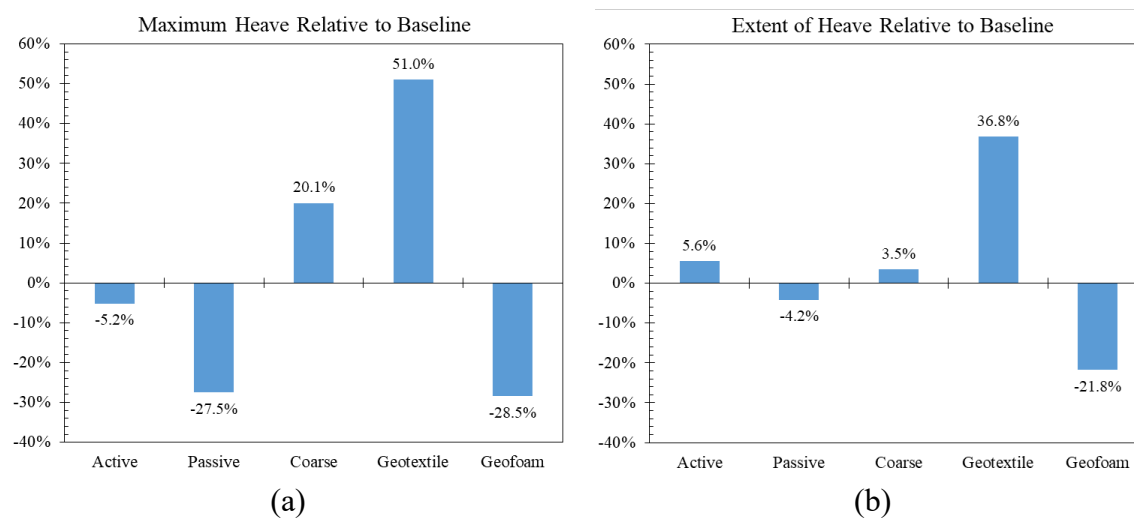


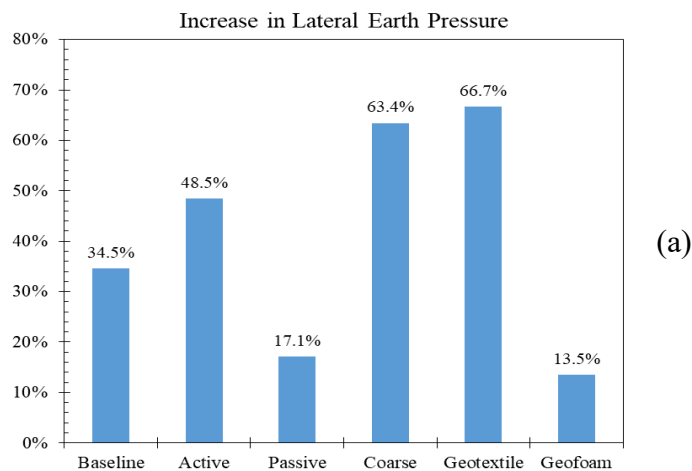
Figure 6.31: Comparison of all configurations relative to baseline for: a) maximum heave; and b) extent of heave beyond settlement region

Another insightful metric for comparing the different testing configurations is the increase in lateral earth pressure during a rotation series of equal magnitude. Figure 6.32 presents this percentage increase from minimum to maximum lateral earth pressure measured in the most forward position (into the soil mass) for testing configurations across a single rotation series. It is readily observed that in the first two rotation series, the geofoam configuration performs the best with the smallest percentage increase from the lowest pressure movement into the soil mass to the highest-pressure movement into the soil mass. The degrees of rotation for these series in this configuration were approximately 0.64° and 0.96° respectively corresponding to an absolute movement of 1.28° and 1.92° from the most backward to most forward position. Considering the absolute movements of this configuration, it is surprising to see such a small increase in lateral earth pressure relative to the active and passive movement tests since their absolute movements

in these series were only 0.64° and 1.28° respectively. As a result, it is reasonable to conclude that the geofoam material is an excellent inhibitor of lateral earth pressure ratcheting in structures subject to this magnitude and quantity of repeated movements.

Figure 6.32 also demonstrates that the coarse interface and wrap-around geotextile configurations performed the worst in nearly all rotation series as it relates to lateral earth pressure ratcheting. Clearly, the coarse interface develops adverse effects for the performance of the retained soil as has been exhibited throughout the experimental results. It was not expected however that the geotextile configuration would perform in this way. It is likely the interaction of the geotextile reinforcement with the retained soil, which resulted in an influence of soil displacements at a greater distance from the rotating wall (as shown in the displacements tracked in Figure 6.30 and Figure 6.31), that also caused larger increases in lateral earth pressure.

It has been shown that the geofoam inclusion configuration results in some of the smallest increases in lateral earth pressure and the least amount of heave throughout testing. Furthermore, smooth interfaces allow for the least amount of soil settlement. Considering these performance characteristics, it is expected that the best performing configuration would be one with a geofoam inclusion connected to the rotating wall that is then coated with a thin metal sheeting at the interface with the retained soil. This would ideally capture the best performance characteristics of each testing configuration.



(a)

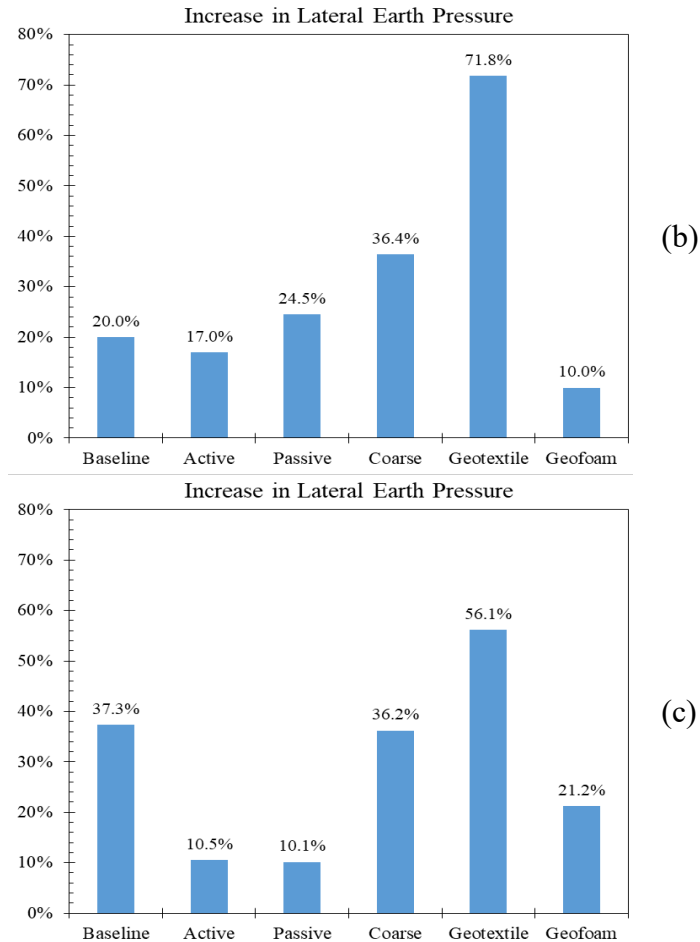


Figure 6.32: Comparison of all configurations' increase in lateral earth pressure from minimum to maximum measured in: a) first series of rotations; b) second series of rotations; and c) third series of rotations

6.6. Digital Image Correlation

While the visual analysis of soil deformations along with data collected using PCs on the wall in different arrangements of the wall have been very informative, it was decided to revisit the experimental component to perform more advanced analysis with the use of advanced Digital Image Correlation (DIC). This would enable the research team to gain better understanding of subsurface soil movement in ways normal visual inspection would not be able to.

To date, many freely/commercially available DIC programs have been developed to enable researchers track differences between successive images of the phenomenon of interest to understand the extent of change. A good example of such phenomenon in geotechnical engineering is development of shear bands in a shallow foundation loading experiment where the soil is placed behind transparent walls. For the purposes of this research, it was decided to use a very well-known MATLAB application called geoPIV-RG (Stanier et al., 2015), which was specifically developed for tracking movements in granular media.

As it was found that images captured for the previously explained testing program, may not be proper to use with this program, it was decided to run a new baseline test with new and improved camera equipment and use the DIC software to track soil particle movement across the cycles. In this baseline test, 20 cycles of loading, where each cycle included 0.25-in movement in the passive and then active direction, were imposed.

The deformation of the backfill soil can be visually expected in Figure 6.33. As can be seen, although it is clear that settlement immediately behind the wall increases as number of cycles increases, not much more can be interpreted with normal visual inspection.

There were nearly 220 images captured during this test (one image per 0.125 in movement of the top of the wall). Next, the images were processed using the DIC capabilities of geoPIV-RG and the software calculated many outputs including data showing the extent of vertical/horizontal movements, strains, shear bands, volumetric changes, etc. For the primary analysis, it was decided to focus on the vertical settlement data is the primary data of interest.

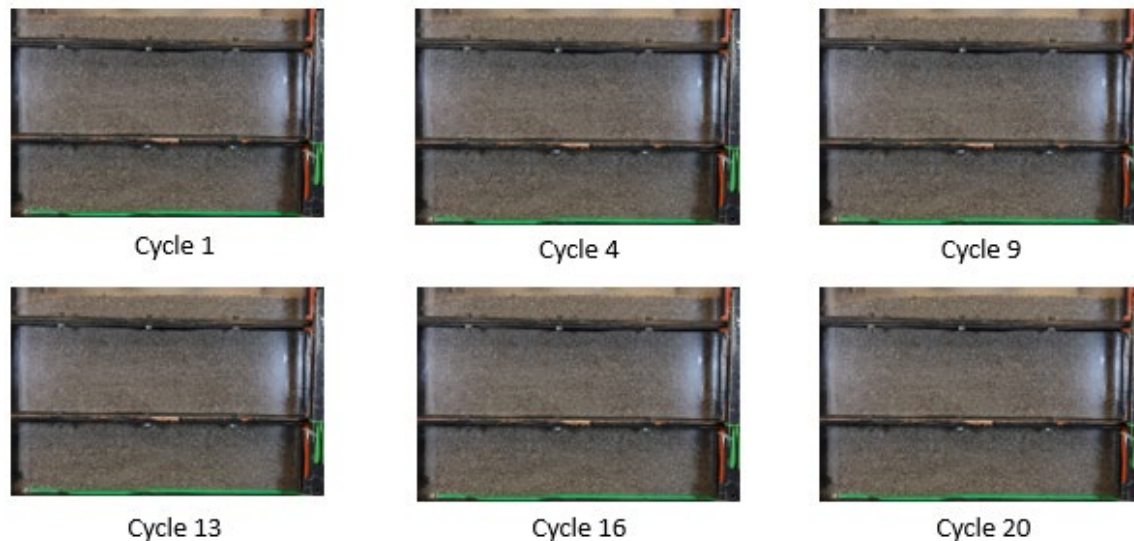


Figure 6.33: Side view of experimental setup (baseline test)

The settlement results can be seen in Figure 6.34, where warmer colors represent areas of higher magnitude vertical settlement. As can be seen, the extent of vertical settlement is actually quite larger than what is immediately visible in the images taken of the wall. Therefore, although it is only within 1 ft of the wall where the majority of settlement happens, it may be reasonable to assume that settlement would accumulate over time within the first 2-3 ft of the wall in large number of cycles, which is relevant to actual field conditions.

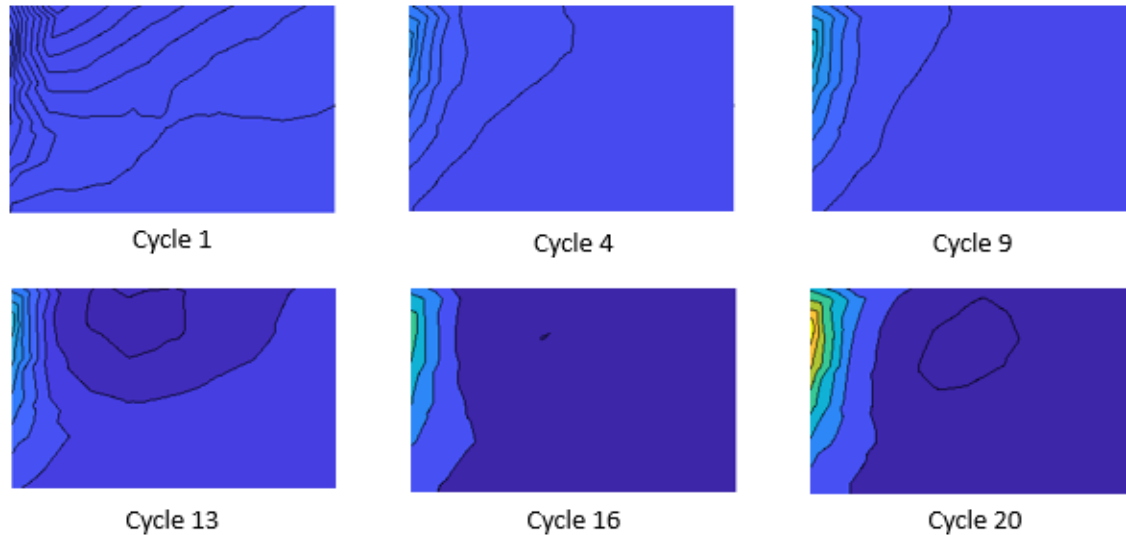


Figure 6.34: Vertical settlement contour plots for baseline test

6.7. Conclusions of the Experimental Component

The experimental component helped understand the effect of various boundary conditions on the cyclic behavior of backfill soil in Semi-Integral/Integral Abutment Bridges (SIAB/IAB).

Some of the most important findings from this component include:

- Increasing the roughness of the soil-wall interface negatively affects soil settlement near the interface by causing deeper settlements, which also extended to a distance beyond the location of the wall compared to all other tests
- Earth pressure ratcheting can be manifested both in the form of increases in lateral earth pressure with repeated movements to uniform rotations, as well as with decreases in rotation angle with repeated cycles to uniform loads
- Wrap-around geotextile reinforcement, and to a lesser extent a rough interface, were found to result in more heaving of the soil (considered a negative effect on performance) when compared to the baseline at some distance from the rotating wall
- The increase in lateral earth pressure acting upon a structure subjected to repeated loading into and/or away from a retained soil can be reduced using geofoam inclusions at the location of soil-structure interaction

Moreover, it was discovered that DIC algorithms can be effectively used to understand the behavior of soil under cyclic loading in this experimental setup. As demonstrated, it can clearly visualize the extent and magnitude of vertical settlement across the soil body and help predict the soil settlement in large cycles. The main drawback of using DIC algorithms is that this method is

extremely computationally intensive as calculations for the baseline cycle took over 20 hours to complete.

Chapter 7. Field Monitoring of Mack Creek Semi-integral Bridge

7.1. Introduction to Mack Creek Bridge Field Monitoring

A major goal of this project was to design and implement an instrumentation program at two Semi-Integral Abutment Bridges (SIAB) in the State of Texas. The first SIAB selected was a bridge replacement project at County Rd 2133, at Mack Creek, between US 79 and FM 1990. (The second SIAB selected was a bridge replacement project on TX-240 outside Haynesville, TX, over China Creek, which is discussed in Chapter 8.)

7.2. Field Monitoring of Mack Creek SIAB

7.2.1. Initial Instrumentation Plan (Summer 2017)

In summer of 2017, Mack Creek Bridge was instrumented using five Geokon model 4810 Vibrating Wire (VW) contact pressure cells. Two pressure cells were mounted vertically on each of the two abutment backwalls, prior to backfilling with crushed rock, spaced at uniform increments along the width of the backwall at the deepest location the dimensions of the cells would allow. The readings from the pressure cells would thus represent lateral earth pressure acting upon the abutment backwalls. A fifth pressure cell was also installed on a section of sheet piling that serves as the southern wingwall to the northwestern abutment. A location was chosen on the sheet piling far enough away from the backwall so that movements due to temperature changes would not affect the lateral earth pressure on the cell. Two Geokon model 8002-4 LC2X4 VW data loggers serve the five pressure cells and are mounted on the underside of the bridge near the west abutment. In addition to collecting pressure and temperature readings from the pressure cells in the soil, the data loggers themselves record temperature, which is representative of the ambient air temperature at the site. The location of the installed pressure cells and data loggers is shown in Figure 7.1.

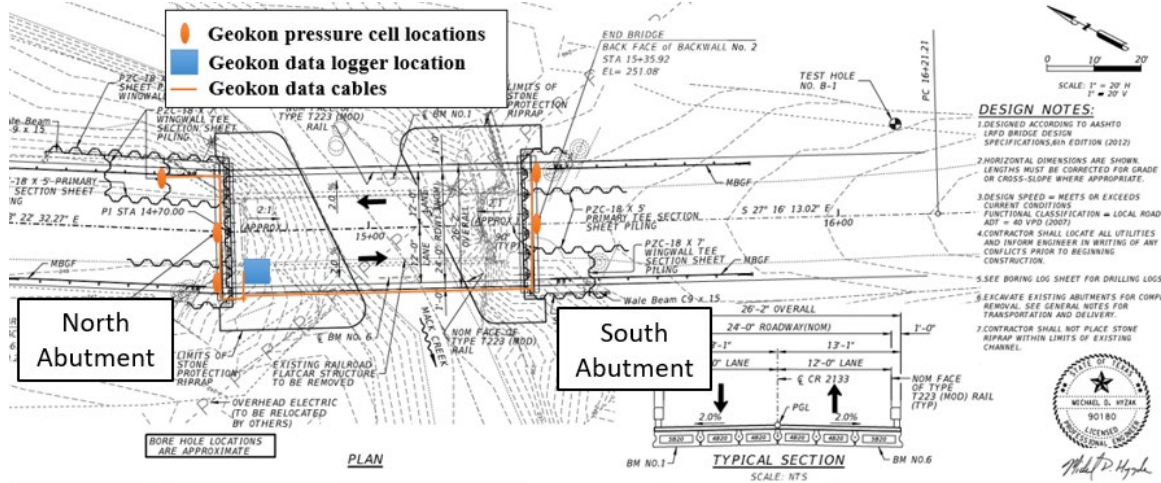


Figure 7.1: Location of installed pressure cells and data loggers

In January 2020, it was decided to install some of the sensors originally intended for China Creek Bridge on Mack Creek as the construction of China Creek had been delayed beyond initial expectations to collect additional data to better understand the performance of Mack Creek Bridge.

Figure 7.2 presents the lateral earth pressure recorded from the south abutment pressure cells, Figure 7.3 presents the lateral earth pressure recorded from the north abutment pressure cells, and Figure 7.4 presents the pressure recorded from the northeast wingwall (control sensor). In each of these figures, the lateral earth pressure is plotted against the Y-axis on the left, and temperature at the site is also plotted against the Y-axis on the right. The reported temperatures in these figures represents an average of the temperature sensors in the two data loggers that were suspended under the bridge on the south side. Prior to presenting these temperature recordings as representative of ambient air temperature, their validity was confirmed against readings from a nearby weather station in Palestine, TX.

Several interesting trends can be observed in the data recorded from the north and south abutment pressure cells. Firstly, a setting period can be identified where, despite the large temperature fluctuations of the initial months, the pressure seems to be increasing on the north abutment and decreasing on the south abutment on average. After the end of August 2017, average pressure remains relatively constant on both abutments until winter.

Another trend observed in fall and winter is that although daily fluctuations in pressure can be as big as the preceding summer, there are many occasions where the range of daily fluctuation is relatively small. This is most likely due to smaller duration of direct solar radiation on bridge deck due to larger number of cloudy days, the shorter duration of days and the lower angle of incidence of solar rays on the surface of the earth in winter and fall. However, it should also be noted that the largest pressures until the end of the first winter were recorded in the second half of November, when there seems to be a relatively significant increase in temperature bringing

the ambient temperature back to lower summer temperatures. While this temperature is not as high as what was experienced in the summer, it results in the generation of pressures higher than those previously seen.

This appears to be due to a phenomenon called pressure ratcheting, which is likely to be found in structures that undergo cyclic movements in active/passive directions. Although the ratcheting mechanism in soil is not well understood yet, it is believed that in order for the soil to undergo pressure increase in passive directions, it must first experience collapse under active condition before being moved in passive direction again. This hypothesis can explain why majority of pressure magnitude increase happens during the colder months of the year where the soil is more likely to experience active condition when the bridge shrinks the most due to shorter days, lower temperatures and less daily solar radiation. As can be seen in the reported data, this incident gets repeated several times during fall and winter, generating pressures slightly higher than what was observed in the preceding summer.

This hypothesis also explains why despite experiencing very high pressures during the warm seasons, pressure magnitude does not increase considerably during these months; this is because although the bridge length is at its largest due to warmer temperatures, longer days and higher solar radiation levels, these conditions do not allow the bridge to cool down much during the nights and therefore the bridge probably does not shrink enough to allow the soil to enter active state. As a result, pressures remain high but there is no significant ratcheting observed.

Moreover, the trend observed in data gathered in May 2019 further supports the ratcheting hypothesis. As can be seen, the average pressure on the south abutment has approximately doubled by the first summer and tripled by the second summer (Figure 7.5); this causes the south abutment to experience pressures ranging from 1 psi to close to 9 psi on many days of the summer. However, such an increase is not observed in the north abutment (Figure 7.6), where the average pressure remained relatively constant in the first year (close to what was observed at the end of the “setting period” [August 2017]) and showed a slight increase during the second year as the warm season approached. Nonetheless, even for the north abutment, the magnitude of daily fluctuations in pressure seem to be about 50% higher than what was observed right after construction, which also could be a sign of “ratcheting behavior.” While the factors that caused this drastic difference in behavior are not fully understood at this point, this may be partly explained by differences in the geology, bridge geometry and topography of the two sides, as shown in

Figure 7.7. It can be seen that the bridge deck is not constructed horizontally and there is 0.8-1.6% downward grade toward the north abutment, which may in turn cause the abutment displacements to be different than one another and not exactly half of total bridge length on either side. A hypothesis is that the slope of the bridge allows the south abutment wall to move more than the north abutment one that is “pinned down” by the sine component of the weight of the bridge. Moreover, upper layers of natural soil between the two abutments are different where

the north abutment has silty soil on top and the south abutment has clayey sand and low plasticity clay. However, these hypotheses can only be verified once a sophisticated numerical model that accounts for the complete geometry of the bridge is constructed.

Regarding the yearly variation in temperature (Figure 7.8), it is apparent that ambient temperature has increased by 3.6 to 5.4 degrees (F) on average from one summer to another but the magnitude of daily fluctuations is not changed notably.

Additionally, the temperature recorded by the sensors installed on the abutment walls are presented in Figure 7.9. There are several interesting trends apparent in this figure. Firstly, it is apparent that the pressure cells do not sense daily hourly changes in temperature as was recorded in the ambient temperature data. This is partly because these sensors are buried at the bottom level of the abutment wall and are in contact with the concrete. Therefore, they are most likely to sense the temperature changes in the concrete and backfill as heat diffuses into these media. This explanation also explains why the peaks in sensor temperatures occur slightly after there is a peak in average ambient temperature. Moreover, it can be seen that the sensors have recorded higher temperatures in the summer months and close to average ambient temperatures in the other months. This points to the possibility that solar radiation is affecting these recording; in summer months, where solar radiation is more intense and has longer duration per day, deck surface and asphalt surface can get considerably hotter than the ambient and cause the sensors to also record higher temperatures on average.

In addition to the earth pressure cells on the bridge abutments, the data from the control pressure cell on the northeast wingwall is presented in Figure 7.4. As expected, the pressure fluctuations with temperature changes for this pressure cell are small when compared to those on the abutment backwalls. Minor fluctuations do occur, however, but reduce in magnitude over time. The fluctuations in pressure readings from this cell may also be a result of extreme temperature changes within the transducer housing of the sensor itself. Since the control sensor is mounted to a sheet pile that has the outside face exposed to the atmosphere, the sheet pile may absorb high levels of thermal energy in days of intense sunshine. Accordingly, the heated sheet pile passes heat onto the transducer house of the pressure cell. It can be seen that the range of temperature fluctuations for this sensor were much larger than other for the other sensors mounted on the backwall. Therefore, the fluctuations observed in the control earth pressure cell are likely due to the fact that this sensor is affected more by the changes in climate which could make corrections for temperature-related effects less effective. However, although small seasonal changes in stress is seen in this sensor, the pressure recordings remain relatively constant and provide a good reference for comparison with other sensors.

In November 2019, another visit to Mack Creek Bridge was made to assess the conditions of the bridge and collect new instrumentation data. Unfortunately, processing of the data gathered on this trip revealed that a problem affected most of the installed sensors and caused incorrect measurements by the logger.

Unlike the trend observed over the past two years, the pressures in the south abutment were seen to consistently decrease in July 2019 (Figure 7.2). At this point, this change in behavior cannot be easily explained seeing as the temperature record is similar to the previous two summers. One possible explanation is that high pressures generated in the backfill has created a crack in the structure or enabled the soil to find a “way out” of the backfill, letting the pressure decrease over July and August 2019, despite the daily cyclic loads applied due to bridge expansion.

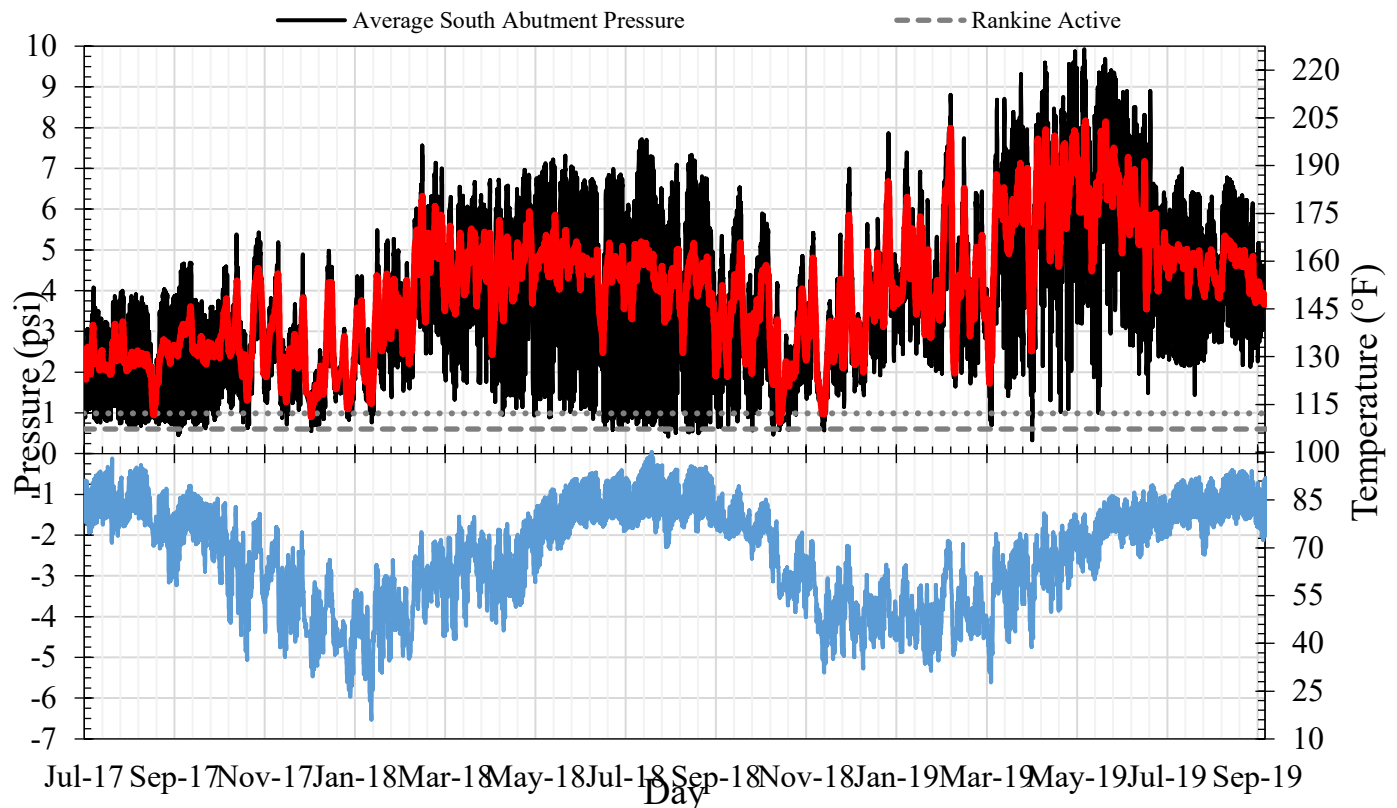


Figure 7.2: Average pressure reading of two contact pressure cells on Mack Creek Bridge south abutment and average temperature reading of two data loggers beneath bridge

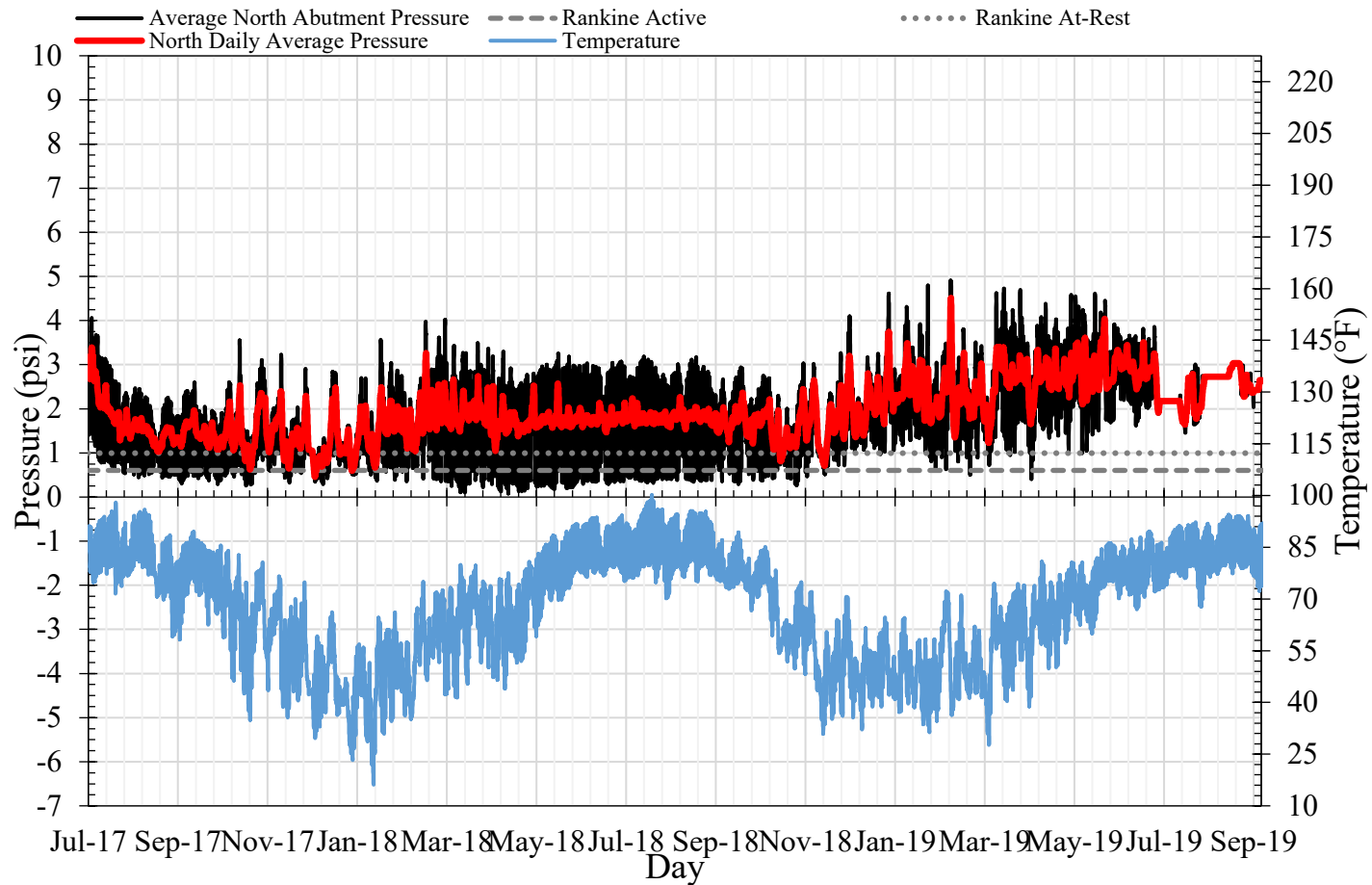


Figure 7.3: Average pressure reading of two contact pressure cells on Mack Creek Bridge north abutment and average temperature reading of two data loggers beneath bridge

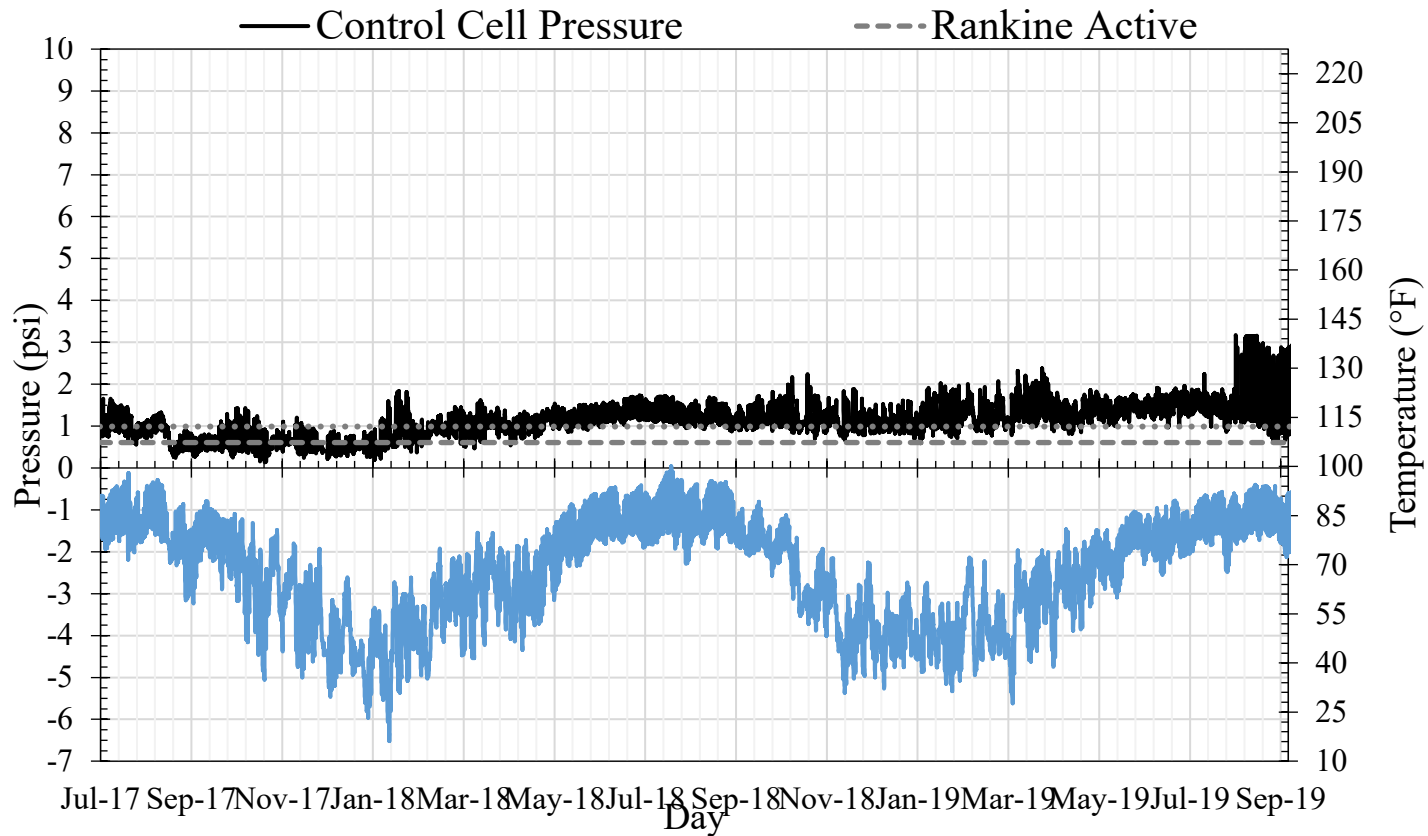


Figure 7.4: Pressure reading of control contact pressure cell on Mack Creek Bridge north wingwall and average temperature reading of two data loggers beneath bridge

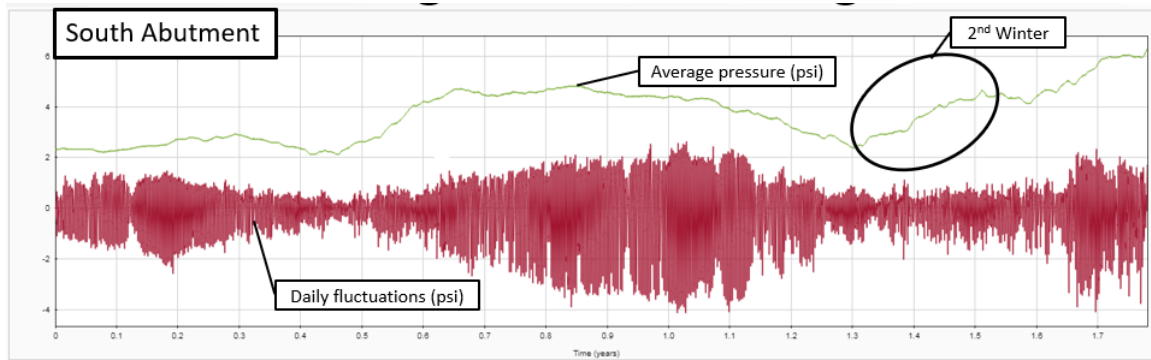


Figure 7.5: Average and daily fluctuations of pressure behind south abutment backwall

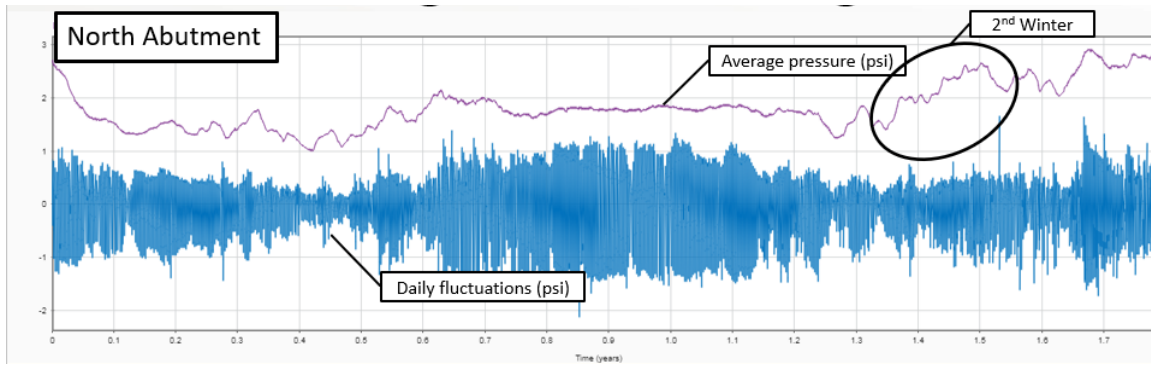


Figure 7.6: Average and daily fluctuations of pressure behind the north abutment backwall

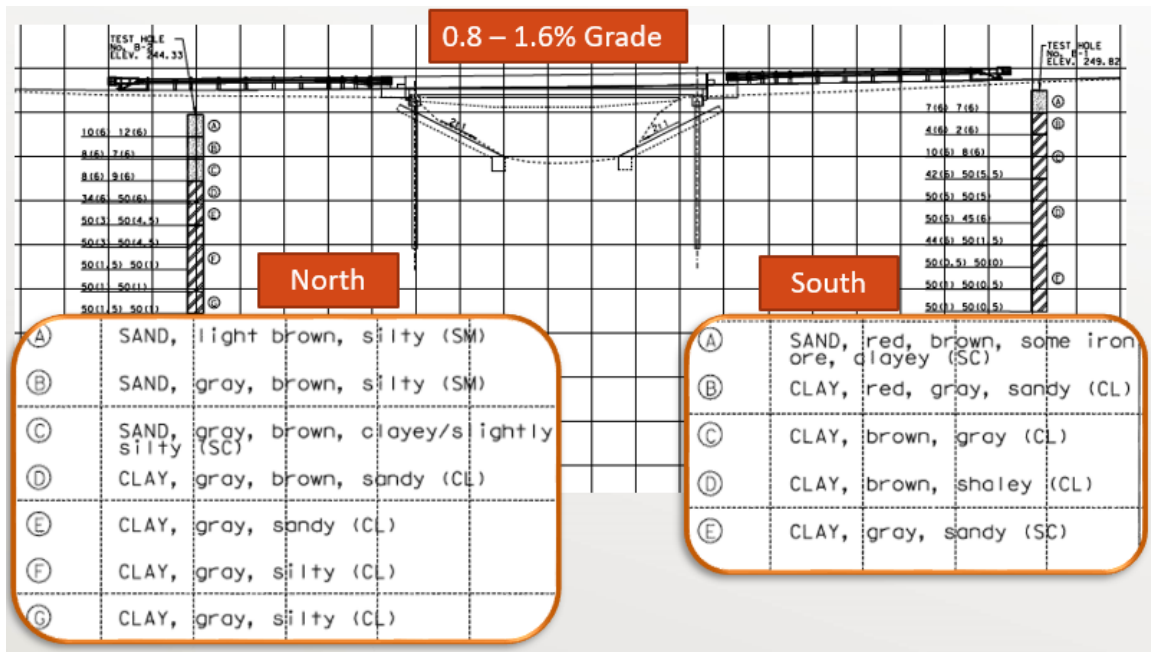


Figure 7.7: Site profile for Mack Creek Bridge

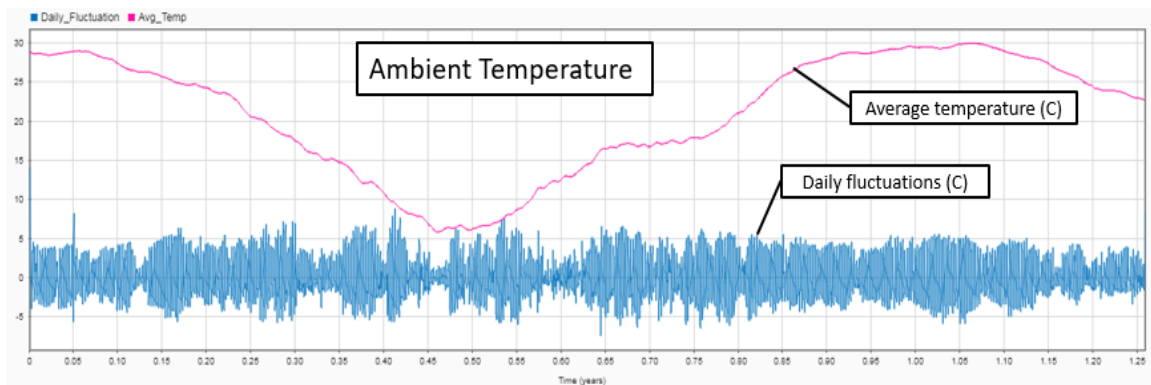


Figure 7.8: Average and daily fluctuations of ambient temperature as recorded by data loggers beneath the bridge

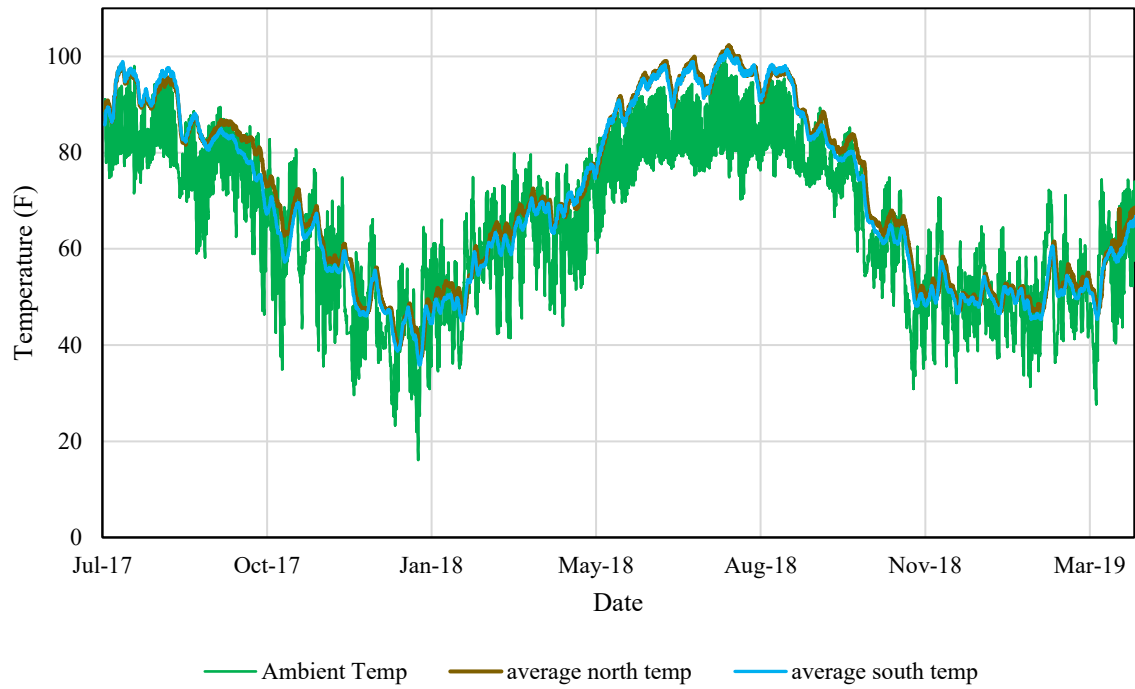


Figure 7.9: Temperature variations in mounted pressure cells as compared with ambient temperature

7.2.2. Additional Instrumentation of Mack Creek SIAB (Winter 2020)

After facing the difficulties in determining the exact magnitude of displacement at the ends of Mack Creek Bridge as input for the numerical model, it was decided to take advantage of the delay in construction of China Creek Bridge and install additional sensors, originally meant for China Creek Bridge, on Mack Creek Bridge. The new equipment was mounted on the bridge in January 2020, the details of which are provided in the following subsections.

7.2.2.1. Assembly and In-house Testing

A new F-rated enclosure was purchased to house the sensors and loggers for this temporary monitoring project. Once the arrangement of components inside the enclosure was decided, holes were drilled in the steel mounting panel and the components were wired accordingly (Figure 7.10). Once the sensors were placed inside the enclosure, a “peep hole” for the laser distance meter was carved out of the side of the enclosure and covered with plexiglass. This would help protect the sensor from the environment while allowing it to make measurements. Before placement of the plexiglass, it was verified that plexiglass does not absorb a significant amount of infrared light emitted by the sensor. The finished assembly is shown in Figure 7.11. In addition to the laser distance meter, a ClimaVue50, SI-111SS and two crackmeters were deployed as well to get more familiar with how these sensors work and test their performances in the field. Most importantly, it was decided to use a cell modem to facilitate data collection and test the remote data collection capability, which would be more important for China Creek SIAB due to the project location’s distance from Austin, TX. To power this setup, it was decided to use one of the solar panels purchased for monitoring of China Creek.

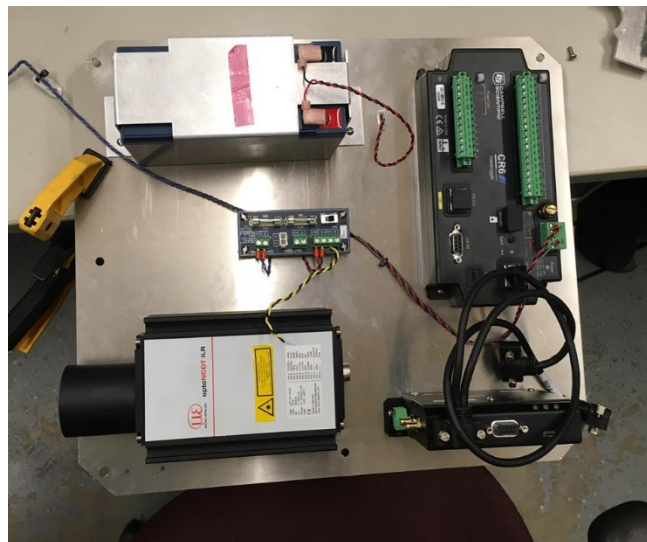


Figure 7.10: Assembly of sensor and logger equipment for temporary additional instrumentation of Mack Creek SIAB

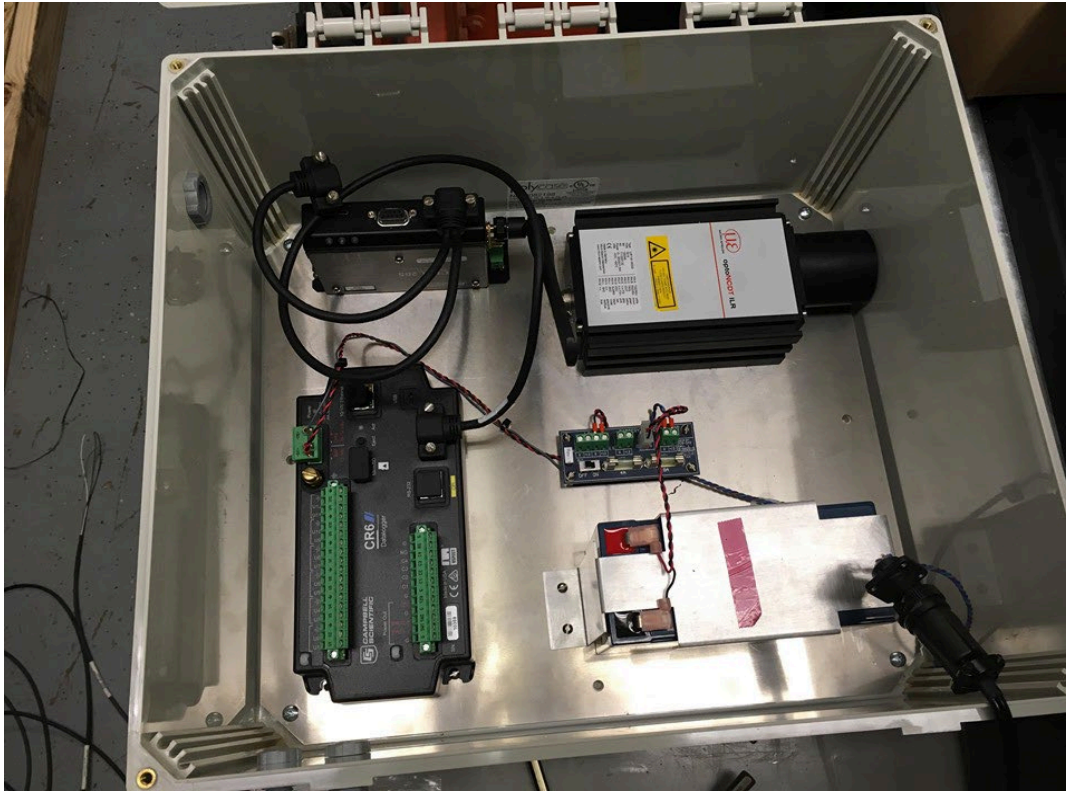


Figure 7.11: Enclosure assembled for additional monitoring of Mack Creek SIAB

As the research team had no prior field experience with this kind of instrumentation setup (wireless data transmission, solar powered, etc.), it was decided to test the equipment on the rooftop of the Civil Engineering Department at UT Austin, as shown in Figure 7.12. In this picture, the enclosure is set next to the wall on the right side, while the solar panel, ClimaVue50 and SI-111SS instrumentation are placed on the left.

This initial test led to the discovery that the wireless data transmission block of the code developed was causing more power draw than the solar panel could compensate for. This eventually led to system shutdown and therefore the code was adjusted accordingly.

Over time, the CRBasic code has undergone many revisions to optimize the performance of the system and currently it is capable of turning on the modem at a certain time for a certain duration, automatically sending data through email and is also capable of sending text alerts when battery voltage drops below a certain number, threatening shutdown or incorrect measurements. An important advantage of having wireless connection to the logger is that it enables the user to update the program running on the logger without having to be physically present at the location and monitor the performance of the new code while in office.



Figure 7.12: Testing of equipment on rooftop of Civil Engineering Department at UT Austin

7.2.2.2. Data Collection, Processing and Visualization Program

As mentioned in the previous section, the CRBasic code was developed so that the sensor measurements done each day would be sent via email to a specified email address so that the users would not have to wait for the exact time the cellular modem is turned on to download the newly acquired data. For this purpose, a specific email account was created to solely receive emails from the data logger and an email is sent everyday with data collected over the preceding 24 hours. It is possible to have the data logger send all the data each time it sends an email but it will not be efficient/economical considering the upload time of the larger files for the logger and data costs.

As this is a long-term monitoring program, it is evident that the research team would have to combine many small data files to visualize the results, which would be very tedious if done manually every time. Therefore, a Python program was developed to help with data collection, processing and visualization. Python is a popular, high-level programming language used in a large variety of applications, especially in data sciences and scientific applications.

As the research team deemed it beneficial to be able to execute the code when needed and on any computer device needed, it was decided to develop this code in “Google Colab”. Google colab is a Jupyter notebook environment that does not require the user to install any software on his/her personal computer to write or execute the code. Instead, the code is executed by a virtual machine dedicated to the user’s account and so all that is needed for the code to work is an up-to-date browser and working internet connection.

The flowchart in Figure 7.13 shows the general processes handled by the code developed, which will be explained in following subsections.

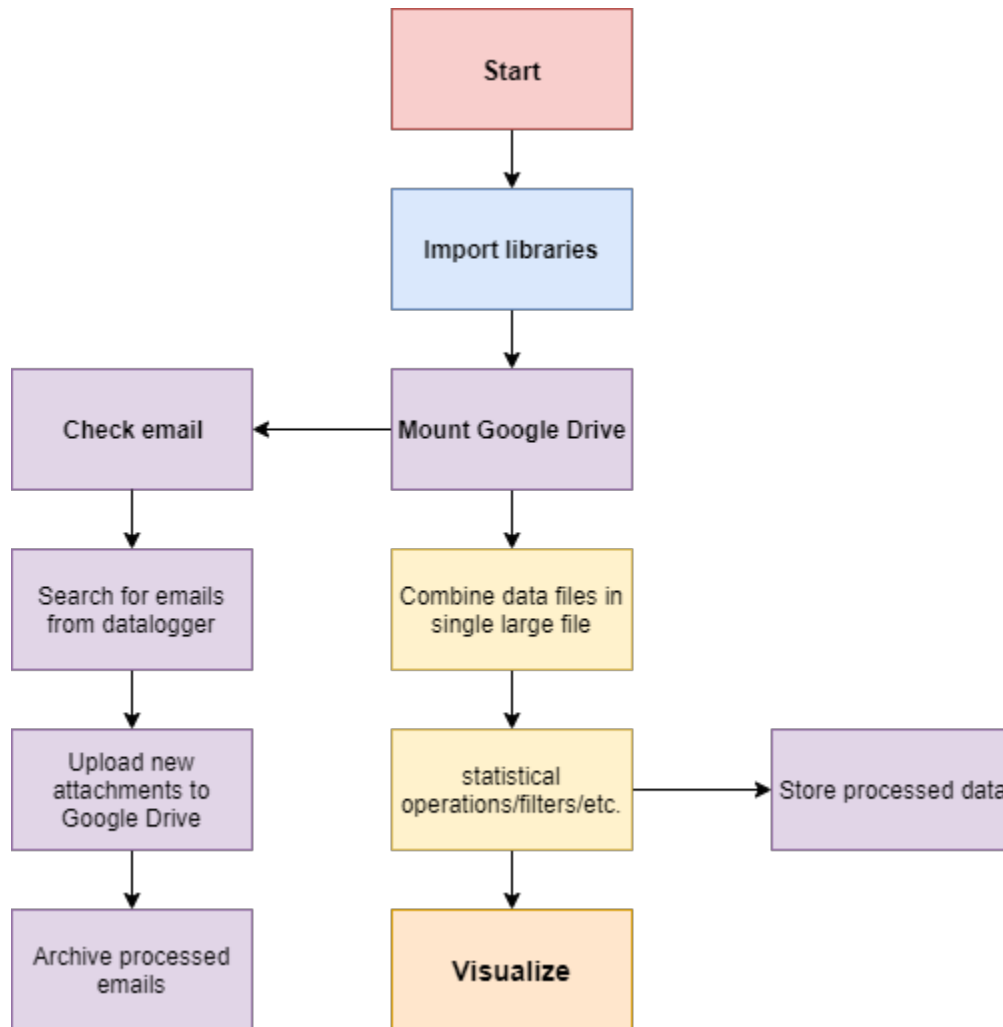


Figure 7.13: Flow chart of the Python program developed for data collection, processing and visualization

7.2.2.2.1. Python Libraries

Although Python comes with a pre-installed standard library, many functions such as plotting, filtering, advanced mathematical operations, file management, etc. are not readily available. These functionalities are added by finding the appropriate library and importing them in the program to make their instructions available for use. Some of the libraries used for this code are:

- Os (file management)
- Numpy (mathematics)
- Impalib and email (email-related operations)

- Pandas (data file processing/reading and writing data files)
- Plotly (data visualization)

More details about these libraries can be found in their respective documentation and websites.

7.2.2.2.2. File Management

The most important function of this code is to automate the process of checking email for new data sent from the data logger, download the attachments, upload them to Google Drive and combine them in one single file with previously downloaded files.

For this purpose, a code was developed that would login to the email address where data logger messages are received (Figure 7.14). Once logged in, all the relevant emails that match the description of what is expected from data logger are searched for and their attachments are downloaded. Once downloaded, these messages are archived to avoid processing them again on future executions of the code (Figure 7.15).

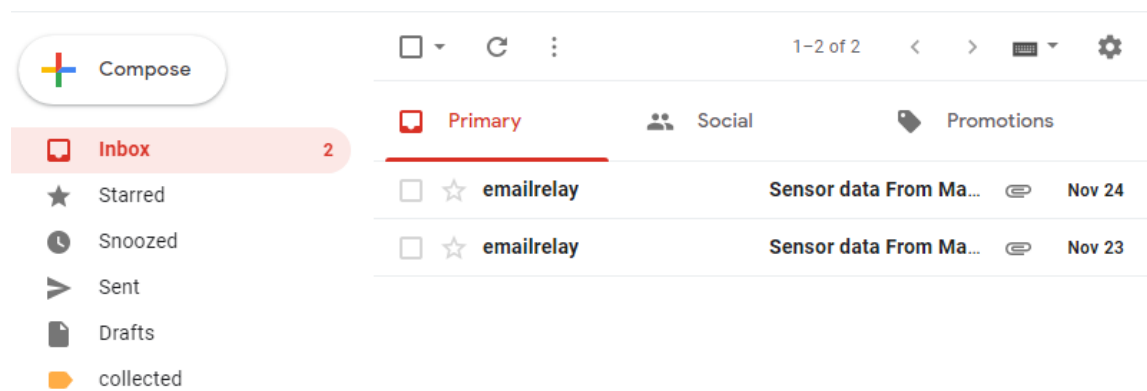


Figure 7.14: New messages received from data logger

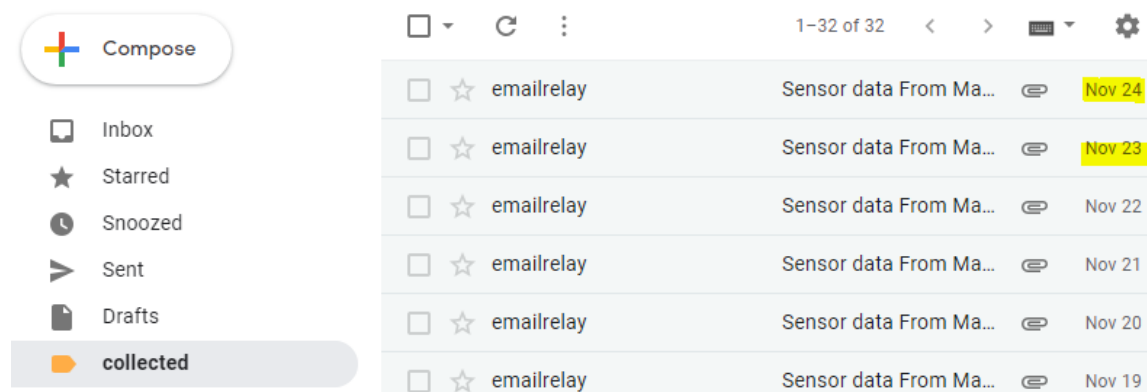


Figure 7.15: Archived messages post-processing by Python

Next, the downloaded attachments are directly uploaded to a Google Drive location to enable ease of access and data sharing when needed.

After the email-related operations are executed, a separate algorithm is executed that will look into the contents of the Google Drive for unprocessed files and would add them to the “master file,” which contains all data previously processed or creates a new “master file” if one does not exist yet. An example output of this algorithm is shown in Figure 7.16.

This simple algorithm provides a great time-saving advantage over the manual alternative, which is opening multiple CSV files in Excel and copying and pasting data to create a “master file” that is also prone to human errors.

```
Output.csv already exists.
New files found in folder.
Output.csv was updated!
CELL_DIAG30.dat Moved to gdrive/cr6data/Processed
SensorData30.dat Moved to gdrive/cr6data/Processed
CELL_DIAG31.dat Moved to gdrive/cr6data/Processed
SensorData31.dat Moved to gdrive/cr6data/Processed

Here's how Output.csv looks like:
Number of records = 768
```

	TIMESTAMP	RECORD	BatteryV	ChargeIn	ChargeOut	LithiumV	PTemp_C	TT_C_Avg	SBT_C_Avg	SlrFD_kW_Avg
0	TS	RN	Volts	Volts	Volts	Volts	Deg C	Deg C	Deg C	kW/m^2
1	2019-10-23 15:00:00	0	13.81	0	0	3.788	27.9	38.5	28.94	0.837
2	2019-10-23 16:00:00	1	13.8	0	0	3.786	28.71	35.29	29.31	0.677

Figure 7.16: Example output of file management algorithm developed in Python

An advantage of using Pandas library to interpret datafiles is that it is capable of interpreting timestamp data automatically, which would be very handy in calculating statistics such as daily/monthly averages or maxima with a single line of code.

7.2.2.2.3. Visualization

Perhaps the most complex part of the algorithm developed so far is that dedicated to visualization of the acquired data as it is perhaps the most significant step in gaining an understanding of data gathered from the field.

As a result, the research team decided to get familiar with the extensive plotting library offered by Plotly to help visualize the collected time series along with helpful statistics in an interactive manner. The interactivity of this algorithm is deemed a huge advantage over conventional plotting methods using Excel as that process can be extremely cumbersome when dealing with large number of variables. To give an idea, the small number of sensors planned for additional instrumentation of Mack Creek, provide more than 20 independent measurements every hour. Plotting this many variables, especially if new data is to be added everyday would be very hard to manage if done manually using a spreadsheet program such as Excel.

An example output of the plotting algorithm is shown in Figure 7.17. This mini-program would allow the user to load the “master file” and create an interactive time-history plot of past measurements, equipped with a handy range slider to allow the user to focus on a certain portion of data as desired. Moreover, a histogram of daily averages, maxima and minima for the variable in focus are plotted as well to aid in understanding the data. Most importantly, a dropdown menu (shown on the left side of Figure 7.17) has been programmed that allows the user to select the variable to be plotted with a simple click.

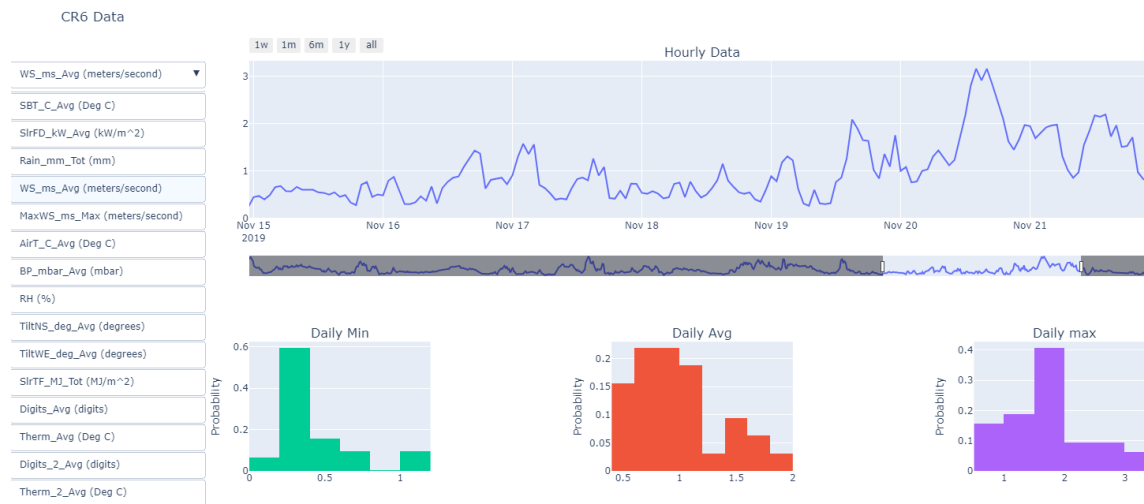


Figure 7.17: Example output of plotting program developed in Python

As demonstrated, programming tedious and repetitive tasks, such as data collection, storage, processing and plotting, saves a significant amount of time and eliminates room for error. In the future, interactive tools that would enable noise filtering capabilities are expected to be added as well.

7.2.2.3. Field Installation

When testing the new equipment on the Civil Engineering building rooftop concluded and final revisions to the logger program were made, the research team planned a field visit to Mack Creek to mount the new set of sensors on the bridge to begin collecting previously uncollected complementary data. As shown in Figure 7.18, the logger equipment, laser source, solar panel, ClimaVue50, SI-111SS and one of the crackmeters were installed on the south abutment, and the laser target and a crackmeter were installed on the north abutment. The data logger was programmed to take measurements three times per hour and store average/maximum values of recordings (depending on parameter). The logger was also programmed to communicate the collected values every day at noon.

In Figure 7.19, equipment installed on the south abutment is shown. Although no flooding/submersion is anticipated in this location, the enclosure and cable glands were tested against prolonged submersion up to 3 ft and this enclosure should therefore safeguard the

equipment against surface water and rain for the duration of the project. As can be seen in Figure 7.19(b), a rain guard was attached to the laser's peep hole to minimize splashback and accumulation of dirt due to rain and reduce the need for maintenance. The enclosure containing the laser source is installed on top of the backwall while the crackmeter is attached to both backwall and pile cap.



Figure 7.18: Equipment installed on Mack Creek SIAB in January 2020

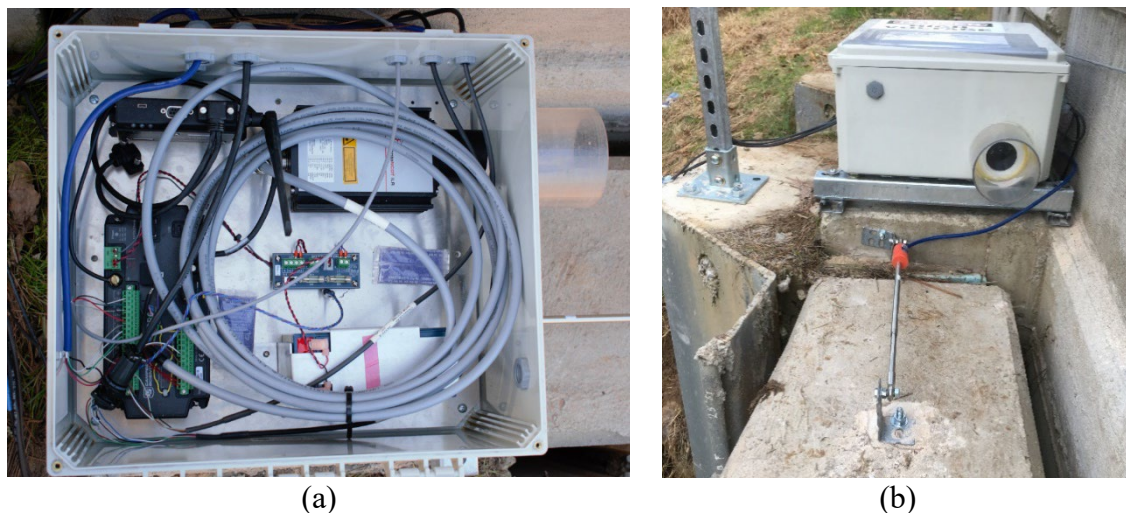


Figure 7.19: Closeup of equipment installed on south abutment: (a) logger equipment and laser distance meter; and (b) crackmeter installed between backwall and pile cap + loggerbox

A closeup of the components installed on the north abutment is shown in Figure 7.20. The laser target is installed on top of the backwall to capture the total expansion/contraction of the deck as deck and backwall are connected in SIAB structures. Similar to the south abutment, the crackmeter is connected to both backwall and pile cap to capture the relative displacement between the two.



Figure 7.20: Closeup of equipment installed on north abutment, laser target and crackmeter installed between backwall and pile cap: (a) view from behind; and (b) top view

Finally, a 10-ft unistrut section was used as a pole to install solar panel, ClimaVue50, SI-111SS and lightning protection equipment (Figure 7.21). This pole was placed as far from the road as possible on the edge of the wingwall. The solar panel faces south to catch the most sun and ClimaVue50 was equipped with a bird spike kit to prevent issues arising from birds sitting on top of the device. Moreover, SI-111SS, which has a 22° half angle field of view was mounted near the top and pointed at the deck in such way that full field of view of the device, covers the deck and not the surroundings. This device is designed to measure the average temperature of the surface it is pointed at, based on the infrared radiations coming from the target surface.



Figure 7.21: Closeup of pole-mounted equipment on south abutment, which includes solar panel, ClimaVue50, SI-111SS and lightning protection device: (a) installation of SI-111SS for measuring deck surface temperatures; and (b) closeup of SI-111SS

7.2.2.4. Analysis of Data Collected Through Additional Instrumentation

The newly mounted sensors provided the research team with a trove of new information collected and analyzed daily by an automated cloud-based Python program.

Perhaps the most important variable measured through the new monitoring program is the continuous measurement of changes to bridge length, which previously was not possible. The deck length changes since the moment of installation is presented in Figure 7.22. Since the original length of the bridge was not known, the measured length from the moment of laser installation was used as a baseline length to calculate the expansion/contraction of the bridge. During this monitoring period, it is evident that the bridge length has changed by more than 1.5 inches, which is quite significant. As can be seen, the bridge has experienced a relatively large amount of contraction during the extremely cold weather brought by winter storm Uri in February 2021. However, despite the continued measurements by the laser distance meter during this event, some of this data is considered invalid as the temperature has dropped below the sensor's standard operating temperature. Overall, based on nearly three years of monitoring, we can see nearly 1 inch of change in the total length of the bridge, excluding the winter storm event of 2021.

Additionally, a histogram depicting the daily changes in bridge length is created. As can be seen in Figure 7.23, in a given day, the bridge length has changed between 0.05 to 0.5 in. with most common values between 0.12 to 0.2 in. As reported in Chapter 6, even such seemingly small cycles of movements can contribute to large settlements in the backfill. All in all, it would be interesting to see how this histogram develops over the coming seasons and conduct additional experiments depending on the new information gathered.

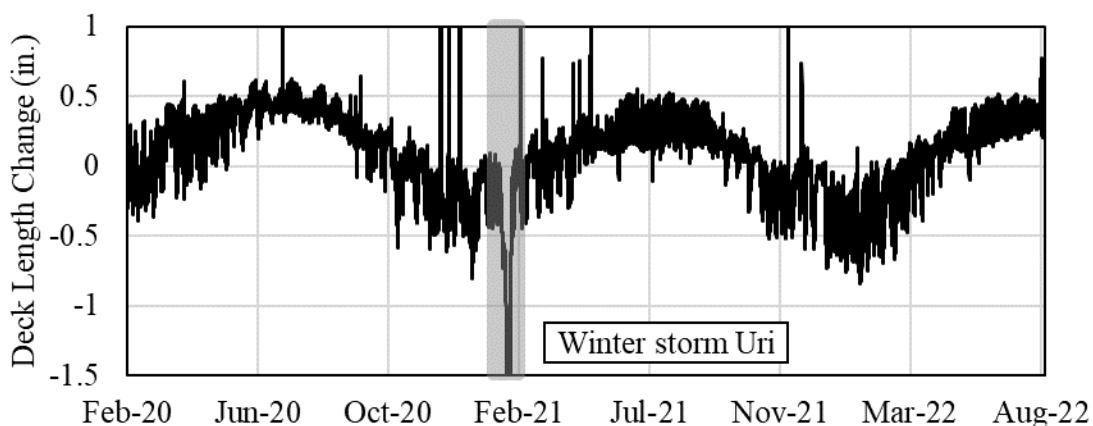


Figure 7.22: Mack Creek Bridge deck length change

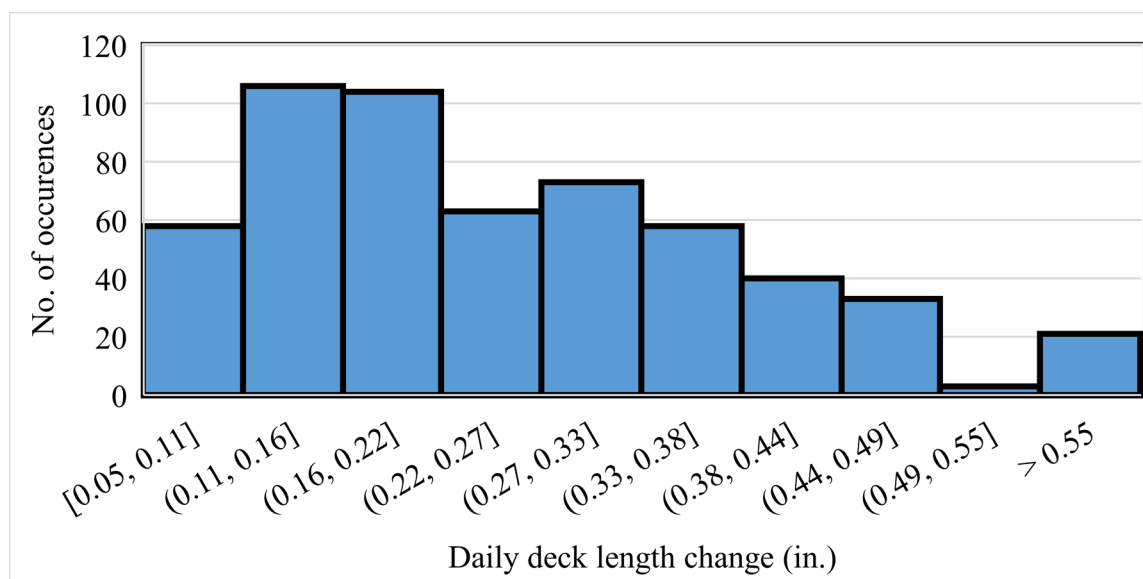
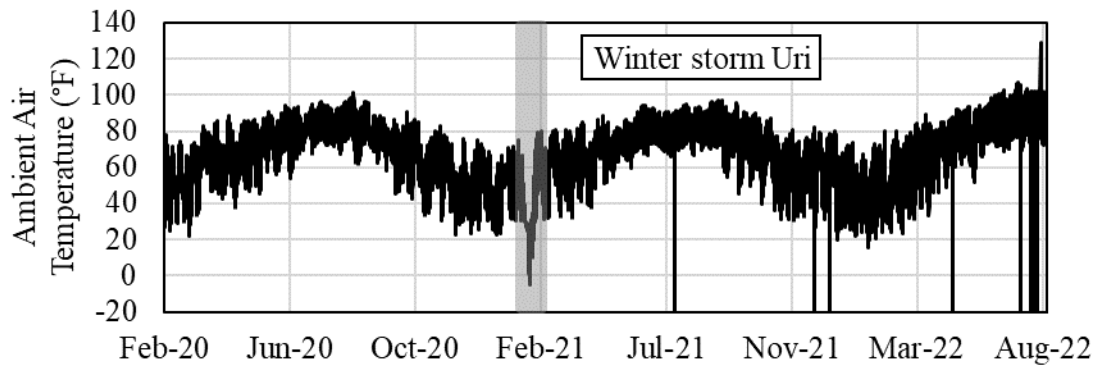
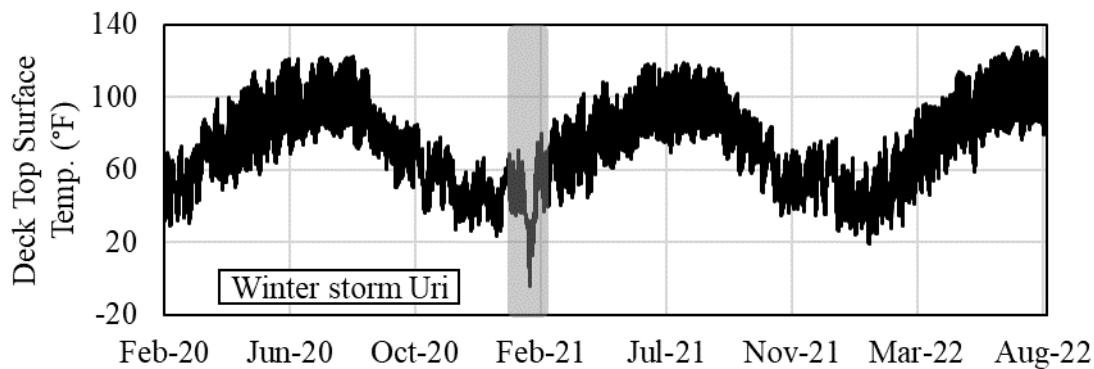


Figure 7.23: Histogram of daily changes in bridge length

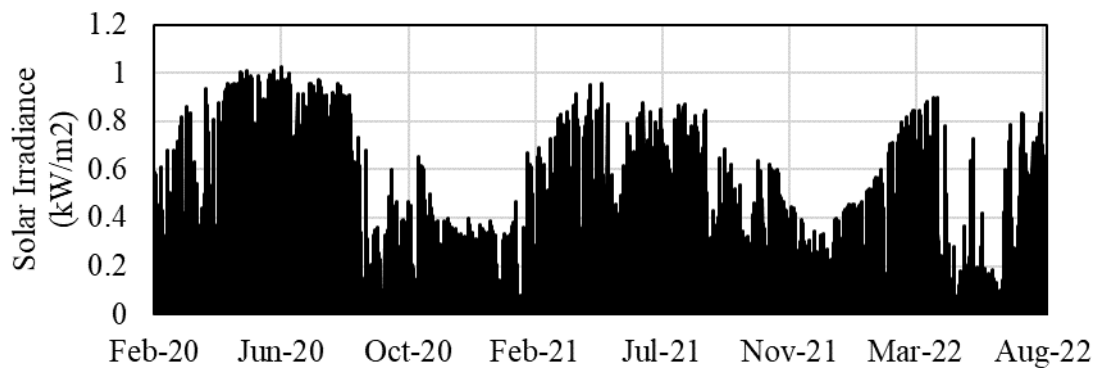
In Figure 7.24, the ambient air temperature recorded by ClimaVue50 and the concrete deck top surface temperature recorded by SI-111SS from Mack Creek Bridge are presented. As can be seen, these parameters are generally different and can vary by up to 20°F at a given time but it is important to keep track of both as they pertain to the top and bottom thermal boundaries. The thermal gradient created in the cross section of the bridge due to solar radiation and the rate of heat flow in the deck can cause curvature in the deck and girders as well as its expansion/contraction. While ambient air temperature can be higher than the deck surface temperature during the winter, the increase in solar radiation intensity means the deck surface temperature can be much hotter than the ambient air temperature in spring and summer. Moreover, the deck surface generally remains hotter than the ambient air throughout the night as the deck concrete stores heat during the day. As expected, it can be seen that temperatures rise from winter to summer, explaining the increase in average length of the deck over this period.



(a)



(b)



(c)

Figure 7.24: (a) Deck surface temperature; (b) ambient air temperature; and (c) solar irradiance at Mack Creek Bridge

A simple statistical analysis of deck and ambient air temperature reveals that the bottom and top surface of the deck are exposed to considerably different temperature ranges each day. It is apparent that on average, the deck surface is subject to more drastic changes in temperature each day (30°F on average), which is likely due to the effect of solar radiation and wind, while the ambient air temperature generally changes by roughly 20° F each day. Considering the extremes, deck surface temperature is subject to more extreme changes (up to 45° F) in a given day while the ambient air temperature generally does not change more than 38° F. This signifies a need for

a thorough analysis of the bridge deck profile to quantify the thermal gradient existing within the structure that can be related to the thermal expansion/contraction of the deck at any given time.

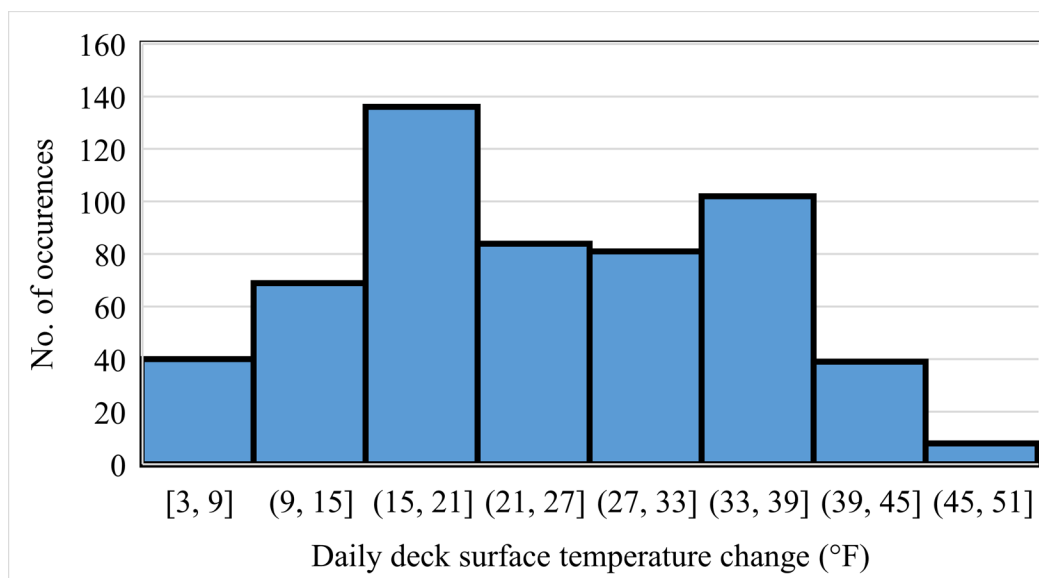


Figure 7.25: Histogram of daily deck surface temperature changes

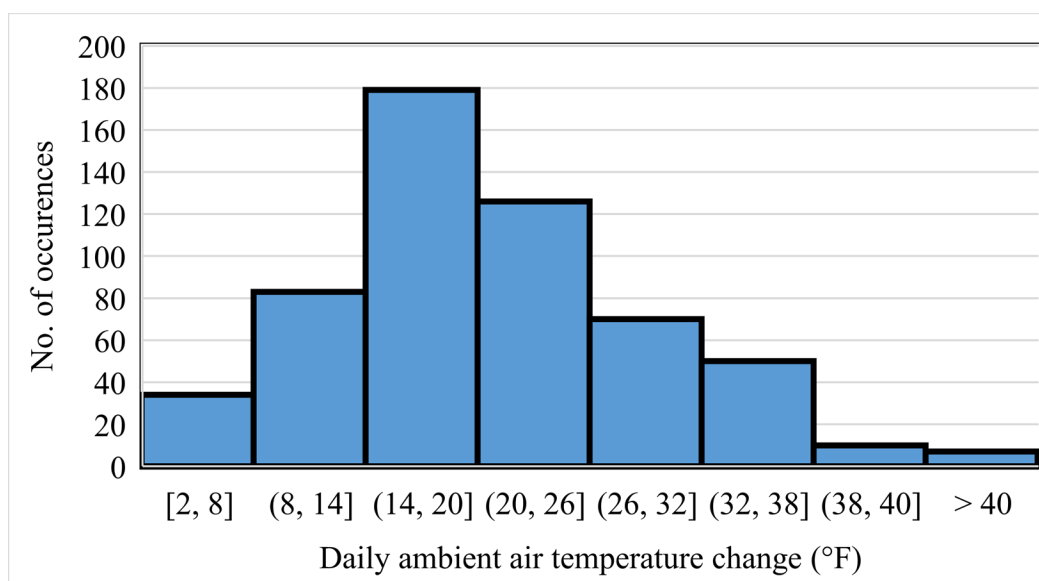


Figure 7.26: Histogram of daily ambient temperature changes

In absence of the exact temperature profile of the bridge deck, we can still perform a simplified check on the collected data using the suggested coefficient of thermal expansion value by the AASHTO LRFD Bridge Design Manual (2018), assuming the whole deck is in thermal equilibrium with ambient air temperature as an upper limit. According to Section 5.4.2.2 of the AASHTO LRFD Bridge Design Manual, in absence of laboratory data, the coefficient of thermal expansion for normal weight concrete can be taken as $6.0 \times 10^{-6}/^{\circ}\text{F}$, therefore by considering the maximum and minimum ambient temperatures recorded since January 2020, we have:

$$\Delta L = \alpha \cdot \Delta T \cdot L_0 = 6 \cdot 10^{-6} \cdot 70 \cdot 68.4 \cdot 12 = 0.34 \text{ in.}$$

As we can see, the calculated range of deflection, with the conservative assumption about temperature, is close to half of what has been recorded using the laser device. One explanation for this discrepancy could be that the real coefficient of thermal expansion for the bridge is higher than the assumed value. However, we should also take into consideration the fact that this is not a free-moving system and not all the components that may affect the movement of the bridge, including geometry, interaction with backfill and pile caps, shrinkage, creep and cracking of the concrete, are accounted for in this simple formula.

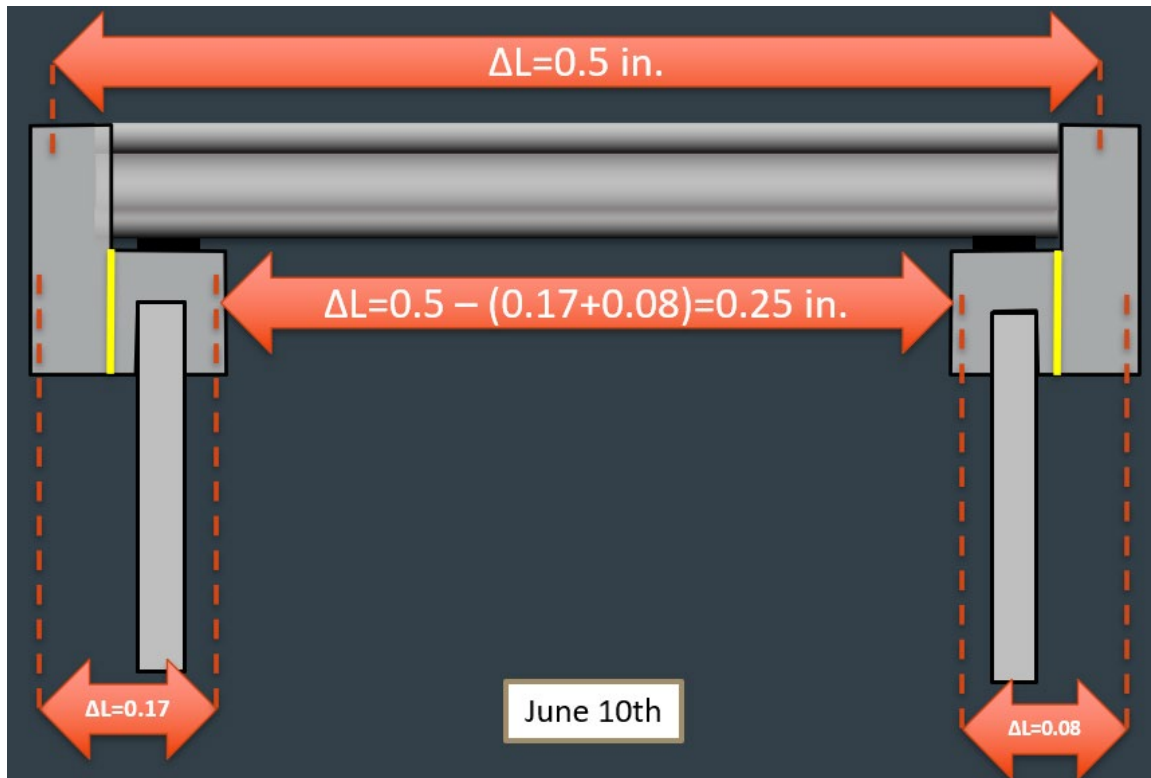


Figure 7.27: Illustration showing lateral deformation at abutment caps due to interaction between deck and abutment caps

In fact, a look at the data collected from the crackmeters (Figure 7.28), and comparison with recordings from the laser device (Figure 7.22), reveals that the bridge deck is pushing both pile caps inward as the sum of displacements recorded by the crackmeters are significantly smaller than the total displacement recorded by the laser device (Figure 7.27). This inward push of pile caps by the bridge deck is expected to be caused by two main factors:

1. Bridge construction was finished in July, which comes with much higher temperatures on average than those the bridge experiences in winter
2. Concrete shrinkage, which would result in permanent reductions in the length of concrete members over time, therefore the deck should be shorter in July 2020, compared to when

it was originally built even if the exact same temperatures are experienced. According to Section 5.4.2.3.3 of AASHTO LRFD Bridge Manual:

$$\epsilon_{sh}(t) = k_s k_{hs} k_f k_{td} 0.48 \times 10^{-3}$$

As this equation is time-dependent, we will attempt to calculate shrinkage strain at roughly 1000 days after construction.

$$\epsilon_{sh}(t) = 0.70 \cdot 0.8 \cdot 1 \cdot 0.96 \cdot 0.48 \times 10^{-3} = 0.26 \times 10^{-3} \rightarrow \Delta L_{sh} \cong 0.21 \text{ in.}$$

The factors used for calculation of shrinkage are experimental. These factors were estimated using the relative humidity data (Figure 7.29) gathered since the installation of new equipment as well as the information reported in the bridge drawings.

Other than increasing temperatures, lateral resistance at both pile caps is also contributing to expansion of the bridge deck, which changes non-linearly with displacement. Additionally, both crackmeters are not expanding at the same rate, which is likely due to the fact that the bridge is slightly sloped and not perfectly horizontal. This asymmetrical behavior was also observed between the earth pressures recorded on both walls, which was attributed to the bridge's slope toward the southern end.

Another interesting observation in the crackmeter data is the apparently permanent deformation of 0.05 and 0.1 in. in the installed crackmeters when comparing the first, second and third year data. It is hypothesized that as the size of the gap between the abutment cap and abutment wall increases, it can get filled with small debris particles, preventing its closure when the temperature decreases. This behavior, which likely occurred in previous years as well, is expected to cause larger lateral loading of the foundation in the future. Similar behavior has also been recorded by China Creek sensors.

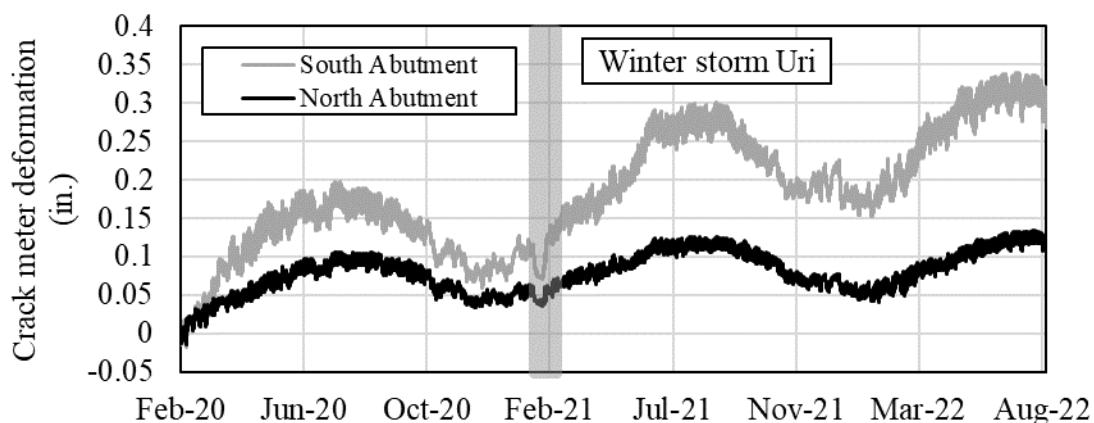


Figure 7.28: Relative displacement between pile caps and abutment backwalls as recorded by crackmeters

Although the extent of the interaction between backwall, pile cap and backfill soil is not fully understood at this point, it is clear that the backwalls are exerting cyclical lateral forces on both

pile caps, which may also lead to permanent deformations in the backfill and soil supporting the sheet piles over time. Therefore, the newly collected data is indicative of a need to consider more parameters, such as thermal profile, shrinkage, creep and asymmetry, in the numerical simulation of the bridge to gain a better understanding of the performance of this structure.

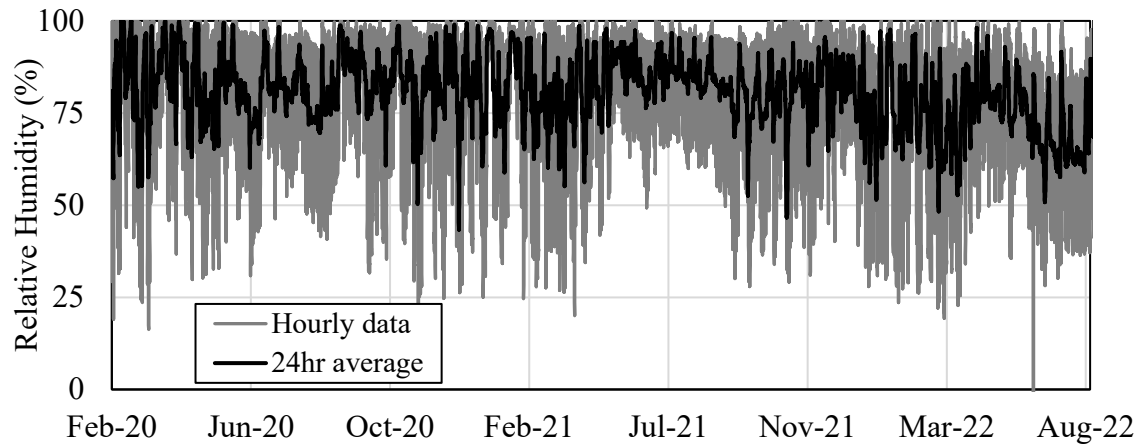


Figure 7.29: Changes in relative humidity of ambient air at Mack Creek

7.3. Analysis of the Performance of Mack Creek Bridge

Several conclusions regarding the field behavior of Mack Creek Bridge can be made based on the data collected in phase 1 and phase 2.

One topic investigated using the collected data is the conditions that lead to earth pressure increase due to ratcheting. A closer look at the earth pressure data reveals that the magnitude of summer daily earth pressure changes is larger than the winter months, while average daily earth pressure remains nearly constant throughout the summer months. In contrast, the magnitude of daily earth pressure change in winter appears to be relatively smaller for most days when compared with the summer months. This contrast in behavior is better illustrated in Figure 7.30, where daily earth pressure changes in July and November 2018 are compared. It can be seen that for the range of 42.8 to 53.6 °F daily temperature change (horizontal axis), the magnitude of earth pressure change is drastically different between the two months (0.725 – 2.901 psi in November vs. 4.351 – 7.252 psi in July). Therefore, the magnitude of daily earth pressure fluctuation does not appear to correlate with the magnitude of daily ambient air temperature change at all.

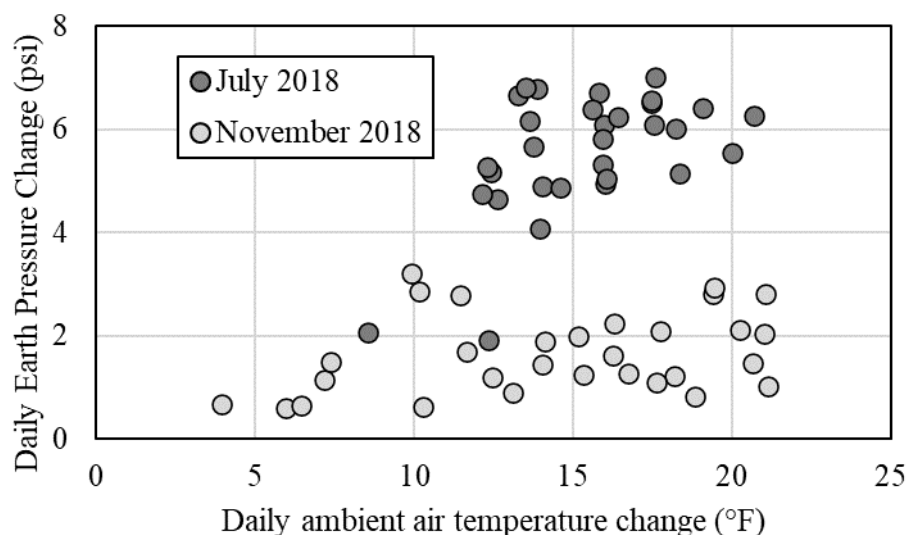


Figure 7.30: Daily ambient temperature change vs daily earth pressure change at south abutment wall (November and July 2018)

In addition to the seasonal contrast in daily earth pressure fluctuation range mentioned earlier, there also appears to be a seasonal difference between how average daily earth pressure changes in the colder seasons versus the warmer seasons. For example, a close look at the south abutment earth pressure and air temperature data in Figure 7.2 reveals that the peak average daily earth pressure (black line) is actually reached during the middle of February each year, while the ambient air temperature is far below the summer high temperatures and this earth pressure is barely exceeded during the ensuing warmer months. In fact, while the daily average ambient air temperature remains relatively constant during the November 2018 to February 2019 period, the south abutment earth pressure continuously increases during this period.

To analyze this behavior, an algorithm was developed to find the most prominent periods of sustained earth pressure increase in the south abutment earth pressure data. This algorithm was designed to find the local maxima and minima (extrema) with the minimum prominence (distance between the peak and the base) of 1.31 psi in the south abutment earth pressure dataset. To reduce the effect of short-term fluctuations on the analysis and ensure the selected points represent a period of sustained elevated earth pressures, the algorithm was set to detect such points in the five-day rolling average of earth pressure data.

The points that satisfied the above-mentioned criteria were used to calculate percent earth pressure change between two succeeding local extrema and the result was plotted against the average air temperature that was experienced during that period. For example, during the January – February 2018 period, when the average air temperature was 49.1 °F, the average south abutment earth pressure increased by 230% (from 1.595 to 5.221 psi).

The result of this analysis is shown in Figure 7.31(a). This data indicates that major pressure increases occur during the colder months of the year at temperatures far below the maximum annual temperatures. Moreover, the magnitude of this increase is largest during the coldest periods and smallest during the warmest periods. To better visualize this data, Figure 7.31(b) was developed as well. This plot shows the average south abutment pressure versus the average ambient air temperature during the sustained earth pressure increase periods identified by the algorithm.

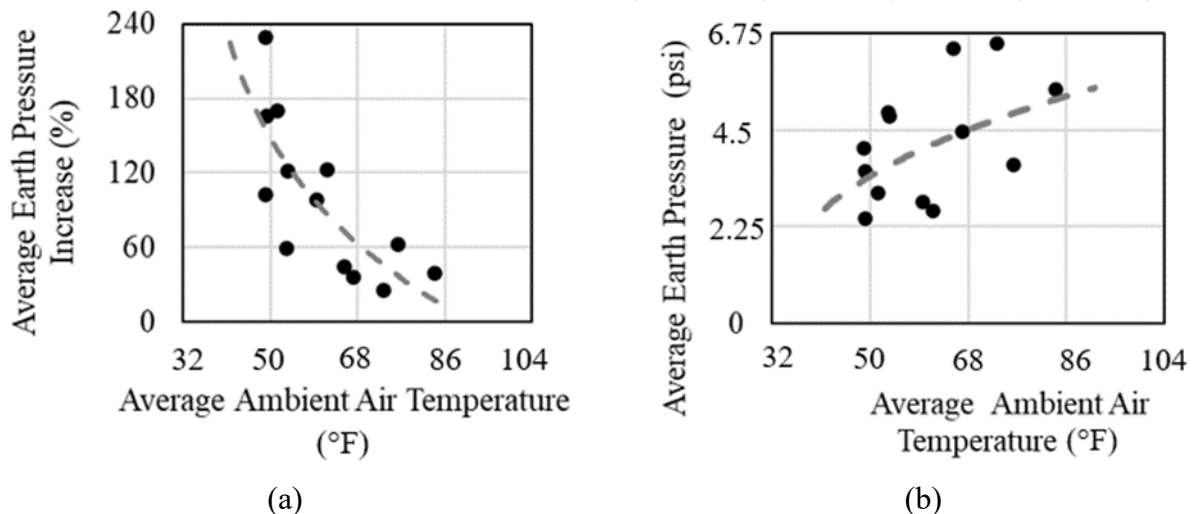


Figure 7.31: (a) South abutment average earth pressure percentage increase vs average ambient air temperature during identified periods of sustained earth pressure increase; and (b) south abutment average earth pressure vs average ambient air temperature during identified periods of sustained earth pressure increase

According to the experimental studies of Clayton et al. (2006), one of the leading causes of stress increase in coarse-grained soils is the readjustment of particles at or close to the active state. Therefore, considering the completion of the bridge during the summer, the backfill soil is more likely to experience active or close to active conditions during the winter, at least partially explaining the larger pressure increases observed during the periods of colder temperature as characterized in Figure 7.31.

Based on the analysis above, it can be hypothesized that such earth pressure increases can be a bigger issue for bridges constructed in locations where the magnitudes of daily and annual temperature changes are larger, especially if the bridge deck is constructed during the hottest times of the year. Moreover, this can be a bigger issue for longer bridges and/or bridges that exhibit asymmetrical behavior due to factors such as construction practices, design or site topography.

7.4. Conclusions on Field Monitoring of Mack Creek SIAB

The data recorded is very exciting because it highlights the importance of considering thermal effects in the design of Semi-Integral/Integral Abutment Bridges (SIAB/IAB).

The bridge deck was observed to expand and contract daily with changes in temperature and climate. The abutment walls also experience a wide range of daily stresses throughout the life of the structure. In Mack Creek Bridge, it was observed that the pressure on the southern backwall increased on average about 100% each year over the course of the two years since construction, highlighting a need to better understand the ratcheting phenomenon to mitigate crack development in weak spots such as structural joints or wingwalls.

Another interesting trend observed is that while the highest magnitude earth pressures were generally recorded during the warm months of the year, the increase in this parameter actually happens during the cold months. The current hypothesis is that for ratcheting to occur, the soil needs to be allowed to enter the active state before being pushed in the passive direction again.

Data collected from Mack Creek pressure cells indicated a change in earth pressure during summer 2019, which is not consistent with the expected behavior considering data from the preceding two years. The earth pressures on the south abutment were observed to start dropping significantly beginning in July 2019, even though these levels were expected to remain almost the same as those recorded earlier in the summer. One possible explanation for this is that the backfill soil may have found a way to relieve the increasing earth pressures due to the expansion of the deck; it is possible that the soil found a crack in the structure to spill through as pressures increased. Visual inspection of the wingwalls on a subsequent visit revealed signs of backfill loss through the gaps at the end of the sheet piles, which may explain the pressure drop in the backfill.

It was also observed that both abutments did not behave similarly despite being under similar conditions. Several hypotheses could account for this discrepancy. The Mack Creek Bridge drawings indicate that the bridge deck is not horizontal and is sloped down toward the north abutment. Moreover, the top soil layers near the north abutment are classified as silty sand while the top soil layers near the south abutment are classified as clayey sand. These differences reveal that the bridge is asymmetric and explain the discrepant pressure recordings from both abutments. Additional numerical analysis and data from subsequent monitoring will help clarify the mechanisms behind this problem.

In January 2020, a new set of sensors was installed on Mack Creek Bridge as construction of China Creek Bridge progressed. This new set of sensors enabled the research team to collect accurate environmental data, such as ambient air temperature, solar radiation intensity, etc., as well as direct measurements of changes in deck length and relative displacement between backwalls and pile caps. A comparison of the magnitude of deck length changes with the

magnitude of relative displacements between pile caps and backwalls suggested that the backwalls were pushing the pile caps toward the creek, causing them to experience daily cycles of lateral loading. This is a plausible explanation as bridge construction was finished in July 2017 (the hottest time of year/greatest deck length with no shrinkage). The magnitude of displacements was slightly larger than that calculated following the procedure detailed in the AASHTO LRFD Bridge Design Manual (2018) and therefore a more sophisticated analysis is needed to better understand the bridge behavior. The crackmeter data collected from Mack Creek Bridge suggests that the gap between abutment caps and abutment walls is filling with debris, leading to larger abutment cap deformations. While both crackmeters show that the size of the gap is increasing each year, the south abutment gap appears to be experiencing more deformation.

Chapter 8. Field Monitoring of China Creek Semi-integral Bridge

8.1. Initial Conditions of China Creek Bridge

As previously mentioned, another component of this project is the instrumentation and monitoring of China Creek Semi-Integral Abutment Bridge (SIAB) outside of Haynesville, TX. Although this project was planned to start in the summer of 2018, it has been delayed for various reasons. First, TxDOT delayed construction of this project until fall 2018 due to the presence of migratory bird nests underneath the bridge (Figure 8.1). Shortly thereafter, a project start date of November 2018 was communicated and then also delayed due to large amounts of rainfall in fall 2018.



Figure 8.1: Swallow nests under China Creek Bridge

However, despite these delays, a brief visit to the China Creek Bridge site was planned in August 2018 to familiarize the research team with the site and inspect the structure to be replaced.

During this visit, the high water levels in the creek (Figure 8.2) made it impossible to inspect the bridge from underneath and look for signs of deterioration. This indicates that subsequent

surveying trips should be planned such that rainfall events are avoided to keep track of surveying targets properly.

Despite the limitations caused by high water level, the bridge was examined from the distance. It was observed that the existing bents underneath the bridge had experienced corrosion damage (Figure 8.3). Moreover, it was observed that during precipitation events, water easily found its way through the joints of the bridge, which caused damage to the concrete made evident by the appearance of the concrete surface close to the joints (Figure 8.4).



Figure 8.2: High water level in China Creek after a precipitation event in August 2018

In addition, although it appeared that the asphalt pavement had been repaved several times, there were still small cracks near the edges of the road where the approach slab reached the bridge deck (Figure 8.5), which means that backfill settlement is an ongoing issue for this settlement. However, it will be hard to judge its severity of this problem due to lack of monitoring information on this bridge.



Figure 8.3: Corroded bents under China Creek Bridge to be replaced



Figure 8.4: Seepage of water through deck joints



Figure 8.5: Cracked edge of pavement at end of the approach slab due to backfill settlement

Overall, the initial visit to China Creek proved to be very beneficial despite the limitations caused by the high water table. It helped the researchers to get familiarized with the location of the project as well as some of the common issues in the existing structure, which are hoped to be avoided by SIAB technology. For example, one of the main advantages of SIAB technology is the omission of joints that would reduce the amount of seepage on concrete surfaces.

In addition, another purpose for this trip was to assess the possibility of transferring acquired instrumentation data over the internet to monitor changes on the bridge more frequently and more closely. Based on the tests conducted in the location of the bridge, it is possible to transmit data via the internet and in real time.

8.2. Instrumentation Plan for China Creek SIAB

After extensive literature review, talking with instrumentation professionals, holding technical discussions with instrumentation companies and seeking feedback from TxDOT staff, a thorough instrumentation plan for monitoring the performance of China Creek Bridge has been designed.

This instrumentation plan features an array of sensors capable of directly measuring:

- Earth pressures acting on abutment walls and wingwalls

- Lateral displacement within the backfill soil
- Vertical settlement within the backfill soil
- Displacement of structural components relative to each other
- Tilt of structural components
- Strains in backwall, deck and girders
- Temperature gradient within the concrete mass and soil
- Solar radiation, wind, humidity, ambient temperature
- Deck surface temperature
- Deformation of the drilled shafts
- Total shrinkage and expansion of the bridge

While the majority of the sensors (earth pressure cells, strain gauges, etc.) benefit from the Vibrating Wire (VW) technology (manufactured by Geokon), there are several sensors that rely on digital outputs and more complex programming and setup (weather station, shape array, infrared radiometer, etc.). Moreover, the designed bridge monitoring system comes in rugged weatherproof enclosures, is powered by solar energy and is capable of transmitting data/alerts over cellular network and radio frequency.

As described in previous sections, there will be a large variety of sensors implemented in this project, most of which benefit from the VW technology. Each of these sensors comes with a very detailed manual that describes the operation principles, programming, installation and troubleshooting instructions. A brief description of each sensor is provided in subsequent sections.

8.2.1. Logger Equipment

As described in the previous section, the logger equipment is housed in two rugged weatherproof enclosures and installed at opposite ends of the bridge on a pole to keep it above the predicted flood elevation as this bridge gets flooded several times a year.

A picture of the enclosure is shown in Figure 8.6. As can be seen, the logger equipment consists of a CR6 data logger manufactured by Campbell Scientific, an AM416 16-channel multiplexer manufactured by Campbell Scientific, 15V DC rechargeable power supply, RF 401A spread spectrum radio (Campbell Scientific), cellular modem and an external model 8032 Geokon multiplexer (Figure 8.7).

As described on Campbell Scientific's website, "The CR6 Datalogger (Figure 8.8) provides fast communication, low power requirements, built-in USB, compact size, and high analog input accuracy and resolution. It uses universal (U) terminals to allow a connection to virtually any sensor—analog, digital, or smart. This multipurpose data logger is also capable of doing static vibrating-wire measurements."

Therefore, this data logger can be programmed to take hourly measurements using all sensors for the duration of this project, and has the ability to transmit data wirelessly between the two stations at opposite ends of the bridge via RF401 components (Figure 8.9) and to the base station in Austin via the cellular modem (Figure 8.10). To ensure proper cellular coverage is received at the location of interest, a high gain external cellular antenna was purchased to be used in conjunction with the cellular modem. Overall, this provides fast and secure access to the data every day and eliminates the need to travel to the bridge site just for the purposes of data collection.

To increase the number of sensors that can be measured using the CR6 data logger, two 16-channel multiplexers were used. These multiplexers enable the data logger to rotate through an array of sensors connected to individual channels on the multiplexers and measure them one by one while occupying the same number of channels as one VW sensor for each multiplexer and therefore provide a low-cost alternative to expanding the limitations on number of sensors that can be read every hour. However, the drawback to using multiplexers instead of a dedicated data logger is that sensors connected through the multiplexer cannot be measured simultaneously or faster than a certain rate. However, this issue is not be a drawback in this project where measurements are planned to be taken once to several times every hour.

A handheld VW readout device (Figure 8.11) was purchased from Geokon to inspect the sensors right after installation in the field and take zero readings as it may not be possible to setup the final logger system before construction is completed and sensors are buried in the soil or embedded in the concrete.

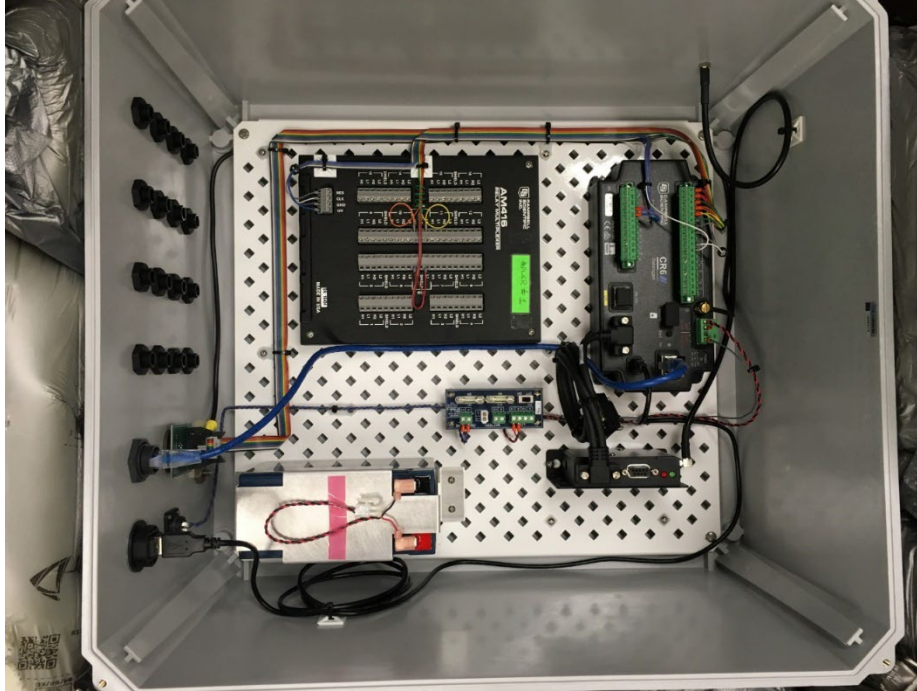


Figure 8.6: Logger equipment in NEMA enclosure

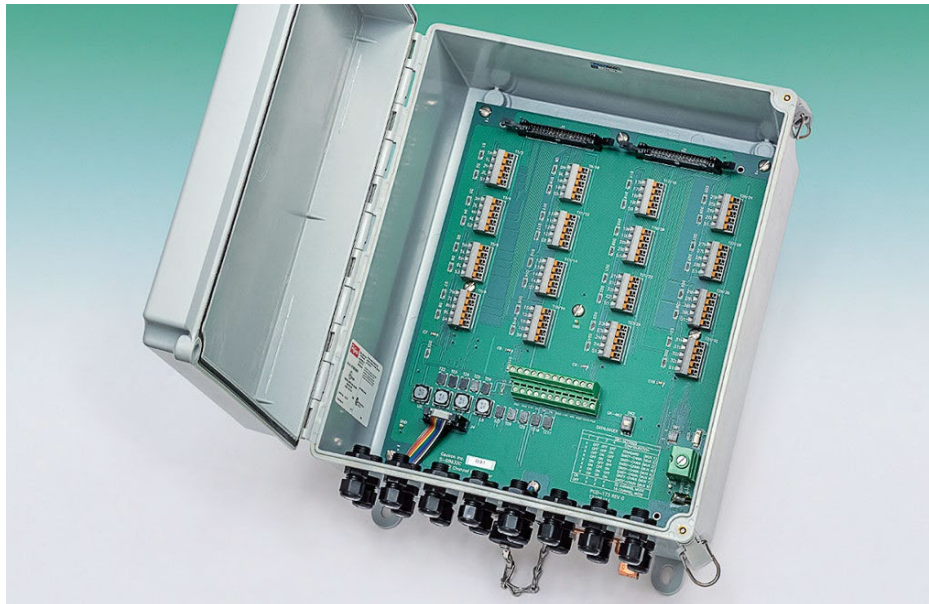


Figure 8.7: External Geokon model 8032 multiplexer (geokon.com)



Figure 8.8: CR6 data logger (campbellsci.com)



Figure 8.9: RF401 radio (campbellsci.com)



Figure 8.10: CELL205 cellular modem (campbellsci.com)



Figure 8.11: GK-404 handheld VW readout device (geokon.com)

8.2.1.1. Earth Pressure Cells

After thorough investigation of various solutions for direct measurement of earth pressure in the market, it was decided to use model 4815 granular type earth pressure cells (Figure 8.12) manufactured by Geokon for this project. Unlike other earth pressure cells manufactured by Geokon, this model has been manufactured with two thick plates (to reduce the effect of point loading) that are welded together at a flexible hinge. The deformation of these plates causes a change in the pressure of fluid inside the cell, which in turn affects the magnitude of tension acting on the VW transducer attached to the cell. These sensors are planned to be installed at different elevations along the height of the backwalls on either side, on the backfill side of the pile caps and on the wingwalls.



Figure 8.12: Model 4815 earth pressure cell (geokon.com)

As the stiffness of the pressure cell is different from the surrounding soil in the field, installing these cells in the field may trigger a stress redistribution causing erroneous earth pressure readings. To reduce this effect, it is recommended by the manufacturer to install these cells on the back of the form before concrete pour, using double headed nails to result in a flush surface (Figure 8.13).

The specifications for this sensor are presented in Table 8.1. To further increase the accuracy of these sensors and considering the range of earth pressures expected, the manufacturer agreed to manufacture the sensors with a custom range of 25 psi. The proposed installation location of these sensors is shown in Figure 8.14.

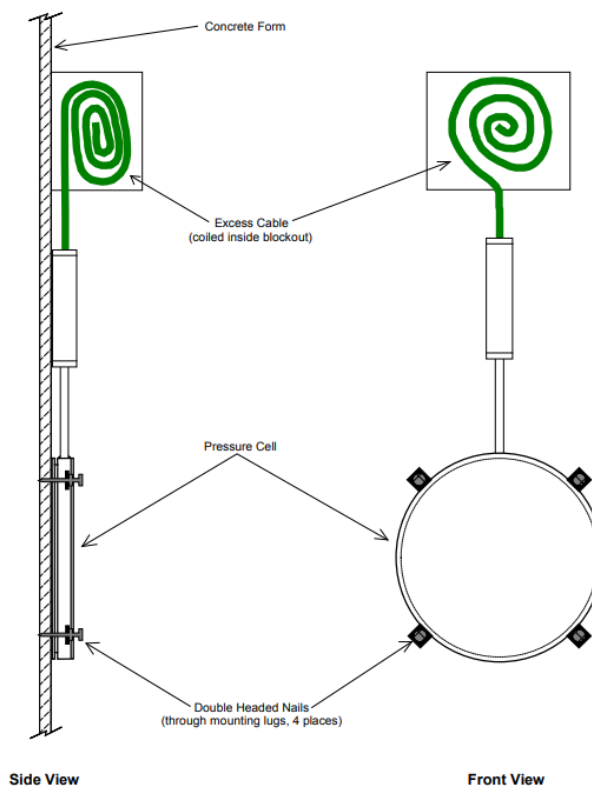


Figure 8.13: Suggested installation procedure for earth pressure cells (geokon.com)

Table 8.1: Specifications for model 4815 pressure cell (geokon.com)

Specifications

Standard Ranges ¹	350, 700 kPa; 1, 2, 3, 5 MPa
Over Range	150% F.S. (maximum)
Resolution	0.025% F.S.
Accuracy ²	±0.1% F.S.
Temperature Range ¹	−20°C to +80°C
Height × Diameter ¹	26 × 230 mm

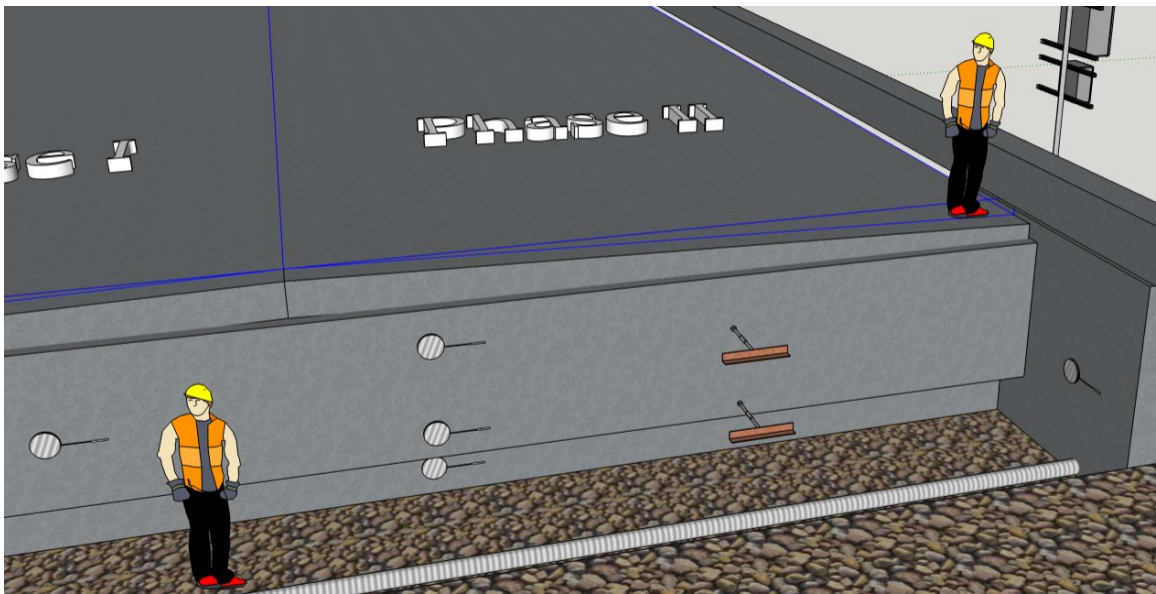


Figure 8.14: Proposed installation location of pressure cells and soil extensometers on east abutment

8.2.1.2. Soil Extensometers

To track the lateral movements of the backfill soil relative to the abutment walls, several Geokon model 4435 soil extensometers (Figure 8.15) are installed on either side at different elevations along the abutment backwalls. These sensors are made of a VW transducer that is calibrated to measure displacement between the two ends of the sensor. The transducer of this sensor is housed in a rugged Sch. 40 telescopic pipe that changes length as the flanges are extended/compressed relative to each other due to soil movement.

To extend the capabilities of these sensors, they can be connected in series by sharing a flange to obtain a lateral displacement profile. However, in this project, it was decided to use one extensometer at each installation location due to the fact that it is not expected to see considerable lateral movements beyond the length of one soil extensometer. The specifications for this sensor are presented in Table 8.2. For this project, sensors with a 4-in range were selected considering the sensitivity of these sensors to being overextended and the level of accuracy offered at this range.

The proposed installation location of these sensors is shown in Figure 8.14.

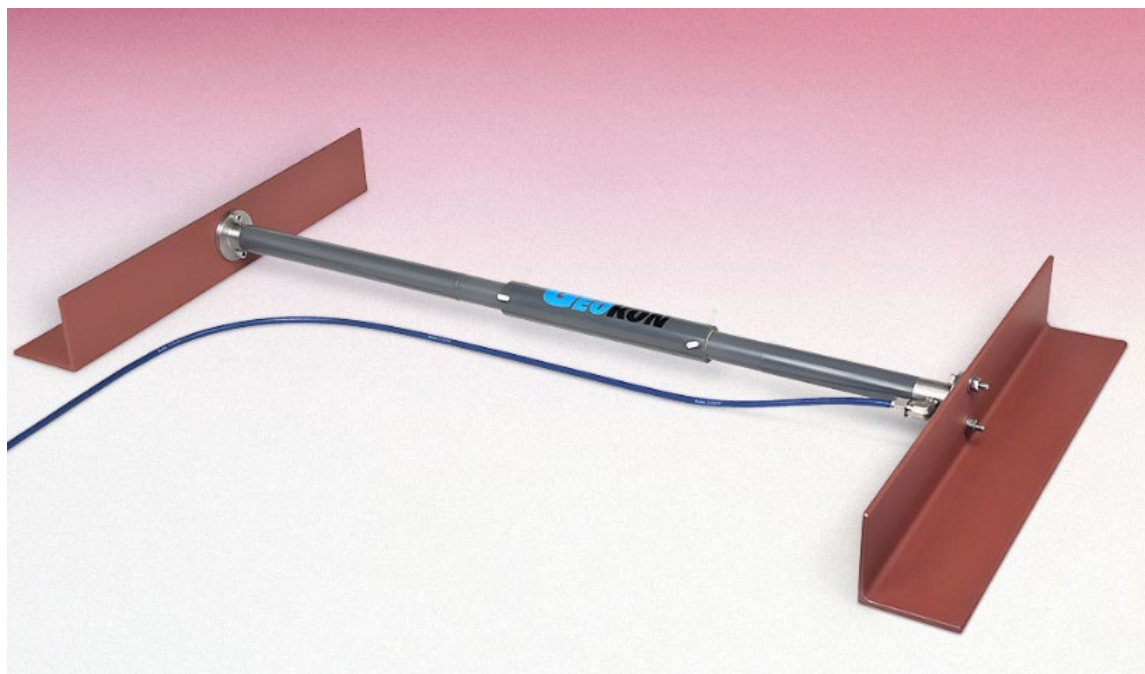


Figure 8.15: Model 4435 soil extensometer (geokon.com)

Table 8.2: Specifications for model 4435 soil extensometer (geokon.com)

Specifications

Standard Ranges ¹	25, 50, 100, 150, 300 mm
Resolution ²	0.025% F.S.
Accuracy ³	±0.1% F.S.
Nonlinearity	<0.5% F.S.
Temperature Range ¹	-20 °C to +80 °C
Minimum Gauge Length	610 mm
Diameter	27 mm (pipe), 33 mm (slip coupling), 51 mm (flange)
Flange (L × W × H)	610 × 75 × 75 mm

8.2.1.3. Deformation Meter

To measure the settlement of backfill through time, it was decided to utilize model 4430 deformation meters (Figure 8.16) installed vertically near the center of the backfill and close to abutment backwall where the largest settlements are expected. In addition, it was decided to place additional deformation meters near the corners of backfill where the abutment backwall meets the wingwalls. These sensors are very similar in construction to the soil extensometers and differ in that end flanges have been switched to circular plates. For installation, one end of the

sensor will be buried in the natural soil about 1 ft below the backfill and the other end will be placed near the top of the backfill and below the approach road's pavement.

This is one of the most sensitive sensors installed considering it must be buried vertically inside the backfill and protected from construction activities as backfill material is being poured and compacted.

There are several options for continuous measurement of settlement within the soil mass, such as the Geokon model 4660 settlement system, which uses hydraulics principles to calculate settlement of a settlement plate attached to a tube filled with a hydraulic solution that is connected to a reservoir. However, the past experience of the research team has shown that although this approach appears more logical, it does not work well in practice if the reservoir and tube are subjected to different temperatures than the buried settlement plate due to uneven expansion of the hydraulic fluid in different parts of the system. Therefore, it was decided to go with a displacement transducer that is completely buried in the soil.

The specifications for this sensor are similar to what is reported in Table 8.2 for model 4435 soil extensometer.



Figure 8.16: Model 4430 deformation meter (geokon.com)

8.2.1.4. Concrete Embedment Strain Gauges

One of the most important measurements in this monitoring program is the measurement of strains and temperature across the various structural components, including deck, girders,

abutment walls and piles, as these measurements will serve as boundary conditions in subsequent numerical/mathematical analysis of loads imposed on the structure due to deformation of the bridge.

Therefore, it was decided to place 10 model 4200 concrete embedment strain gauges (Figure 8.17) in the deck of China Creek Bridge. These sensors were distributed evenly at the top and bottom of the deck concrete in the long direction of the bridge. Additionally, six of these sensors were placed along the height of the backwall to measure strain and thermal gradients as displacement occurs. Several strain gauges were also placed at one of the pile heads to measure the load transfer to the bridge support system.

Moreover, additional sensors are to be embedded in the reinforced concrete approach to track movements and forces acting on the reinforced concrete approach slabs as well.

In addition, several model 4200L concrete embedment strain gauges (Figure 8.18) were purchased to measure strains due to concrete shrinkage in the curing stage and strains perpendicular to the bridge direction (mainly affected by temperature changes). It was decided to use model 4200L instead of 4200 for this purpose because 4200L gauges have a lower stiffness modulus and would therefore deform due to shrinkage of concrete in the curing stage. These sensors are able to record strains with a 1 micro-strain resolution and maximum 15 micro-strain accuracy over a total range of 3000 micro-strains.

An example installation location for these strain gauges is shown in Figure 8.19.

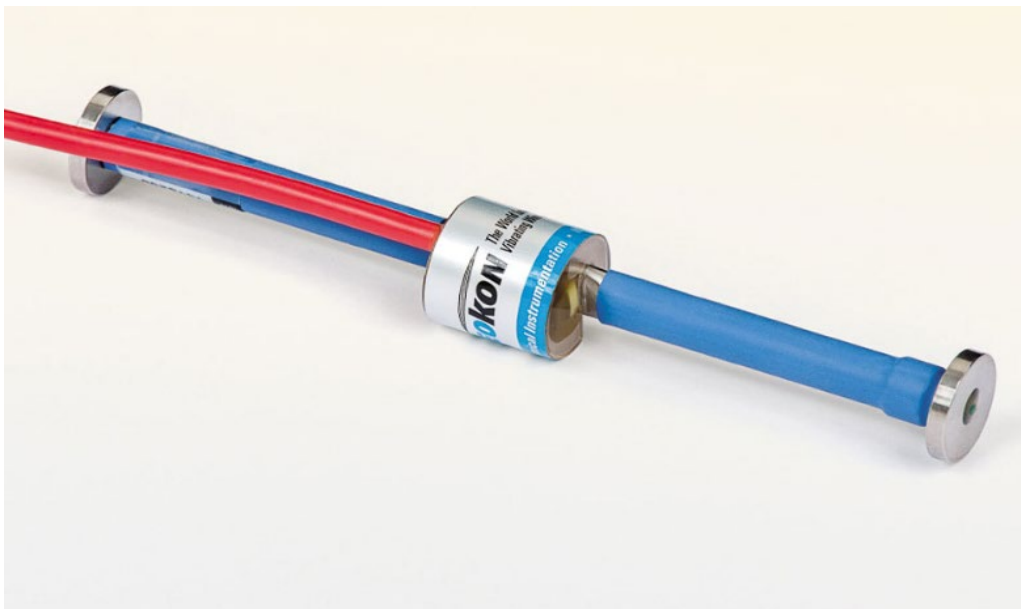


Figure 8.17: Model 4200 concrete embedment strain gauge (geokon.com)

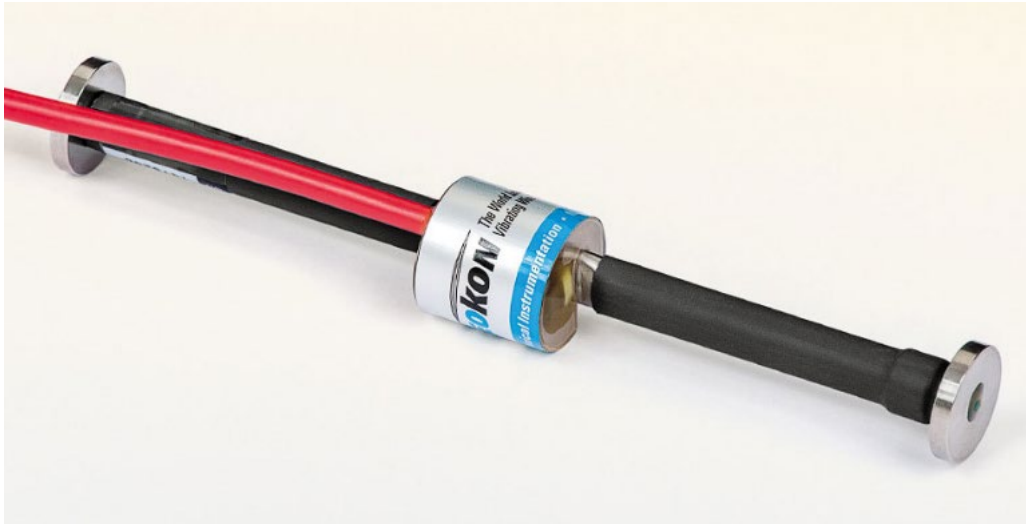


Figure 8.18: Model 4200L concrete embedment strain gauge

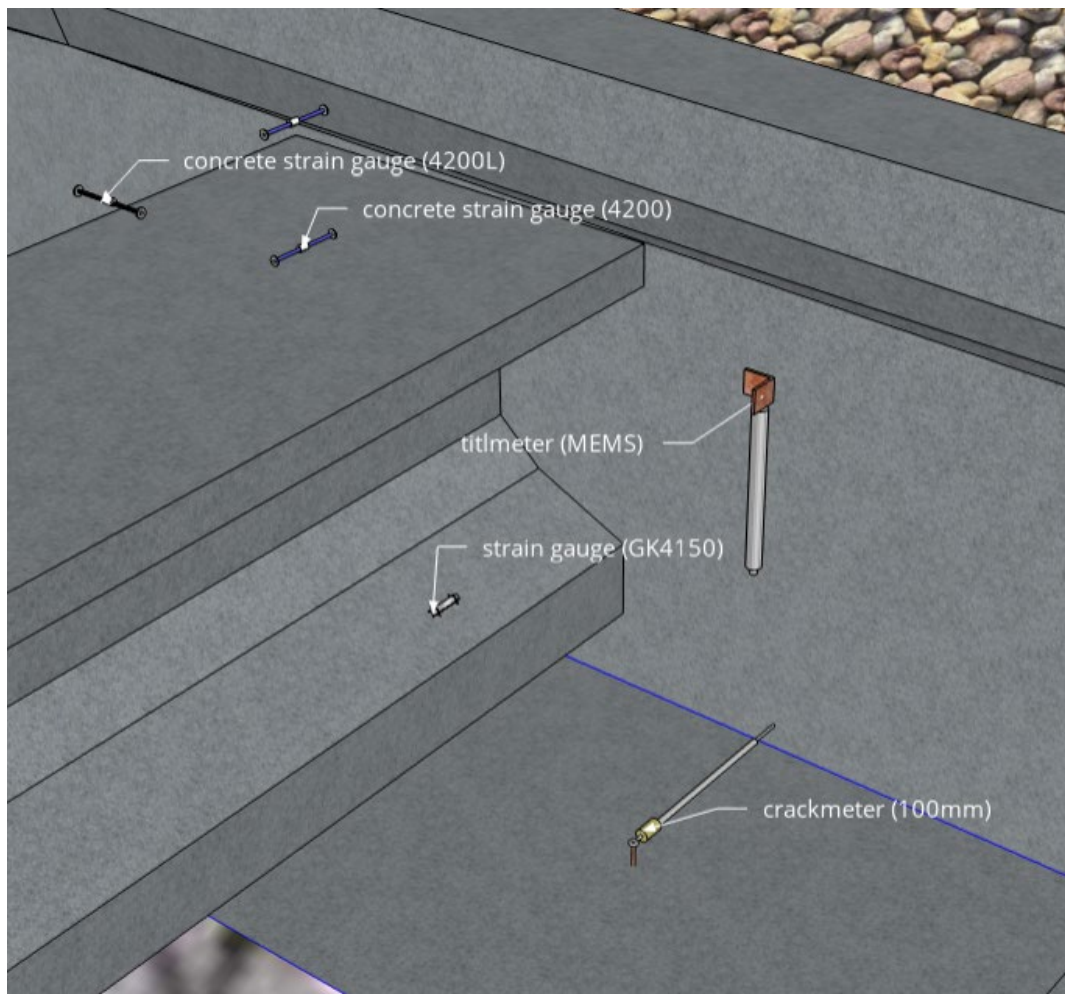


Figure 8.19: Example installation location for strain gauges, tiltmeters and crackmeters (west side of China Creek Bridge)

8.2.1.5. Miniature Strain Gauges

In addition to the deck, it is also deemed beneficial to monitor the deformation and temperature of precast girders as well. As these components are precast, it is not possible to embed a sensor in them. To this end, model 4151 miniature strain gauges (Figure 8.20) by Geokon were purchased. These strain gauges can be attached to the concrete surface by drilling 0.25-in-deep holes with 0.125-in diameters. Although these sensors should not be damaged by being submerged in water, they can be further protected from the environment (especially flash floods) by installing a cover plate and protecting the ends. These sensors are to be installed on top of the bottom flange at five different locations along the length of one of the girders as shown in Figure 8.19.

The miniature nature of these sensors enabled the research team to install them on the surface of the precast concrete girders, as the pegs on these sensors are small enough to not penetrate to the location of the pre-stressed tendons.

The specifications for these sensors are similar to the model 4200 strain gauges introduced in the previous section.

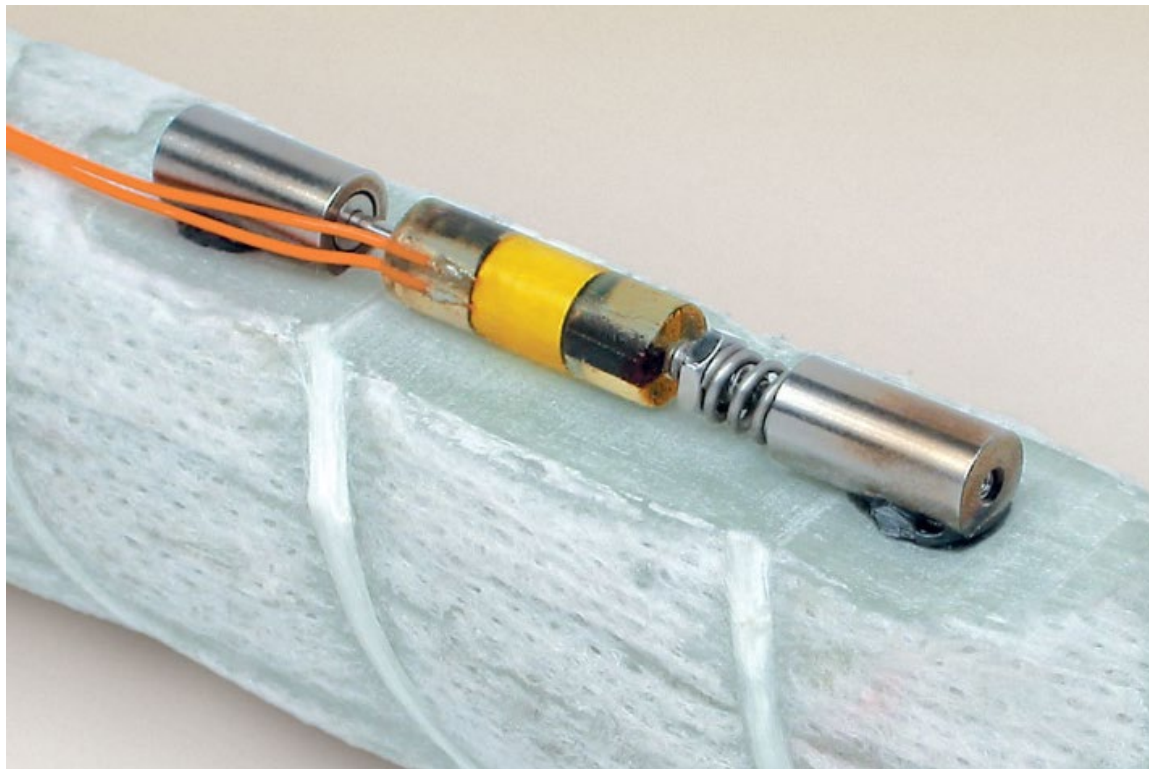


Figure 8.20: Model 4151 miniature strain gauge (geokon.com)

8.2.1.6. Crackmeters

To measure relative displacement between two separate structural components in the bridge, it was decided to utilize model 4420 crackmeters (Figure 8.21) from Geokon. This sensor is comprised of a VW displacement transducer that is housed inside a steel shaft and is connected to two anchors that can be mounted on separate structures to capture their relative displacements in the direction of interest.

For this project, these transducers were installed between the pile cap and abutment backwalls (Figure 8.19), between wingwall and bridge deck and between beam seat and approach slab at either side of the bridge. Where needed, the sensors were customized to have a universal joint at one end to simplify installation and make readings more accurate.

The specifications for this sensor are presented in Table 8.3.



Figure 8.21: Model 4420 crackmeter (geokon.com)

Table 8.3: Specifications for model 4420 crackmeter (geokon.com)

Specifications

Standard Ranges ¹	12.5, 25, 50, 100, 150 mm
Resolution	0.025% F.S.
Accuracy ²	±0.1% F.S.
Nonlinearity	<0.5% F.S.
Temperature Range ¹	−20 °C to +80 °C
Lengths ³	318, 343, 397, 555, 645 mm (transducer)
Diameter	8 mm (shaft); 25 mm (coil)

8.2.1.7. Tiltmeters

In addition to the previously discussed sensors that measure pure displacement in the direction of the sensors, it was decided to install a tiltmeter (Figure 8.22) on either side of the bridge (Figure 8.19) to capture the tilt of the abutment backwalls, as it is possible for the backwall to experience tilt due to variable magnitudes of earth pressure and the cantilever nature of the abutment backwall.

Unlike the previously discussed sensors, this sensor is a Micro-Electro-Mechanical Systems (MEMS) sensor, which offers a high range with high sensitivity and accuracy in measurements. The specifications for this sensor are presented in Table 8.4.



Figure 8.22: Model 6160 MEMS tiltmeter (geokon.com)

Table 8.4: Specifications for model 6160 MEMS tiltmeter (geokon.com)**Specifications**

Standard Range ¹	±15°
Resolution	±0.02 mm/m (±4 arc seconds)
Sensor Accuracy ²	±0.05 mm/m (±10 arc seconds)
Sensor Output	6160A/B ±4 V @ ±15° 6160C/E Digital
Shock Survival	2000 g
Temperature Range ¹	-20°C to +80°C
Dimensions (L × Ø)	6160A 219 × 32 mm (sensor) 6160B/C/E 362 × 32 mm (sensor)

8.2.1.8. Shape Array

To monitor displacements of the foundations relative to their bases, it was decided to install a string of shape arrays (Figure 8.23) in one of the drilled shafts on the east side. A 35-ft string of SAAV sensors was selected for installation and consists of 20-in instrumented segments (MEMS sensors) joined at joints that can bend up to 90 degrees in all directions (Figure 8.24).

For installation, these segments are to be slowly lowered down into an existing casing and then compressed into the casing so the joints push into the walls of the casings firmly, after which the string is held compressed using a special clamping system as depicted in the specifications for this sensor (Table 8.5).

Table 8.5: Specifications for SAAV static measurements (measurand.com)

ANGULAR RANGE OF MEMS SENSORS	± 360° (software selection required for 2D/3D modes)
RANGE OF 3D MODE (VERTICAL)	± 60° with respect to vertical
DEFORMATION ACCURACY ^{1,2,3}	± 1.5 mm for 32 m ShapeArray
RESOLUTION OF SINGLE SEGMENT	+/- 1 arcsecond ⁴
AZIMUTH ERROR IN JOINTS	< ±0.01°
LONG-TERM RELIABILITY MTBF ⁵	38 years for 32 m ShapeArray



Figure 8.23: SAAV array on reel prior to installation (measurand.com)

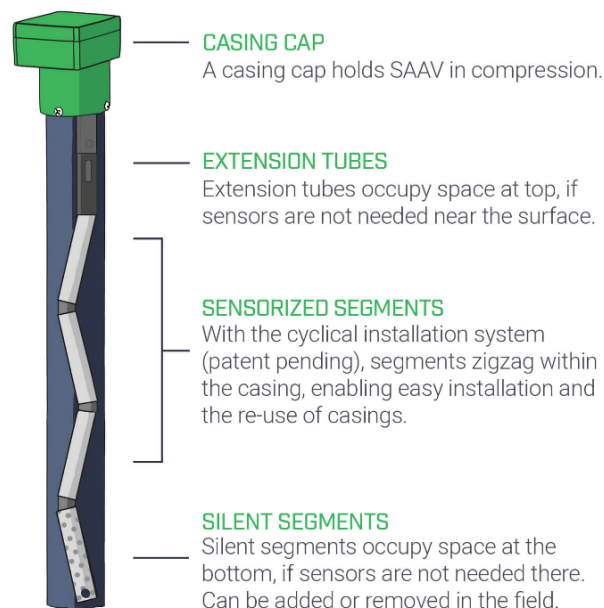


Figure 8.24: Schematics for installation of SAAV in an inclinometer casing (measurand.com)

8.2.1.9. ClimaVue50 Compact Weather Station

After the experience gained through monitoring Mack Creek Bridge, a weather station system that can accurately measure ambient temperature, solar radiation, humidity, rain and general climate conditions was considered necessary to better understand thermally induced strains in the monitored structure.

After a thorough investigation, it was decided to install a ClimaVue50 compact weather station (Figure 8.25), which houses a pyranometer, anemometer, temperature sensor, drip counter gauge and relative humidity sensor in a 4-in x 13.4-in housing that can be installed on top of a pole.

Using this sensor would enable the research team to accurately estimate the amount of thermal energy absorbed by the structure that would cause it to expand or contract.



Figure 8.25: ClimaVue50 sensor (campbellsci.com)

8.2.1.10. SI-111SS Infrared Radiometer

In addition to the previously described list of sensors to capture movements and thermal gradients in various components of the structure, it was decided to also install one SI-111SS infrared radiometer (Figure 8.26), which is capable of measuring the temperature of an object's surface using infrared at specific intervals. This sensor consists of a thermopile that measures an object's surface temperature and a thermistor that measures the sensor body temperature to correct the thermopile readings. This sensor is accurate to 0.2 degrees Celsius in a range from 14 to 149°F. The field of view for this sensor is a 22-degree half-angle.



Figure 8.26: SI-111SS infrared radiometer (campbellsci.com)

8.2.1.11. OptoNCDT ILR 1181-30 Laser Distance Meter

Following the monitoring program implemented at Mack Creek Bridge and subsequent numerical simulations, the need to collect an accurate time-history of bridge expansion/contraction was identified. A device that could be powered by a CR6 data logger and measured as needed with a sufficient level of accuracy was sought.

The OptoNCDT ILR 1181-30 (Figure 8.27) is an industrial grade, time-of-flight laser distance meter that compares the returned laser pulse with the laser pulse shot to find the arrival time of the reflected wave and calculates distance using the travel speed of the laser. This device is capable of measuring distances up to 500 ft with a resolution of 0.004 in and repeatability of <0.02 in, which fits the needs of this project perfectly.

This sensor is capable of transmitting data in both serial (e.g. RS-422) and analog (4-20 mA) outputs. For the purposes of this project, the sensor was first connected to a PC using the serial interface to set the correct settings. It was then connected to the data logger and its output measured using the analog (4-20 mA) output.

Analog/4-20 mA measurements are a simple method of transmitting data for analog sensors. In this mode, an expected range of measurements is passed to the sensor. For example, the logger is to measure distances between 10 and 20 ft. Then, when the sensor is powered and measures distances, it will generate a current with an intensity between 4 mA and 20 mA proportional to the distance it measures. For example, if the distance to target is 15 ft, the sensor will generate a 12 mA current.

This sensor has a relatively high power consumption rate compared to any of the other sensors used as it was developed for industrial applications and not long-term field-monitoring applications; if kept on continuously, it can drain the battery in a matter of few hours. Therefore, CR6's switched power port feature should be used to help with saving power especially if measurements are to be taken far apart from each other.

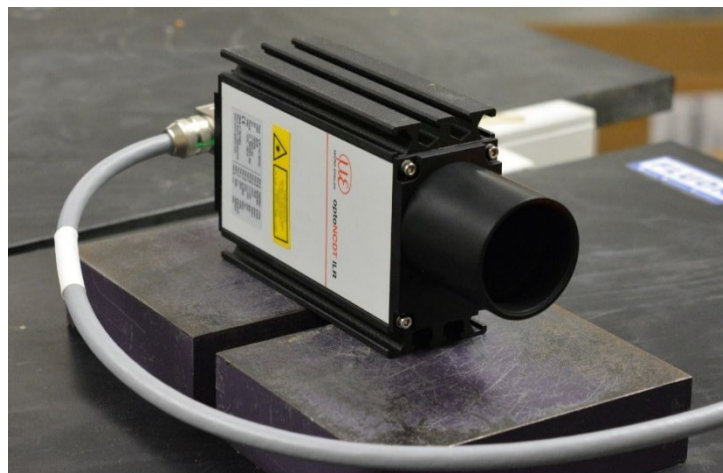


Figure 8.27: OptoNCDT ILR 1181-30 laser distance meter

8.2.2. Logger Programming

As introduced in Section 8.2.1, CR6 is a very versatile data logging device capable of measuring outputs from various types of sensors. As each port on this device can be configured for various functions to help power and measure different kinds of sensors, this device needs to be programmed using a programming language called CRBasic to set various parameters.

In addition to programming the data logger using CRBasic, a Python program was developed to aid in collection, processing and visualization of the data as this task may become cumbersome if done manually in long-term monitoring programs.

8.2.2.1. CRBasic

CRBasic is a high-level programming language developed by Campbell Scientific to help users program data loggers manufactured by Campbell Scientific. A general structure of a CRBasic program is shown in Figure 8.28.

As there appeared to be no freely available guide for learning how to program in CRBasic, the research team spent many days on learning this language and developing the right program for the job through numerous communications with Campbell Scientific technicians, studying the CRBasic documentation and example programs found in different manuals.

At the beginning of the program, all the variables used for storing sensor measurements or performing mathematical operations are declared. An example of these declarations is shown in Figure 8.29. As can be seen, the variable declaration transmits information about the name of the variable, its expected “behavior” and the data type to the data logger. Therefore, it is necessary to pay attention to the type of data being stored in each variable and make sure it matches the variable’s function within the program.

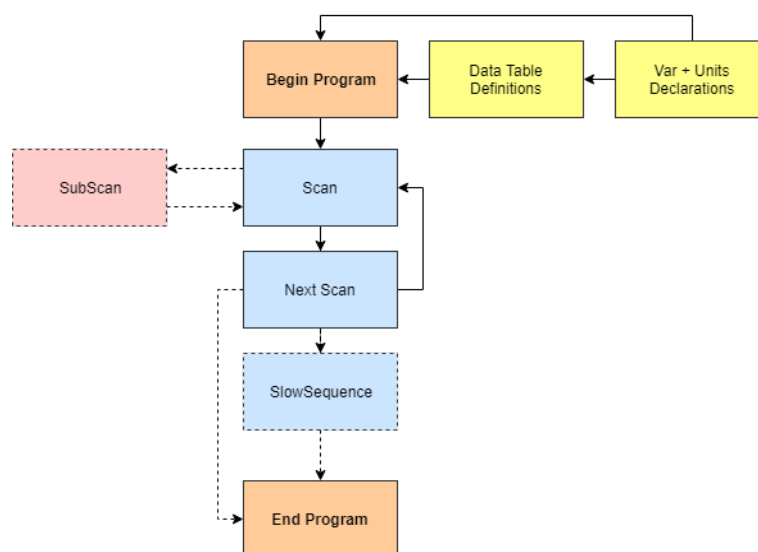


Figure 8.28: General scheme of a CRBasic program

After the variables are defined, data tables should be defined. An example data table definition is shown in Figure 8.30. A data table definition basically tells the logger which variables it should store on its disk for future data collection. Therefore, if a sensor is measured by the logger at each scan, if it is not called in a table definition block, its values will not be recorded for future data collections; it will only be stored in the logger's memory until the next scan takes place.

An interesting feature of data table definition blocks is allowing the user to perform simple statistical operations (averaging, maximum calculations, etc.) on measured data before storage by setting a different frequency of writing measurements and scanning the sensors. For example, the logger can be setup so that it measures wind speed four times in an hour and stores only the average or standard deviation of the four readings. This will help increase the value of data collected while using the same amount of disk space as just sampling at the top of the hour.

```

16 'EmailReady() variables
17 Public Email_message(2) As String * 150
18 Public Email_relay_server_response(2) As String * 100
19 Public Email_tx_success(2)
20
21
22 Dim TT_K
23 Dim SBT_K
24 Dim m
25 Dim b
26 Public cell_rssi As Long: Units cell_rssi = DB
27 Public cell_ip_address As String * 40

```

Figure 8.29: Variable declarations in CRBasic

```

105 Units TiltNS_deg=degrees
106 Units TiltWE_deg=degrees
107
108 'Define Data Tables
109 DataTable(CELL_DIAGNOSTICS, True, -1)
110   Sample(1, cell_state, String)
111   Sample(1, cell_status, String)
112   Sample(1, cell_rssi, IEEE4)
113   Sample(1, cell_ecio, FP2)
114   Sample(1, cell_rsrq, FP2)
115   Sample(1, cell_rsrp, IEEE4)
116   Sample(1, cell_ip_address, String)
117   Sample(1, cell_this_months_usage, FP2)
118 EndTable

```

Figure 8.30: Example data table definition in CRBasic

Once variables and data tables are defined, the main body of the program begins with a BeginProg instruction (Figure 8.31). After the BeginProg instruction, the user can set various

settings for the data logger including connected cellular modem settings, passing values to variables used during scans before the first scan begins.

What is defined inside a scan loop is what tells the logger how to control its different ports; these instructions tell the logger that:

1. What port is used to power a sensor
2. What port should be used to make a measurement (e.g. voltage difference between adjacent ports)
3. What type of measurement should be done (VW measurement, SDI-12, etc.)
4. How to handle unexpected data (e.g. what to write to a variable expecting to store wind speed (numeric) but sensor returns “nan” because it could not make a correct measurement)
5. Applying calibration factors to measured data
6. Communication (emailing data, sending text alerts when an alarm is triggered, etc.)

An example scan loop is shown in Figure 8.32. Depending on how the code in a scan loop is written, CR6 will decide to compile it in either sequential or pipeline mode; this means the program will evaluate the program to recognize whether different lines of the code need to be executed in the order written or if the logger can execute them in the order it finds best.

As mentioned in Section 8.2.1.11, the laser distance meter needs to be turned off between scans to conserve battery power as leaving it on will drain the battery in only a few hours. To remedy this issue, the switched output port of CR6 was used to turn on the sensor before measurement and to turn it off once the measurement is made. As this sensor requires a small amount of time to warm up, an instruction was used to delay execution of measurement instruction for a set amount of time until the sensor warms up. These instructions are an example of when the code needs to be compiled in sequential mode as the order of execution of instructions makes a difference.

```

145 BeginProg
146   m1=(RE-RB)/16R 'optioncdt
147   b1=RB-4R*m1 'optioncdt
148   SetSetting("CellPwrStartTime",780) 'Power on time in minutes in minutes; 780 = (13*
149   SetSetting("CellPwrDuration",90) 'Number of minutes to remain powered on after "cel.
150   SetSetting("CellBillingDay",15) 'Tells modem what day of the month to rollover its .
151   cell_ip_address=PPPOpen() 'Just make sure we are ready to go!
152   Email_message(1)= "This is an automatic email message from the datalogger station "
153   Email_message(1)= Email_message(1) & "Sensor data are attached."
154   Email_message(2)= "Hey Handsome! This is an automatic email message from the datalog
155   Email_message(2)= Email_message(2) & "Cell Diagnostics data are attached."
156
157 'Main Scan
158 Scan(15,Min,1,0)

```

Figure 8.31: Main body of a CRBasic program

```

157 'Main Scan
158 Scan(15,Min,1,0)
159 'SI-111SS Precision Infrared Radiometer measurements 'TT_C' and 'SBT_C'
160 'Measure SI-111SS sensor body thermistor temperature
161 Therm109(SBT_C,1,U2,U1,0,60,1,0)
162 'Measure SI-111SS output of thermopile
163 VoltDiff(TTmV,1,mV200,U3,True,0,60,1,0)
164 'Calculate slope (m) and offset (b) coefficients for target temperature calculation
165 m=1528894770+(9519931*SBT_C)+(96898*SBT_C^2)
166 b=-3689625+(-249586*SBT_C)+(-851*SBT_C^2)
167 SubScan (1,Min,15)
168     SDI12Recorder(CVData(),C1,"0","R7!",1,0,-1)
169     'Convert fractional relative humidity into percent relative humidity
170 TriggerSequence(1,-1)
171 If TimeIsBetween(780,870,1440,Min) 'If time = the range cell modem is on
172     TriggerSequence(1,0) 'Trigger occurs for SlowSequence
173 EndIf
174 'Default CR6 Datalogger Battery Voltage measurement 'BattV'
175 Battery(BattV)

```

Figure 8.32: Scan loop example in CRBasic

Although not always necessary, it is possible to define SubScan and SlowSequence loops when needed. SubScans allow the user to make measurements of certain sensors at a faster rate compared to the rest. On the other hand, SlowSequences enable the logger to give lower priority to certain actions in case there is worry that a lower priority time-consuming action (such as emailing data) may prevent the logger from performing a higher priority action (measuring sensors at specified intervals). It is possible to define multiple SlowSequence and SubScan loops in a single program if needed.

```

279 SlowSequence
280 Do
281     WaitTriggerSequence
282     Email_tx_success(1) = EmailRelay(EMAIL_TO_ADDRESS,EMAIL_SUBJECT_1,Email_message(1),Email_relay_server_respor
283     Email_tx_success(2) = EmailRelay(EMAIL_TO_ADDRESS,EMAIL_SUBJECT_2,Email_message(2),Email_relay_server_respor
284 Loop
285 EndSequence
286 EndProg

```

Figure 8.33: SlowSequence example in a CRBasic program

While a relatively small program (300 lines) was developed for collection of data from Mack Creek SIAB, the China Creek SIAB program ended up being more than 4,000 lines of CRBasic code carefully developed to control and measure all the installed sensors and peripherals, communicate data between the loggers, email the data and establish a remote cellular connection on a given schedule.

8.2.3. Construction Sequence of China Creek Bridge Replacement

The construction of China Creek Bridge faced numerous delays in construction due to inclement weather and unforeseen field conditions. As a result, the contractor was still awaiting the installation of drilled shafts in June 2019, which was delayed due to the discovery of buried steel H-piles where the new shafts were to be placed. Therefore, the first half of the bridge was completely demolished at that point and the debris was carried away. The demolition of the first half of the bridge using heavy machinery is shown in Figure 8.34. Also, to protect the active

roadway on the other half of the bridge, a temporary soil-nail wall was constructed to prevent the active roadway from settling and keep the road open. A picture of this temporary support is shown in Figure 8.35.



Figure 8.34: First half of old China Creek Bridge demolition



Figure 8.35: Installation of soil nail wall as temporary support for active roadway crossing the undemolished half of China Creek Bridge (Picture provided by Samuel Groves)

After encountering the buried obstructions in June/July 2019, construction of drilled shafts was delayed until mid-November 2019. A trip to China Creek for the day of drilled shaft construction was planned to document the construction process and also gather soil cuttings from the drilling operations as we were not given the opportunity to collect high quality soil samples to test in the lab and gain a better understanding of the soil properties at the site.

Two-and-a-half-gallon Ziploc bags were used to collect soil cuttings every time the drill bit was raised from the hole (Figure 8.36), when the drill operator was asked to stop for a few seconds to allow the research team to collect two to three large scoops of soil off the auger blades before dumping the soil in a pile by the drilling rig. In the end, nearly 40 bags of soil were collected and carried by car to UT Austin for further analysis (Figure 8.37).

During the collection of cuttings, the top 15 to 20 ft of soil appeared to be a mix of sandy materials mixed with highly plastic clayey soil with no visible layering changes. The material deposited in this depth were once removed to remove the buried obstruction and placed back after removal of the obstruction. According to the TxDOT supervisor, sheepfoot rollers were used to recompact the as it was being placed back. Therefore, the soil cuttings, even though highly disturbed, should still be a good representative of soils in place up to the depth of about 20 ft. Another important observation made was of signs of groundwater flow at depths of about 20 ft as well; the samples removed from this depth were found to be very sticky and wet relative to what was recovered above that depth. After reaching this depth, the rig operator placed a permanent casing in the hole due to the presence of collapsible soils at the top (Figure 8.38).

At a depth of about 25 ft and deeper, the cuttings recovered appeared brittle and flaky, which is known as gray shale (Figure 8.39). The heap of soil removed by the auger is shown in Figure 8.40, in which broken flakes of gray shale (covered in powdered red dirt) can be easily seen on top while the remolded wet/plastic material can be seen below.

Once the target depth was reached, the rebar cage (Figure 8.41) was gently lowered into the hole while construction workers attached plastic spacers to the rebar on all sides to maintain the minimum cover. As no spacers/cushions were used for the bottom of the longitudinal rebars, the contractor kept the rebar cage from touching the bottom of the hole by temporarily propping it with a wooden log (Figure 8.42). In this case, the contractor planned to adjust the final height of the rebar cage when concrete is poured.



Figure 8.36: Drill bit exiting hole to dump excavated soil



Figure 8.37: Soil cuttings collected during drilling operations in November 2019



Figure 8.38: Casing used for top 20 ft of drilled shafts



Figure 8.39: Gray shale covered with powdery red dirt recovered from a depth of 30 ft



Figure 8.40: Heap of soil excavated from drilled shaft (Note broken shale pieces on top (25 ft and below) and wetter/plastic material removed beforehand)



Figure 8.41: Lowering of rebar cage



Figure 8.42: Propping rebar cage to keep it off the bottom of the hole before concrete pouring

By the end of February 2020, the contractor finished forming the pile caps and wingwalls and placed the girders and precast panels for the first phase in position. As the precast/pre-stressed girders were stored in a remote location for more than a year, they had experienced a significant creep resulting in excessive camber when initially brought to the site. Therefore, the contractor decided to wait for the precast panels placed on top to reverse part of this creep before forming the backwalls.

As work on forming the backwalls began (Figure 8.43), the research team visited the site during the first week of March 2020, to place the first set of instrumentation, earth pressure cells (GK-4810) on either wall to be cast in concrete.

Unlike the procedure followed in Mack Creek, it was decided to mount the pressure cells on the inside of the wooden forms, nailed to the forms. This way, once the forms are removed, the surface of the pressure cell will be flush with the concrete and potentially eliminate any errors due to arching effect. As experienced during laboratory calibration of these sensors, due to difference in stiffness of the steel plate and the soil, if the sensor is mounted on the surface of the concrete (as opposed to being flush with it), some arching effects would occur resulting in higher magnitudes of stress being recorded by the cell. Another improvement over the procedure followed in Mack Creek is elimination of the need to place a sand cushion around the sensor to prevent point-loading effects. These cells were designed with thicker steel to give correct readings when in contact with granular media.



Figure 8.43: Forming of abutment backwalls after placement of girders and precast panels, March 2020 (east abutment)

In Figure 8.44, the earth pressure cell installed on the west abutment is shown. As can be seen, once the concrete is placed, this sensor will be integrated with the backwall and its exposed face will be directly in contact with the granular backfill. The cables for these sensors were routed through the polystyrene to the inside of the bridge and coiled up above the pile cap, awaiting the installation of data loggers. Baseline measurements of the installed cells were taken upon installation using GK-404 handheld logger.

The concrete was placed the day after installation and a subsequent visit was made during the form removal process to examine the finished surface. As expected, the finished surface looks great and the concrete placement did not cause the pressure cell to move away from the form (Figure 8.45). Upon form removal and before placement of the backfill, another set of measurements were made using the handheld GK-404 logger.

The remainder of the pressure cells were installed on the backwall, pile cap and wingwalls during the second phase of the construction.



Figure 8.44: Top view of earth pressure cell (GK-4810) installed on inside of form on west abutment backwall, March 2020 (photographer standing on one precast panel placed on deck)



Figure 8.45: Finished surface of east abutment backwall with pressure cell (GK-4810) installed between two girders on left, March 2020

Shortly after the removal of the forms, the backfill was placed and rebars for the bridge deck were placed. Although placement of concrete-embedded strain gauges in the deck was originally planned for the second phase of construction, this task was expedited in an attempt to collect more data considering bridge construction was extremely delayed.

For instrumentation of the deck, a total of 11 concrete strain gauges were brought to the site. Ten of these strain gauges were model GK-4200 that were placed in evenly spaced pairs (top and bottom of the deck profile) along the longitudinal axis of the deck. The other one was a GK-4200L placed perpendicular to the longitudinal axis of the bridge (Figure 8.46) close to the first pair of GK-4200s near the west abutment. The difference between the two types is that GK-4200L has lower stiffness and so it can capture early shrinkage deformations of the concrete as well, while the other ones will not deform until the concrete sets and reaches higher stiffness.



Figure 8.46: GK-4200L as installed on the deck, perpendicular to the direction of the bridge, March 2020

A pair of GK-4200 installed on the deck is shown in Figure 8.47. As can be seen, one is attached to the bottom of the top rebar with the help of zipties and blocks of Styrofoam as a spacer and the other is installed near the bottom (top of the girder). As there are no rebars at the bottom, a set of zipties were wrapped between two “U” shaped hooks of the girder and the strain gauges were tied to those as shown in Figure 8.47.

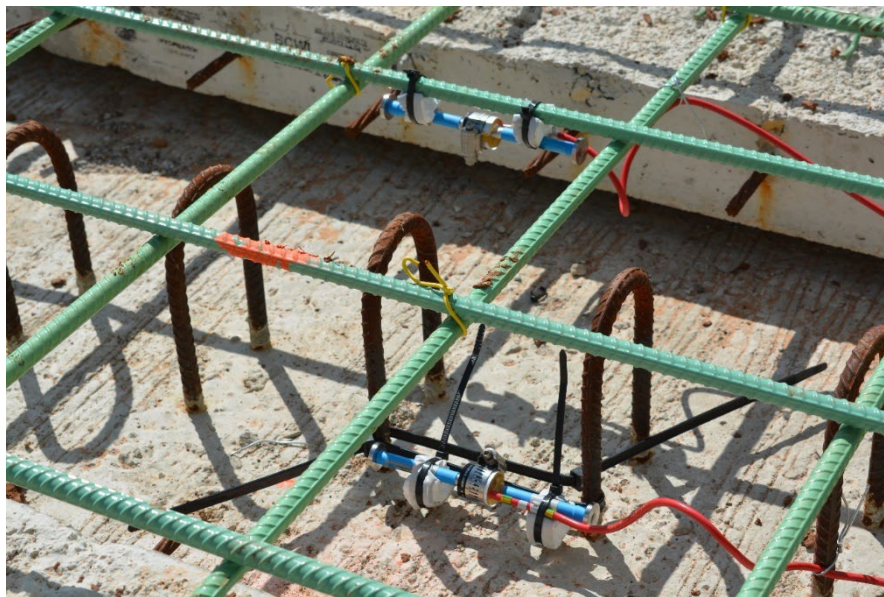


Figure 8.47: A pair of GK-4200 strain gauges installed on the deck during phase 1 of construction

Unlike other Geokon sensors, the sensor body of the GK-4200 is manufactured separate from the cable and transducer and needs to be assembled in the field. Therefore, each sensor/cable does not carry a unique serial number tag. A binary codebook was designed to keep track of the cables and position of the sensors attached to them. An example of the binary code applied is shown in Figure 8.49 where yellow/green tape represent ones and gray tape represents zeroes. The same code is applied to the other end of the cable, which is routed through a small gap to the top of the pile cap (Figure 8.49), helping identify which cable belongs to which sensor. In the end, these cables were coiled and routed through a block of wood (Figure 8.50) with pre-drilled holes in a specific order, in case the tape is removed due to weathering or a possible flood event. In the end, baseline values for each strain gauge were recorded using the handheld GK-404 logger.



Figure 8.48: Different colored tape represents binary values to help identify sensor



(a)



(b)

Figure 8.49: (a) Strain gauge cables were routed underneath the bridge through a small gap between foam boards; and (b) coiled strain gauge (red) and earth pressure cell (blue) wires



Figure 8.50: Predrilled block of wood used to help keep track of cables coming from embedded strain gauges

In late March 2020, the research team was notified that deck concrete was successfully placed and the sensors appear to have stayed in place (Figure 8.51 to Figure 8.53). Due to the COVID-19 pandemic-related travel guidelines issued by the University of Texas at Austin, the research team was not able to make subsequent visits to oversee deck concrete placement and record the sensor outputs thereafter or while the concrete set. While the time-rate of deformations were not expected to be captured during this time, the sensors were still expected to capture deformations, and total deformation during this period would be known at the next field visit.



Figure 8.51: Concrete placement on deck, phase I, March 2020



Figure 8.52: Finished deck surface, phase I, March 2020



Figure 8.53: Covered deck surface after concrete placement, phase I, March 2020

The work on phase 2 of the bridge proceeded rather quickly compared with phase 1. This required the research team to make frequent visits to the site to install the planned sensors for different parts of the bridge over spring and summer 2020.

The first set of instrumentation for phase 2 began after conclusion of demolition activities and by the start of excavation activities for the drilled shafts. As the construction crew began the excavation activities, the research team prepared Sch. 40 PVC conduits for installation inside the drilled shaft's rebar cage for the center drilled shafts on both sides of the bridge. The purpose of the 40-ft PVC conduits was to serve as housing for the SAAV sensors that are intended to capture potential lateral deformations in the drilled shafts.

To alleviate transportation of PVC conduits, the pipe sections were cut into manageable 5-ft sections that could be easily transported by car from Austin to Wichita Falls (Figure 8.54). The day before the excavation, these pipe sections were assembled at the location using PVC cement and various types of couplers to ensure the finished conduit does not collapse during the installation phase (Figure 8.55). Because the rebar cage was to be lifted only from one end by the crane prior to installation in the hole, a significant amount of bending was expected to occur in the cage and the conduit attached to it. Therefore, several methods of reinforcement were used to ensure the joints are just as strong as the uncut portions of the conduit through the use of heavy duty PVC cement and hose clamps as shown in Figure 8.56.



Figure 8.54: Five-ft PVC conduits transported to China Creek Bridge to house SAAV sensors in drilled shafts (conduits pictured have been assembled into 10-ft sections using PVC cement and couplers)



Figure 8.55: PVC conduits assembled into 40-ft sections using additional couplers and joint reinforcement



(a)



(b)

Figure 8.56: Reinforcement of PVC conduit joints: (a) threaded couplers + heavy duty PVC cement; and (b) compression couplers + flexible couplers + hose clamps

Furthermore, to reduce stresses on the pipe and joints, heavy duty zipties and hose clamps were used roughly every 3 ft to secure the PVC conduit against the spiral rebars of the drilled shaft in the order shown in Figure 8.57. The final result of attaching the assembled PVC conduit to the rebar cage can be seen in Figure 8.58 where the conduit runs in the space between two vertical rebars from top to bottom of the cage. While all the different types of reinforcements used for the assembly of this conduit may not have been necessary, the cost of adding these layers of reinforcement far outweighs the cost of potential damages to the conduit during construction; a failure of the PVC during construction is equal to the loss of opportunity for the installation of a very expensive and important sensor as there will be no chance to repair or replace

As depicted in Figure 8.58, the conduit is several feet longer than the drilled shaft, which accounts for the height of the abutment cap. Following its construction, the SAAV sensors were installed.



(a)



(b)

Figure 8.57: Attachment of 40-ft PVC conduit to rebar cage: (a) heavy duty zipties used on either side of joints; and (b) combination of steel hose clamps and heavy duty zipties used at each middle section



Figure 8.58: Assembled PVC conduits attached to drilled shafts to serve as SAAV housing

In addition to the planned instrumentation of the drilled shafts with SAAV, three pairs of strain gauges were attached to the east-center drilled shaft at a 5-ft distance from the top. The goal for the installation of these sensors is to gain a better understanding of vertical and horizontal loads applied to the drilled shafts and obtain an estimate of skin friction for the top 10 ft.

A close-up view of the instrumented rebar cage used for the center drilled shaft on the east abutment is shown in Figure 8.60. The strain gauges were installed in pairs according to the expected direction of bending to decouple compression from bending strains.

After the completion of instrumentation tasks intended for rebar cages and end of excavation activities, the construction crew proceeded to carefully lift the rebar cages using cranes and front loaders and place them inside their holes (Figure 8.61).



Figure 8.59: Strain gauges attached to long rebars of drilled shafts

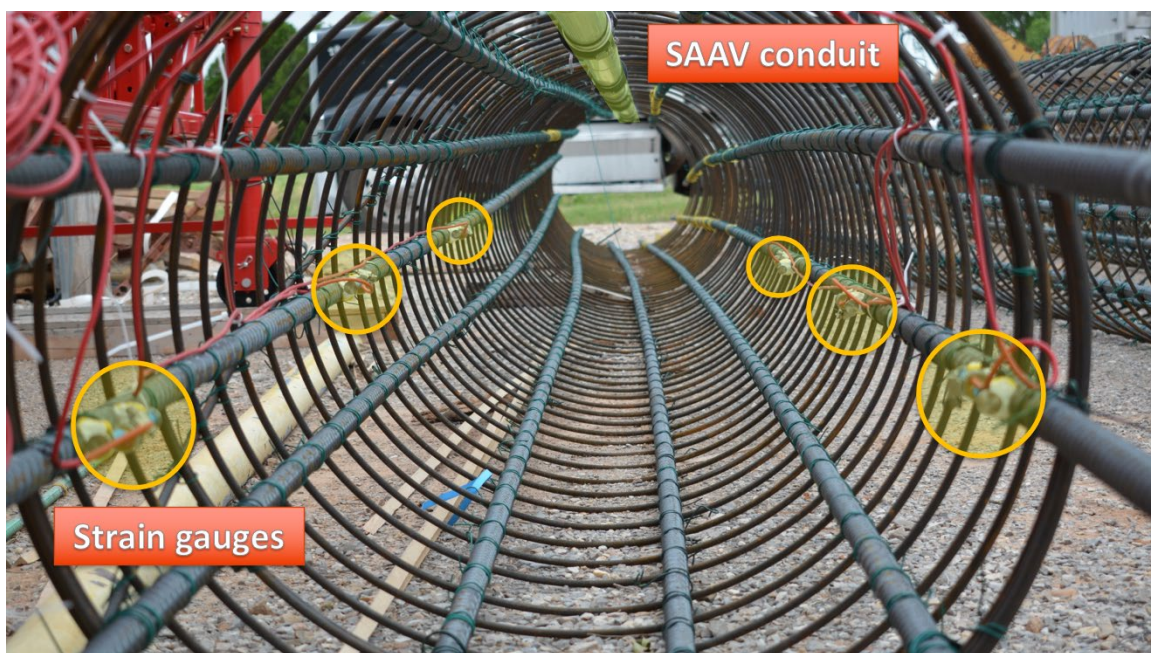


Figure 8.60: Instrumented rebar cage intended for China Creek Bridge east-center drilled shaft, phase 2



(a)



(b)



(c)



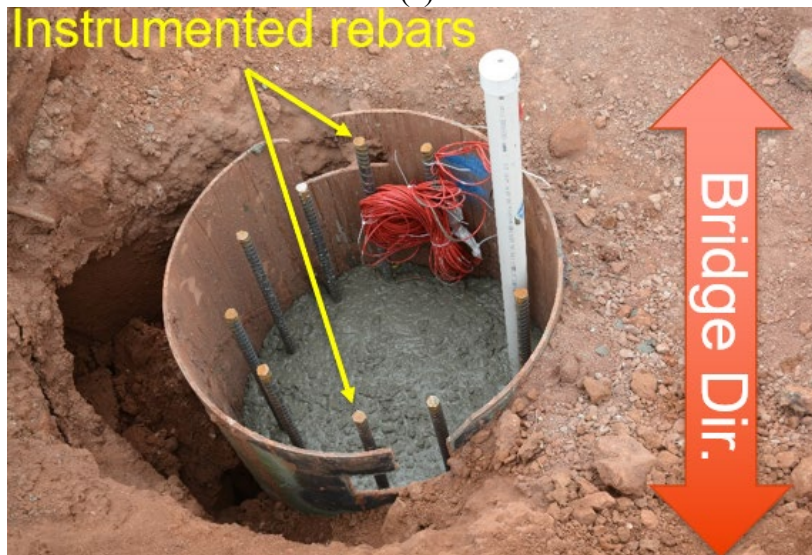
(d)

Figure 8.61: Installation of east abutment instrumented drilled shaft: (a) lift and transportation to drilled shaft location of rebar cage using a front loader; (b) rebar cage raised from the top using a crane (note the extent of curvature on the rebar cage and PVC conduit); (c) lowering of rebar cage into the hole; and (d) final placement of rebar cage before concrete is poured

Once the drilled shafts are placed and excavation machinery are removed from the location, concrete is pumped into the drilled shafts and the final adjustments on the rebar cage are made to ensure the orientation of sensors are correct for the expected direction of movement.



(a)



(b)

Figure 8.62: (a) Concrete being pumped into drilled shaft; and (b) final orientation of instrumented shaft and sensors

One week after construction of the drilled shafts, the construction crew began forming the abutment caps (Figure 8.63). For this stage, the research team intended to install earth pressure

cells on the side facing the backfill to record earth pressure acting on the abutment caps and any potential changes in them.



Figure 8.63: Formwork for construction of pile caps and wingwalls

As can be seen in Figure 8.64, earth pressure cells are mounted on the inside of the form at the mid-height of the abutment cap and near the location of the center drilled shafts. Once the forms are stripped, the earth pressure cells will be flush with the concrete surface. Also, it can be seen in Figure 8.64(a) that once the abutment cap is poured, roughly 1 ft of the SAAV conduit will be sticking out of the top, leaving enough room to lower the SAAV into the conduit and clamp it at the top, per installation requirements.



(a)



(b)

Figure 8.64: (a) West abutment cap pressure cell (before formwork completion); and (b) east abutment pressure cell (after formwork completion)

Upon completion of formwork, abutment cap sensor installation and routing of the sensor wires to a suitable location, the abutment cap was poured with a concrete tremie (Figure 8.65).



(a)



(b)

Figure 8.65: (a) Pouring concrete for abutment cap with a concrete tremie (west abutment); and (b) completion of abutment cap surface (notice SAAV conduit sticking out between two girder pedestals)

Immediately after pouring the abutment caps, the construction crew began the formwork on the wingwalls, which were cast integrally with the abutment cap but in a separate pour. Before the forms were installed, the research team took the time to mount an earth pressure cell on each side to measure changes in earth pressure on the wingwalls due to movements in the backwalls. The earth pressure cells were mounted at a location close to the surface of the abutment backwall, and the forms were clearly marked with spray paint to ensure installation of the cells at the correct locations (Figure 8.66).



(a)



(b)

Figure 8.66: Installation of earth pressure cells on wingwall forms to measure backfill pressure acting on wingwalls

Upon completion of abutment cap and wingwall construction, another visit was made to the site to install the SAAV sensors before the girders were placed. As can be seen in Figure 8.67, the SAAV was shipped on a reel that needed to be carefully unspooled as the sensor was fed into the conduit. This installation is best done with at least two people to ensure SAAV segments bend as little as possible during installation as the joints are vulnerable to snapping if bent too much. Once the SAAV is fully lowered into the conduit, the extension fiber glass tube is attached to the top, and the whole sensor is lifted several times and rammed into the conduit (pumping motion) to ensure the sensor has fully settled into the conduit and all joints are compressed against the walls. This step is very important because if the sensor is not fully settled into the conduit, SAAV may slowly settle over the first few weeks after the installation causing errors in the readings. Once the sensor is settled, the extension piece is cut using a hacksaw and clamped to the top of the conduit using the compression clamp provided by the manufacturer. This

compression clamp ensures there is certain amount of vertical compressive force acting on the SAAV segments to prevent them from moving out of place and generating readings that are not from deformations of the structure being monitored. Once the compression clamp is assembled, the installation verification tool provided by the manufacturer is used to ensure the amount of tilt recorded at each SAAV segment is within the expected range given the internal diameter of the conduit chosen (Figure 8.68). By analyzing the sensor readings from all segments of the SAAV, and given the internal diameter of the casing, the tool calculates amount of compression on the system, total compression required, tilt angle of each segment and whether these angles exceed the minimum tilt angle expected for the casing chosen. If the tilt angle of the majority of the segments pass the angle calculated by the software, a green light is given and the installation is considered successful (Figure 8.68).



Figure 8.67: SAAV installation in east abutment center drilled shaft

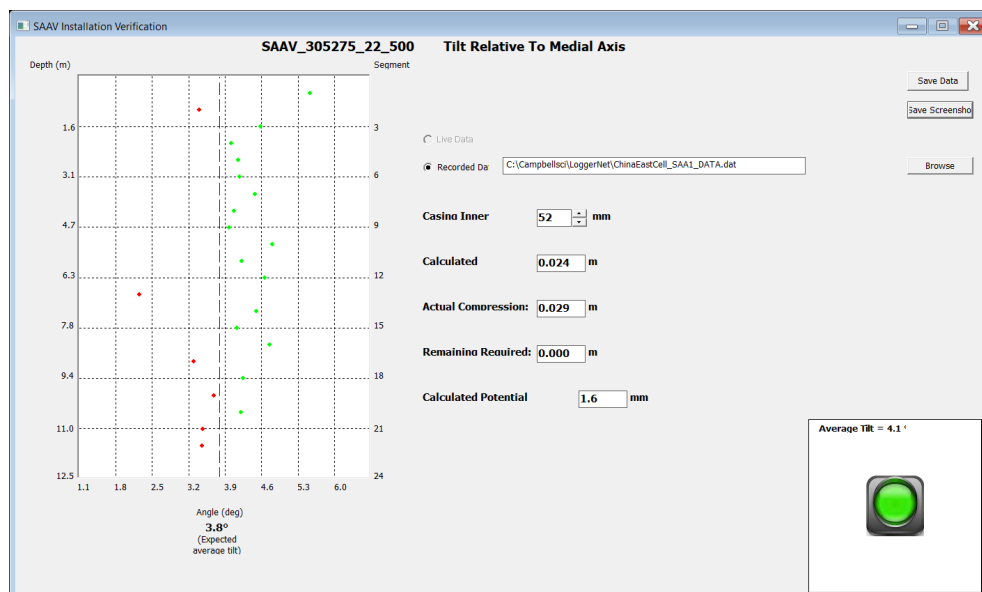


Figure 8.68: SAAV verification tool screen (green light indicates successful installation)

Once the installation is completed, SAAV conduits are capped using 4-in. PVC conduits to prevent water/debris from entering the conduits and interfering with the performance of the system (Figure 8.69). This is very important because if water enters the conduits and freezes over the cold season, the pressure due to expansion of water can cause serious harm to the sensors.



Figure 8.69: Capped SAAV conduit on east abutment

After the girders are placed, a set of five VW miniature strain gauges are mounted on the bottom flange of the middle girder of the bridge at a spacing of 15 ft. For the installation of these sensors, a drilling guide (Figure 8.70) is used to make shallow holes in the bottom flange of the girder that are the same distance as the pegs on the strain gauges. For drilling, extra care was taken to not drill holes deeper than necessary to minimize the risk of damaging pre-stressed reinforcement in the girders. Next, these holes are cleaned using canned air and filled with quick-setting epoxy before setting the strain gauges. The strain gauges are held in place using a piece of duct tape until the epoxy sets (Figure 8.71). In the end, a metallic cover is epoxied on top of these gauges to protect them from potential flood debris. The finished installation can be seen in Figure 8.72.

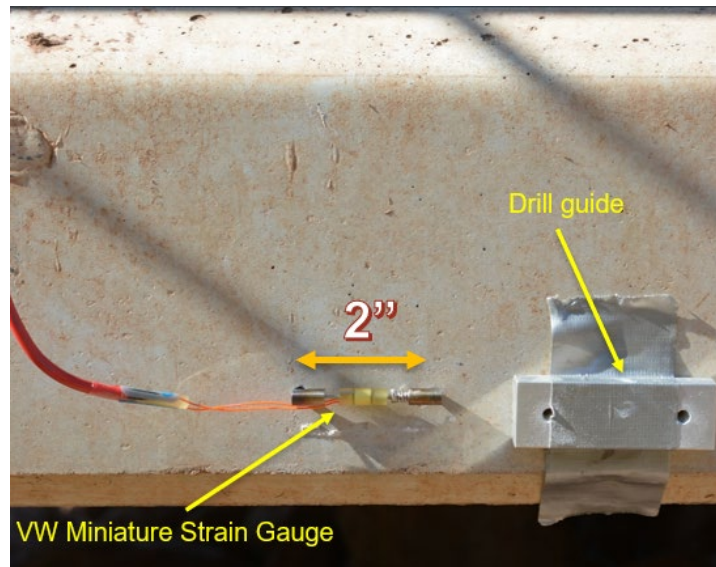
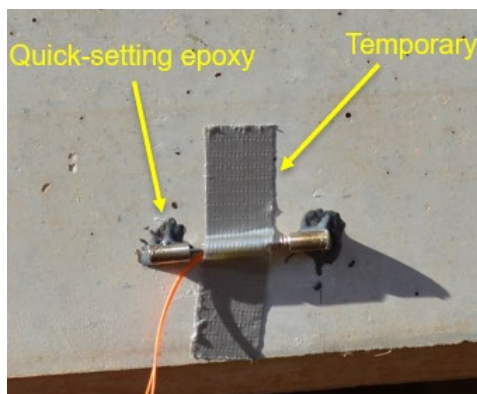


Figure 8.70: Miniature strain gauge next to drill guide used for installation on side of bottom flange of bridge girder



(a)



(b)

Figure 8.71: Installation of miniature strain gauges on bridge girder: (a) epoxied strain gauge; and (b) strain gauge installation (cables are routed along top flange)



Figure 8.72: Mounted miniature strain gauges on bottom flange of middle girder

As the abutment backwalls were formed, it was decided to attach three pairs of strain gauges to the rebars in different locations and orientations to record strains in the backwall due to changes in backfill pressure as well as have measure of heat flow in the backwall using the thermistors of these sensors (Figure 8.73). In addition to the strain gauges, two pairs of earth pressure cells were also mounted to the back of the forms intended for each backwall to complement the measurements made by the earth pressure cells mounted during the phase 1 of the construction (Figure 8.74).

Once the backwalls were formed, precast concrete panels were placed in between the girders using a crane, as shown in Figure 8.75. Thereafter, placement of the deck rebar, deck concrete and abutment backwalls was completed on the same day (Figure 8.76).



Figure 8.73: Location of three pairs of concrete-embedded strain gauges on east abutment backwall



Figure 8.74: Pair of earth pressure cells mounted on back of form intended for west abutment backwall



Figure 8.75: Placement of precast concrete panels on deck



Figure 8.76: Phase 2 deck concrete placement

As the concrete for the deck was delivered, the research team prepared two instrumented fresh concrete sample cylinders (Figure 8.77) using low modulus VW strain gauges. This was done to monitor thermal and shrinkage strains occurring in the concrete used in the deck without the influence of other live or dead loads as well as structural constraints. One of these cylinders is intended to be placed on a wingwall to catch direct sunlight and the other is placed under the bridge to be only influenced by ambient temperature. It is hoped that the data collected from these two instrumented cylinders will help the researchers better define the coefficient of thermal expansion as well as shrinkage of the concrete used in this bridge.



Figure 8.77: Instrumented concrete sample cylinders

After the completion of the bridge deck, the research team began installing the backfill sensors, which included backfill settlement sensors and soil extensometers, both of which are made of VW displacement transducers housed in a Sch. 40 PVC conduit and measure the distance between their flanges. The installation of the settlement sensor was one of the trickiest installations in this project as it required several feet of excavation below the backfill. For this purpose, a two-man gas-powered auger was rented to excavate a hole deep enough. Next, the settlement sensor was placed into the hole and set in place by adding quick-mix concrete, mixed onsite using a drill equipped with a paddle mixer attachment. This point below the backfill serves as the reference point for backfill settlement measurements (Figure 8.78)

To better understand how settlement in the backfill occurs, it was decided to spread the settlement sensors in different directions on each side. As a result, the settlement sensors were placed at different distances from the abutment backwall and centerline of the bridge (Figure 8.79).



(a)



(b)

Figure 8.78: Installation of VW displacement transducers to be used as backfill settlement sensors: (a) hole excavation using auger; and (b) vertical sensor placement in hole



(a)



(b)

Figure 8.79: Settlement sensor installation locations: (a) west abutment; and (b) east abutment

To monitor horizontal movements in the backfill due to expansion/contraction of the bridge deck, two daisy-chained extensometers were installed in each backfill as well. Each of these extensometers was attached to a pre-machined angled iron flange that would extend or compress the displacement transducer upon engagement with the backfill soil.

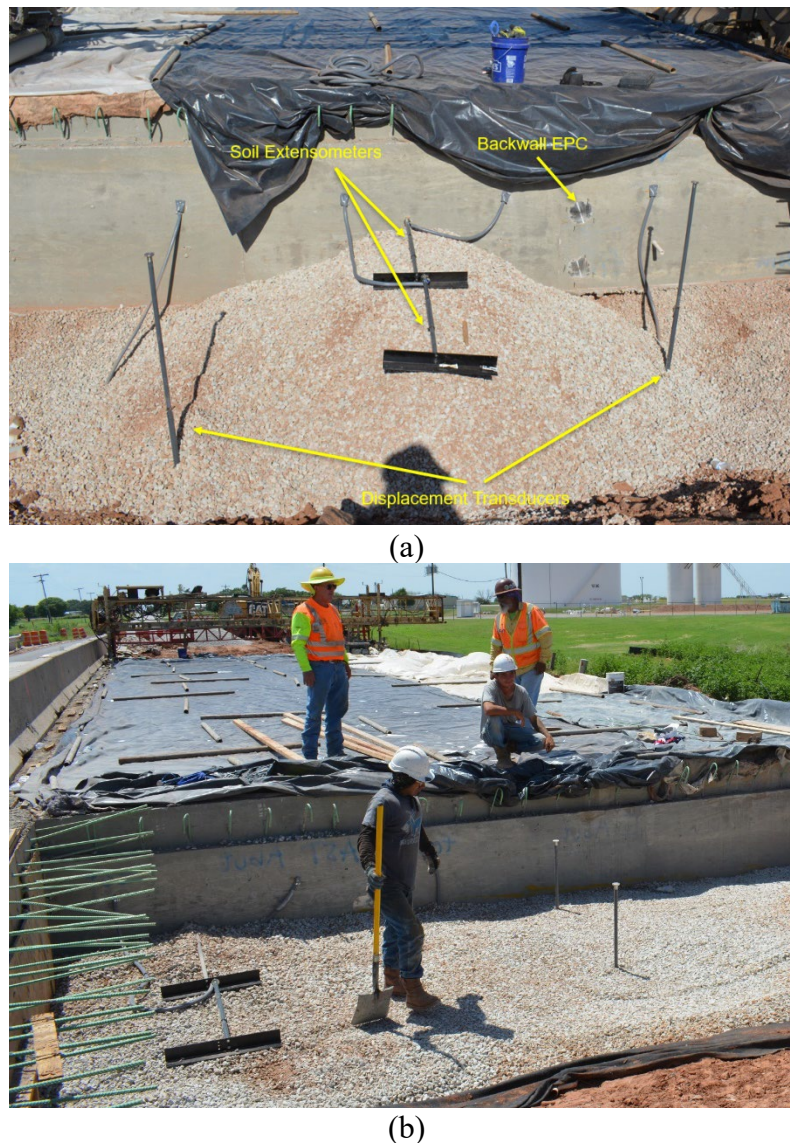


Figure 8.80: Soil extensometer installation in backfill: (a) west abutment; and (b) east abutment

Once the backfill is placed all the way to the top, a large and heavy stainless steel plate was attached to the top flange of the settlement sensors to ensure the top flange follows the motion of the backfill soil at the surface (Figure 8.81). These plates were tested prior to installation to ensure they are heavy enough to compress the displacement transducer under their own weights considering the sliding resistance provided by the set screws and tapes on the body of the sensor.



Figure 8.81: Stainless steel plates attached to top flange of settlement sensors

After the construction crew finished the placement of backfill material, work on forming the sleeper slab and approach slab began. No sensors were planned for this phase of the construction but because not enough backfill material was delivered to the site, a small amount of cobble-sized stone (material used for construction of silt fence on the creek) was used to even the surface at the location near the west sleeper slab.

After the completion of the approach slabs, three VW crackmeters were placed on each side to monitor relative displacement between the sleeper slab & approach slab (Figure 8.82), approach slab & wingwall (Figure 8.83) and abutment cap and backwall (Figure 8.84) on each side of the bridge. A tiltmeter was also installed on each side to measure any potential tilt in the backwalls due to thermal cycles of the bridge.

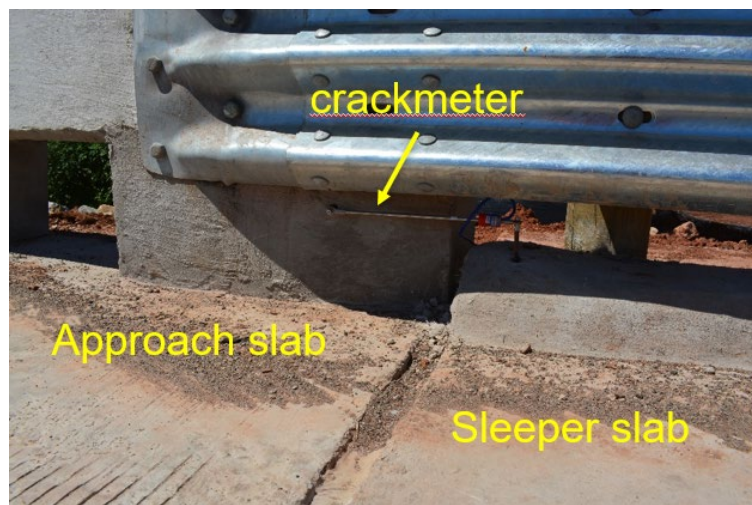


Figure 8.82: Crackmeter installed for measuring relative displacement between approach slab and sleeper slab

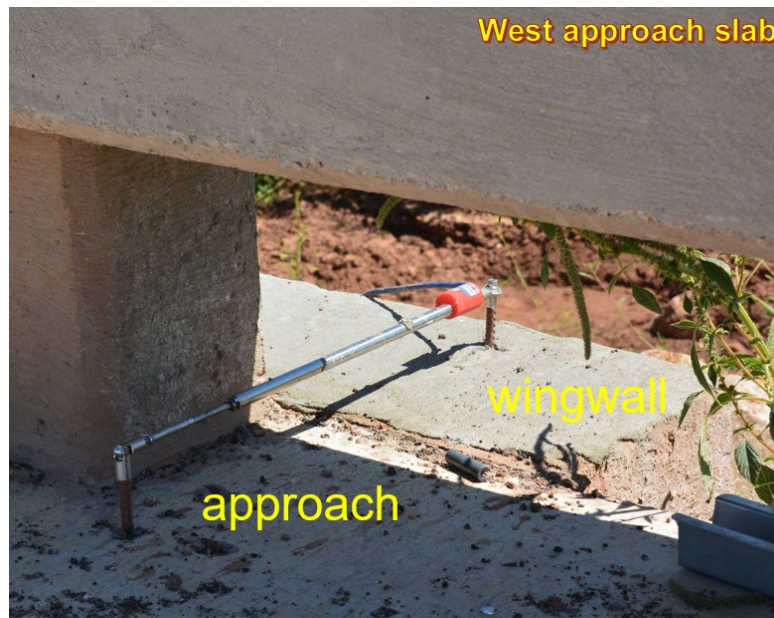


Figure 8.83: Crackmeter installed for measuring relative displacement between approach slab and wingwall

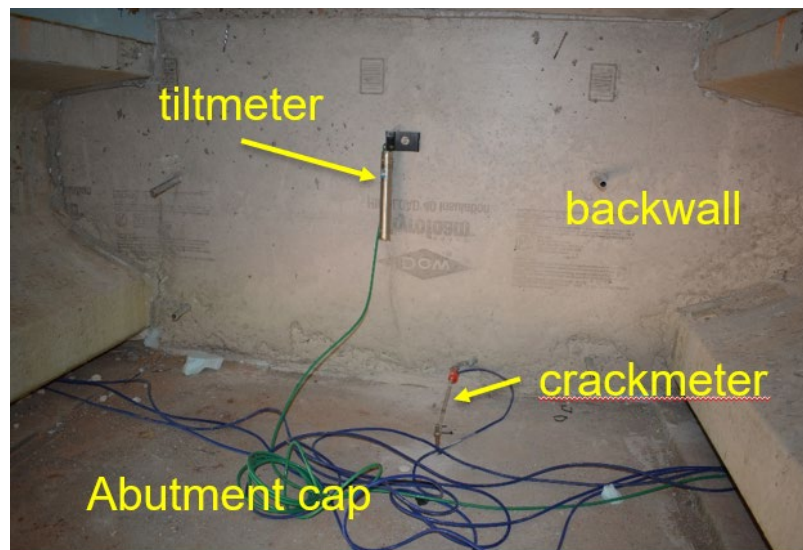


Figure 8.84: Crackmeter installed for measuring relative displacement between abutment cap and abutment backwall + tiltmeter installed on abutment backwall

The purpose of these crackmeters is to see if there is any relative motion occurring between these structural components as they are not constructed integrally and it is possible to see relative movement between these components due to a variety of reasons including pressures generated in the backfill and thermal expansion of concrete.

Due to the frequent flooding of China Creek, which passes below the bridge, it was decided to instrument the structure with two piezometers as well to track significant flood events and see if there are any changes in the other parameters associated with the floods. To this end, one

piezometer was installed inside the backwall with the tip of the piezometer in contact with the backfill soil (Figure 8.85). The other piezometer was installed on the abutment cap's creek side to help track how high the water in the creek rises, when it reaches the height of the abutment cap (Figure 8.86).

The last set of sensors intended for China Creek Bridge were mounted on a 10-ft superstrut mounted on the southwestern wingwall of the bridge. These sensors help measure weather-related parameter (ClimaVue50) and deck surface temperature (SI-111SS infrared radiometer). In addition, a powerful cell antenna is mounted to help establish a remote connection with the data logger using a cell modem.

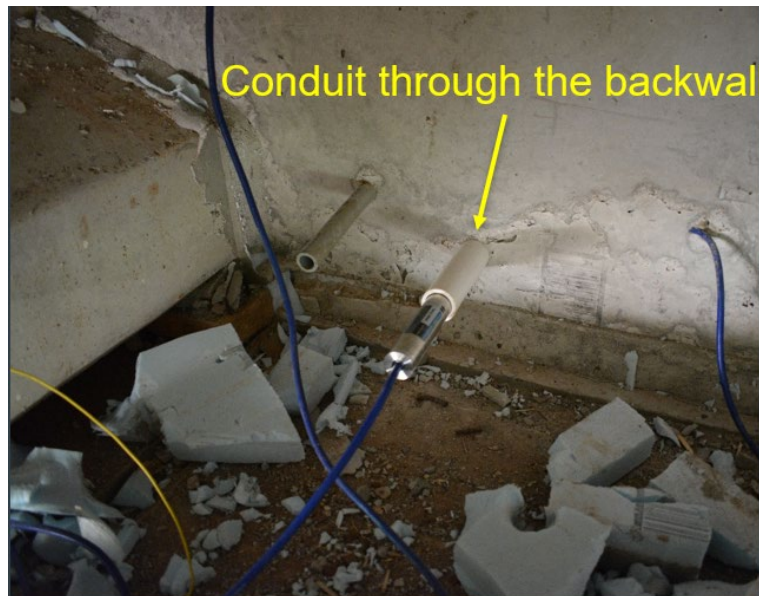


Figure 8.85: Piezometer measuring water pressure in backfill, prior to installation (sensor is fully inserted and sealed on the back to prevent water infiltration from creekside in case of flooding)



Figure 8.86: Creekside piezometer installed on abutment cap

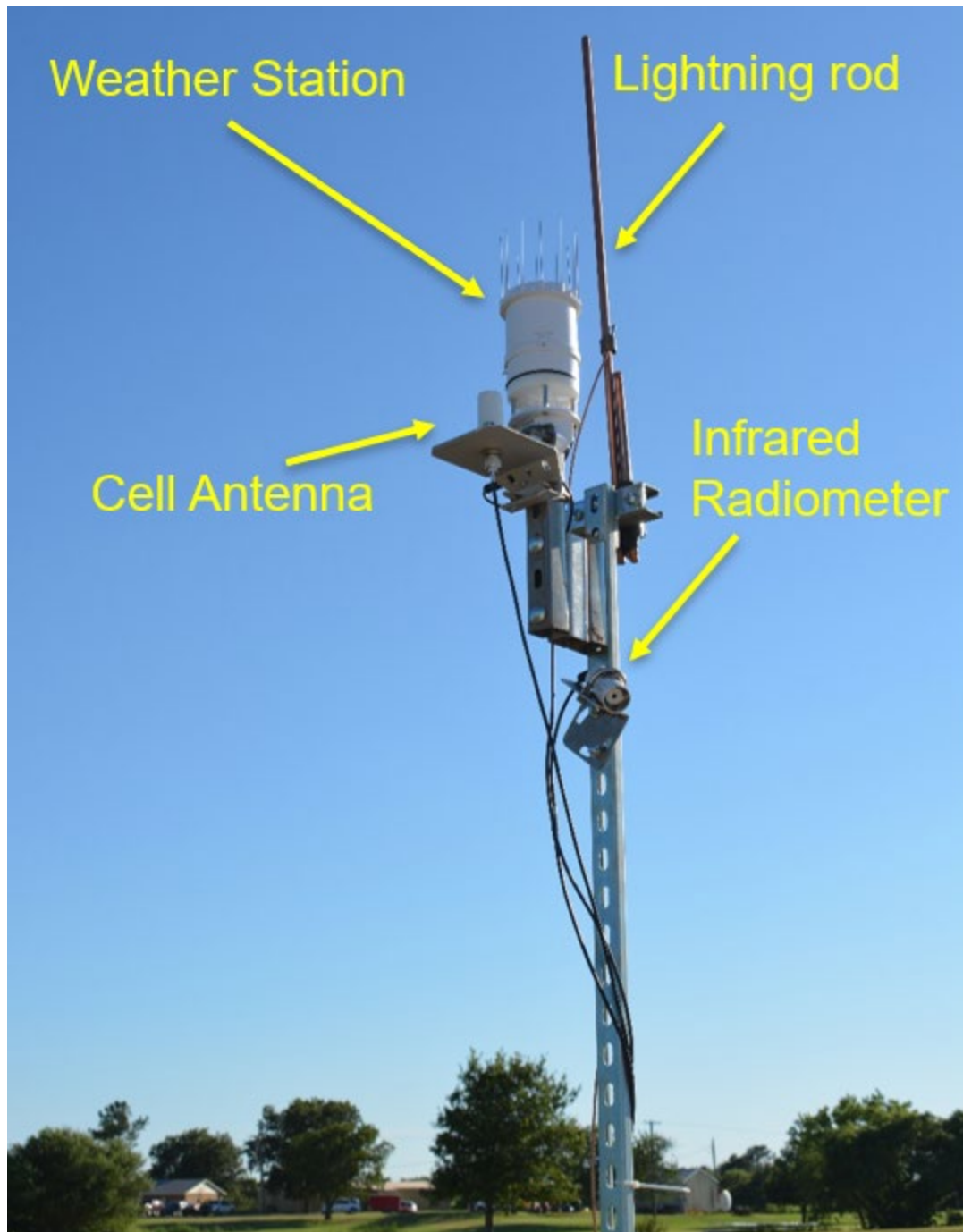


Figure 8.87: Superstrut mounted on southwest wingwall; infrared radiometer is pointed toward deck surface to measure surface temperature

To power the data logger system, two 40W solar panels equipped with 12V charge controllers were installed on the south railing of the bridge, with one on each end (Figure 8.88). Installing these solar panels on the south side enables them to produce maximum amount of electricity to ensure continuous operation of the data loggers with the help of sealed lead acid batteries placed inside the data logger enclosures.



Figure 8.88: Solar panel mounted on south railing of east end of China Creek Bridge



Figure 8.89: China Creek Bridge construction completed and opened to traffic on July 31, 2020

After the completion of construction (Figure 8.89), pre-assembled data logger enclosures were brought to the site and were mounted upside-down under the deck between two adjacent girders.

The data logger enclosures were mounted underneath the bridge and at the request of TxDOT to minimize the potential for tampering by hiding them from plain sight. However, due to history of flooding under the bridge (recent instances of flood reaching the deck height), extra measures had to be taken to protect the system from water damage as none of these components are waterproof. The first measure taken in waterproofing the enclosures was to switch the original enclosures provided by the manufacturer with IP68-rated enclosures fitted with IP68-rated cord grips. To test the performance of these enclosures under continuous submersion, they were filled with heavy metallic pieces and placed inside a 50-gal. drum filled with water for two days to confirm if any water ingress occurred. A considerable amount of water ingress, due to a faulty cord grip, was found to have occurred on the first attempt. After the faulty cord grip was replaced, a second attempt was made and no signs of water intrusion were found. Therefore, despite the equipment being IP68-rated, the research team determined a high likelihood of at least one piece of faulty equipment potentially undermining the integrity of the whole system. Consequently, in addition to the IP68-rated cord grips and enclosures, several additional measures were taken to ensure no water ingress occurred in cases of heavy flooding events:

1. The enclosures are mounted at the highest point possible below the deck, which is directly under the precast concrete panels
2. Enclosures are mounted upside down with cord grips as close to the lid as possible. This arrangement leads to the creation of an air pocket inside the enclosure, which would keep water out even if faulty cord grips are in place (Figure 8.90). The working principle is that if there is no place for the air molecules to escape from, water pressure from the outside would only lead to compression of the air pocket, not its drainage; therefore, the air pressure developed in the air pocket will be equal to the water pressure from outside and no flow can occur. This phenomenon is similar to how a shallow diving helmet does not get filled with water despite not being sealed at the bottom.

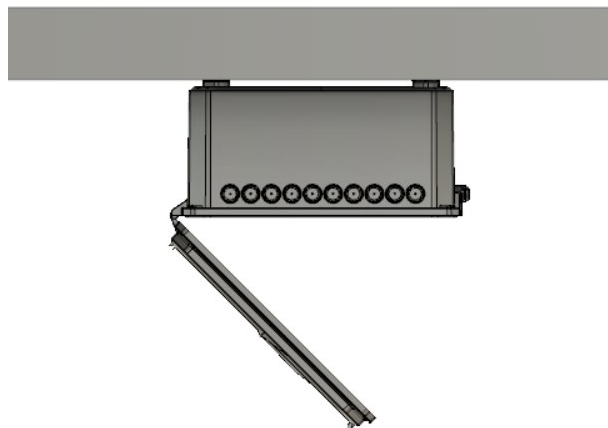


Figure 8.90: Upside-down installation of logger enclosures mounted to bottom of deck; to prevent water damage to housed equipment, all cord grip holes need to be as close to lid as possible

3. It is expected that an even larger air pocket can form in the space between adjacent girders since girders are cast into the backwall at the end and the precast concrete panels and deck concrete seal the top. With no place for the air to escape from, water should not be able to rise much in between the girders even if it reaches the deck height on the outside.

Therefore, four layers of protection were devised to prevent flooding of the enclosures, given the steep cost of equipment loss.

A major downside to the previously explained installation method is that accessing the logger equipment for wiring or troubleshooting becomes significantly harder as all work has to be done in a cramped overhead space (Figure 8.91). To put things in perspective, there are roughly 75 sensors installed, each of which have at least five wires, amounting to more than 350 wire connections to be made on an overhead terminal while balancing on riprap in a cramped space in late-July heat. Given the volume of the work, it took nearly two weeks to route the cables on the abutment caps and connect them to the pre-assigned terminals on the data loggers and multiplexers.

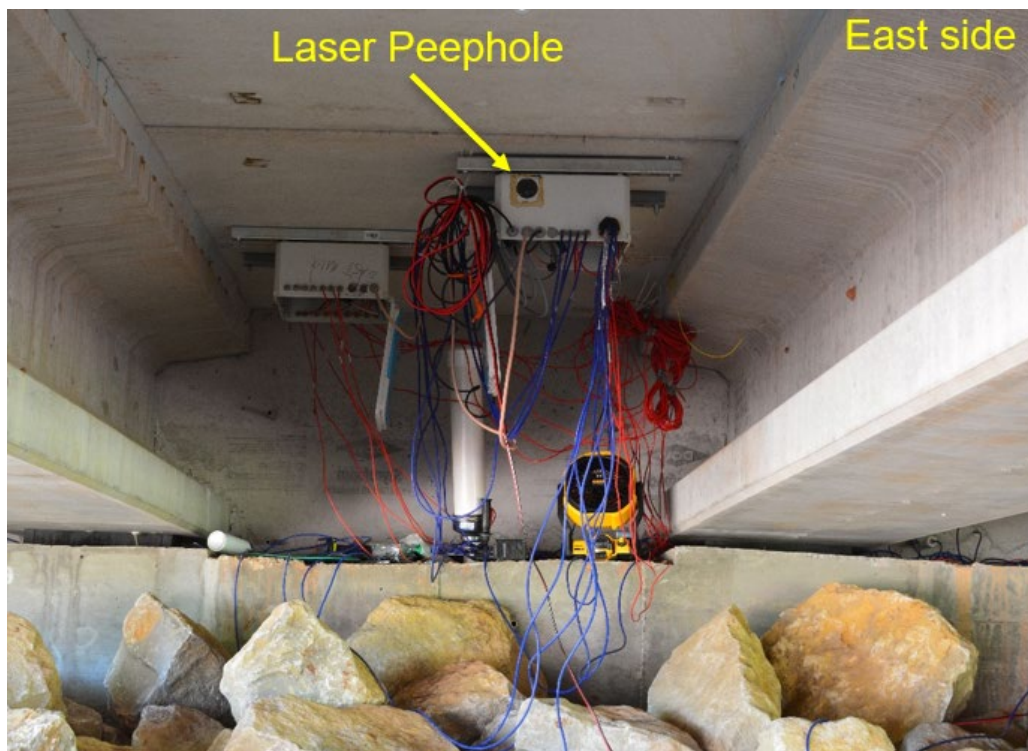


Figure 8.91: Wiring of the east side data logger station, equipped with a laser distance meter (fun fact: the battery-operated fan pictured was our best defense against the late-July heat and creekside mosquito swarm while wiring the loggers)

In October 2020, a trip was made to the bridge site. The purpose of this trip was to troubleshoot remote connectivity issues, replace a faulty multiplexer and to collect soil samples collected by

Terracon for subsequent characterization at the University of Texas at Austin. During this trip, it was discovered that rodents were attempting to build nests on top of the abutment cap in the space between backwall and bearing pads under the girders. These rats also appear to have been very attracted to the sensor cables being routed on top of the abutment caps and had managed to extensively damage some of these cables by chewing them. As a result, several cables had lost connectivity and one had completely disappeared! The disconnected cables were spliced quickly and reconnected to the data loggers. After the discovery of rodents under the bridge, it was decided to protect the cables by adding flexible PVC conduits around the cables as an added layer of protection. Since the wires were already attached to the data loggers, the PVC conduit was cut open lengthwise using a utility knife and fitted around the cables. This action was taken as our best chance to at least temporarily keep the rodents away from the cables until a more permanent solution can be found and applied in a subsequent visit.



Figure 8.92: PVC pipes to protect cables routed on top of abutment caps

After talking with other professionals experienced with outdoor wiring, it was decided to use a harder material to protect the cables from rodents as there has been instances of rodents chewing through flexible conduits and even aluminum. For this purpose, Sch. 40 1.5-in PVC pipes were cut in half lengthwise using a bandsaw and carried to the bridge site. The two halves of the PVC pipe were then placed around the cables and clamped together using hose clamps (Figure 8.92). The majority of the cables were covered using this method, except at the locations of cable entry or behind the bearing pads, which were protected through the addition of a thick layer of expandable foam.

8.3. Analysis of the Performance of China Creek Bridge

8.3.1. Analysis of the Data from the Monitoring System

In this section, the data collected from the instrumentation of China Creek SIAB is presented and analyzed. As explained in the previous sections, the sensors used were embedded in different components of the bridge throughout the construction progress from March to July 2020. After construction was completed, the logger equipment was brought to the field and mounted under the bridge. Due to the amount of time required for wiring the data loggers (more than 350 wires) and several issues encountered in the field, including cell and radio connectivity issues, faulty multiplexer replacement and rodent problems, official data collection began in October 2020. However, in anticipation of delayed data collection, zero readings of all sensors were recorded prior to and right after installation of each sensor and will be used to estimate changes in sensor readings during the initial 2.5 months of bridge operation.

A comprehensive Python program has been developed to aid in post-processing of data gathered from 70+ sensors installed on the bridge. This program allows for automatic collection of the raw data, conversion to physical measurements (e.g. transducer frequency measurement to micro-strains), filtering bad measurements and creating an interactive dashboard for plotting and interactive filtering of data. While majority of the work on this program is done and the program's main components have been tested separately multiple times, more work still needs to be done to fully integrate this program into the work flow of analyzing the data coming from China Creek Bridge.

While there were significant concerns regarding the operation of sensors and data loggers during the record freezing temperatures and snow fall caused by winter storm Uri in the second week of February 2021, all equipment remained fully operational during this period and recorded very valuable data from these extreme weather conditions. During this period, the oversized solar panels still managed to charge the batteries (though at a lower rate), the batteries remained operational despite the extreme below freezing temperatures and no electronics appear to have been damaged.

The data collected from the laser distance meter in fall 2020 is presented in Figure 8.93. As recorded by early laser distance meter measurements, China Creek Bridge was thought to have undergone length changes of up to 1.75 inches per day during fall 2020. This magnitude of movement was much larger than expected when compared with Mack Creek data and was a cause for concern based on the experimental behavior observed in large scale laboratory experiments conducted earlier during this project. However, with collection of more data from the laser distance meter as well as the concrete-embedded strain gauges, it is believed that there are issues with the laser distancemeter data and large parts of the data gathered through this sensor cannot be trusted without secondary verification. To verify the results, a separate variable

based on the measurements coming from all concrete-embedded strain gauges in the bridge deck was created. To keep the level of noise under control, median of all of these measurements was taken as the average longitudinal strain of the bridge deck. This data is plotted side by side with the laser distancemeter data in Figure 8.94. As can be seen the data from the strain gauges follows the same trends as laser distancemeter but does not produce the same large magnitudes of deck length change in occasions where it occurs in the laser distancemeter data. Moreover, the strain gauge data is consistent with experimental values of the coefficient of thermal expansion for concrete. The deck length change data calculated based on strain gauge data is presented in Figure 8.95.

The deck length change data gathered so far shows daily length change cycles of about 0.1 inches, while the total length of the bridge changed approximately 0.55 inches within the monitoring period. Had the winter storm not occurred this year, we would have expected to see only about half this total length change during this monitoring period.

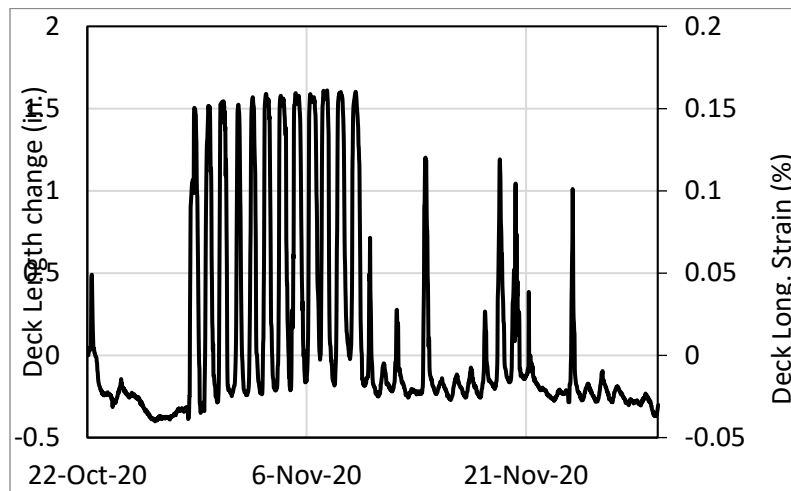


Figure 8.93: Deck length change measured by laser distance meter

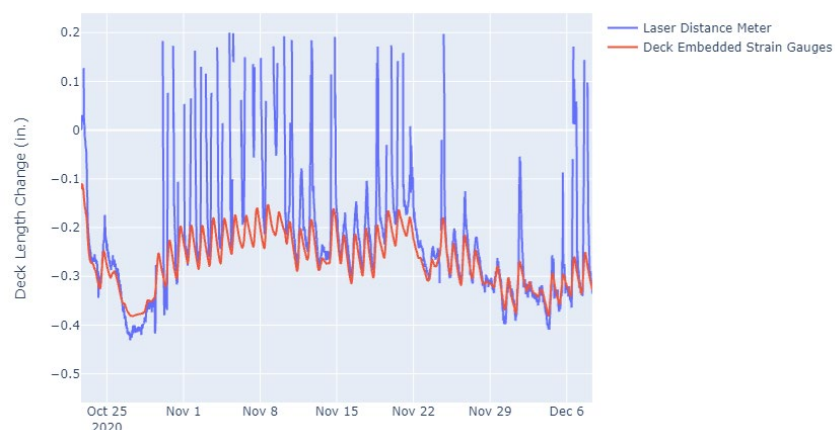


Figure 8.94: Comparison of laser distance meter and deck strain gauges for measuring deck length change

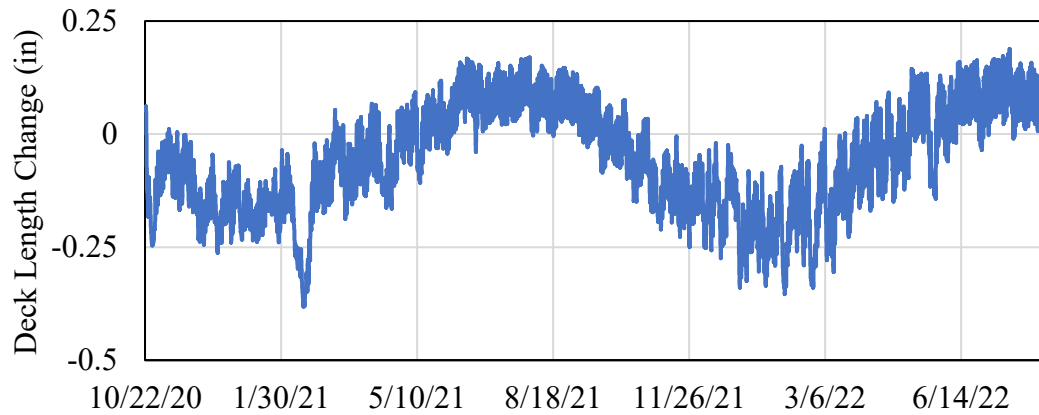
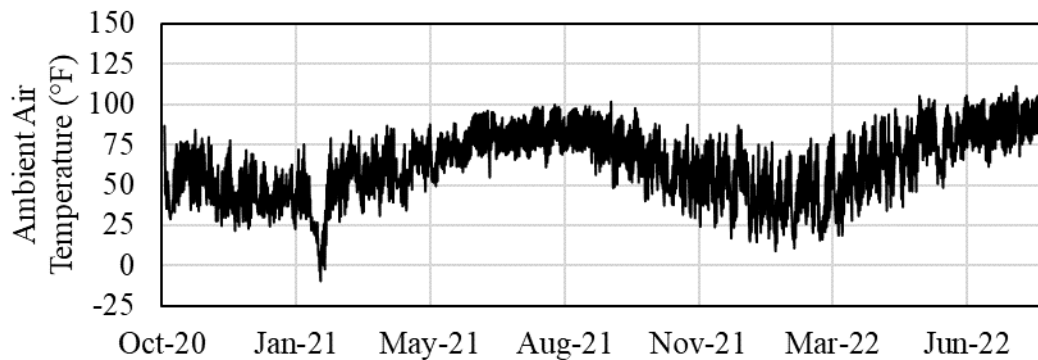
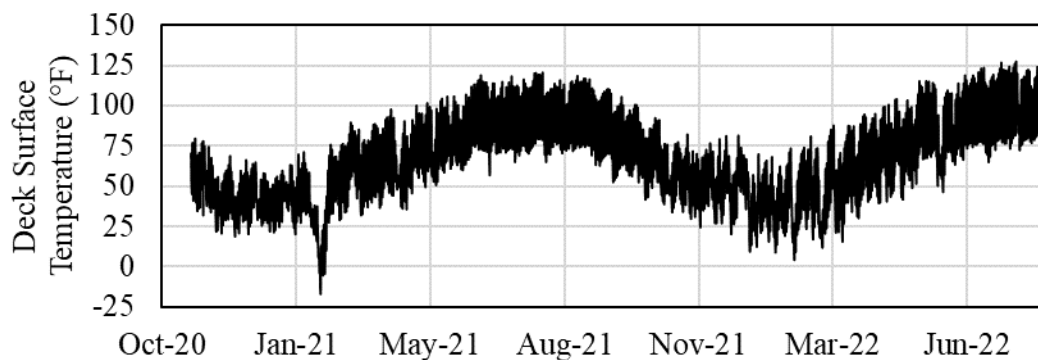


Figure 8.95: Deck length change calculated using embedded strain gauge data

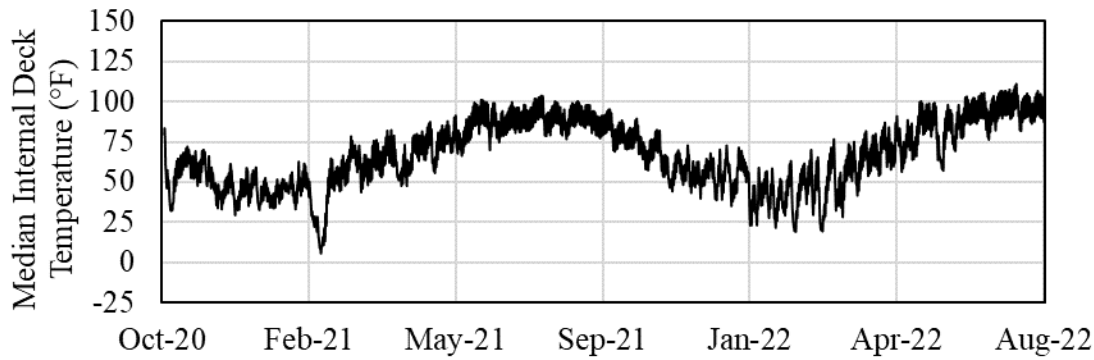
The ambient air temperature data from the bridge is presented in Figure 8.96. As can be seen, deck surface and average deck temperature have generally been slightly colder than the ambient air temperature during the fall and winter monitoring period.



(a)



(b)



(c)

Figure 8.96: Temperature data collected from China Creek SIAB (missing deck surface temperature data is due to rodent activity)

The average deck temperature as measured by embedded strain gauge thermistors appears to undergo smaller magnitudes of daily fluctuations when compared with deck surface and ambient air temperature records. This is completely reasonable and is due to slower transmission of heat within concrete and the larger specific heat of concrete compared to air. As evident by the data, the concrete mass temperature fluctuates by about 15-20 °F on a typical fall and winter day at this location. Regarding the measurements made during the second week of February, it is likely that the measured deck surface temperatures are from the surface of snow, not concrete and the entire deck must have had a uniform temperature close to ambient air temperature as evident by the weather station and strain gauge thermistor measurements; the long week of cloud-covered skies and snow-covered surfaces must have contributed to this temperature distribution. In the warm seasons, the daily change in deck surface temperature and median internal deck temperature appears to be considerably larger than the colder months. This explains why there is larger daily deck length changes occurring in the warmer months. However, it is still interesting to note that unlike the considerably larger magnitude changes observed in daily ambient air and deck surface temperature records, the magnitude of temperature within the concrete mass is much smaller and not much higher than the colder months, resulting in only slightly larger daily deck length change magnitudes in the warmer months.

With the exceptionally warm summer of 2022, it can be seen that the deck surface temperature has reached 125°F on several dates and the median internal deck temperature has reached 105°F on several dates. Therefore, the internal deck temperature in summer 2022 was approximately 10°F higher than the preceding year.

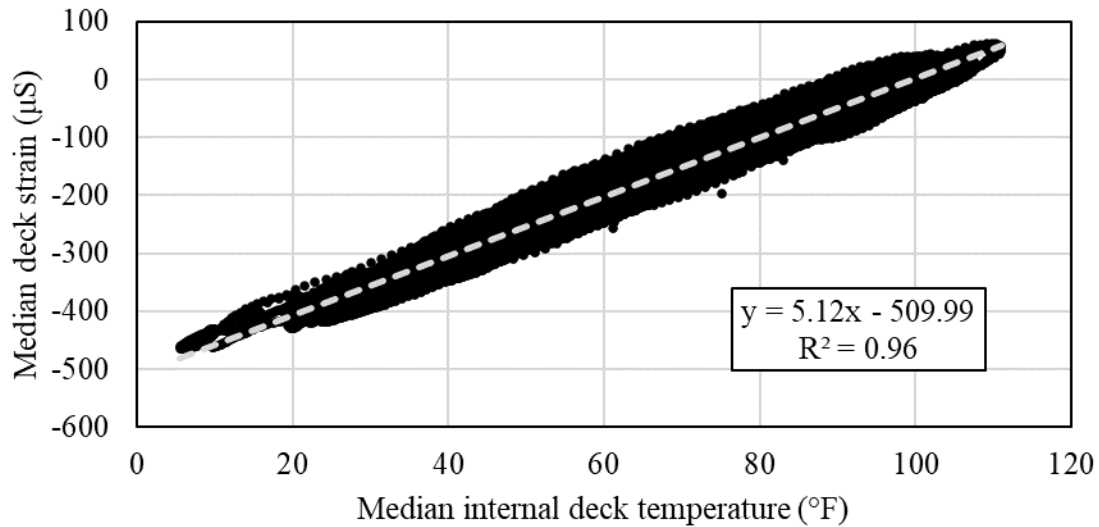


Figure 8.97: Internal deck temperature vs deck strain

To understand the behavior of the bridge due to thermal expansion, the deck length change data is plotted against the internal deck temperature in Figure 8.97. The highly linear distribution of data in this plot ($R^2 = 0.96$) is evidence that the bridge has been freely expanding and contracting due to temperature changes during fall and winter. Regression analysis of this data reveals that an average length change of 0.05 inches is expected per 10 °F deck temperature change for this bridge.

To demonstrate the difference between the performance of different temperature records in predicting bridge movements, the ambient air temperature collected from the weather station at the bridge site is plotted against the deck length change data in Figure 8.98. The higher level of scatter in this plot ($R^2 = 0.89$) shows that ambient air temperature data is not as good of an indicator for predicting total bridge length change. While the level of error in estimating displacements given ambient air temperature records may seem low (e.g., 0.15 inches at 50 °F), this is a relatively short single-span bridge and the level of error is expected to be several times higher for a multiple span bridge, resulting in miscalculations for expansion joint demands.

Similar trends can be observed from other temperature records collected from other temperature sensors such as those of data logger panels and deck surface temperatures. Therefore, for high precision prediction of expansion joint demands for bridges in a given geographical location, it is necessary to create a model that can predict temperatures within the deck profile using available climate records and theoretical heat flow solutions.

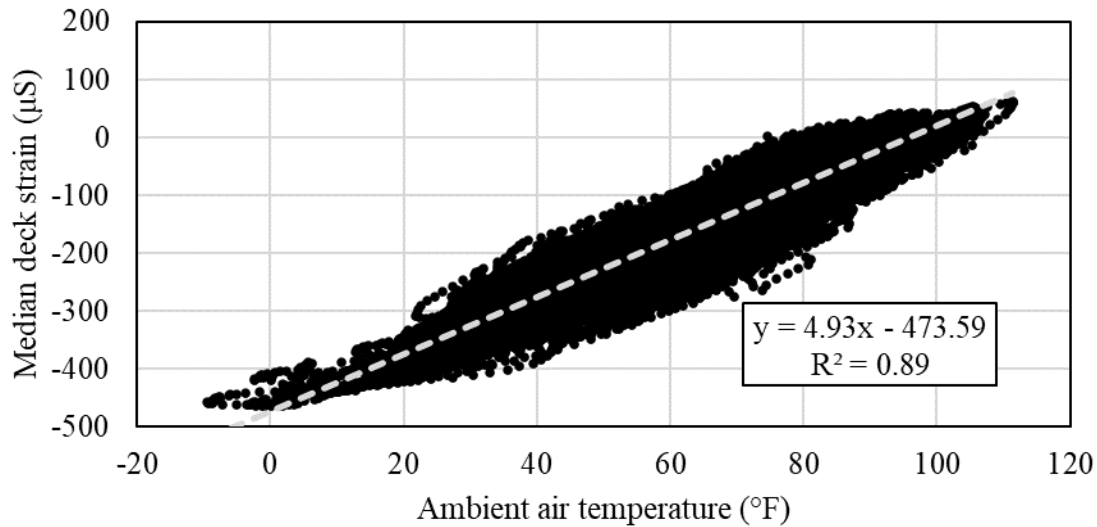


Figure 8.98: Ambient air temperature vs deck strain

As mentioned in previous subsections, several crackmeters were installed on China Creek Bridge to measure relative displacement between various components of the bridge.

As an important component of this monitoring program, the expansion joints placed at the ends of the approach slabs were fitted with crackmeters. The data from these sensors is plotted in Figure 8.99. As can be seen, the response of the two expansion joints to thermal expansion/contraction of the bridge has not been equal, with the larger displacements occurring on the west side of bridge. The collected data shows negligible levels of displacement in the east side up until February 2021 (Winter storm Uri). However, after the winter storm, similar levels of movements are observed on both sides of the bridge.

The crackmeter data collected so far shows that the expansion joints must be able to maintain their integrity under daily cyclic movements of 0.05 inches and overall expansion/contraction of up to 0.5 inches to avoid damage to the joint, roadway and structure. Interestingly, several sudden jumps in the data collected from the east abutment expansion joints can be seen. It is possible that some type of slippage is occurring within the displacement transducer components that has resulted in these readings. Overall, both crackmeters indicate that the expansion joints get stretched by approximately 0.2 inches over the fall and winter due to contraction of the bridge and they do not appear to compress within the summer months. This shows that the preformed material used in the expansion joints is too stiff to compress during the expansion of the bridge and as a result the approach slabs must have been moving in response to the bridge expansion over the spring and summer months.

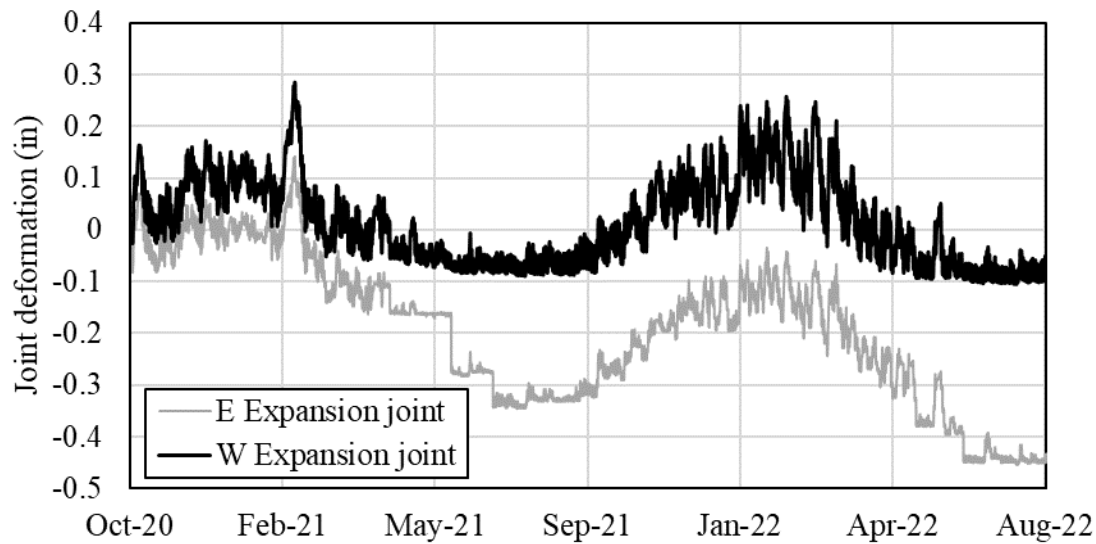


Figure 8.99: Joint movement as recorded by crackmeters installed between approach slab and sleeper slab

The data from the crackmeters installed between abutment caps and backwalls is presented in Figure 8.100. It is evident by the east abutment data that until February 2021, there has been virtually no movement between east abutment wall and east abutment cap and majority of the movement has occurred on the west abutment. However, with rising temperatures in March, we are starting to see the gap size between abutment caps and backwalls increasing in both abutments. The data collected from the warmer season shows that after the extremely cold days of February 2021, the gap between abutment cap and abutment wall on both sides appears to be deforming at a similar rate. This suggests that there is nearly equal backfill resistance on both sides after the winter storm leading to a more symmetrical expansion behavior. One possible explanation for this is that the bridge could have contracted enough in February 2021 to let both abutment backfills experience active condition, leading to loss of compaction and lower resistance in the east backfill compared to before the winter storm.

As shown in Figure 8.101, the total of these two crackmeter readings is not equivalent to the total change in deck length change. The difference from the two parameters serves as a sign for lateral deformation of abutment caps under thermal contraction and shrinkage of the deck. While this data cannot indicate how much each abutment cap has moved at a given time, it can tell us that in total there is nearly 0.2 inches of displacement between the two abutment caps in the colder months and 0 to 0.1 inches in the summer. This data clearly shows that the foundation of the bridge experienced daily lateral loading cycles that were stronger during the colder months. The shape array data would show a clear picture of how lateral movements occur in the drilled shafts and abutment caps.

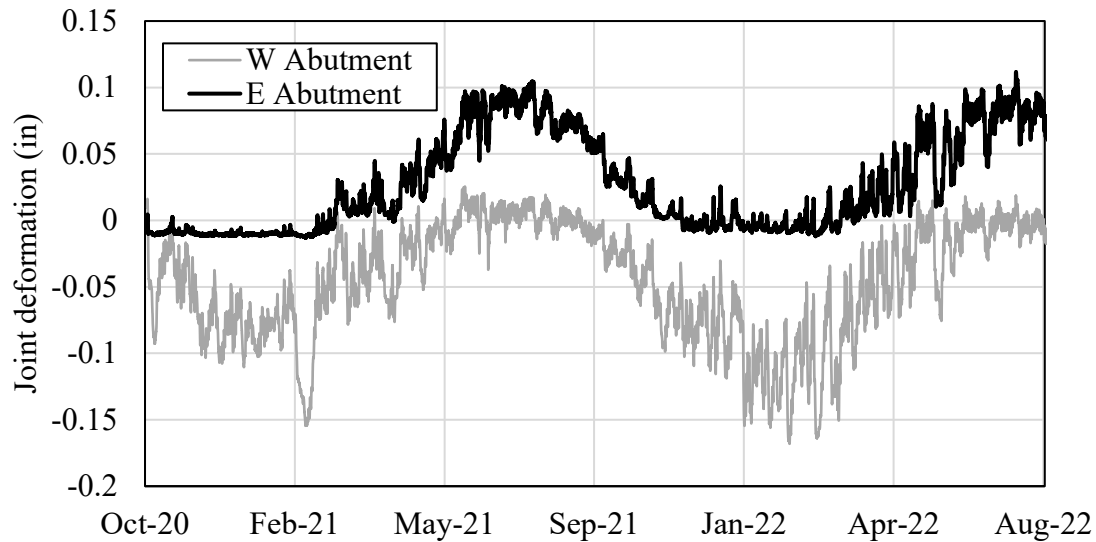


Figure 8.100: Relative displacement between abutment caps and backwalls

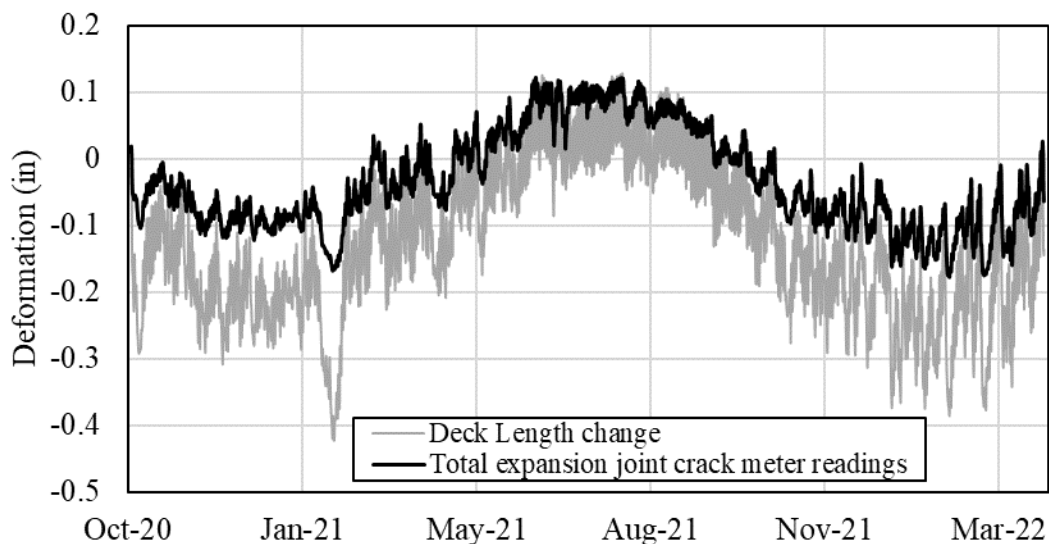


Figure 8.101: Total cap/backwall crackmeter readings vs total deck length change

A pair of crackmeters was also installed to monitor displacements in the wingwall due to backfill pressure changes. The data from these two crackmeters is shown in Figure 8.102. Overall, it appears that very small magnitude displacements occur at the wingwall due to changes in backfill pressure. While the displacement magnitudes are quite small at this point, we can clearly see larger magnitude displacements occurring over the summer (higher lateral earth pressure) compared to the winter.

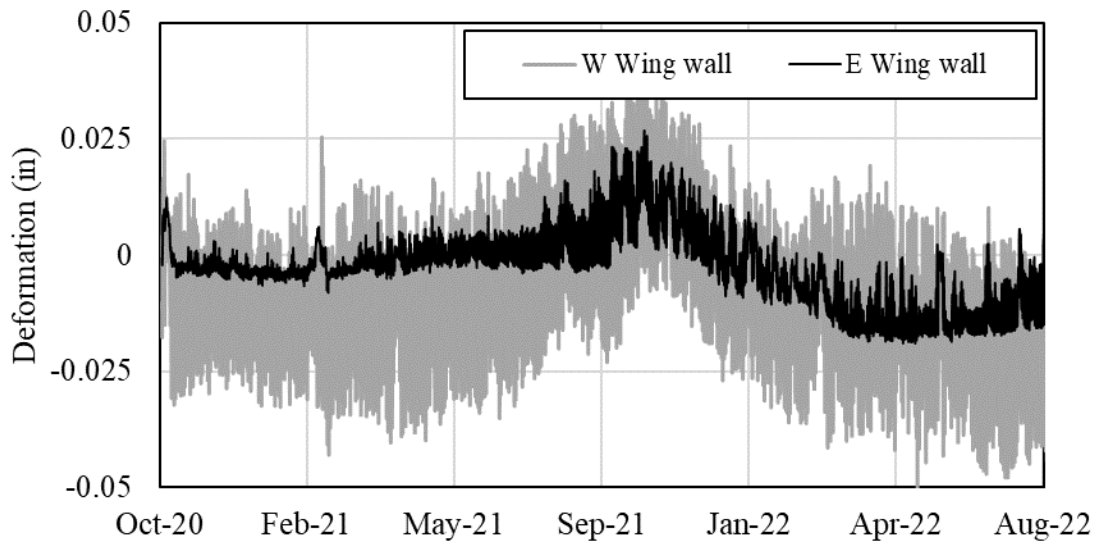


Figure 8.102: Relative displacement between top of wingwall and approach slab

The data from the settlement sensors installed during Phase 2 of the construction in the east abutment backfill is presented in Figure 8.103. It can be seen that more than 1 inch of settlement is registered by both sensors since the time of installation and settlement appears to be increasing steadily over time. It is interesting to note that a small portion of the settlement recorded by the sensor installed closer to the abutment wall (sensor 2) is “recovered” during the periods of temperature increase (bridge expansion). Backfill heaving was observed during the large-scale laboratory experiments as well. Another interesting observation is that the rate of settlement appears to be affected by the season, with a higher settlement rate experienced over the colder months compared to the warmer months.

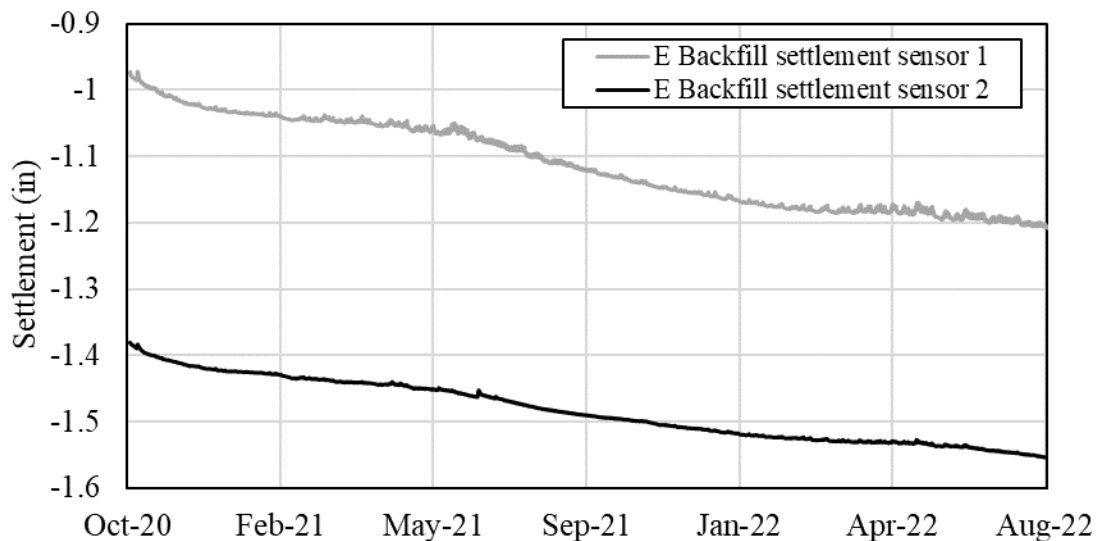


Figure 8.103: East abutment backfill settlement

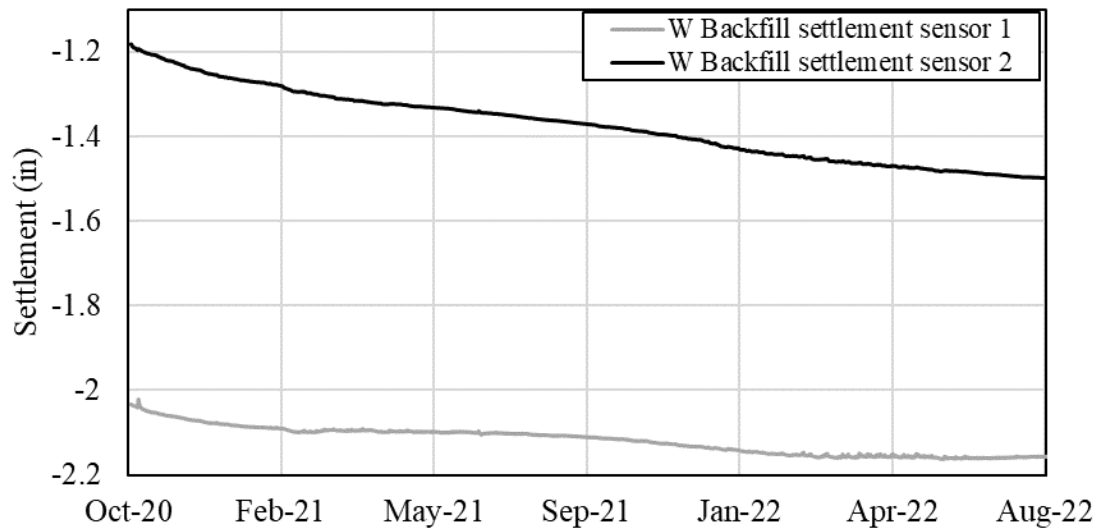


Figure 8.104: West abutment backfill settlement

The backfill settlement data from the west abutment is presented in Figure 8.104. Sensor 1 is placed closer to the abutment wall while sensor 2 is placed farther back. As can be seen, a larger magnitude of settlement is recorded for the west abutment as compared with the east abutment (almost double). This result is expected considering the larger magnitude of movements occurring on the west side of the bridge as recorded by the crackmeters.

Considering the data obtained from all four settlement sensors in the backfill, at least the backfill within the flat portion of the excavation area is providing no support to the approach slab. Based on the available data, it is recommended that approach slabs for SIAB with granular backfill be constructed considering the development of such large voids underneath, so they do not get severely damaged due to the lack of vertical support. Given these results, it was decided to search for methods that could help determine the unsupported length of the slabs. Ground Penetrating Radar (GPR) was chosen as a viable option for this problem. The proposed solution was put to test in a site visit conducted in summer 2021. The results and description of the GPR survey are presented in Section 8.3.2 of this chapter.

The data coming from the pair of strain gauges installed at each end of the approach slabs also shows signs of tension developing in the slabs when comparing the average strains at each end of the slabs. This data for both slabs is plotted in Figure 8.105. At this stage, it is hard to draw conclusions regarding this data for design purposes, especially as the magnitude of these strains do not seem to be very concerning for design purposes. It is most likely that the installation of polyethylene sheets as bond breakers during the construction of the slabs has served the structure well by preventing the formation of cemented bonds and keeping friction at a minimum.

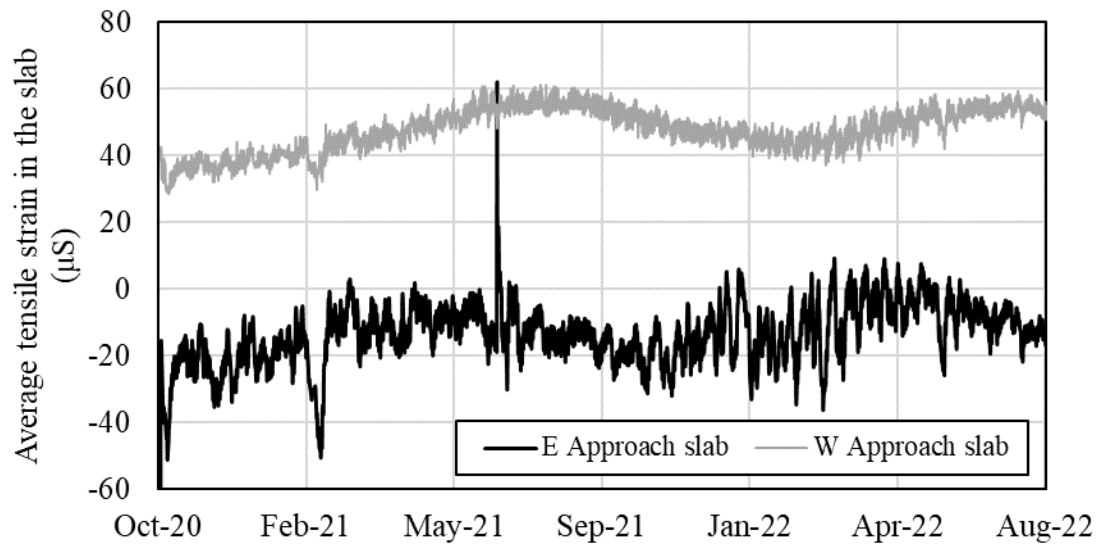


Figure 8.105: Difference between average strains recorded at opposite ends of each approach slab

As mentioned earlier, each abutment is fitted with several earth pressure cells to record earth pressure distribution and how it changes against the abutment wall, wingwalls and abutment caps. The data from the pressure cells are presented in Figure 8.106 and Figure 8.107. The plotted data has undergone a secondary correction to compensate for the effect of concrete embedment and the interactions due to unequal thermal expansion/contraction of the earth pressure cell and its surrounding concrete. The calibration factor for this process was calculated using the records collected during the February 2021 winter storm with the assumption that during this period, each earth pressure cell has experience active earth pressure levels.

Expectedly, the largest earth pressures are observed during the warm season. However, lateral earth pressure does not appear to increase with depth as the highest earth pressures are recorded by the top and bottom earth pressure cells. The wingwall EPC and abutment cap EPC also indicated pressure increases due to thermal expansion of the bridge in the summer, resulting in their displacements.

Overall, the earth pressure levels appear to have increased by nearly 50 psi in summer 2022 compared to the preceding summer. This pressure increase is recorded by all installed EPCs and is a product of ratcheting in the abutment backfills. It will be interesting to see how this behavior evolved in the long-term and if any ratcheting occurs, as was observed in Mack Creek Bridge.

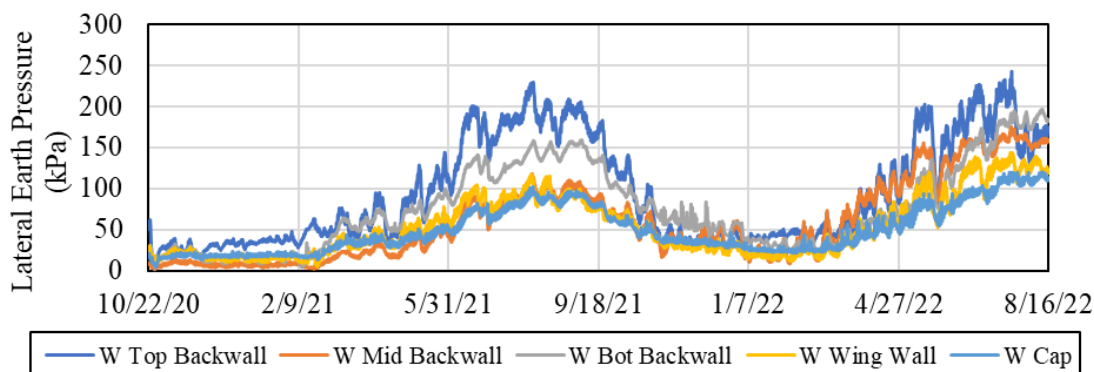


Figure 8.106: West abutment earth pressure cell measurements

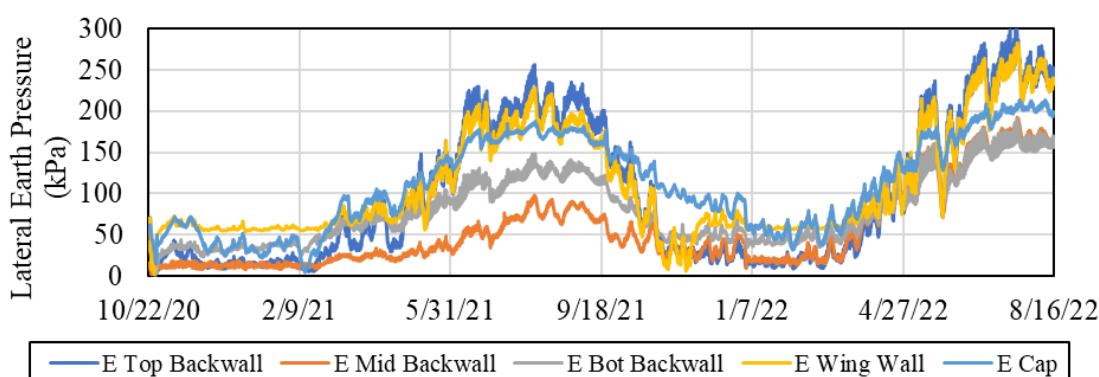


Figure 8.107: East abutment earth pressure cell measurements (note: 1 kPa = 0.000145038 psi)

Due to observation of several flood events before and during the construction of China Creek Bridge, it was decided to install a set of piezometers, one on the abutment cap to measure creek level rises and one in the backwall to measure pore pressures in the backfill. The data collected so far is shown in Figure 8.108. The cap piezometer data indicates that there has been several flood events over the monitoring period. However, it would be hard to estimate the flood level based on the piezometer readings alone as we have no measure of the flow velocity in the creek. It is also possible that the large readings by the cap piezometer are not accurate because they indicate either an extremely high flood depth or a very high velocity of flow and in addition there are no similar readings made by the east abutment piezometer.

Fortunately, no damage to the data logging equipment occurred. Currently, there appears to be a spike in the east approach slab tensile strain data (Figure 8.105) at the same time that this flood event has occurred. However, this is not considered a concerning event given the relatively low magnitude of these strains in general. The large spike observed in the west abutment cap piezometer data is considered a measurement error as it is not corroborated by a similar measurement on the east side piezometer.

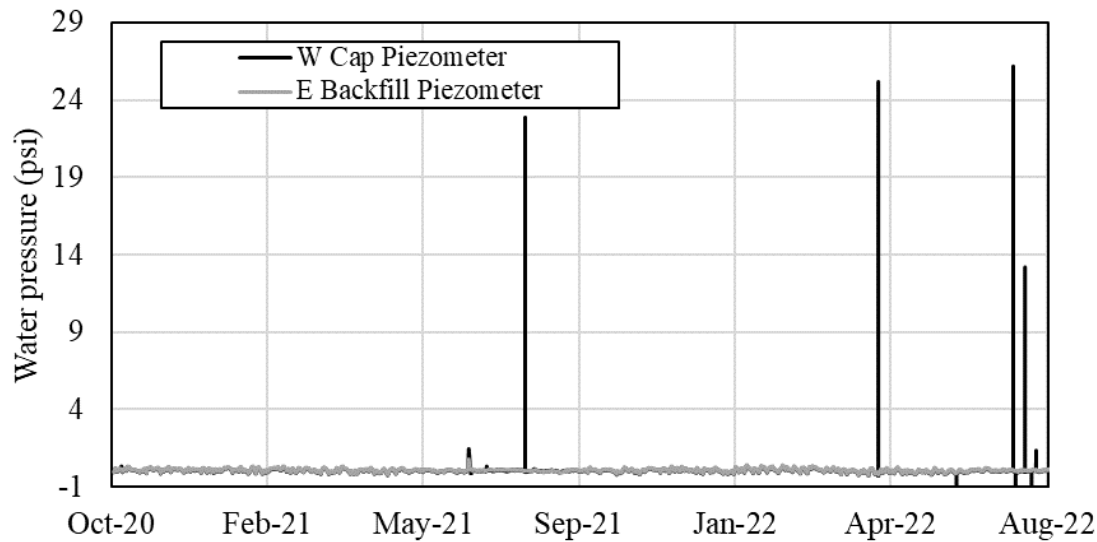


Figure 8.108: Piezometer readings

To better understand the interaction between abutment wall and backfill, a tiltmeter was installed on each abutment wall to capture any rotational movement/bending occurring in the abutment walls. This data is plotted in Figure 8.109. As can be seen, the magnitude of tilt in the east abutment backwall is relatively smaller in the east abutment, compared to the west abutment. This is likely due to smaller magnitude displacements in the east direction and slightly smaller earth pressures developed within the east abutment backfill. The west abutment wall however has experienced tilts up to 0.4 degrees due to thermal expansion/contraction of the bridge.

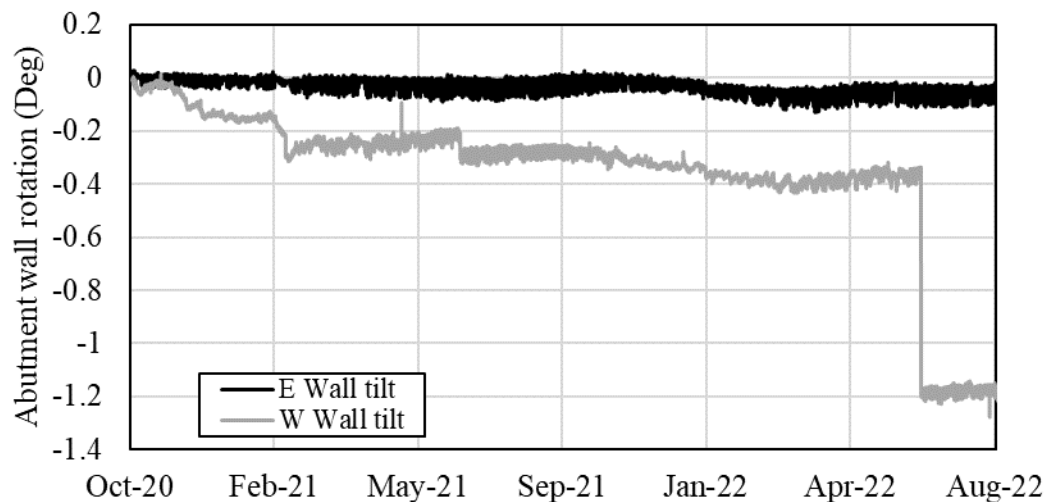


Figure 8.109: Abutment wall tiltmeter readings (+ denotes tilt toward creek)

To verify whether the change in tilt of the west abutment wall is due to development of curvature in the deck, and to understand whether the existing thermal gradients in the deck lead to curvature, Figure 8.110 was developed. A linear regression line fit for each curve reveals a slope

of 1.0 and a coefficient of determination of +0.99. This data shows that the thermal gradient and/or interaction with abutment backfill has not led to changes in curvature of the deck elements so far and the rotation of the west abutment is likely due to interaction with the abutment cap and backfill alone. Had any curvature in the deck occurred, the data should have shown a non-linear scatter with a slope other than 1.

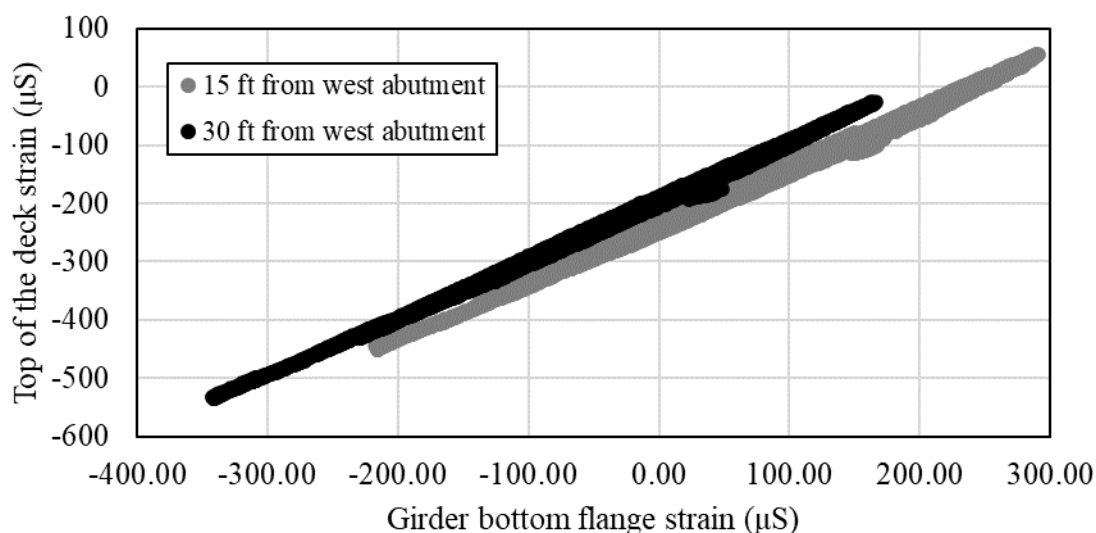


Figure 8.110: Scatter plot of strains at the top of the deck vs strains at the bottom of the girder at 15 and 30 ft from west abutment wall

Based on the data collected from Mack Creek's second set of instrumentation, it was speculated that the foundation in SIAB may be subjected to lateral loading due to effects of concrete shrinkage as well as thermal strains. As a result, a drilled shaft on each end of the bridge was instrumented using a shape array to continuously capture deformations in the drilled shafts. This data is presented in Figure 8.111. Positive deformation in both cases is deformation toward the center of the deck (creek). Therefore, it can be seen that due to contraction (bridge was completed in summer), as well as concrete shrinkage strains, both drilled shafts are being pushed toward the creek through the interaction between abutment wall and abutment cap. And the magnitude of this movement seems to be slightly higher in the west abutment as shown in Figure 8.112. As expected, the largest magnitude of this movement belongs to the time of the winter storm Uri where the east and west drilled shafts have experienced 0.1 and 0.15 inches of deformation respectively at peak deformation. These numbers are calculated in reference to the beginning of the monitoring period and the total deformation since construction is expected to be higher.

The data plotted in Figure 8.112 shows the general deformation trends at the top of the drilled shaft/bottom of the abutment cap as well as smaller daily fluctuations. The magnitude of daily fluctuations appear to be very small and typically in the order of 0.01 inches. While these values appear to be very small, a fatigue analysis can help determine if these levels of deformation for

the drilled shaft are capable of causing any substantial damage during the lifetime of the structure.

On another note, the data plotted in Figure 8.112 shows that while the east drill shaft moved back to zero displacement, the west abutment drilled shaft did not and 0.07 inches of seemingly permanent deformation were accumulated over this monitoring period. Similar behavior has also been observed in the Mack Creek Bridge where it appears that the gap between the abutment wall and abutment cap must have been filled with debris, leading to permanent deformations. It would be interesting to see how this trend continues over the course of this monitoring program.

By comparing the 2022 shape array data with the preceding year we can see that the the both drilled shafts have experienced a slight shift toward the east direction. As a result, the west abutment cap has moved by 0.03 inches toward east and the east abutment cap has moved by 0.02 inches toward east. Based on the collected data, this shift appears to be occurring over the spring and summer months. At this point it is not clear what is the true cause of this behavior. Moreover, it would be interesting to see if this behavior continues in the coming years as well, as more data is being collected.

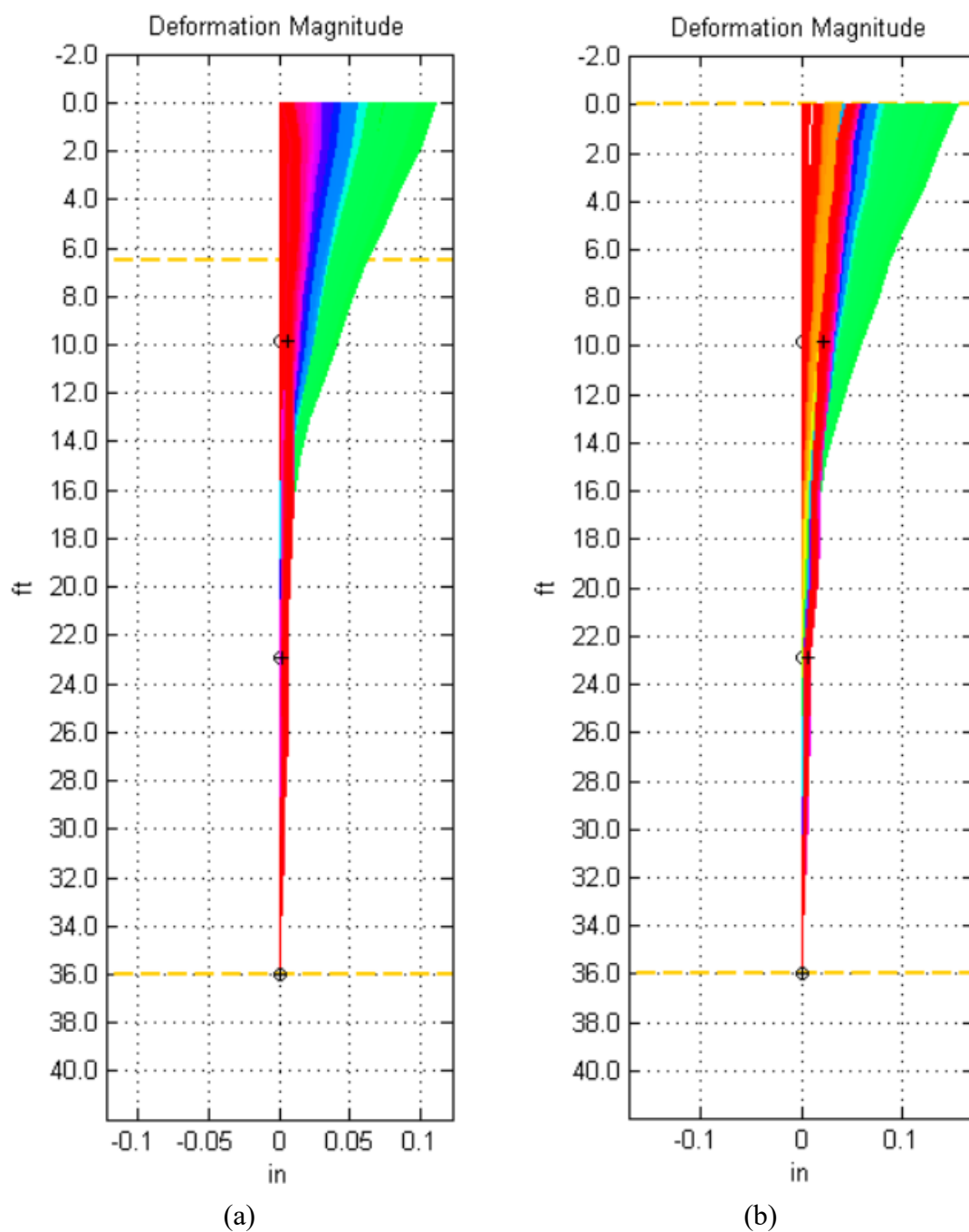


Figure 8.111: Deformation profile snapshots of drilled shafts: (a) east abutment; and (b) west abutment (positive deformation is toward center of bridge/creek)

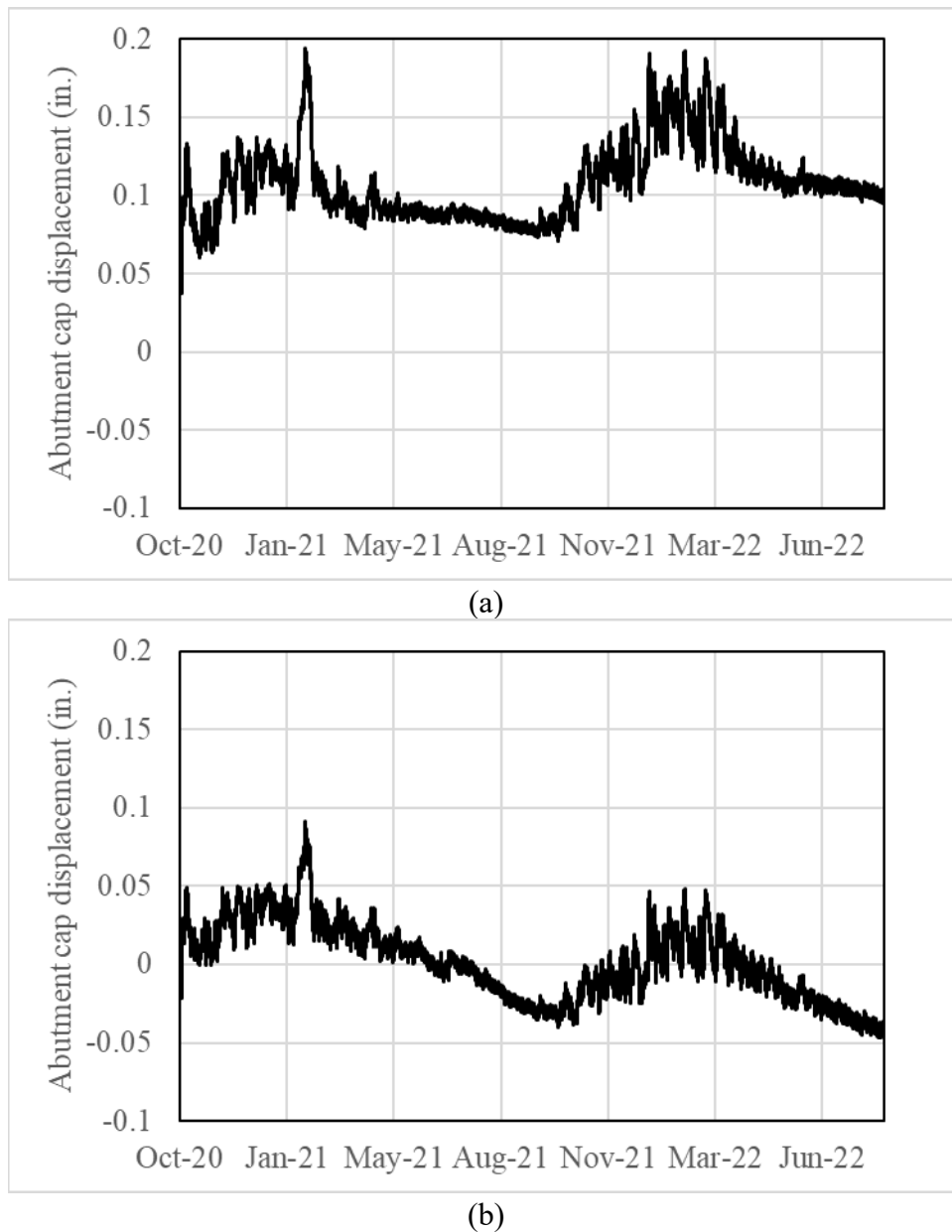


Figure 8.112: Abutment cap displacement records: (a) east abutment; and (b) west abutment

To better understand the significance of the drilled shaft deformation due to thermal expansion/contraction of the bridge deck, a program is being developed to estimate bending moments acting on the drilled shafts due to interaction with the superstructure.

A sample deflection profile of the instrumented west abutment drilled shaft is presented in Figure 8.113. As the data indicates, the west abutment cap had moved by 0.12 in toward the center of the bridge at 7:30 pm on December 5, 2020, due to the decrease in temperature from the time of construction (July 2020) to December 2020.

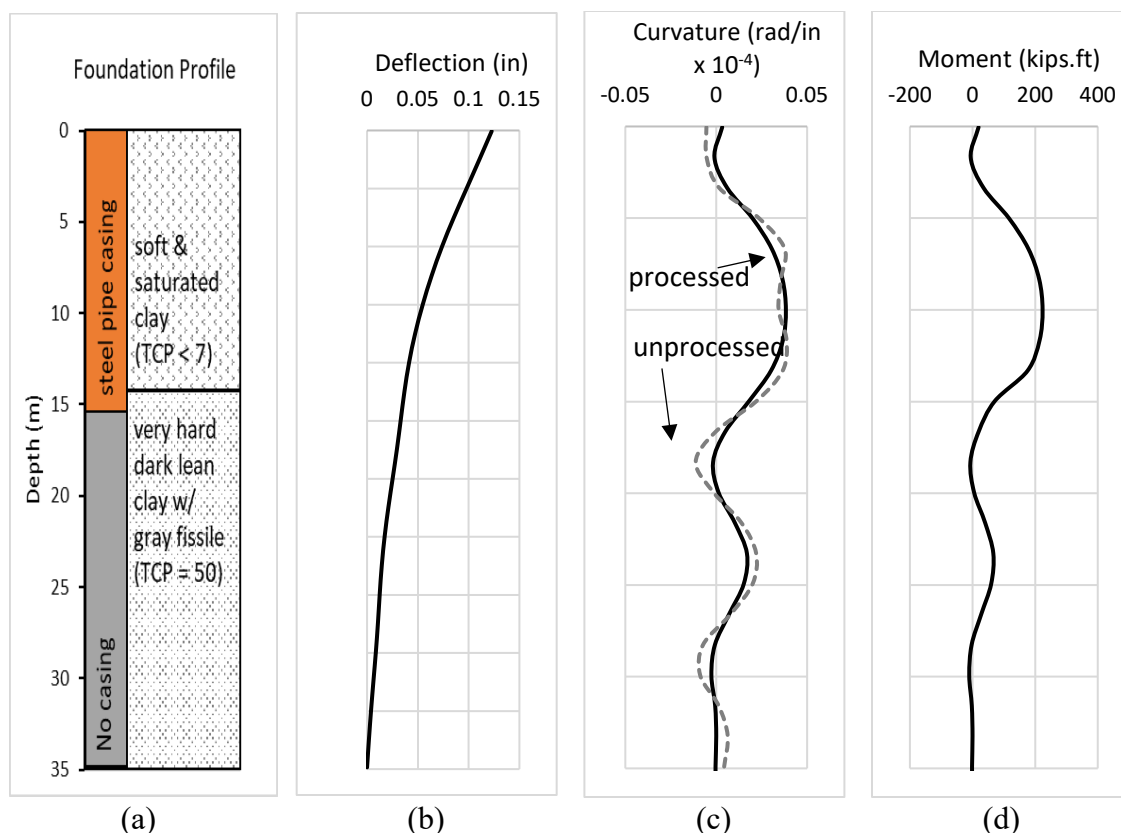


Figure 8.113: West abutment drilled shaft profiles: (a) foundation profile; (b) deflection profile; (c) curvature profile; and (d) moment profile (shape array data captured at 7:30 pm on December 5, 2020)

In addition to the deflection profile of the drilled shafts, it is theoretically possible to calculate other parameters of interest such as the moment profile. For this purpose, the curvature profile of the foundation needs to be calculated. Mathematically, curvature profile can be obtained by taking the second differential of the deflection profile using Equation. 1. In this equation, “y” is the nodal deflection and “h” is the segment length as shown in Figure 8.114.

$$\frac{d^2y}{dx^2} = \frac{y_{m+1} - 2y_m + y_{m-1}}{h^2} \quad (\text{Equation. 1})$$

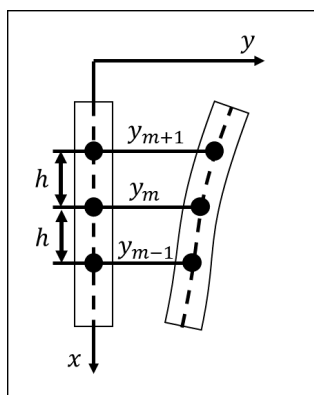


Figure 8.114: Schematic of a deflected drilled shaft

As the shape array only provides discrete displacement measurements at the nodal locations, calculating the second derivative of the unprocessed deflection profile using finite difference method can result in unrealistic spikes in the profiles. As such, the performance of several filters including rolling average, rolling median and Savitzki-Golay on smoothing the data were evaluated. For the early data, processing the deflection data with a moving average filter with a window size of 3 was found to be the most effective method in removing the noise in curvature data. The small window size resulted in minimal alteration of the deflection data while also minimizing noise in the curvature profile. The calculated curvature profile is shown in Figure 8.113(c).

To obtain the moment profile, flexural stiffness properties of the instrumented sections were calculated using the LPILE software (Wang et al., 2022). As previously mentioned, the top 16 ft of the drilled shafts are encased permanently, while the bottom section only consists of reinforced concrete, resulting in a larger flexural rigidity for the top section. As such, the moment profile of the west abutment drilled shaft for the sample data is calculated using the shape array data and flexural stiffness analysis done using LPILE. The resulting profile is shown in Figure 8.113(d). In this instance, it appears that a maximum moment of 225 kips.ft occurred at a depth of 10 ft, within the encased section of the drilled shaft. The moment within the bottom segment of the drilled shaft, which was embedded in the hard and blocky stiff clay, was significantly smaller and reached a maximum of 75 kips.ft. The moments and curvature values experienced at this point were within the elastic range according to the moment-curvature diagram obtained for each section.

The analysis procedure described above can be expanded to evaluate the maximum moment acting on the drilled shafts at any point in time. Additionally, to understand the significance of the lateral loads imposed on the drilled shafts due to thermal expansion/contraction of the bridge, the calculated moment profiles can be compared with the section's cracking moment. This comparison will provide a measure of what level of the section's elastic flexural capacity is reached. The result for the early data collected from the instrumented west abutment drilled shaft are plotted in Figure 8.115. As can be seen, during this period, the abutment cap moved by 0.1 to 0.17 inches toward the center of the bridge, resulting in a maximum bending moment of 150 to 240 kips.ft in the drilled shaft. For reference, the calculated concrete cracking moment for this section is 363 kips.ft, which means that the calculated bending moments are within the elastic range, but they reach values as high as 63% of the cracking moment of the section during this period. This may be a cause for concern as more extreme weather conditions may be experienced in the future, leading to larger bending moments in the section. The maximum moments during this period all occurred within the top (steel-encased) segment of the drilled shaft, which was not a surprising behavior considering the top 16 ft is embedded in a relatively soft saturated layer of clay (compared to the bottom segment, which is embedded in a dry, very stiff layer of clay).

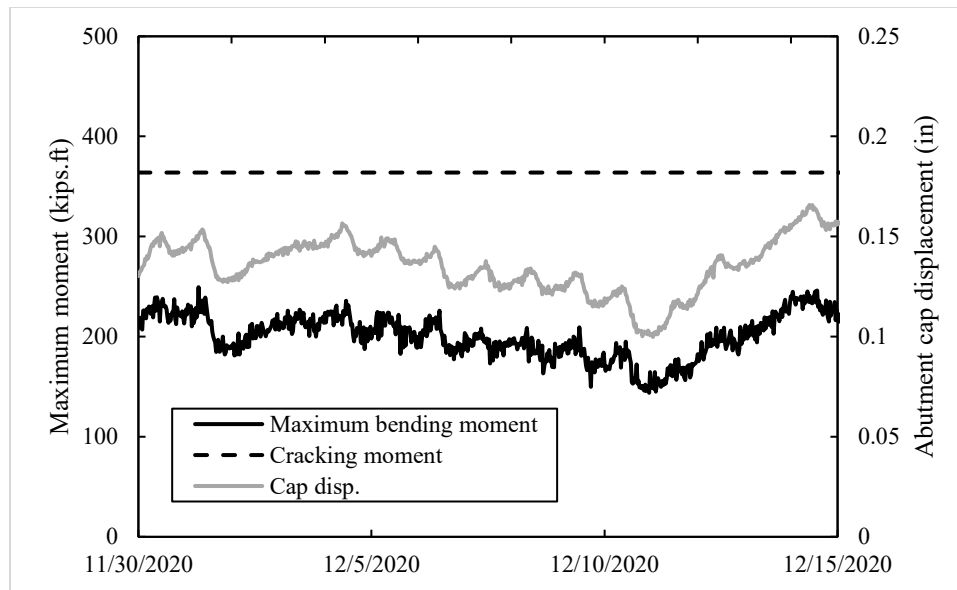


Figure 8.115: Instrumented west drilled shaft's maximum moment and abutment cap displacement data
(Note: positive displacement signifies drilled shafts bending toward center of bridge)

8.3.2. Analysis of the Data from Field Survey Campaigns

While the majority of the data from China Creek is collected remotely through various structural and geotechnical sensors, it is important to also collect field survey data to aid in the interpretation of the sensor data and better judge the performance of the structure.

To save on travel costs, a request was made to the area office regarding occasional visits to the bridge to take pictures of the expansion joints and make notes of any cracks or signs of settlement around the structure.

An area office technician visited the site on February 22, 2021 and looked for signs of damage while taking pictures of the expansion joints at the end of the approach slabs. During this visit, no signs of damage were observed on or around the bridge structure. A main concern at the time was over-extension of the expansion joints on the west end of the bridge due to unusually cold temperatures that were experienced the week before due to winter storm Uri. However, the photos received (Figure 8.116) show no signs of damage to the expansion joints on either end.



Figure 8.116: West approach expansion joint appears to be intact and undamaged (photograph taken by Samuel Groves, TXDOT, on February 22, 2021)

In August 2021, it was decided to visit the China Creek Bridge site to survey the bridge, look for signs of damage and check on the installed sensors after one year of being in service. The visual survey concluded there were no visible signs of damage to any components of the bridge, which was welcome news, especially compared to Mack Creek Bridge, which had developed significant bumps at the ends of the bridge within the first year of operation.

Another activity planned in this visit was to assess the feasibility of using GPR as a non-destructive testing method to survey backfill settlement beneath the approach slabs. For this purpose, 25 individual GPR surveys were conducted in different directions and at different locations around the bridge as shown in Figure 8.117. The main challenge with using GPR is the detrimental effect that conductive objects (such as rebars) have on the quality of the surveys, making it very challenging to detect changes in depth when multiple layers of rebar in different directions are present at the top. Since GPR survey results require extensive post-processing to reveal the desired subsurface information, it was decided to run many different surveys with different settings and decide which settings work best for this site after all surveys were carefully processed and compared with each other to form a basis of future surveys.

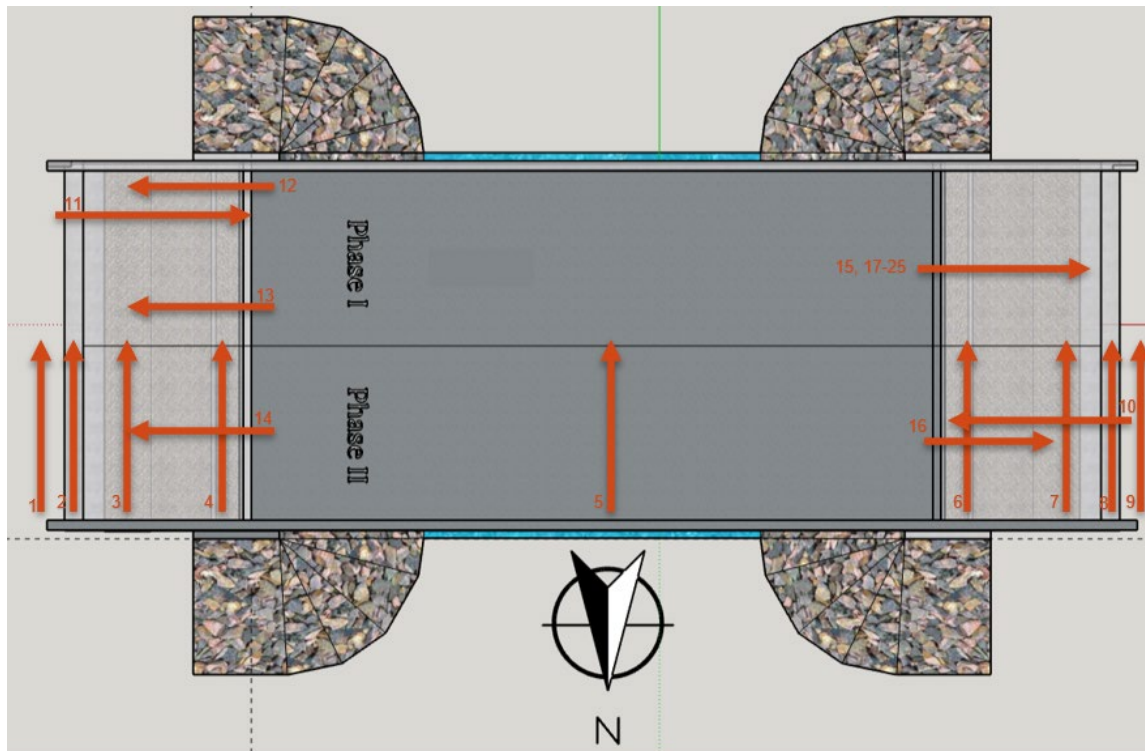


Figure 8.117: China Creek Bridge GPR survey locations (August 2021)

A portion of the raw GPR data from survey #3 (NE Approach slab) is shown in Figure 8.118. As can be seen, the top reinforcement bars make very clear hyperbolic ringing marks on the data and appear to be roughly 12 inches apart in this location, which matches the drawings. Another recognizable artifact is the thin air gap at the very top, between the bottom of the GPR and top of the concrete slab, which is shown by a prominent positive peak followed by a prominent negative peak. These peaks can help identify the surface location in all GPR surveys. There also appears to be a more faded hyperbolic shape below the top level rebars, likely from the bottom rebars. As can be seen, it is much harder to see them because of how the top level rebars tend to absorb the electro-magnetic (EM) waves and limit the visibility of objects below them. Lastly, there appears to be a significant phase change in the signal at about a 15-in depth, which may signify a change in material (concrete to air or concrete to gravel).

Regarding the depth of the artifacts, GPR only measures the travel time of the EM wave that reflects from different depths and converts the travel time to distance by using a parameter called the “dielectric constant.” Dielectric constant is a physical parameter that can be used to estimate the travel speed of EM waves in a material as shown in the following equation:

$$v = \frac{c}{\sqrt{\epsilon_r}}$$

In this equation, c is the speed of light and ϵ_r is the material’s dielectric constant (relative permittivity), which can range from 1 (air) to infinite (metals). It is the contrast between the dielectric constant of adjacent materials that causes changes in the amplitude and phase of the

reflected EM wave at different depths. A list of dielectric constants for materials commonly encountered in construction settings is shown in Table 8.6. It can be generally said that stronger dielectric constant contrasts result in larger amplitude reflected signals and if the deeper material has a lower dielectric contrast, it will be seen as a bright spot (positive peak) and if it has a higher dielectric contrast, it will be seen as a dark spot. Therefore, air voids beneath the slab should be seen as a positive (bright) peak while the top of a rebar should be seen as a negative (dark) peak.

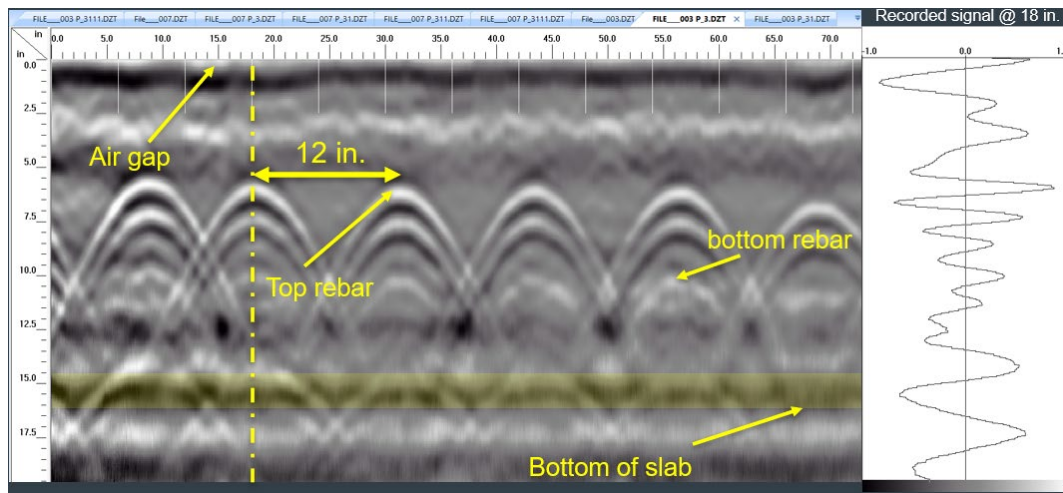


Figure 8.118: Raw GPR data recorded during survey #3 at northeast approach slab, perpendicular to the roadway direction

Table 8.6: Dielectric constant for some materials commonly encountered in construction settings

Material	Dielectric Constant	Material	Dielectric Constant
Air	1	Wet Sandstone	6
Snow Firm	1.5	Wet Granite	6.5
Dry Loamy/Clayey Soils	2.5	Travertine	8
Dry Clay	4	Wet Limestone	8
Dry Sands	4	Wet Basalt	8.5
Ice	4	Tills	11
Coal	4.5	Wet Concrete	12.5
Asphalt	5	Volcanic Ash	13
Dry Granite	5	Wet Sands	15
Frozen Sand & Gravel	5	Wet Sandy Soils	23.5
Dry Concrete	5.5	Dry Bauxite	25
Dry Limestone	5.5	Saturated Sands	25
Dry Sand & Gravel	5.5	Wet Clay	27
Potash Ore	5.5	Peats (saturated)	61.5
Dry Mineral/Sandy Soils	6	Organic Soils (saturated)	64
Dry Salt	6	Sea Water	81
Frozen Soil/Permafrost	6	Water	81
Syenite Porphyry	6		

Overall, it can be seen that it can be relatively challenging to obtain subsurface information using GPR when multiple layers of reinforcement bars are present, the true dielectric constant of the

material is not known and this constant is spatially variable due to heterogeneity of concrete, presence of rebars, air voids and gravel at the same place. However, there are several post-processing tools developed to specifically deal with these issues and present a clearer picture of the subsurface than what is seen in Figure 8.118.

The first step in correcting raw GPR data is called Time Zero Adjustment. In this step, a vertical shift in data is applied so that the start of the displayed data is the pavement surface. This step is done manually by picking the first negative peak in the data (increase in dielectric constant for moving from air to concrete). The result of this adjustment is shown in Figure 8.119.

The next step is called migration analysis, which is considered an essential processing step for surveys that include conductive materials such as rebars, metallic pipes, etc. As shown in Figure 8.118, these objects tend to produce a hyperbolic ringing noise in the data that obscures many other details in the profile. Since the shape of this hyperbola is dictated by the dielectric constant of the surrounding medium, one can use these artifacts to estimate the dielectric constant of the surrounding medium and also remove most of this noise from the data. The processing software used for this purposes, requires the user to fit a “ghost” hyperbola on top of the data to help the software in identifying these artifacts. Once this “ghost” hyperbola is fitted, a much cleared image of the subsurface is obtained, as shown in Figure 8.120.

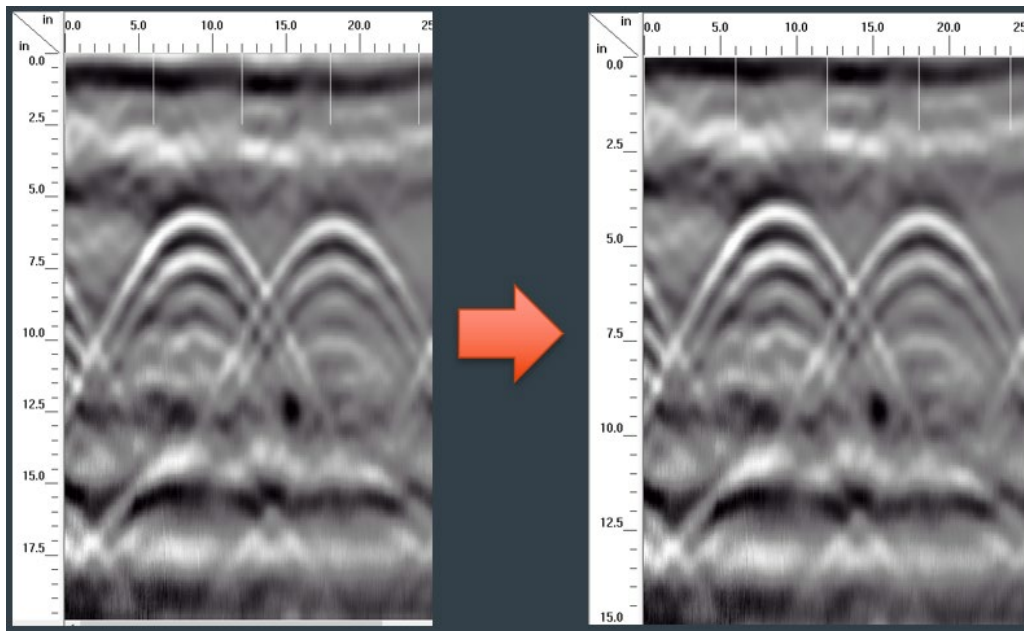


Figure 8.119: Application of Time Zero Adjustment to raw GPR data

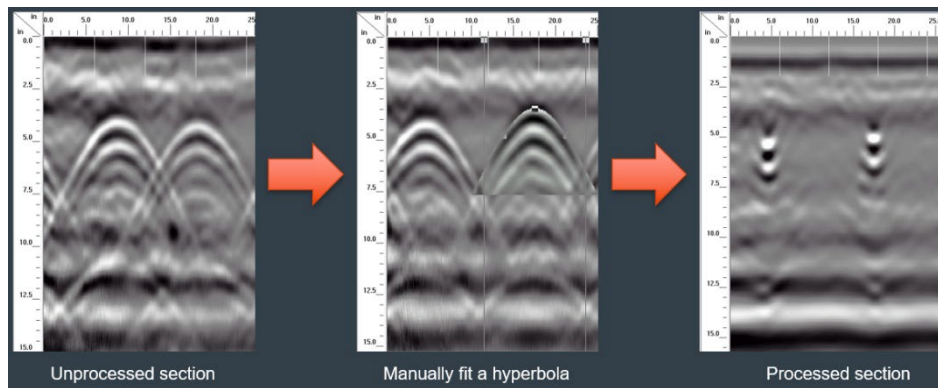


Figure 8.120: Migration processing of GPR data

With the corrected dielectric constant obtained from the migration process, a more accurate estimate of the depth is now obtained. For example, the unprocessed data puts the top rebars at about 3 inches below the concrete surface, while the updated data shows them at roughly 4 inches below the surface.

Another processing option that should be used with care is a process known as “deconvolution.” The purpose of deconvolution is to remove multiple reflections from the same object to reduce noise and prevent them from showing as multiple layers in the GPR profile. However, this process is not 100% accurate and can remove important information in some cases. Therefore, it should be used with care. The result of this analysis is shown in Figure 8.121. As can be seen, this process makes the GPR profile look much sharper with some features becoming less pronounced in the resulting GPR profile.

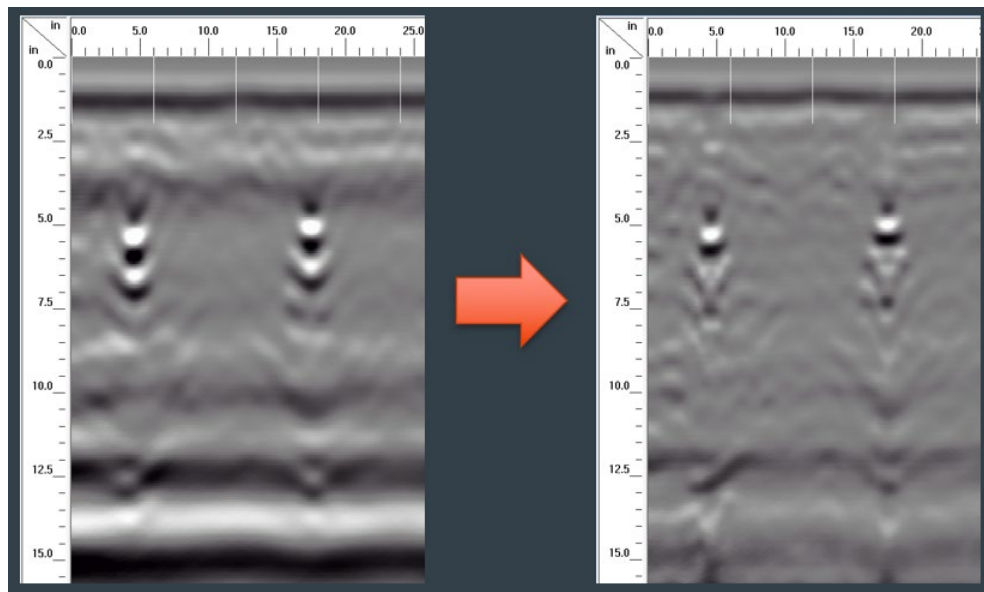


Figure 8.121: Deconvolution processing of GPR data

The processed GPR profile for survey #3 is shown in Figure 8.122. As can be seen, this profile is much clearer than the initial profile shown in Figure 8.118. The top rebars are very visible due to their high dielectric constants and it can be seen the actual spacing of them varies between 9 to 14 inches in this location with the rebar cover being between 4 to 6 inches in this section. However, the main purpose of this survey was to assess the feasibility of using GPR to detect air voids beneath the approach slab. As can be seen, there is a positive peak (bright line) at about a 13-in depth running across the section, denoting a decrease in dielectric constant (concrete to air) and another negative peak (dark line) at about a 14.5-in depth, denoting an increase in dielectric constant (air to gravel). If the interpretation is correct, then there exists a gap that is roughly 1 inch thick in this location.

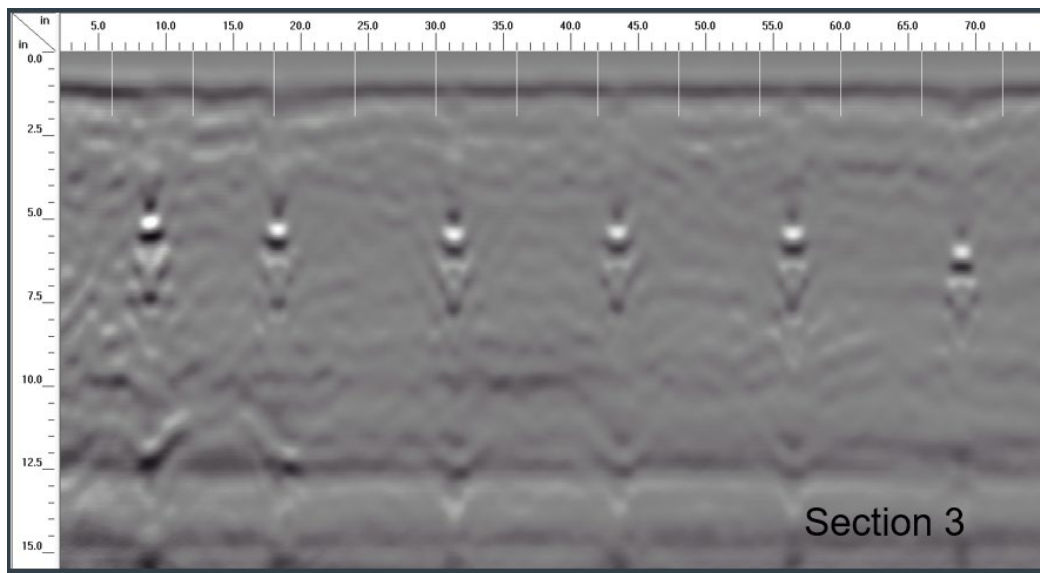


Figure 8.122: Processed GPR profile of section #3 on NE approach slab

The settlement sensors installed on the east abutment measured close to 2 inches of settlement close to the abutment wall. Therefore, it is not unrealistic to expect 1 inch of settlement at a location farther from the abutment wall. On the other hand, the reflection at the bottom of the slab is not quite strong, and it is possible that what is assumed to be an air void is caused by multiple reflections from the same boundary.

As shown in Figure 8.117, 40% of the GPR surveys were conducted on the southwest approach slab at the same location and same direction. The purpose of these surveys was to evaluate the effect of different device input settings on the recorded data to decide which options would work best for this site. The southwest approach was chosen for this purpose because of the amount of fill settlement observed at that location during the second phase of construction. Moreover, the settlement sensors also indicate larger settlement occurring on the west side, making it the better choice for testing the feasibility of using GPR to map fill settlement and estimate the unsupported length of the approach slab in this bridge.

Among the surveys conducted, survey 25 was found to produce the best result overall. The GPR profile is shown in Figure 8.123. As can be seen, the surface of the backfill is highly visible in this GPR survey with areas closer to the wall showing slightly more settlement than areas farther from the wall. What is more important is that nearly 8.5 ft of the approach slab is not supported by the backfill due to excessive backfill settlement. Fortunately, this slab appears to be strong enough that this has not resulted in any visible cracking in the slab yet. However, the approach slab is experiencing loading conditions it was not specifically designed for and may have a reduced service life due to an increased rate of fatigue.

The thickness of this air gap appears to be about 2.5 inches according to the GPR profile and it is interesting to note that this matches very well with what is recorded by the west abutment settlement sensors.

Another interesting note about this GPR profile is that the concrete cover for the top rebar appears to be about 6 inches (instead of the specified 4 inches) and the thickness of the slab is about 15 inches (instead of the specified 13 inches). This extra thickness in concrete may be a “happy” mistake by the contractor that provides additional bending strength to the structure.

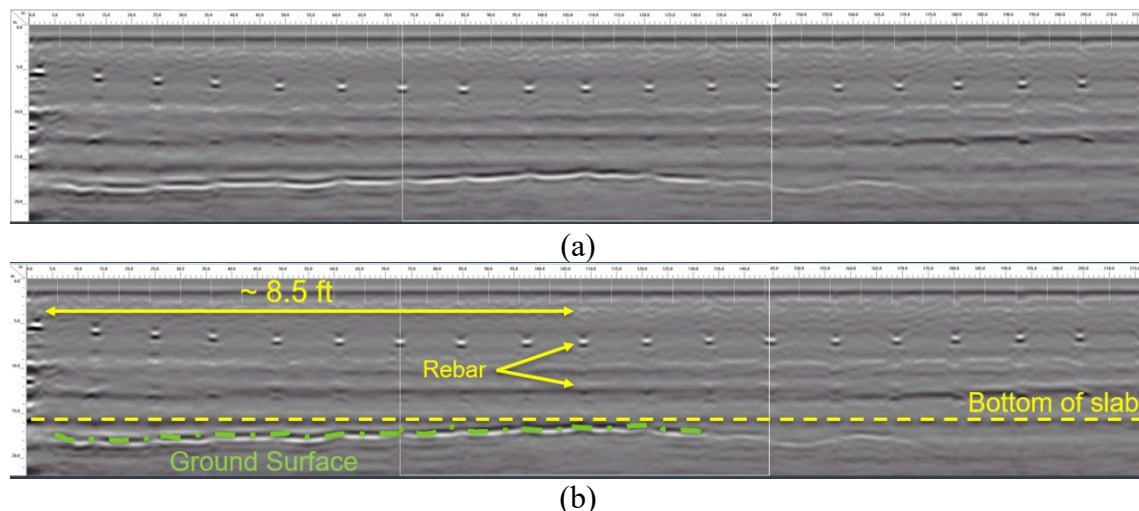


Figure 8.123: Processed GPR profile for section 25: (a) unannotated; and (b) annotated

While the research team has been able to continuously monitor settlement at the location of the installed settlement sensors with success, this data cannot provide any information about other locations farther from the abutment walls with certainty. GPR has proven to be a very valuable tool in providing a continuous profile of the subsurface at the desired location and help the research team determine what parts of the slab are left completely unsupported and how this phenomenon evolves seasonally and yearly. The downside of this tool is that the analysis of the data is much more complicated and it requires a visit each time measurements need to be taken. However, it is believed that this data can be very valuable to the design of future SIAB constructed using granular backfill. The knowledge of the expected unsupported length can help the design engineers to design more resilient slabs for jointless bridges.

8.4. Conclusions on Field Monitoring of China Creek SIAB

A very thorough monitoring program was designed for the SIAB over China Creek outside Wichita Falls, TX. The design of this system was guided by the experiences gained through the instrumentation of Mack Creek Bridge, discussion with professionals and various manufacturers, and academics. The goal of this instrumentation program is to monitor stresses, strains and thermal gradients induced on the structure after construction. China Creek SIAB was completed and opened to traffic on July 31, 2020. All sensors were successfully installed in their pre-assigned locations and the remote data collection program started in October 2020. A program for efficient post-processing of data collected from the 70+ sensors installed on China Creek Bridge was also developed.

After a comparison of laser distance meter data with strain gauge data and theoretical values for the coefficient of thermal expansion of concrete, it was determined that the laser data collected from China Creek Bridge was prone to error. Therefore, the strain gauge data was used to correct the laser distance meter data and produce an accurate deformation record of the deck. The data shows a total decrease in length of nearly 0.6 in since October 2020, most of which occurred on the west side of the bridge as shown by the crackmeter data.

A regression analysis of different temperature records collected from thermistors, the weather station and other sensors against the deck length change shows that the best estimator of deck length is a deck-embedded thermistor that produces a coefficient of determination of 0.96. While other temperature records, such as ambient air temperature, still correlate with changes in deck length, they produce a relatively coefficient of determination $R^2 = 0.87$, and using them to estimate expansion joint demands will require the use of a larger factor of safety.

Visual inspection of the expansion joints in February 2021 revealed no signs of damage due to the extremely cold weather. A main concern in the design of SIAB is the development of gaps in the expansion joints due to thermal contraction, which could fill up with debris, preventing the joints from expanding in subsequent warm seasons and resulting in damage to the structure or roadway. Overall, the crackmeter data from the expansion joints indicated that while the joint width increased each fall and winter, the expansion joint did not experience compression during the warm season. This revealed that the preformed boards are relatively rigid and do not compress due to thermal expansion of the bridge. As a result, the sleeper slab must have displaced each spring and summer, leading to the development of a bump behind the sleeper slabs.

A comparison of the data recorded by strain gauges installed at the top of the deck and bottom of the girders indicated no sign of bending due to existing temperature gradients across the deck profile. However, small signs of rotation were observed in the west abutment wall as the temperature rose, possibly due to the interaction between the abutment wall, abutment cap and backfill.

The settlement sensors installed in the backfill on both sides of the bridge recorded 1 to 2 inches of settlement in the backfill area. This indicated that the approach slab did not receive any vertical support from the backfill at least within 5 ft of the abutment wall. The backfill settlement data also showed that the settlement in the backfill occurred at a nearly constant rate, with a small recovery in settlement during warmer weather.

The data collected from approach slab strain gauges established that small levels of compressive and tensile strains (± 40 microstrains) developed in the slabs due to temperature changes and friction at the base of the slabs. The small magnitude of these strains confirmed that a complete debonding of the base of the slab and backfill occurred, which demonstrates the effectiveness of using two layers of polyethylene as bond breaker to prevent formation of cemented bonds during slab construction.

The data from shape arrays installed in the drilled shafts illustrated that both drilled shafts were subjected to lateral loading due to shrinkage and thermal strains of the deck. The data indicated bending toward the center of the bridge (creek) during fall and winter months, which was consistent with the research team's expectations. In addition, a slight shift toward the east abutment was detected by both shape arrays. Though this shift appears to occur over the spring and summer months, the cause is not very well understood.

Following the successful capture of drilled shaft deformation profiles, an algorithm was developed to estimate bending moment profiles of the drilled shafts. The analysis results indicate that relatively large moments developed within the upper portion of the drilled shafts due to thermal contraction of the bridge deck. While the calculated moments for the earlier data collected were within the elastic range, the moment magnitudes were relatively large and may lead to cracking in cold temperatures or as the gap between abutment cap and abutment wall gets filled with debris.

The earth pressure data collected indicated that some ratcheting occurred at China Creek Bridge as well. Overall, the measured earth pressures increased by nearly 25% from summer 2021 to summer 2022 due to ratcheting. This ratcheting also affected the wingwalls and abutment caps of the bridge. Interestingly, the highest earth pressure on both abutments was measured by the EPC installed closest to the top of the wall, indicating that the earth pressure does not increase with depth as assumed in classic gravity retaining wall design procedures.

Chapter 9. Analysis Of Soil-structure Interaction Data From China Creek Semi-integral Bridge

9.1. Introduction to the Analysis of China Creek SIAB Soil-structure Interaction Data

Conventional bridge construction often includes expansion joints placed at the ends of the bridge and in between spans. This design choice is made to minimize the development of secondary stresses in components of the bridge superstructure due to movements such as those induced by thermal strains, shrinkage, creep, and abutment settlement (Burke, 2009). Moreover, expansion joints can potentially prevent interaction between the abutment and the bridge superstructure during its thermal expansion and contraction. However, many studies have shown that bridge expansion joints are highly susceptible to deterioration and damage while in service. In particular, expansion joints expose the abutment caps, girders and bearings to moisture, deicing salts, abrasives, chemicals, and other debris, causing extensive damage to the structure and an accelerated degradation rate (Purvis and Berger, 1983). While periodic replacement of damaged expansion joints can maintain their intended function, the damage to the structural elements will be comparatively difficult, if not entirely unfeasible, to remedy. Furthermore, maintenance of expansion joints is typically expensive and can exceed its initial cost of construction. As a result, many transportation agencies have started pursuing jointless bridge designs, such as Semi-Integral Abutment and Integral Abutment Bridges (SIAB and IAB, respectively).

In SIAB, the deck, girders, and abutment walls are integrated during construction, and superstructure loads are transferred to the abutment caps and foundation via bearings. On the other hand, in IAB, the bearings are also eliminated, resulting in a seamless connection between the superstructure and substructure. According to Burke (2009), the adoption of IAB and SIAB in the US began in Ohio nearly a century ago.

A key factor in selecting between adoption of SIAB/IAB is the foundation type of the bridge. IAB require comparatively flexible foundation elements that would provide limited restraint against thermal expansion of the superstructure. As a result, many transportation agencies in the US require the use of steel H-piles with the weak axis oriented toward the IAB. In contrast, SIAB are often preferred when site conditions preclude the use of flexible foundation systems (e.g., pile driving is unfeasible or uneconomical). However, in either case, thermal expansion and contraction of the superstructure may result in daily cyclic interaction of the abutment walls with the abutment backfills.

The cyclic soil-structure interaction that develops in semi-integral and integral bridge abutments has been investigated through several studies over the past few decades. Through long-term field monitoring programs, this interaction has been found to cause increased abutment earth pressure (also known as ratcheting) and settlement of the backfill (Mofarraj and Zornberg, 2022; Huntly

and Valsangkar, 2013; England et al. 2000; Frosch and Lovell, 2011; Civjan et al., 2013). Based on a series of cyclic triaxial tests, Clayton et al. (2006) attributed the ratcheting in sand particles to an accumulation of plastic strains and gradual changes in the fabric structure due to cyclic loading of the sand particles. Accordingly, ratcheting was observed in both densely- and loosely-packed specimens. However, long-term field monitoring studies have provided mixed results regarding the occurrence of ratcheting in IAB and SIAB. While some researchers have clearly observed seasonal increases in lateral earth pressures (e.g., Mofarraj and Zornberg, 2022; Huntly and Valsangkar, 2013), others have reported contradicting observations (Civjan et al., 2013; Ooi et al, 2020).

According to Oesterle and Tabatabai (2014), the complexity and uncertainty in the behavior of jointless bridges resulted in the adoption of an empirical design approach for these structures. Jointless bridges were initially limited to short lengths and their continued success led to increasingly longer bridge structures over time. Accordingly, the design procedures and guidelines established by various transportation agencies were developed primarily based on empirical rules. Therefore, significant insight can be gained by generating detailed field results on the long-term behavior of SIAB and IAB that would enable development of a rigorous design approach for such structures.

The purpose of this study is to provide additional insight into the long-term behavior and performance of SIAB. To this end, a pilot semi-integral highway bridge was constructed in Wichita County, TX in 2020 by the Texas Department of Transportation (TxDOT). This structure was instrumented with over 75 sensors that operated during and after its construction. A detailed description of the instrumentation system and its development is provided in Section 8.2. This paper's focus is on providing insight specifically into the quantification of the soil-structure interaction occurring in the abutments and on the evaluation of the affects that such interaction has on the behavior of the superstructure and abutment backfill.

In the following sections, a description of the instrumented SIAB structure is presented, followed by a detailed analysis and discussion of the instrumentation data relevant to the soil-structure interaction in the abutments. The insight provided by such analysis into the effect of daily and seasonal temperature variations on the bridge behavior is finally discussed in detail.

9.2. Bridge Description

China Creek SIAB was built on Texas State Highway 240 outside Wichita Falls, TX, in summer 2020. A schematic of this bridge is shown in Figure 9.1. The bridge is 90.2 ft long and 45.9 ft wide with two traffic lanes. China Creek Bridge was constructed to replace an older bridge, and it was constructed in two phases to keep the road open to traffic during construction. The eastbound lane was completed in April 2020 and the westbound lane in July 2020.

The bridge superstructure consists of Tx34 prestressed concrete I-beam girders, precast concrete panels between the girders, and a cast-in-place concrete deck. The abutment walls are integrally connected to the deck and measure 4.1 ft deep. The deck connects to the approaching roadway via 19.7-ft-long reinforced concrete approach slabs that are structurally connected to the deck and abutment wall on one end and rest on the sleeper slabs on the other. Because the abutment wall extends below the top of the abutment cap, the gap between the abutment wall and abutment cap was filled with a 1.97-in-thick closed-cell foam, which was also initially used as formwork for the construction of the abutment walls.

The bridge is supported by four 36.1-ft-deep drilled shafts on each side, each of which are 2.95 ft in diameter. Per TxDOT specifications, Type AS select fill (TxDOT Item 423) was used as abutment backfill, which consists of crushed gravel with 50% or more of the particles ranging in size from 0.47 to 2.95 in and a fines content not exceeding 5%. Figure 9.2 pictures the abutment backfill material.

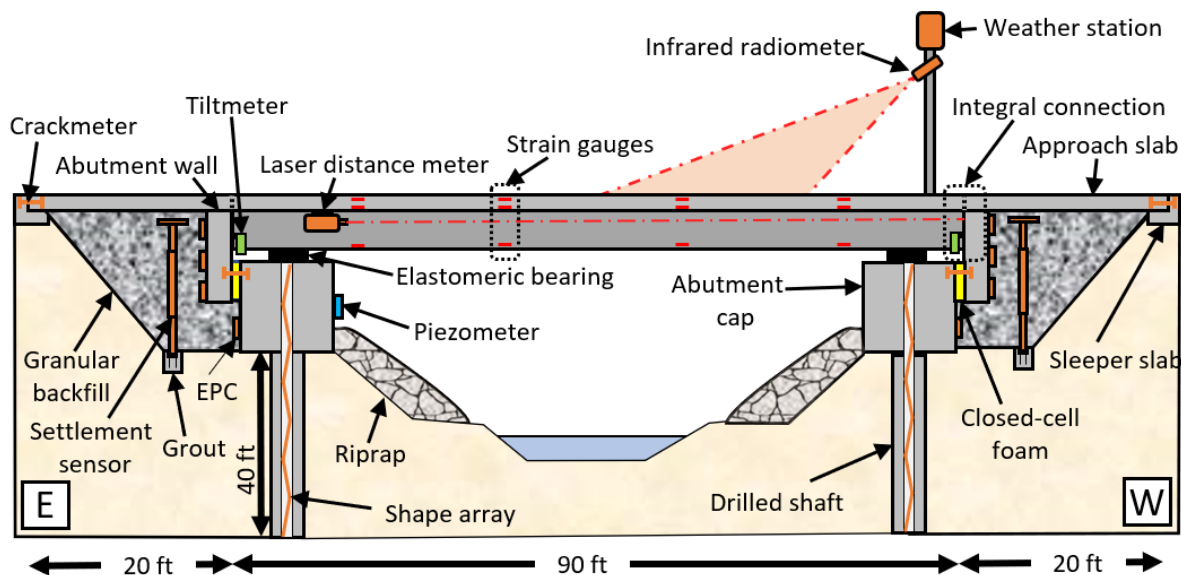


Figure 9.1: Schematic of China Creek SIAB and location of installed sensors

9.3. Instrumentation Description

As depicted in Figure 9.1, a large array of geotechnical, structural and climate-related instruments were installed on various bridge components. The bridge monitoring program was developed to provide a comprehensive overview of the development of stresses and strains in and around the structure. Moreover, this instrumentation scheme allows for the measurement of displacements of multiple bridge components (such as abutment walls and caps) independently.

Since this study aims at understanding the soil-structure interaction in the abutment area, data analysis and discussion focuses primarily on movements of the abutment walls, backfill earth

pressure distribution, backfill settlement and ratcheting. Figure 9.2 presents the primary instrumentation and abutment backfill sensors prior to placement of the backfilling on the west abutment.

The earth pressure cells (Geokon model 4815) measure the lateral earth pressures acting on the abutment walls (at three different depths), abutment caps (mid-height) and wingwalls (mid-height, close to the abutment walls). The vertical settlement sensors consist of 7.6-ft-long telescopic displacement transducers (Geokon model 4430) installed vertically within the abutment fill. The bottom of these sensors was grouted below the backfill (Figure 9.1) and the top was attached to a 0.98-ft x 0.98-ft stainless steel plate seating at the top of the backfill (Figure 9.2). The data collected from the settlement sensors was validated using Ground Penetrating Radar (GPR) measurements.

To estimate the lateral compression of the backfill material, two daisy-chained 3.3-ft-long horizontal soil extensometers (Geokon model 4435) were installed on each abutment. One end of each set of soil extensometers was attached to the abutment wall and the other end was placed within the backfill, as shown in Figure 9.2. These sensors can measure the average compression and extension of the backfill at the sensor locations. The data collected by these sensors can provide stiffness information of the abutment backfill as well as additional insight on the factors affecting the thermal expansion of the bridge.

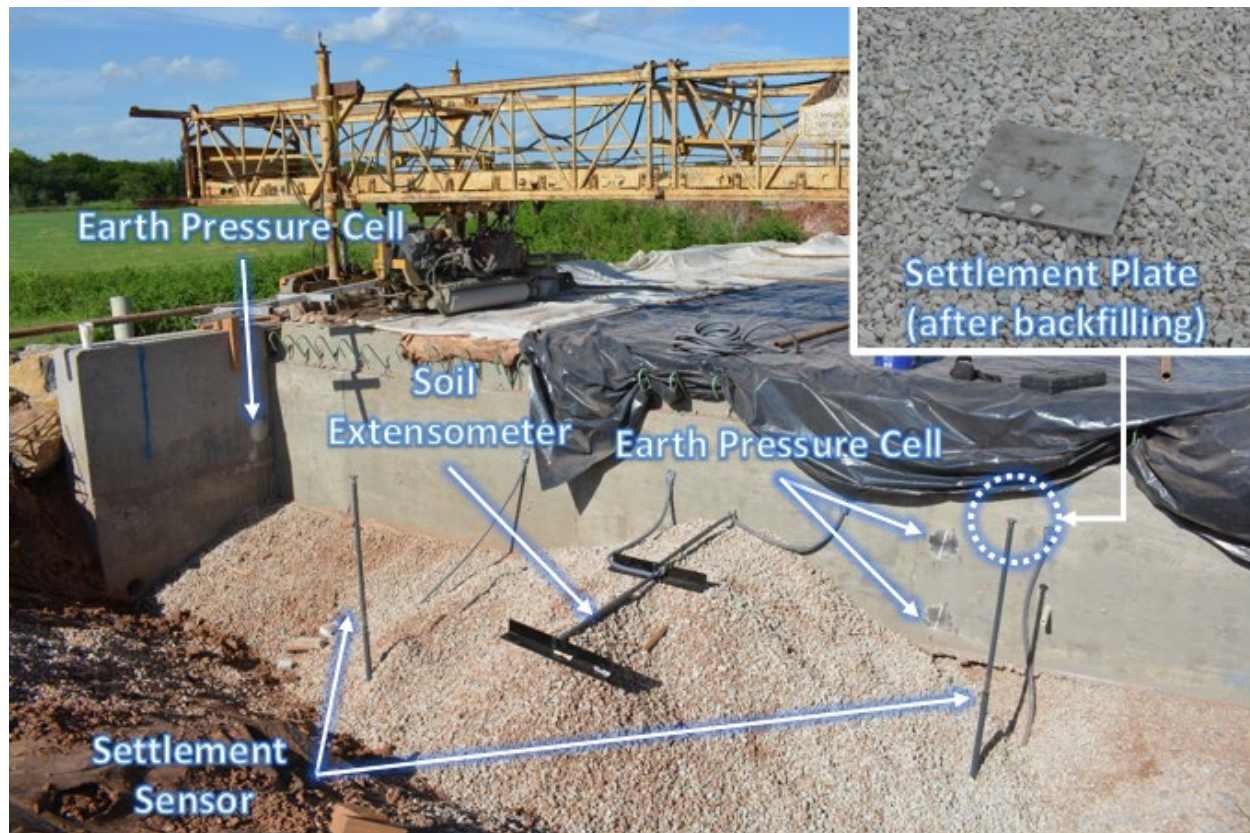


Figure 9.2: Instrumentation and backfilling of China Creek Bridge west abutment; top right inset shows a close-up of steel plate attached to top of settlement sensors after backfill placement

In addition to the aforementioned sensors in the abutment area, shape arrays, abutment cap crackmeters and deck strain gauges were also installed as part of this project. The data measured by these additional instruments were used to calculate abutment cap and abutment wall movements, which provide additional detail on the soil-structure interaction in this semi-integral bridge abutment. The instrumentation data was collected every 30 minutes by Campbell Scientific CR6 data loggers. While the sensors' zero measurements correspond to readings taken immediately after their installation (during bridge construction), the data collection campaign began in October 2020, after construction had been completed, data loggers had been installed and measurement issues were successfully troubleshoot.

The subsequent discussion of instrumentation data is grouped into three main categories: thermal expansion of the superstructure; backfill earth pressures; and backfill settlements.

9.4. Thermal Expansion and Contraction of the Bridge

The ambient air temperature data (Figure 9.3) was collected using the weather station installed on site, as shown in Figure 9.1. This data indicates temperature changes ranging from -9.4°F to 113°F during the monitoring period. The lowest temperature recorded as part of this study was

caused by winter storm Uri in February 2021, which resulted in record low temperatures and snowfall across the State of Texas for nearly a week. As revealed by the ambient air temperature data, temperature fluctuations are significantly larger during the colder fall and winter months of the year compared to the warmer spring and summer months. For example, the ambient air temperature over one week in winter 2021 was observed to fluctuate by 86°F, while temperature changes of more than 68°F during the summer are not typically observed, with the temperature remaining consistently high.

As illustrated by the monitoring results presented in Figure 9.4, changes in climate conditions affected the thermal expansion and contraction of the bridge. The design of the monitoring program facilitated the determination of the changes in bridge length through two independent, redundant methods. The first method requires using the average strain measurements from the strain gauges installed on the bottom flange of the girder (see Figure 9.1). The second method involves tracking the displacement of abutment walls via the drilled shaft shape arrays and abutment cap crackmeters, and determining the change in their distance at each measurement. As illustrated by the two methods of measuring length changes presented in Figure 9.4, both methods rendered very similar predictions during fall, winter, and spring (when ambient temperature remained below 77°F), while a slight mismatch in daily variations is observed during the warmer months. However, the strong overall correlation between the two sets of measurements ($R^2 = 0.91$), which were obtained independently, provides good evidence of the high reliability of the field data collected as part of the monitoring program. The calculations, based on shape array and crackmeter data, are considered to be the most accurate of the two data sets, as these sensors were individually calibrated, whereas the Geokon Model 4151 strain gauges were batch-calibrated, which may result in slight inaccuracies.

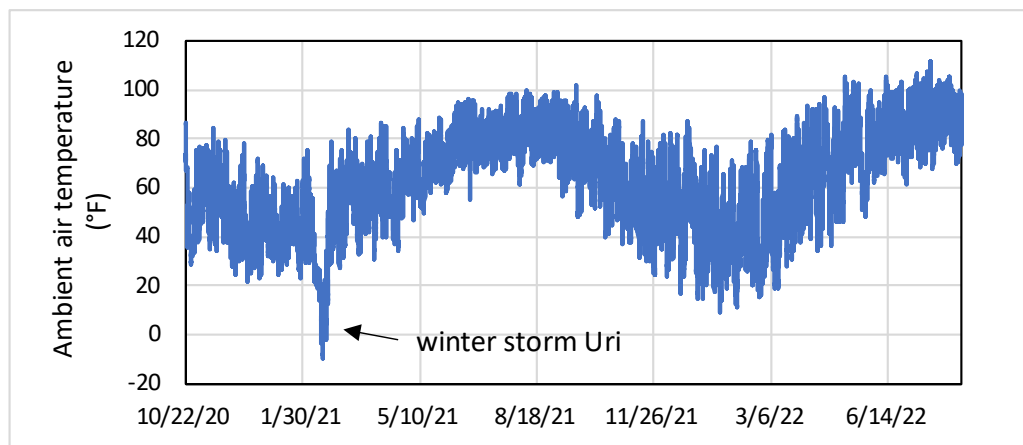


Figure 9.3: Ambient air temperature time-history data collected from China Creek Bridge site

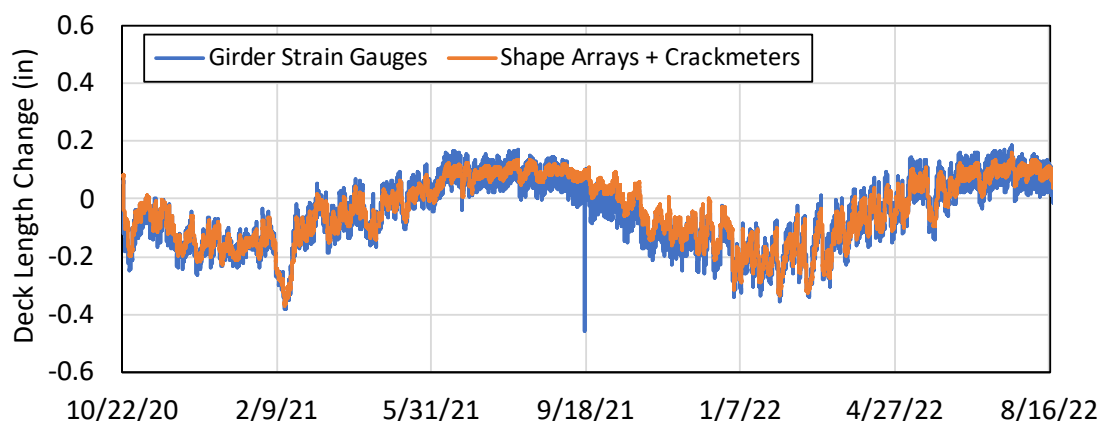


Figure 9.4: Time-history of changes in bridge length measured using girder-mounted strain gauges compared to foundation shape array and abutment cap crackmeter measurements

Overall, the data shown in Figure 9.4 indicates that the 90.2-ft-long bridge experienced approximately 0.51 in of thermal expansion/contraction over the monitoring period. Using as a reference the bridge length at the time of construction completion (July 2020), the bridge experienced a maximum thermal expansion of 0.16 in during both summers (2021 and 2022) in the monitoring program, and a maximum thermal contraction of approximately 0.37 in during the winter storm of February 2021. On a smaller timescale, thermal expansion/contraction behavior is observed to vary distinctively depending on the season. The consistently high temperatures of the summer months typically produce comparatively smaller changes in bridge length, of 0.04 to 0.08 in, happening daily and the average length of the bridge typically not changing by more than 0.08 in over the summer months. On the other hand, during the cold winter months, daily changes of 0.16 in or more in bridge length are commonly observed and the average bridge length was observed to change by up to 0.32 in during the winter months.

The availability of field temperature and displacement data allows the back-calculation of the Coefficient of Thermal Expansion (CTE) of the structure. Specifically, the thermal expansion of a linear structure can be calculated as follows:

$$\Delta L = CTE \times \Delta T \times L_0 \quad \text{Equation 1}$$

Where “ ΔL ” is the change in bridge length, “ ΔT ” is the change in the structure’s internal temperature, and “ L_0 ” is the initial length of the structure at the time of construction.

Therefore, the CTE can be obtained by finding the slope of the linear regression line fitted to the average strain measurement ($\Delta L/L_0$) recorded by the deck strain gauges versus the average internal deck temperature measured by their thermistors. The deck-embedded strain gauges were selected for this analysis because they are expected to provide a more accurate measurement of the concrete temperature than the girder strain gauges, as the latter are mounted on the concrete surface.

Figure 9.5 presents the deck strains and corresponding concrete temperature data. According to the AASHTO LRFD Bridge Design Manual (2017), the CTE of normal weight concrete ranges from 5.4 to $14.4 \times 10^{-6}/^{\circ}\text{C}$. In the absence of project-specific data, a CTE of $10.8 \times 10^{-6}/^{\circ}\text{C}$ is recommended by AASHTO (2017). Therefore, the estimated CTE of $9.0 \times 10^{-6}/^{\circ}\text{C}$, based on a linear regression analysis of the strain gauge data (Figure 9.5), falls well within the expected range and is very similar to AASHTO's recommended design value, which bolsters confidence in the field monitoring data.

As stated previously, the positions of both abutment walls were tracked independently using the installed shape arrays and crackmeters. The abutment wall displacement data is shown in Figure 9.6. The plotted data shows the time-history of the positions of the east and west abutment walls relative to their original positions upon completion of construction. Positive displacement values in this figure indicate that the abutment wall has displaced toward the backfill (passive backfill movements) while negative values indicate that the abutment wall has displaced away from the backfill (active backfill movement).

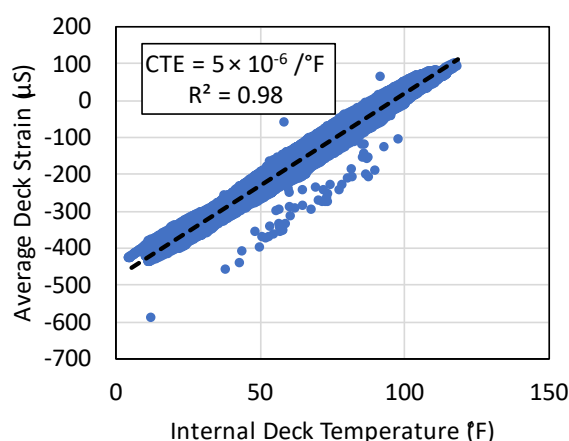


Figure 9.5: Coefficient of Thermal Expansion (CTE) calculation based on deck strain gauges

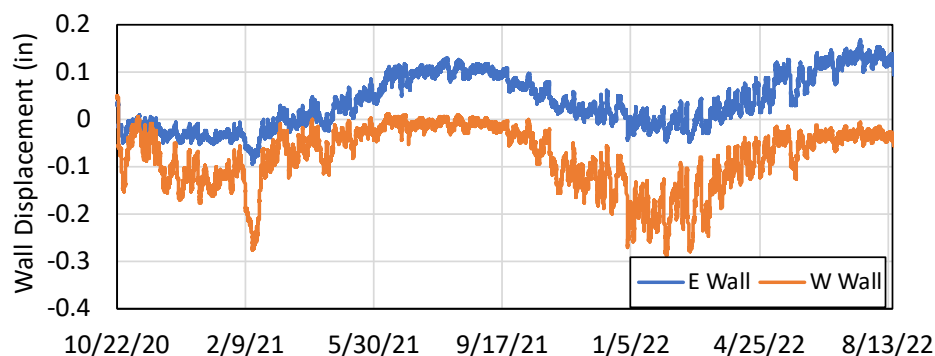


Figure 9.6: Time-history of east and west abutment wall displacement relative to their original positions at completion of construction

The displacement data in Figure 9.6 shows that thermal expansion and contraction in the west abutment wall was comparatively larger than in the east abutment wall, revealing an asymmetric displacement response of the bridge. In addition to the observed difference in abutment wall displacement magnitudes, the direction of displacement and seasonal behavior observed appears to be asymmetrical as well. It is observed that the west abutment wall primarily moved from its initial position to positions up to 0.28 in away from the abutment backfill, which occurred during both winters in the monitoring period. On the other hand, the east abutment wall moved among positions 0.04 to 0.08 in away from the abutment backfill (winter months) to 0.12 in toward the abutment backfill (summer months). Consequently, while both abutment walls experienced cyclic displacement toward and away from the abutment backfills due to thermal expansion/contraction of the bridge, their behavior was highly asymmetrical. This behavior was unexpected because the structure is geometrically symmetrical as shown in Figure 9.1. For design purposes, the displacement magnitudes of the two bridge abutments due to bridge deck expansion and contraction are often considered to be the same (e.g., for design of joints and bearings). However, asymmetrical displacements of abutment walls have been previously reported in field monitoring studies of jointless bridges (Abendroth et al., 2007; Huffaker, 2013; Ooi et al. 2010).

An evaluation of the data recorded during winter storm Uri (February 2021) illustrates this asymmetry well: the east abutment wall displaced approximately 0.08 in away from the east abutment backfill, while the west abutment wall displaced some 0.2 in (i.e., 2.5 times more) away from the west abutment backfill. The results also reveal that from spring to summer 2021, the east abutment wall displaced approximately 0.12 in toward the east abutment backfill, which is somewhat larger than the 0.08 in displacement recorded for the west abutment wall.

Overall, the east and west abutment walls have experienced displacements of up to 0.16 and 0.3 in since construction was completed, respectively. Consequently, the typical design assumption of attributing half the total expected thermal displacements to each abutment is neither a conservative nor realistic assumption considering the total 0.51 in thermal expansion/contraction of the bridge length (Figure 9.4). The thermal displacement data collected in this study indicates that an appropriate design approach would be to consider that a single abutment wall may experience displacements consistent with approximately 70% of the expected total change in bridge length. Among the bridge design manuals published by various transportation agencies in the United States, design recommendations have been identified in the State of Ohio's Bridge Design Manual (ODOT, 2020), which recommends considering 2/3 of the total bridge length as expansion length for each abutment wall. The following analysis, based on abutment wall displacement records, demonstrates how the direction of thermal expansion and contraction of the bridge changes throughout the year, resulting in the asymmetrical wall displacement behavior shown in Figure 9.6.

Considering that thermal strains cause the two abutment walls in a bridge to always move in opposite directions, there will be a point along the length of the bridge deck that experiences zero displacement at any given time. Figure 9.7 shows a schematic view of a bridge with the ends of deck moving by ΔL_1 and ΔL_2 in the opposite directions due to thermal expansion of the bridge deck. Consequently, a point can be imagined along the length of the bridge that does not experience any displacement due to thermal expansion/contraction of the bridge. This Neutral Thermal Expansion Point (NTEP) is positioned such that the displacement of each abutment wall is proportional to the distance of that abutment wall to the NTEP. In this analysis, the distance of each abutment wall to the NTEP is identified as the effective thermal expansion length (L_e). While it is conceivable that the NTEP may fall outside the bridge deck (e.g., if the west sleeper slab is fully anchored causing the bridge to only expand eastward), observing that the abutment walls have always moved in the opposite direction due to thermal expansion/contraction of the bridge reveals that the NTEP lies within the length of the bridge. Consequently, the sum of the effective thermal expansion lengths would be equal to the total length of the deck (L_0), as shown in Figure 9.7.

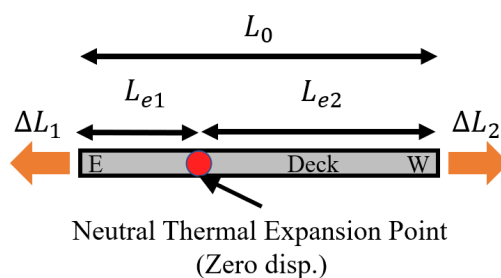


Figure 9.7: Diagram showing Neutral Thermal Expansion Point (NTEP) and effective expansion length for each abutment wall

Having determined the magnitude and direction of displacement at each end of the bridge, the relative position of the NTEP at the China Creek Bridge was calculated and is shown in Figure 9.8. The results in this figure correspond to the distance from the east abutment wall to the NTEP normalized in relation to the total bridge deck length. For example, L_{e1}/L_0 equal to 50% indicates that the effective expansion length for both abutment walls is the same and the bridge is expanding/contracting symmetrically. As illustrated by the results in Figure 9.8, the position of the NTEP varied considerably over the monitoring period, ranging from 25% to 70%.

During the colder winter months, the NTEP distance has remained within 25 to 35% of the bridge length, meaning that the effective expansion length for the west abutment wall is three to four times larger than that for the east abutment wall. This observation implies that during the colder months, when the bridge length has decreased due to contraction, the majority of the temperature-induced changes in bridge deck length resulted in displacements of the west abutment. During the warm summer months, the NTEP distance ranged from 60 to 70% of the

bridge length, which indicates that bridge thermal expansion resulted in larger displacements of the east abutment wall compared to the west abutment wall.

Overall, it appears that the bridge only experienced symmetrical thermal expansion/contraction ($L_{e1}/L_0 = 50\%$) during a comparatively small period during the monitoring period. Instead, the bridge primarily experienced expansion toward the east abutment and contraction away from the west abutment. Given this trend of monitoring results, it would be worthwhile to investigate whether the bridge experiences a permanent shift over time or returns to the same position after a yearly cycle.



Figure 9.8: Time-history of NTEP distance from east abutment wall, normalized to total length of bridge

Having established the position of both abutment walls relative to the time of construction, the position of the bridge midpoint can also be tracked at any given time. Such results are shown in Figure 9.9. In this figure, positive values indicate that bridge midpoint has moved toward the east abutment. Figure 9.9 data indicates that the bridge midpoint has experienced displacements of 0.08 to 0.12 in during each annual cycle. While much of the displacements are recovered (see for example the midpoint position changing from 0.06 in, in October 2021, to 0.12 in, in February 2021, and returning to 0.06 in, in April 2021), there appears to be a small seemingly permanent shift occurring during the summer months. For example, the bridge midpoint position changed from 0.03 in, in April 2021, to 0.06 in, in August 2021, indicating a seemingly permanent eastward shift.

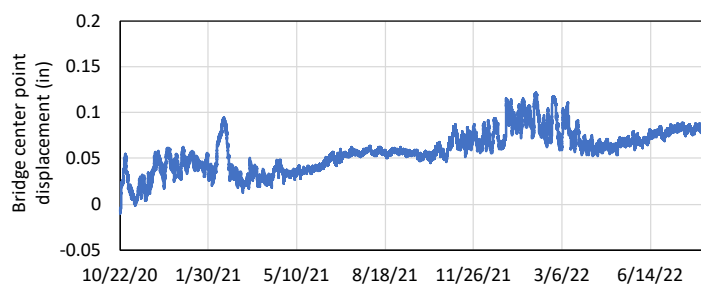


Figure 9.9: Time-history of change in bridge midpoint position relative to time of construction (positive values indicate that midpoint has moved eastward)

To better understand the reasons behind the asymmetrical response to changes in temperature exhibited by China Creek Bridge, factors that could potentially affect the direction of the bridge thermal expansion/contraction were evaluated. Figure 9.10(a) displays a simplified soil-structure interaction diagram showing the elements that resist a bridge's thermal expansion/contraction.

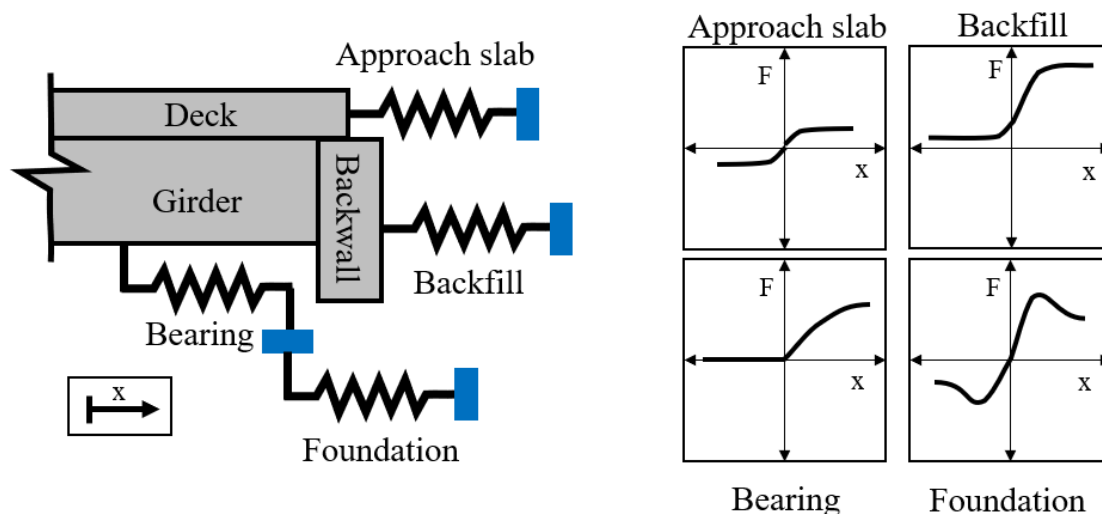
The resisting elements include abutment backfill, foundation, bearings, and approach slab.

Typical load-displacement behavior of these components is shown in Figure 9.10(b). To satisfy force equilibrium, the sum of the reaction forces from the approach slab, backfill, bearings, and foundation from the two abutments should be equal. A symmetrical response can be expected if the different resisting elements exhibit the same stiffness on both ends of the bridge.

Consequently, considering the asymmetrical behavior described previously, it may be concluded that some of these resisting elements exhibit a higher stiffness on one of the abutment walls than on the other. While it may be reasonable to consider that the elastomeric bearings exhibit a similar shear-deformation behavior because they are manufactured under rigorous quality control standards, several of the other elements may be a source of unequal resistance in the two abutments, including the following:

1. Difference in the backfill compaction can result in a difference in the stiffness of the abutment backfills against lateral loading
2. Differences between the foundation soil stiffnesses between the two abutments
3. Differences in the sliding resistance of the approach slabs due to factors such as backfill settlement

Considering the potential role of the backfill stiffness variation as a cause for asymmetric thermal expansion/contraction of the bridge, the following section presents and discusses the data collected from earth pressure cells installed in the abutment area.



(a)

(b)

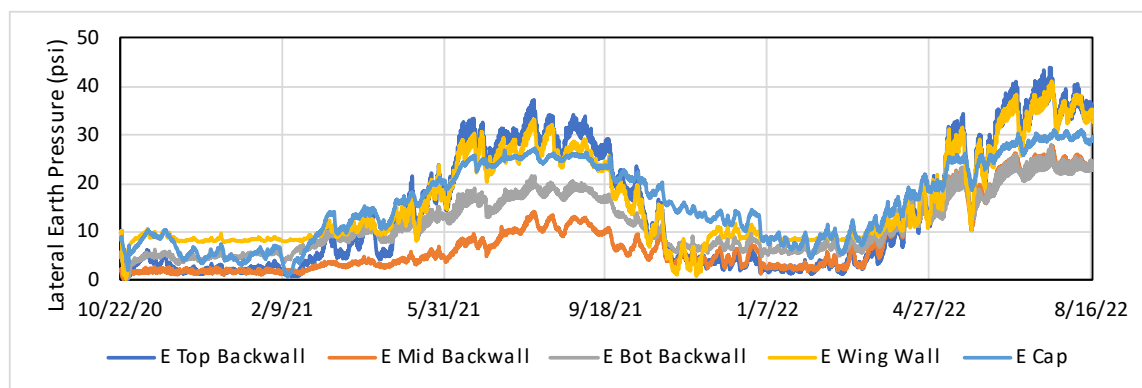
Figure 9.10: Semi-integral bridge abutment resistance model: (a) diagram showing elements that resist thermal expansion/contraction of an SIAB; and (b) hypothetical force-displacement diagram of resisting elements (positive 'x' signifies abutment wall displacement toward backfill)

9.5. Lateral Earth Pressures on Abutment Walls

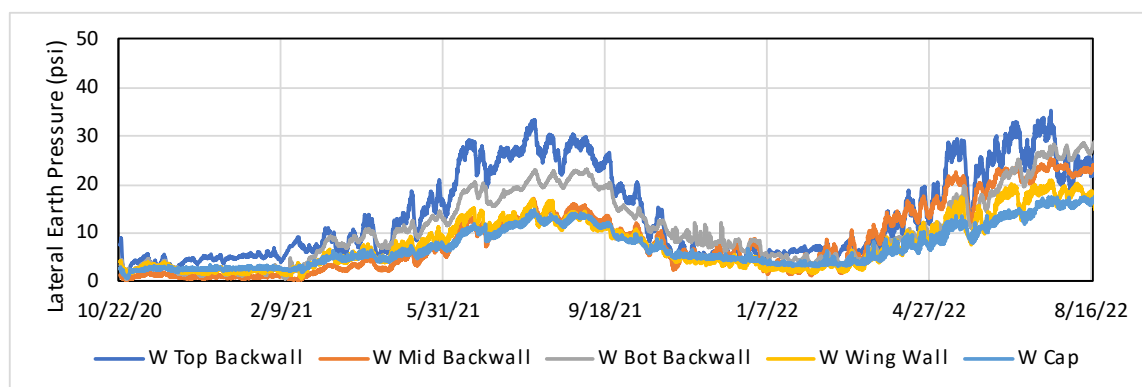
The lateral earth pressure data collected from the east and west abutment walls are presented in Figure 9.11(a) and Figure 9.11(b), respectively. Specifically, the graphs show the time histories of lateral earth pressure measurements from the five Earth Pressure Cells (EPCs) installed in each abutment wall. Three EPCs were installed on the 4.1-ft-deep abutment walls at depths of 1.2 ft, 2 ft and 3.5 ft from the top, and are referred to in Figure 9.11 as “top backwall,” “mid backwall” and “bot backwall,” respectively. In addition, one EPC was installed at mid-height of each abutment cap and at mid-height of the north wingwalls, approximately 1.15 ft from the abutment walls.

Overall, the lateral earth pressures measured by the EPCs can be observed to vary considerably depending on the location and time of year. The lowest earth pressures were recorded during each fall and winter (ranging from 1.45 to 7.25 psi depending on the location), while the highest earth pressures were recorded from late spring to early fall each year (ranging from 14.5 to 43.51 psi depending on the location). These trends are expected, as comparatively higher earth pressures are consistent with the expected expansion of the bridge deck during summers toward the abutment backfill (overall movements in the passive direction) while lower earth pressures are anticipated with the expected contraction of the bridge deck during winters, with abutment walls retracting from the backfill (overall movements in the active direction).

The data recorded over the nearly two years of abutment earth pressure monitoring show signs of ratcheting in both abutments. For example, the maximum earth pressure recorded at the location of the top EPC on the east abutment wall increased by 7.25 psi (i.e., about 20%) from summer 2021 to summer 2022. A similar trend can be observed among other EPC records as well. This indicates that the earth pressures acting on the abutment walls, abutment caps and wingwalls exhibited an overall increasing trend with time. The abutment wall displacements slightly changed from summer 2021 to summer 2022 due to the bridge shifting over time (Figure 9.9). As a result, the east abutment wall moved slightly more in the passive direction (expected to cause relatively larger lateral earth pressures) in summer 2022 compared to summer 2021 and the west abutment wall moved slightly more in the active direction (expected to cause relatively smaller lateral earth pressures) in summer 2022 compared to summer 2021. However, ratcheting is clearly observed in the EPC data collected from both abutments.



(a)



(b)

Figure 9.11: Time-history of lateral earth pressures recorded in: (a) east abutment; and (b) west abutment

The data on lateral earth pressures acting on the wingwalls and abutment caps, also presented in Figure 9.10, indicate that the thermal expansion of the bridge also significantly affects the earth pressure acting on these components. It bears reiterating that the wingwall EPCs on China Creek Bridge are installed very close to the abutment wall. The higher confinement of the backfill in this region can potentially explain the similar trends between the readings collected by the wingwall EPCs and those collected by the EPCs installed in the abutment walls. However, the earth pressure acting on the far end of the wingwalls is expected to be comparatively lower, and the plotted data should therefore not be considered the representative average earth pressure acting on this component. In the case of the abutment caps, the change in lateral earth pressure is attributed to the displacement of the abutment caps themselves. The recorded data indicates that earth pressures as high as 29 psi were recorded on the east abutment cap due to thermal expansion of the bridge.

Regarding the variation of lateral earth pressures with depth, the results in Figure 9.11 indicate that the highest earth pressure readings were recorded by the top EPC (i.e., the shallowest), with earth pressures reaching 43.5 psi. While this trend with depth may appear inconsistent with typical lateral earth pressure distribution in conventional walls (i.e., lateral earth pressure

increasing linearly with depth), several studies (e.g., Huntly and Valsangkar, 2008; Civjan et al., 2004), have also found a non-linear distribution of earth pressures with depth while monitoring integral bridge abutment walls. While this observation is not consistent with expected earth pressure distribution based on classic earth pressure theories (e.g., Rankine, 1857), there are other factors that can help explain why lateral earth pressure behind semi-integral bridge abutment walls would not increase linearly with depth.

Firstly, it is established in the available literature that the lateral earth pressure magnitude behind retaining walls is a function of the displacement of the wall (e.g., Clough and Duncan, 1991). Therefore, the points along the semi-integral bridge abutment wall can be expected to experience different lateral earth pressure magnitudes if the movement of the abutment wall is not purely translational, but a combination of rotation and translation. Furthermore, it has been shown that the magnitude of earth pressure increase due to ratcheting is a function of lateral compression/extension cycle magnitude (e.g., Clayton et al., 2006). Accordingly, larger displacement cycles can result in a faster rate of ratcheting.

Lastly, the top two-thirds of the abutment wall is directly supported by the girders while the bottom third of the wall is cantilevered and consequently more flexible, which can potentially affect soil arching and stress redistribution, especially as the backfill material is granular (crushed gravel). This arrangement is also analogous to a shallow footing with an off-center axially-loaded column. Therefore, similar to how soil reaction is expected to decrease from directly below the column to the far edge of the shallow footing, larger magnitude lateral earth pressures can be expected near the top of the abutment wall compared to the bottom of the abutment wall.

While traditional lateral earth pressure concepts do not completely explain the development of higher lateral earth pressures near the top of the abutment walls during the summer months, the other concepts explained above can potentially explain the observed variation of lateral earth pressure with depth. According to the bridge deck temperature distribution model proposed in Branco and Mendes (1993), the deck concrete on top of the girders is expected to experience a wider range of temperatures on most days due to the effect of environmental factors such as solar radiation, thermal convection at the concrete surface, wind, and thermal radiation. As such, the deck concrete, in comparison with the bottom of the girder, is expected to heat up faster and to a higher temperature as well as cool down quicker during the night. This difference in the range of temperatures is also expected to result in a slightly different magnitude of thermal expansion cycles, with larger magnitude cycles occurring near the top of the bridge in comparison with the bottom of the girder.

Since strain gauges were installed at three different depths within the bridge superstructure (girder and deck slab), it is possible to directly verify whether larger thermal expansion cycles occur near the top of the deck. For this purpose, the ratio of daily thermal strains between the top of the deck and bottom of the girder was determined. Figure 9.12 presents these results. For

reference, the approximate location of the strain gauges used in the analysis is depicted in the bottom right corner of the figure. Values greater than one in Figure 9.12 indicate that the top of the girder has experienced more thermal expansion than the bottom (in a 24-hour period), meaning that the top of the abutment walls have moved farther than the bottom. Furthermore, the opposite holds true for the few instances where the thermal expansion ratio is seen to fall below one.

Overall, the points near the top of the wall not only experienced larger displacement magnitudes, but also larger daily displacement cycles compared to the bottom of the wall. These two observations along with the potential effect of soil arching and variation of the abutment wall's rigidity with depth due to how it is connected to the girders can potentially explain why significantly higher earth pressures were recorded near the top of the abutment wall in comparison to the bottom of the wall.

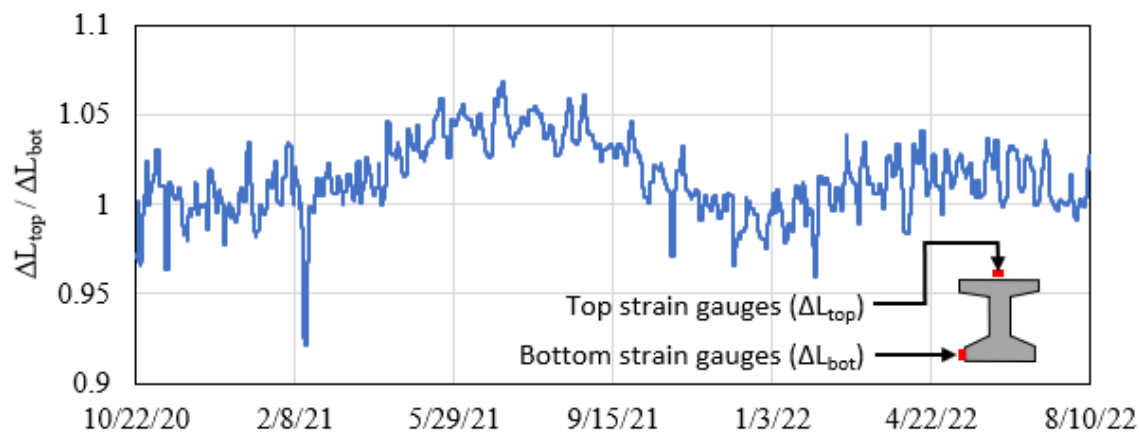


Figure 9.12: Time-history plot of ratio between thermal expansion of deck slab right above girder's top flange relative to bottom of girder (girder top-to-bottom thermal expansion ratio)

With the earth pressure data recorded during the monitoring period, it is possible to investigate the causes of the bridge asymmetric thermal expansion/contraction, as previously discussed in Section 9.5. Specifically, the lateral thrust (i.e., total force) acting on each abutment was estimated using the lateral earth pressures defined by the EPCs installed on each wall. The lateral thrust results are presented in Figure 4.13. For reference, the lateral thrust predicted using the conventional Coulomb (1776) and Rankine (1857) lateral earth pressure theories (considering the backfill friction angle of 42°) are also shown in Figure 9.13. The results indicate that the lateral thrust acting on both abutment walls reached values that were 2 to 2.5 times higher than Rankine's passive thrust estimate. However, these values are still below the value corresponding to Coulomb's passive thrust force. Moreover, it can be observed that the ratcheting phenomenon resulted in an increase of the average summer lateral thrust of approximately 25%, from summer 2021 to summer 2022.

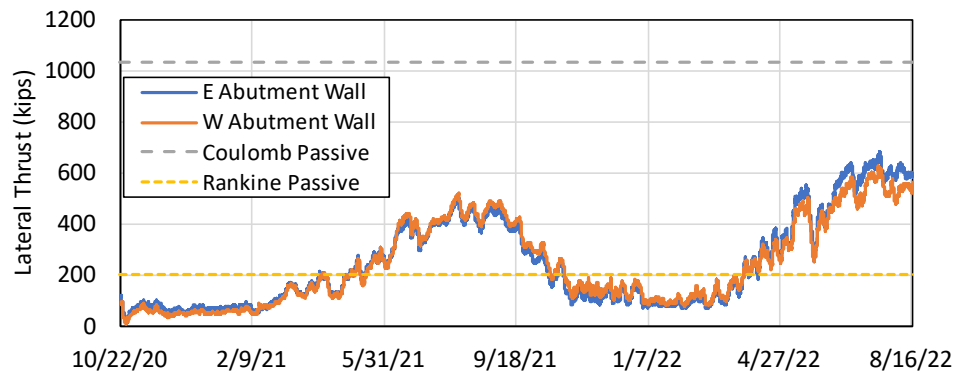


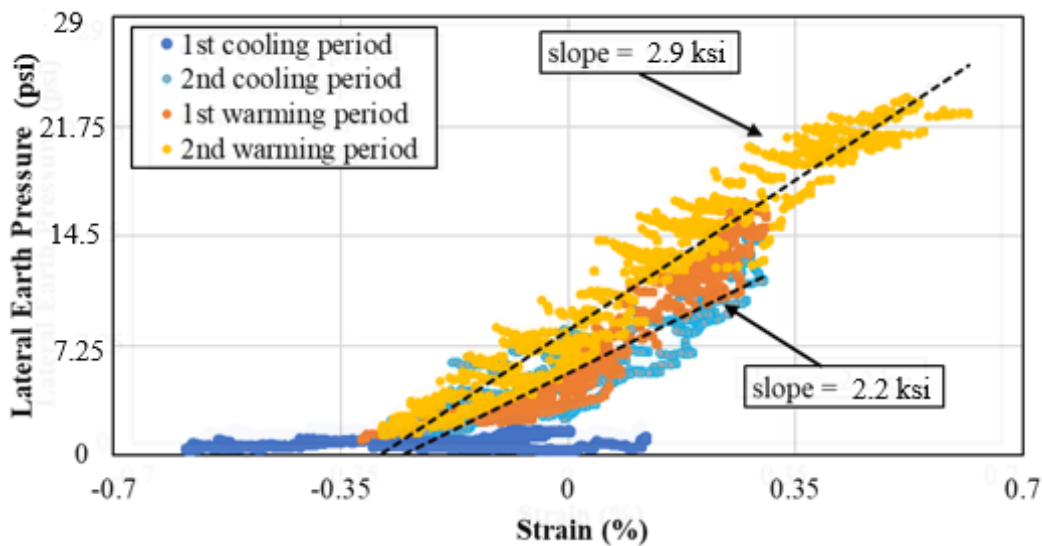
Figure 9.13: Time-history plot of lateral thrust force acting on abutment walls estimated from EPC readings

The results in Figure 9.13 also indicate that the time-history of lateral thrust corresponding to the backwalls of the west and east abutments are remarkably similar. Consequently, the difference between the ultimate resistance offered by the backfill on either end of the bridge is essentially negligible. This is revealing, particularly considering the asymmetric abutment wall displacement records discussed in Section 9.5. Consequently, the stiffness of the abutment backfills is expected to be notably different to result in a nearly identical amount of lateral thrust in response to different magnitudes of abutment wall movement. The horizontal soil extensometers installed at the mid-depth of each abutment wall (Figure 9.2) allow defining the relationship between the average lateral compression and extension of the backfill soil mass within 3.28 ft of the abutment walls and the lateral earth pressures acting at mid-depth of the abutment walls. Figure 9.14 displays the results of such an evaluation. To facilitate the discussion of observed trends, the data is grouped into warming and cooling periods. In this analysis, “warming period” refers to the period when the bridge primarily experienced thermal expansion (i.e., April to August) and the cooling period is when the bridge primarily experienced thermal contraction (i.e., October to March). In this analysis, positive strain measurements correspond to lateral compression of the backfill the approximate stiffness of the backfill material is defined for the two warming periods on record using linear regression.

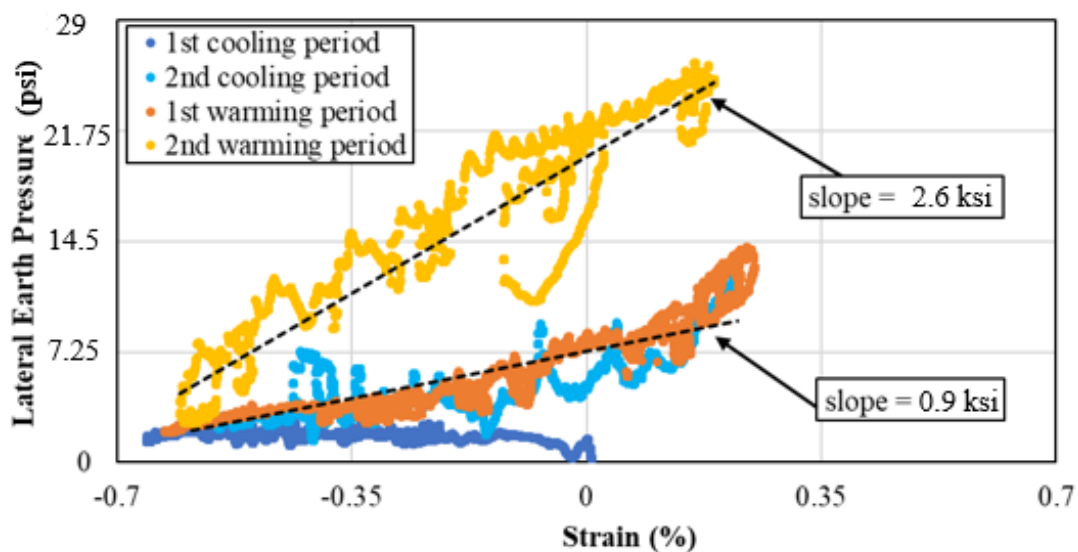
The seasonal stress-strain behavior presented in Figure 9.14 indicates that the stiffnesses of the abutment backfill in the east and west abutments are very different. For example, during the first warming period (orange markers), the predicted east abutment backfill stiffness (870.2 psi) was less than half that of the west abutment backfill (2.18 psi). While the stiffness of the east abutment backfill increased significantly over the second warming period (yellow markers), it was still slightly less than that of the west abutment backfill. The identified discrepancies in backfill stiffness are consistent with the bridge’s tendency for eastward thermal expansion during the warming period.

The results presented in Figure 9.14 also provide further evidence of ratcheting and the effect of cyclic lateral loading on the stiffness of the abutment backfill. Specifically, the results in Figure

9.14 show that during the second warming period (yellow markers), the stiffness of the east abutment backfill had increased by 200% and the stiffness of the west abutment backfill increased by 33% compared to the stiffness estimated for the preceding year. The results in the figure also indicate that the discrepancy in backfill stiffnesses between the east and west abutments decreased significantly from the first to the second year. Therefore, while such discrepancy in backfill stiffness is deemed to be a significant factor affecting the asymmetrical thermal expansion of the bridge, it is possible that such thermal response will become more balanced (i.e., symmetrical) over the long-term. This is considering that the increasing trend of backfill stiffnesses will lead to east and west backfill stiffness values becoming closer in magnitude.



(a)



(b)

Figure 9.14: Measured stress – strain behavior for abutment backfills at abutment wall mid-depth: (a) east abutment; and (b) west abutment (Note: positive strain values indicate backfill compression)

9.6. Abutment Backfill Settlements

In addition to the influence of thermal expansion/contraction cycles on increasing backfill lateral earth pressure, it is important to also understand their effect on the settlement of the abutment backfill. This is a relevant topic because backfill settlement may lead to the development of a bump at the end of the bridge when flexible approach pavements are used or lead to a faster rate of fatigue and cracking in rigid approach slabs. The next section presents observations on the settlement of abutment backfills at China Creek Bridge.

In this section, the data collected from the four backfill settlement sensors (see Figure 9.1 and Figure 9.2) is evaluated. Figure 9.15 displays the settlement data collected by these sensors. Unlike most other data presented herein, the settlement data was defined in reference to the sensor readings taken at the start of the monitoring period (October 2020) as opposed to the time of sensor installation (June 2020) to facilitate a side-by-side comparison. However, during the period between June 2020 to October 2020 (not included in Figure 9.15), the west abutment sensors recorded settlements of 1.18 and 1.97 in, while the settlements recorded by the east abutment sensors were 0.98 and 1.38 in of settlement. The higher on average settlement recorded for the west abutment backfill from June to October 2020 could be attributed to the larger active direction displacement of the west abutment wall compared to the east abutment wall.

Focusing on the backfill settlement data shown in Figure 9.15, it is observed that the four sensors recorded settlements ranging from 0.12 to 0.32 in over the monitoring period. In this dataset, the two highest settlement magnitudes were recorded by the sensors installed closest to the abutment wall (approximately 2.6 ft away), while the sensors installed nearly 5.9 ft away from the abutment wall recorded smaller settlement magnitudes. The measurement of higher magnitude settlements closer to the abutment wall is consistent with the findings of Walter (2018) based on large-scale experimental testing of integral abutments. It is possible that the partial collapse of the soil near the abutment wall (within the active wedge) may have led to a higher rate of settlement in the vicinity of the abutment walls in comparison to points farther away.

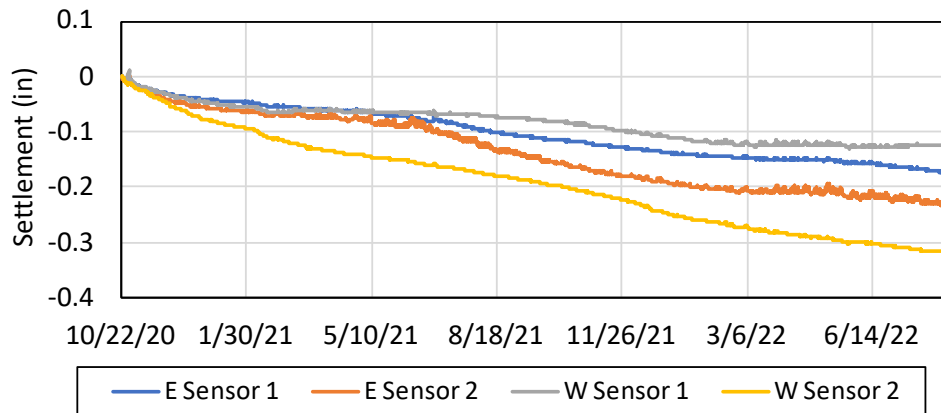


Figure 9.15: Time-history of settlement data collected from four backfill settlement sensors, calculated relative to start of monitoring (10/22/2020)

While the data collected during the monitoring period indicates that the settlement in both abutments increases with time, on a smaller time-scale some of the backfill settlement was observed to be recovered (i.e., resulting in soil heaving). A close-up of the settlement data measured by one of the east abutment settlement sensors along with the east abutment wall displacement is shown in Figure 9.16. The results in this figure indicate that the abutment wall displacement toward the backfill is accompanied by a decrease in settlement (heaving) such that there is an overall decrease in settlement during the first four days of this data set. However, the overall trend suggests that the lateral wall displacements in the passive direction do not cause as much heaving as abutment wall displacements in the active direction cause backfill settlement. Therefore, the settlement of the abutment fill tends to increase over time.

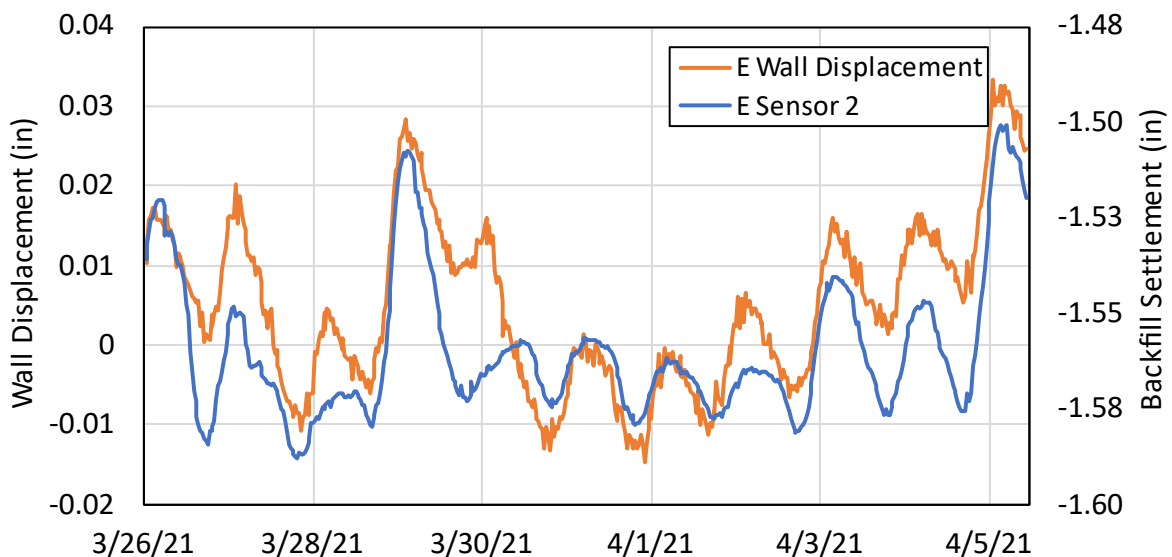


Figure 9.16: East backfill settlement and wall displacement during a 10-day period in October 2021

While the settlement sensors do not indicate the extent of the backfill area affected by settlement, it is apparent that at least a third of the reinforced concrete approach slabs are no longer resting in direct contact with the abutment backfill soil. This loss of vertical support results in larger shear stresses and bending moments being experienced by the approach slabs, possibly leading to damage and cracking if not properly designed. Despite the increased loading of the approach slabs, no sign of damage was observed on the approach slabs during the visual inspection of the structure. This is because of the conservative assumption, at the design stage, that no vertical support would be provided by the backfill. However, the settlement observed is undesirable and signifies an area with a large potential for improvement. Such improvements may be achieved by adopting materials and construction techniques that help mitigate backfill settlement, reduce loads on the approach slabs and increase the service life of the structure.

9.7. Conclusions on the Analysis of China Creek SIAB Soil-structure Interaction Data

This chapter presents the results from nearly two years of monitoring a pilot Semi-Integral Abutment Bridge (SIAB) in North Texas. Through the comprehensive instrumentation program developed for this study, the thermal expansion and contraction of the bridge superstructure, displacement of the abutment walls and soil-structure interaction within the abutments were successfully captured. These findings facilitate understanding the effect of soil-structure interaction on the performance and behavior of SIAB with unreinforced granular abutment backfills and can be utilized to improve the design and long-term performance of future SIAB structures.

The following conclusions were drawn from the analyses of the data presented in this chapter:

- The abutment wall movements in response to the thermal expansion/contraction of the bridge superstructure can be highly asymmetrical even if the structure is symmetric in geometry. The time-history data for the abutment wall positions indicated highly asymmetric displacements of these components. Compared to the east abutment wall, the west abutment wall experienced significantly more displacement away from the abutment backfill due to thermal contraction of the bridge during the winter months. However, more displacement occurred in the east abutment compared to the west abutment during the summer months.
- The position of the neutral thermal expansion point in SIAB can change seasonally and is rarely in the midpoint of the bridge. Consequently, in China Creek Bridge, it was found that it would be more realistic to use 70% of the total bridge length for estimating the range of movement at the abutment walls due to thermal expansion/contraction of the bridge as opposed to half the bridge length.

- The recommended Coefficient of Thermal Expansion (CTE) by AASHTO (2018) was found to be adequate for predicting the thermal expansion of the instrumented structure. The 90.2-ft-long bridge superstructure experienced nearly 0.47 in of thermal expansion/contraction over the monitoring period, with a CTE of $9.0 \times 10^{-6}/^{\circ}\text{C}$, falling within the expected range for normal weight concrete structures.
- Semi-integral bridge abutment backfills were found to be susceptible to ratcheting caused by the cyclic movement of the abutment walls. In China Creek Bridge, the maximum annual backfill lateral earth pressures were seen to increase by approximately 20% over a year reaching values as high as 43.5 psi.
- Lateral earth pressures do not necessarily increase with depth in semi-integral bridge abutment backfills. Through the analysis of China Creek Bridge data, it was concluded that the larger displacement cycle magnitude near the top of the abutment walls compared to the bottom of the walls as well as the larger rigidity of the abutment wall in the top two-thirds of the wall can cause the lateral earth pressures to be significantly higher near the top of the wall, compared to the bottom of the wall.
- Ratcheting in SIAB can also affect the wingwalls and abutment caps. The earth pressure data collected from China Creek Bridge indicates that the abutment caps and wingwalls also experienced significant lateral earth pressure increase during the summer months. EPCs installed on abutment caps and wingwalls indicated that the lateral earth pressure acting on these components changes seasonally, similar to the abutment walls, and that they are also affected by ratcheting.
- The asymmetric displacement of the SIAB abutment walls was attributed to the difference in stiffness of the abutment elements (e.g., backfill) between the two abutments. In China Creek Bridge, it was observed that the lateral thrust acting on the east and west abutment walls matched very closely during the monitoring period despite the significant difference in abutment wall movement records between the two abutments.
- The lateral thrust acting on semi-integral bridge abutment walls can exceed Rankine's passive thrust. In China Creek Bridge, the lateral thrust acting on the abutment walls reached approximately 60% of Coulomb's passive thrust estimate by the end of summer 2021. It is possible that the lateral thrust will continue to increase in the coming years as more ratcheting occurs.
- The close match between the two abutments' lateral thrust data and mismatch between the abutment walls' displacement data revealed a discrepancy between the stiffnesses of the abutment backfills. The relatively stiffer west abutment backfill was identified as the

cause of the bridge's tendency for eastward expansion during the spring and summer months.

- The stiffness of the semi-integral bridge abutment backfills can significantly change over time due to ratcheting. In China Creek Bridge, the measured seasonal stress-strain behavior of the abutment backfills indicated that the west abutment backfill was stiffer than the east abutment and both abutment backfill stiffnesses increased each year. The data also indicated that the difference between the abutment backfill stiffnesses decreased each year and it is therefore possible that the thermal expansion of the bridge will occur more symmetrically in the long-term.
- Unreinforced granular backfills in SIAB are highly susceptible to settlement due to daily and seasonal cyclic abutment wall displacements. In China Creek Bridge, the settlement of the abutment backfills was measured using four settlement sensors, which recorded 30 to 2.28 in of settlement over the monitoring period. Some asymmetry was observed as well, indicating that more settlement occurred within the west abutment backfill. This is likely due to the larger active direction displacement history of the west abutment wall compared to the east abutment wall.
- The settlement records indicated that backfill settlement and heave occur each day as the abutment walls move away and toward the backfill because of the thermal expansion/contraction of the superstructure. The magnitude of heave has typically been smaller than the magnitude of settlement, leading to increased settlement over time. While the observed settlement rate in China Creek Bridge has changed seasonally, no signs of abutment backfill settlement reaching an asymptotic value has been observed during the monitoring period.
- Abutment backfill settlement can lead to a partial loss of vertical support for the approach slabs in SIAB. In China Creek Bridge, the settlement data indicates that at least a third of the approach slabs are no longer vertically supported by the abutment backfills and the size of the void continues to increase with time. As the void grows larger, the magnitude of stresses acting on the approach slabs due to traffic loads increases as well. Consequently, the loss of vertical support for the approach slabs may result in a higher rate of fatigue and deterioration, thereby affecting the service life of the structure.

Chapter 10. Analysis of Foundation Monitoring Data from China Creek Semi-integral Bridge

10.1. Introduction to the Analysis of China Creek SIAB Foundation Monitoring Data

Semi-Integral and Integral Abutment Bridge (SIAB/IAB) construction is becoming increasingly common, both in the USA and worldwide. The main characteristic of these bridges is the elimination of expansion joints at the ends of the deck and in between spans. However, the abutment wall and abutment caps are not integrally connected to allow the superstructure to move independently from the substructure. Unlike SIAB, IAB are continuous single- or multi-span bridges in which the superstructure is constructed integrally with the substructure.

The increasing popularity of these structures can be attributed to the number of issues associated with deck expansion joints. Deck expansion joints are typically used to alleviate stresses in the structure caused by phenomena associated to shrinkage, creep, thermal expansion/contraction, and differential settlement of piers and abutments (Burke, 2009). However, as noted in Purvis and Berger (1983), several problems are associated with deck expansion joints, including the high rate of wear and tear, exposure of the structure to harmful chemicals and relatively high cost of initial construction and maintenance. Therefore, many transportation agencies throughout the world have opted for other alternatives such as SIAB and IAB.

A brief look at the SIAB and IAB details from within the United States alone reveals significant differences among the designs adopted in each state. For example, according to Maruri and Petro (2005), while many states require H-pile foundations oriented toward the weak bending axis for IAB to increase flexibility, some states require them to be oriented toward the strong axis and some even allow the use of drilled shafts, which are typically more rigid than H-piles. Moreover, while lateral loading is considered in the design of IAB foundations, such loading has typically not been considered in the design of SIAB foundations. These discrepancies are further reflected in the development of instrumentation programs implemented to monitor the behavior of IAB and SIAB. While long-term studies on the behavior of IAB foundations could be identified (Ooi et al, 2010; Lawver et al, 2000; Abendroth et al, 2005), the authors were not able to find studies on lateral loading of SIAB foundations in the technical literature.

Despite the lack of focus on possible lateral loading of SIAB foundations, a prior investigation of the behavior of a pilot SIAB in Texas, described in Mofarraj and Zornberg (2022), found evidence of lateral movements in the abutment caps though the magnitude of the loads remained unknown. Applying the lessons learned from the pilot instrumentation program, a more comprehensive bridge monitoring program was developed for a second SIAB in Texas involving over 70 sensors and including a dedicated foundation monitoring system.

This chapter provides an analysis of the data obtained from monitoring lateral deformations of the foundation elements in China Creek SIAB and characterizes the deflection and lateral loads acting on the bridge foundations due to thermal expansion and contraction of the superstructure.

10.2. Description of China Creek Bridge

China Creek SIAB is a state highway bridge built in 2020, outside Wichita Falls, TX. A schematic of this bridge is shown in Figure 10.1. The bridge is 90.2-ft-long and has two traffic lanes. The superstructure includes prestressed concrete I-beam girders, precast concrete panels between the girders, and a cast-in-place reinforced concrete overlay. The abutment walls are integrally connected to the deck and are 4.1 ft deep. The bridge is supported by four 36.1-ft-deep drilled shafts on each side that are 2.95 ft in diameter each. The deck connects to the approaching roadway via 19.7-ft-long reinforced concrete approach slabs that are structurally connected to the deck and abutment wall on one end and rest on sleeper slabs on the other. The gap between the abutment wall and abutment cap was filled with a 1.97-in-thick closed cell foam as displayed in Figure 10.1.

While forming the abutment walls, a very stiff closed cell foam was used on the inner facing of the abutment walls. Although most of this material was removed after the construction, the portion between the abutment cap and abutment wall was left in place (Figure 10.1). Considering the stiffness of this material, it was expected that the contraction of the deck due to shrinkage and changes in temperature would likely contribute to lateral deflection of the drilled shafts. Furthermore, the development of friction and shear at the base of the elastomeric bearing pads due to expansion and contraction of the deck may also induce lateral loads acting on the drilled shafts in spite of the semi-integral nature of the bridge (Han et al., 2019).

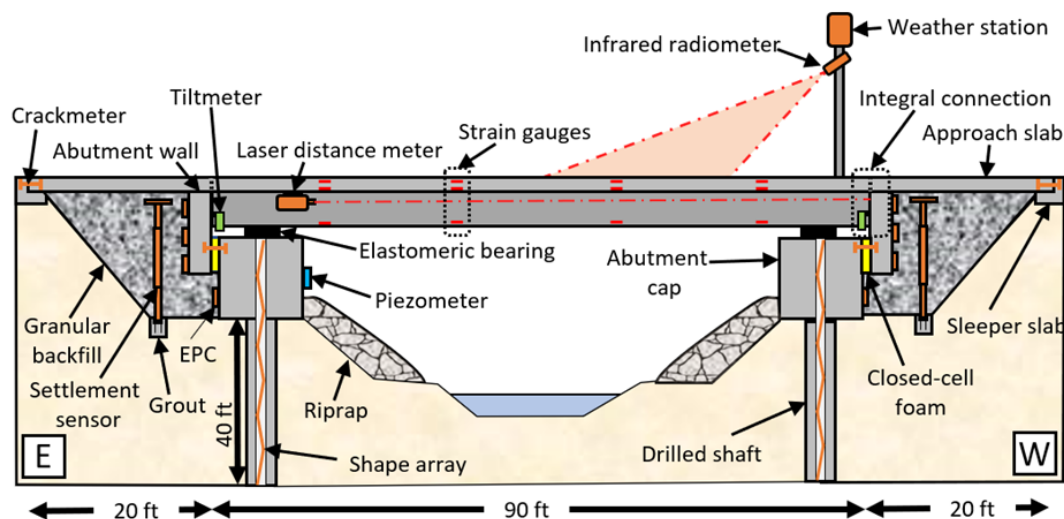


Figure 10.1: Schematic of China Creek SIAB and installed sensors (EPC: Earth Pressure Cell)

10.2.1. Geotechnical Characterization of the Foundation Soil

Prior to bridge construction, 39.4-ft-deep borings were conducted on each side of the bridge for subsurface characterization. The materials recovered from these borings on the top 13.1 ft revealed the presence of lean soft clay deposits. Specifically, the material recovered from 7.2- to 13.1-ft-deep were described as very soft and saturated. Below 13.1 ft, the recovered materials involved mainly stiff and dry lean clay, while the soil below 22.9 ft appeared very hard and blocky.

In addition to the physical characterization of the in-situ soils, a series of Texas Cone Penetration (TCP) (TEX 132-E, 1999) tests were performed at 4.9-ft intervals. A TCP count of 50 (maximum blow count) was reached for depths below 13.2 ft, making it a well-suited bearing stratum for drilled shaft foundation. However, the top 13.2 ft of the boring logs consisted of soils with TCP counts ranging from 3 to 7, which is associated with soft to medium soils, according to Touma and Reese (1972). Considering the characteristics of this top soil layer, a decision was made to protect the drilled shafts from side-wall caving using 13.2-ft-long steel casings.

10.3. Instrumentation Overview

During the construction of China Creek Bridge, over 70 sensors were installed to monitor various aspects of bridge behavior and performance. The installed sensors are shown in Figure 10.1.

The lateral displacements of drilled shafts were obtained using shape arrays (Measurand SAAV), which were installed during bridge construction within the drilled shafts. They consist of a series of rigid segments connected with joints that allow movement in any direction but prevent twisting. Each segment is instrumented with a triaxial Micro-Electro-Mechanical Systems (MEMS) gravity sensor for measuring tilt in two perpendicular directions. The sensor data is used to calculate the relative position of each joint compared to other joints. Therefore, by knowing the absolute position of one joint, the position of all other joints can be calculated. In this report, the bottom of the drilled shaft is assumed stationary under normal operating conditions for calculating the absolute displacement of the abutment caps. The potential errors associated with this assumption will be discussed in the next section. According to the manufacturer, this instrument has a precision of ± 0.02 in (0.5 mm) for a 98.4-ft array.

Figure 10.2 shows the installation of the drilled shaft rebar cage (fitted with a 2.76-in PVC conduit) as well as the installation of the shape array in one of the drilled shafts of China Creek Bridge. The shape arrays used in this study consist of 22 1.6-ft-long segments, each of which provide a 3-D deformation profile of the drilled shafts. While continuous data collection began in October 2020, initial sensor readings were recorded immediately after installation of the shape arrays in June 2020 and before placement of the bridge girders.

To capture the changes in ambient air temperature at the bridge site, a ClimaVue50 weather station was installed at the site. In addition, to measure the thermal expansion contraction of the bridge, 15 concrete strain gauges (Geokon model 4200 and 4151) were installed on the bridge superstructure to measure deck and girder strains across the length of the bridge. Lastly, the displacement of the semi-integral abutment walls relative to the abutment caps were measured using a set of Geokon model 4420 crackmeters. These crackmeters essentially measure the change in the width of the expansion joint between the abutment caps and abutment walls, which can also be used to estimate the shear strains on the elastomeric bearings beneath the girders.



(a)



(b)

Figure 10.2: Shape array installation: (a) installation of drilled shaft rebar cage fitted with a shape array casing; and (b) installation of shape array inside casing after abutment caps were formed

10.4. Instrumentation Data

The time-history of the ambient air temperature data collected at the bridge site is presented in Figure 10.3. As can be seen, the ambient air temperature over the monitoring period ranged from -4°F to 113°F . Seasonally, it can be seen that daily variation of temperature during the summer months is 59°F to 68°F . On the other hand, during the winter months, the ambient air temperature has changed by 68°F to 86°F in a given day. The sharp decrease in ambient air temperature in February 2021 was due to an extreme weather event (winter storm Uri) that affected the entire State of Texas as well as the rest of the country and resulted in nearly a week of subfreezing temperatures and record snowfall events in this area.

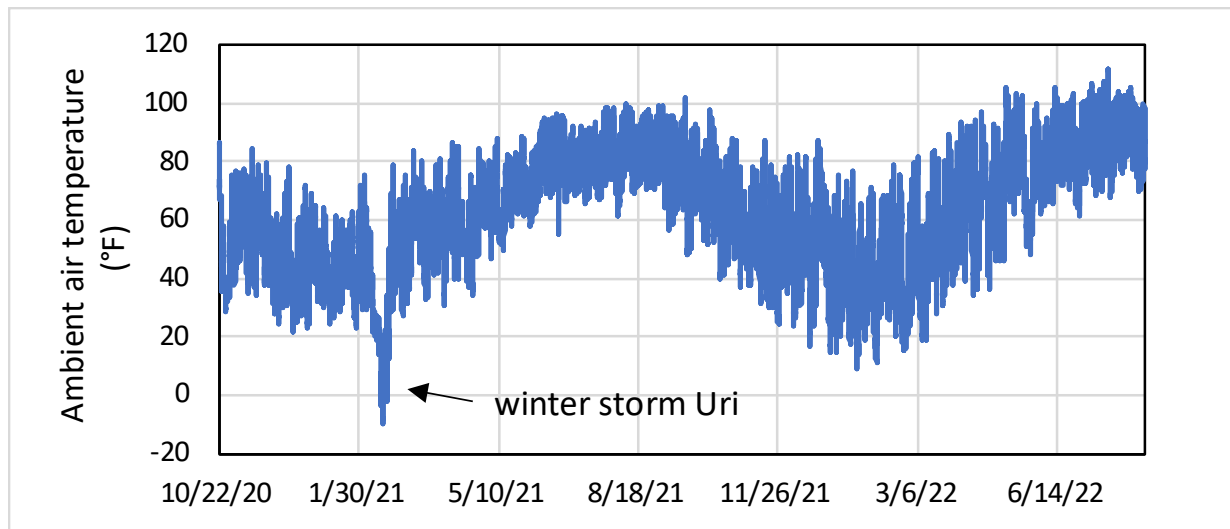


Figure 10.3: Time-history of ambient air temperature data collected using on-site weather station

The daily and seasonal changes in ambient air temperature have expectedly resulted in thermal expansion/contraction of the bridge. The thermal expansion/contraction of the bridge was calculated using a series of strain gauges installed on one of the bridge girders. The time-history of the thermal expansion/contraction of the bridge is shown in Figure 10.4. In this plot, each point indicates how much the length of the bridge has increased/decreased relative to the initial length of the bridge in July 2020. For example, the length of the bridge increased by up to 0.14 in, in summer 2021, and decreased by up to 0.35 in, in winter 2021, relative to its initial length.

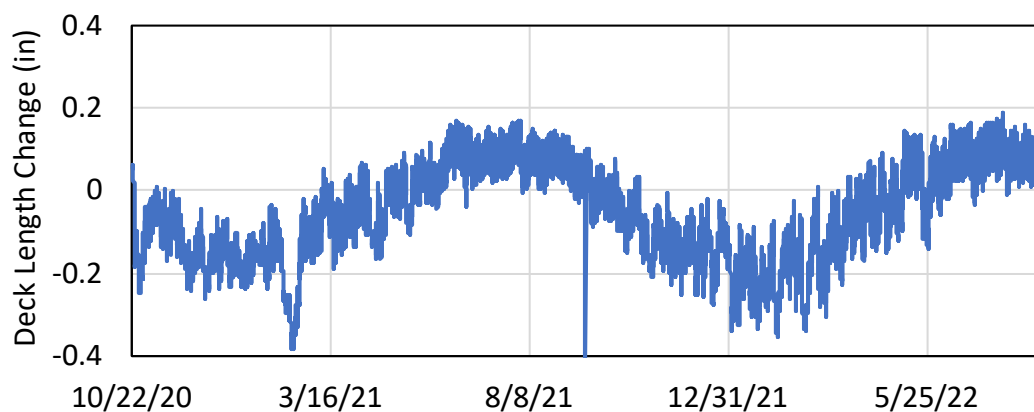


Figure 10.4: Time-history of changes in deck length (deck thermal expansion/contraction)

Because the deck and girders are not rigidly connected to the abutment cap and foundations in SIAB, it is expected that the thermal expansion/contraction of the bridge results in opening/closing of the expansion joints between the abutment caps and abutment walls. The changes in the width of these expansion joints was successfully captured using crackmeters. The

crackmeter data is presented in Figure 10.5. The presented data shows the change in the joint width relative to the initial width of the joints. As such, positive values indicate that the distance between the abutment wall and abutment cap has increased, and negative values show the opposite. In addition, the crackmeter readings also indicate the shear displacement of the elastomeric bearings (see Figure 10.1). In this bridge, the bearing shear is transferred to the abutment caps and can cause lateral loading of the foundations. Furthermore, zero crackmeter readings indicate contact between the abutment wall, expansion joint materials (stiff geofoam) and abutment caps, and negative readings indicate compression of the expansion joint materials. As can be seen, the change in the width of the expansion joints does not occur symmetrically in this bridge. For example, during the winter months, the east abutment expansion joint width has returned to its original width (zero crackmeter readings) while the negative values recorded by the west abutment crackmeter indicate compression of the geofoam installed at the joint. In either case, the crackmeter readings indicate that there has been contact between the abutment cap and abutment walls due to contraction of the bridge in the winter months, which can also lead to lateral loading of the foundations.

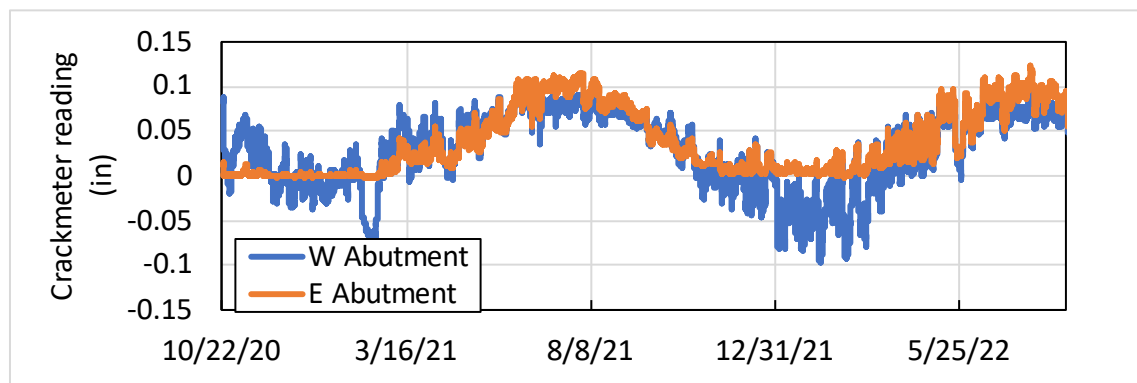


Figure 10.5: Time-history of change in expansion joint width between abutment caps and abutment walls measured by crackmeters

The time-history of the abutment cap displacement data is plotted in Figure 10.6. This data was measured using the shape arrays installed in the drilled shafts. The displacement values indicate changes in position of the abutment caps compared to their initial position at the time of construction. As such, positive values in this plot indicate displacement away from the abutment backfill and negative values indicate the opposite.

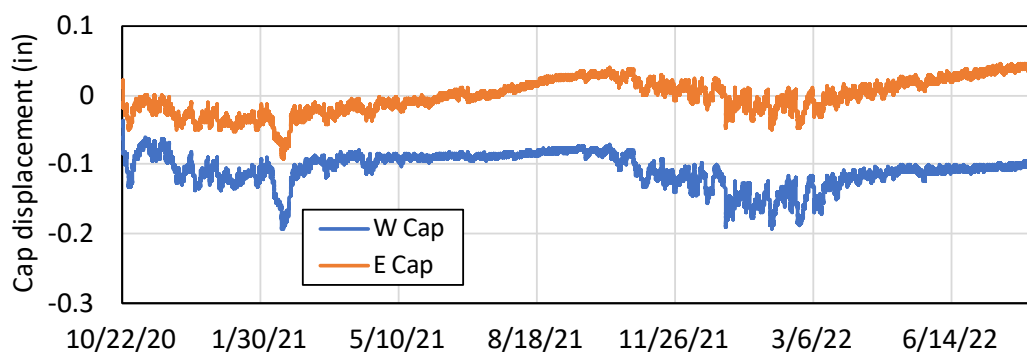


Figure 10.6: Time-history of abutment cap displacement data measured by drilled shaft shape arrays

As the shape array data shows, the abutment caps are moving everyday in response to the thermal expansion/contraction of the bridge. However, the abutment cap movements are highly asymmetrical. For example, during the winter storm event of February 2021, the east abutment cap moved approximately 0.08 in toward the center of the bridge, while the west cap moved approximately 0.2 in toward the center of the bridge, relative to their initial position at the time of construction. Additionally, it can be seen that overall, the west abutment cap has moved farther away from its original position compared to the east abutment cap at all instances. Seasonally, it can be seen that the east abutment cap has experienced movements toward the backfill during summer 2021 and 2022, while the west abutment cap has always stayed in a position closer to the center of the bridge compared to its initial position. A similar asymmetric response to thermal expansion/contraction of the bridge was also observed during the assessment of backfill lateral earth pressures described in Section 9.5.

Overall, it appears that the west drilled shafts have experienced larger displacements compared to the east drilled shafts during the periods of bridge contraction (e.g., winter months). In contrast, the east drilled shafts have experienced larger displacements during the periods of bridge expansion compared to the west drilled shafts (e.g., summer months).

To help understand the shape array and crackmeter measurements better, a sketch of changes in the abutment area at the time of construction as well as when the abutment walls move toward or away from the abutment backfill is shown in Figure 10.7.

As shown in Figure 10.7(b), the expansion joint width increases during bridge expansion (positive crackmeter readings), which implies that the shear stress in elastomeric bearings increases and causes lateral deflection of the drilled shafts toward the abutment backfill. On the other hand, during bridge contraction (Figure 10.7[c]), the abutment wall makes contact with the abutment cap and the lateral loading applied to the abutment caps would be either equal to the contact forces alone or the sum of the contact forces and the bearing shear (if the expansion joint material is compressed during contact). Both cases have been observed in this project. For example, during the winter storm of February 2021, the east abutment cap moved by 0.08 in,

while the expansion joint width remained unchanged relative to the time of construction. This implies that the east abutment cap moved because of the contact forces between the east abutment cap and wall but no bearing shearing was applied. On the other hand, during the same period, the west expansion joint width decreased by 0.08 in and the abutment cap moved by 0.2 in due to bridge contraction. This observation implies 0.08 in of shear displacement for the west bearings in addition to the contact forces between the west abutment cap and wall.

The cyclic lateral loading of SIAB foundations is typically not considered in their analysis and design. In fact, no prior reports of such behavior have been found in the available literature. However, as demonstrated by the shape array data, SIAB foundations can also experience cyclic lateral loading in response to the thermal expansion/contraction of the bridge superstructure. In the next section, the data collected from the shape arrays and crackmeters are further analyzed to help understand the interaction between the superstructure and the foundation elements and the implications of this interaction on the long-term performance of SIAB.

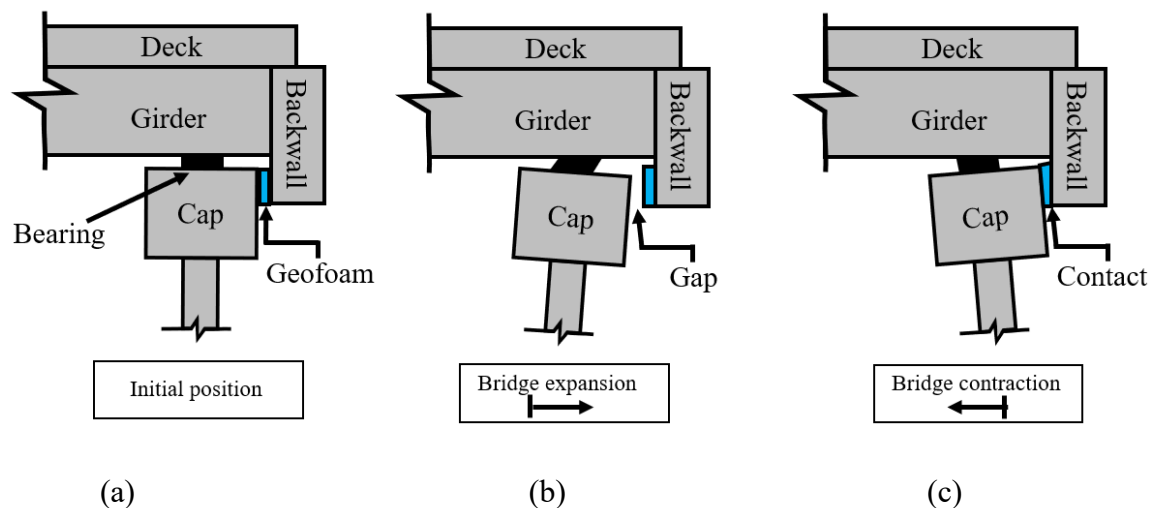


Figure 10.7: Sketch of changes in abutment area in response to bridge thermal expansion/contraction: (a) initial position; (b) bridge expansion; and (c) bridge contraction

10.5. Analysis of Drilled Shaft Behavior

As noted earlier, the deflection profile of the drilled shafts is recorded using the installed shape arrays. The deflection profile of the drilled shafts can be used to estimate the curvature and bending moment profile of the drilled shafts as well. Two instances of the deflection, curvature and moment profile for the west drilled shaft are shown in Figure 10.8.

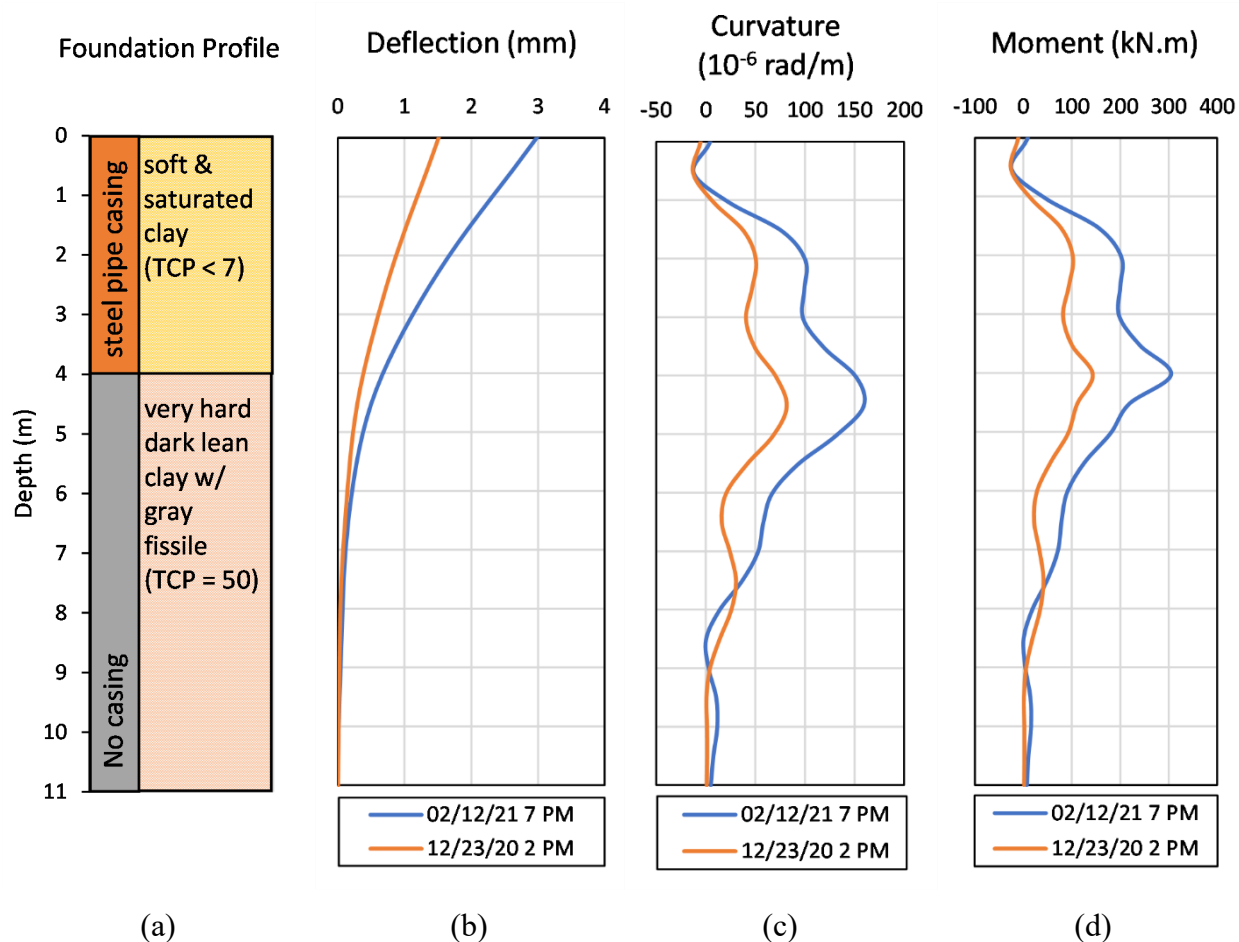


Figure 10.8: West abutment drilled shaft profiles on two different dates: (a) subsurface profile; (b) lateral deflection profile; (c) curvature profile; and (d) flexural moment profile

The shape of the deflection profiles shown in Figure 10.8 resembles short pile behavior (e.g., Broms, 1964) and indicates that the foundation is most likely rotating about a point within the hard clay layer. While determining the position of this point can slightly affect the displacement estimates for all points along the drilled shafts (typically by less than 0.004 in), it will not affect the calculation of curvature and bending moments, which is the primary focus of this section. To investigate the effect of thermal expansion/contraction of the bridge on the foundations, a Python code was developed to analyze each recorded deflection profile and calculate the maximum bending moments acting on the east and west abutment drilled shafts.

The time-history of the maximum bending moments acting on the drilled shafts is presented in Figure 10.9. This dataset includes the time-histories of the maximum bending moment in both directions (bending toward and away from the backfill) because the direction of the lateral loading changes depending on the season.

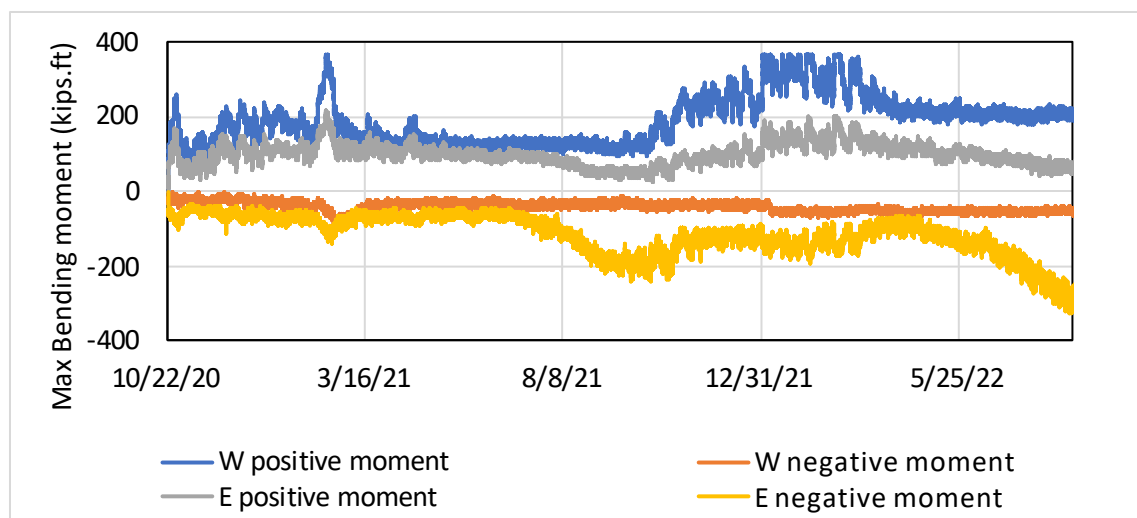


Figure 10.9: Maximum bending moment acting on drilled shafts (positive bending moments indicate bending toward bridge center as sketched in Figure 10.7)

As shown in Figure 10.9, the maximum positive bending moment acting on the drilled shafts has been typically larger than the negative bending moments when the cap was pushed toward the center of the bridge (sketched in Figure 10.7[c]). For example, because the west drilled shaft was primarily pushed toward the center of the bridge, the positive moments were always larger than the negative moments and the largest positive bending moments were experienced during the winter months when the bridge has experienced thermal contraction. On the other hand, the negative bending moments were typically larger than the positive bending moments when the abutment caps were pushed toward the backfill (sketched in Figure 10.7[b]). This case is primarily observed for the east drilled shafts during the summer months when the abutment cap was pushed toward the backfill. It can be seen that during both summers, the positive bending moment for the east drilled shaft decreased and the magnitude of the negative bending moments increased.

Overall, the data presented in Figure 10.9 confirms that SIAB foundations can experience significant cyclic lateral loading in response to the thermal expansion/contraction of the structure. This is considered an important finding with major design and analysis implications because SIAB foundations are typically only designed for the axial load bearing capacity. However, as the data shows that only a few millimeters of movement at the abutment caps in response to the thermal expansion/contraction of the bridge has resulted in the development of very large bending moments. For reference, the estimated cracking moment for the drilled shafts is 361.4 kip.ft, which appears to have been reached on several instances for the west drilled shaft according to the analysis performed.

There are certain caveats to the analysis such as the fact that the cracking moment is determined based on the 28-day compressive strength of the lab-tested concrete samples, which can potentially differ from the actual strength of the drilled shaft concrete after several months or

years of curing in field conditions. Another caveat is that the analysis is based on the finite difference analysis of the discrete measurements of the deflection profile by the shape arrays, which is affected by the precision of the sensors as well as the limitations of calculating the curvature profile of the drilled shafts (second order differential of the deflection profile) using finite difference method. Therefore, the observed trends and estimated values in Figure 10.9 are primarily discussed qualitatively in this study and issues such as cyclic fatigue and cracking potential of the drilled shafts will not be discussed based on this data.

Considering the abutment cap data (Figure 10.6 and Figure 10.9) in conjunction with the thermal expansion/contraction and crackmeter data (Figure 10.4 and Figure 10.5), it can be seen that the response of the drilled shafts to thermal expansion/contraction of the bridge has slightly changed in the second year of monitoring in comparison to the first year. For example, it can be seen that the bridge thermal expansion/contraction and the abutment cap crackmeter records (Figure 10.4 and Figure 10.5) are virtually similar between the summers of 2021 and 2022. However, neither of the abutment caps returned to the same position in summer 2022, as summer 2021. As shown in Figure 10.6, the west abutment cap has moved an additional 0.02 in toward the center of the bridge (eastward movement) from August 2021 to August 2022. Similarly, the east abutment cap has also moved by 0.01 in toward the abutment backfill (eastward movement) from August 2021 to August 2022. The eastward movement of both drilled shafts has also resulted in a 50 to 60% increase in the maximum bending moments of the east and west drilled shafts, from summer 2021 to summer 2022. This signifies that, much like the soil-structure interaction in IAB and SIAB abutments, the interaction of the superstructure with the foundations is also a long-term phenomenon and foundation loads in SIAB can actually increase over time and potentially cause long-term performance issues.

Another observation regarding the foundation behavior is the continued displacement of the east abutment cap toward the abutment backfill in summer and fall 2021, despite the decreasing trends in the expansion joint width, which is proportional to the bearing shear stress. As sketched in Figure 10.7(b), during the period of August to October 2021, the lateral load transferred to the abutment caps is through shearing of the elastomeric bearings. Therefore, it is reasonable to expect that the decreasing trend in the expansion joint width from August 2021 to October 2021 would result in the reduction of lateral loads applied to the east abutment cap during this period as well. Moreover, it is often expected that smaller lateral loads result in smaller lateral deflection of the drilled shafts. However, the instrumentation data indicates that the abutment cap continued to move farther in the direction of the backfill.

To provide a better view of this behavior, the time-history of the east abutment cap displacement and crackmeter readings is shown in Figure 10.10. Looking at the periods highlighted using orange and blue rectangles (periods 1 and 2), it can be seen that the abutment cap moved farther toward the backfill when the expansion joint width increased (increasing bearing shear) and moved away from the backfill when the expansion joint width decreased (decreasing shear).

However, a close look at the period highlighted using a green rectangle (period 3) reveals that during this period, the expansion joint width has slightly changed during the highlighted days, but it has remained relatively constant on average and so has the bearing shear. On the other hand, the abutment cap has continued to move toward the east cap during this period. Many other similar periods can be identified through a close look at the data presented in Figure 10.10. It is believed that the key to understanding this behavior is in understanding the response of clay deposits to cyclic loading by deep foundations.

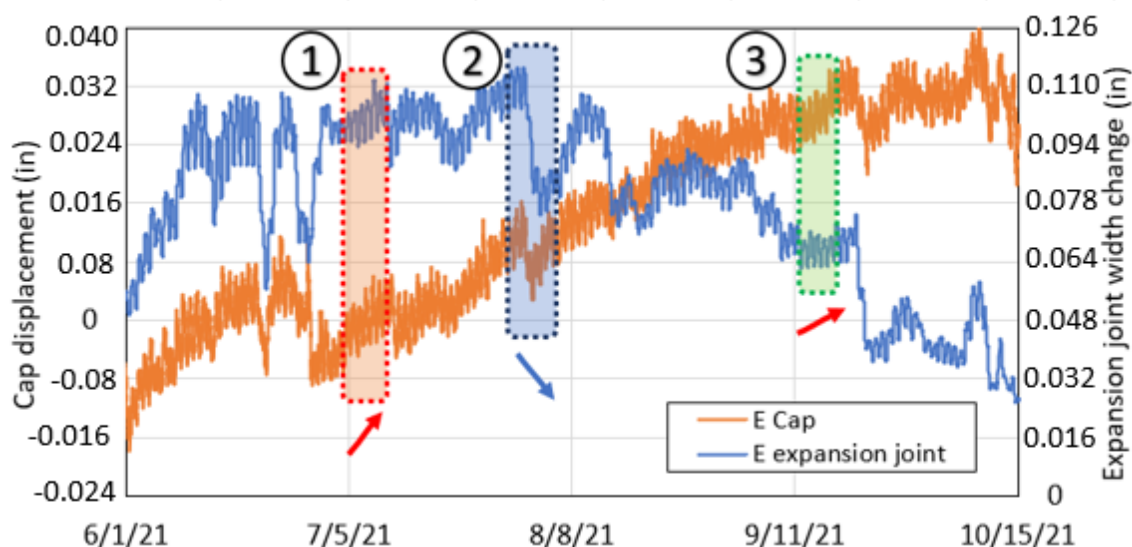


Figure 10.10: Time-history of changes in east abutment cap position and expansion joint width (arrows indicate abutment cap general displacement direction during highlighted periods)

The soil resistance-deflection behavior of clays under static and cyclic loading conditions has been studied extensively by researchers in the past (Matlock, 1970; O'Neill and Dunnavant, 1984; Reese and Welch, 1975). A well-known method for analyzing the soil response to lateral loading involves modeling the foundation soils as a series of layers that provide the resistance (P) for a specific level of deflection (y). This method is also conventionally known as the “p-y analysis method.” To understand the observed behavior in Figure 10.10, the p-y analysis framework based on the typical behavior of cyclically loaded clays (e.g., Matlock, 1970) can be used to qualitatively assess the underlying mechanisms.

To aid this discussion, a sketch of the p-y behavior occurring under each of the three highlighted conditions in Figure 10.10 is presented in Figure 10.11. In Figure 10.11(a), the typical response of the foundation soils to a cyclic loading regime that increases in magnitude over time (period 1 in Figure 10.10) is shown. In this case, part of the pile deflection is due to the accumulation of plastic strains during daily thermal expansion/contraction and part is due to the increasing soil resistance demand from the lateral load increase, which require larger soil deflection to provide enough resistance. Figure 10.11(b) shows the effect of load reduction on the lateral deflection of the drilled shafts (period 2 in Figure 10.10). In this period, the lateral deflection of the pile is

slightly reduced due to the reduction in the lateral load, however, the decrease in lateral deflection and the decrease in the load would not be proportional. Figure 10.11(c) shows the typical response of a clay deposit experiencing cyclic loads of similar magnitude (period 3 in Figure 10.10). As can be seen, repeated loading can result in the accumulation of plastic strains in the clay deposit and as the number of cycles increases, larger deflections are needed to provide the same level of resistance to the applied loads. Therefore, the behavior described above can explain why the east abutment cap has continued moving toward the abutment backfill, despite the overall decreasing trend in the bearing shear force during periods such as August to October 2021.

Overall, it can be seen that the daily thermal expansion/contraction of the bridge can result in slow accumulation of plastic strains in the foundations of SIAB and cause the foundations to slowly shift over time. As shown in Figure 10.9, this behavior can also cause larger stresses in the foundations over time (larger magnitude negative bending moments in the east drilled shaft in summer 2022 compared to summer 2021) and negatively affect the overall performance of the foundation elements over time. Therefore, it is highly recommended to assess the long-term performance of SIAB foundations, especially those founded in clay deposits, against the cyclic lateral loads transferred to the abutment caps from thermal expansion/contraction of the bridge superstructure.

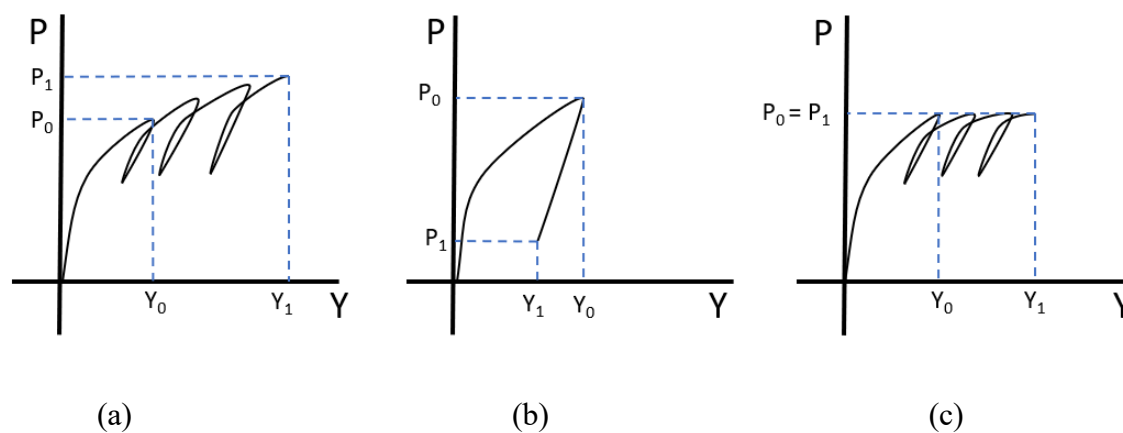


Figure 10.11: Sketch of cyclic p - y behavior of foundation soil in different conditions: (a) period of average daily temperature increase; (b) period of average temperature decrease; and (c) period of no change in average daily temperature

10.6. Conclusions to the Analysis of China Creek SIAB Foundation Monitoring Data

Two years of instrumentation data obtained from monitoring an SIAB constructed near Wichita Falls, TX was evaluated to assess the performance and behavior of deep foundations in SIAB due to thermal expansion/contraction of the superstructure. The deflection profile of the instrumented drilled shafts was collected using shape arrays. The shape array data was evaluated

in conjunction with bridge thermal expansion/contraction data and abutment cap expansion joint monitoring data. The collected data was used to evaluate short-term and long-term trends in the response of the foundation elements to the thermal expansion/contraction of the superstructure.

After careful evaluation of the filed monitoring data, the following conclusions were drawn:

- Despite the lack of an integral connection between the superstructure and foundation elements in this SIAB, SIAB foundation elements still experience cyclic lateral loading and deflection in response to the thermal expansion/contraction of the bridge.
- The collected data indicates that the east and west abutment caps moved 0.08 and 0.2 in toward the center of the bridge, respectively, due to bridge contraction in the winter. For reference, China Creek Bridge experienced nearly 0.35 in of thermal contraction in winter 2020.
- In spite of the symmetrical geometry of the bridge, the response of SIAB foundations to thermal expansion/contraction of the bridge can be asymmetrical and also vary seasonally. For example, in China Creek Bridge, the west abutment cap experienced larger displacements and bending moments compared to the east abutment cap in the winter months, while the east abutment cap experienced larger displacements during the summer months compared to the west abutment cap.
- The instrumentation data also revealed that the cyclic loading of SIAB foundations placed in clay deposits can lead to accumulation of strains in the clay deposit. This phenomenon resulted in a slow increase in the displacement of the east and west abutment caps from August to October 2021 in China Creek SIAB. As a result, both abutment caps moved slightly eastward from time of construction to the end of the monitoring period.
- While SIAB foundations are not typically designed for cyclic lateral loading caused by the thermal expansion/contraction of the superstructure, the observed trends indicate that it would be highly beneficial to assess the long-term performance of SIAB foundations in response to the daily and seasonal thermal expansion/contraction of the bridge. Designing the structure for these loads can help improve the long-term performance of these structures.

Chapter 11. Compilation of Design Concepts, Limitations and Details

11.1. Introduction to the Compilation of Design Concepts, Limitations and Details

The ultimate goal of this project is to provide recommendations regarding the construction of future SIAB/IAB structures in the State of Texas.

In this section, the aim is to provide practical design recommendations regarding the construction and design of SIAB/IAB structures that could later be implemented in the Texas Bridge Design Manual. These recommendations are a culmination of information gathered through the two bridge monitoring campaigns in Texas, an experimental component, a numerical component, parametric evaluations, literature reviews and review of state of practice in other DOTs.

Before presenting the proposed design details, the relevant observations from the two field monitoring campaigns are presented to provide the necessary background in support of the proposed abutment details for future Texas SIAB.

11.2. Design Recommendations

The recommendations regarding the design of future SIAB/IAB structures, based on information synthesized in different tasks are presented in separate subsections as follows.

11.2.1. Backfill Placement/Protection

In summer 2019 a significant lateral earth pressure drop in Mack Creek Bridge's backfill was observed. This was an unexpected behavior as the highest pressures of the year were observed during these months in previous years. Moreover, based on the expectation that the bridge is at peak expansion during the summer, it was expected to see a rise in lateral earth pressures, not a gradual drop.

Upon inspection of the bridge, it was discovered that some of the soils placed behind the wingwalls had been likely lost through erosion. Further examining the photographs documenting various stages of the construction also revealed that given enough pressure/displacement, the backfill soil could move past the sheet piles and spill over to the area behind the wingwalls (Figure 11.1).

Therefore, it is expected that the cyclic expansion/contraction of the bridge, which led to increases in lateral earth pressure on the backfill, caused some of the backfill soil to be lost, leading to further settlement of the approach roadway.

While possible movements within backfill is not a great concern in conventional bridges due to presence of expansion joints, care must be taken in design of SIAB/IAB structures regarding how the backfill may move out of place over time, leading to settlement. It may be possible to limit these effects by use of material capable of absorbing parts of this displacement (such as geofabric attached to backwall) or by altering the geometry of wingwalls to contain the backfill material better.

Overall, it is recommended to support the backfill in both parallel and perpendicular directions to the bridge using geotextiles. A wrap-around layer of woven geotextile fabric perpendicular to the bridge direction is expected to prevent loss of backfill through the gaps behind or in front of the wingwall.



Figure 11.1: Backfill material flowing behind wingwall

A phenomenon similar to what was observed at Mack Creek Bridge was also observed at China Creek Bridge. As previously mentioned, China Creek Bridge was built in two phases to keep the road open while replacing the old bridge. A problem with this phased construction is that the contractor needed to come up with a good shoring system to contain the backfill placed on phase 1 during the construction of phase 2. In this bridge, the contractor decided to use wooden forms as a retaining wall to keep the backfill in place. As became evident a few months into construction, the wooden forms began to buckle out of plane due to pressure exerted from the backfill soil, which continued to increase from the completion of phase 1 (March 2020) to the completion of phase 2 (July 2020). The expansion of the bridge due to temperature changes must have led to a significant increase in lateral earth pressures in the backfill and caused buckling of

the wooden forms, which is the weakest part of the structure containing the soil. These effects can be seen in Figure 11.2. In June 2020, the wooden form seen in Figure 11.2 had moved out of plane by nearly 8 inches and a close inspection of the backfill through the gaps showed nearly 6 inches of settlement in the backfill as well.



Figure 11.2: Buckling of wooden forms retaining the backfill placed during phase 1 on the west end of the bridge

Even though this type of phased construction may not be regularly used in the future, the importance of containing the backfill properly to avoid settlement and backfill loss during the lifetime of the structure should nonetheless be highlighted.

Based on the observations in China Creek Bridge, the authors recommend that temporary shoring structures be properly designed by taking earth pressures generated in the backfill due to temperature changes into account and treated as an earth retaining structure with low tolerance for lateral deformations. The tolerance for lateral deformation is very important because in this structure, any lateral deformation is equivalent to settlement of the backfill, which is highly undesirable.

The data collected from crackmeters installed in China Creek Bridge suggest the bridge is not symmetrically expanding in both directions due to changes in temperature. Looking back at the construction records, one likely cause of this issue is the sequence of construction. After the construction of the decks, east abutment fill was placed a few days before the west abutment fill and it was also compacted by vibratory compactors during placement. If we imagine the bridge at the time where one side has compacted fill and the other side has no fill, it is easy to envision

the bridge would only expand toward the side that offers no resistance reaching its maximum length around noon, which is when the west abutment fill was placed few days later in the hottest month of the year. It is easily imaginable that once the bridge cools down and its length decreases, the deck will move away from the west fill, causing collapse of the fill (west backfill losing its compaction, even if it was compacted during placement). Therefore, for the remainder of the life of the bridge, the west abutment is the path of least resistance toward thermal expansion of the bridge unless temperature drops so far that even the east abutment fill reaches active condition. This incidentally is what happened during February 2021 with record low temperatures of winter storm Uri. After this event, we can observe small movements in the east abutment as well.

Based on these observations, it is recommended that the contractor keeps in mind the effect of providing uneven support to abutments during construction as it could result in uneven deformation of abutments, uneven loading of expansion joints and possibly higher maintenance needs. Uneven placement of backfill in China Creek occurred because not enough backfill material was delivered at the time and the contractor had to wait for another shipment. In these situations, it is recommended to either wait until sufficient backfill material is delivered for both abutments or both abutments be backfilled halfway until the rest of the backfill material is delivered. It is also recommended to perform backfilling activities in the afternoons after peak temperature has reached or plan these activities for colder days if feasible.

11.2.2. Rigorous Quality Control

Upon completion of Mack Creek Bridge, the bumps at the ends of the bridge began to develop rather quickly. While this can be expected of SIAB/IAB structures, which lack the expansion joints typical in conventional bridges, a review of photographs taken during construction revealed that the majority of this settlement could be attributed to placement of low-quality fill (Figure 11.3) as base material for the asphalt pavement and not providing an appropriate separation layer to prevent infiltration of the low-quality fill into the backfill. Although the drawings had called for adequate base material and installation of a filter fabric, in practice, the natural sandy/clayey soil found at the site was used on top of the backfill and the filter fabric used barely covered the top of the backfill (Figure 11.4) to provide complete separation of backfill and base material.

Perhaps a major cause of confusion in this part is due to the novelty of this design and can be overcome once contractors and supervising engineers are made fully aware of the ramifications of not catching such mistakes.

It is possible to reduce the chances of such mistakes occurring as those observed in China Creek Bridge drawings. In China Creek, it was decided to construct a reinforced concrete approach slab right on top of the backfill soil, eliminating the need to place separate base material. Moreover, the contractor is required to place one layer of filter fabric and two layers of PET membrane to

isolate the approach slab from the backfill. However, as the construction of the bridge is not completed yet, it is still early to judge whether such modifications can resolve this issue.



Figure 11.3: Sandy/clayey soil excavated from the site was used as base material for the approach roadway



Figure 11.4: No separation between base material and backfill material

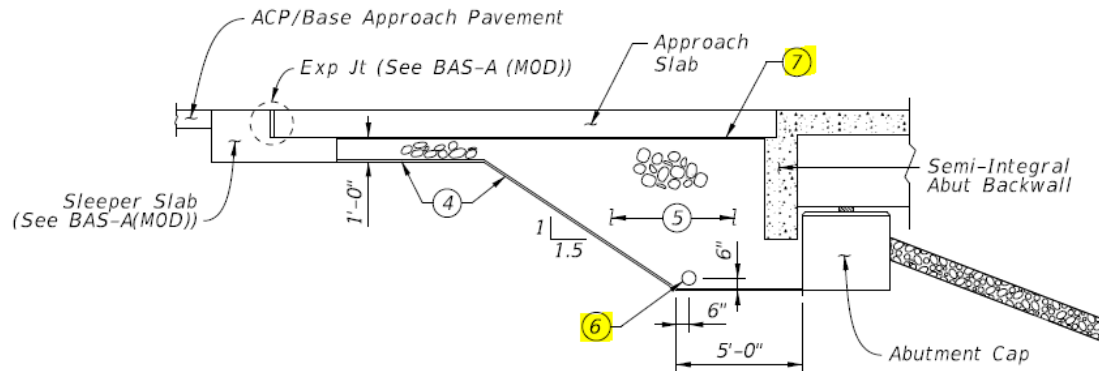
Similar quality control issues were also encountered in China Creek Bridge due to the inclusion of design items that do not appear for the construction of conventional bridges. The first error encountered was the contractor neglecting to use two layers of polyethylene below the approach slab to serve as a bond breaker with the granular backfill below. Luckily, this issue was pointed out by the research team before the approach slab was fully formed and all approach slabs were constructed according to the specifications.

Another construction issue, which was not fixed, was the contractor missing the details regarding the drainage pipes to be used in the backfill. In this case, even though the contractor constructed the wingwalls with holes in them (Figure 11.5) for the drainage pipe to pass through, no pipe was actually placed and bridge construction was completed without this item.

Interestingly, both issues encountered in China Creek Bridge come from not fully reading/ignoring the same detail in the bridge drawings (Figure 11.6). A possible solution to this is to train employees/contractors on these changes, include these “uncommon” design items in bold typeface and even provide 3D views that better showcase these design items.



Figure 11.5: According to drawings, a perforated drainage pipe was planned to pass through the wingwall (west abutment view, phase 2)



SECTION SHOWING APPROACH

- ④ Compact bottom excavation in accordance with Item 132.3.4, "Ordinary Compaction", except smaller "jumping jack" equipment or similar may be used in lieu of proof rolling. After compacting, provide a layer of Type 1 Filter Fabric in accordance with DMS-6200 "Filter Fabric". Provide for the entire interface between subsurface soil and select fill. Provide a 6" minimum upturn against sleeper slab and abutment cap, bonding to concrete with an approved adhesive. Materials, equipment, and labor are considered subsidiary to Item 132.
- ⑤ Provide select rock fill in the form of Grade 3 Aggregate per Item 421.2.6 or Type AS or DS select fill per Item 423.2.4.2. Compact as directed by the Engineer.
- ⑥ Provide a 6" Dia Type 6 or Type 8 pipe underdrain in accordance with Item 556 for the full width of the bridge. Slope to drain and outfall through the header bank slope as directed by the Engineer.
- ⑦ Provide an initial layer of filter fabric (meeting same requirements of note 4) on top of the finished surface of the select fill. On top of filter fabric, provide two layers of polyethylene sheet (minimum thickness 6 mils each) conforming to ASTM E 1745 Performance Class A. Place all layers to create a smooth debonding surface to allow sliding movement of approach slab without undulation or voids. Materials, equipment, and labor are considered subsidiary to Item 422 Approach Slab.

Figure 11.6: Approach slab drawings and construction details mistakenly overlooked during bridge construction

11.2.3. Foundation Design

The information gathered using the equipment placed on Mack Creek in January 2020 reveals that while the bridge goes under daily cycles of thermal expansion/contraction, the width of the gap between backwalls and pile caps are not changing as much. This leads to the conclusion that the pile caps are being pressed inward toward the creek and therefore experience daily cycles of lateral movement as bridge expands/contracts. The data collected from the instrumentation of China Creek Bridge, confirms this hypothesis with displacements of up to 0.15 inches recorded since October 2020.

In a conventional bridge design, foundations are designed for compression according to the Texas Bridge Design Manual-LRFD (2015) as the girders merely sit on bearing pads placed on girders and are not expected to transfer significant lateral forces to the pile caps. On the other hand, in both Mack Creek and China Creek SIAB, the deck is integrated with the backwall, which is located on the outside of the pile caps and the gap between backwall and pile caps is filled with a very stiff EPS or bituminous fiber board layer with low compressibility.

In SIAB/IAB structures, as the bridge deck undergoes shrinkage and/or experiences lower temperatures than when the concrete was placed/cured, the abutment backwalls are expected to push on the pile caps, causing lateral movements/forces at the head of the pile.

The extent of these displacements is a function of climate variables such as temperature extremes, daily changes in temperature, relative humidity of the air, and non-climate parameters such as deck length, deck cross section geometry, season of completion, material properties, in-situ soil, etc.

This problem can become more pronounced in bridges that have a longer span and are constructed in locations with more extreme changes in temperature.

Several different approaches can be considered to mitigate this issue:

1. Design the foundation for the cyclic lateral load imposed considering the shrinkage, creep and daily temperature variations of the deck as dependent on the location of the bridge and its length.
2. Alter the geometry of the backwall so once the deck contracts, there is no contact between the backwall and pile cap due to expansion/contraction of the bridge deck. An example of such a design is shown in Figure 11.7. This option requires good installation of waterproofing material to prevent seepage between the joints, which was found to be tricky in the experience of other DOTs such as OHDOT.
3. Choose filler material placed between the backwall and pile cap, in terms of thickness and type, that is capable of fully absorbing the expected displacement and remains elastic at the expected range of daily cycles of displacements throughout the life of the structure. This option could help keeping the deck sealed against water while protecting the foundation from unnecessary lateral loading.

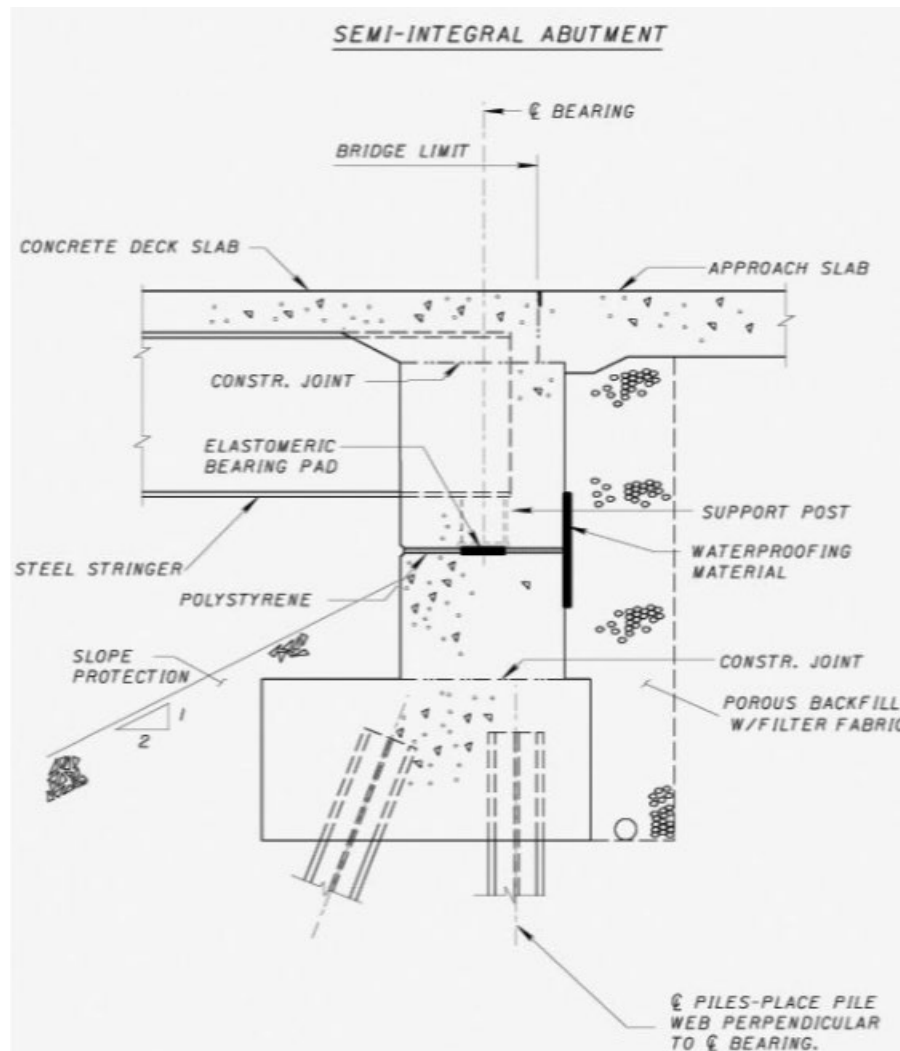


Figure 11.7: Example SIAB design by OHDOT

11.2.4. Season of Completion

Various sources in the literature as well as the completed numerical simulation point out that there can be differences in the performance of the bridge based on the time the deck is cast.

For example, the result of laboratory tests reported by (Xu et al., 2007) suggests that generally cyclic loading leads to much larger pressures when the soil is allowed to experience active state before being pushed in passive direction; if the soil only goes from at rest state to passive and back, it will not experience large increases of pressure.

Moreover, the numerical simulations as reported in Appendix B suggest that if the bridge is completed in the colder months of the year, as opposed to the hottest months, the backfill will experience smaller settlements and smaller increases in lateral earth pressures.

In addition, it is expected that if the bridge is completed during the cold seasons, the thermal expansion of the bridge will negate some of the effects of shrinkage of the deck during warmer seasons while if it were completed in warmer months, thermal contraction effects will be added to the shrinkage effects when weather gets colder.

Since in many occasions it may not be possible to plan the season of completion, it is still advised to leave operations such as deck concrete pouring or placement of backfill for periods of relatively cooler weather, such as colder days of the week according to forecasts or even afternoon/evening times. Any such efforts are expected to help with the long-term performance of the structure and are supported by observations made during the construction of China Creek and Mack Creek Bridge as well as experience of other DOTs with construction of SIAB.

11.2.5. Surface Runoff Management

It is recommended to design proper drainage system in the vicinity of SIAB and approach slabs to keep water away from the shoulders of the approach slabs and abutment caps as much as possible. As evident in Mack Creek Bridge, large voids have begun forming under the guardrails and behind wingwall sheetpiles due to erosion caused by surface water runoff. Over time, this erosion can lead to loss of backfill and formation of voids beneath the approach slab.

It is also a possibility to start seeing erosion effects in China Creek Bridge as well because the approach slabs are only provided with drainage curbs on one side.

11.2.6. Approach Pavement Design

As flexible pavements follow the profile of the subsurface closely and as settlement of granular backfill soil can almost always be expected, it is recommended to use rigid reinforced concrete pavements that can maintain profile despite formation of voids and gaps in the backfill.

In this case, reinforcement should be provided assuming partial or (conservatively) complete loss of vertical support from the backfill.

A conservative design can assume no support from backfill, designing the approach slabs as simply supported structures. In Mack Creek Bridge, there is already visual evidence of backfill loss. Moreover, the data from settlement sensors installed in China Creek Bridge reveal more than 1 inch of settlement from all sensors for at least half the length of the approach slabs.

11.3. Proposed Semi-integral Bridge Abutment Details

After careful consideration of the performance of the two pilot Semi-Integral Abutment Bridges (SIAB) in Texas as well as a review of the details used by other transportation agencies across the United States, the following design details are proposed.

The proposed abutment design for future TxDOT SIAB is shown in Figure 11.8. This design includes several important modifications compared to the previous abutment details used for the construction of China Creek and Mack Creek SIAB. Most notably, this design incorporates the use of woven geotextiles in (1) the abutment area and (2) around the sleeper slab. In addition, a layer of soft and compressible geofoam is placed between the abutment wall and backfill. The justifications and recommendations for successful execution of these details are presented below.

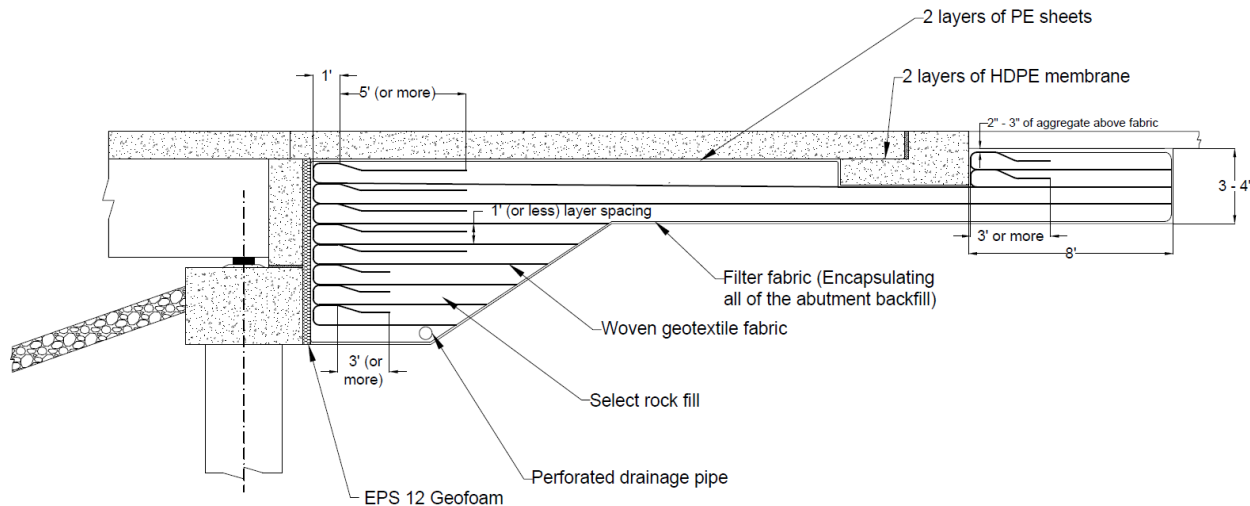


Figure 11.8: Proposed abutment detail for future TxDOT bridges

11.3.1. Woven Geotextile Fabric

As discussed earlier, the development of settlements within the backfill has been largely associated with the thermal contraction of the deck. As the coarse granular backfills have no cohesion, they are susceptible to partial collapse and settlement close to the abutment walls due to loss of lateral support from the abutment walls during thermal contraction of the bridge. In this case, closely spaced geosynthetic layers can provide tensile strength to the soil mass and “lock” the aggregates in place when the abutment wall moves away from the fill and minimizing particle movements.

Over the past few decades, several transportation agencies such as Colorado DOT, Kansas DOT, New Mexico DOT, Louisiana DOT, and Wyoming DOT have successfully used geosynthetic reinforced backfills for the construction of SIAB and IAB. Reportedly, the use of geosynthetic reinforcement has led to significant reduction of backfill settlement and lateral earth pressures acting on the abutment walls. In addition, during the experimental component of this research, the use of wrap-around reinforcement led to significant reduction of backfill settlement and reduction of lateral earth pressures acting on the abutment walls. It is recommended to follow the guidelines provided in FHWA Geosynthetic Reinforced Soil Integrated Bridge System Synthesis report (FHWA-11-027) for the design of reinforced abutment backfills for future TxDOT SIAB.

While backfill performance can be improved with the use of different types of geosynthetics (e.g., woven geotextiles, geogrids), the use of woven geotextiles is recommended for adoption by TxDOT. This recommendation is mainly based on the ease of installation of wrap-around woven geotextiles. Woven geotextiles are significantly more flexible, comparatively easier to transport, very flexible, and can provide a comparatively better barrier against erosion compared to geogrids.

In addition to adopting the use of geotextiles to stabilize the fill next to the abutment walls, their use is also recommended for the area underneath and behind the sleeper slabs as shown in Figure 11.8. This configuration can significantly improve the long-term performance of the sleeper slab by providing a comparatively stiff foundation for the sleeper slab and minimizing its settlement under the traffic loading. Similar details have been successfully used by several other transportation agencies such as Colorado DOT, New Mexico DOT and Tennessee DOT. The two layers of wrap-around reinforcement placed behind the sleeper slab and beneath the asphalt approach roadway are expected to reduce the differential settlement (bump development) between the sleeper slab and the approaching roadway and minimize the need for pavement maintenance at this segment.

To optimize the performance of the reinforced abutment, it is recommended to:

1. Maintain reinforcement layer spacing of 1 ft or smaller.
2. Properly compact the backfill materials on each lift.
3. Extend the wrap-back portion at least 5 ft behind the abutment walls and at least 3 ft behind the abutment caps.
4. Place approximately 2 to 3 inches of aggregate over the top geotextile layer behind the sleeper slab to minimize damage to the geotextile that could result from asphalt pavement construction.
5. Avoid running compaction equipment directly on top of the geotextile.
6. Wrap the geotextile layers against the wingwalls and temporary shoring structures (in case of phased construction).

This design offers a high degree of versatility that allows refinement in future projects as more performance data is collected from the first bridges constructed this way. While 1 ft reinforcement spacing appears to be a common detail and has been used successfully, this spacing can be easily adjusted for cost and performance optimization. It is not recommended to use spacing smaller than 6 in. (constructability) or larger than 16 in. (diminishing the positive effects of closely-spaced reinforcement).

11.3.2. Select Rockfill

A relatively wide range of coarse aggregates can be used successfully for this application. According to FHWA-HRT-17-080 (2018), it is possible to use either well-graded or open-graded aggregates for this purpose. For well-graded aggregates, it is recommended to use aggregates with a maximum aggregate size of 0.5 to 2 inches, less than 12% fines and an internal friction angle of 38° or higher. For open-graded aggregates, a maximum aggregate size of 0.5 to 1.5 inches and internal friction angle of 38° or higher are recommended. In open-graded aggregates, it is recommended to limit the percent passing the No. 50 sieve to 5% maximum. The maximum grain sized recommended in this document is mainly to ensure constructability and allow for efficient compaction within the confines of the abutment.

Given the FHWA specifications, grades 3, 4 and 5 crushed stone aggregates, per TxDOT item 421.2.6, seem to be good candidates for use in the proposed abutment details.

One of the most important aspects related to the backfill aggregate is proper compaction. For this purpose, it is highly recommended that the contractor perform a test strip compaction with the procured aggregate to determine the required compaction effort to reach a state of “no movement.” Additionally, the contractor can use this information to estimate how much loose aggregate is needed to achieve a specific compacted lift height during the backfilling process. In the absence of a test strip, it is recommended to compact aggregates in 6-in. lifts using at least three passes of hand-operated compaction equipment such as a jackhammer or vibratory plate compactors.

Proper compaction is considered a critical aspect of the abutment construction as loose aggregates will experience gradual compaction over time due to abutment wall movements, ground vibrations generated from heavy traffic, etc. As explained earlier, post-construction compaction and settlement of the backfill will result in the loss of vertical support for the approach slabs and faster deterioration of these bridge components.

It is highly recommended that the contractor perform abutment backfill placement on both sides of the bridge as symmetrically as possible. In SIAB, bridge expansion/contraction will lead to abutment wall movements from the moment the abutment walls are cast. If compacted backfill is placed on one end of the bridge while the other abutment has not been backfilled yet, the bridge will primarily expand toward the side with no backfill (path of least resistance). As a result, bridge contraction will also primarily cause abutment wall movement away from the second backfill, leading to loss of compaction and immediate settlement of the second abutment’s backfill. This can also lead to unequal backfill stiffnesses between the first and second backfill, causing asymmetrical thermal expansion/contraction of the bridge. Therefore, it is highly recommended to maintain symmetry during the construction of the bridge abutments.

11.3.3. Compressible Inclusion

Another relatively common component found in SIAB and IAB details across the country is the usage of a buffer material between the backfill and abutment wall. The purpose of this buffer system is to minimize the effect of bridge thermal expansion/contraction on the abutment backfill and prevent ratcheting and backfill settlement.

Several State DOTs, such as Kansas, Colorado, New Mexico, and Virginia, have adopted the use of a layer of geofabric attached to the abutment wall in standard SIAB and IAB. The thickness of this layer in the reviewed standard drawings has ranged from 3 inches to 2.5 ft. Alternatively, other State DOTs have adopted abutments where a 4 to 6 in. void is incorporated between the abutment backfill and abutment wall. In Wyoming, this gap was created by using collapsible corrugated cardboard at the face of the abutment wall during backfill construction. The cardboard is stiff enough to support the backfilling process without experiencing excessive compression. However, the cardboard would lose its strength upon wetting and deteriorate shortly thereafter.

Given the additional complexity of abutment construction with a gap between abutment wall and backfill, it is recommended to install a layer of soft and compressible EPS on the abutment wall. The thickness and stiffness of the material should be selected such that it maintains integrity and does not get compressed beyond the elastic range during backfill compaction but soft enough that it absorbs thermal expansion of the bridge superstructure instead of transferring the wall displacement to the backfill. Overall, EPS 12 conforming to ASTM D6817 is a good candidate for this application. EPS 12 is among the softest commercially available geofabrics and has been found to maintain its integrity for this application.

Commercially available EPS geofabric maintains elasticity up to 1% strain and compression beyond 1% will lead to permanent deformation. This magnitude of permanent deformations is not a concern in geosynthetic reinforced abutments as the geosynthetic reinforcement is expected to support the backfill in the absence of lateral support. Therefore, it is recommended to select an EPS layer thickness that is two to three times larger than the expected abutment displacement.

The usage of a compressible inclusion is strongly discouraged in the absence of backfill reinforcement. As large-scale laboratory test results show, a compressible inclusion can slow ratcheting and backfill settlement in the initial thermal expansion cycles. However, this material tends to compress under strains larger than 1%, leading to larger backfill settlement magnitudes compared to cases with no compressible inclusion. Therefore, unless the thickness of the EPS layer is more than 100 times the expected abutment wall displacement, its usage is expected to have a detrimental effect on the long-term performance of the unreinforced backfill.

Another viable alternative to EPS 12 is “Elasticized Polystyrene,” which is engineered to compress when pressure is applied and return to its initial state when pressure is relieved. This

material exhibits linear-elastic behavior up to 10% strain with a compressive strength of 5 psi at this strain.

11.3.4. Filter Fabric

Filter fabric is considered another important component of this design. For best performance, it is recommended that the filter fabric be placed on all sides of the backfill. While this has been noted in the drawings of China Creek and Mack Creek Bridges, the details did not clearly show the need to encapsulate the fill on the sides (against the wingwalls) as well. In Mack Creek Bridge, this missing detail appears to have allowed for the erosion of the backfill material placed near the wingwalls. Therefore, there should be a layer of filter fabric between the backfill and excavation surfaces, wingwalls, approach slab, sleeper slab, approach roadway and EPS layer. The successful execution of this item will significantly reduce the possibility of erosion and fines migration and is expected to significantly improve the long-term performance of the abutment backfill.

11.3.5. Wingwalls

For SIAB, it is recommended that the length of the wingwalls be determined based on the extent of the excavation area and completely cover the sides of the excavated abutment area. This modification result in two potential benefits:

1. Limiting the infiltration of surface water runoff into the backfill area, which can cause erosion and settlement.
2. Preventing the backfill aggregate from “spilling” outside in the area behind the wingwalls. Thermal expansion of the superstructure can lead to increased pressure within the backfill, which can lead to aggregates being pushed behind the wingwalls if they are not extended far enough.

The wingwalls may conform to the shape of the excavation area to facilitate a cost-effective construction.

11.3.6. Approach Slab Bond Breaker

The use of two sheets of minimum 6 mil PE on top of the filter fabric was observed to be effective at preventing bonding between the approach slab and backfill soil in China Creek Bridge.

The data collected from China Creek revealed that the sleeper slab moves significantly with thermal expansion and contraction of the superstructure. This can lead to settlement just behind the sleeper slab and development of a bump. To create a smooth interface between the approach slab and sleeper slab, it is recommended to use two sheets of 60 mil smooth HDPE membranes

in between the sleeper slab and the approach slab. To enhance the performance of this bond breaker, a lubricant such as wax can be used between the HDPE layers to further reduce the interface friction and promote sliding.

11.3.7. Foundation Design

The instrumentation data collected from both instrumented SIAB indicates that the thermal expansion/contraction of the bridge deck also causes cyclic movements of the abutment caps. In the case of China Creek Bridge, it is speculated that cyclic loading of the drilled shafts has led to cyclic deterioration of the clayey foundation soils and resulted in increasing displacement magnitudes of the foundations over time and slight eastward displacement of the bridge as well. It is recommended that the designer considers lateral loading of the SIAB foundations due to interaction with the superstructure, bearing shear transfer and abutment backfill pressure increase in the design of SIAB foundations. One solution to minimize the effect of cyclic degradation of the foundation soils is to increase the embedment depth of the deep foundations such that the lateral foundation behavior is more similar to a long pile (double-curvature form) instead of short piles (single curvature). The determination of sufficient embedment depth requires detailed lateral behavior analysis using geotechnical analysis software such as LPILE (Ensoft, inc.) with pile cap movements determined based on the expected movement of the abutment walls due to thermal loads and other applicable live loads.

11.3.8. Thermal Movements

Based on the instrumentation data collected from China Creek Bridge, it was found that the thermal expansion of the bridge can be predicted with sufficient accuracy using the methods described in AASHTO LRFD Bridge Design Specifications. However, the collected data from both bridges indicates the thermal expansion/contraction of the bridge does not occur symmetrically and that the ratio of thermal movements between the abutments can vary significantly throughout the year with one abutment experiencing up to twice as much thermally-induced displacements than the other abutment. As asymmetrical thermal expansion of the bridge can happen due to a variety of factors, some of which can be unpredictable, it is recommended to estimate that each abutment wall can experience up to 70% of the total expected annual thermal expansion/contraction.

11.3.9. Abutment Earth Pressures

Due to cyclic interaction between the bridge abutment walls and the abutment backfills, backfill earth pressure changes daily and seasonally. Highest annual earth pressures are typically experienced during the warmest times of the year and the lowest earth pressures are typically experienced during the coldest times of the year. As the collected instrumentation data from both bridges indicate, passive abutment earth pressures exceeded Rankine's passive earth pressure

after a few years of ratcheting. Maximum earth pressures in unreinforced backfill can increase each year due to ratcheting and reach the theoretical limit of Coulomb's passive earth pressure in long-term. Additionally, it was observed that in a given year, the maximum and minimum annual abutment earth pressures were experienced several times. In Texas, the largest magnitude earth pressure cycles were observed during the winter and spring months where the bridge temperature can decrease substantially overnight and quickly increase during the day due to the strong sun, causing large abutment wall displacement cycles.

It is speculated that in reinforced abutments, the effect of ratcheting would be minimized and the abutment earth pressure can be estimated based on the expected wall movement magnitudes with more certainty.

Appendix A. Relevant Information on the Survey of State DOTs and Texas Districts

This appendix complements the information presented in Chapter 3 regarding the surveys sent to State DOTs and Texas Districts regarding the use of Integral/Semi-Integral Abutment Bridges (IAB/SIAB). Sub-appendix A.1: Phase 1 Questionnaire of State DOT Survey, presents the phase 1 questionnaire sent to US DOTs. Sub-appendix A.2: Phase 2 Questionnaire of State DOT Survey, presents the phase 2 questionnaire sent to US DOTs. Sub-appendix A.3: TxDOT District Survey, presents the internal TxDOT survey sent to 25 TxDOT Districts. Sub-appendix A.4: MnDOT IAB/SIAB Design Details, presents MnDOT design details of IAB/SIAB abutments, approaches and an overall design guidance document. Sub-appendix A.5: Oklahoma DOT CLSM Backfilling Specifications, presents information provided by Oklahoma DOT on the Controlled Low Strength Material (CLSM) reported to provide better performance with IAB/SIAB and corresponding approach slabs when used as a backfill material. Sub-appendix A.6: PennDOT Approach Slab Details, presents bridge approach slab details provided by PennDOT.

A.1: Phase 1 Questionnaire of State DOT Survey

1. Does your agency allow for design and construction of IAB?
 - a. Yes
 - b. No
 2. How many IAB are you aware of in your agency's jurisdiction? If none, please explain why and skip to question 6.
 - a. (essay format)
 3. What type of bridge superstructures does your agency allow in IAB projects?
 - a. Reinforced Concrete Beams
 - b. Prestressed Concrete Beams
 - c. Steel Beams
 - d. Other
 4. What kind of foundation is required for IAB?
 - a. Drilled Shaft
 - b. Precast Concrete Pile
 - c. Steel H Pile
 - d. Steel Sheet Pile
 - e. Other
 5. What type of backfill is required for IAB?
 - a. (essay format)
 6. Does your agency allow for design and construction of SIAB?
 - a. Yes
 - b. No
 7. How many SIAB are you aware of in your agency's jurisdiction? If non, please explain why and skip to question 11.
 - a. (essay format)
-

8. What type of bridge superstructures does your agency allow in SIAB projects?
 - a. Reinforced Concrete Beams
 - b. Prestressed Concrete Beams
 - c. Steel Beams
 - d. Other
9. What kind of foundation is required for SIAB?
 - a. Drilled Shaft
 - b. Precast Concrete Pile
 - c. Steel H Pile
 - d. Steel Sheet Pile
 - e. Other
10. What type of backfill is required for SIAB?
 - a. (essay format)
11. Based on your responses we may wish to contact you or send a follow-up survey with more detailed questions regarding IAB and/or SIAB. Would you be willing to respond to additional questions?
 - a. Yes
 - b. No
12. What is your name, position title, phone number, and email?
 - a. (essay format)
13. What agency are you representing and where is it located?
 - a. (essay format)

A.2: Phase 2 Questionnaire of State DOT Survey

TxDOT Project 0-6936

Integral Abutment Bridge Survey

University of Texas at Austin



Survey of Integral Abutment Bridge Use and Design Criteria



Notes on completing the survey	
1) Please provide answers to questions in cells with blue tinted background 2) If information is unknown for a particular question, please place a dash in the answer cell (e.g. -) 3) Please complete as much of the survey as possible, spend as much time as you see fit. A partially completed survey is more beneficial than no response at all.	
History of Integral/Semi-Integral Abutment Bridges within the State	
1) When was the first integral bridge constructed?	
a. First fully integral bridge	
b. First semi-integral bridge	
c. First deck-extended bridge	
2) How many bridges have been constructed to date?	
a. Fully integral bridge	
b. Semi-integral bridge	
c. Deck-extended bridge	
3) What was the main reason that prompted the use of integral bridges?	
4) How many poorly performing/failure cases have been identified?	
5) What were the problems experienced with integral bridges in the past?	
6) How were the problems solved?	
7) What are the types of foundation soil in your state common to bridge structures?	



Survey of Integral Abutment Bridge Use and Design Criteria



Design of Integral/Semi-Integral Abutment Bridges within the State	
1) What are the types of integral bridges used?	
a. Are fully-integral abutments and piers allowed?	<input type="text"/>
b. Are semi-integral abutments and piers allowed?	<input type="text"/>
c. Are deck-extensions allowed?	<input type="text"/>
d. Are there any other types used?	<input type="text"/>
Questions pertaining to fully-integral abutment bridges (FIAB)	
2) Are pile foundations always required for fully-integral abutment bridges?	<input type="text"/>
3) Are steel piles used, and if so list the section type(s) used?	<input type="text"/>
4) What is the minimum pile length below the bottom of the abutment stem for steel piles?	<input type="text"/>
5) How are the steel pile foundations oriented?	<input type="text"/>
6) Are precast/prestressed concrete piles used?	<input type="text"/>
7) What is the minimum pile length below the bottom of the abutment stem for concrete piles?	<input type="text"/>
8) Are drilled shaft foundations used?	<input type="text"/>
9) What is the minimum drilled shaft length below the bottom of the abutment stem?	<input type="text"/>
10) Do you account for the bending forces in the piles? If so, how?	<input type="text"/>
11) What type of backfill material is required, and what the compaction requirements?	<input type="text"/>
12) Is even fill on both front and back of the substructure required?	<input type="text"/>
13) Is a compressible material between the abutment and retained soil required?	<input type="text"/>
14) What type of approach slabs are used and are they required?	<input type="text"/>

16) Do you design the abutment stems for full passive earth pressure? If not, what is the earth pressure accounted for?	<input type="text"/>
17) Are the wingwalls allowed to be cast rigidly with the abutment stem? If not, how are wing-walls connected with the bridge structure?	<input type="text"/>
18) How does the foundation soil impact the design of the integral abutment and corresponding foundation?	<input type="text"/>
19) How is the bridge expansion behavior accounted for in terms of interface with asphaltic and concrete deck pavements?	<input type="text"/>
20) What are the design tools used? (computer models, charts, etc.)	<input type="text"/>
21) Do you consider the beam ends to be simply supported, fully fixed, or other?	<input type="text"/>
22) Does your agency use steel beams with FIAB? (If not, proceed to question 28)	<input type="text"/>
23) What is the limit for an individual span length with steel beams?	<input type="text"/>
24) What is the limit for overall span length with steel beams?	<input type="text"/>
25) What is the maximum skew angle permitted with steel beams?	<input type="text"/>
26) What is the maximum grade of the roadway with steel beams?	<input type="text"/>
27) What is the maximum bridge width with steel beams?	<input type="text"/>
28) Does your agency use reinforced concrete beams with FIAB? (If not, proceed to question 35)	<input type="text"/>
29) What is the limit for an individual span length with concrete beams?	<input type="text"/>
30) What is the limit for overall span length with concrete beams?	<input type="text"/>
31) What is the maximum skew angle permitted with concrete beams?	<input type="text"/>
32) What is the maximum grade of the roadway with concrete beams?	<input type="text"/>

Phase 2 Questionnaire of State DOT Survey

TxDOT Project 0-6936

Integral Abutment Bridge Survey

University of Texas at Austin

33) What is the maximum bridge width with concrete beams?	<input type="text"/>
34) Does your agency account for shrinkage of the concrete beams in the FIAB design?	<input type="text"/>
35) Does your agency use precast/prestressed concrete beams with FIAB? (If not, proceed to question 42)	<input type="text"/>
36) What is the limit for an individual span length with precast concrete beams?	<input type="text"/>
37) What is the limit for overall span length with precast concrete beams?	<input type="text"/>
38) What is the maximum skew angle permitted with precast concrete beams?	<input type="text"/>
39) What is the maximum grade of the roadway with precast concrete beams?	<input type="text"/>
40) What is the maximum bridge width with precast concrete beams?	<input type="text"/>
41) Does your agency account for creep and shrinkage of the precast concrete beams in the FIAB design?	<input type="text"/>
Questions pertaining to semi-integral abutment bridges (SIAB)	
42) Are pile foundations always required for semi-integral abutment bridges?	<input type="text"/>
43) Are steel piles used, and if so list the section type(s) used?	<input type="text"/>
44) How are the steel pile foundations oriented?	<input type="text"/>
45) Are precast/sprestressed concrete piles used?	<input type="text"/>
46) Are drilled shaft foundations used?	<input type="text"/>
47) Do you account for the bending forces in the piles? If so, how?	<input type="text"/>
48) What type of backfill material is required, and what the compaction requirements?	<input type="text"/>
49) Is even fill on both front and back of the substructure required?	<input type="text"/>
50) Is a compressible material between the abutment and retained soil required?	<input type="text"/>
51) What type of approach slabs are used and are they required?	<input type="text"/>

52) Do you design the top of the abutment stems for full passive earth pressure? If not, what is the earth pressure accounted for?	<input type="text"/>
53) Are the wingwalls required to be cast with the lower non-moving portion of the abutment stem? If not, what requirements are in place for wing-walls?	<input type="text"/>
54) How does the foundation soil impact the design of the semi-integral abutment and corresponding foundation?	<input type="text"/>
55) How is the bridge expansion behavior accounted for in terms of interface with asphaltic and concrete deck pavements?	<input type="text"/>
56) What are the design tools used? (computer models, charts, etc.)	<input type="text"/>
57) Do you consider the beam ends to be simply supported, fully fixed, or other?	<input type="text"/>
58) Does your agency use steel beams with SIAB? (If not, proceed to question 64)	<input type="text"/>
59) What is the limit for an individual span length with steel beams?	<input type="text"/>
60) What is the limit for overall span length with steel beams?	<input type="text"/>
61) What is the maximum skew angle permitted with steel beams?	<input type="text"/>
62) What is the maximum grade of the roadway with steel beams?	<input type="text"/>
63) What is the maximum bridge width with steel beams?	<input type="text"/>
64) Does your agency use reinforced concrete beams with SIAB? (If not, proceed to question 71)	<input type="text"/>
65) What is the limit for an individual span length with concrete beams?	<input type="text"/>
66) What is the limit for overall span length with concrete beams?	<input type="text"/>
67) What is the maximum skew angle permitted with concrete beams?	<input type="text"/>
68) What is the maximum grade of the roadway with concrete beams?	<input type="text"/>

69) What is the maximum bridge width with concrete beams?	<input type="text"/>
70) Does your agency account for shrinkage of the concrete beams in the SIAB design?	<input type="text"/>
71) Does your agency use precast/prestressed concrete beams with SIAB? (If not, proceed to question 78)	<input type="text"/>
72) What is the limit for an individual span length with precast concrete beams?	<input type="text"/>
73) What is the limit for overall span length with precast concrete beams?	<input type="text"/>
74) What is the maximum skew angle permitted with precast concrete beams?	<input type="text"/>
75) What is the maximum grade of the roadway with precast concrete beams?	<input type="text"/>
76) What is the maximum bridge width with precast concrete beams?	<input type="text"/>
77) Does your agency account for creep and shrinkage of the precast concrete beams in the SIAB design?	<input type="text"/>
Questions pertaining to general design of FIAB & SIAB	
78) What are the temperature ranges in your state that IAB are designed for?	<input type="text"/>
79) What are the humidity ranges in your state, and how are IAB designed for them if applicable?	<input type="text"/>
80) How does the design load impact the bridge type selection?	<input type="text"/>
81) How does the annual average daily traffic (AADT) impact the bridge type selection?	<input type="text"/>

**Survey of Integral Abutment Bridge Use and Design Criteria**

Construction and Maintenance of Integral/Semi-Integral Abutment Bridges within the State	
1) What types of equipment are used for the construction of a FIAB?	<input type="text"/>
2) What is the time difference in construction between a FIAB and a conventional bridge?	<input type="text"/>
3) What types of equipment are used for the construction of a SIAB?	<input type="text"/>
4) What is the time difference in construction between a SIAB and a conventional bridge?	<input type="text"/>
5) What are the materials used for embankment and filling for FIAB and SIAB?	<input type="text"/>
6) How often do FIAB require maintenance, and what type of maintenance has been typical?	<input type="text"/>
7) How often do SIAB require maintenance, and what type of maintenance has been typical?	<input type="text"/>

Additional notes on submitting the survey
1) Please submit responses to Jakob Walter at the following email address: Jakob.Walter@utexas.edu
2) Please include in your response any governing codes for the design and detailing of FIAB and SIAB that you are willing and able to share with TxDOT and the University of Texas at Austin.
3) Please list any additional information you believe may be beneficial to enhance your survey response.

A.3: TxDOT District Survey

Introduction

The TxDOT Research and Technology Implementation Office in conjunction with The University of Texas at Austin is investigating the efficacy of integral and semi-integral abutment bridges for Texas conditions. The following survey is intended to provide vital information to the research team regarding current and potential future bridges in the State of Texas. Your responses are greatly appreciated and will be used to guide the development of new bridge design details in the state. Thank you for your time.

Glossary of Terms

This survey focuses on the design, construction, and associated maintenance of bridges within various Texas Districts. Please read the following glossary of terms below before continuing to the questions.

- Conventional Bridge – a bridge with a superstructure isolated from approaching roadway with thermal expansion joints and isolated from substructure with bearings or rollers. The superstructure is allowed to expand and contract without interacting with the deep foundations or approach roadway.
 - Integral Abutment Bridge (IAB) – consists of a continuous pavement between approaching road and bridge deck with no thermal expansion joints. Additionally, bridge girders are rigidly connected with abutment backwall creating a moment-resisting connection. No bearing pads or rollers are used between the girders and a beam seat.
 - Semi-Integral Abutment Bridge (SIAB) – consists of a continuous pavement between approaching road and bridge deck with no thermal expansion joints. Additionally, bridge girders are rigidly connected with abutment backwall creating a moment-resisting connection. Bearing pads may be used between the girders and a beam seat.
 - If your district constructs a unique type of bridge not listed above (e.g. shallow foundation on MSE wall for abutment) please provide a description in the box below
 - o (essay format)
1. What bridge types are currently used in your district?
 - o Conventional
 - o IAB
 - o SIAB
-

- ☐ Other
 - 2. What is the most commonly specified or preferred bridge type in your district? Rank the types below with 1 being the most common.
 - ☐ Prestressed Concrete Box Beam Bridge
 - ☐ Prestressed Concrete I-Girder Bridge
 - ☐ Prestressed Concrete Slab Beam Bridge
 - ☐ Cast-In-Place Concrete Slab Span Bridge
 - ☐ Concrete Slab and Girder (Pan Form) Bridge
 - ☐ Steel Beam Bridge
 - ☐ Prestressed Concrete Deck Slab Beam Bridge
 - ☐ Prestressed Concrete X-Beam Bridge
 - ☐ Other (type and ranking)
 - 3. On average, what is the maintenance interval for thermal expansion joints on bridges (cleaning, resealing, replacing, etc.) within your district?
 - ☐ 0 – 5 years
 - ☐ 6 – 10 years
 - ☐ 11 – 15 years
 - ☐ 16 – 20 years
 - ☐ 21 – 25 years
 - ☐ 26 – 30 years
 - ☐ 31 – 35 years
 - ☐ 36 – 40 years
 - ☐ 41+ years
 - 4. What are the major problems driving maintenance of bridges in your district?
 - ☐ Deck Problems
-

- ☐ Embankment Stability Issues
 - ☐ Substructure Displacements
 - ☐ Superstructure Cracking/Spalling
 - ☐ Other (please explain)
 - 5. How does maintenance of bridges typically affect traffic in your district?
 - ☐ Severe impact on traffic
 - ☐ Moderate impact on traffic
 - ☐ Minimal impact on traffic
 - ☐ No impact on traffic
 - ☐ Other (please explain)
 - 6. What are the common foundation types used for bridges in your district?
 - ☐ Drilled Shafts
 - ☐ Concrete Piling
 - ☐ Steel H-Piling
 - ☐ Steel Sheet Piling
 - ☐ Other (please explain)
 - 7. Does your District have a preference for the use of approach slabs on bridges?
 - ☐ Use on all bridges (on and off system bridges)
 - ☐ Use on all on-system bridges
 - ☐ Use selectively depending on selective factors
 - ☐ Do not use
 - 8. What approach slab standards does your district use?
 - ☐ Statewide BAS-A and BAS-C
 - ☐ District Modified (please explain)
-

9. The perceived benefits of IAB and SIAB from other DOTs throughout the United States and abroad include reduced bridge deck maintenance, faster construction, and reduced cost in design and construction. Furthermore, this technology has been shown in many cases to reduce the severity and likelihood of the “bump at the end of the bridge” condition. Potential adoption of this technology in Texas is currently being researched and input regarding its feasibility from all TxDOT districts is appreciated.
- o My district would consider adopting IAB/SIAB technology
 - o My district would NOT consider adopting IAB/SIAB technology
10. Are there any concerns that your district may have regarding IAB/SIAB technology?
- o Construction Issues
 - o Long Term Performance Issues
 - o Thermal Expansion Issues
 - o Approach Slab Issues
 - o Pavement to Approach Slab Issues
 - o Other (please explain)
11. Does your district foresee any additional benefits from IAB/SIAB technology in your region?
- o Reduction of the Bump at the End of the Bridge
 - o Elimination of Expansion Joints
 - o Improved Design of Abutment Backwalls
 - o Reduced Number of Bearing Assemblies
 - o Elimination of Abutment Seats
 - o Reduction in Routine Maintenance
 - o Other (please explain)
12. An approach slab used in conjunction with an IAB/SIAB bridge would need to accommodate the movement of the bridge at this interface with the approaching concrete or asphalt pavement. What type of joint system would your District prefer, given the performance of joints used between approach slabs and concrete pavement?
-

- o Wide Flange Pavement Terminal Joint
- o Backer Rod with Silicone Seal
- o Other (please explain)

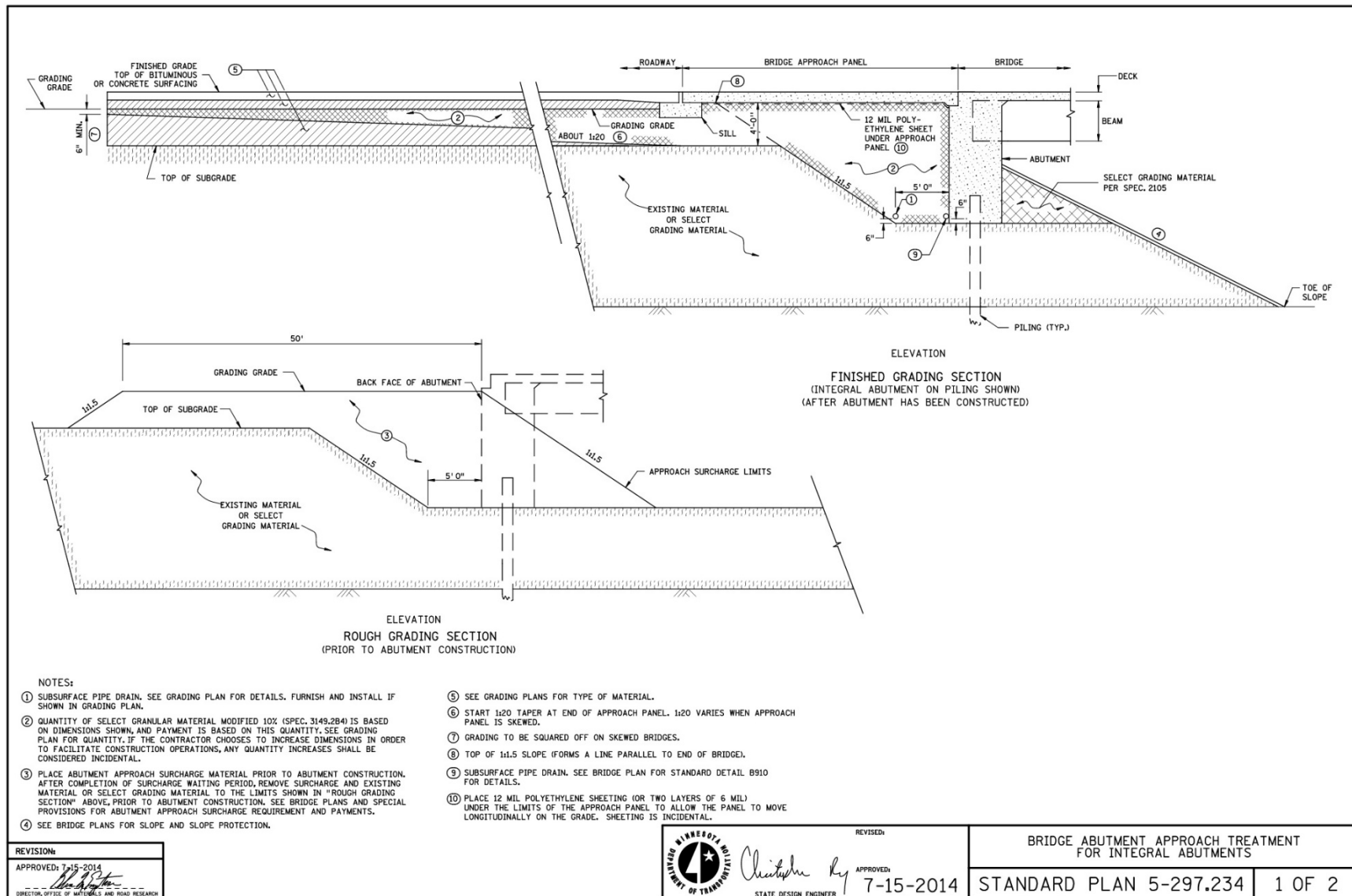
13. What is your position title and what TxDOT district are you representing?

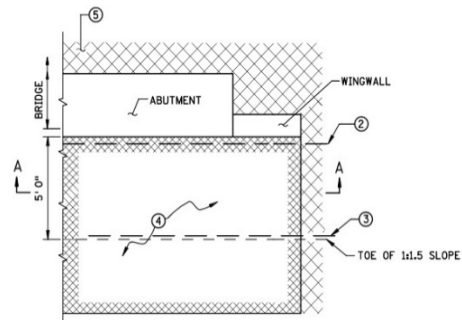
- o (essay format)

14. Depending on your responses, we may be interested in contacting you for additional information. If you would willing to respond to a potential follow-up request, please provide your name, phone number, and email address.

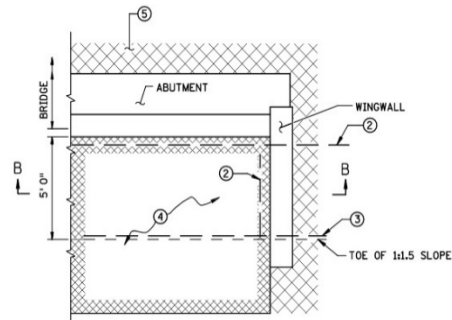
- o (essay format)

A.4: MnDOT IAB/SIAB Design Details

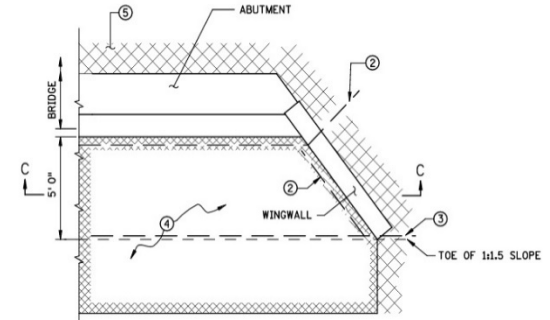




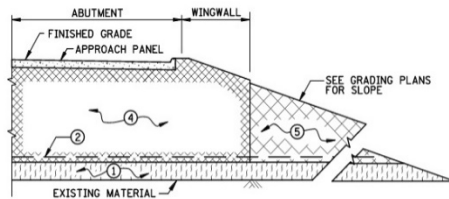
PARTIAL PLAN VIEW AT ABUTMENT
(WINGWALL AT 180°) (FINISHED GRADING)



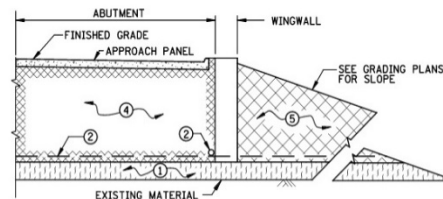
PARTIAL PLAN VIEW AT ABUTMENT
(WINGWALL AT 90°) (FINISHED GRADING)



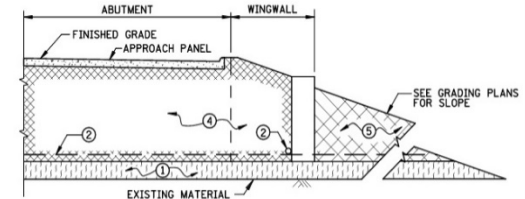
PARTIAL PLAN VIEW AT ABUTMENT
(WINGWALL AT ANY OTHER ANGLE) (FINISHED GRADING)



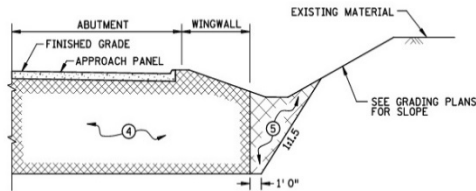
FINISHED GRADING SECTION A-A
(FILL SECTION)



FINISHED GRADING SECTION B-B
(FILL SECTION)



FINISHED GRADING SECTION C-C
(FILL SECTION)



FINISHED GRADING SECTION A-A
(CUT SECTION)
(BRIDGE DETAIL B910 DRAIN NOT SHOWN)

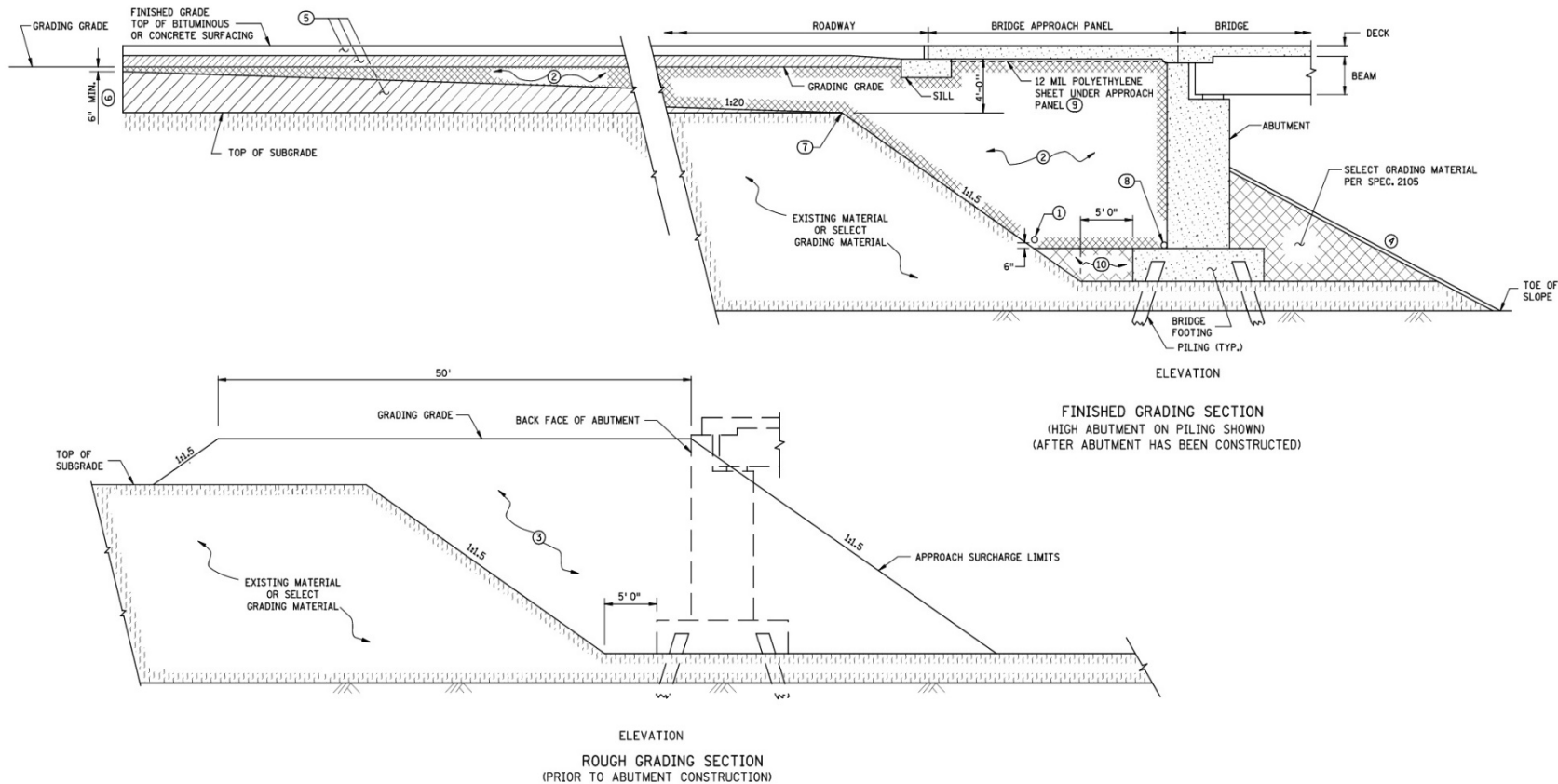
NOTES:

- ① EXISTING MATERIAL OR SELECT GRADING MATERIAL (SPEC. 2105).
- ② SUBSURFACE PIPE DRAIN. SEE BRIDGE PLAN FOR STANDARD DETAIL B910 FOR DETAILS.
- ③ SUBSURFACE PIPE DRAIN. SEE GRADING PLAN FOR DETAILS. FURNISH AND INSTALL IF SHOWN IN GRADING PLAN.
- ④ QUANTITY OF SELECT GRANULAR MATERIAL MODIFIED 10% (SPEC. 3149.2B-4) IS BASED ON DIMENSIONS SHOWN, AND PAYMENT IS BASED ON THIS QUANTITY. SEE GRADING PLAN FOR QUANTITY. IF THE CONTRACTOR CHOOSES TO INCREASE DIMENSIONS IN ORDER TO FACILITATE CONSTRUCTION OPERATIONS, ANY QUANTITY INCREASES SHALL BE CONSIDERED INCIDENTAL.
- ⑤ SELECT GRADING MATERIAL (SPEC. 2105).

REVISION:
APPROVED: 7-15-2014
DIRECTOR, OFFICE OF MATERIALS AND ROAD RESEARCH

MINNESOTA DEPARTMENT OF TRANSPORTATION
STATE DESIGN ENGINEER
APPROVED: 7-15-2014

BRIDGE ABUTMENT APPROACH TREATMENT FOR INTEGRAL ABUTMENTS
STANDARD PLAN 5-297.234
2 OF 2



NOTES:

- ① SUBSURFACE PIPE DRAIN. SEE GRADING PLAN FOR DETAILS. FURNISH AND INSTALL IF SHOWN IN GRADING PLAN.
- ② QUANTITY OF SELECT GRANULAR MATERIAL MODIFIED 10% (SPEC. 3149.284) IS BASED ON DIMENSIONS SHOWN, AND PAYMENT IS BASED ON THIS QUANTITY. SEE GRADING PLAN FOR QUANTITY. IF THE CONTRACTOR CHOOSES TO INCREASE DIMENSIONS IN ORDER TO FACILITATE CONSTRUCTION OPERATIONS, ANY QUANTITY INCREASES SHALL BE CONSIDERED INCIDENTAL.
- ③ PLACE ABUTMENT APPROACH SURCHARGE MATERIAL PRIOR TO ABUTMENT CONSTRUCTION. AFTER COMPLETION OF SURCHARGE WAITING PERIOD, REMOVE SURCHARGE AND EXISTING MATERIAL OR SELECT GRADING MATERIAL TO THE LIMITS SHOWN IN "ROUGH GRADING SECTION" ABOVE, PRIOR TO ABUTMENT CONSTRUCTION. SEE BRIDGE PLANS AND SPECIAL PROVISIONS FOR ABUTMENT APPROACH SURCHARGE REQUIREMENT AND PAYMENTS.

- ④ SEE BRIDGE PLANS FOR SLOPE AND SLOPE PROTECTION.
- ⑤ SEE GRADING PLANS FOR TYPE OF MATERIAL.
- ⑥ GRADING TO BE SQUARED OFF ON SKEWED BRIDGES.
- ⑦ TOP OF 1:1.5 SLOPE (FORMS A LINE PARALLEL TO END OF BRIDGE).
- ⑧ SUBSURFACE PIPE DRAIN. FURNISH AND INSTALL AT TOP OF BRIDGE FOOTING IF BRIDGE DETAIL B910 IS INCLUDED ON BRIDGE PLAN.

- ⑨ IF THE APPROACH PANEL IS TIED TO THE ABUTMENT WITH REINFORCEMENT BARS, PLACE 12 MIL POLYETHYLENE SHEETING (OR TWO LAYERS OF 6 MIL) UNDER THE LIMITS OF THE APPROACH PANEL TO ALLOW THE PANEL TO MOVE LONGITUDINALLY ON THE GRADE. SHEETING IS INCIDENTAL.
- ⑩ SELECT GRADING MATERIAL (SPEC. 2105) SHALL BE COMPACTED AND MEET THE MOISTURE REQUIREMENTS OF 2105. SELECT GRANULAR MATERIAL MODIFIED 10% (SPEC. 3149.284) MAY BE USED IN LIEU OF SELECT GRADING MATERIAL AS PER SPEC. 2105.

REVISION:
APPROVED: 7-15-2014
DIRECTOR, OFFICE OF MATERIALS AND ROAD RESEARCH

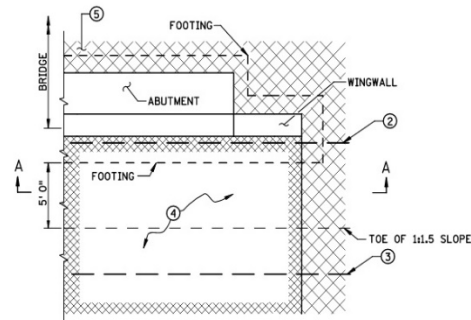


REVISOR:
 APPROVED: 7-15-2014
 STATE DESIGN ENGINEER

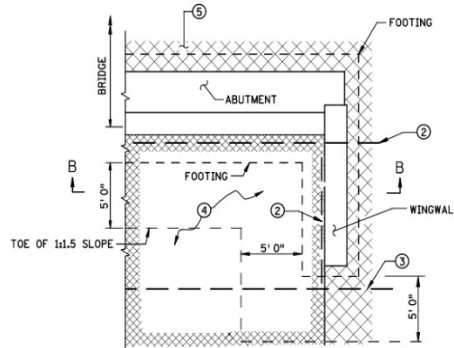
BRIDGE ABUTMENT APPROACH TREATMENT
 FOR ABUTMENT ON FOOTING

STANDARD PLAN 5-297.233

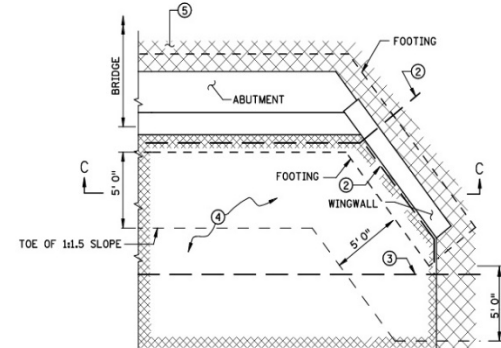
1 OF 2



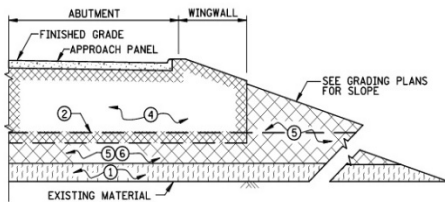
PARTIAL PLAN VIEW AT ABUTMENT
(WINGWALL AT 180°) (FINISHED GRADING)



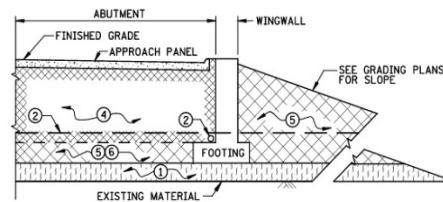
PARTIAL PLAN VIEW AT ABUTMENT
(WINGWALL AT 90°) (FINISHED GRADING)



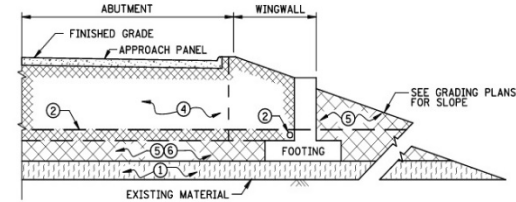
PARTIAL PLAN VIEW AT ABUTMENT
(WINGWALL AT ANY OTHER ANGLE) (FINISHED GRADING)



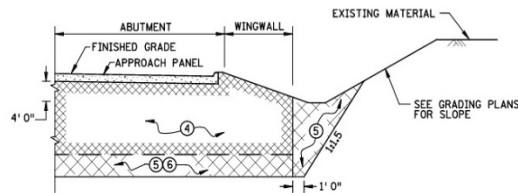
FINISHED GRADING SECTION A-A
(FILL SECTION)



FINISHED GRADING SECTION B-B
(FILL SECTION)



FINISHED GRADING SECTION C-C
(FILL SECTION)




FINISHED GRADING SECTION A-A
(CUT SECTION)
(BRIDGE DETAIL B910 DRAIN NOT SHOWN)

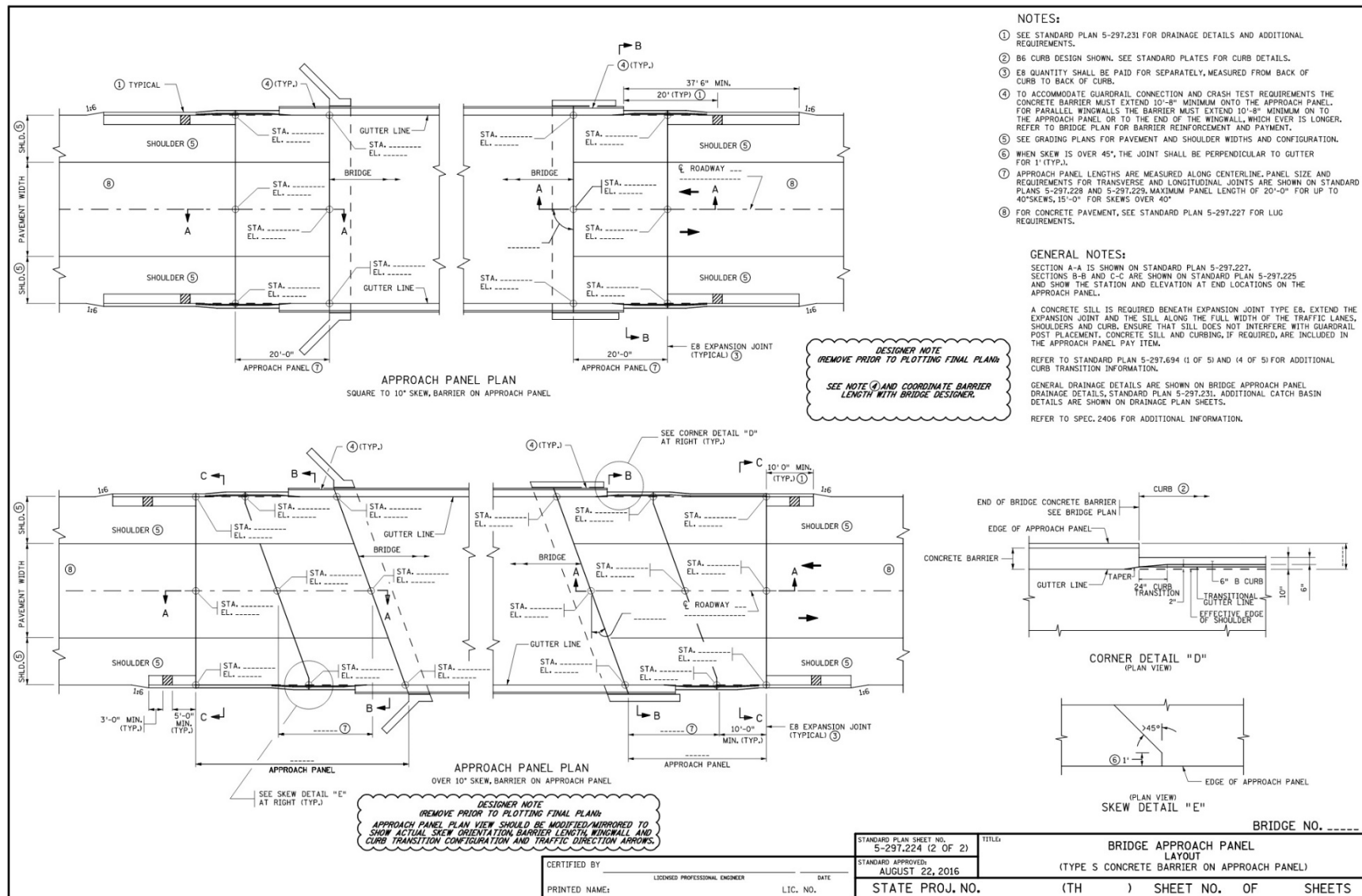
NOTES:

- ① EXISTING MATERIAL OR SELECT GRADING MATERIAL (SPEC. 2105).
- ② SUBSURFACE PIPE DRAIN, FURNISH AND INSTALL AT TOP OF BRIDGE FOOTING IF BRIDGE DETAIL B910 IS INCLUDED ON BRIDGE PLAN.
- ③ SUBSURFACE PIPE DRAIN. SEE GRADING PLAN FOR DETAILS. FURNISH AND INSTALL IF SHOWN IN GRADING PLAN.
- ④ QUANTITY OF SELECT GRANULAR MATERIAL MODIFIED 10% (SPEC. 3149.284) IS BASED ON DIMENSIONS SHOWN, AND PAYMENT IS BASED ON THIS QUANTITY. SEE GRADING PLAN FOR QUANTITY. IF THE CONTRACTOR CHOOSES TO INCREASE DIMENSIONS IN ORDER TO FACILITATE CONSTRUCTION OPERATIONS, ANY QUANTITY INCREASES SHALL BE CONSIDERED INCIDENTAL.
- ⑤ SELECT GRADING MATERIAL (SPEC. 2105).
- ⑥ MATERIAL SHALL MEET THE COMPACTION AND MOISTURE CONTENT REQUIREMENTS OF SPEC. 2105. SELECT GRANULAR MATERIAL MODIFIED 10% (SPEC. 3149.284) MAY BE USED IN LIEU OF SELECT GRADING MATERIAL (SPEC. 2105).

REVISION:
APPROVED: 7-15-2014
DIRECTOR, OFFICE OF MATERIALS AND ROAD RESEARCH

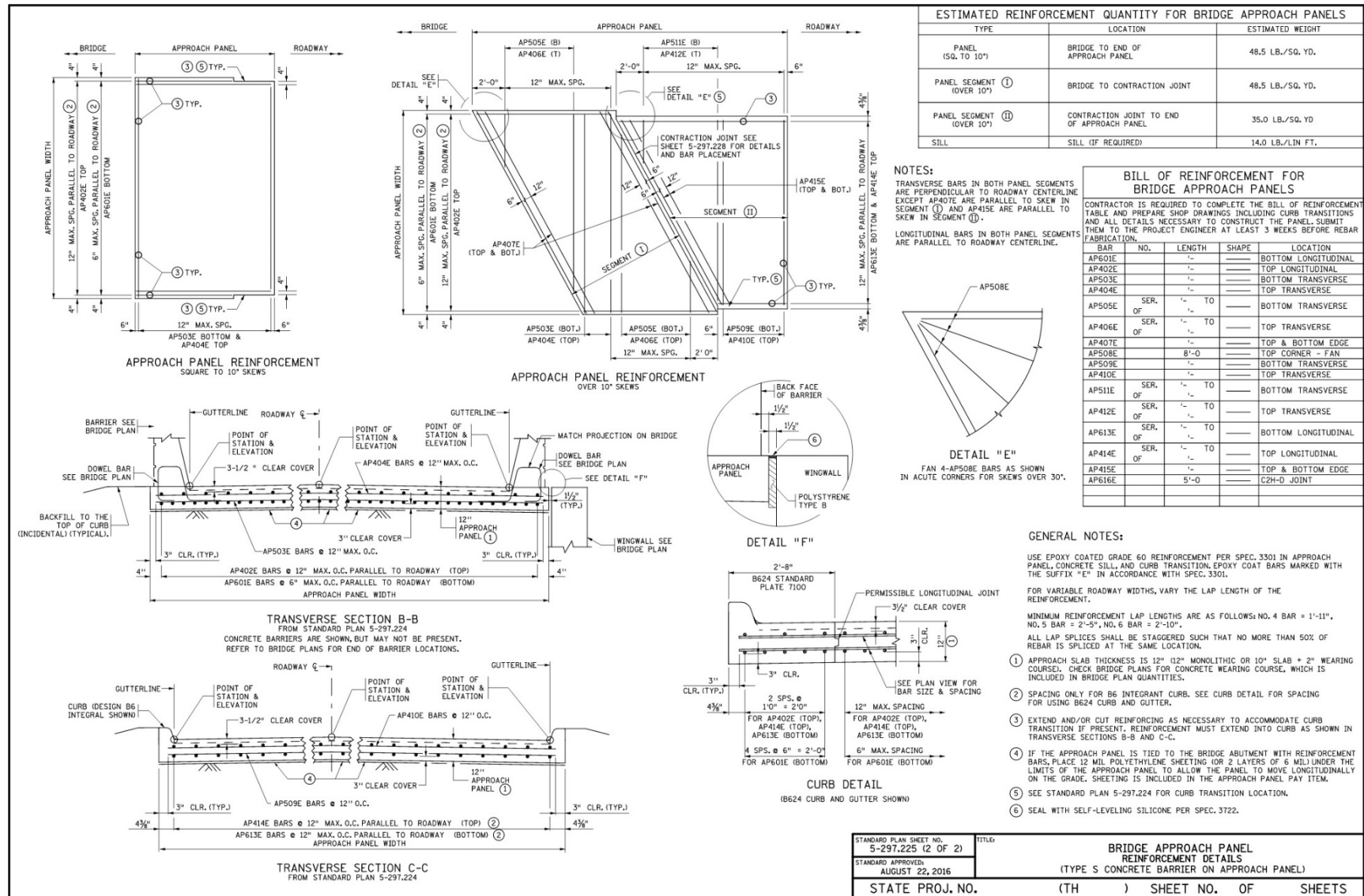
	REVISED: APPROVED: 7-15-2014 STATE DESIGN ENGINEER
---	--

BRIDGE ABUTMENT APPROACH TREATMENT FOR ABUTMENT ON FOOTING	
STANDARD PLAN 5-297.233	2 OF 2



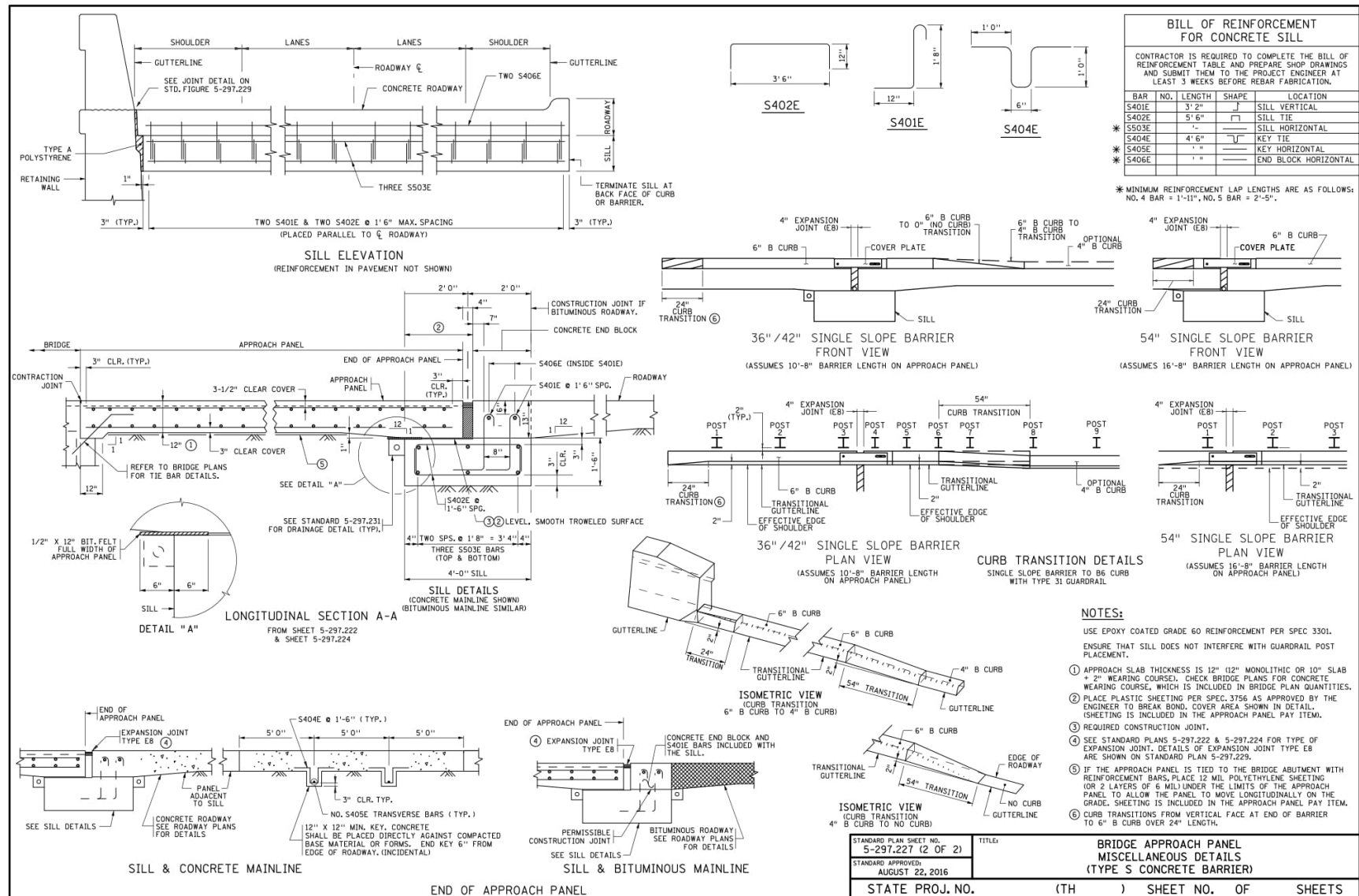
AUGUST 22, 2016

5-297.224 (2 OF 2)



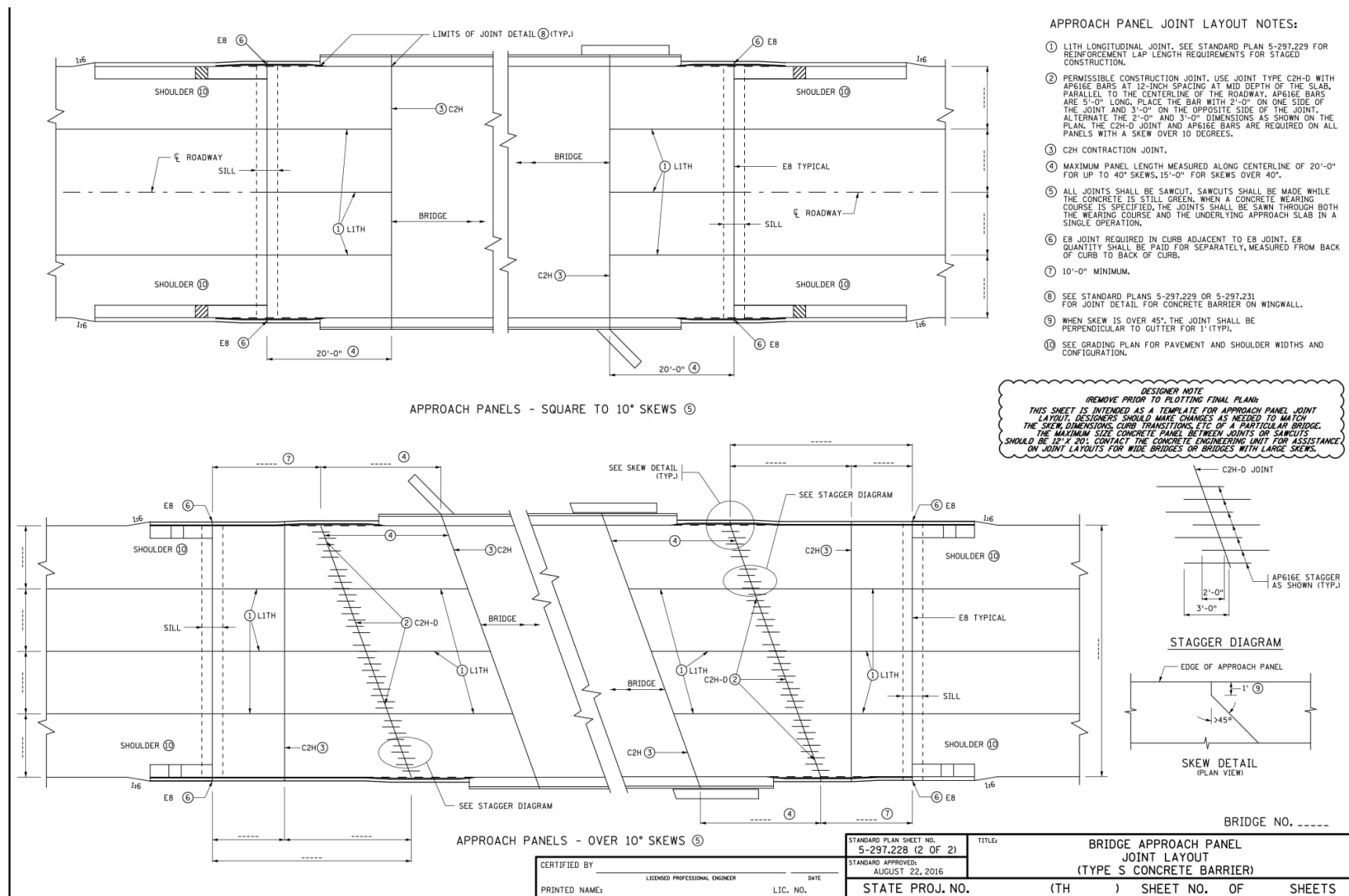
AUGUST 22, 2016

5-297.225 (2 OF 2)



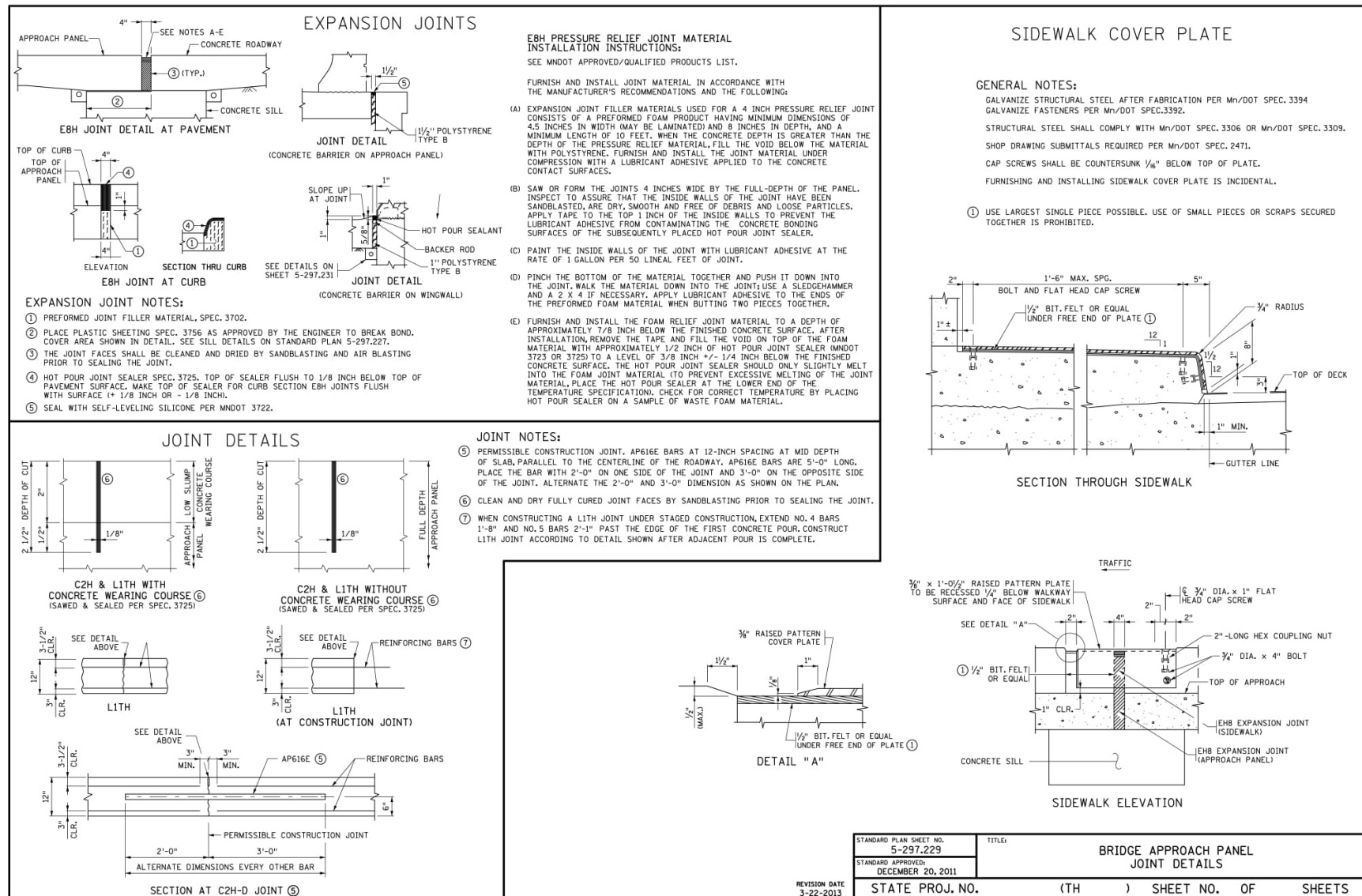
AUGUST 22, 2016

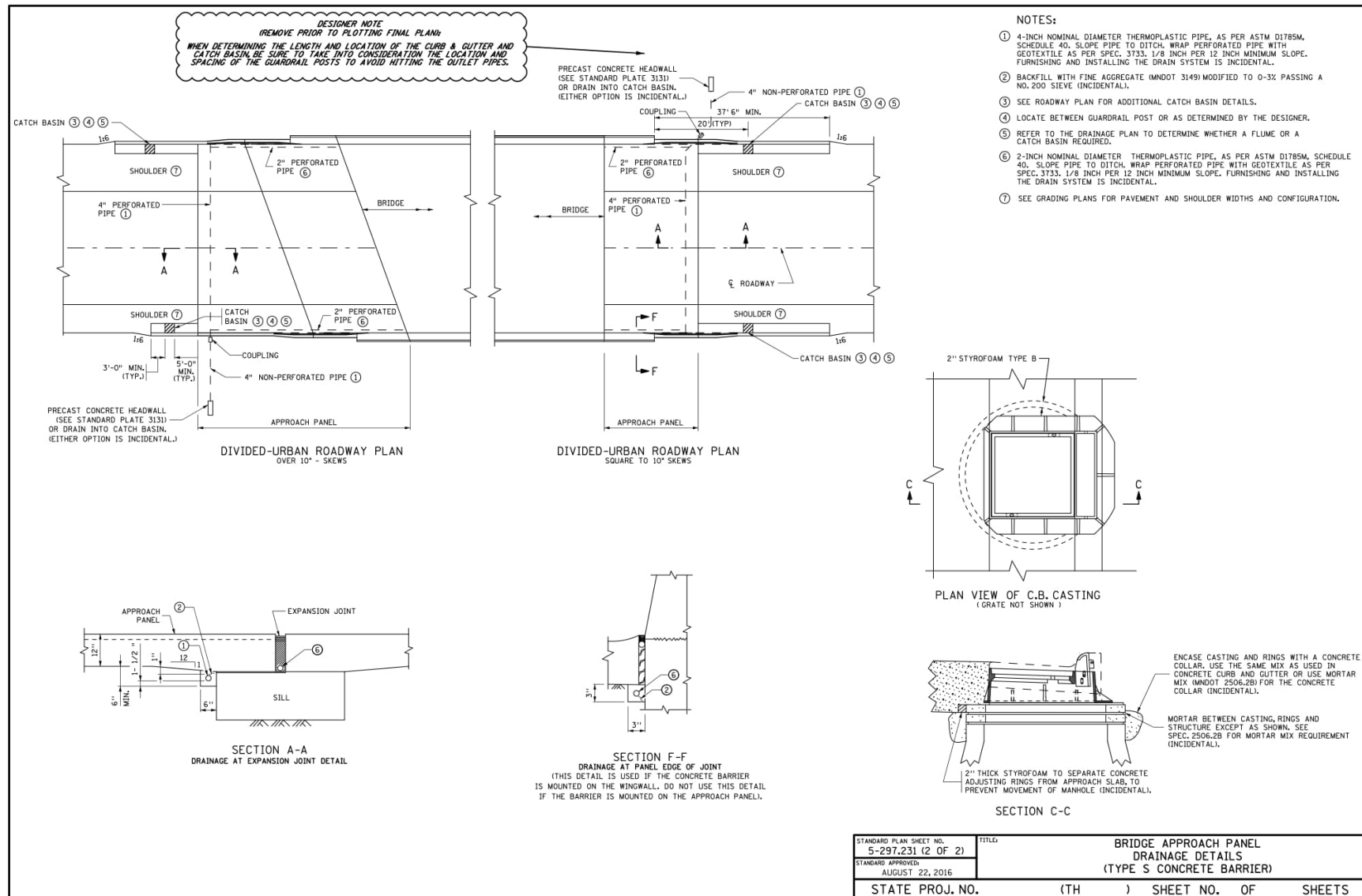
5-297.227 (2 OF 2)



AUGUST 22, 2016

5-297.228 (2 OF 2)





AUGUST 22, 2016

5-297.231 (2 OF 2)

**11. ABUTMENTS,
PIERS, AND
WALLS**

This section contains guidance for the design and detailing of abutments, piers, retaining walls, and noise walls. Abutments and piers are used to support bridge superstructures, whereas walls primarily function as earth retaining structures. In most cases, abutments, piers, and walls are reinforced concrete elements.

The preferred details for connecting the superstructure to the substructure are dependent on the geometry and type of bridge. For example, flexible substructure units supported by a single line of piles may be constructed integral with the superstructure. Conversely, stiff substructure units are detailed with expansion bearings between the superstructure and substructure to reduce the design loads in the substructure units.

11.1 Abutments**General**

Abutments function as both earth retaining structures and as vertical load carrying components. Integral and semi-integral abutments are designed to accommodate movements at the roadway end of the approach panel. Parapet abutments are detailed to accommodate movements with strip seal or modular expansion joint devices between the concrete deck and the abutment end block.

Railroad bridge abutments shall be designed according to the *AREMA Manual for Railway Engineering, Volume 2*, for the live load specified by the railroad. Design all other abutments according to the *AASHTO LRFD Bridge Design Specifications*. The Duluth Mesabe & Iron Range Railway requires a special live load. The live load surcharge is found by taking the axle load and distributing it over an area equal to axle spacing multiplied by the track spacing, generally 70 square feet. Do not reduce the surcharge loading for skew.

Refer to Article 2.4.1.6.2 when locating utilities near an abutment. When footings are perched on an embankment, consult with the Regional Construction Engineer regarding the use of spread footings.

Abutment Type Selection

Integral abutments are the preferred type of abutment when all of the following criteria are met:

- The bridge length and skew meet one of the following:
(See Figure 11.1.1)
 - Bridge length \leq 300 feet and skew \leq 20 degrees
 - Bridge length \leq 100 feet and skew \leq 45 degrees
 - Bridge length is between 100 feet and 300 feet, and

skew $\leq [45 - 0.125 (L - 100)]$ degrees, where L is the length of the bridge in feet.

- Bridge horizontal alignment is straight. Slight curvature can be allowed, but must be considered on a case-by-case basis.
- The length of wingwall cantilevers are ≤ 14 feet (measured from the back face of abutment to the end of the wingwall).
- Abutment wingwalls do not tie into roadway retaining walls.
- Bridge configuration allows setting the abutment front face exposure on the low side of the bridge at 2 feet.
- Maximum abutment stem height $\leq 7'-0"$
- Depth of beams is ≤ 72 inches.

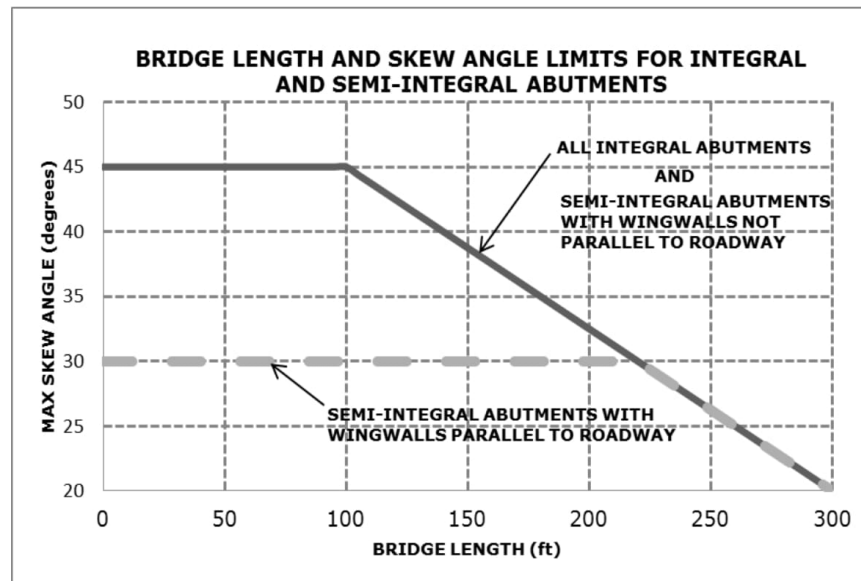


Figure 11.1.1

Semi-integral abutments are the preferred type of abutment when the following circumstances apply:

- The wingwall length, abutment exposure or superstructure depth requirements for integral abutments cannot be met.
- The bridge length and skew meet the requirements given above for integral abutments, except that when wingwalls are parallel to the roadway, the maximum skew limit for semi-integral abutments is 30 degrees. (See Figure 11.1.1.) Also, note that a guide lug is required for skews greater than 30 degrees to limit unwanted lateral movement.

Parapet abutments should only be considered where integral and semi-integral abutment criteria cannot be met.

A parapet abutment supported by a pile foundation can be used behind a mechanically stabilized earth (MSE) retaining wall where high abutments would be required and where it is economical to use an MSE wall. Locate the front face of the MSE wall a minimum of 6'-0" from the centerline of bearing. Do not batter the piles. Place the bottom of the abutment footing and the bottom of the MSE wall cap at the same elevation. Slope protection between the abutment and the MSE wall cap should not exceed a 1V:4H slope.

Detailing/Reinforcement

For bridge rail sections that extend beyond the bridge ends and connect to guardrail, it is preferable to locate them on top of the approach panel rather than on top of the wingwall. However, for situations where the wingwalls tie into roadway retaining walls, be aware that this will result in an offset between the wingwall and roadway retaining wall. In this case, additional coordination with the roadway designer will be required.

Extend architectural rustications 2 feet below the top of finished ground.

As a minimum, tie abutment and wingwall dimensions to the working points by providing distances normal and parallel to the center line of bearing from working points to the following points:

- Centerline of piles at abutment footing corners
- Corners of abutment front face
- Corners of abutment fillets
- Wingwall ends at front and back face of wall

The gutter line, the edge of deck, and the centerline of the fascia beam should be illustrated and labeled in the corner details.

To facilitate plan reading, label the ends of the abutments in the details (South End, North End, etc.).

Label all construction joints and identify the nominal size of keyways.

Where conduit extends through an abutment, provide horizontal dimensions from a working point to the location where the conduit penetrates the front face of the abutment or the outside face of the wingwall. The elevation at mid-height of the conduit should also be provided.

For presentation clarity, detail abutments with complicated layouts on separate sheets. Identical abutments (except for minor elevation differences) should be detailed on common sheets.

The minimum depth for the paving bracket is 1'-4".

On footing details, dimension the lap splice length for bent dowel bars. For straight dowel bars, dimension the embedment or projection length.

If the railing contains a separate end post (supported on the abutment), show the end post anchorage reinforcement in the abutment details.

Membrane waterproofing (per Spec. 2481.3.B) shall be provided for construction joints, doweled cork joints, Detail B801 contraction joints, and on wall joints below ground. Waterproofing is not required at the top of parapet expansion block joints.

All reinforcement, except that completely encased in buried footings or otherwise indicated in this section, shall be epoxy coated. The minimum size for longitudinal bars in abutment and wingwall footings is #6.

Figure 11.1.2 illustrates cover and clearance requirements for abutments.

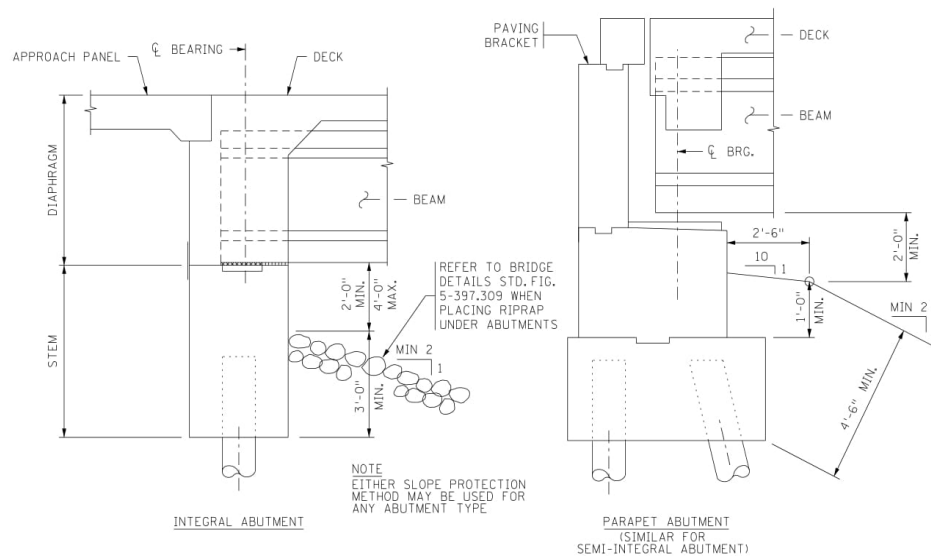


Figure 11.1.2
Cover and Clearance Requirements

For skewed abutments, acute angles are not allowed at corners where wingwalls intersect with the abutment stem. Instead, provide a 6 inch minimum chamfer or "square up" the corner to the wingwall at all acute angle corners.

Provide shrinkage and temperature reinforcement per Article 5.2.6.

Detail sidewalk paving brackets with the same width and elevation as the roadway paving bracket. Sidewalks are to be supported on abutment diaphragm or abutment backwalls and detailed to "float" along adjacent wingwalls.

For semi-integral and parapet abutments, avoid projections on the back of abutments that are less than 4'-6" below grade. If shallower projections are necessary, slope the bottom to minimize frost heave effects.

For additional guidance on reinforcement detailing, see the web published document, *Suggested Reinforcement Detailing Practices*, which can be found at <http://www.dot.state.mn.us/bridge/standards.html>.

11.1.1 Integral Abutments

An integral abutment consists of an abutment stem supported by a single line of piles. The superstructure girders or slab bear on the stem. An abutment diaphragm is poured with the deck and encases the girders. The diaphragm is connected to the stem, making the superstructure integral with the abutment. Figure 11.1.1.2 shows typical integral abutment cross-section details and reinforcement. Figure 11.1.1.3 shows typical partial elevation details and reinforcement. Figure 11.1.1.4 shows Section A-A through the partial elevation. The reinforcement in these figures is typical for an integral abutment design based on the **Integral Abutment Reinforcement Design Guide** found in this section. For abutments that do not meet the design guide criteria, these figures may not accurately reflect the final abutment design.

Geometry

Use a minimum thickness of 3 feet for the abutment stem. For skewed bridges, increase the abutment thickness to maintain a minimum of 5 inches between the beam end and the approach slab seat (See Figure 11.1.1.2). Set the abutment stem height to be as short as practical while meeting the embedment and exposure limits shown in Figure 11.1.2. The preferred abutment stem height on the low side of the bridge is 5 feet, with 3 feet below grade and 2 feet exposure. (Note that the 4'-6"

minimum depth below grade requirement for abutment footings does not apply to integral abutment stems.)

Orient H-piling such that weak axis bending occurs under longitudinal bridge movements. Limit the use of CIP piling to bridges 150 feet or less in length. Minimum pile penetration into abutment stem is 2'-6". Avoid using 16" CIP and HP 14 piles or larger because of limited flexibility.

When the angle between the back face of wingwall and back face of abutment is less than 135 degrees, provide a 2'-0" x 2'-0" corner fillet on the back face of the wingwall/abutment connection. Include the fillet along the height of the abutment stem only, stopping it at the top of the stem.

Wingwalls and the end diaphragm are intended to move as a single unit. Do not include a gap between wingwalls and the abutment diaphragm. Detail rebar to cross the joint between the diaphragm and the wingwalls.

Detail integral abutments with a drainage system (Detail B910). Outlet the 4 inch drains through wingwalls and backslopes.

Limit the length of the wingwall cantilever to 14 feet measured from the back face of abutment to the end of the wingwall.

Refer to Figure 11.1.1.1a and 11.1.1.1b regarding the following guidance on integral abutment permissible construction joints. Unless indicated otherwise on the preliminary plan, place a permissible horizontal construction joint in the wingwall at the elevation of the abutment stem/diaphragm interface, running the entire length of the wingwall. For abutments with wingwalls parallel to the roadway, include a permissible vertical construction joint that is an extension of the wingwall back face through the abutment diaphragm, running from the bridge seat to the top of the wingwall. For abutments with flared wingwalls, include a permissible vertical construction joint where the wingwall connects to the abutment fillet (if provided) or abutment stem, running from the bridge seat to the top of the wingwall. Show membrane waterproofing along the inside face of all construction joints. Inclusion of these permissible construction joints allows the contractor the option of casting the upper portion of the wingwall separately or with the diaphragm and deck. Note that the upper portion of the wingwall is always to be paid for as abutment concrete, even when it is placed with the diaphragm. These permissible construction joint options may be limited for aesthetic reasons by the Preliminary Bridge Plans Engineer based on guidance from

AUGUST 2016**LRFD BRIDGE DESIGN****11-7**

the Bridge Architectural Specialist. In those cases, acceptable construction joint locations are to be shown on the preliminary plan.

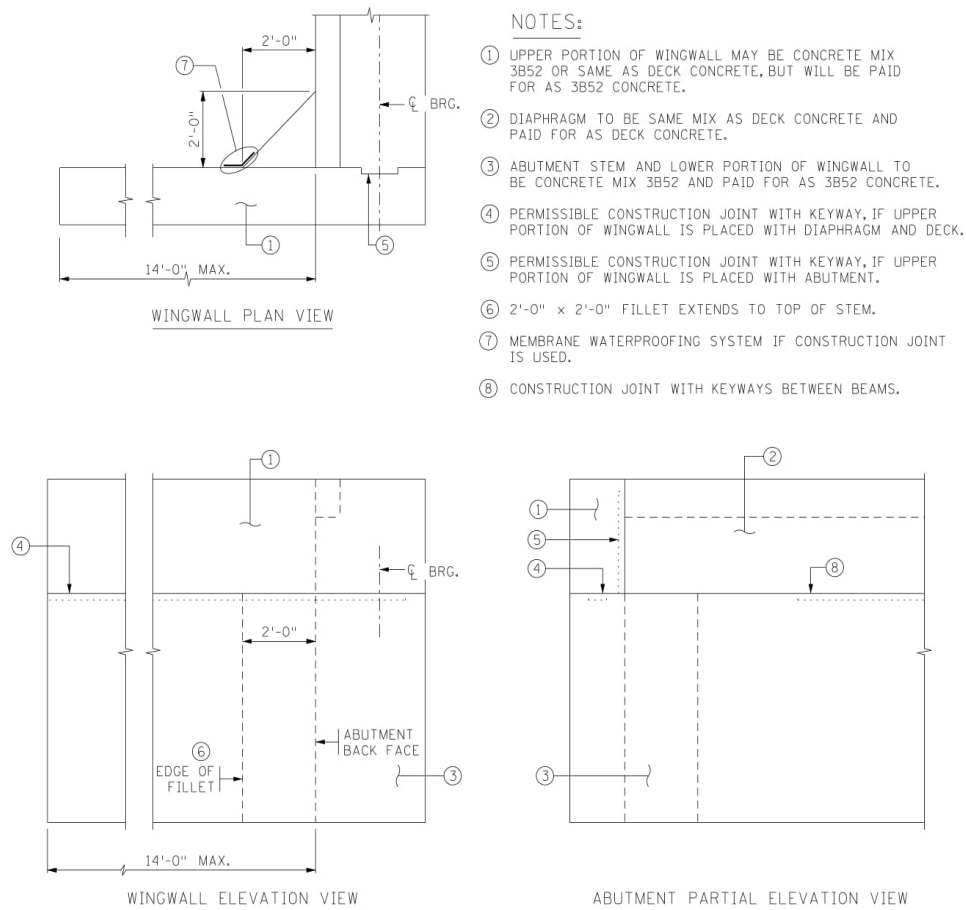


Figure 11.1.1.1a
Permissible Construction Joints For Integral Abutments With
Wingwalls Parallel to Roadway

JULY 2016

LRFD BRIDGE DESIGN

11-8

NOTES:

- ① CONSTRUCTION JOINT AT TOP OF ABUTMENT STEM WITH KEYWAYS BETWEEN BEAMS.
- ② PERMISSIBLE CONSTRUCTION JOINT WITH KEYWAY, IF UPPER PORTION OF WINGWALL IS PLACED WITH DIAPHRAGM AND DECK.
- ③ PERMISSIBLE CONSTRUCTION JOINT WITH KEYWAY (ABOVE ABUTMENT STEM), IF UPPER PORTION OF WINGWALL IS PLACED WITH ABUTMENT.
- ④ MEMBRANE WATERPROOFING SYSTEM IF CONSTRUCTION JOINT IS USED.

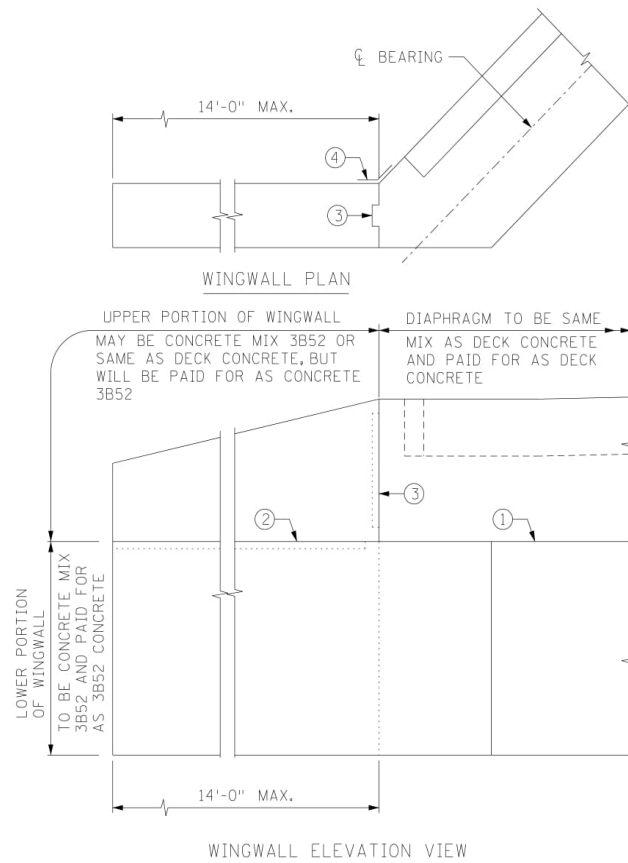


Figure 11.1.1.1b
Permissible Construction Joints For Integral Abutments With
Flared Wingwalls

JULY 2016

LRFD BRIDGE DESIGN

11-9

For new bridges, tie the approach panel to the bridge with stainless steel dowel bars that extend at a 45 degree angle out of the diaphragm through the paving bracket seat and bend horizontally 6 inches below the top of the approach panel. (See bar S605S, Figure 11.1.1.2.) For repair projects, provide an epoxy coated dowel rather than stainless steel due to the shorter remaining life of the bridge. Include a ½ x 7 inch bituminous felt strip on the bottom of the paving bracket to allow rotation of the approach panel.

JULY 2016

LRFD BRIDGE DESIGN

11-10

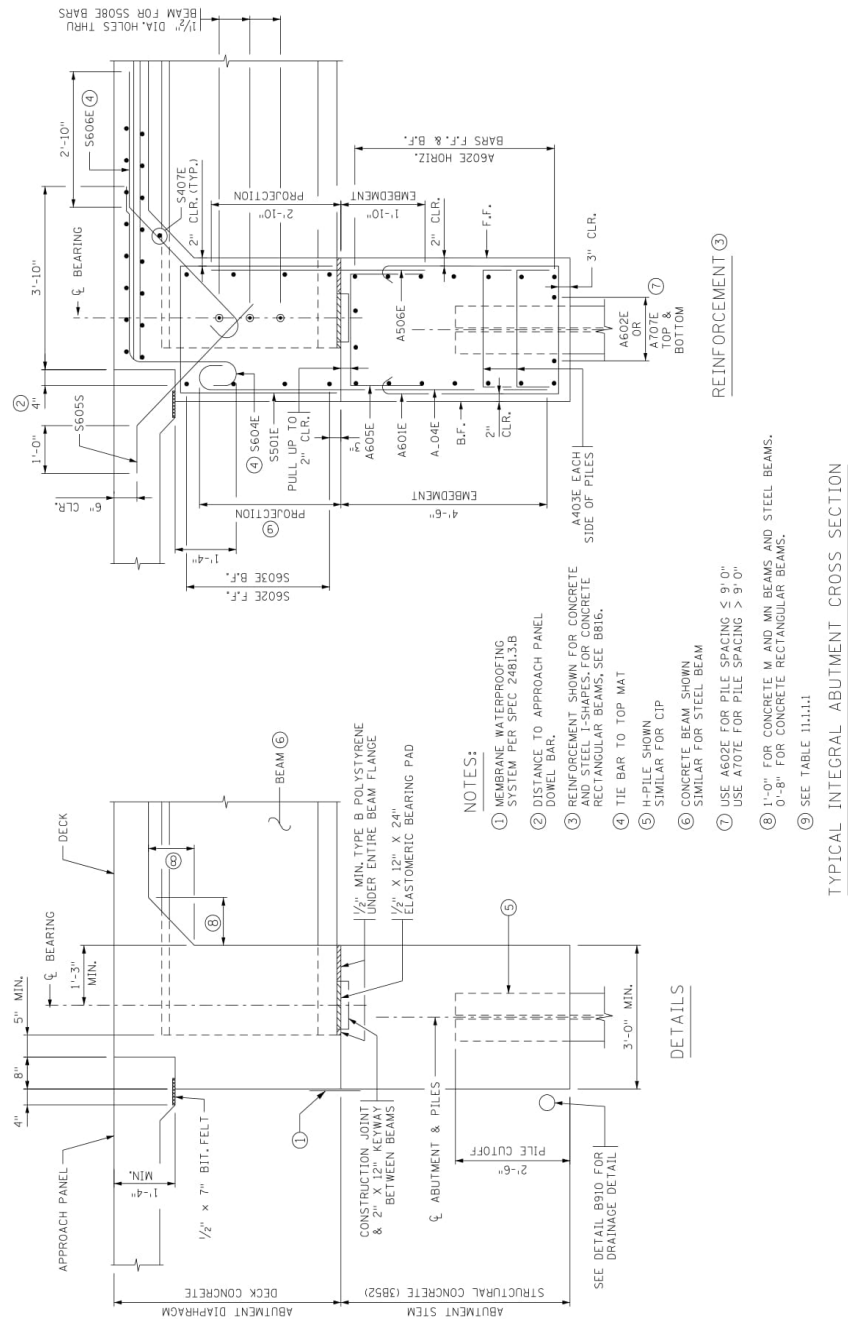


Figure 11.1.1.2

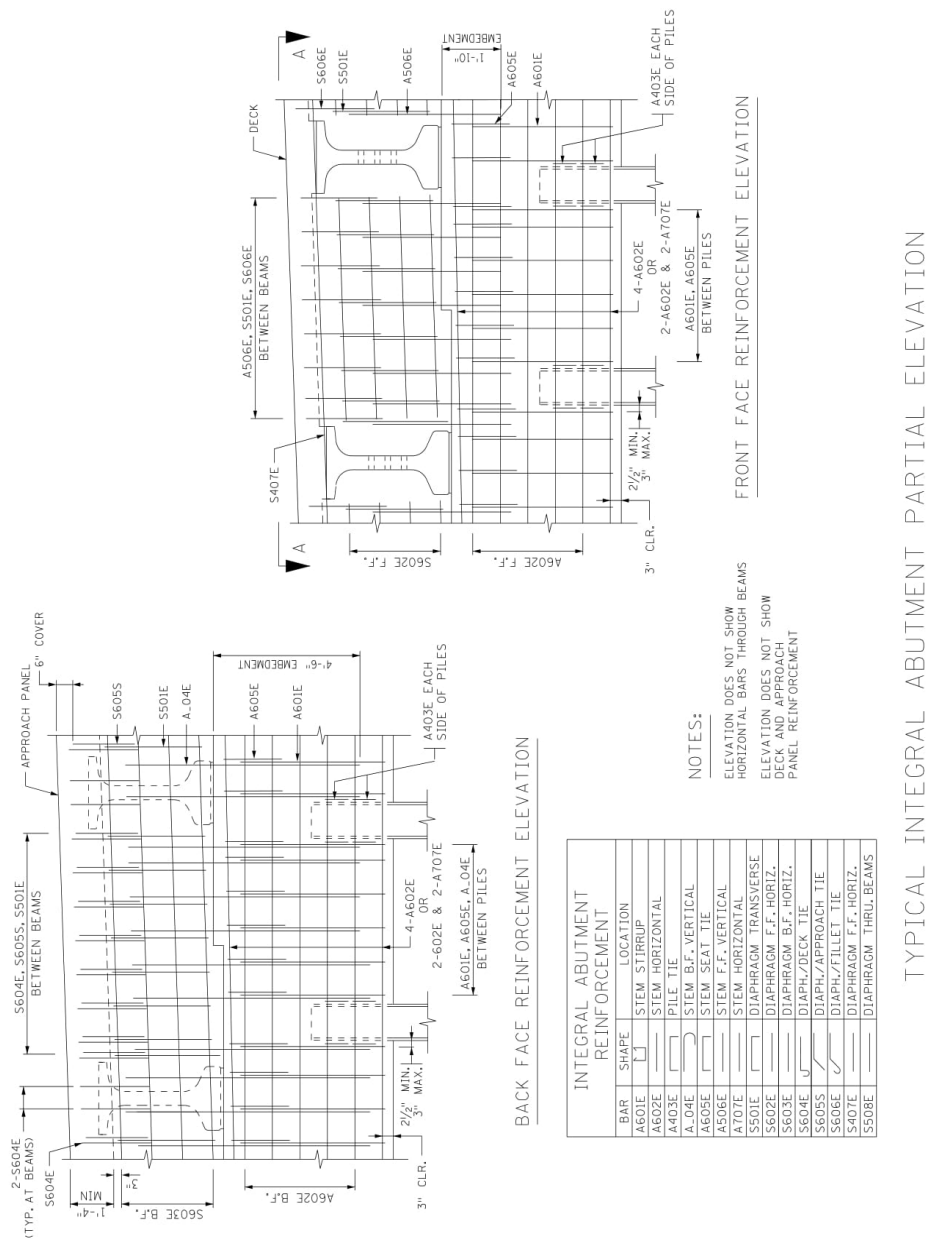
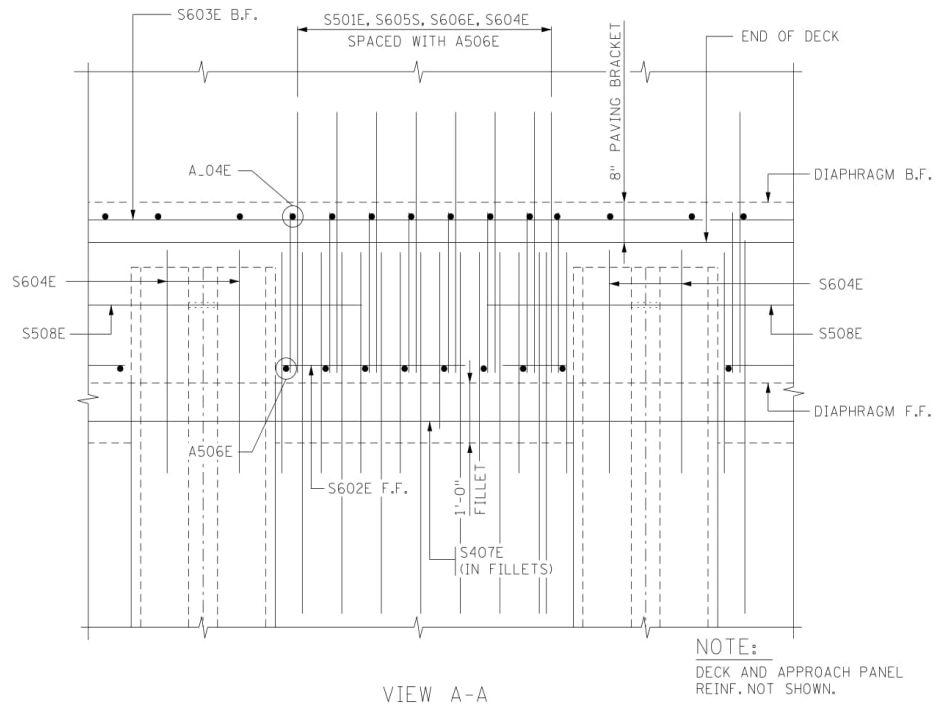


Figure 11.1.1.3

JULY 2016

LRFD BRIDGE DESIGN

11-12

**Figure 11.1.1.4****Integral Abutment Reinforcement Design Guide**

Integral abutment reinforcement may be designed using the following guidance on beam and slab span bridges where all of the following criteria are met:

- All requirements of Articles 11.1 and 11.1.1 of this manual are met
- Beam height $\leq 72''$
- Beam spacing $\leq 13'-0''$
- Pile spacing $\leq 11'-0''$
- Factored pile bearing resistance $\phi R_n \leq 165$ tons
- Maximum abutment stem height $\leq 7'-0''$
- Deck thickness plus stool height $\leq 15.5''$

For beam heights that fall in between current MnDOT prestressed beam sizes (i.e. steel beams), use the values corresponding to the next largest beam height in the tables. Detail reinforcement using Figures 11.1.1.2 through 11.1.1.4.

For abutment stem shear reinforcement, use #6 bars spaced at a maximum of 12 inches between piles along the length of the abutment. These bars are designated A601E and A605E in Figures 11.1.1.2 and 11.1.1.3.

For abutment stem back face vertical dowels, select bar size, spacing and length from Table 11.1.1.1. Embed dowels 4'-6" into the stem. These bars are designated A_04E in Figures 11.1.1.2 and 11.1.1.3. Where table shows a maximum spacing of 12", space A_04E dowels with the abutment stem shear reinforcement (A601E) between piles. Where table shows a maximum spacing of 6", space every other A_04E dowel with the abutment stem shear reinforcement (A601E) between piles.

**Table 11.1.1.1 Abutment Stem Vertical Dowels
(A_04E) Minimum Required Bar Size and Length**

Beam Size (in)	Bar Size & Max Spacing	Bar Projection into Abutment Diaphragm
14	#5 @ 12"	8"
18	#6 @ 12"	1'-0"
22	#6 @ 12"	1'-4"
27	#6 @ 12"	1'-9"
36	#7 @ 12"	2'-6"
45	#7 @ 12"	3'-3"
54	#6 @ 6"	4'-0"
63	#6 @ 6"	4'-9"
72	#6 @ 6"	5'-6"

For abutment stem front face vertical dowels, use #5 bars spaced at a maximum of 12 inches between beams. These bars are designated A506E in Figures 11.1.1.2 through 11.1.1.4. Do not space with the other abutment stem reinforcement, but instead space with the abutment diaphragm transverse bars (S501E).

For abutment stem front and back face horizontal reinforcement, use #6 bars spaced at a maximum of 9 inches. These bars are designated A602E in Figures 11.1.1.2 and 11.1.1.3. Account for changes in abutment seat height by varying bar spacing or the number of bars.

For the abutment stem top and bottom longitudinal bars, use 4-#6 bars on the top and bottom faces of the stem for piles spaced at 9 feet or less. These bars are designated A602E in Figures 11.1.1.2 and 11.1.1.3. When pile spacing exceeds 9 feet, use #6 bars in the corners with two additional

#7 bars on the top and bottom faces of the stem. These bars are designated A602E and A707E in Figures 11.1.1.2 and 11.1.1.3.

Include 2-#4 pile ties on each side of each pile. These bars are designated A403E in Figures 11.1.1.2 and 11.1.1.3.

For abutment diaphragm transverse reinforcement, use #5 bars, which are designated S501E in Figures 11.1.1.2 through 11.1.1.4. Space them at a maximum of 12 inches between beams, matching the abutment stem front face vertical dowels (A506E).

For abutment diaphragm deck ties, approach panel ties and fillet ties, use #6 bars spaced at a maximum of 12 inches between beams to match the abutment stem front face vertical dowels. These bars are designated S604E, S605S and S606E, respectively in Figures 11.1.1.2 through 11.1.1.4. Additionally, place S604E and S605S bars outside the fascia beams to the end of the diaphragm. Do not place S606E fillet ties outside of the fascia beams. Place two additional S604E diaphragm deck ties at equal spaces at the end of each beam.

Provide 1-#4 horizontal bar in the fillet area of the abutment diaphragm that runs the width of the fillet. This bar is designated S407E in Figures 11.1.1.2 through 11.1.1.4.

For abutment diaphragm front face and back face horizontal reinforcement, use equally spaced #6 bars. These bars are designated S602E and S603E, respectively in Figures 11.1.1.2 through 11.1.1.4. Determine the number of bars using Table 11.1.1.2.

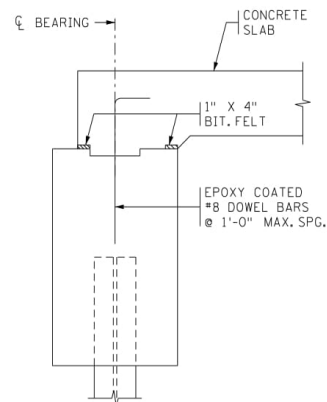
Table 11.1.1.2
Abutment Diaphragm Horizontal Bars (S602E & S603E)
Minimum Required Number of #6 Bars, Each Face

Beam Size (in)	Beam Spacing (feet)				
	≤ 9	10	11	12	13
14	2	2	2	2	2
18	2	2	2	2	2
22	2	2	2	2	2
27	3	3	3	3	3
36	3	3	3	3	4
45	4	4	4	4	5
54	5	5	5	5	6
63	6	6	6	7	7
72	7	7	7	8	9

For abutment diaphragms of concrete slab bridges, provide a minimum of two #6 bars in both the front face (S602E) and back face (S603E) with a maximum spacing of 12 inches.

For skews less than or equal to 20 degrees, place end diaphragm transverse bars (S501E), slab dowels (S606E), and approach panel dowels (S605S) perpendicular to the centerline of bearing. When skews exceed 20 degrees, place bars parallel to the working line.

For bridges on the local system, pinned connections between the abutment stem and diaphragm are allowed in instances where the material encountered in the soil borings for the bridge is very stable and abutment movement from slope instabilities is very unlikely. Pinned connections should be limited to concrete slab bridges with skews less than 30 degrees that have abutment stem exposure heights set at no greater than 2 feet at the low point. Provide #8 dowels at 1'-0" maximum spacing along the centerline of bearing, and a strip of 1" x 4" bituminous felt along the front edge of abutment stem and back edge of slab to allow rotation. See Figure 11.1.1.5. For all other cases, use a fixed connection similar to that shown in Figures 11.1.1.2 through 11.1.1.4.



ABUTMENT CROSS SECTION WITH PINNED CONNECTION

(STEM & SLAB REINF. NOT SHOWN)

Figure 11.1.1.5

Integral Abutment General Design/Analysis Method

Design piling for axial loads only. Assume that one half of the approach panel load is carried by the abutment. Distribute live load over the entire length of abutment. Apply the number of lanes that will fit on the superstructure adjusted by the multiple presence factor. Use a minimum of four piles in an integral abutment.

For integral abutments that do not meet the **Integral Abutment Reinforcement Design Guide** criteria found in this section, use the methods outlined below to design the reinforcement.

Design vertical shear reinforcement in the abutment stem for the maximum factored shear due to the simple span girder reactions, including the dynamic load allowance of 33%. Consider the stem to act as a continuous beam with piles as supports.

Punching shear of the piles can be assumed to be satisfied and need not be checked.

Design abutment stem backface vertical dowels for the passive soil pressure that develops when the bridge expands. Assume the abutment stem acts as a cantilever fixed at the bottom of the diaphragm and free at the bottom of the stem. Referring to Figure 11.1.1.6, determine the passive pressure p_p at the elevation of the bottom of the diaphragm and apply as a uniform pressure on the stem.

$$p_p = k_p \cdot \gamma_{\text{soil}} \cdot h_{\text{soil}}$$

$$k_p = \tan^2 \left(45 + \frac{\phi}{2} \right)$$

Where:

k_p = coefficient of passive pressure

γ_{soil} = unit weight of backfill soil

h_{soil} = height of soil from top of deck to top of stem
(see Figure 11.1.1.6)

ϕ = angle of internal friction of the backfill material (use 30 degrees)

Then design for a moment M_{up} equal to:

$$M_{up} = \gamma_{EH} \cdot \left(\frac{p_p \cdot h_{stem}^2}{2} \right)$$

A load factor for passive earth pressure is not specified in the LRFD specifications. Use the maximum load factor for active earth pressure, $\gamma_{EH} = 1.50$.

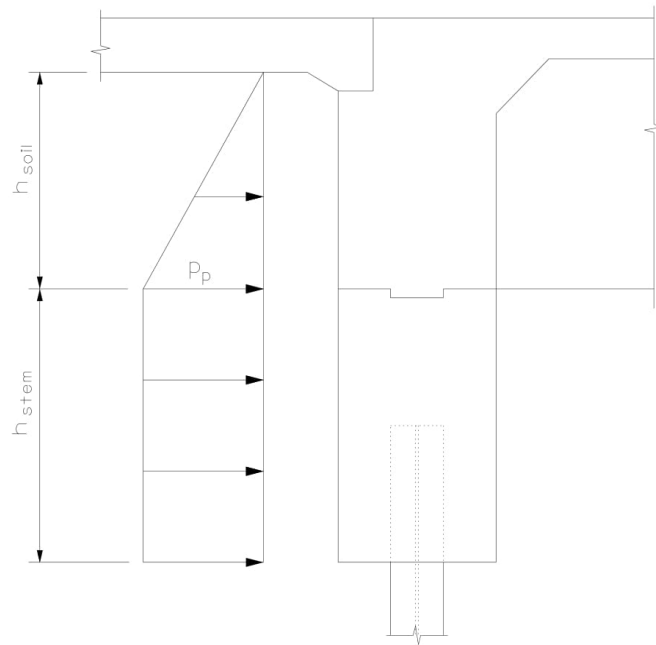


Figure 11.1.1.6

Design abutment stem front and back face horizontal bars for the passive soil pressure which results when the bridge expands. Consider the stem to be a continuous beam with piles as supports and design for a moment of:

$$M_{up} = \gamma_{EH} \cdot \left(\frac{w_p L^2}{10} \right)$$

Where:

w_p = passive pressure calculated at the elevation of the bottom of abutment diaphragm and applied as a uniform pressure on the abutment stem
 $= p_p \cdot h_{\text{stem}}$
 L = pile spacing

Design abutment stem top and bottom horizontal bars for vertical loads due to girder reactions, including dynamic load allowance of 33%. Consider the stem to be a continuous beam with piles as supports. Also, check that the front and back face horizontal bars meet the longitudinal skin reinforcement provisions of LRFD Article 5.7.3.4.

Similar to abutment stem, design abutment diaphragm horizontal bars for the passive soil pressure which results when the bridge expands. For this case, consider the diaphragm to be a continuous beam with the superstructure girders as supports.

For crack control checks, assume a Class 1 exposure condition ($\gamma_e=1.00$).

For size and spacing of all other abutment diaphragm bars, refer to the **Integral Abutment Reinforcement Design Guide**.

11.1.2 Semi-Integral Abutments

Semi-integral abutments are similar to integral abutments in that the superstructure and approach panel are connected and move together. Unlike integral abutments, the superstructure is supported on bearings that allow movement independent from the abutment stem. The abutment stem is stationary and is supported by a spread footing or a pile cap on multiple rows of piles. Figure 11.1.2.1 illustrates typical semi-integral abutment cross-section details and reinforcement.

Geometry

Skews on semi-integral abutments are limited to 30 degrees when wingwalls are parallel to the roadway in order to prevent binding of the approach panel/wingwall interface during thermal movement. For other wingwall configurations, bridge length and skew limits are the same as those for integral abutments. Whenever the skew is greater than 30 degrees, provide a concrete guide lug to limit unwanted lateral movement.

Refer to Figure 11.1.2 for minimum cover and clearance requirements. Provide a minimum abutment stem thickness of 4'-0".

Provide pedestals under the bearings and slope the bridge seat between pedestals to provide drainage toward the abutment front face. A standard seat slope provides one inch of fall from the back of the seat to the front of the seat. In no case should the slope be less than 2 percent. Set pedestals back 2 inches from front face of abutment. Minimum pedestal height is to be 3 inches at front of pedestal. Preferred maximum pedestal height is 9 inches. Provide #5 reinforcing tie bars at 6 inch to 8 inch centers in both directions under each bearing. For bearing pedestals over 9 inches tall, provide column ties in addition to other reinforcement. Provide 2 inches of clear cover for horizontal pedestal bars in the bridge seat. Provide a minimum of 2 inches of clear distance between anchor rods and reinforcing tie bars.

Provide a 3 inch minimum horizontal gap between the abutment diaphragm lug and abutment stem.

When the angle between the back face of wingwall and back face of abutment is less than 135 degrees, provide a 2'-0" x 2'-0" corner fillet on the back face of the wingwall/abutment connection. Extend the fillet from the top of footing to the top of abutment stem on the back face.

Provide a vertical construction joint at the abutment to wingwall connection. Detail the joint location with the goal of making it inconspicuous by considering the wingwall layout, abutment skew angle, fascia beam offset distance from the abutment edge, and aesthetic treatment. For wingwall layout parallel to the roadway, the preferred construction joint location is through the thickness of the abutment in a plane coincident with the back face of the wingwall. For abutments with geometry or aesthetic features that preclude this, another location such as at a vertical rustication line in the abutment or wingwall front face is appropriate. When aesthetic features govern the joint location, the Preliminary Bridge Plans Engineer will provide acceptable construction joint locations in the preliminary plan based on guidance from the Bridge Architectural Specialist. Avoid horizontal construction joints in the wingwall unless absolutely needed. If horizontal joints are needed, locate the joints at a rustication line.

Provide 1 inch of Type B (low density) polystyrene in the vertical gap between the end diaphragm and back face of wingwall. Also, provide 1 inch of Type A (high density) polystyrene in the horizontal gap between the end diaphragm lug and abutment stem. Additionally, provide a membrane waterproofing system with a 1 inch backer rod to allow movement to occur without tearing the waterproofing. Note that the membrane waterproofing and backer rod are incidental to the "Structural

JULY 2016

LRFD BRIDGE DESIGN

11-20

Concrete (____)" and the geotextile filter is incidental to the "Bridge Slab Concrete (____)". See Figures 11.1.2.1 and 11.1.2.2 for details.

Place 1½ inches of Type B (low density) polystyrene between the edge of the approach panel and the back face of the wingwall to minimize binding of the approach panel on the wingwall interface during thermal movement. See approach panel standard plan sheets 5-297.225 and .229 for more details.

Detail semi-integral abutments with a drainage system behind the wall (Detail B910). Outlet the 4 inch drains through the wingwalls and backslopes.

For new bridges, tie the approach panel to the bridge with stainless steel dowel bars that extend at a 45 degree angle out of the diaphragm through the paving bracket seat and bend horizontally 6 inches below the top of the approach panel. (See bar #6S, Figure 11.1.2.1.) For repair projects, provide an epoxy coated dowel rather than stainless steel due to the shorter remaining life of the bridge. Include a ½ inch x 7 inch bituminous felt strip on the bottom of the paving bracket to allow rotation of the approach panel.

JULY 2016

LRFD BRIDGE DESIGN

11-21

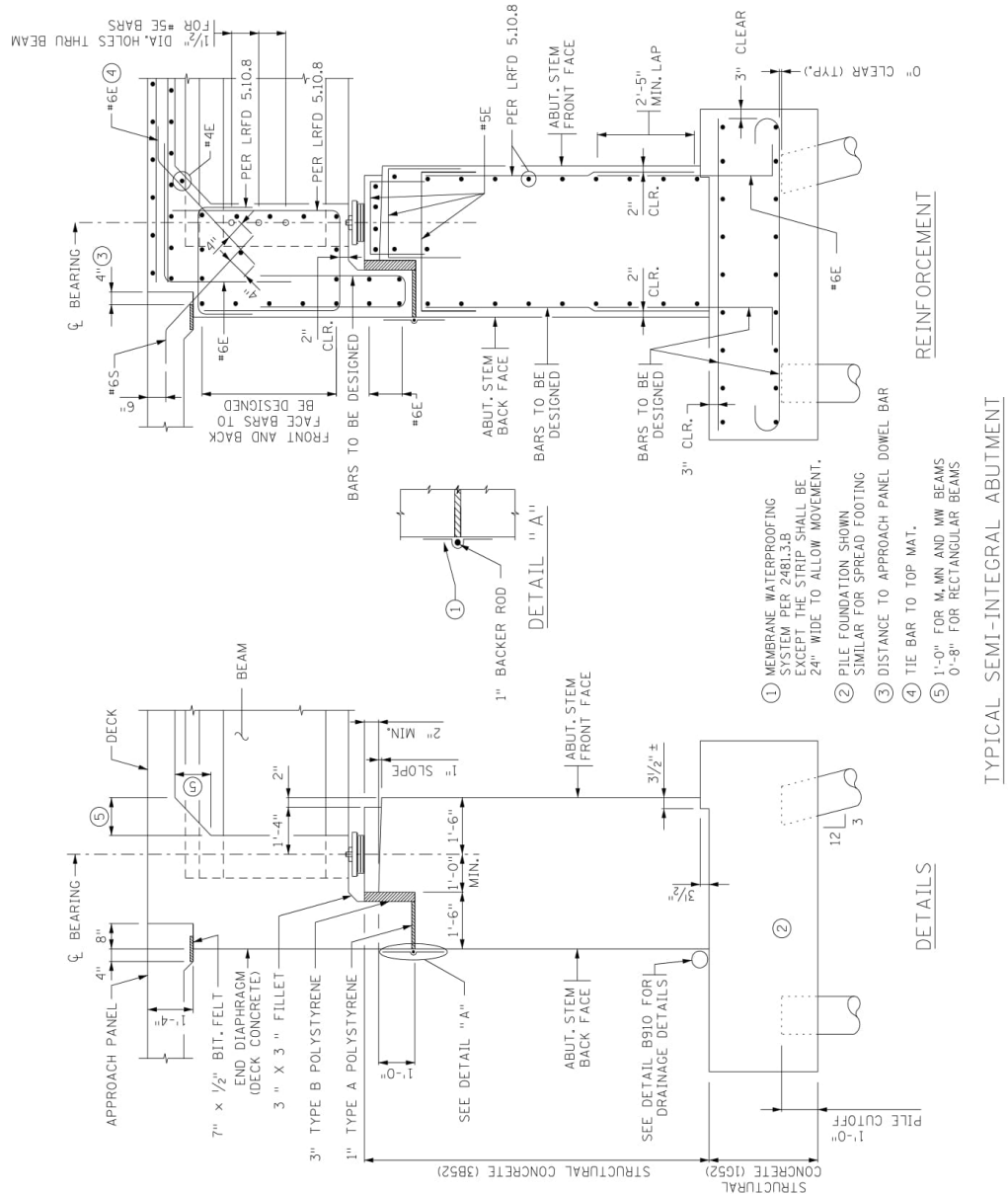


Figure 11.1.2.1

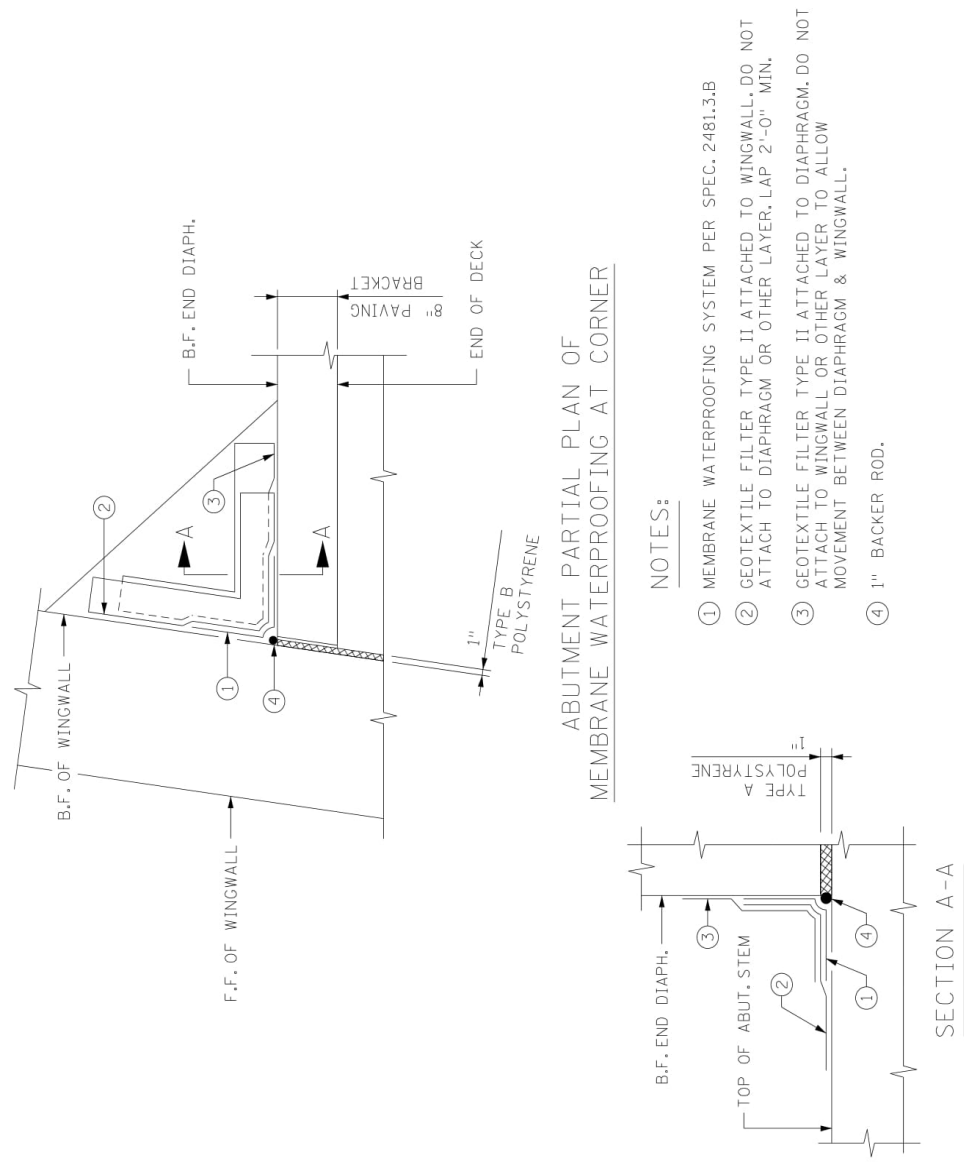


Figure 11.1.2.2

Design/Analysis

For single span bridges, provide fixity at one of the abutments.

Design semi-integral abutment stem, footing, and piles in accordance with Article 11.1.3 of this manual under **Design/Analysis**, except modify the Construction Case 1 loading as follows:

Construction Case 1a – Strength I ($0.90DC+1.00EV+1.50EH+1.75LS$)
Abutment stem has been constructed and backfilled, but the superstructure and approach panel are not in place. Use minimum load factors for vertical loads and maximum load factors for horizontal loads. Assume a single lane (12 foot width) of live load surcharge (LS) is acting on abutments less than 100 feet long measured along the skew. Apply two lanes of LS for abutments 100 feet or longer.

Construction Case 1b – Strength I ($0.90DC+1.00EV+1.50EH+1.75LS$)
Abutment has been constructed and the superstructure is in place. All of the backfill has been placed, but the approach panel has not been constructed. Use minimum load factors for vertical loads and maximum load factors for horizontal loads. Assume a single lane (12 foot width) of live load surcharge is acting on abutments less than 100 feet long measured along the skew. Apply two lanes of LS for abutments 100 feet or longer.

Design abutment diaphragm front and back face horizontal bars for the passive soil pressure which results when the bridge expands.

Design abutment diaphragm vertical bars found in the lug to resist the passive pressure that develops when the bridge expands. Assume the diaphragm lug acts as a cantilever fixed at the bottom of the diaphragm.

Semi-integral abutment diaphragm horizontal reinforcement can be designed using the **Integral Abutment Reinforcement Design Guide** found in this section, provided all of the criteria for the design guide are met. When using this guide for semi-integral abutments, the stem height requirement may be ignored. Design front and back face horizontal bars using Table 11.1.1.2, and place 4 additional #6 bars in the diaphragm lug. (See Figure 11.1.2.1).

For skews less than or equal to 20 degrees, place diaphragm transverse bars, slab dowel, and approach panel dowel bars perpendicular to the centerline of bearing. When skews exceed 20 degrees, place bars parallel to the working line.

For semi-integral abutments with total heights (stem plus footing) of less than 15 feet, use vertical contraction joints spaced at approximately 32 feet (see Detail B801). For semi-integral abutments with total heights greater than or equal to 15 feet, use construction joints (with keyways) spaced at approximately 32 feet.

11.1.3 Parapet Abutments

Parapet abutments have backwall or parapet elements that are separate from the end diaphragms in the superstructure. Low parapet abutments have total heights (from top of paving block to bottom of footing) of less than 15 feet. High parapet abutments have total heights equal to or greater than 15 feet. If the total height of the abutment is more than 40 feet, counterforts should be considered.

Geometry

Refer to Figure 11.1.2 for minimum cover and clearance requirements.

When the angle between the back face of wingwall and back face of abutment is less than 135 degrees, provide a 2'-0" x 2'-0" corner fillet on the back face of the wingwall/abutment connection. Extend the fillet from the top of footing to 1 inch below the top of abutment parapet on the back face and provide a 1 inch thick polystyrene bond breaker between the top of fillet and approach panel.

Provide a vertical construction joint at the abutment to wingwall connection. Detail the joint location with the goal of making it inconspicuous by considering the wingwall layout, abutment skew angle, fascia beam offset distance from the abutment edge, and aesthetic treatment. For abutments without maskwalls that have a wingwall layout parallel to the roadway, the preferred construction joint location is at the end of the corner fillet and running through the wingwall thickness. For bridges with mask walls, the preferred construction joint location is through the thickness of the abutment in a plane coincident with the back face of the wingwall. This helps to prevent development of mask wall horizontal cracks at the top of the bridge seat that extend horizontally into the wingwall. For abutments with geometry or aesthetic features that preclude use of the preferred location, another location such as at a vertical rustication line in the abutment or wingwall front face is appropriate. When aesthetic features govern the joint location, the Preliminary Bridge Plans Engineer will provide acceptable construction joint locations in the preliminary plan based on guidance from the Bridge Architectural Specialist. Avoid horizontal construction joints in the wingwall unless absolutely needed. If horizontal joints are needed, hide the joints by locating at a rustication line.

A.5: Oklahoma DOT CLSM Backfilling Specifications

501.04

EXCAVATION AND BACKFILL FOR STRUCTURES

(e) *Approval of Foundation*

Notify the Engineer when the excavation is ready for inspection. Place the footing concrete after the Engineer approves the excavation and foundation material. Unless otherwise approved by the Engineer, do not place concrete under water.

B. Backfilling

(1) General

Place and compact backfill (to the existing ground line) and embankments in accordance with Section 202, "Earthwork," unless modified by Subsection 501.04.B(1). If excavation does not yield enough suitable material for backfill, provide additional backfill material in accordance with Subsection 501.02, "Materials."

Unless otherwise required by the Contract, backfill excavated spaces unoccupied by permanent structures up to the surface of the surrounding ground and allow for settlement. Uniformly backfill around the sides of the structure to ensure equal density of the surrounding ground, and neatly grade its top surface. Do not place rocks larger than 3 in [75 mm] against concrete surfaces.

Place and compact fill for retaining walls, abutments, wingwalls, and bridge bents in layers no greater than 6 in [150 mm] thick. Uniformly backfill around the sides of the structure to ensure equal loading. Compact backfill within, or beneath, embankments within roadways in excavated areas, or in front of abutments and retaining walls or wingwalls to the same density required for the embankments. Unless otherwise required by the Contract, compact fill in embankments to at least 95 percent of standard density in accordance with AASHTO T 99.

Place backfill against structure concrete only when the concrete reaches the required compressive strength in accordance with Subsection 509.04.I(2), "Earth Loads."

To prevent horizontal movement of abutments and wingwalls, place backfill on the outside faces before backfilling the inside faces. The Department will not allow jetting the backfill behind abutments or wingwalls. Operate rollers, vibrators, or other compactors parallel to the outside lines of box culverts and cross-drain wingwalls. Compact areas inaccessible to rolling equipment with mechanical tampers.

(2) Placing CLSM

Fill the excavation with approved CLSM uniformly around the structure to the elevation shown on the Plans. Place CLSM in lifts no deeper than 4 ft [1.2 m]. Subsequent lifts of CLSM may be placed when the preceding lift supports foot traffic. Begin placing specified fill material over the CLSM when the water is gone from the surface of the CLSM, or as directed by the Engineer.

(3) Disposal of Surplus

Clean construction areas in accordance with Subsection 104.10, "Final Cleanup." Do not place excess material in the streambed. Remove obstructions that may collect drift, induce scour, or endanger the work as approved by the Engineer. Dispose of excess excavated and removed materials.

270

501.06 BASIS OF PAYMENT

The Department will pay for each pay item at the contract unit price per the specified pay unit as follows:

Pay Item:	Pay Unit:
(A) <i>STRUCTURAL EXCAVATION, UNCLASSIFIED</i>	Cubic Yard [Cubic Meter]
(B) <i>SUBSTRUCTURE EXCAVATION, COMMON</i>	Cubic Yard [Cubic Meter]
(C) <i>SUBSTRUCTURE EXCAVATION, ROCK</i>	Cubic Yard [Cubic Meter]
(D) <i>UNCLASSIFIED BACKFILL</i>	Cubic Yard [Cubic Meter]
(E) <i>SELECT BACKFILL</i>	Cubic Yard [Cubic Meter]

272

EXCAVATION AND BACKFILL FOR STRUCTURES

501.06

Pay Item:	Pay Unit:
(F) <i>GRANULAR BACKFILL</i>	Cubic Yard [Cubic Meter]
(G) <i>CLSM BACKFILL</i>	Cubic Yard [Cubic Meter]

The Department will pay for the volumes of *Unclassified Excavation*, calculated in accordance with Subsection 501.05.B(1), "Unclassified Excavation," in accordance with Section 202, "Earthwork."

The Department will consider the cost of removal and disposal of obstructions, as defined in Subsection 501.01.C, "Obstructions," to be included in the Contract unit price for the relevant excavation pay item, unless specifically included in other pay items. The Department will pay for volumes of removed obstructions at twice the Contract unit price for the relevant excavation pay item for which the obstruction was encountered.

The Department will consider the cost of removing volumes of water, disposing of excess material, and excavation for placing sway bracing, sash bracing, and bulkheads on timber substructures to be included in the Contract unit price for the relevant excavation pay item.

The Department will pay for the volume of soft and yielding material removed and a like volume for replacement material from the bottom of box footings as *Structural Excavation, Unclassified* at the Contract unit price.

The Department will consider backfilling around structures below the existing ground line to be included in the contract unit price for the relevant excavation pay item.

The Department will not pay for excess concrete when the Contractor omits footing backforms and fills the excavation with concrete in accordance with Subsection 501.04.A(2)(a), "General."

701.19 CONTROLLED LOW-STRENGTH MATERIAL

A. General

Controlled Low-Strength Material (CLSM). A low strength grout backfill material consisting of portland cement, fly ash, fine aggregate, and water.

The Department will allow the use of an air entraining agent.

B. Mix Design

Design the mix using absolute volumes. Use at least 20 lb/yd³ [12 kg/m³] of portland cement in the mix design. Submit the proposed mix design with trial batch testing data before use. Include the weight [mass], specific gravity, material source, and material requirements for each ingredient. Include the flowability results, unit weight [mass], and trial batch strength tests. The Department will allow the submittal of previously used and successful mix designs without retesting if material sources have not changed. Provide materials in accordance with the following sections and subsections for CLSM:

Material:	Section or Subsection:
Portland Cement	701.02
Fly Ash	702
Fine Aggregate	701.05
Water	701.04
Air Entraining Agents	701.03

C. Sampling and Testing

Test CLSM in accordance with the following methods:

- Conduct the flow test in accordance with ASTM D 6103. Provide a CLSM spread diameter of 8 in [200 mm] or greater.
- Conduct the unit weight [mass] tests in accordance with ASTM D 6023. The Resident Engineer will reject batches with a unit weight [mass] that deviates 5 percent or more from the mix design value.
- Conduct the compressive strength tests in accordance with ASTM D 4832. Provide a CLSM compressive strength at 28 days from 100 psi to 800 psi [700 kPa to 5,500 kPa]. Earlier strength tests may be performed to confirm that the material reaches the minimum strength, but are not required by the Contract.

579

A.6: PennDOT Approach Slab Details

GENERAL NOTES:

- DESIGN SPECIFICATIONS:
 - AASHTO, LRFD BRIDGE DESIGN SPECIFICATIONS AND AS SUPPLEMENTED BY THE DESIGN MANUAL, PART 4, STRUCTURES.
 - DESIGN IS IN ACCORDANCE WITH THE LOAD AND RESISTANCE FACTOR DESIGN METHOD (LRFD).
- CONSTRUCTION SPECIFICATIONS AND WORKMANSHIP:
 - PROVIDE MATERIALS AND PERFORM WORK IN ACCORDANCE WITH THE CURRENT VERSION OF THE PENNSYLVANIA DEPARTMENT OF TRANSPORTATION PUBLICATION 408, AASHTO/AWS/DI.5M/DI.5 - BRIDGE WELDING CODE AND THE CONTRACT SPECIAL PROVISIONS. (USE AWS/DI.1/DI.1M FOR WELDING NOT COVERED IN AASHTO/AWS/DI.5M/DI.5.)
- ALL DIMENSIONS SHOWN ARE HORIZONTAL, EXCEPT AS NOTED.
- DIMENSIONS SHOWN ARE FOR A NORMAL TEMPERATURE OF 68 DEGREES F.
- REINFORCEMENT IN SOME SECTIONS IS NOT SHOWN FOR CLARITY.
- IF NEEDED DETAILS ARE NOT FOUND IN THIS STANDARD A SPECIAL SUBMISSION REQUESTING APPROVAL FOR SPECIFIC DETAILS MUST BE MADE TO THE CHIEF BRIDGE ENGINEER.

MATERIAL NOTES:

- PROVIDE THE FOLLOWING CONCRETE CLASS:
 - PROVIDE CLASS A CEMENT CONCRETE IN SUPPORT PEDESTALS BELOW THE BRIDGE SEAT CONSTRUCTION JOINT FOR TYPE 4 APPROACH SLAB.
 - PROVIDE CLASS AA CEMENT CONCRETE IN APPROACH SLAB TYPES 1, 2 AND 4, SLEEPER SLABS, BARRIERS, SUPPORT PEDESTALS ABOVE THE BRIDGE SEAT CONSTRUCTION JOINT AND DRAIN TROUGH.
 - PROVIDE CLASS AA/C CEMENT CONCRETE IN APPROACH SLAB TYPES 3 AND 5.
 - A HIGHER CLASS OF CONCRETE MAY BE SUBSTITUTED FOR A LOWER CLASS OF CONCRETE AT NO ADDITIONAL COST TO THE DEPARTMENT.
- REINFORCEMENT STEEL:
 - PROVIDE GRADE 60 DEFORMED REINFORCING BARS THAT MEET THE REQUIREMENTS OF ASTM A615, ASTM A996, OR A706. DO NOT WELD REINFORCEMENT BARS UNLESS SPECIFIED. DO NOT USE RAIL STEEL A996 IN BARRIERS OR WHERE BENDING OR WELDING OF REINFORCEMENT BARS IS INDICATED.
 - EPOXY COAT ALL REINFORCEMENT BARS.
 - PROVIDE MINIMUM LAP AND EMBEDMENT LENGTH FOR REINFORCING BARS IN ACCORDANCE WITH BC-735M.
- FABRICATED STRUCTURAL STEEL:
 - PROVIDE STRUCTURAL STEEL CONFORMING TO AASHTO M270 GRADE 36 (ASTM A709, GRADE 36) UNLESS NOTED OTHERWISE.
- NEOPRENE COMPRESSION SEALS:
 - PROVIDE MATERIALS AND DETAILS IN ACCORDANCE WITH BC-766M.
- NEOPRENE STRIP SEAL DAMS:
 - PROVIDE MATERIALS AND DETAILS IN ACCORDANCE WITH BC-767M.
- TOOTH EXPANSION DAMS:
 - PROVIDE MATERIALS AND DETAILS IN ACCORDANCE WITH BC-762M.

APPROACH SLAB TYPES	
TYPE	DESCRIPTION
1	CONCRETE APPROACH SLAB
2	CONCRETE APPROACH SLAB WITH SUPERPAVE ASPHALT OVERLAY
3	ABUTMENT WITH BACKWALL WITH ATTACHED CONCRETE APPROACH SLAB AND NEOPRENE STRIP SEAL DAM
4	ABUTMENT WITH BACKWALL WITH ATTACHED INTEGRAL CONCRETE DRAIN TROUGH AND TOOTH EXPANSION DAM
5	CONCRETE APPROACH SLAB WITH INTEGRAL ABUTMENT

NOTE: ASPHALT OVERLAY IS NOT PERMITTED ON APPROACH SLAB TYPES 1, 3, 4 AND 5.

INDEX OF SHEETS

SHEET NO.	SHEET TITLE
1	GENERAL NOTES - 1
2	GENERAL NOTES - 2
3	TYPE 1 AND TYPE 2 - SECTIONS AND DETAILS
4	TYPE 1 AND TYPE 2 - PLAN 1
5	TYPE 1 AND TYPE 2 - PLAN 2
6	TYPE 1 AND TYPE 2 - PLAN 3
7	TYPE 1 AND TYPE 2 - PLAN 4
8	TYPE 1 THRU TYPE 4 - TRANSVERSE SECTION WITH ATTACHED BARRIERS
9	TYPE 1, 2 AND 4 - DETAILS 1, 2 AND 3
10	TYPE 1 AND TYPE 2 - DETAIL 4
11	TYPE 1 AND TYPE 2 - DETAIL 5
12	TYPE 1 AND TYPE 2 - DETAIL 6
13	TYPE 1 AND TYPE 2 - DETAIL 7
14	TYPE 1 AND TYPE 2 - DETAIL 8
15	TYPE 1 AND TYPE 2 - DETAIL 9
16	TYPE 1 AND TYPE 2 - DETAIL 10
17	TYPE 1 AND TYPE 2 - DETAIL 11
18	TYPE 1 AND TYPE 2 - DETAIL 12
19	TYPE 3 - PLAN 1 AND SECTION
20	TYPE 3 - PLAN 2
21	TYPE 3 - PLAN 3
22	TYPE 3 AND TYPE 5 - DETAILS 13, 14 AND 15
23	TYPE 5 - DETAILS 16, 17 AND 18
24	TYPE 3 - DETAILS 19 AND 20
25	TYPE 3 - DETAILS 21 AND 22
26	TYPE 4 - PLAN 1 AND SECTION
27	TYPE 4 - PLAN 2
28	TYPE 4 - PLAN 3
29	TYPE 4 - DETAIL 23
30	TYPE 4 - DETAIL 24
31	TYPE 4 - DETAIL 25
32	TYPE 4 - DETAIL 26
33	TYPE 4 - DRAIN TROUGH DETAILS 1
34	TYPE 4 - DRAIN TROUGH DETAILS 2
35	TYPE 5 - PLAN AND SECTION

RC-12M	BACKFILL AT STRUCTURES	BC-788M	TYPICAL WATERPROOFING AND EXPANSION DETAILS
RC-20M	CONCRETE PAVEMENT JOINTS	BC-799M	MECHANICALLY STABILIZED EARTH RETAINING WALLS
RC-24M	PAVEMENT RELIEF JOINT	BD-601M	CONCRETE DECK SLAB
RC-30M	SUBSURFACE DRAINS	BD-610M	PA BRIDGE BARRIER
RC-50M	GUIDE RAIL TO BRIDGE BARRIER TRANSITIONS	BD-611M	CONCRETE DIAPHRAGM DETAILS FOR STEEL I-BEAM STRUCTURES
BC-703M	THREE-BEAM TO VERTICAL WALL BRIDGE BARRIER TRANSITION CONNECTION	BD-615M	PA HT BRIDGE BARRIER
BC-708M	THREE-BEAM TO PA TYPE 10M BRIDGE BARRIER TRANSITION CONNECTION	BD-617M	PA TYPE 10M BRIDGE BARRIER
BC-709M	PA TYPE 10M BRIDGE BARRIER	BD-618M	CONCRETE VERTICAL WALL BRIDGE BARRIER
	THREE-BEAM TO PA BRIDGE BARRIER TRANSITION CONNECTION	BD-621M	REINFORCED CONCRETE ABUTMENTS
BC-713M	PA BRIDGE BARRIER	BD-622M	R.C. ABUTMENTS WITH BACKWALL
BC-735M	WALL CONSTRUCTION AND EXPANSION JOINT DETAILS	BD-624M	R.C. ABUTMENTS WITHOUT BACKWALL
BC-736M	REINFORCEMENT BAR FABRICATION DETAILS	BD-627M	MOMENT SLABS
BC-739M	BRIDGE BARRIER TO GUIDE RAIL TRANSITION	BD-655M	TYPICAL SUPERSTRUCTURE SECTIONS
BC-752M	CONCRETE DECK SLAB DETAILS	BD-656M	TYPICAL LONGITUDINAL SECTIONS
BC-762M	TOOTH EXPANSION DAM FOR PRESTRESSED CONCRETE AND STEEL BEAM BRIDGES	BD-661M	BOX BEAM REINFORCEMENT DETAILS
BC-766M	PREFORMED NEOPRENE COMPRESSION SEAL JOINT FOR APPROACH SLABS	BD-662M	I-BEAM AND PA BULB-TEE BEAM REINFORCEMENT DETAILS
BC-767M	NEOPRENE STRIP SEAL DAM FOR PRESTRESSED CONCRETE AND STEEL I-BEAM BRIDGES	BD-676M	INTEGRAL ABUTMENTS
BC-775M	MISCELLANEOUS PRESTRESS DETAILS	BD-679M	STRUCTURE MOUNTED SOUND BARRIER WALLS

REFERENCE DRAWINGS

COMMONWEALTH OF PENNSYLVANIA
DEPARTMENT OF TRANSPORTATION
BUREAU OF PROJECT DELIVERY

STANDARD BRIDGE APPROACH SLABS GENERAL NOTES - 1

RECOMMENDED APR. 29, 2016 <i>Thomas P. Meier</i> CHIEF BRIDGE ENGINEER	RECOMMENDED APR. 29, 2016 <i>Brian J. Thompson</i> DIRECTOR, BUREAU OF PROJECT DELIVERY	SHEET 1 OF 35 BD-628M
--	---	--------------------------

INSTRUCTIONS TO DESIGNER NOTES

1. THE INFORMATION SHOWN IN THIS STANDARD IS PROVIDED FOR USE IN THE DEVELOPMENT OF THE CONTRACT DRAWINGS. THE DESIGNER IS RESPONSIBLE FOR THE PRESENTATION OF ALL REQUIRED DETAILS AND NOTES.
2. APPROACH SLAB SKEW ANGLE TO MATCH BRIDGE SKEW ANGLE. BRIDGE SKEW ANGLE MUST BE GREATER THAN OR EQUAL TO 45 DEGREES. IF THE BRIDGE SKEW ANGLE IS LESS THAN 45 DEGREES THE DESIGNER MUST DISCUSS ALTERNATE DETAILS WITH THE BRIDGE DESIGN AND TECHNOLOGY DIVISION.
3. DESIGNER TO DETERMINE AND SPECIFY THE APPROPRIATE TYPE OF APPROACH SLAB REQUIRED ON THE TSM DRAWINGS FOR APPROVAL BY PENNDOT.
4. REFER TO APPROACH SLAB SELECTION CRITERIA TABLE FOR ADDITIONAL INFORMATION.
5. DIFFERENT APPROACH SLAB TYPES ARE PERMITTED ON THE SAME BRIDGE.
6. APPROACH SLABS ARE PERMITTED TO BE USED ON CURVED HORIZONTAL ALIGNMENTS. DESIGNER TO DETERMINE IF THESE DETAILS ARE APPROPRIATE FOR EACH INDIVIDUAL SITUATION.
7. CONTRACT DRAWINGS:
 - PROVIDE COMPLETE DETAILS AND NOTES AS REQUIRED.
 - PROVIDE COMPLETE REINFORCEMENT BAR DETAILS AND BAR SCHEDULE.
 - PROVIDE FINISHED TOP OF CONCRETE ELEVATIONS AT THE BEGIN AND END OF SLABS AND AT 10 FOOT INTERVALS. PROVIDE ELEVATIONS AT THE BASELINE, GUTTER LINES, AND AT BREAKS IN SLOPES.
8. APPROACH SLAB PER RC-23M:
 - APPROACH SLAB DETAILS SHOWN ON RC-23M ARE ONLY PERMITTED WHEN THE BRIDGE IS DESIGNED USING BRADDO, UNLESS OTHERWISE DIRECTED.
 - APPROACH SLAB DETAILS ARE NOT REQUIRED ON THE CONTRACT DRAWINGS WHEN THE BRIDGE IS DESIGNED USING BRADDO, UNLESS OTHERWISE DIRECTED.
 - IF THE APPROACH SLAB IS CONSTRUCTED IN ACCORDANCE WITH RC-23M, THE APPROACH SLAB IS A ROADWAY ITEM, UNLESS OTHERWISE DIRECTED.
9. BRIDGE PAVEMENT ITEMS:
 - BRIDGE APPROACH SLABS ARE TO BE INCLUDED AS PART OF THE LUMP SUM STRUCTURE AND SEPARATED INTO INDIVIDUAL ITEMS, UNLESS OTHERWISE DIRECTED.
 - PROVIDE SEPARATE COLUMNS IN THE QUANTITY BLOCK FOR EACH APPROACH SLAB.
 - APPROACH SLAB AT ABUTMENT 1 / APPROACH SLAB AT ABUTMENT 2
 - PROVIDE SEPARATE ITEMS AND INDICATE THE APPROXIMATE QUANTITY FOR CONCRETE, REINFORCEMENT, NEOPRENE STRIP SEAL DAMS, TOOTH EXPANSION DAMS, PROTECTIVE COATINGS AND ANY OTHER ITEM THAT MAY BE REQUIRED FOR THE CONSTRUCTION OF THE APPROACH SLAB.
 - COMPRESSION SEALS OR INVERTED V JOINT SEALS, WATERSTOP, POLYETHYLENE SHEETING, CLOSED CELL NEOPRENE SPONGE, EPOXY BONDING COMPOUND, SAWING AND SEALING JOINTS, BACKER ROD, AND BITUMINOUS PAPER ITEMS ARE INCIDENTAL TO THE APPROACH SLAB CONCRETE.
 - END COVER PLATES, BOLTS, WASHERS AND THREADED INSERTS FOR TYPE 3 AND 5 APPROACH SLABS ARE INCIDENTAL TO THE NEOPRENE STRIP SEAL DAM.
 - STAINLESS STEEL PLATES, RUBBERIZED TROUGH MATERIAL, GALVANIZED STEEL BARS, STAINLESS STEEL SCREWS, NON SHRINK GROUT, STUDS AND ANCHOR BOLTS REQUIRED FOR THE DRAIN TROUGH FOR TYPE 4 APPROACH SLAB ARE INCIDENTAL TO THE TOOTH EXPANSION DAM PAVEMENT.
 - TYPE 5 APPROACH SLABS:
 - PROVIDE STRUCTURAL BACKFILL IN ACCORDANCE WITH RC-12M. SUBBASE MATERIAL NOT REQUIRED.
10. ROADWAY PAVEMENT ITEMS:
 - SUPERPAVE ASPHALT OVERLAY, ROADWAY PAVEMENT, PAVEMENT RELIEF JOINT, DUCTILE IRON PIPE, INLETS, EXCAVATION, SUBBASE MATERIAL AND SUBGRADE DRAINS ARE ROADWAY PAVEMENT ITEMS.
 - SUBBASE THICKNESS BENEATH THE APPROACH SLABS AND SLEEPER SLABS MUST MATCH THE ROADWAY SUBBASE THICKNESS.
11. SUPERPAVE ASPHALT OVERLAY:
 - THE TYPE OF SUPERPAVE ASPHALT MIXTURE DESIGNS PLACED ON TOP OF THE APPROACH SLAB MUST MATCH THE TYPE OF SUPERPAVE ASPHALT MIXTURE DESIGNS USED ON THE ADJACENT ROADWAY.
 - DESIGNER TO SPECIFY THE REQUIRED SUPERPAVE ASPHALT MIXTURE DESIGNS, FOR THE WEARING AND BASE COURSES, ON THE CONTRACT PLANS. THE DEPTH OF THE COURSES MUST EQUAL 5".
 - ASPHALT OVERLAY IS ONLY PERMITTED ON TYPE 2 APPROACH SLAB.
12. PAVEMENT SUBGRADE DRAIN:
 - PROVIDE SUBGRADE DRAIN, REFER TO RC-30M, ON THE LOW SIDE OF THE SLEEPER SLAB.
13. PROTECTIVE COATINGS:
 - APPLY A PROTECTIVE COATING FOR REINFORCED CONCRETE SURFACES (PENETRATING SEALER, BRIDGE SUPERSTRUCTURE) IN ACCORDANCE WITH PUBLICATION 408, SECTION 1019 TO THE TOP SURFACE OF APPROACH SLAB, EXPOSED SURFACES OF THE SLEEPER SLAB AND TO THE FACE AND TOP SURFACES OF THE BARRIERS. DO NOT PLACE PENETRATING SEALERS ON TOP OF ANY SURFACE THAT RECEIVES ASPHALT OVERLAY.
14. GENERAL INFORMATION:
 - PROVIDE PAYING NOTCH OUT-TO-OUT.
 - THE DETAILS PRESENTED IN THIS STANDARD SHOW A TYPICAL CONCRETE BARRIER. DESIGNER IS RESPONSIBLE TO PROVIDE THE APPROPRIATE DETAILS FOR THE TYPE OF BARRIER REQUIRED.
 - THE DIAPHRAGM REINFORCEMENT CONNECTING THE TYPE 3 APPROACH SLAB TO THE BRIDGE STRUCTURE WAS DEVELOPED BASED ON A HORIZONTAL LOAD EQUAL TO A FRICTION FACTOR OF 0.40 X DEADLOAD OF APPROACH SLAB.
 - DESIGN OF ABUTMENTS AND BEARINGS WITH STRUCTURE SUPPORTED APPROACH SLAB: DESIGNER TO INCLUDE THE FOLLOWING ADDITIONAL VERTICAL LOADS INCURRED FROM THE APPROACH SLAB WHEN DESIGNING THE ABUTMENTS AND BEARINGS.
 - VERTICAL REACTION = $1/2$ DEADLOAD OF APPROACH SLAB + PHL-93 LANE LOAD REACTION FROM APPROACH SLAB.
 - PHL-93 LANE LOAD REACTION IS OBTAINED BY TREATING THE BRIDGE APPROACH SLAB AS A SIMPLE BEAM WHICH SPANS FROM STRUCTURE TO SLEEPER SLAB. DESIGNER MUST DETERMINE MAXIMUM REACTION BASED ON LENGTH OF THE APPROACH SLAB.
 - DESIGN OF BACKWALL WITH BACKWALL SUPPORTED APPROACH SLAB:
 - DESIGNER TO INCLUDE $1/2$ DEADLOAD OF THE APPROACH SLAB, MAXIMUM PHL-93 LIVE LOAD REACTION (AXLES PLUS LANE LOAD) AND BRAKING FORCE WHEN DESIGNING THE BACKWALL.
 - DESIGN OF ABUTMENTS AND BEARINGS TO INCLUDE $1/2$ LIVE LOAD SURCHARGE IN THE DESIGN OF THE ABUTMENT TO ACCOUNT FOR FUTURE CONDITION WITHOUT APPROACH SLABS (I.E., OMIT APPROACH SLAB DEADLOAD AND LIVE LOAD).

CONTRACT DRAWINGS NOTES

- THE FOLLOWING NOTES ARE TO BE PLACED ON THE CONTRACT DRAWINGS
1. CONSTRUCT BRIDGE APPROACH SLAB AFTER THE BRIDGE DECK SLAB IS CONSTRUCTED.
 2. PLACE CONCRETE IN ONE CONTINUOUS OPERATION, UNLESS OTHERWISE INDICATED OR DIRECTED.
 3. TRANSVERSE CONSTRUCTION JOINTS ARE NOT PERMITTED IN THE CONCRETE APPROACH SLAB OR SLEEPER SLAB, UNLESS OTHERWISE INDICATED.
 4. PROVIDE ANY OTHER NOTES AS REQUIRED.

APPROACH SLAB GUIDELINE NOTES

THE FOLLOWING GUIDELINES ARE PROVIDED IN ORDER TO HELP THE DESIGNER DETERMINE THE APPROPRIATE TYPE OF APPROACH SLAB TO BE SPECIFIED ON THE CONTRACT DRAWINGS. DESIGNER TO DISCUSS OPTIONS WITH PENNDOT PRIOR TO TSM SUBMISSION.

1. BRADDO BRIDGES:
 - REFER TO RC-23M. APPROACH SLAB DETAILS ARE NOT REQUIRED ON THE CONTRACT DRAWINGS, UNLESS OTHERWISE DIRECTED.
2. TYPE 1 APPROACH SLAB:
 - PROVIDE TYPE 1 APPROACH SLAB WHEN CONCRETE OR FLEXIBLE PAVEMENT IS SPECIFIED. THE BARRIERS MUST BE CONNECTED TO THE APPROACH SLAB DIRECTLY OR USE MOMENT SLABS CONNECTED TO THE APPROACH SLAB.
3. TYPE 2 APPROACH SLAB:
 - PROVIDE TYPE 2 APPROACH SLAB WHEN FLEXIBLE PAVEMENT IS SPECIFIED. THE BARRIERS MUST BE CONNECTED TO THE APPROACH SLAB, DIRECTLY OR USE MOMENT SLABS CONNECTED TO THE APPROACH SLAB.
4. TYPE 3 APPROACH SLAB:
 - TYPE 3 APPROACH SLABS CONNECTS THE BRIDGE SUPERSTRUCTURE AND BARRIERS WITH THE APPROACH SLAB.
 - PROVIDE TYPE 3 APPROACH SLAB WHEN AN EXPANSION DEVICE IS REQUIRED AND THE DEPARTMENT DIRECTS THE DESIGNER TO RELOCATE THE EXPANSION DEVICE FROM ON THE BRIDGE TO THE END OF THE APPROACH SLAB.
 - DESIGNER TO DETERMINE THE REQUIRED JOINT OPENING AT TIME OF CONSTRUCTION AND THE MOVEMENT REQUIREMENTS OF THE EXPANSION JOINT AT THE END OF THE APPROACH SLAB IN ACCORDANCE WITH THE REQUIREMENTS OF DESIGN MANUAL, PART 4.
4. TYPE 4 APPROACH SLAB:
 - PROVIDE TYPE 4 APPROACH SLAB WHEN AN EXPANSION DEVICE IS REQUIRED AND THE ANTICIPATED JOINT MOVEMENT IS OVER 4". EXTEND THE DECK SLAB CONTINUOUS OVER THE BACKWALL TO THE EXPANSION DEVICE SUPPORTED BY AN INTEGRAL DRAIN TROUGH.
 - DESIGNER TO DETERMINE THE REQUIRED JOINT OPENING AT TIME OF CONSTRUCTION AND THE MOVEMENT REQUIREMENTS OF THE EXPANSION JOINT AT THE END OF THE APPROACH SLAB IN ACCORDANCE WITH THE REQUIREMENTS OF DESIGN MANUAL, PART 4.
6. TYPE 5 APPROACH SLAB:
 - PROVIDE TYPE 5 APPROACH SLAB WHEN INTEGRAL ABUTMENTS ARE SPECIFIED.
 - DESIGNER TO DETERMINE THE REQUIRED JOINT OPENING AT TIME OF CONSTRUCTION AND THE MOVEMENT REQUIREMENTS OF THE EXPANSION JOINT AT THE END OF THE APPROACH SLAB IN ACCORDANCE WITH THE REQUIREMENTS OF DESIGN MANUAL, PART 4, APPENDIX G, SECTION 1.6.
7. TYPE 3 AND 5 APPROACH SLABS ARE NOT PERMITTED IF MECHANICALLY STABILIZED EARTH (MSE) ABUTMENTS AND/OR RETAINING WALLS ARE SPECIFIED. MSE RETAINING WALLS ARE PERMITTED BEYOND THE END OF THE SLEEPER SLAB.
8. REFER TO THE DETAILS FOR BEAM DEPTH LIMITATIONS.

APPROACH SLAB SELECTION CRITERIA TABLE

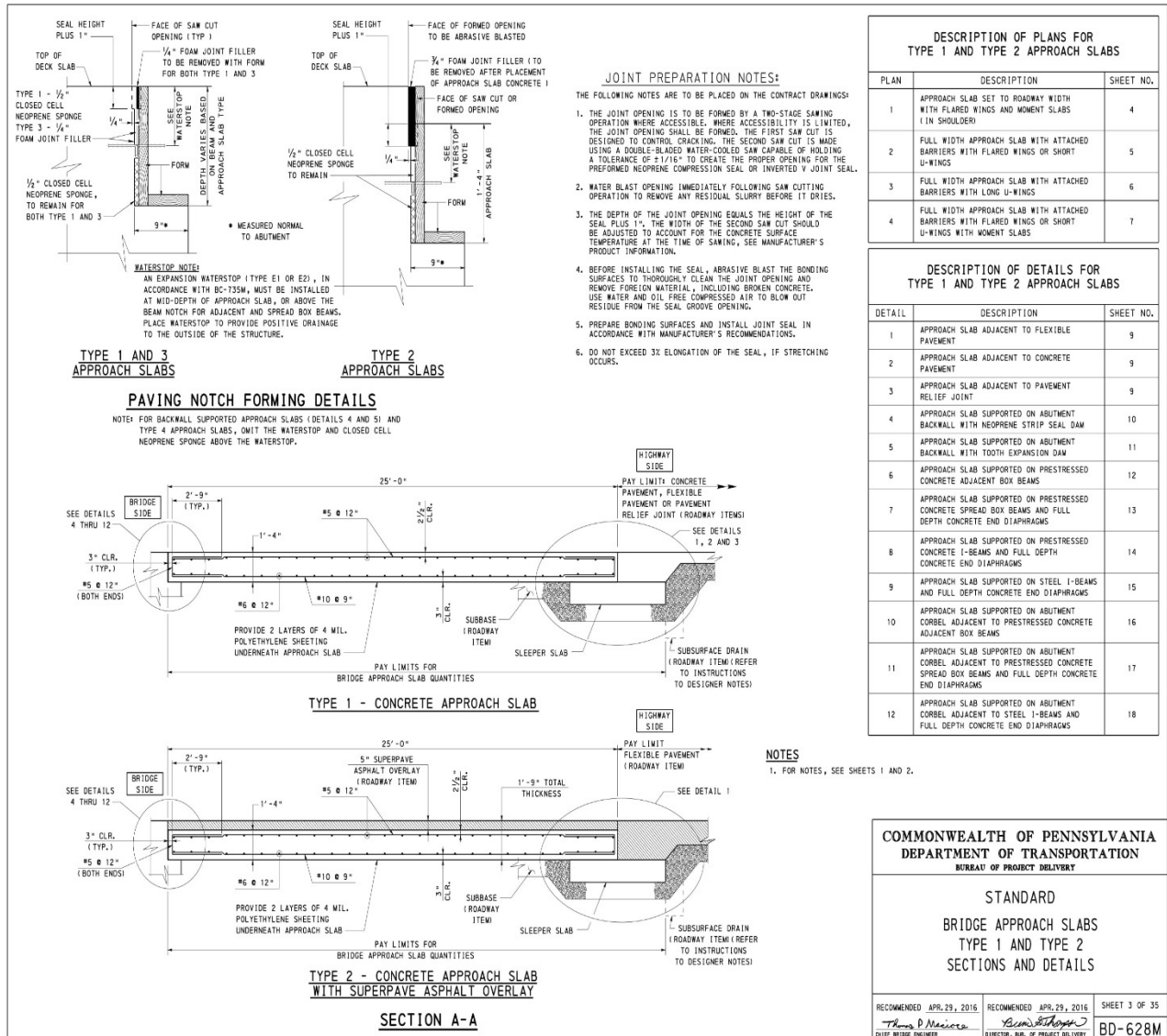
APPROACH SLAB TYPE	ROADWAY PAVEMENT TYPE	MINIMUM SKEW ANGLE (DEGREES)	ABUTMENT WITH BACKWALL?	APPROACH SLAB CONNECTED TO SUPERSTRUCTURE?	SUPERPAVE ASPHALT OVERLAY ON APPROACH SLAB?	EXPANSION JOINT AT END OF APPROACH SLAB
1	CONCRETE	45	N/A	NO	NO	N/A
2	FLEXIBLE	45	N/A	NO	YES	N/A
3	CONCRETE	45	YES	YES	NO	NEOPRENE STRIP SEAL
4	CONCRETE	45	YES	YES	NO	TOOTH EXPANSION DAM
5 (SEE NOTE 1)	CONCRETE	45	N/A	YES	NO	NEOPRENE STRIP SEAL (IF REQUIRED)
	FLEXIBLE	45				

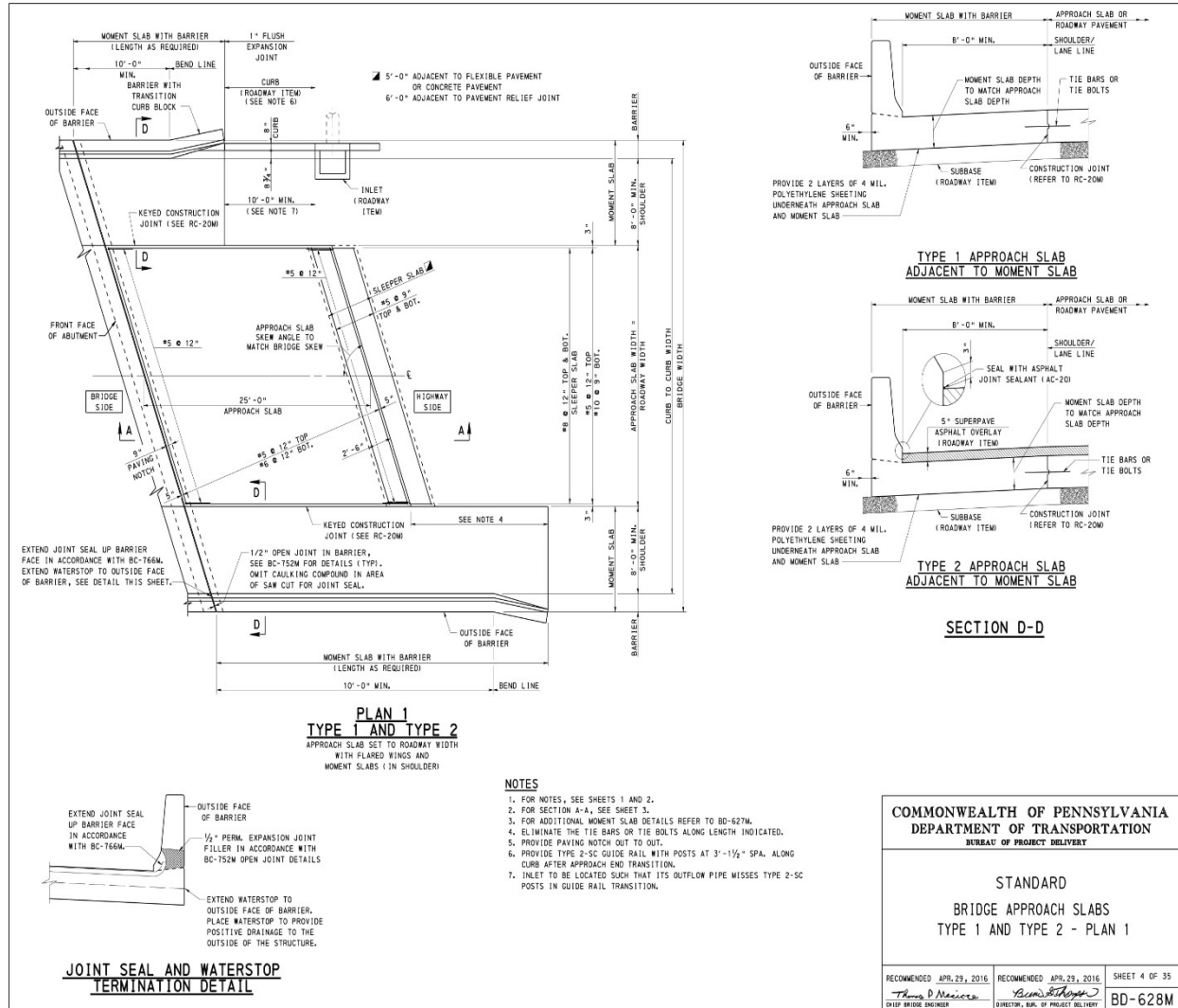
NOTES

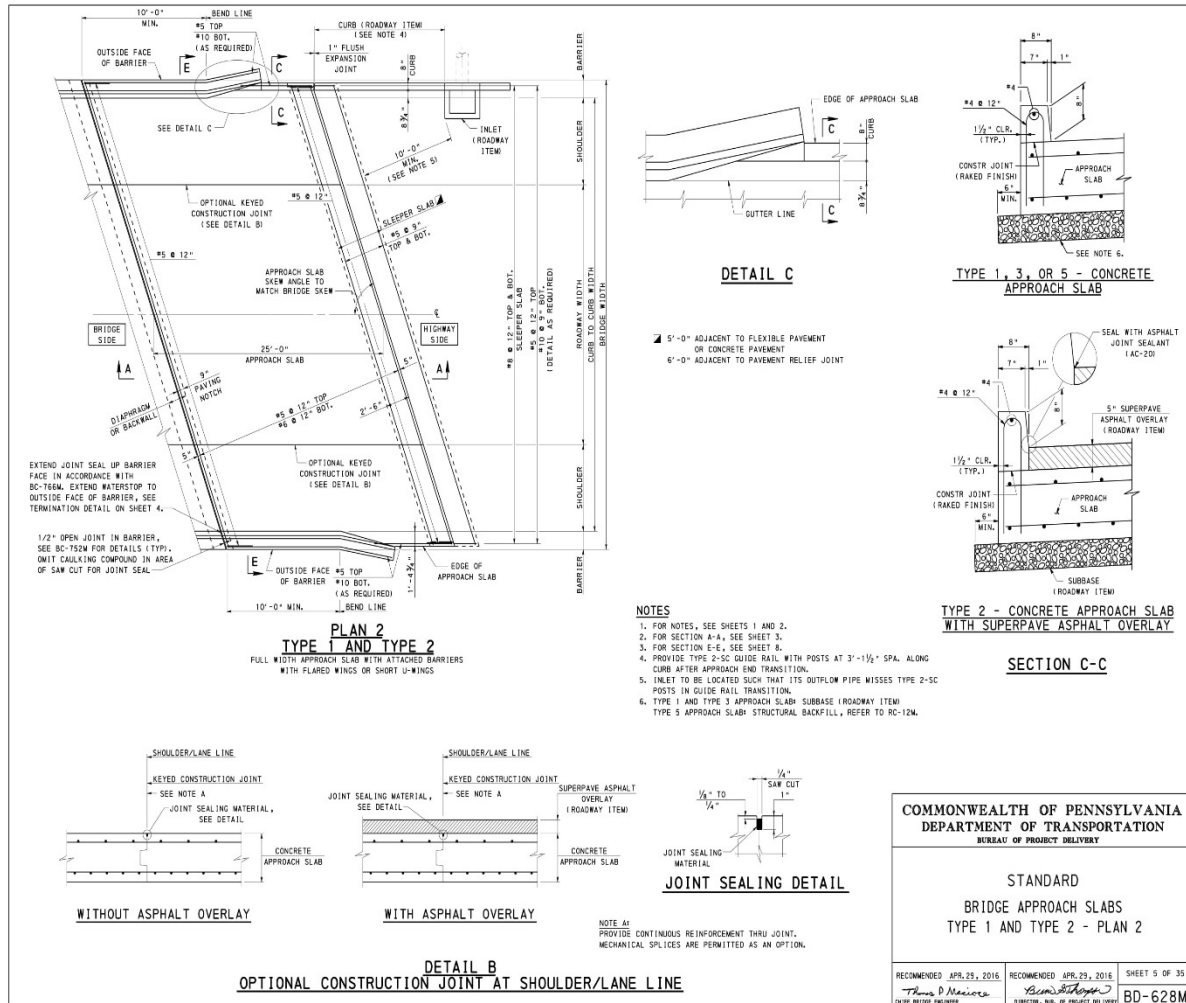
1. SKEW LIMITATIONS PER DESIGN MANUAL, PART 4, APPENDIX G, SECTION 1.2.2 MUST ALSO BE MET IN ORDER TO USE INTEGRAL ABUTMENTS.
2. IF BRIDGE SKEW ANGLE IS LESS THAN 45 DEGREES THE DESIGNER MUST DISCUSS ALTERNATE DETAILS WITH THE BRIDGE DESIGN AND TECHNOLOGY DIVISION.

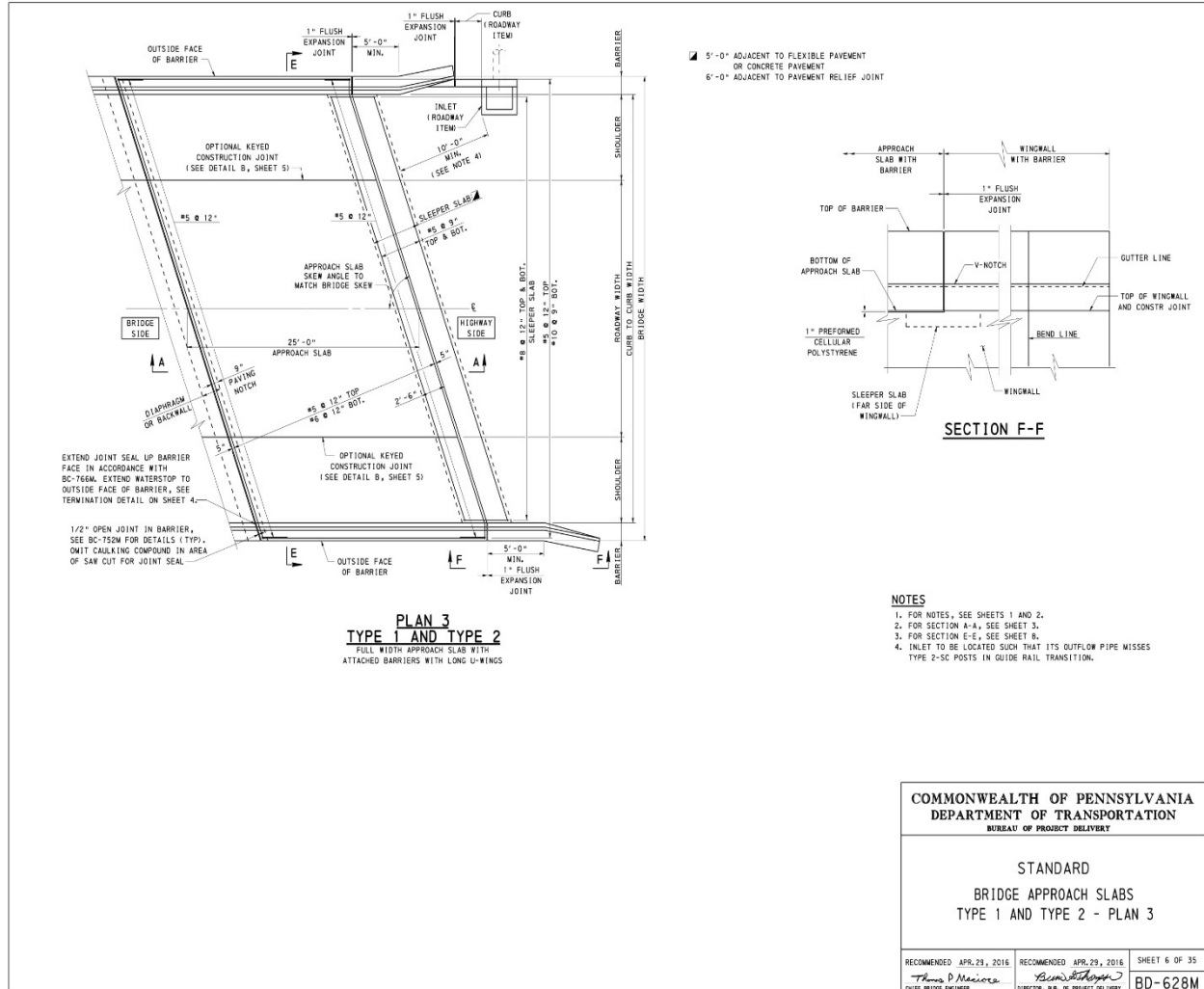
**COMMONWEALTH OF PENNSYLVANIA
DEPARTMENT OF TRANSPORTATION
BUREAU OF PROJECT DELIVERY****STANDARD
BRIDGE APPROACH SLABS
GENERAL NOTES - 2**

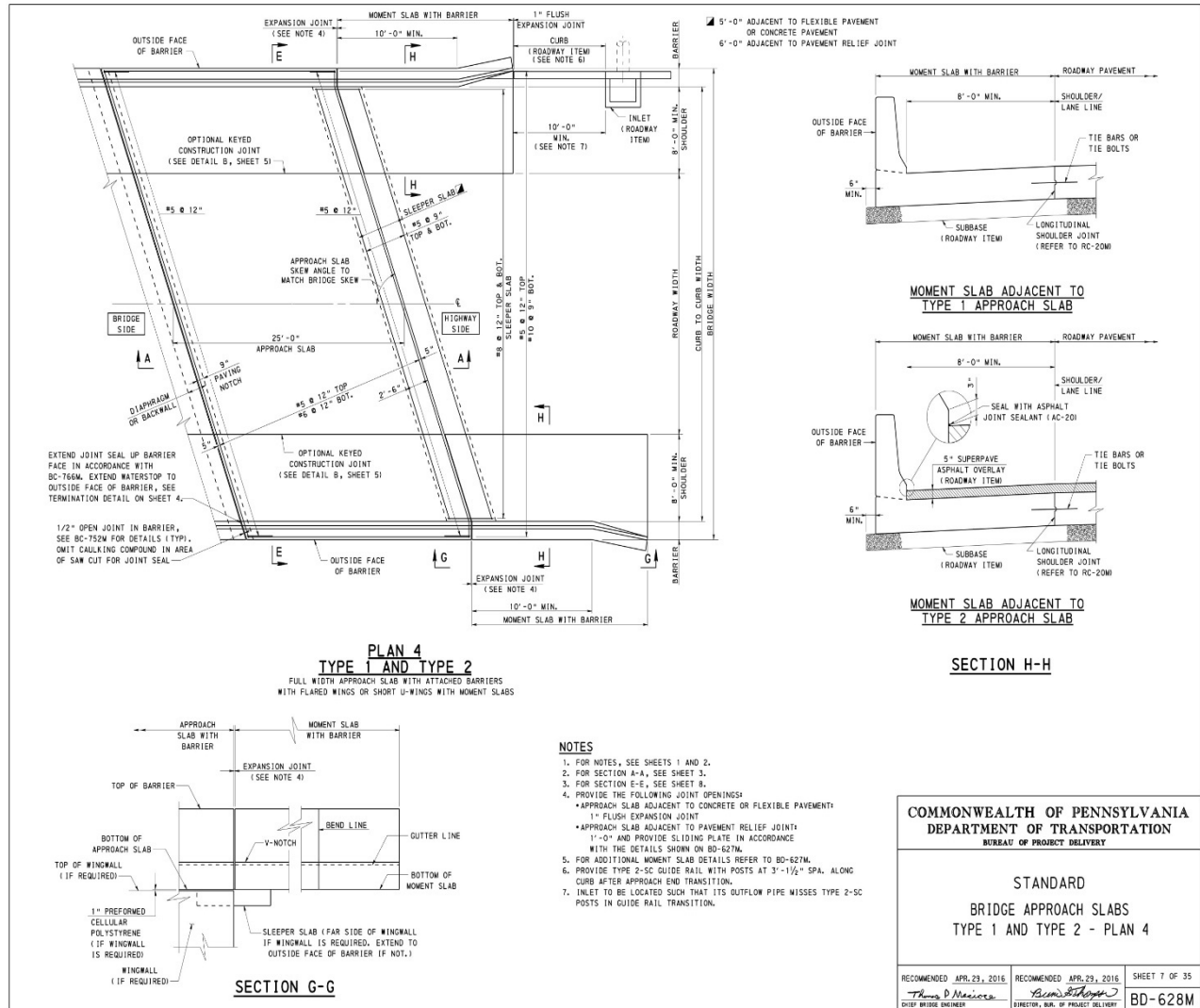
RECOMMENDED APR. 29, 2016 <i>Thomas D. Maciver</i> DIST. BRIDGE ENGINEER	RECOMMENDED APR. 29, 2016 <i>Brian S. Stephens</i> DIRECTOR, BUREAU OF PROJECT DELIVERY	SHEET 2 OF 35 BD-628M
--	---	--------------------------

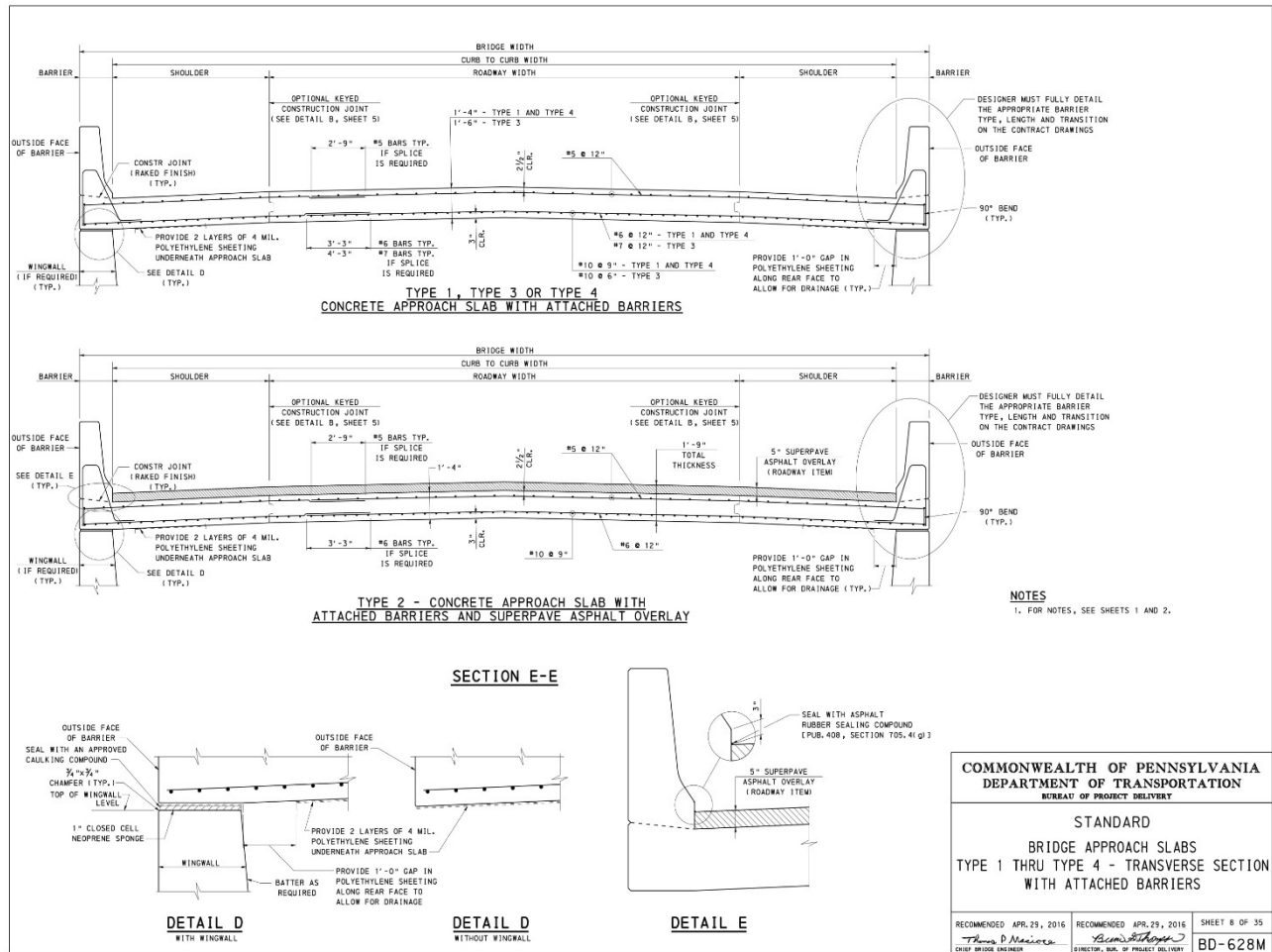


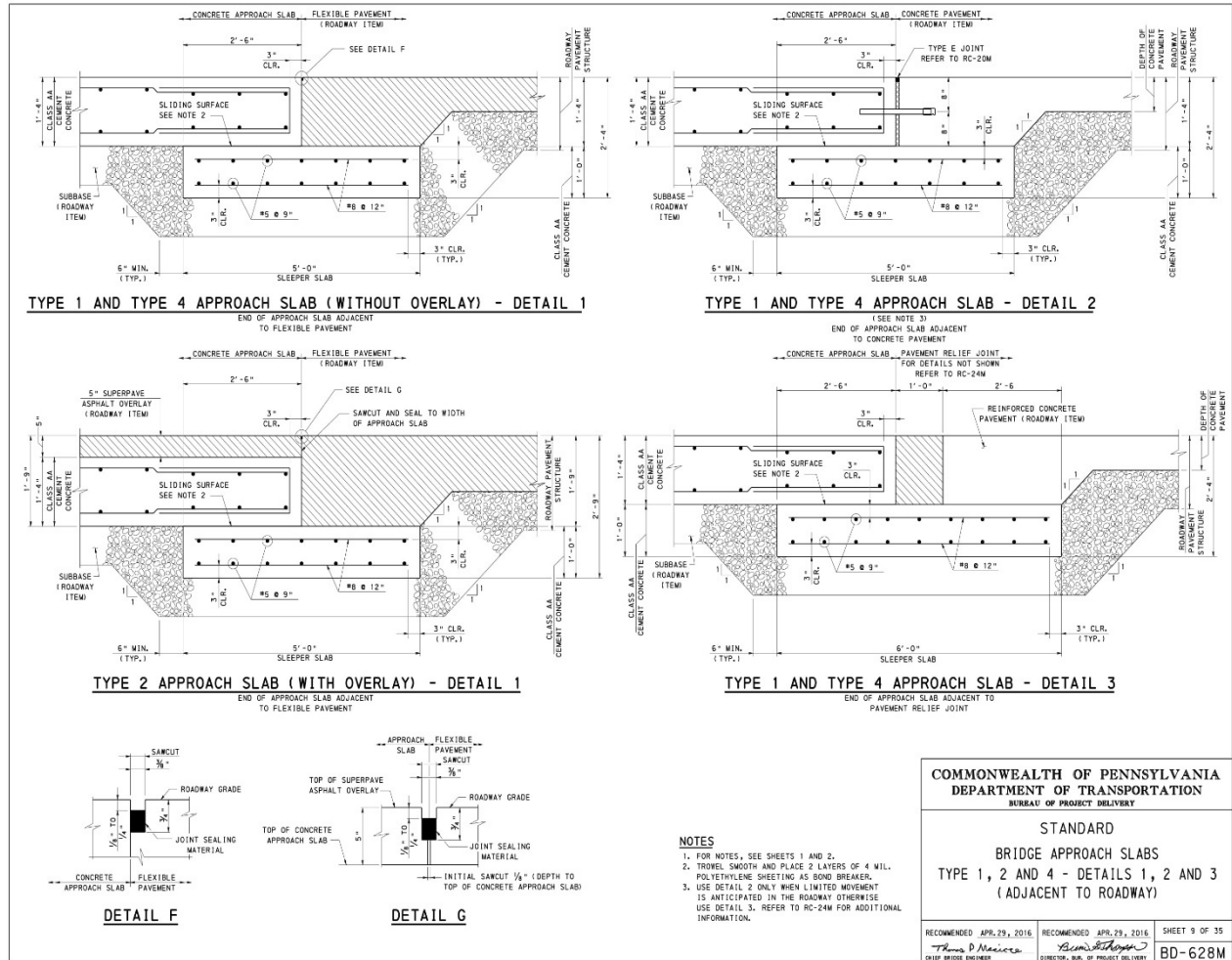


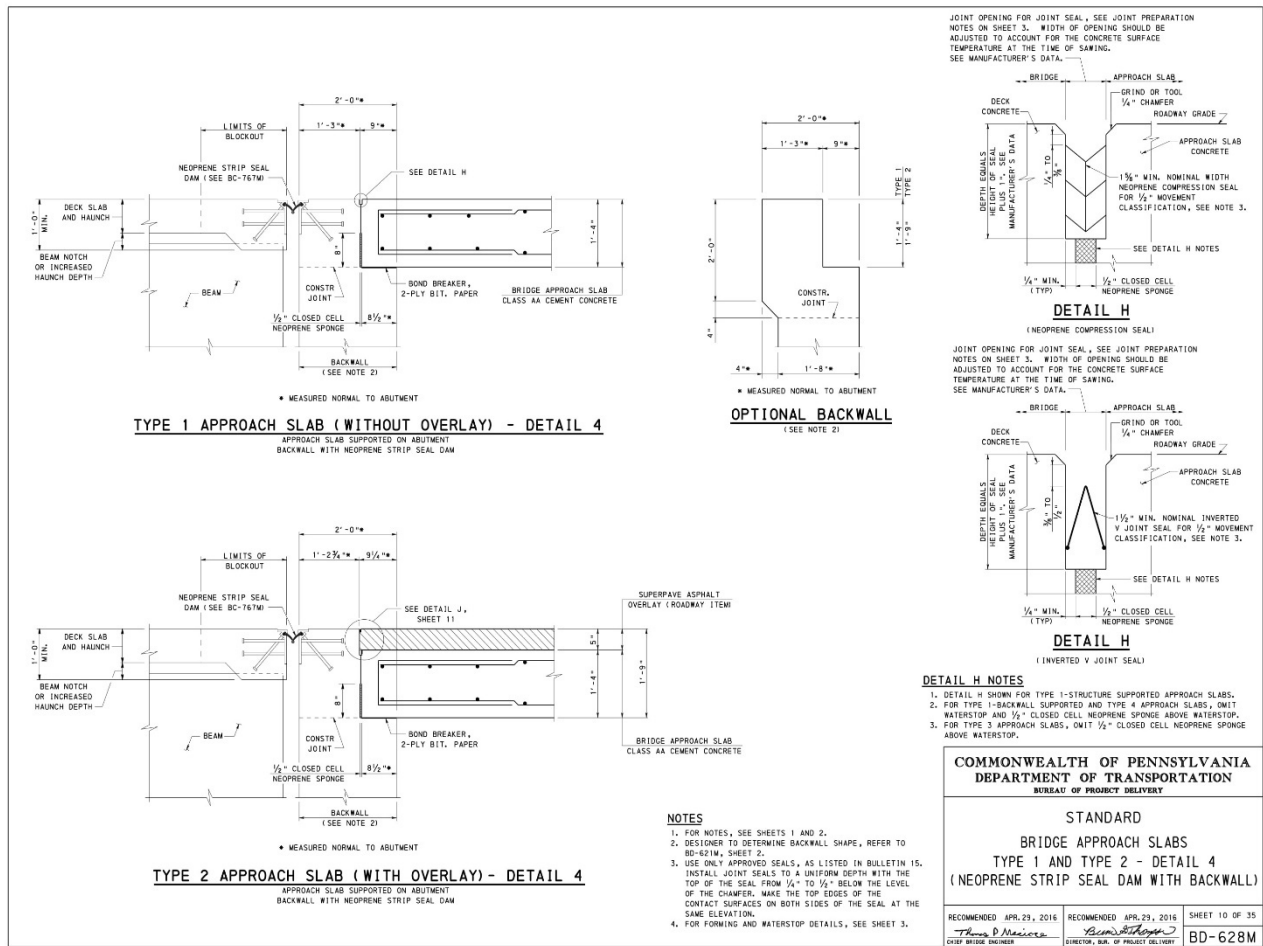


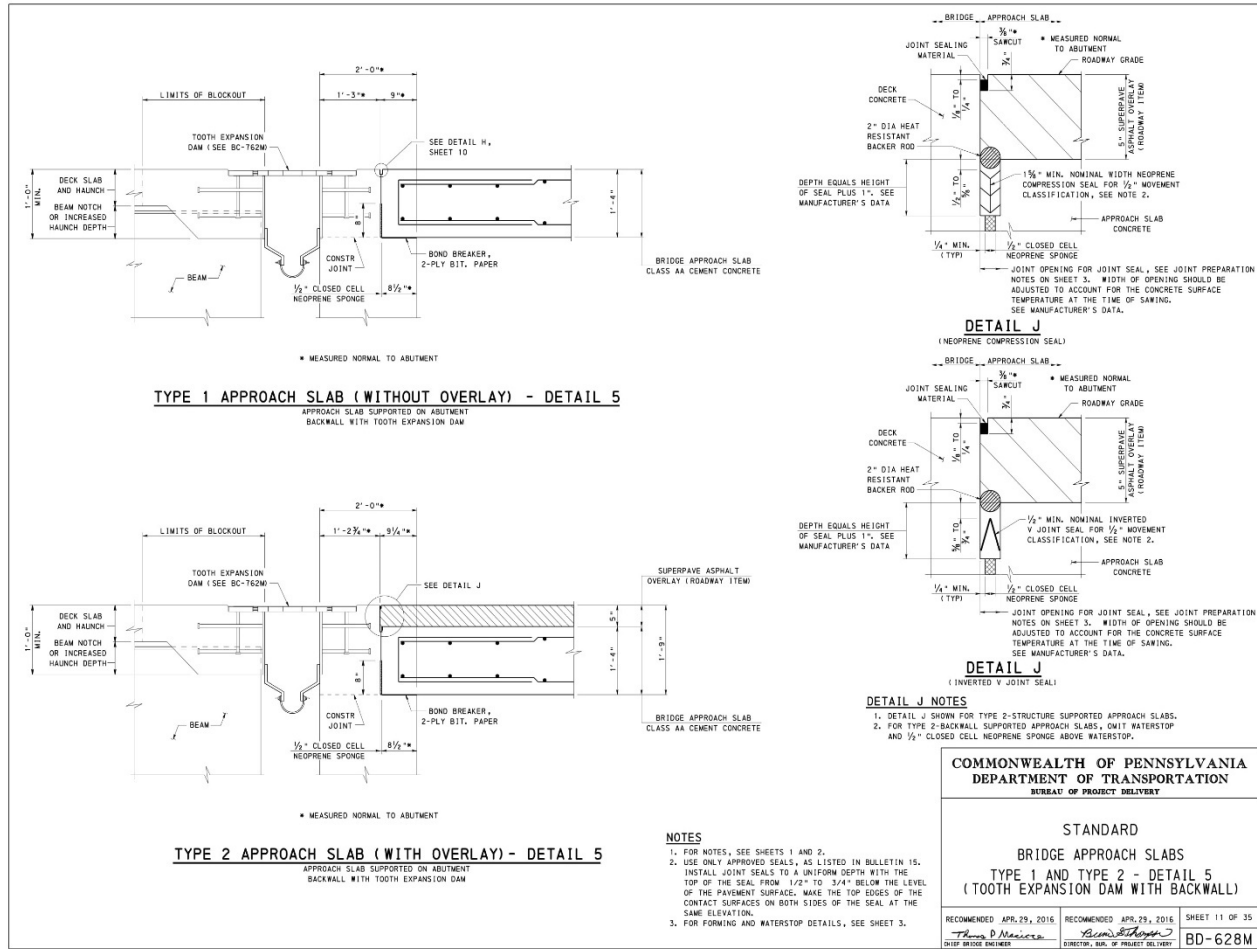




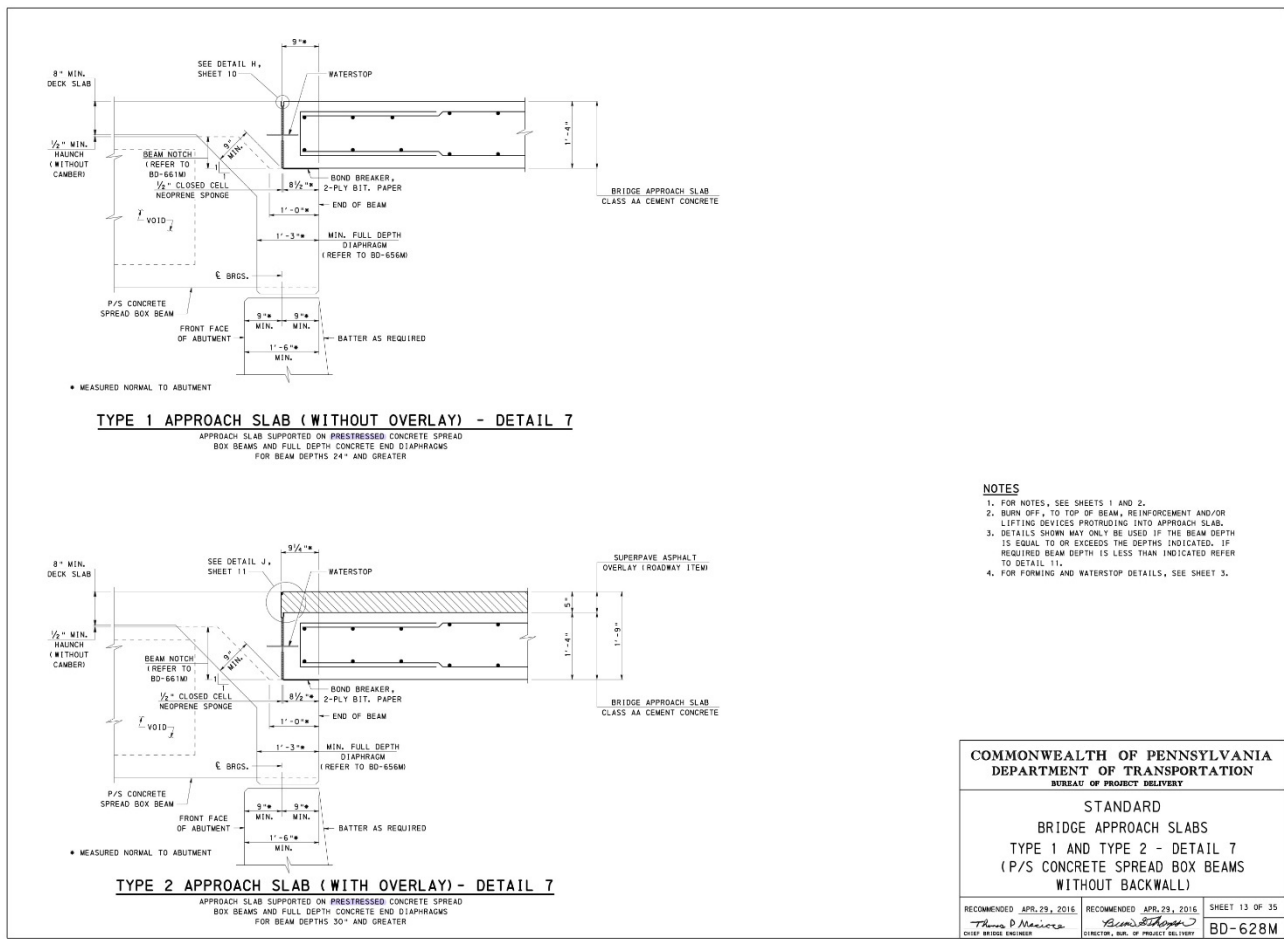


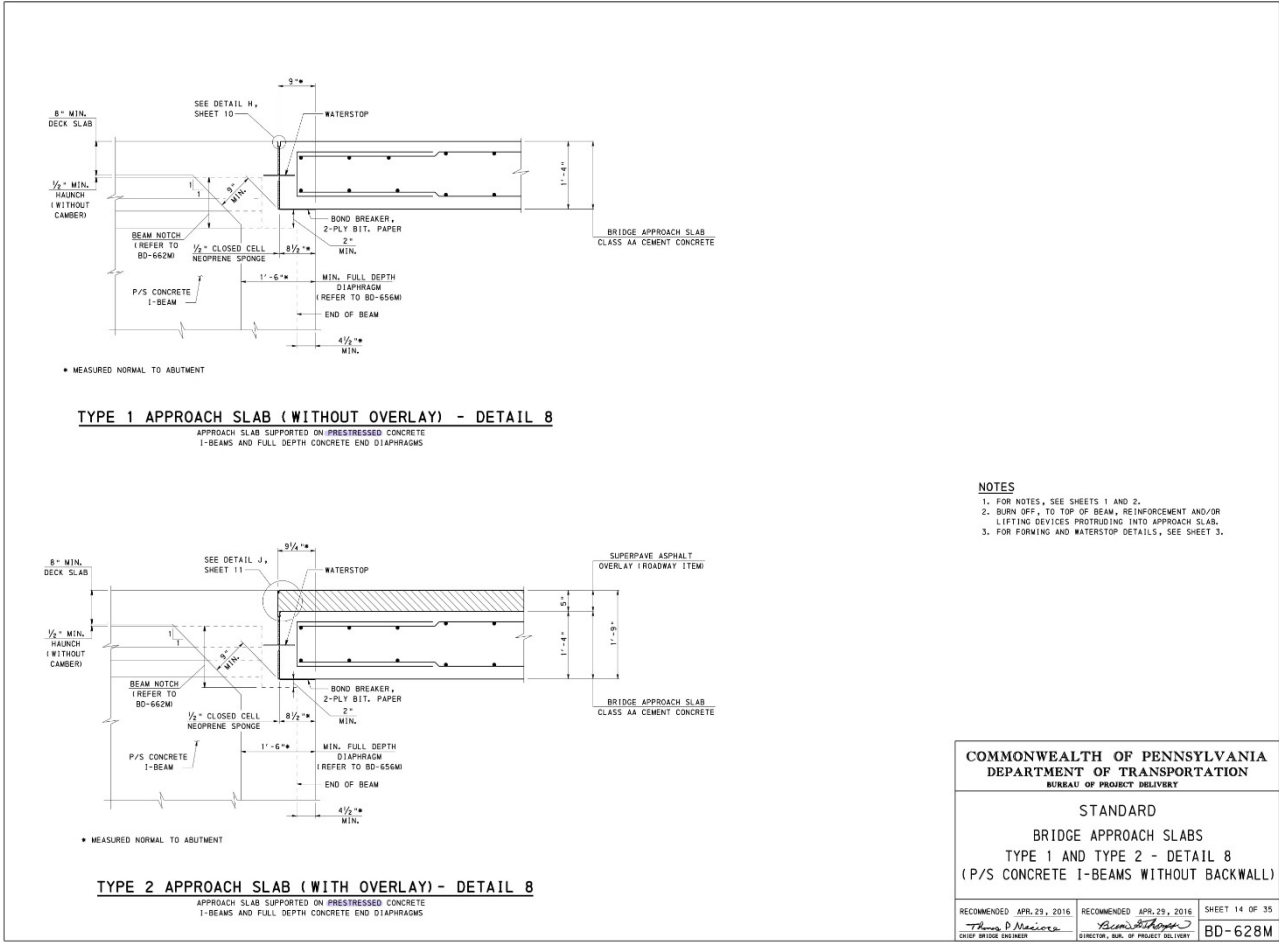


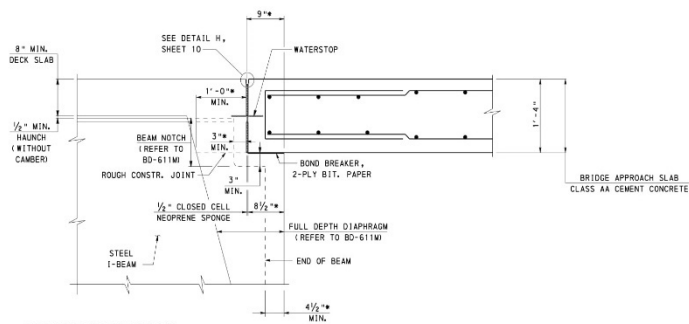








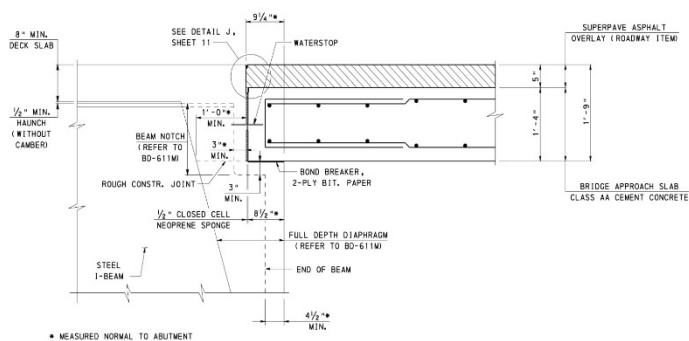




TYPE 1 APPROACH SLAB (WITHOUT OVERLAY) - DETAIL 9

APPROACH SLAB SUPPORTED ON STEEL
I-BEAMS AND FULL DEPTH CONCRETE END DIAPHRAGMS
FOR BEAM DEPTHS 2'-1 1/2" AND GREATER

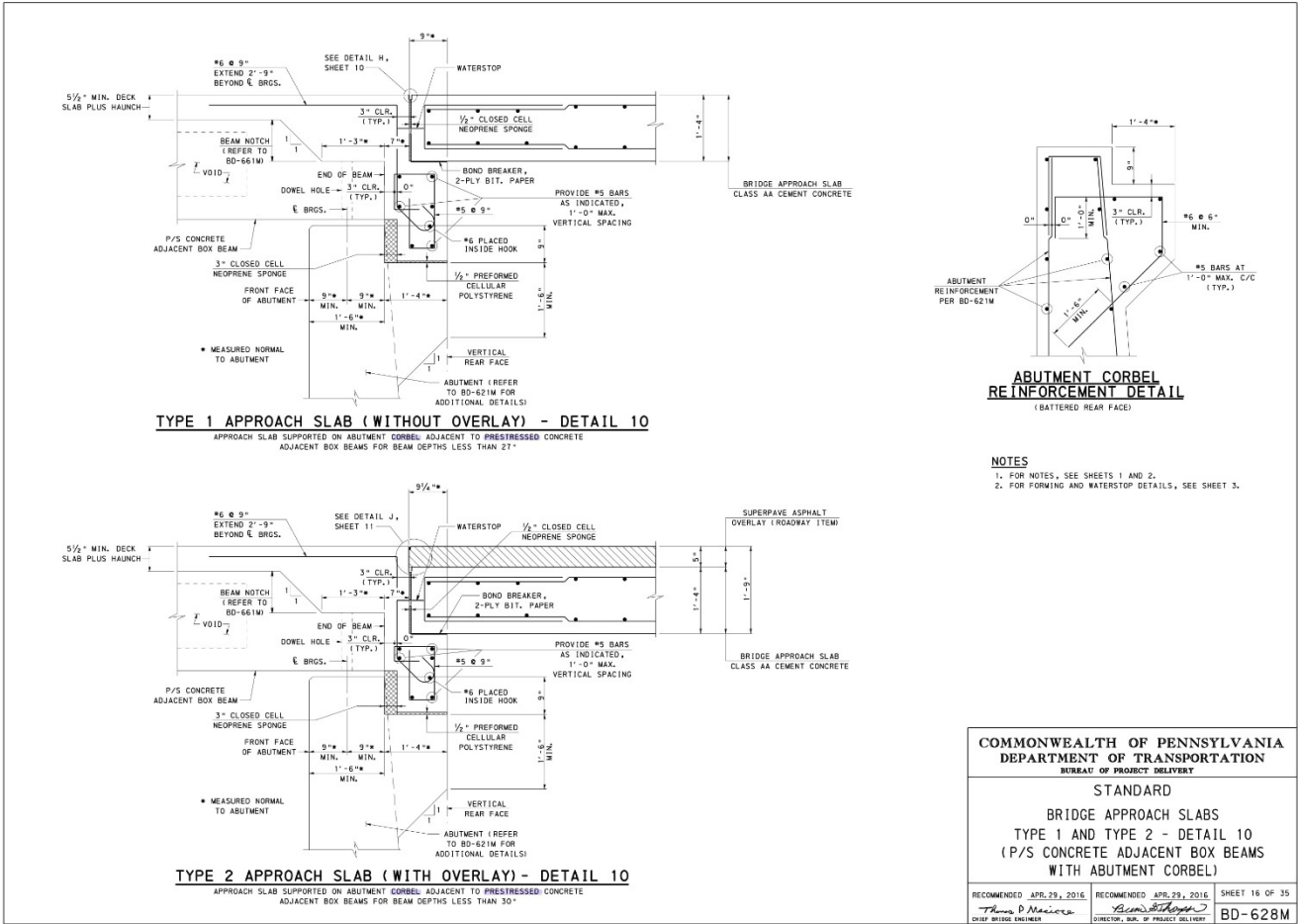
- NOTES**
- 1. FOR NOTES, SEE SHEETS 1 AND 2.
 - 2. DETAILS SHOWN MAY ONLY BE USED IF THE BEAM DEPTH IS EQUAL TO OR EXCEEDS THE DEPTHS INDICATED. IF REQUIRED BEAM DEPTH IS LESS THAN INDICATED REFER TO DETAIL 12.
 - 3. FOR FORMING AND WATERSTOP DETAILS, SEE SHEET 3.

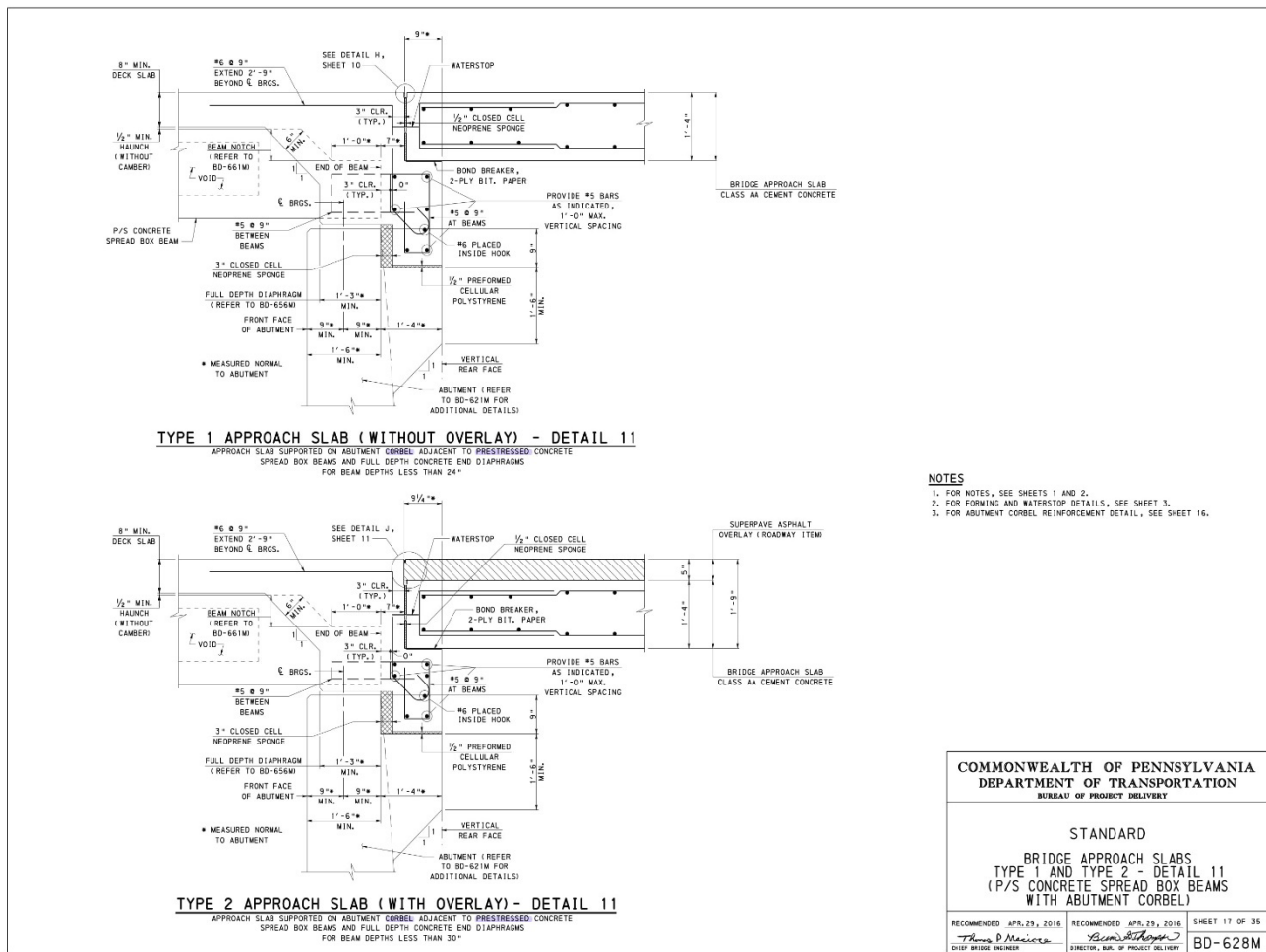


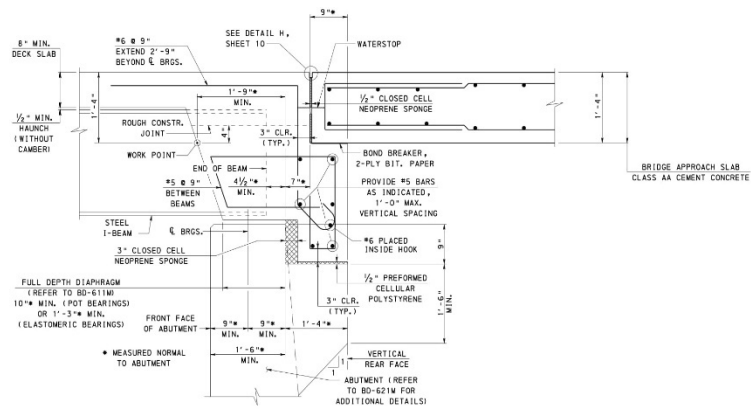
TYPE 2 APPROACH SLAB (WITH OVERLAY) - DETAIL 9

APPROACH SLAB SUPPORTED ON STEEL
I-BEAMS AND FULL DEPTH CONCRETE END DIAPHRAGMS
FOR BEAM DEPTHS 2'-6 1/2" AND GREATER

COMMONWEALTH OF PENNSYLVANIA DEPARTMENT OF TRANSPORTATION BUREAU OF PROJECT DELIVERY		
STANDARD BRIDGE APPROACH SLABS TYPE 1 AND TYPE 2 - DETAIL 9 (STEEL BEAMS WITHOUT BACKWALL)		
RECOMMENDED APR. 29, 2016 <i>Thomas D. McCreary</i> CHIEF BRIDGE ENGINEER	RECOMMENDED APR. 29, 2016 <i>Benjamin J. Thompson</i> DIRECTOR, BUREAU OF PROJECT DELIVERY	SHEET 15 OF 35 BD-628M





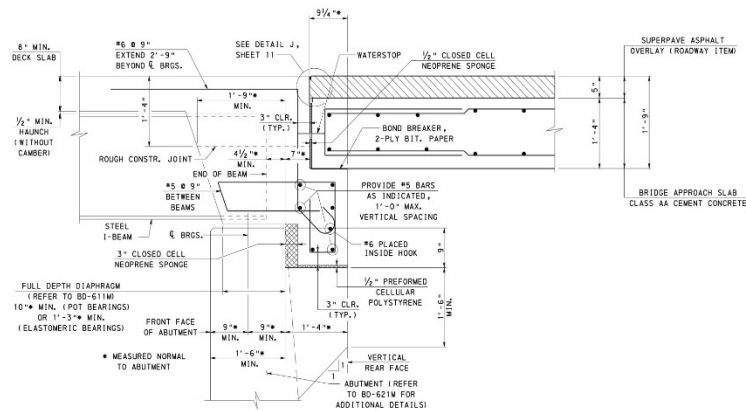


TYPE 1 APPROACH SLAB (WITHOUT OVERLAY) - DETAIL 12

APPROACH SLAB SUPPORTED ON ABUTMENT CORBEL ADJACENT TO STEEL I-BEAMS AND FULL DEPTH CONCRETE END DIAPHRAGMS FOR BEAM DEPTHS LESS THAN 2'-1 1/2"

NOTES

1. FOR NOTES, SEE SHEETS 1 AND 2.
2. FOR FORMING AND WATERSTOP DETAILS, SEE SHEET 3.
3. FOR ABUTMENT CORBEL REINFORCEMENT DETAIL, SEE SHEET 16.



TYPE 2 APPROACH SLAB (WITH OVERLAY) - DETAIL 12

APPROACH SLAB SUPPORTED ON ABUTMENT CORBEL ADJACENT TO STEEL I-BEAMS AND FULL DEPTH CONCRETE END DIAPHRAGMS FOR BEAM DEPTHS LESS THAN 2'-6 1/2"

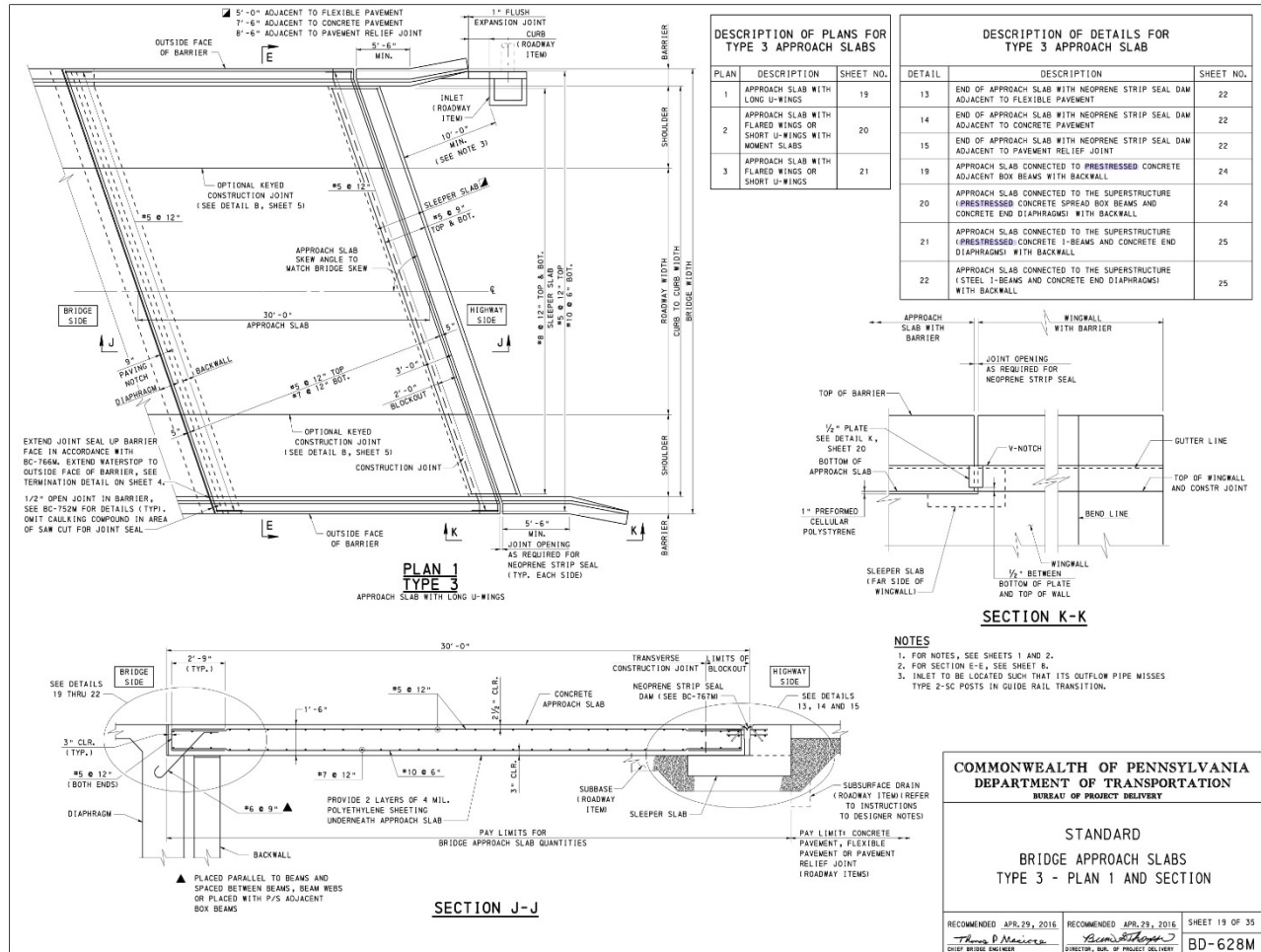
COMMONWEALTH OF PENNSYLVANIA
DEPARTMENT OF TRANSPORTATION
BUREAU OF PROJECT DELIVERY

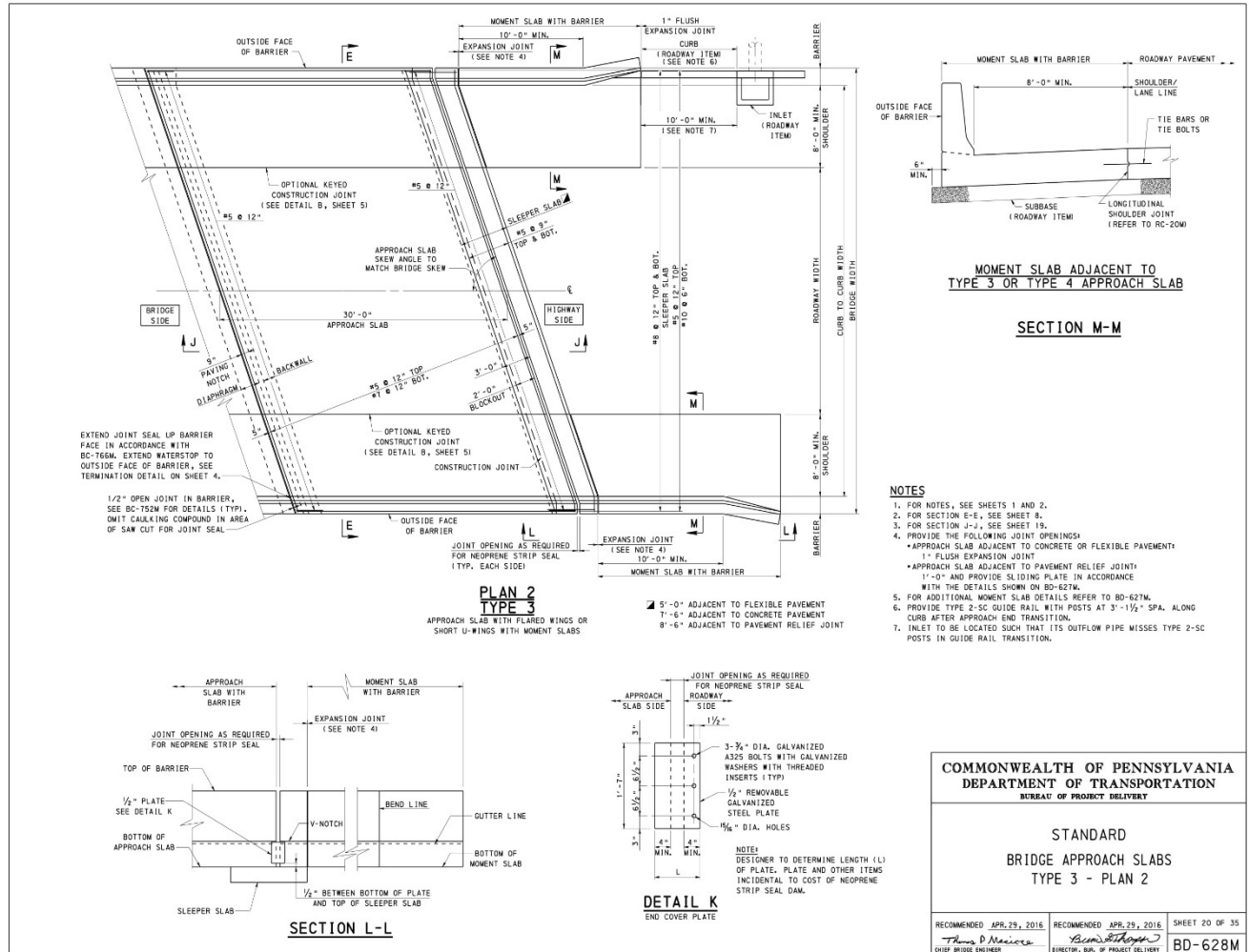
STANDARD
BRIDGE APPROACH SLABS
TYPE 1 AND TYPE 2 - DETAIL 12
(STEEL BEAMS WITH ABUTMENT CORBEL)

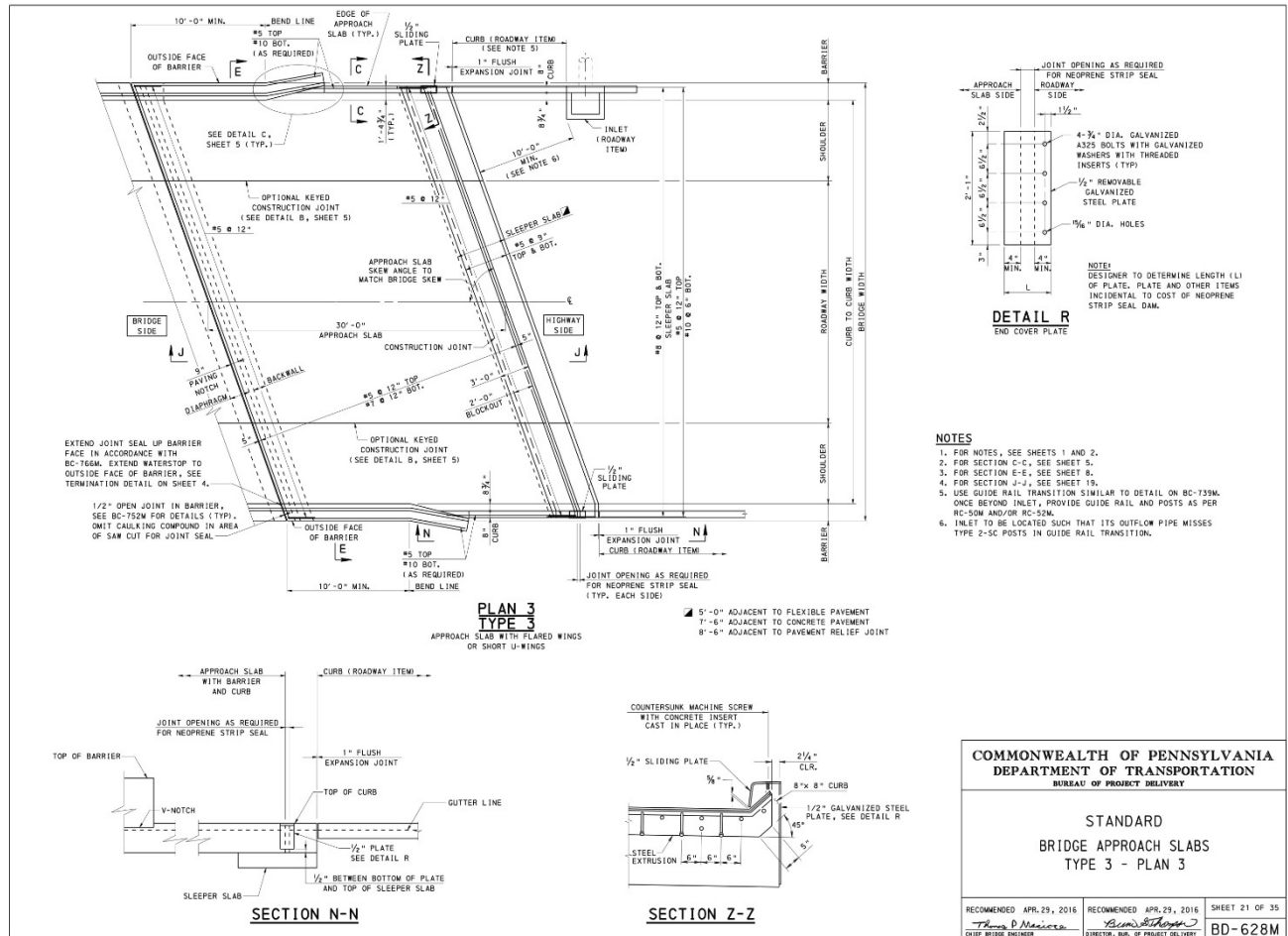
RECOMMENDED APR. 23, 2016
Thomas D. Mancione
CHIEF BRIDGE ENGINEER

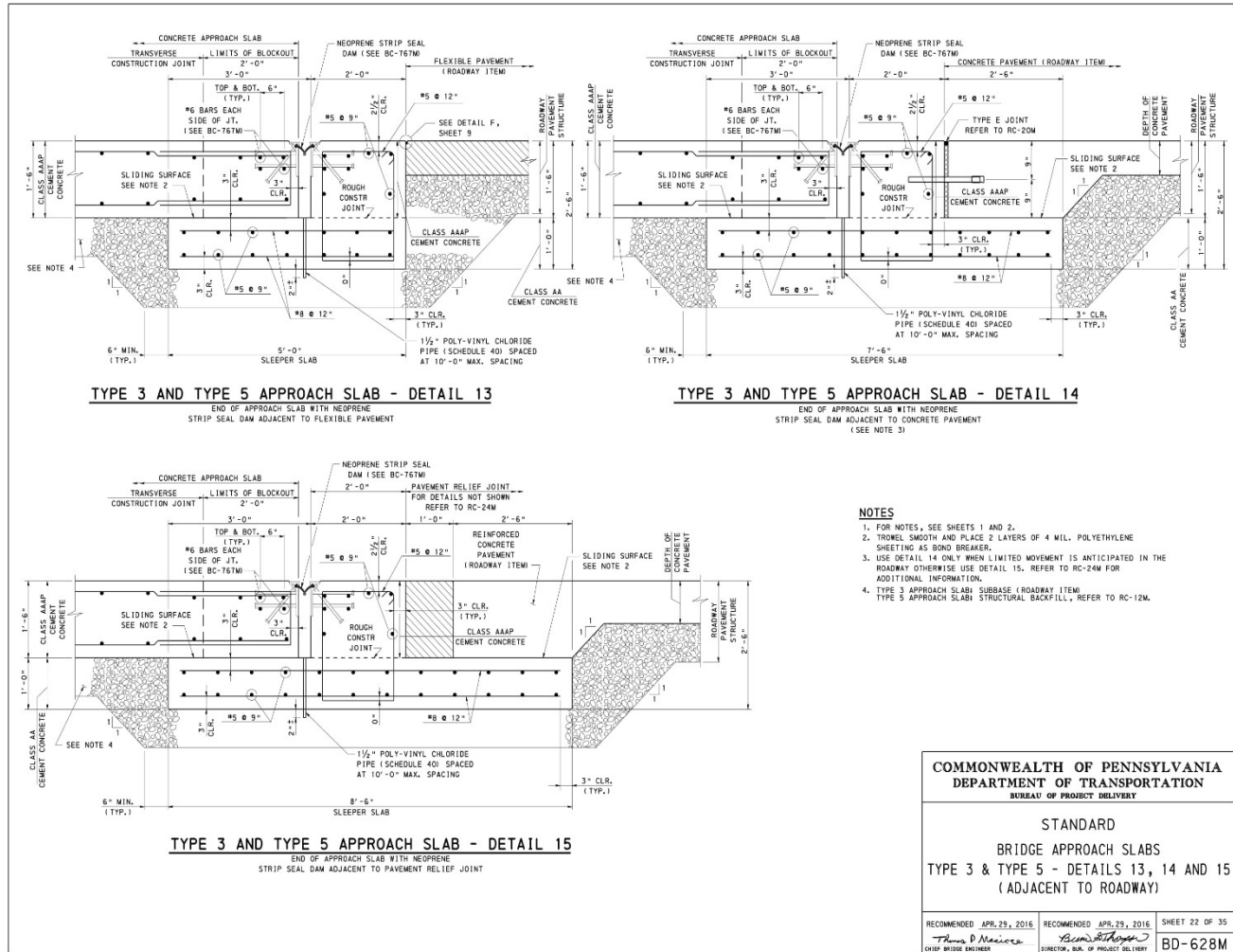
RECOMMENDED APR. 23, 2016
Bryan J. Thompson
DIRECTOR, BUREAU OF PROJECT DELIVERY

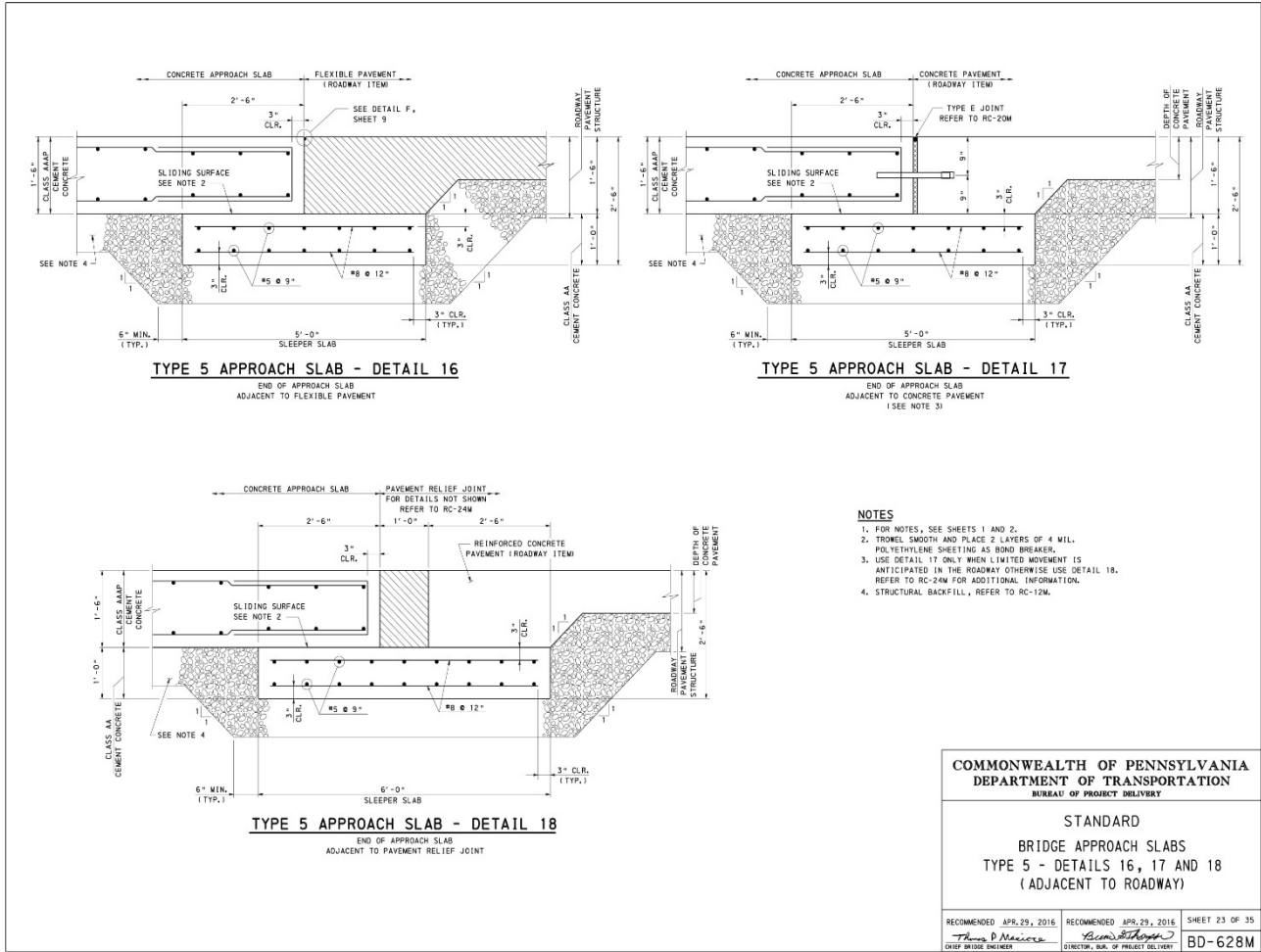
SHEET 18 OF 35
BD-628M

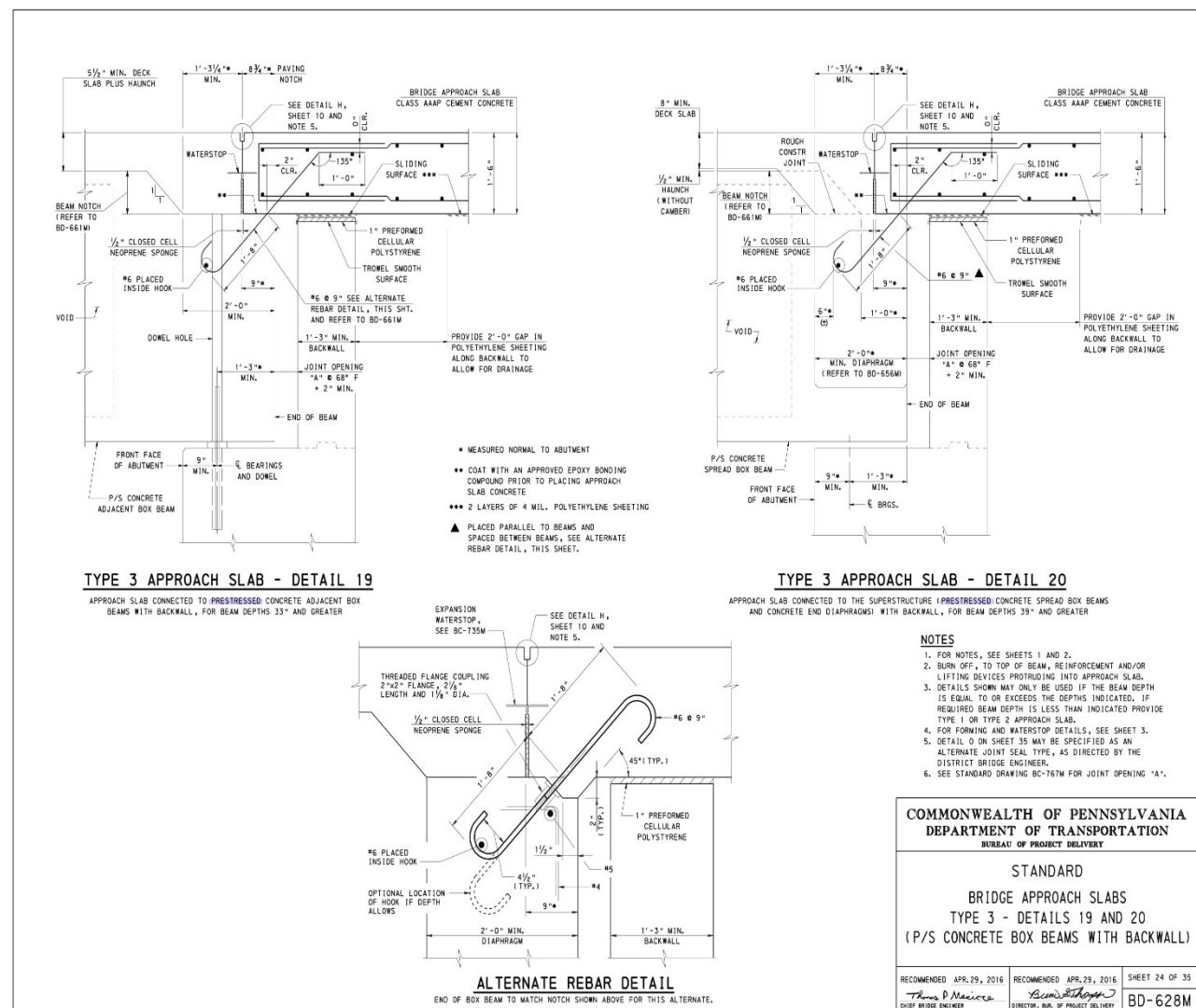


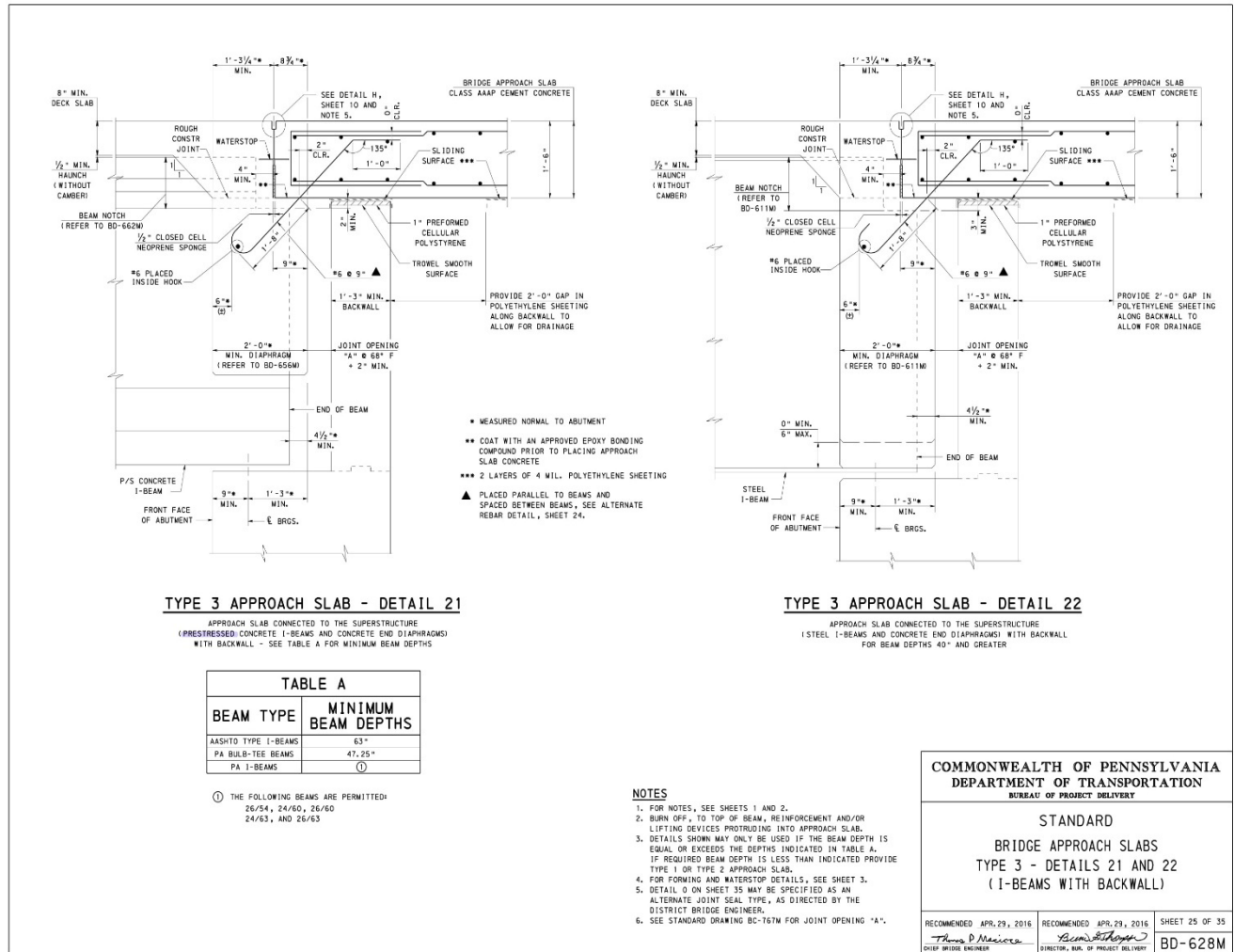


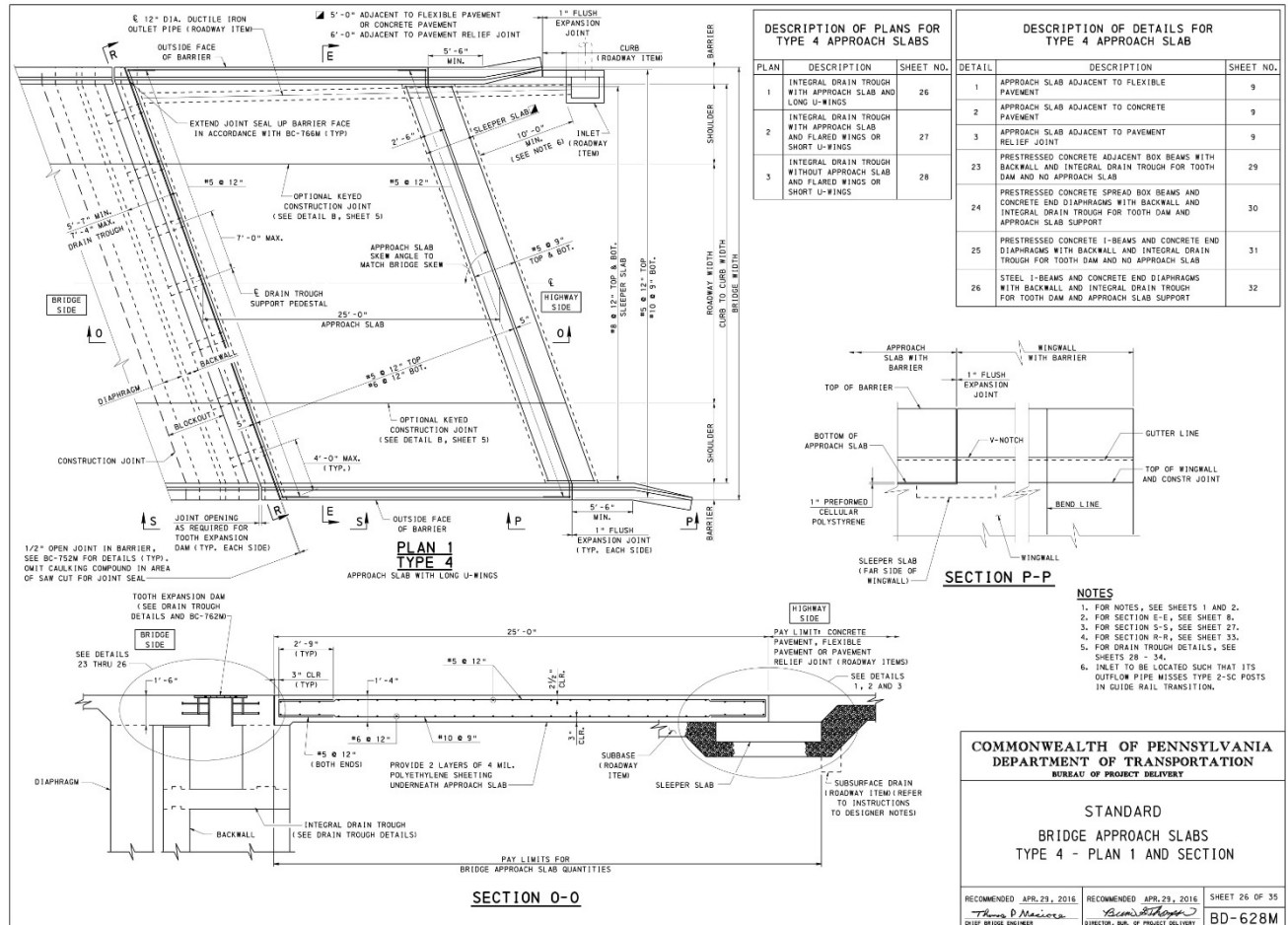


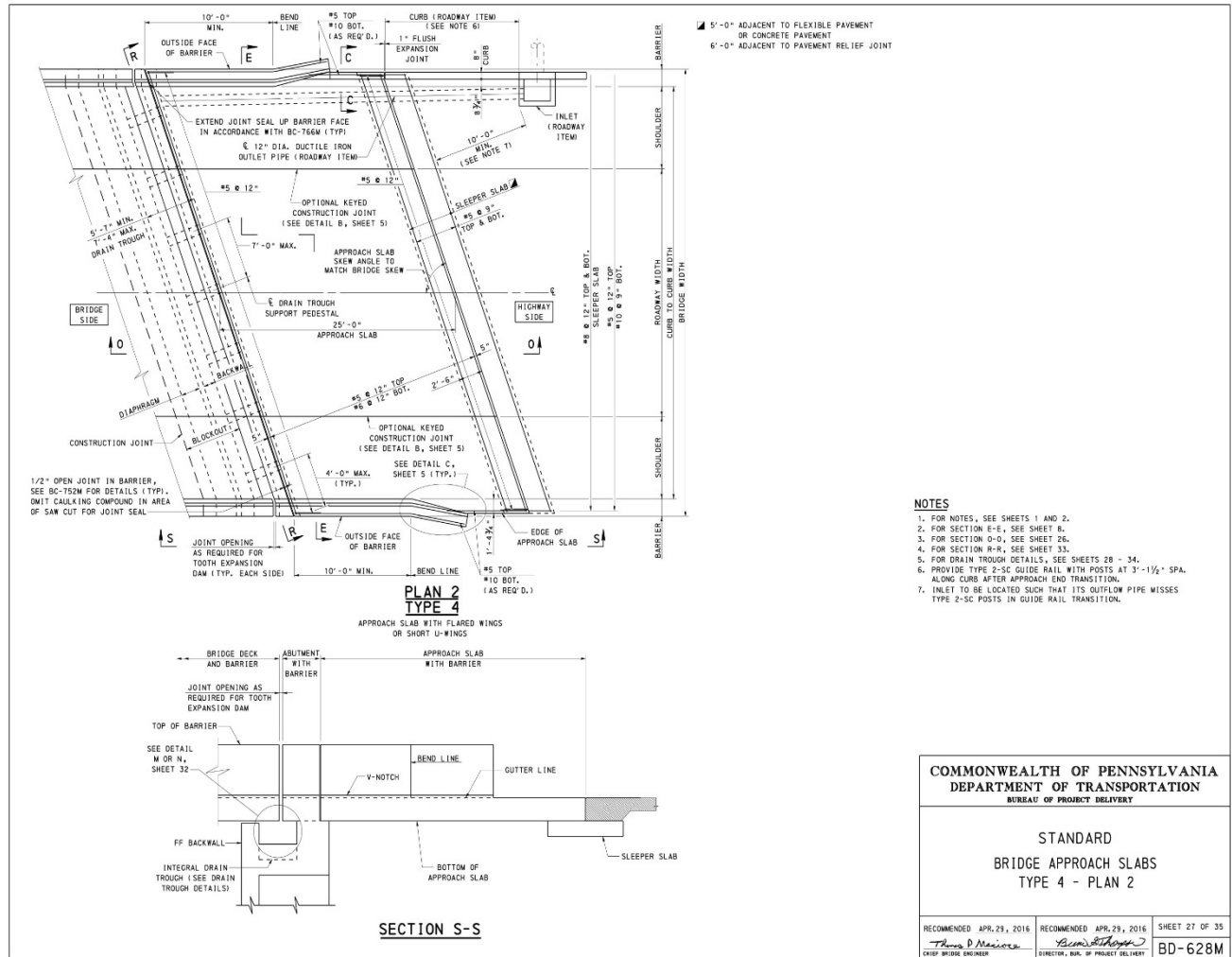


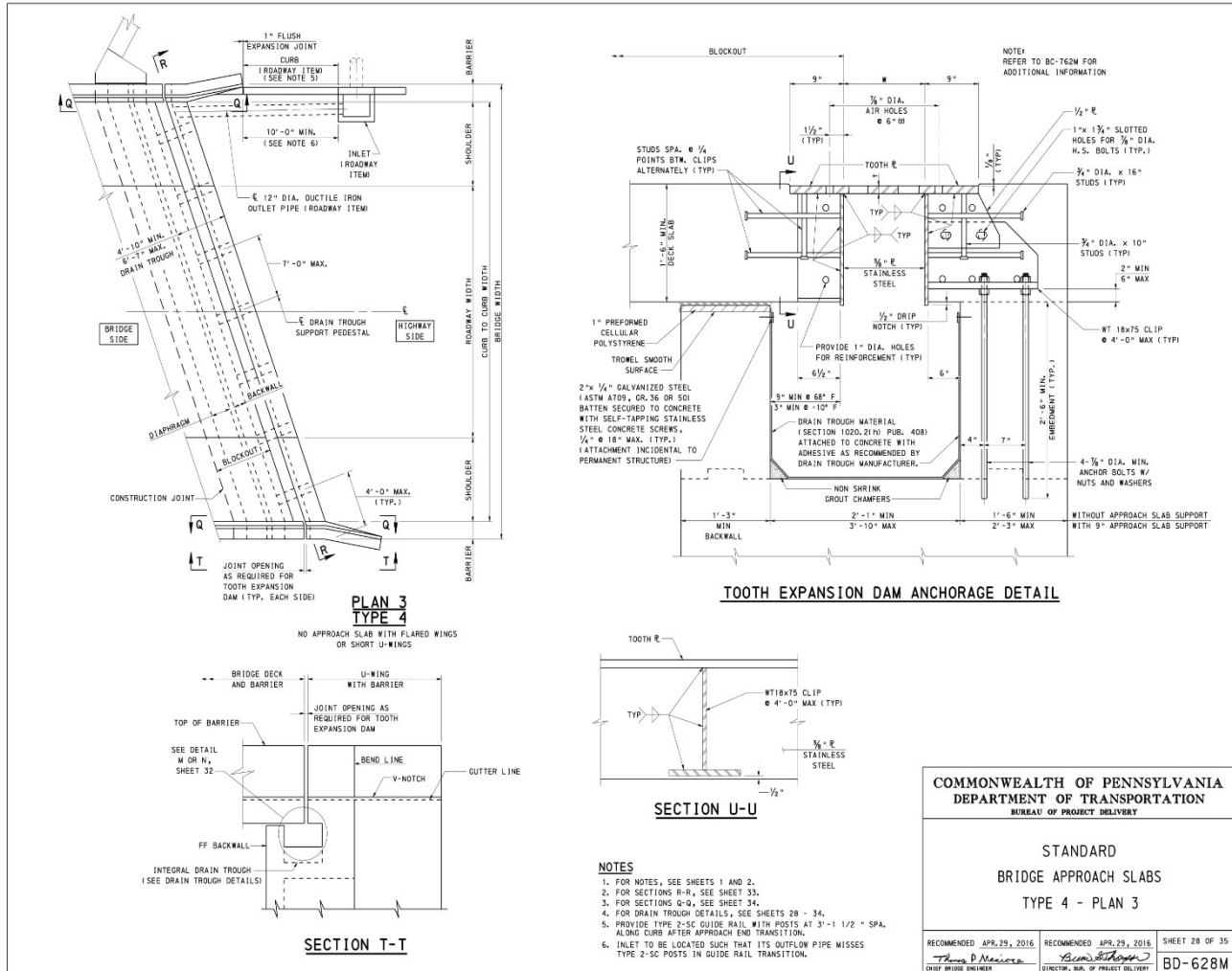


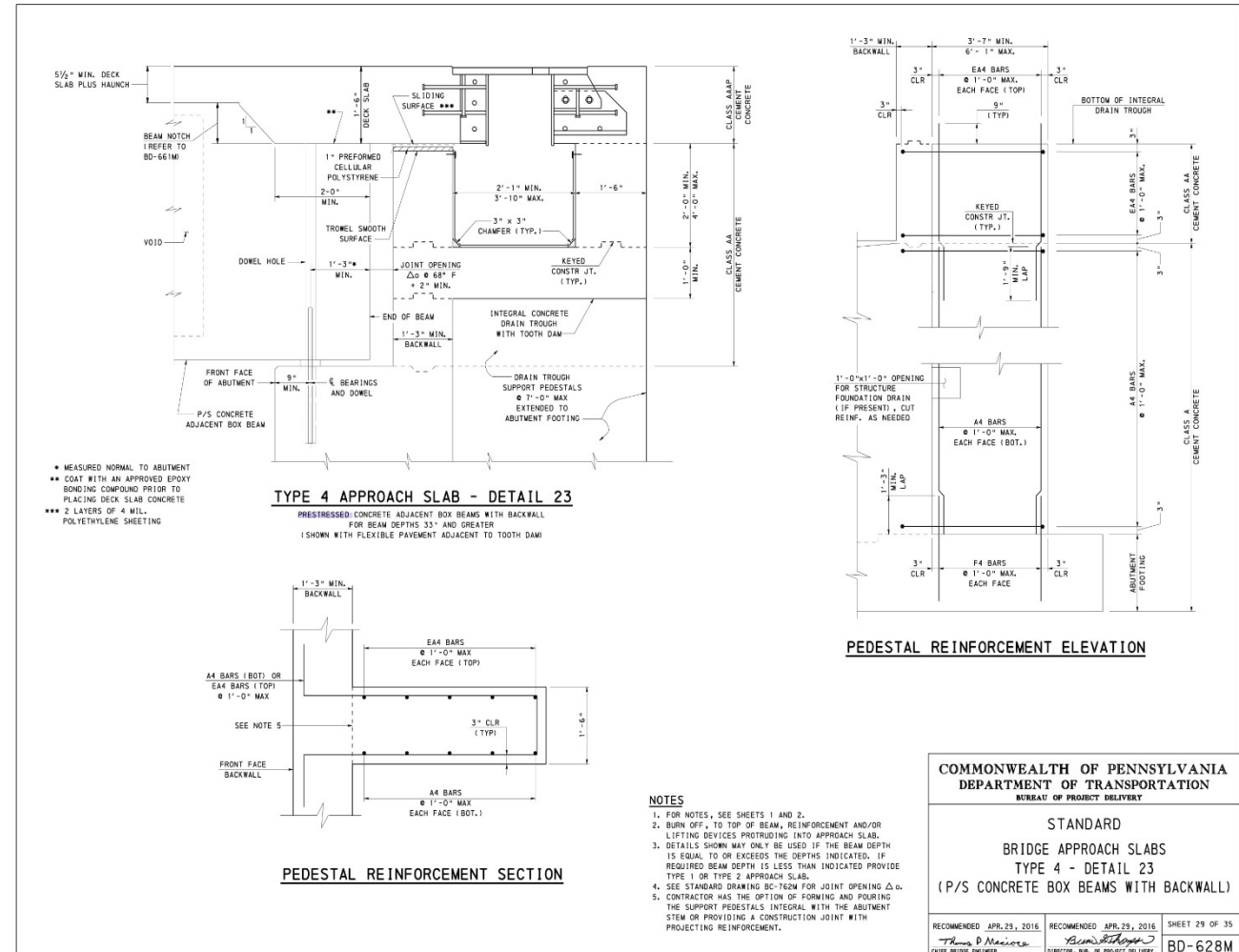


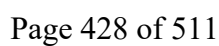


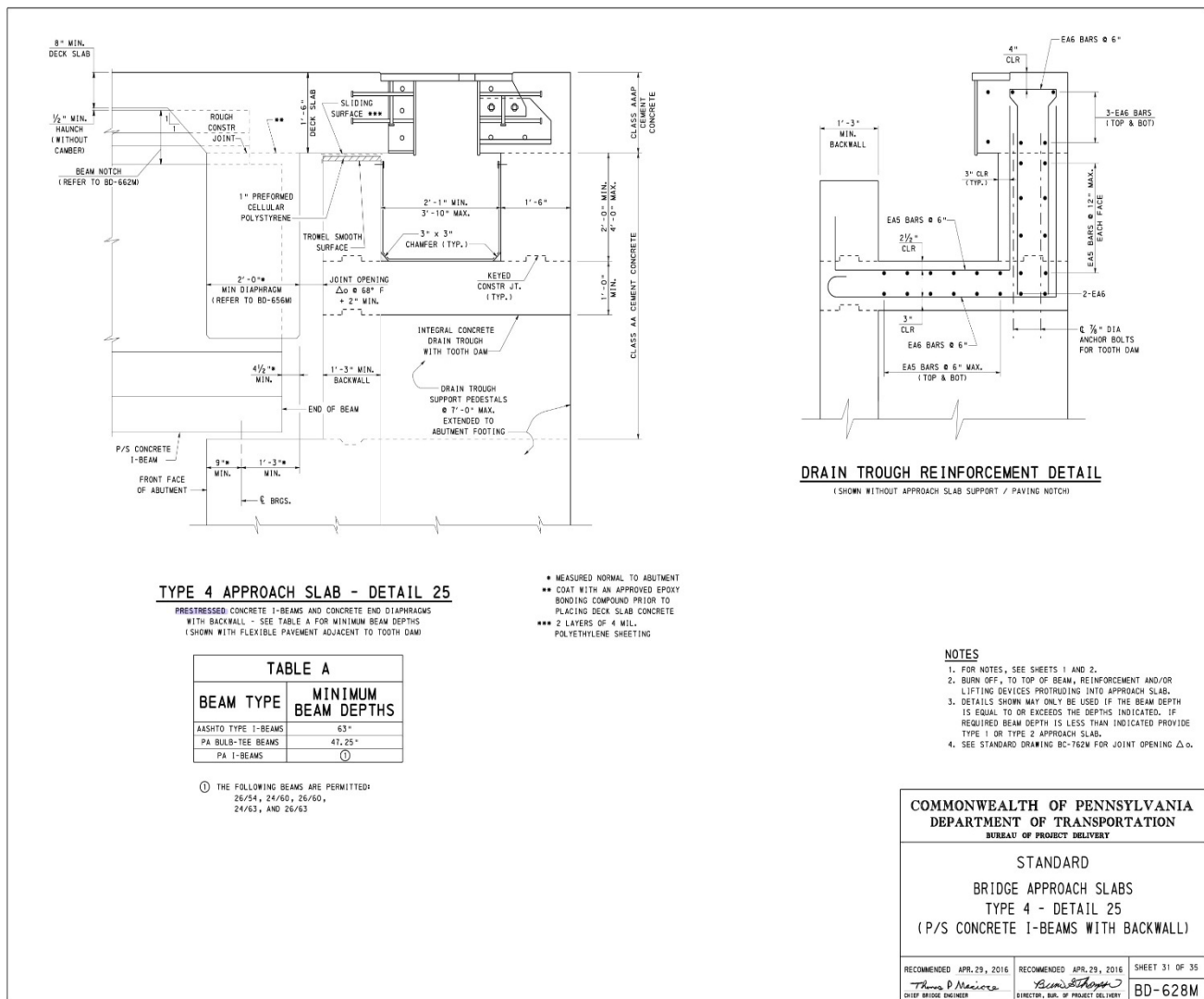


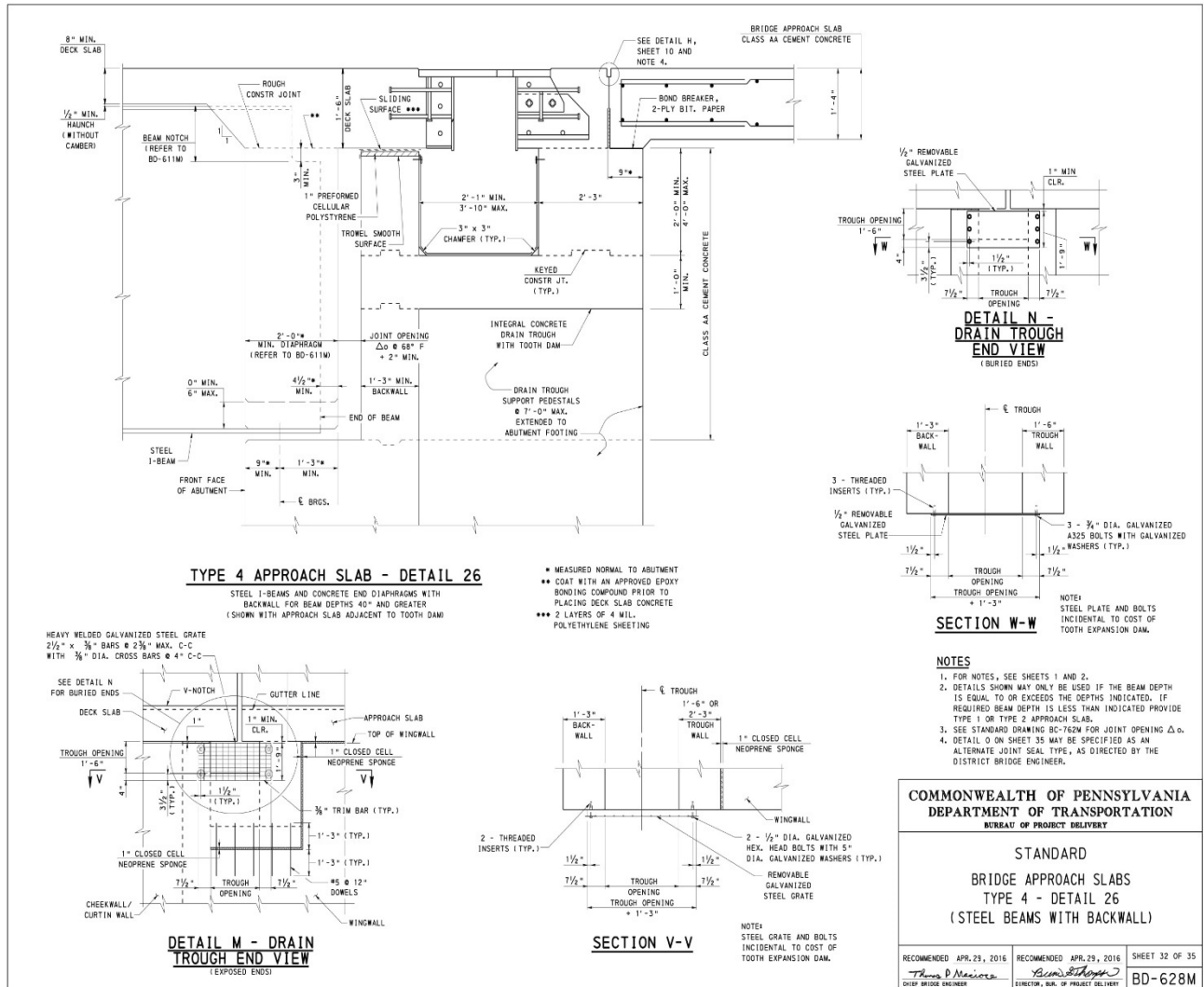


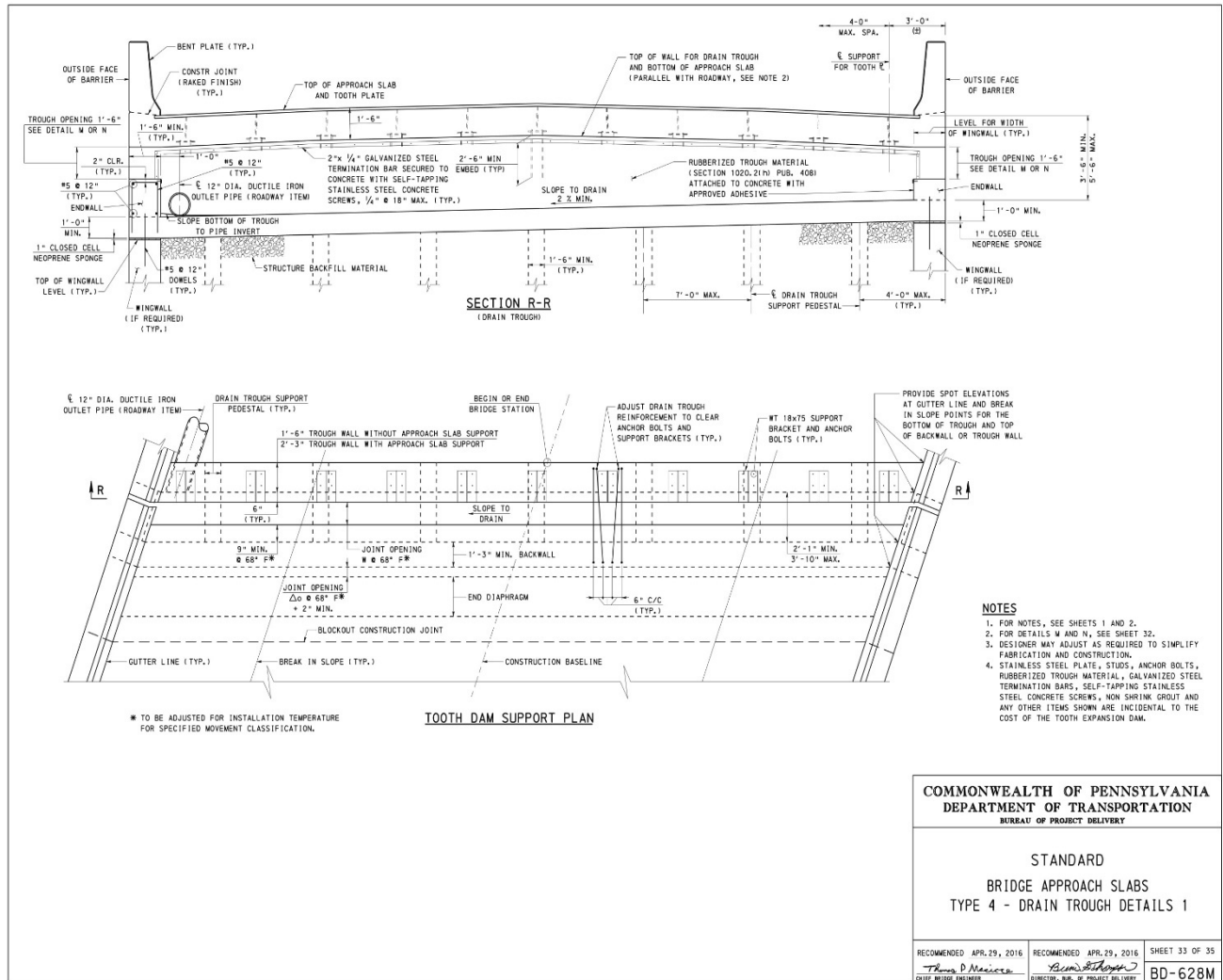


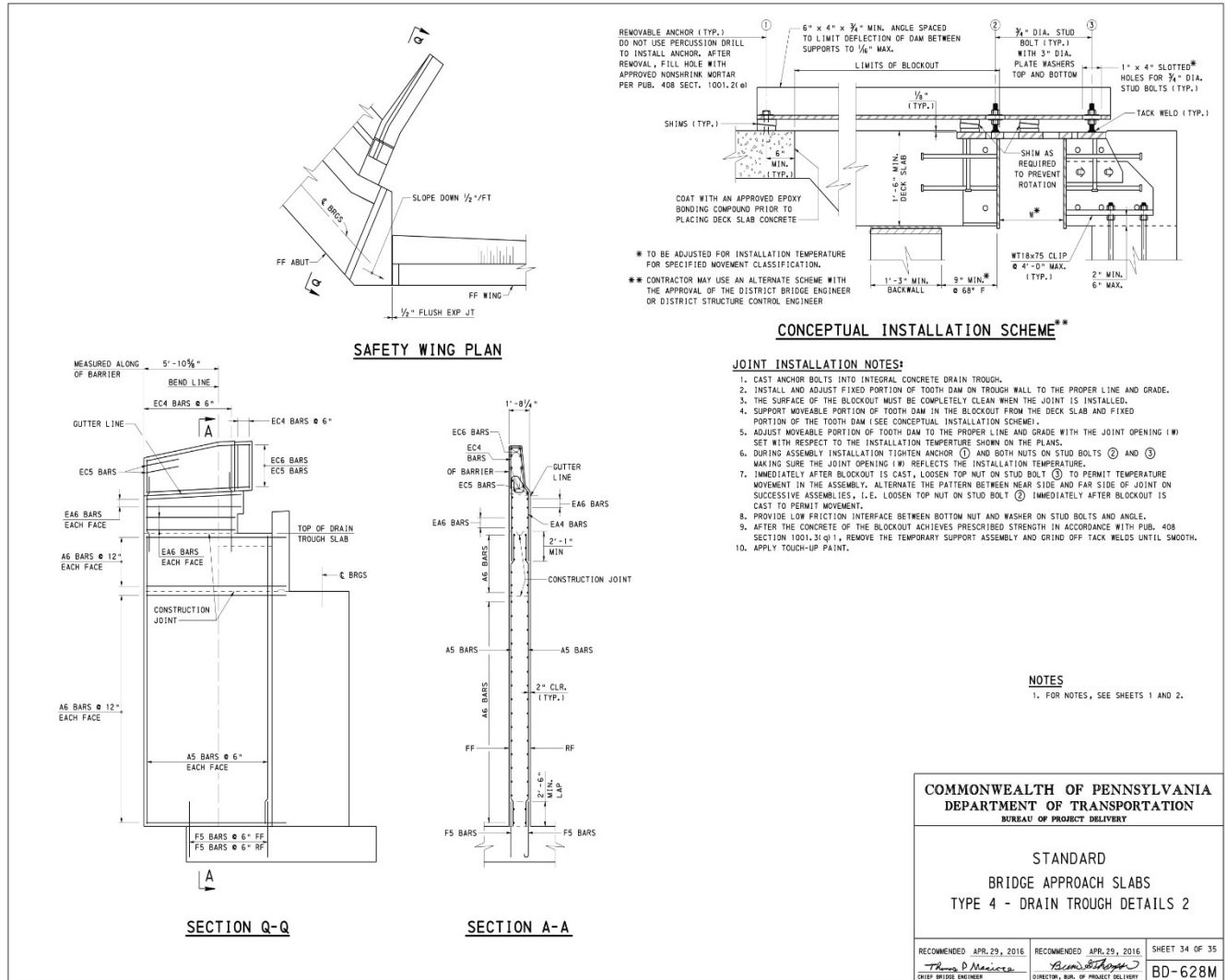


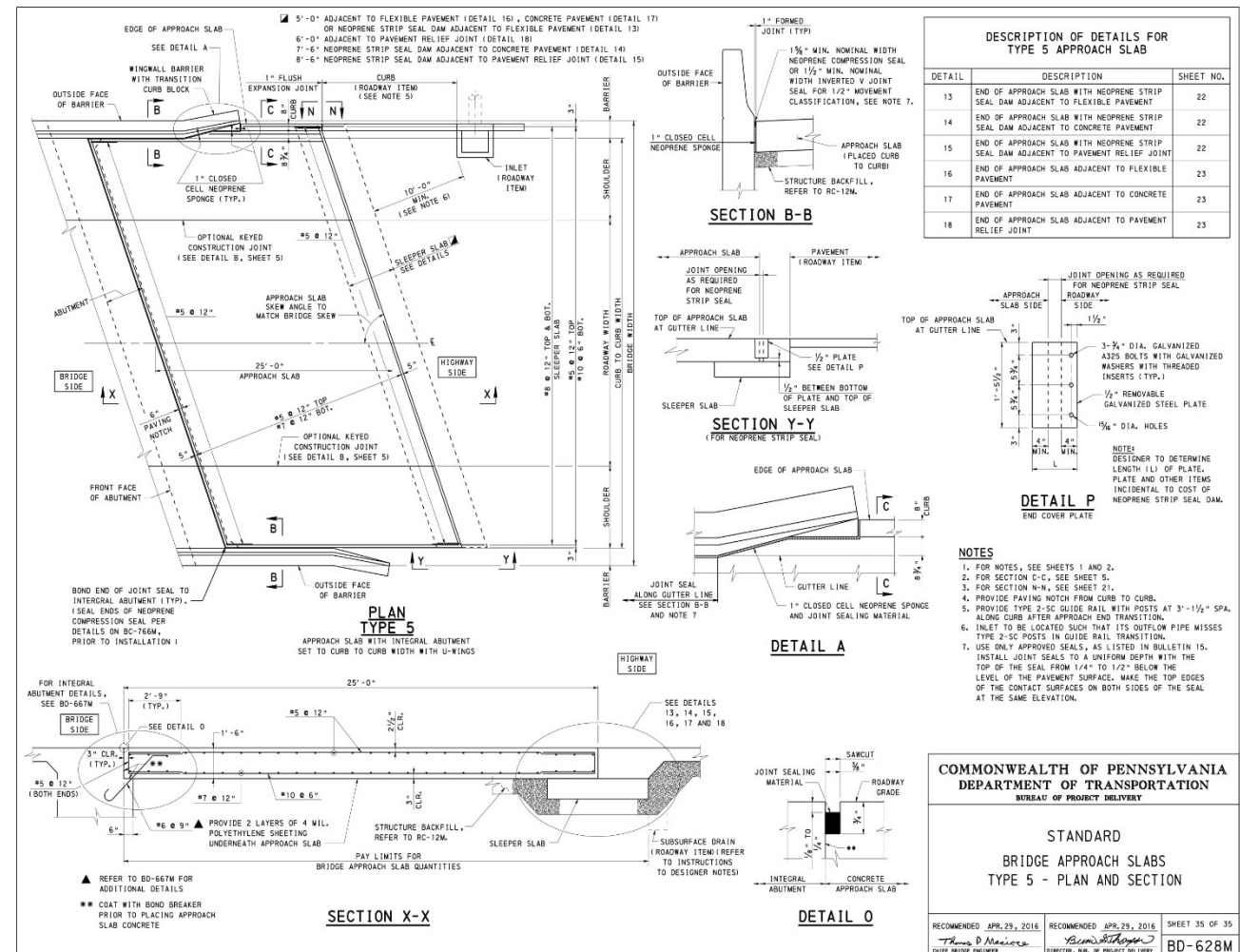












Appendix B. Numerical Simulation and Parametric Evaluation of Integral/Semi-Integral Bridges Considering Representative Ranges of Relevant Parameters

(Contributing authors: Mr. Pedro Silva and Dr. Yuri Costa)

B.1: Introduction to the Numerical Simulations

The goal of the numerical simulations is to evaluate the effect of various parameters that are expected to influence the performance of SIAB/IAB structures using numerical modeling techniques. To perform this analysis, a baseline structure similar to structures constructed in Mack Creek and China Creek are modeled using Plaxis. The loads applied to the structure are estimated based on field measurements and other reasonable assumptions, applicable to environmental conditions found in the State of Texas.

In addition, due to the complexity of the effects of various restraints imposed on a SIAB/IAB structure, it was decided to expand the numerical analysis to include numerical modeling of thermal flow within the bridge deck profile as informed by the data directly measured in the field.

B.2: Finite Element Model of Mack Creek Bridge

As a baseline, a structure similar to Mack Creek is modeled in Plaxis using the information found in the technical drawings of the bridge. The details of this model are described in the following subsections.

B.3: Description of the Finite Element Model of Mack Creek Bridge

The numerical simulations were carried out using the software Plaxis 2D 2016, which uses the Finite Element Method (FEM). Plane-strain conditions were used in a two-dimensional finite element analysis. The geometry of the numerical model was defined based on the information provided by TxDOT (2016). The geometric boundaries of the numerical model were 131.2 ft in length and 65.6 in depth. These dimensions were assumed to be sufficient to avoid boundary interferences (Knappett et al., 2016; Rawat and Gupta, 2017). Figure B.1 and Figure B.2 show the geometry used in the numerical model.

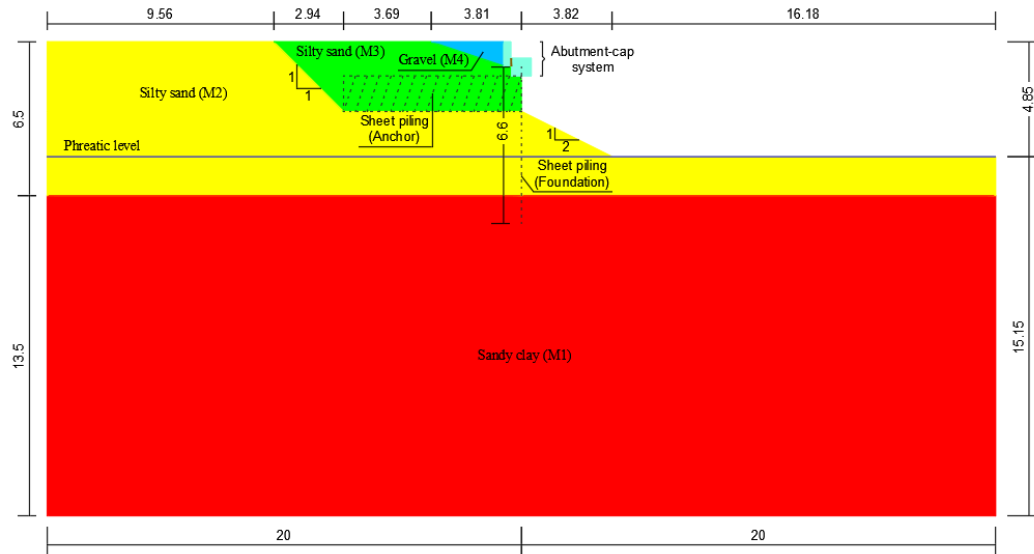


Figure B.1: Numerical model geometry (dimensions in m)

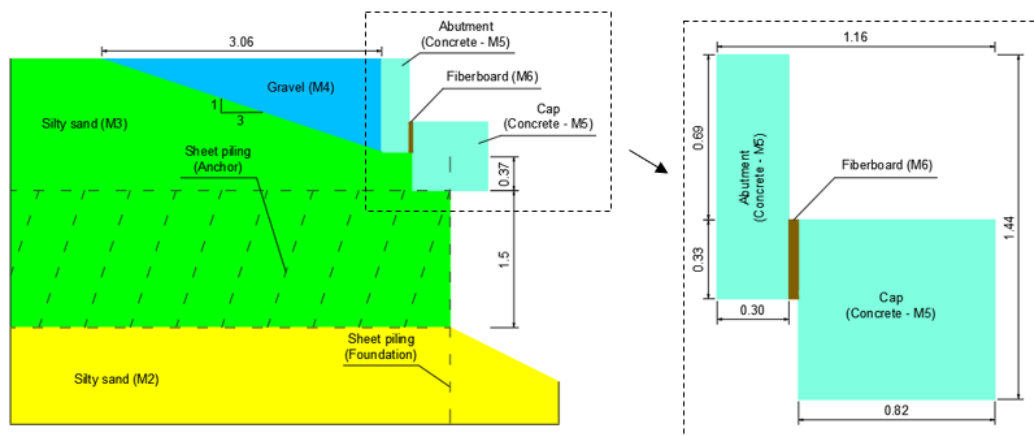


Figure B.2: Detail of the bridge abutment and pile cap (dimension in m)

M3 represents the same soil as M2, but after backfilling; M4 represents the gravel backfill used by the contractor behind the abutment walls; and M6 represents a fiberboard material used to fill the space between the abutment and pile cap (TxDOT, 2016). The soil materials, the reinforced concrete and the fiberboard were represented by using soil clusters. The foundation sheet piles were represented by using plate elements while the anchor sheet piles were represented by using fixed-end anchor elements. Soil-structure interaction was considered by using interface elements with strength reduction factors (R_{inter}) equal to 0.5 for soil-steel interface, and 0.7 for soil-concrete interface. A virtual thickness factor of 0.1 was also applied in the interface boundaries. The finite element mesh used in the numerical simulations was a very fine mesh composed by 15-node triangular elements and with automatic refinement on the interfaces of the soil-structure interaction. Figure B.3 shows the finite element mesh used in the numerical simulations.

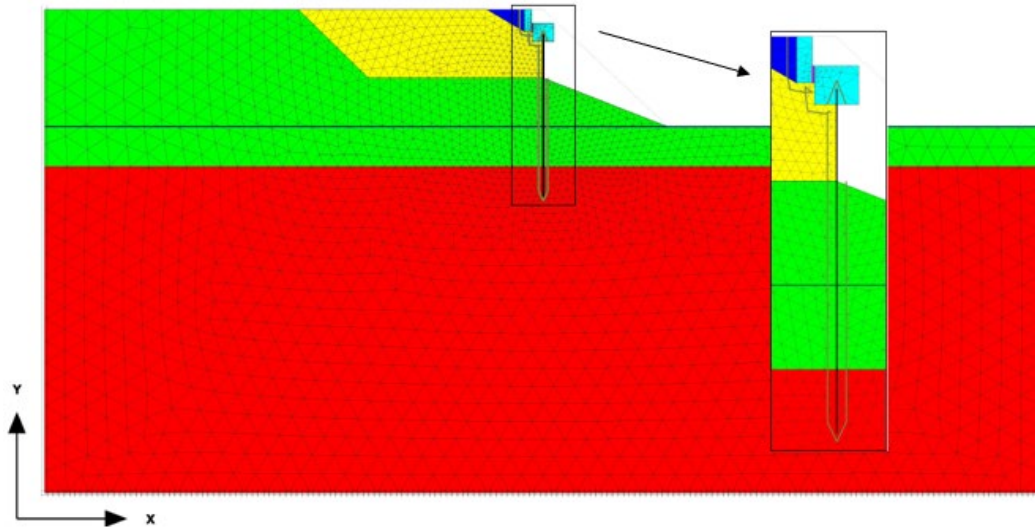


Figure B.3: Finite element mesh of the numerical model

The effect of the bridge superstructure on the abutment and on the foundation was represented in the numerical model by static equivalent loads calculated with the software Ftool (Martha, 2018). A simplified structural analysis was conducted to find the shear force and the bending moment on the abutment and the load on the cap. The superstructure was considered as a single bi-supported beam subjected to itself weight only. A representation of static equivalent loads on the abutment and on the pile-cap is shown in Figure B.4a.

Since Plaxis 2D 2016 does not allow the input of bending moments, this effect was represented by a two-point load on the abutment, as shown in Figure B.4b. The value of the two-point load was calculated by dividing the value of the bending moment by the height of the superstructure. Values of the Shear Force (SF), two-Point Load (PL) and Superstructure Load (SL) on the abutment-cap system used in the Plaxis 2D 2016 numerical model were equal to 5.9 kip.ft/ft, 1.48 kip.ft and 112.85 kip.ft/ft, respectively. A scheme of the effect of the bridge superstructure on the abutment and foundation is shown in Figure B.4.

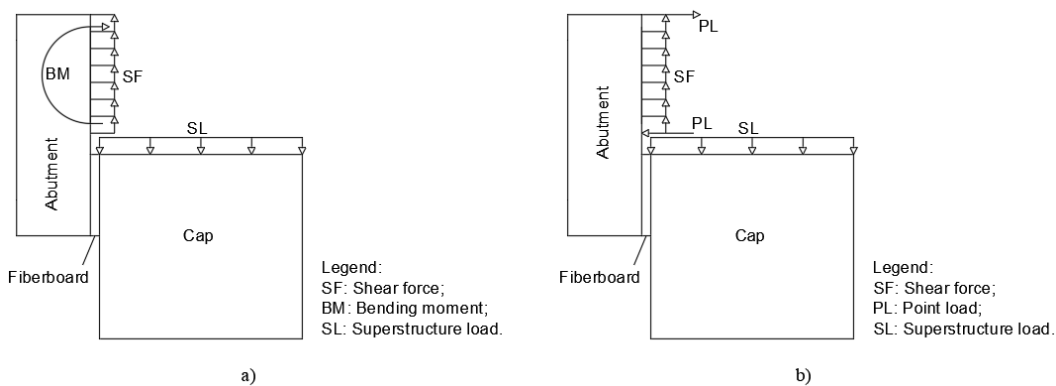


Figure B.4: Representation of the effect of the bridge superstructure: (a) structural analysis; and (b) Plaxis 2D 2016

Prescribed horizontal displacements were used to represent the effects of expansion and contraction of the bridge superstructure on the abutment due to temperature changes. The numerical simulations were performed by applying cycles of calculated prescribed displacements, as to represent the daily expansion and contraction of the bridge.

According to AASHTO (2012), the length variation (ΔL) of the bridge superstructure can be estimated by Equation 1.

$$\Delta L = \alpha * L * \Delta T \quad (1)$$

where: α is the coefficient of thermal expansion of the concrete, L is the length of the bridge superstructure and ΔT is the temperature variation in the bridge superstructure.

The coefficient of thermal expansion assumed for the concrete was $10.8 \times 10^{-6}/^{\circ}\text{C}$ and is in the range recommended by AASHTO (2012) in the absence of laboratory tests or more precise data. The temperature variation (ΔT) was calculated from the daily minimum and maximum temperatures recorded by the temperature sensors.

As an example, to illustrate how displacements were calculated, Figure B.5 presents the ambient air temperatures recorded hourly on 07/14/2017. The temperature decreases from hour 0 to hour 7, when it reaches the minimum value (T_{\min}), and increases from hour 7 to hour 17, when the maximum value is reached (T_{\max}). After reaching the maximum, the temperature decreases again until the next day. The horizontal displacement pushing the abutment backwall against the backfill was calculated using the difference between the temperature at hours 7 and 17 of the day. The horizontal displacement pulling the abutment backwall was calculated using the difference between the maximum temperature found at hour 17 and the minimum temperature of the next day. The decrease in temperature until hour 7 was used in the calculations of the previous day.

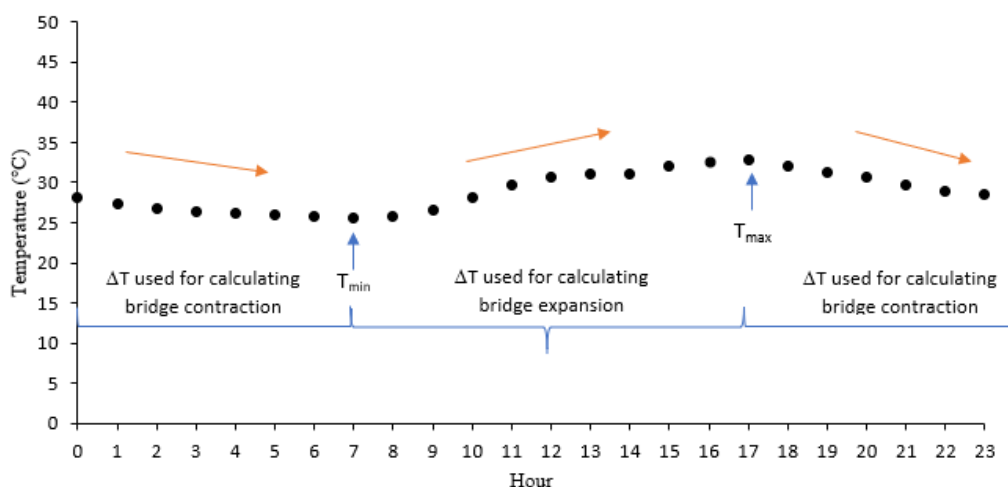


Figure B.5: Ambient air temperature recorded on 07/14/2017

The prescribed horizontal displacements (δh) were calculated by dividing ΔL from Eq. (1) by two. This assumption is believed to be in accordance with field conditions, since both abutments received the same granular backfill against the backwall, which was compacted to the same compaction degree (TxDOT, 2016). Other investigations used the same approach to calculate δh (ex. Karalar and Dicleli, 2018; Murphy and Yarnold, 2018). The estimated prescribed horizontal displacement during the first 100 days of the bridge monitoring are presented in Figure B.6. Displacements ranged within ± 0.04 in.

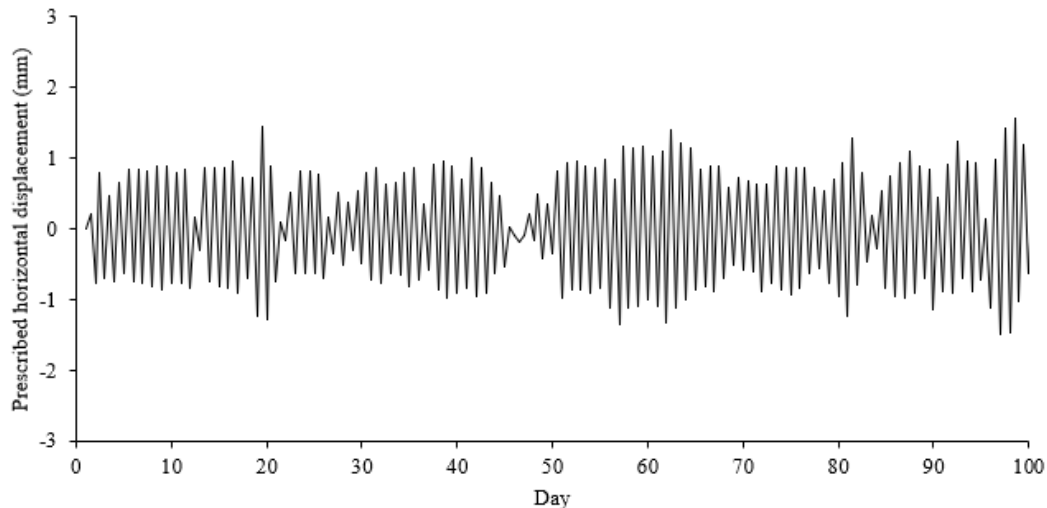


Figure B.6: Estimated prescribed displacement representing the bridge horizontal movements

The height of application of prescribed horizontal displacements was defined at the top of the abutment, as shown in Figure B.7. Solar radiation is the main cause of variations in bridge temperature (Emerson 1977). Assumption of larger lateral displacements at the deck top was considered a realistic approach, since most changes in temperature by solar radiation take place within the upper third of the deck (Emerson, 1977; Rodriguez et al., 2014). Three different possibilities were investigated for defining the best position for the prescribed horizontal displacements at the top of the abutment. Preliminary simulations including the soil-wall interface, the deck-wall interface and at the central section of the abutment yielded virtually the same results. The application point of the horizontal displacement was defined at the soil-wall interface since this is the major section of interest for the present investigation (Figure B.7).

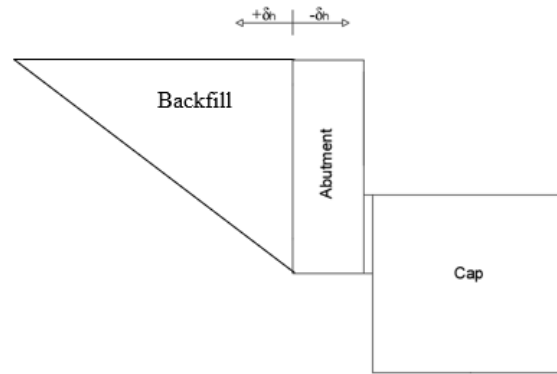


Figure B.7: Representation of the application point of prescribed horizontal displacements

According to Thepchatri et al. (1977) and Arsoy (2000), the most significant factors affecting the temperature variation of the bridge superstructure are solar radiation, ambient air temperature, wind speed, precipitation and thermal properties of structural materials. Combinations of those factors can produce situations in which the temperature of the bridge superstructure is not necessarily equal to the ambient air temperature. Therefore, the effective bridge temperature and, consequently, associated horizontal movements, are very difficult to predict (England et al., 2000).

To simplify the complex mechanisms of interaction of heat transfer and flow involving the bridge structure and environment, the temperature of the bridge abutment was assumed equal to the collected ambient air temperature delayed by 12 to 14 hours. This lag was found by matching the daily peaks of temperature and horizontal stress variations in the field data, as illustrated in Figure B.8.

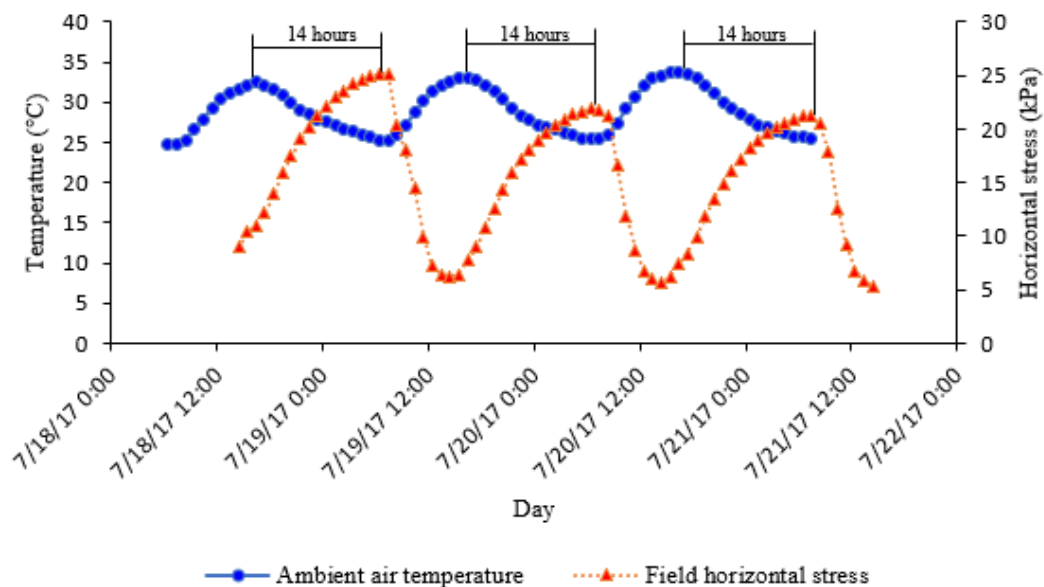


Figure B.8: Example of lag between ambient air temperature and horizontal stresses collected in the field

B.4: Mack Creek Bridge Finite Element Model Results

The numerical model was developed and calibrated based on the field data collected at the bridge's north abutment by Walter (2018). Figure B.9 compares the maximum and minimum daily values of horizontal stresses measured by the pressure cells on the abutment-backfill interface with the corresponding numerical predictions. The numerical stress values represent the average of stresses in six points along the abutment backwall, as to coincide with the position of installation of the pressure cells in the backfill. Predicted and field stresses are also compared in a 1:1 chart (Figure B.10).

The linear adjustment of data shown in Figure B.10 yielded a coefficient of determination (R^2) of 0.77. Also, the inclination of the fitted line is very close to the 1:1 line. It is possible to observe that, in general, predictions with the numerical model produced a good match with field data. The numerical model validation can be considered satisfactory, given the many variables and inherent imprecisions involved in the process overall.

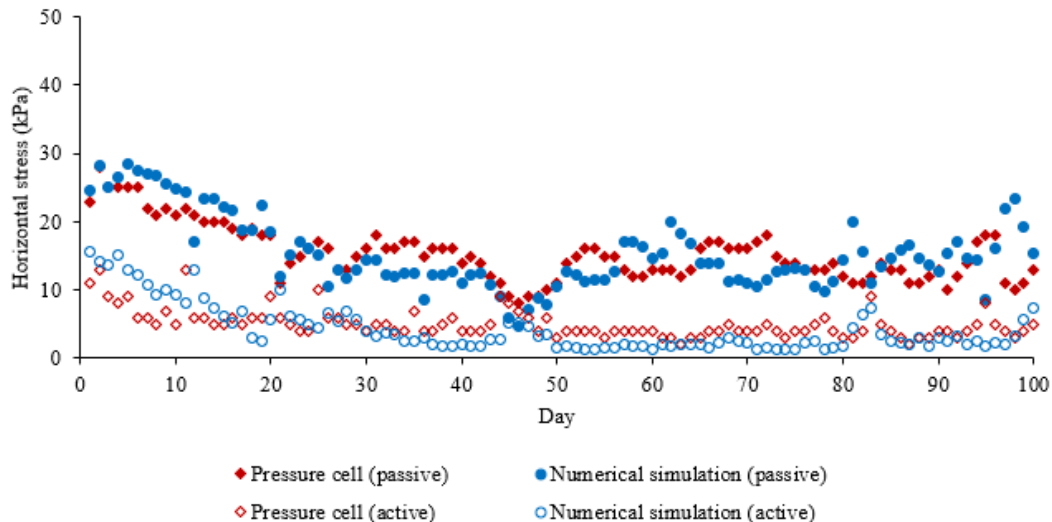


Figure B.9: Comparison between field data and numerical results

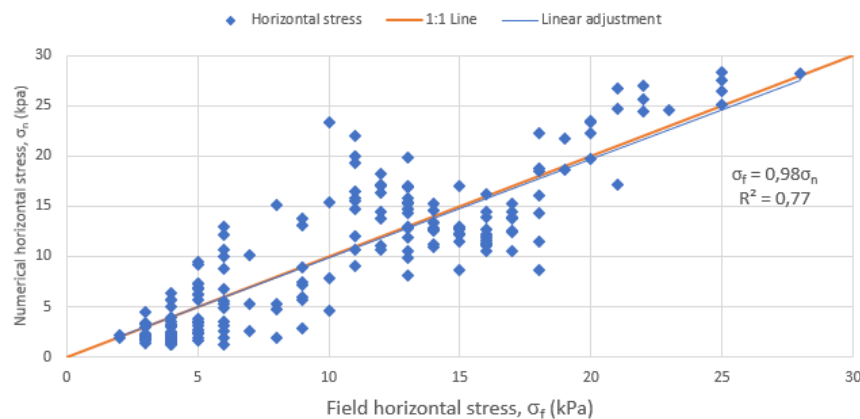


Figure B.10: Dispersion of horizontal stress values

To illustrate the outcome of the developed numerical model, contours of horizontal displacements (u_x) and vertical displacements (u_y) in the soil mass are shown in Figures B.11 and B.12, respectively. The data correspond to expansion and contraction phases on 75th day. Larger soil displacements caused by the cycles concentrate near the top of the abutment backwall and extend to some distance behind it. The soil horizontal displacements for bridge contraction were larger than that for bridge expansion due to the absence of lateral support in the former case (Figure B.11). On the other hand, the soil vertical displacements between the expansion and contraction phases were more similar.

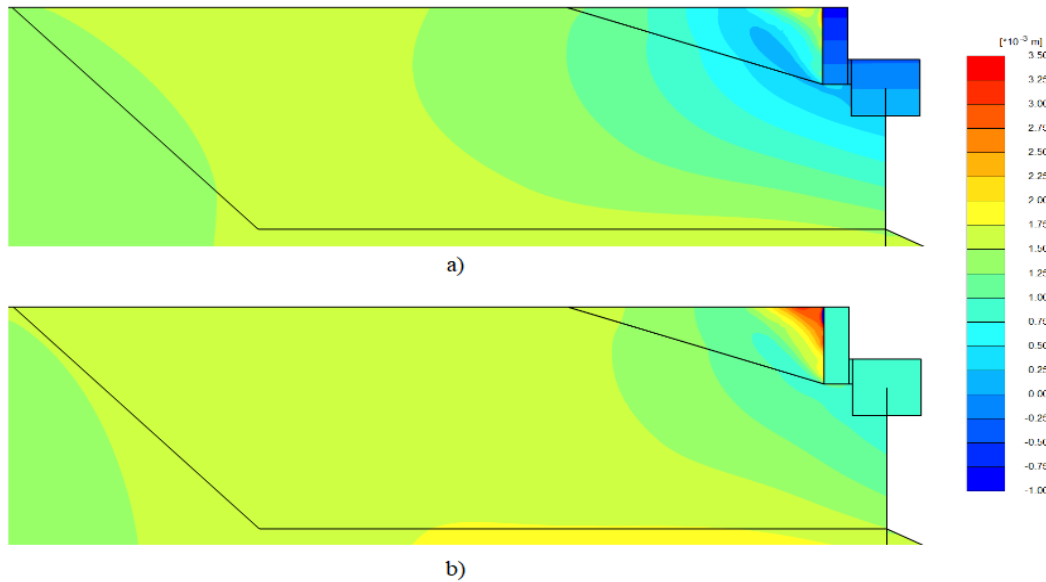


Figure B.11: Horizontal displacement on 75th day: (a) bridge expansion; and (b) bridge contraction

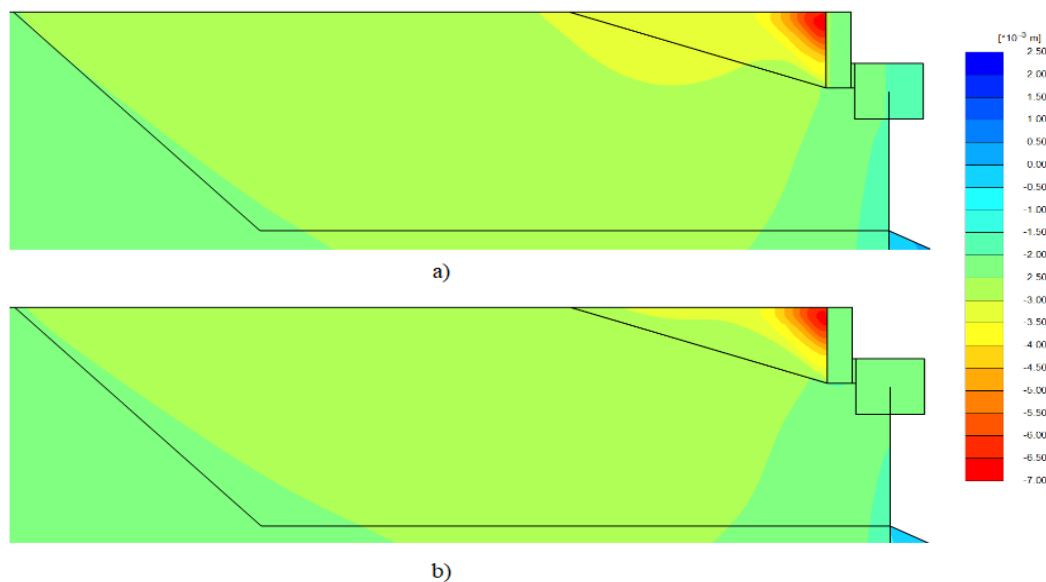


Figure B.12: Vertical displacement on 75th day: (a) bridge expansion; and (b) bridge contraction

Figures B.13 and B.14 show the calculated lateral thrust in the abutment backwall during expansion (passive thrust) and contraction (active thrust) of the bridge, respectively. Variations of the lateral thrust are associated with the daily changes of the imposed horizontal displacements due to temperature fluctuations.

The passive lateral thrust remained below 22.1 kip.ft throughout the entire investigated period (Figure B.13). Trends for the passive lateral thrust can be identified as the days go by. Firstly, the lateral thrust shows a tendency of reduction between the 1st and 46th days. Then, the thrust increases until the 62nd day and reduces until the 78th day. The data becomes too disperse from the 79th day, so that a clear tendency cannot be recognized. The active lateral thrust remained below 7.4 kip.ft during the analyzed period (Figure B.14). The tendencies identified in the variations of the active thrust are firstly characterized by a decrease within the first 20 days, with some scatter occurring between the 20th and 30th days. The thrust becomes constant after the 30th day. The active thrust appeared to be less affected by the daily oscillations of the lateral displacements of the bridge than the passive thrust.

Figure B.15 shows the escalation of the soil vertical displacement (settlement) near the top of the soil-backwall interface. The positive sign in the graph means downward vertical displacement (settlement). Settlements increase with time according to a nearly linear fashion, which show the development of ratcheting with the daily cycles. No stabilization of settlements was noted within those first 100 days of investigation. This figure illustrates the occurrence of strain ratcheting in the backfill soil.

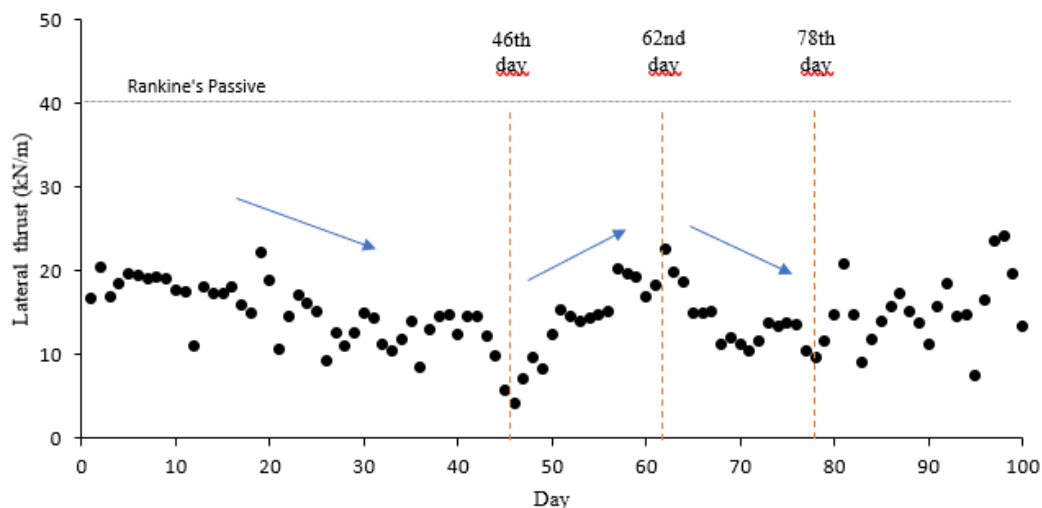


Figure B.13: Passive lateral thrust for bridge expansion

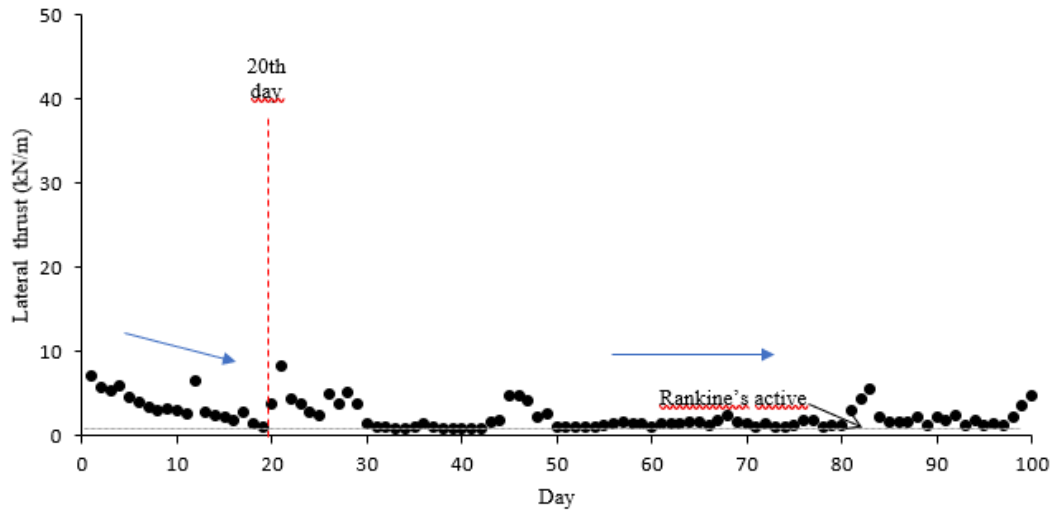


Figure B.14: Active lateral thrust for bridge contraction

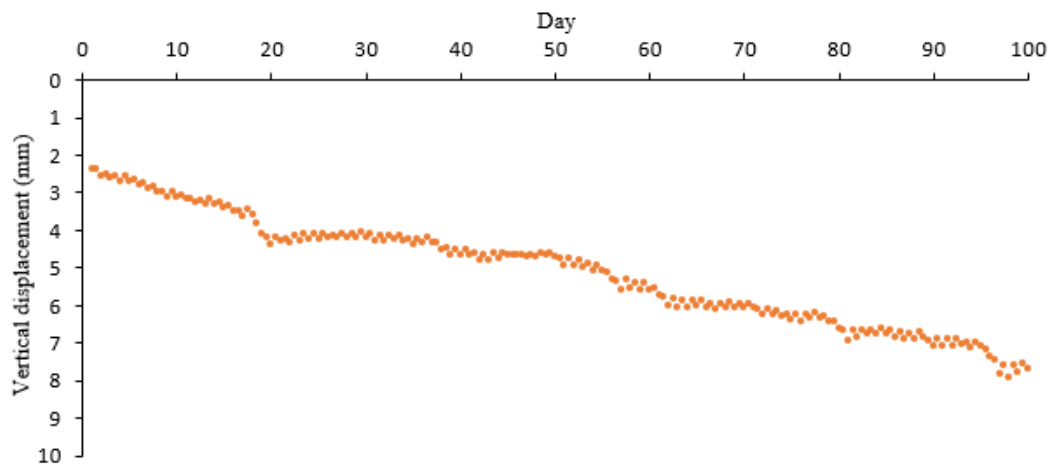


Figure B.15: Vertical displacement of the soil mass close to the abutment

Figure B.16 show the settlement of the soil surface along the distance from the abutment backwall, for selected cycles. The largest displacement occurs at the soil-backwall interface and gradually decreases with the distance from the abutment. The distance of influence can be assumed as 3.28 ft. No heave of the soil surface was observed behind the wall.

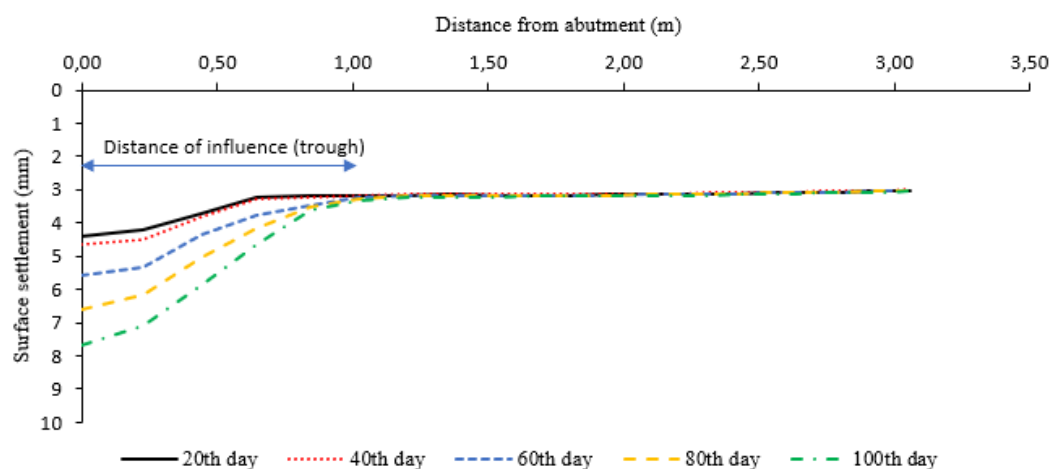


Figure B.16: Settlement of the soil surface behind the bridge abutment

B.5: Preliminary Sensitivity Analyses

B.5.1: Choice of Displacement Amplitudes and Number of Cycles

Sensitivity analyses of parameters of interest were performed after validation of the numerical model. The first parameter of investigation was the amplitude of the prescribed displacement to be used in the numerical simulations. The horizontal displacement magnitudes were chosen based on information from different sources in the literature. Table B.1 presents a compilation of horizontal abutment displacements measured or assumed in various numerical and experimental investigations. It is observed that the relative horizontal displacement, δ_h/h , situates in the range between 0.1% and 0.5%.

Table B.1 - Horizontal abutment displacements from several sources in the literature

Reference	Horizontal displacement δ_h (mm)	Abutment height h (m)	δ_h/h (%)
Ng et al. (1998)	± 6	6.40	0.1
	± 12		0.2
Bloodworth et al. (2012)	± 16	4.00	0.4
Civjan et al. (2013)	± 12	4.00	0.3
	± 20		0.5
Huntley and Valsangkar (2013)	± 15	4.00	0.4
Mitoulis et al. (2016)	± 30	7.00	0.4
Caristo et al. (2018)	± 27	7.00	0.4

The AASHTO LRFD Bridge Design Specifications (AASHTO, 2012) suggest Eq. (1) for estimating the design thermal movement of a bridge deck. Considering that: (a) the minimum (T_{min}) and maximum (T_{max}) ambient temperatures recorded in the field are -17.6°F and $+98.6^{\circ}\text{F}$ (that is, a temperature variation $\Delta T = 113^{\circ}\text{F}$), (b) the deck length (L) is 65.4 ft, and (c) assuming that the concrete thermal expansion coefficient (α) equals $10.8 \times 10^{-6}/^{\circ}\text{C}$, a deck length variation of 0.38 in is obtained with Eq. (1). This would represent a horizontal imposed displacement (δ_h) of 0.19 in for each abutment, which corresponds to a relative horizontal displacement (δ_h/h) of approximately 0.5%. This value can be assumed as a serviceability limit for the bridge under investigation.

Clough and Duncan (1991) provide approximate values of relative movements required to reach passive or active earth pressure conditions, as shown in Table B.2. Based on this information, a horizontal displacement around 4% of the height is needed to achieve passive conditions in a loose granular backfill.

Table B.2 - Approximate values of relative movements required to reach passive or active earth pressure conditions (Clough and Duncan, 1991)

Backfill type	δ_h/h	
	Active	Passive
Dense sand	0.001	0.01
Medium dense sand	0.002	0.02
Loose sand	0.004	0.04
Compacted silt	0.002	0.02
Compacted lean clay	0.01	0.05
Compacted fat clay	0.01	0.05

The AASHTO LRFD Bridge Design Specifications (2012) states that earth pressures used in design of abutments should be selected consistent with the requirement that the abutment should not move more than 1.5 in laterally. This assertion is in line with the assumption of Clough and Duncan (1991). A horizontal displacement of 1.58 in could be assumed as an extreme limit for the displacement of the studied abutment wall. Based on specifications and related past experience of the literature, three horizontal displacements were chosen for the present investigation (Table B.3). The displacements of ± 0.02 in and ± 0.2 in represent serviceability conditions, and the displacement of ± 0.4 in is assumed as an ultimate limit for the bridge abutment.

Table B.3 - Chosen amplitudes of horizontal displacements for present analysis

δ_h (mm)	δ_h/h (%)	Condition
± 0.5	0.05	Serviceability
± 5	0.50	Serviceability
± 10	1.00	Ultimate

A preliminary simulation was performed to find out the number of cycles necessary for the stabilization of the response of the soil-abutment system (steady-state) upon imposed lateral displacements. Limiting the number of cycles can save time and unnecessary computational efforts. Figures B.17 and B.18 show the lateral thrust in the bridge expansion and contraction, respectively, for the prescribed horizontal displacements of ± 0.08 in and ± 0.2 in.

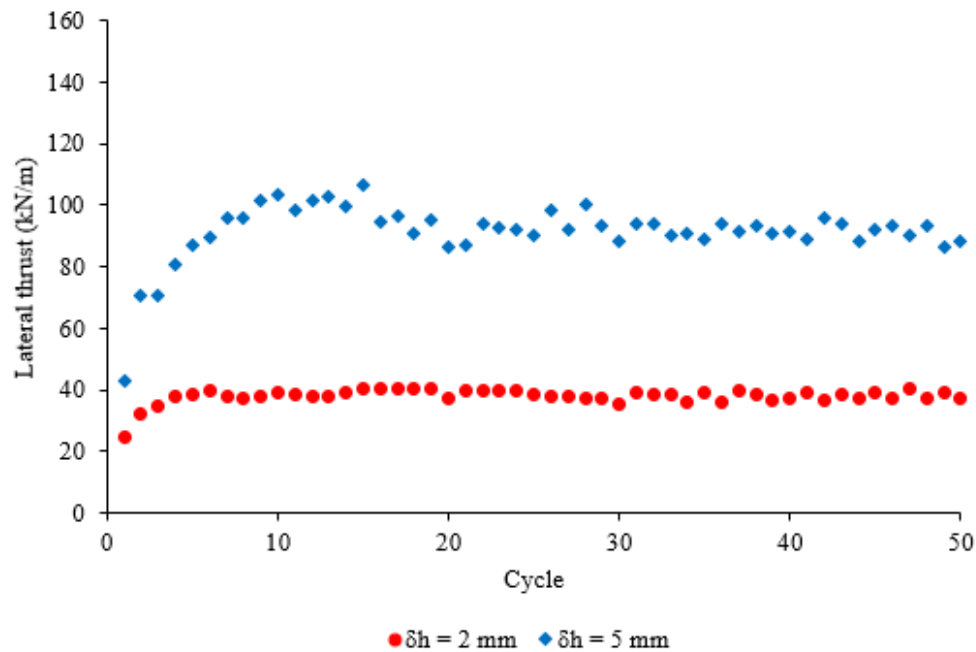


Figure B.17: Lateral (passive) thrust at bridge expansion

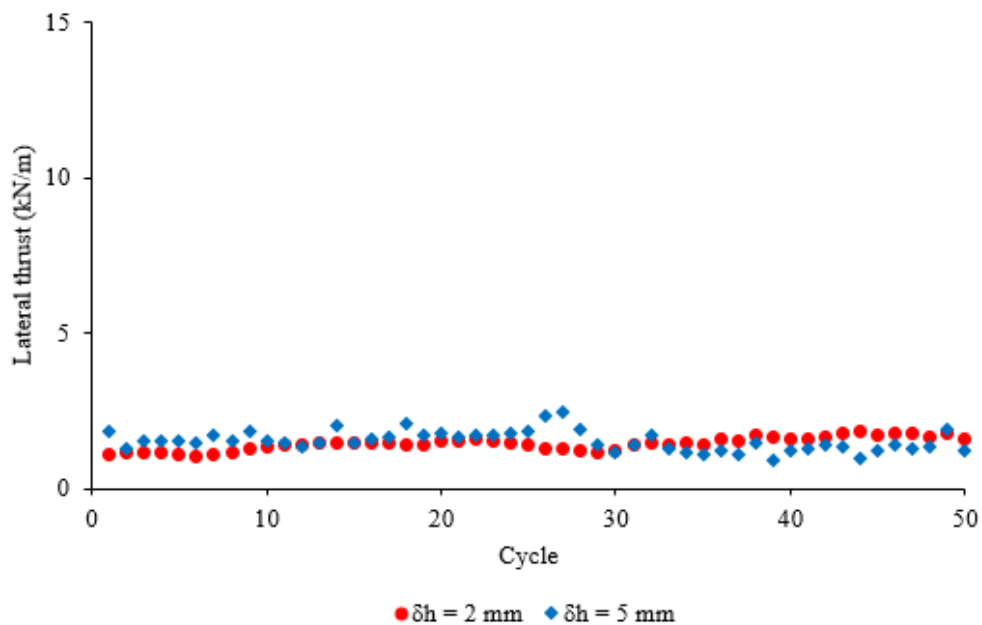
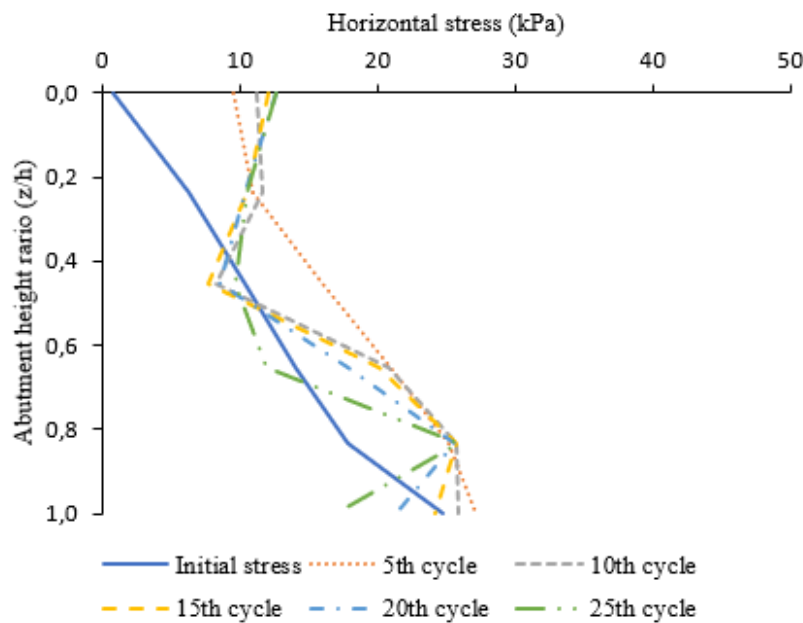


Figure B.18: Lateral (active) thrust at bridge contraction

A tendency for stabilization of the lateral thrust before 15th cycle, for both investigated lateral movements, was identified. On the other hand, the active thrust presented a constant behavior along the cycles since the beginning of movements. Based on this preliminary examination, the subsequent simulations were limited to 50 cycles. Bloodworth et al. (2012) and Caristo et al. (2018) carried out numerical simulations of IAB by applying 100 and 120 cycles, respectively, and found out that 30 cycles were enough for reaching the steady-state in their investigated cases.

B.5.2: Influence of Lateral Displacement Amplitude

Figures B.19 – B.21 show the horizontal stress distribution along the height of the abutment (h) for passive (deck expansion) and active (deck contraction) conditions and displacement amplitudes of ± 0.02 in, ± 0.2 in and ± 0.4 in, respectively. The figures show the horizontal stress against the abutment depth ratio, z/h , where z is the depth from the soil surface, for the 5th, 10th, 15th, 20th and 25th cycles. The distribution of the lateral stress shows a typical triangular shape with the peak wall stress occurring at a depth of approximately 0.65 – 0.85 h . Particularly, active lateral stresses behind the wall were nearly zero within a depth of 0.25 h from the backfill surface. Stresses reduced with increasing cycles of ± 0.02 in and grew with increasing cycles of ± 0.2 in and ± 0.4 in. Variations of passive stresses along the cycles were more marked than active stresses.



a)

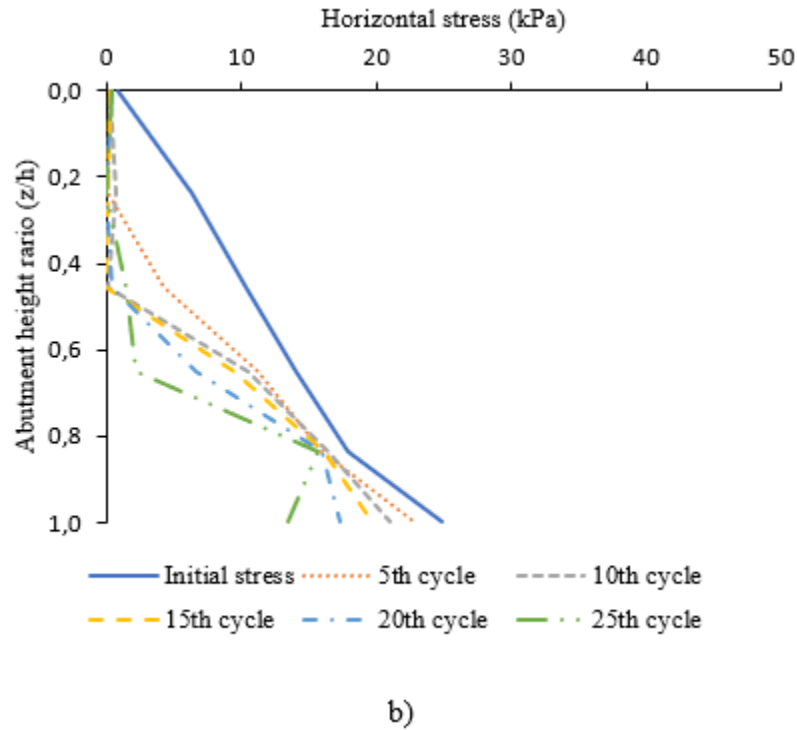
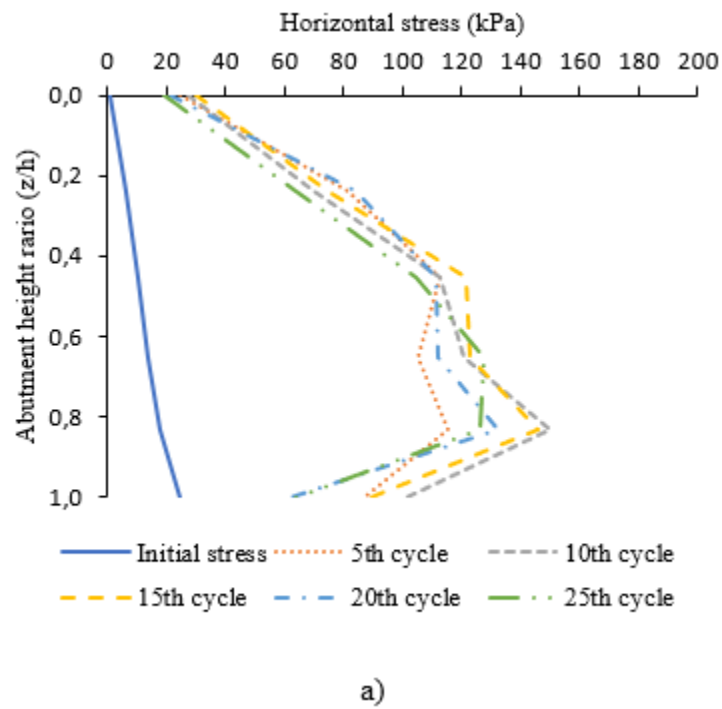
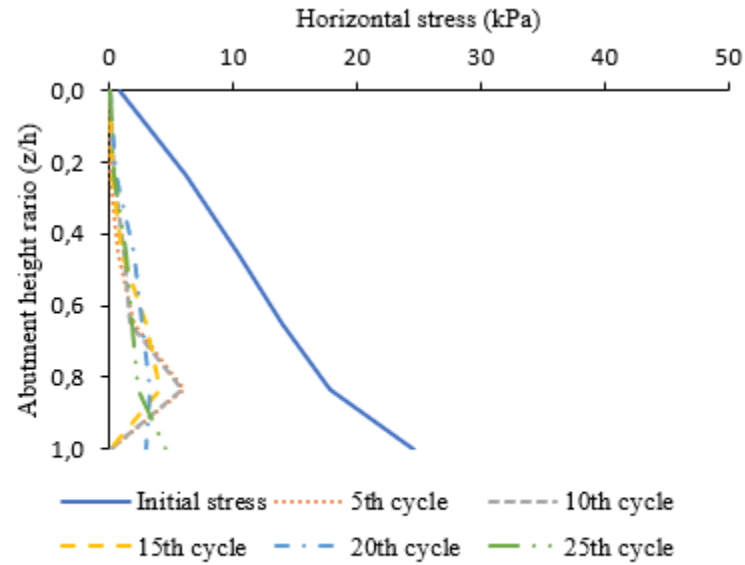


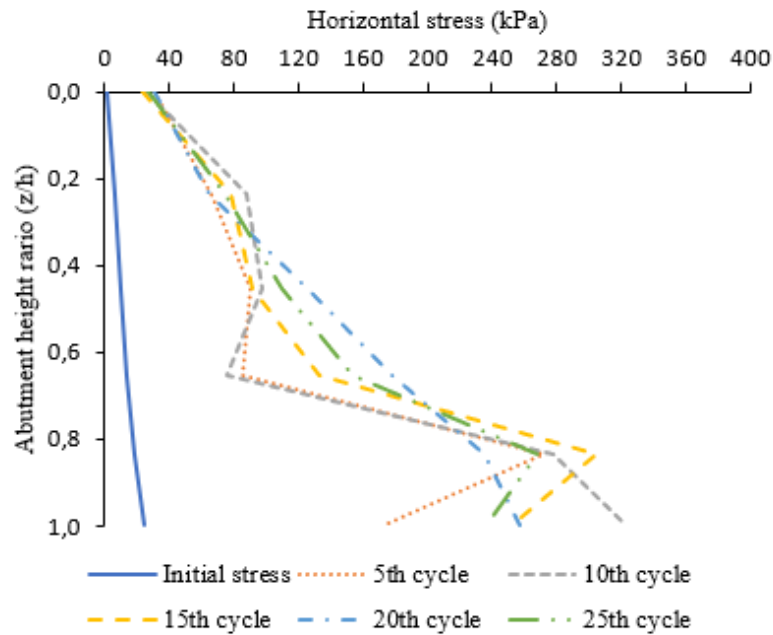
Figure B.19: Lateral stress distribution along the abutment height for $\delta h = \pm 0.50$ mm: (a) bridge expansion; and (b) bridge contraction



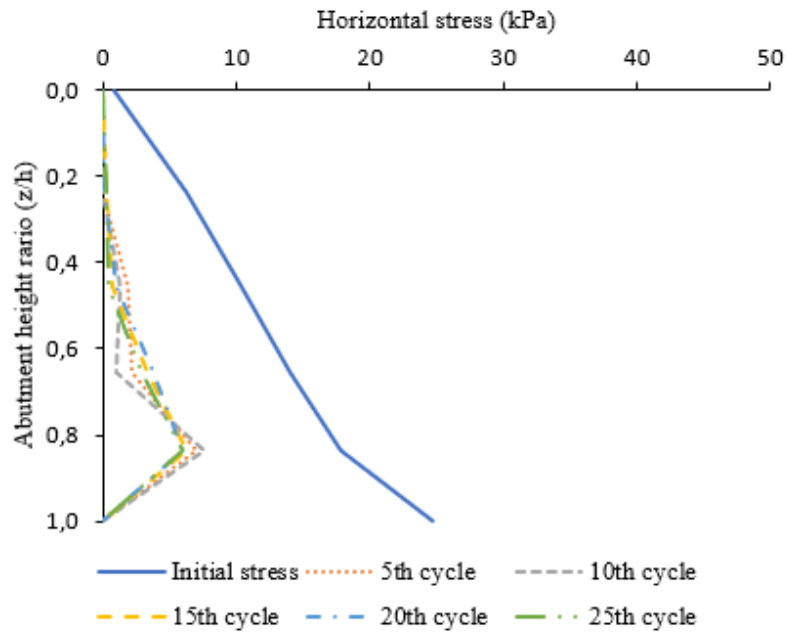


b)

Figure B.20: Lateral stress distribution along the abutment height for $\delta h = \pm 5$ mm: (a) bridge expansion; and (b) bridge contraction



a)



b)

Figure B.21: Lateral stress distribution along the abutment height for $\delta h = \pm 10$ mm: (a) bridge expansion; and (b) bridge contraction

Figures B.22 – B.24 show the evolution of the lateral thrust with the cycles during the phases of expansion and contraction of the bridge, for the prescribed horizontal displacements of ± 0.02 in, ± 0.2 in and ± 0.4 in. For the smaller lateral displacement, it is observed a nearly linear reduction of the lateral thrust before reaching stabilization at the 25th cycle, in both passive and active cases (Figure B.22). However, with the other two higher horizontal displacements, the passive thrust increased until around the 10th cycle and approached a nearly linear stable value, while the active thrust remained virtually constant (Figures B.23 and B.24). It is possible to observe a ratcheting effect occurring with the larger lateral displacements, that is, an increase of the lateral thrust with the cycles. For contraction movements of the bridge, there seems to be no effect of the cycles on the lateral thrust. Figure B.25 compares the curves of the three lateral displacements in the same plot. The degradation of the lateral thrust with small lateral displacements and the escalation with larger displacements was also reported by England et al. (2000) from results of small-scale tests of retaining wall models. It is related with how the horizontal and vertical strains behave with amplitudes. Under low amplitudes of cycles, there is lateral expansion and vertical compression of the soil mass near the backfill. This makes the lateral thrust increase with the cycles. On the other hand, under high amplitudes of cycles, the soil mass near the backfill tends to compress laterally and expand vertically, which causes reduction of the lateral thrust. In both cases, a steady state is reached after a few cycles.

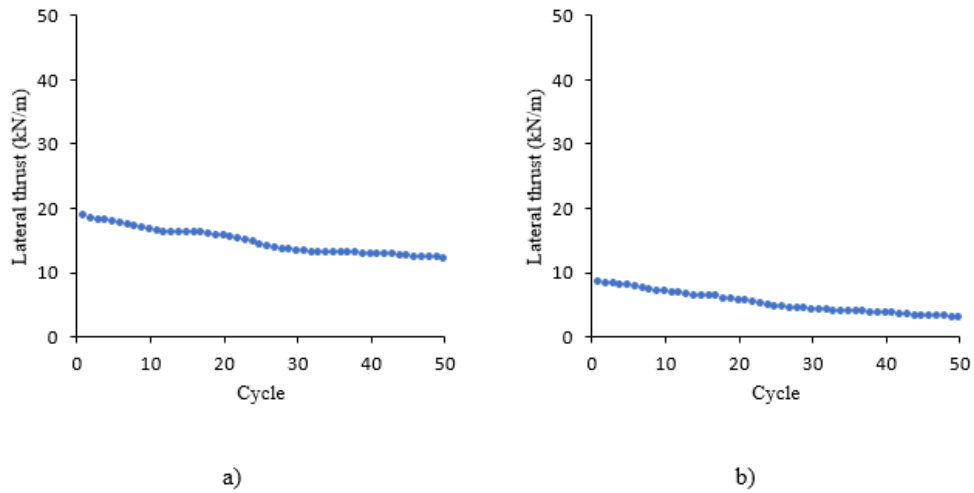


Figure B.22: Lateral thrust for $\delta h = \pm 0.50$ mm: (a) bridge expansion; and (b) bridge contraction

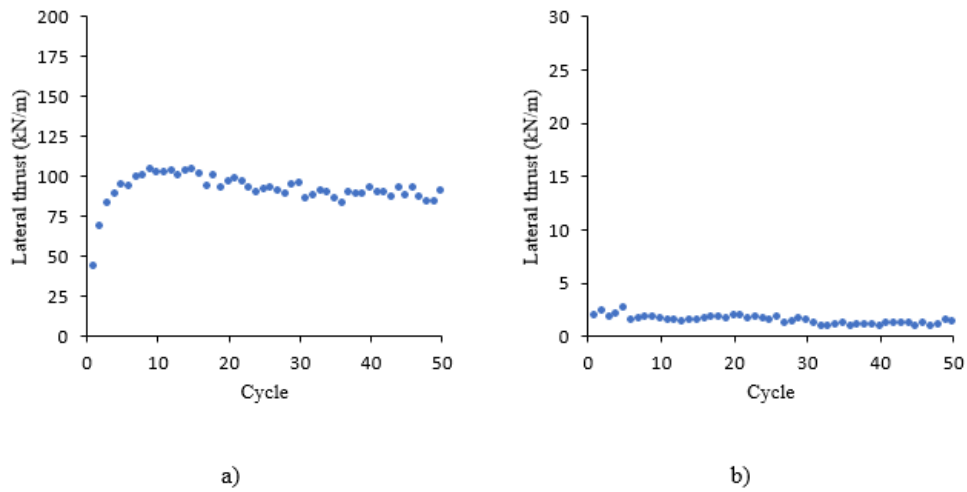


Figure B.23: Lateral thrust for $\delta h = \pm 5$ mm: (a) bridge expansion; and (b) bridge contraction

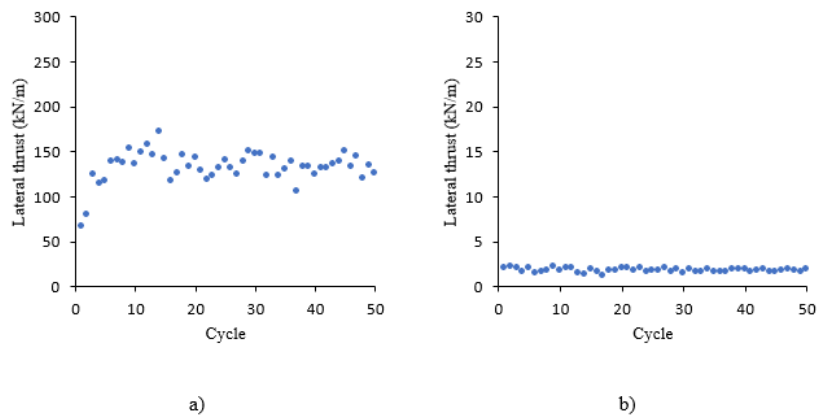


Figure B.24: Lateral thrust for $\delta h = \pm 10$ mm: (a) bridge expansion; and (b) bridge contraction

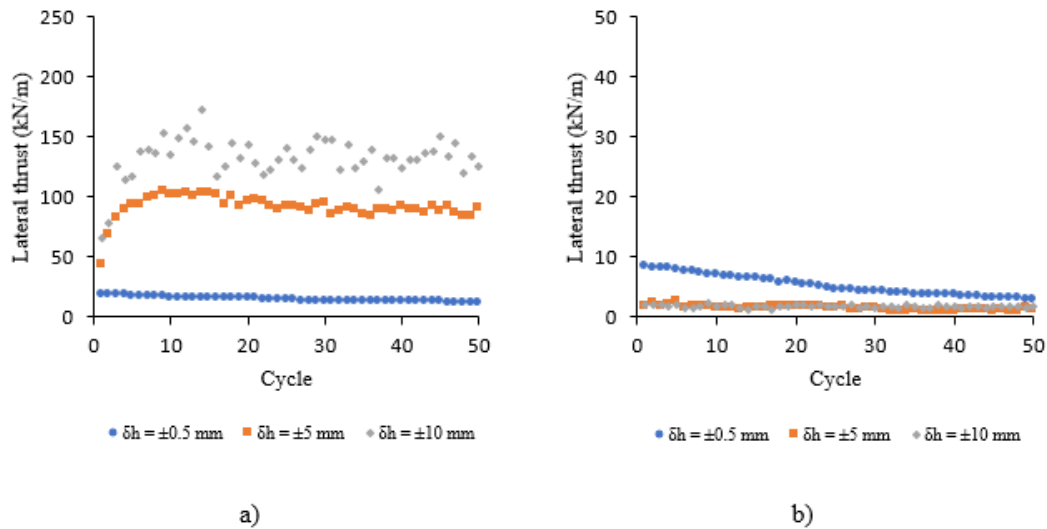


Figure B.25: Comparison of lateral thrust with different amplitudes of lateral displacement: (a) bridge expansion; and (b) bridge contraction

Figures B.26 – B.28 show the variation in the wall reaction ratio (K) during the cyclic process for variations within selected active-passive rotation cycles. K is the ratio of total lateral soil force acting on the wall to the total lateral force of a triangular hydrostatic stress distribution acting over the height of the wall. The figures show the decrease in K with the lateral displacement of ± 0.02 in and the increase in K with the displacements of ± 0.2 in and ± 0.4 in.

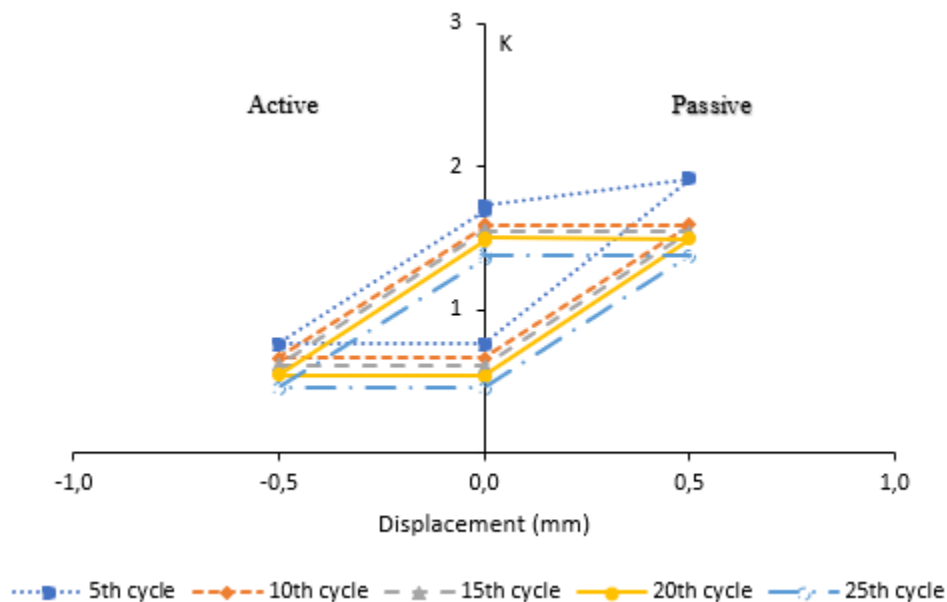


Figure B.26: Variation in wall reaction ratio K during cyclic wall rotations of amplitude ± 0.5 mm

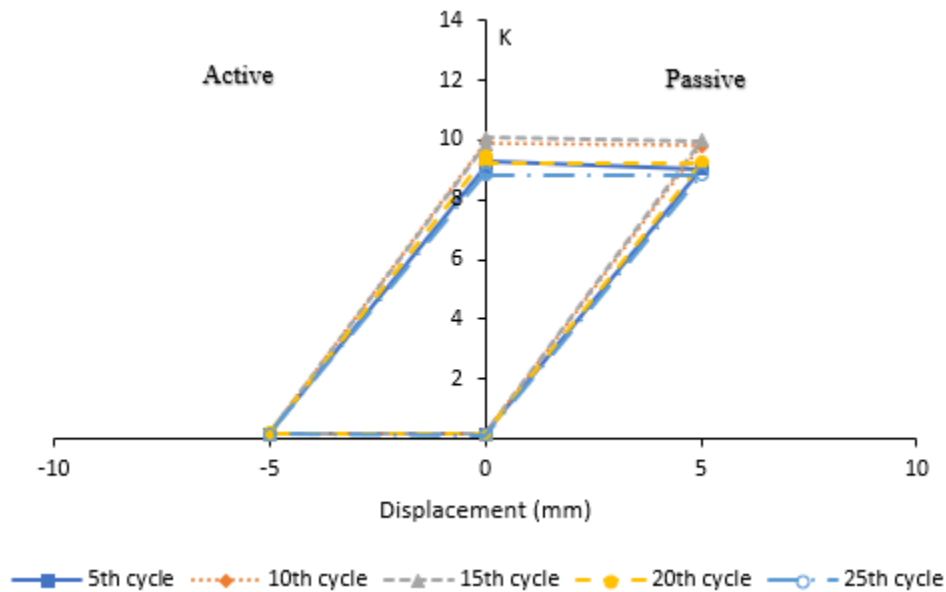


Figure B.27: Variation in wall reaction ratio K during cyclic wall rotations of amplitude ± 5 mm

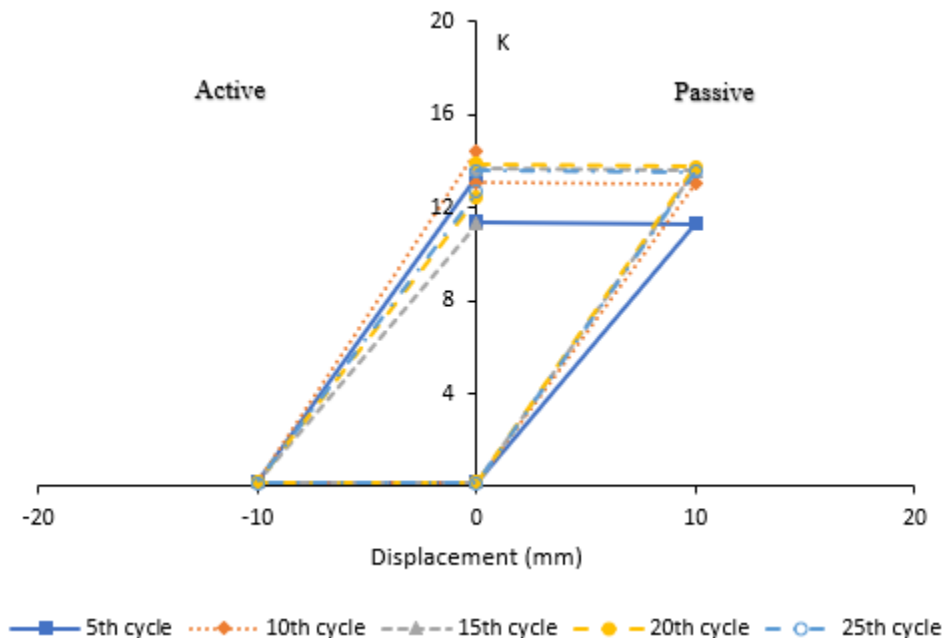


Figure B.28: Variation in wall reaction ratio K during cyclic wall rotations of amplitude ± 10 mm

Profiles of vertical displacements of the soil surface behind the abutment wall are shown in Figures B.29 – B.31. The magnitude of the vertical displacements was found to increase with increasing amplitudes of imposed lateral displacements. The low amplitude cyclic displacement of ± 0.02 in provoked the appearance of a settlement region in the soil mass (Figure B.29), while the higher amplitudes of ± 0.2 in and ± 0.4 in also caused heave of the soil at greater distances from the backwall (Figures B.30 and B.31). Settlements were maximum adjacent to the wall. The

heave of the free-soil surface indicates the existence of a flow mechanism within the backfill. The passive-active wall movements produced a granular flow away from the backwall. The extension of the disturbance in the soil surface increased with increasing amplitude of displacements.

The soil settlement close to the top of the abutment backwall progressively grew with increasing number of cycles and there was no indication that a limiting value was being approached (Figure B.32).

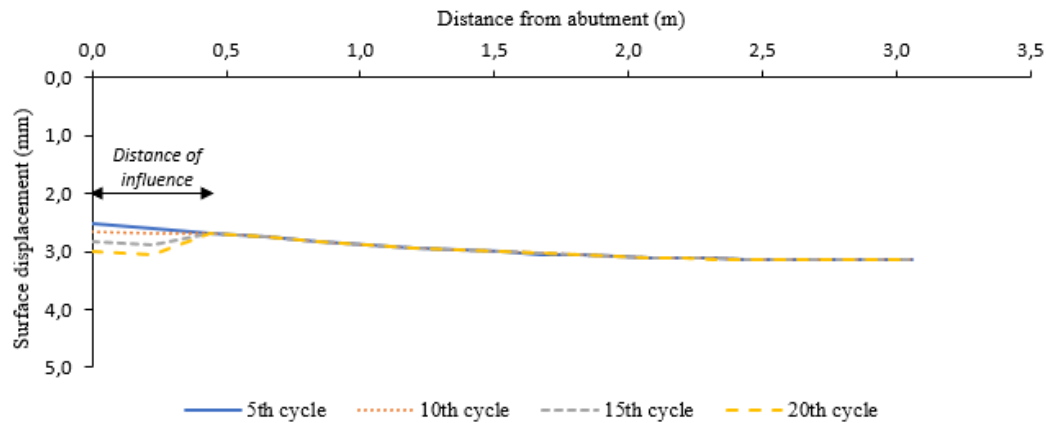


Figure B.29: Profiles of vertical displacements on backfill surface behind bridge abutment with a lateral displacement amplitude of ± 0.5 mm

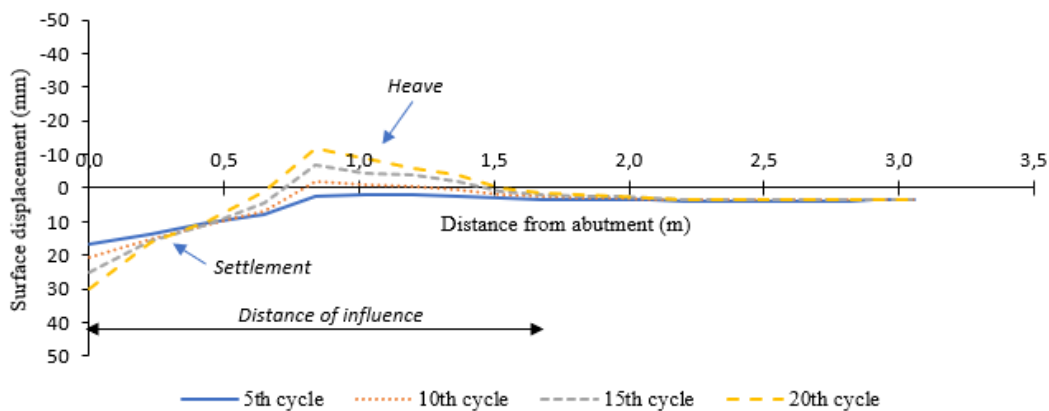


Figure B.30: Profiles of vertical displacements on backfill surface behind bridge abutment with a lateral displacement amplitude of ± 5 mm

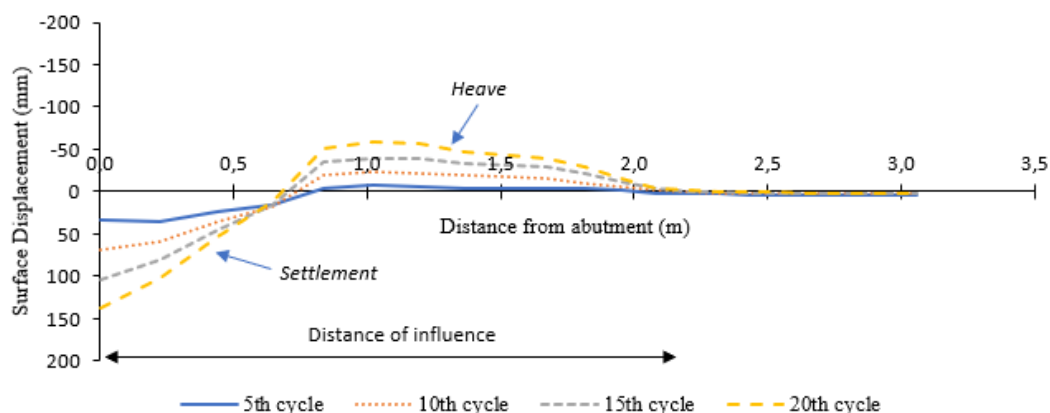


Figure B.31: Profiles of vertical displacements on backfill surface behind bridge abutment with a lateral displacement amplitude of ± 10 mm

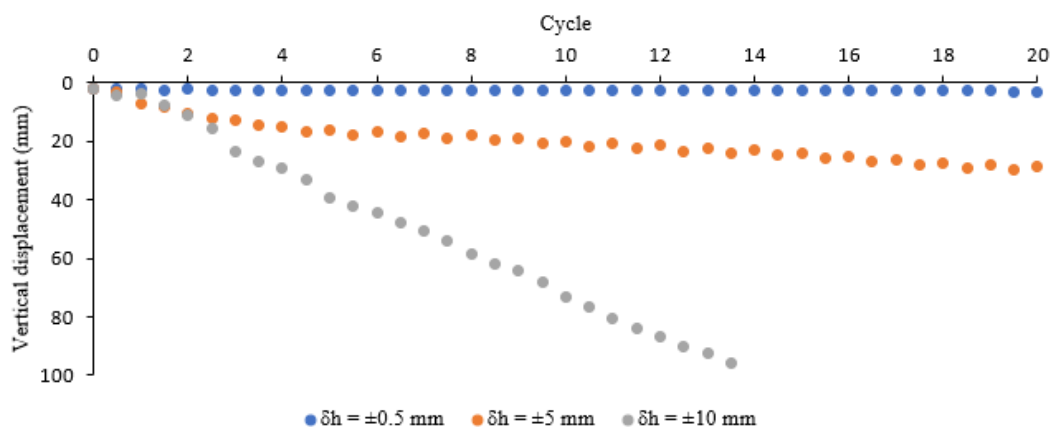


Figure B.32: Settlements close to the top of the abutment backwall for different amplitudes of lateral displacements

B.5.3: Numerical Simulation Considering the Alternative Approach for Modeling the Abutment-cap System

After simulating 100 days of the field data using the geometry described in Section B.3, an alternative approach for modeling the abutment-cap system was proposed to account for the influence of elastomeric bearing pad. The same geometry described in Section B.3 was used but considering the abutment-cap system shown in Figure B.33. The intention to use the alternative approach was to evaluate if the match between field data and simulated results can be improved by inclusion of more structural elements such as the bearing pad and the bridge deck and use this model as a starting point to evaluate possible effects of thermally induced displacements on the bearing pad. Both geometries are still under calibration and may undergo several more cycles of alteration before the optimal finite element model is constructed to perform the final sensitivity analysis and present the final report. Figure B.34 shows the finite element mesh used in the numerical simulations.

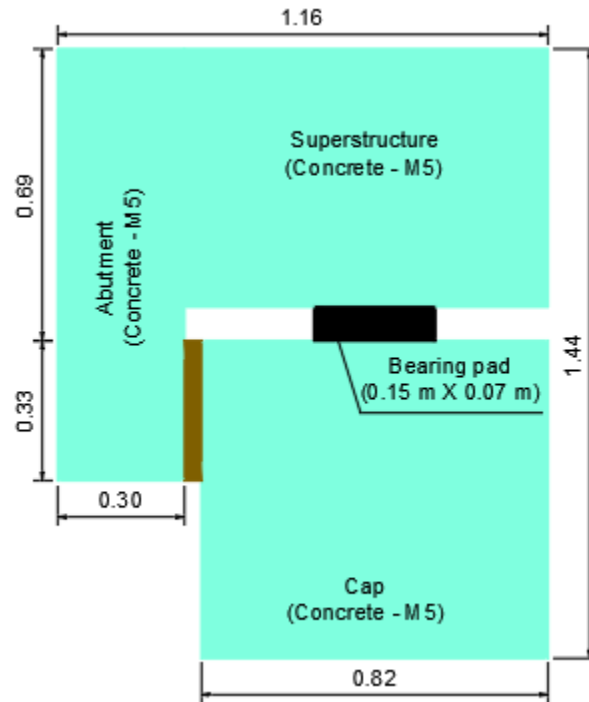


Figure B.33: Detail of proposed alternative abutment-cap system (dimension in m)

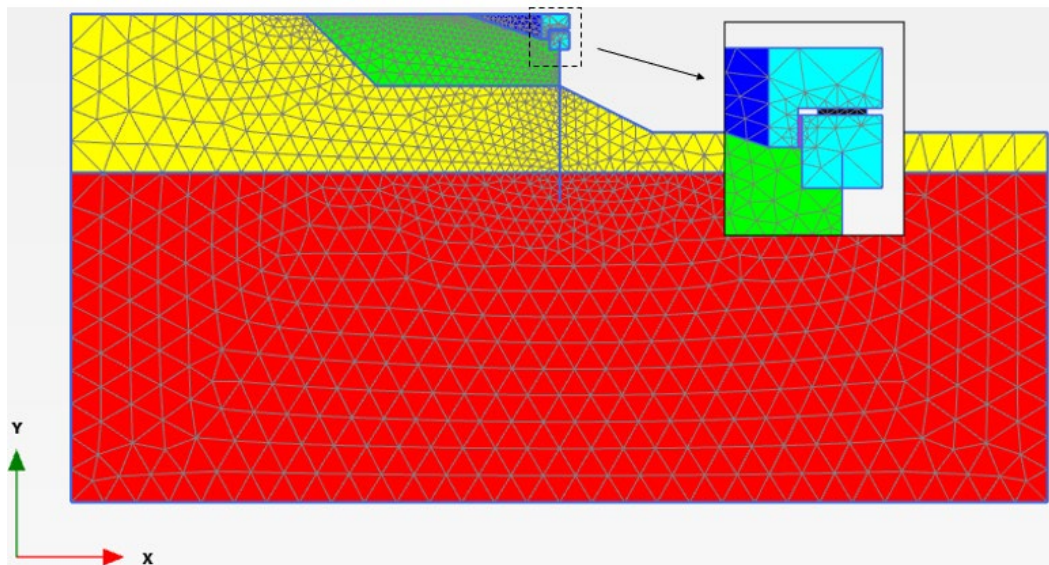


Figure B.34: Finite element mesh of the numerical model

The magnitude of the lateral prescribed displacements was estimated considering the first-year data of the bridge monitoring. The displacement boundary condition was considered to be the same point as defined in Chapter 8. Figure B.35 shows the estimated prescribed horizontal displacement for 360 days of recorded data from Mack Creek Bridge.

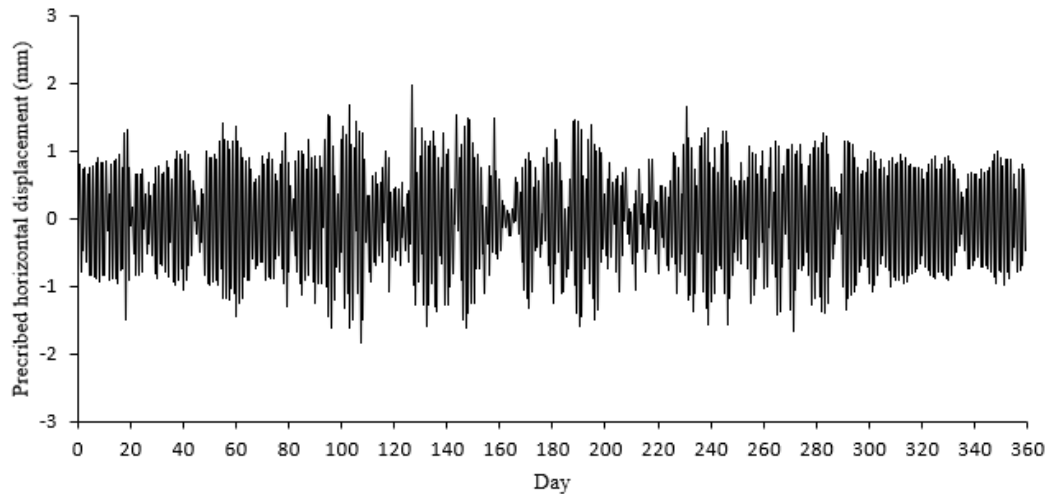


Figure B.35: Estimated prescribed displacement representing horizontal bridge movement

Figure B.36 compares the maximum and minimum daily values of horizontal stresses measured by the pressure cells on the abutment-backfill interface with the corresponding numerical predictions. The numerical stress values represent the average of stresses in six points along the abutment backwall, as to coincide with the position of installation of the pressure cells in the backfill. Predicted and field stresses are also compared in a 1:1 chart (Figure B.37).

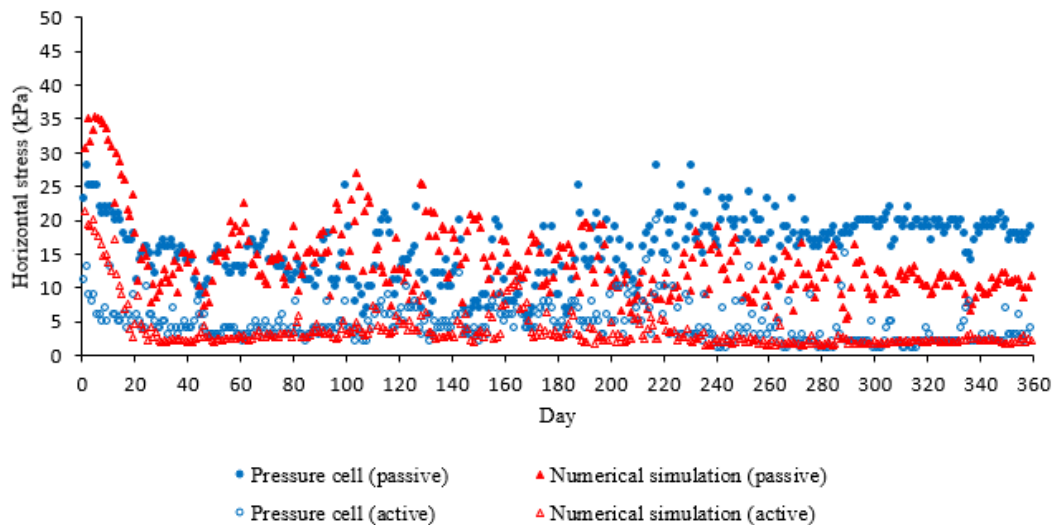


Figure B.36: Comparison between field data and numerical results

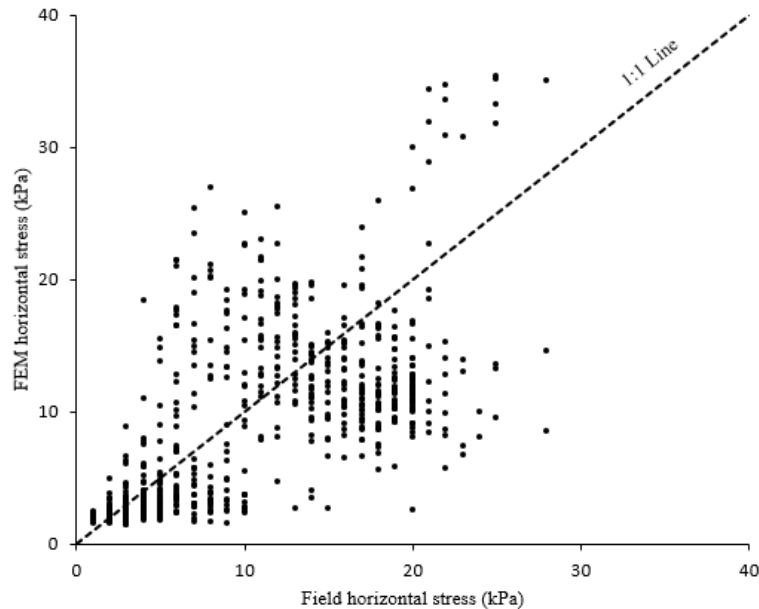


Figure B.37: Dispersion of horizontal stress values

As can be seen in Fig. B.37, there is still considerable dispersion in matching field with numerical results, especially in mid-range pressures. However, the degree of mismatch appears to be slightly smaller when trying to simulate days that had experienced higher pressures. Overall, the numerical model validation cannot be considered satisfactory in its current state and there is a need for exploring a more sophisticated modeling approach that considers more elements, uses more sophisticated material models, etc. These models are currently under development to understand field behavior better.

Figures B.38 and B.39 show the calculated lateral thrust in the abutment backwall during expansion (passive thrust) and contraction (active thrust) of the bridge, respectively. Variations of the lateral thrust are associated with the daily changes of the imposed horizontal displacements due to temperature fluctuations.

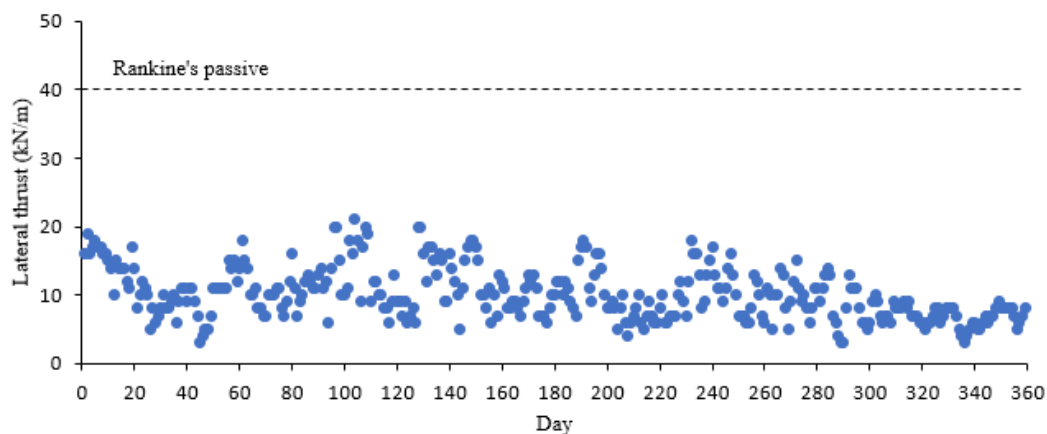


Figure B.38: Lateral thrust in passive direction due to bridge expansion

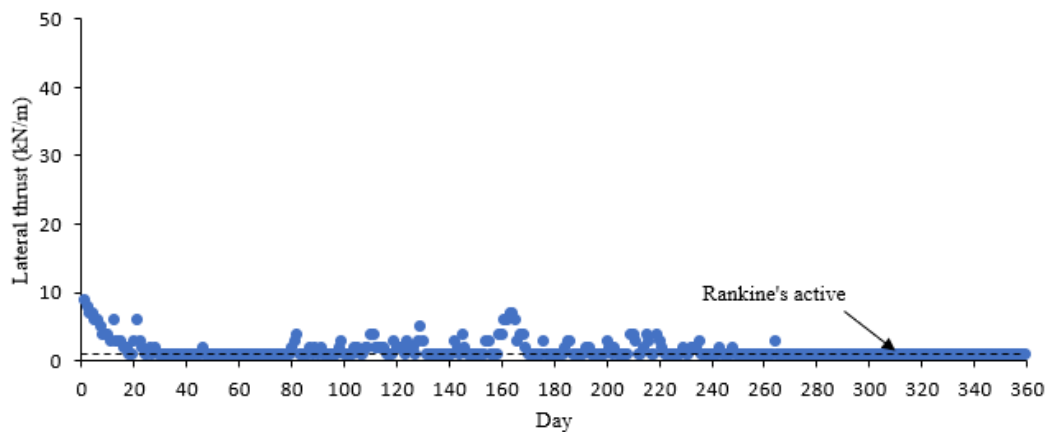


Figure B.39: Lateral thrust in active direction due to bridge contraction

As can be seen, the lateral thrust in the passive direction remained below 22.1 kip.ft throughout the entire period investigated (Figure B.38). Several trends for the lateral thrust in the passive direction can be identified as the days go by. Firstly, the lateral thrust shows a tendency of reduction between the 1st and 50th days. Then, the thrust increases until the 60th day, reduces until the 80th day and increases until 100th day. The data becomes too dispersed from the 100th day and a clear tendency cannot be recognized until the 200th day. The lateral thrust increases again from the 200th to 240th day and decreases again from the 240th to 300th day. Finally, the data shows a tendency of stabilization after the 300th day.

The lateral thrust in the active direction remained below 7.4 kip.ft during the analyzed period (Figure B.39). The tendencies identified in the variations of the lateral thrust in the active direction are firstly characterized by a decrease within the first 20 days, with a tendency of stabilization after the 20th day. The active thrust appeared to be less affected by the daily oscillations of the lateral displacements of the bridge than the passive thrust. This can be explained by the fact that, in practice, relatively small displacements are needed to achieve an active condition, while in the passive direction much larger displacements are required to mobilize the passive earth pressure completely.

Figure B.40 shows the escalation of the soil vertical displacement (settlement) near the top of the soil-backwall interface. The positive sign in the graph means downward vertical displacement (settlement). Settlements increase with time according to a nearly linear fashion, accompanied by the ratcheting phenomenon with the daily cycles. No stabilization of settlements was noted within the first year of investigation. This figure illustrates the occurrence of strain ratcheting in the backfill soil.

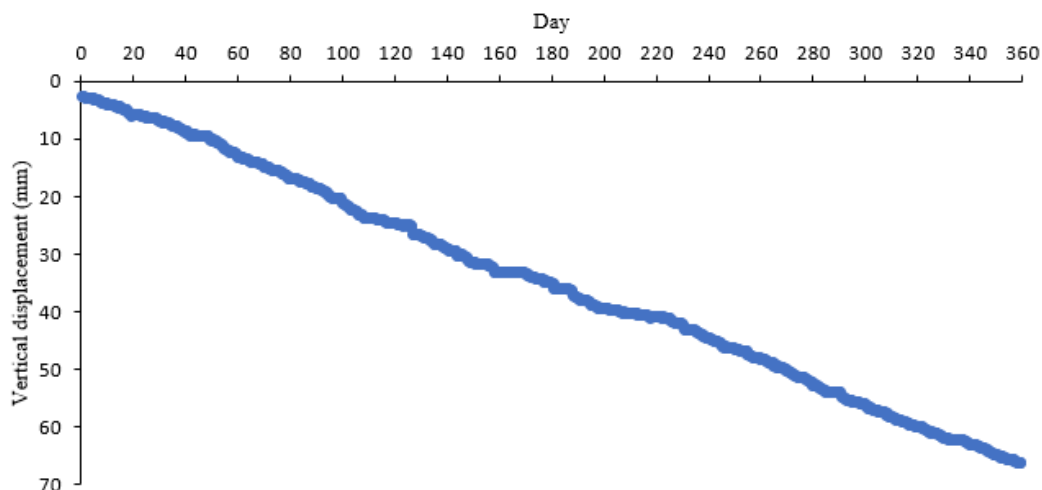


Figure B.40: Vertical displacement of the soil mass close to the abutment

Figure B.41 show the settlement of the soil surface along the distance from the abutment backwall, for selected cycles. The largest displacement occurs at the soil-backwall interface and gradually decreases with the distance from the abutment. The distance of influence can be assumed as 2.6 ft. No heave of the soil surface was observed behind the wall.

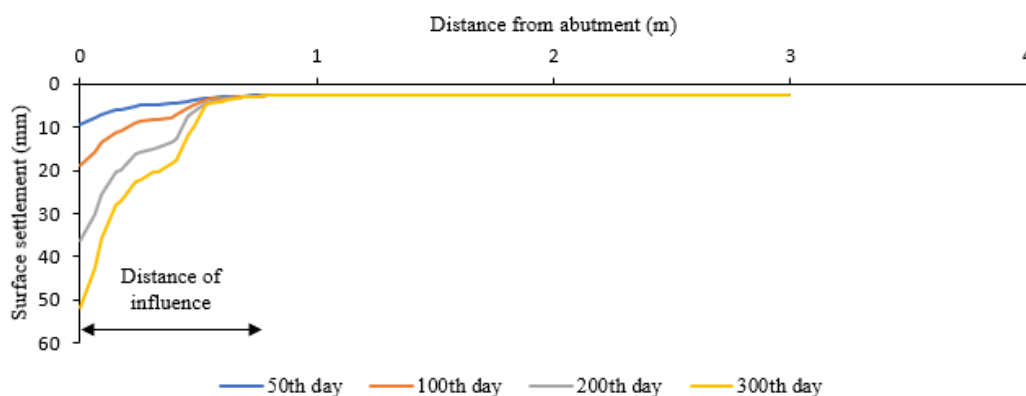


Figure B.41: Settlement of the soil surface behind the bridge abutment

B.5.4: Numerical Simulation Considering the New Numerical Model

B.5.4.1: New Geometry Description

Due to the high computational costs of the preliminary results using the alternative approach, some alterations in the preliminary numerical model geometry were adopted to try a better match between field and numerical data. Figures B.42 and B.43 show the new geometry proposed. The effect of the approach road on the soil was represented by a uniform vertical load at the soil surface from the left boundary to backfill-abutment interface. Due to the absence of information about the asphalt concrete pavement of the approach road, a value of 0.44 psi was adopted based

on preliminary simulations taken place to identify a suitable value that could yield realistic results.

The finite element mesh used was a very fine mesh, composed by 15-node triangular elements, with automatic refinement on the interfaces of soil-structure interaction. An extra refinement was applied on the backfill-abutment section inasmuch as it is the section of interest for the present investigation. Then, the mesh presented 4410 finite elements resulting in 36062 nodes. Vertical boundaries were fixed in x-direction and free in y-direction. The bottom boundary was fixed while the top boundary was free in both directions. Figure B.44 shows the finite element mesh used in the new numerical model.

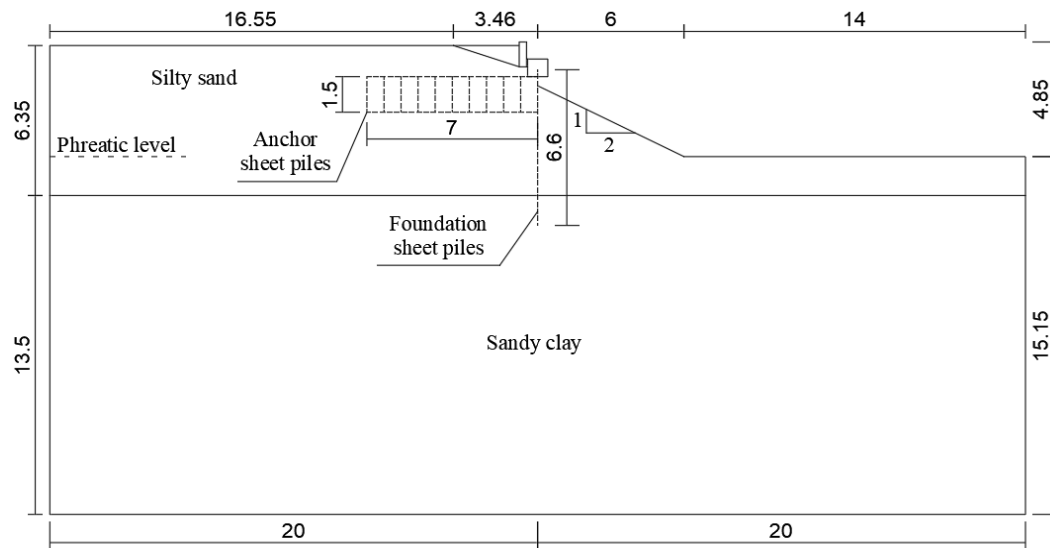


Figure B.42: Geometry used in new numerical model (dimensions in m)

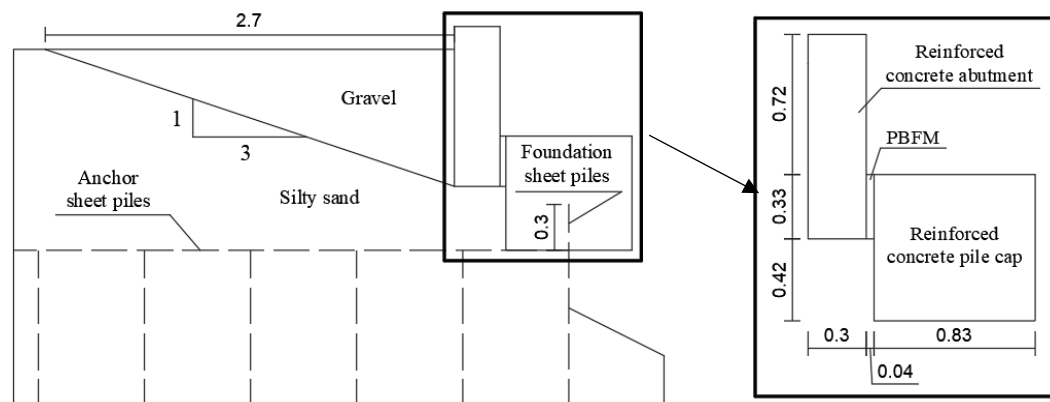


Figure B.43: Geometry details used in new numerical model (dimensions in m)

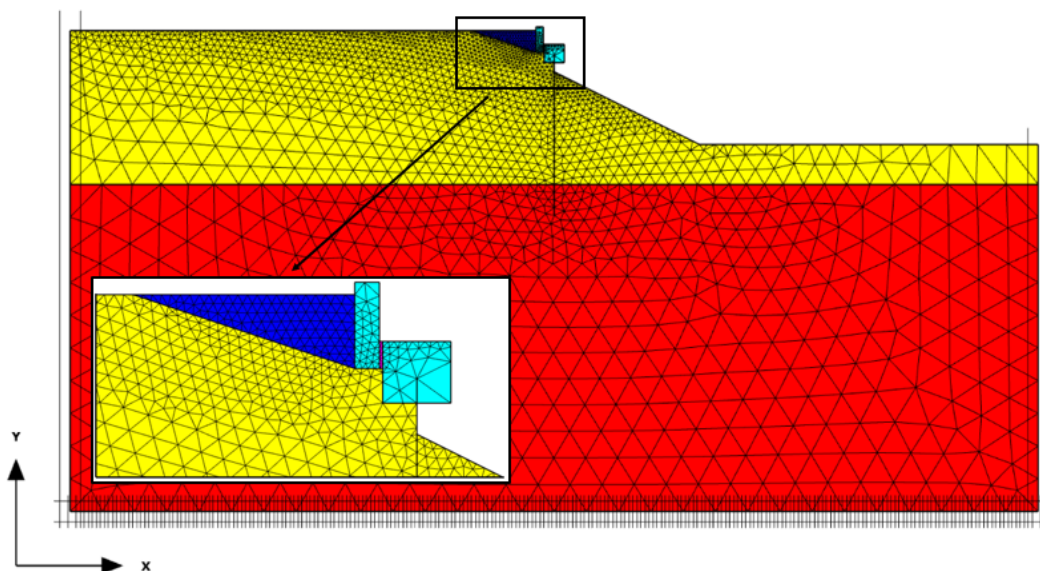


Figure B.44: Finite element mesh used in new numerical model

B.5.4.2: New Geometry Results

The new numerical model was also validated based on field data collected by Walter (2018). Data of a 100-day period since the beginning of field monitoring were considered to avoid high computational costs. The numerical simulations were performed by applying cycles of calculated horizontal prescribed displacements, as described to the preliminary numerical modeling. Figures B.45 and B.46 compare, respectively, the maximum and minimum daily values of lateral earth pressures measured by the pressure cells on the backfill-abutment interface with the corresponding numerical predictions. The numerical lateral earth pressure values represent the average of stresses in eleven stress points on the backfill-abutment interface, as to coincide with the same position of installation of the pressure cells.

Numerical and field daily lateral earth pressures are also compared in a 1:1 chart, as shown in Figure B.47. The linear adjustment of data presented in Figure B.47 yielded a coefficient of determination (r^2) of 0.82, which represents a coefficient of Pearson product-moment correlation (r) of 0.905. Also, the inclination of the fitted line is very close to the 1:1 line. The value of r^2 represents the percentage of variance in one variable that can be explained by the variance in the other variable (SALKIND, 2017). In this case, 82% of the variance in the numerical daily lateral earth pressure is accounted for by the variance in the field daily lateral earth pressure. This means that both variables share 82% of the variance between them.

Additional numerical simulations were carried out with strength reduction factors (R_{inter}) equal to 0.1, 0.3, 0.5, and 0.9. The r and r^2 values produced by these numerical simulations were compared with the r and r^2 values produced by the numerical simulation with $R_{\text{inter}} = 0.7$ (Table B.4) to analyze the influence of R_{inter} in the numerical model validation. The results showed that the best relationship between numerical predictions and field measurements was obtained with

$R_{\text{inter}} = 0.7$. Therefore, the numerical model validation can be considered satisfactory, given the many variables and inherent imprecision involved in the whole calibration process.

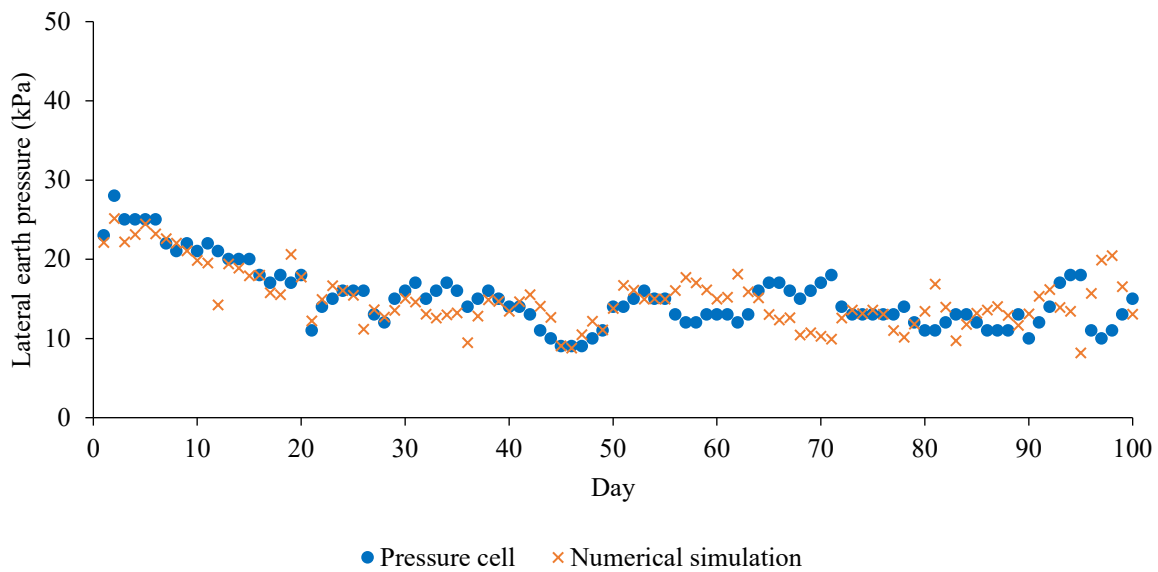


Figure B.45: Comparison between bridge expansion field data and numerical results

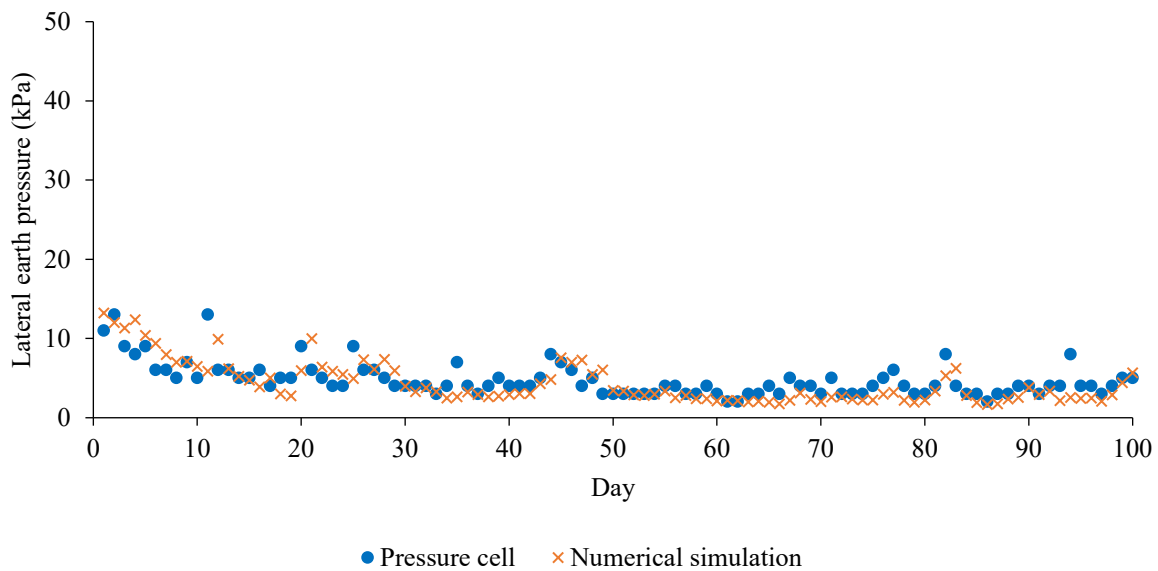


Figure B.46: Comparison between bridge contraction field data and numerical results

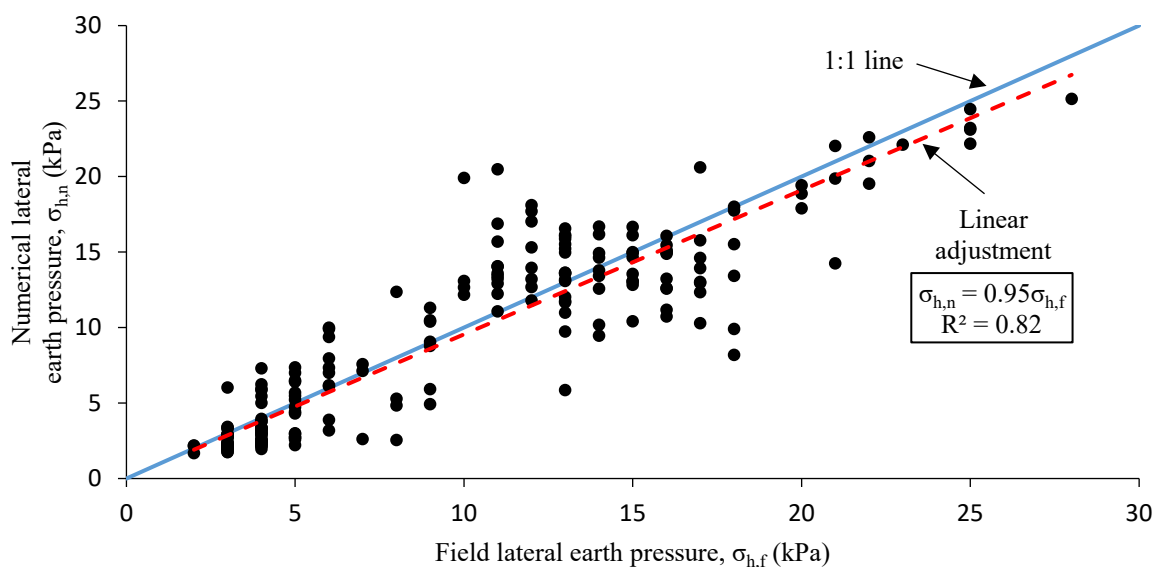


Figure B.47: Dispersion of lateral earth pressures

Table B.4: Relationship between numerical predictions and field measurements for different values of R_{inter}

R_{inter}	r	r^2	Variance	Relationship (SALKIND, 2017)
0.1	0.14	0.02	2%	Weak or no relationship
0.3	0.34	0.12	12%	Weak relationship
0.5	0.35	0.12	12%	Weak relationship
0.7	0.91	0.82	82%	Very strong relationship
0.9	0.20	0.04	4%	Weak or no relationship

According to Salkind (2017), the value of r assesses the relationship between two continuous variables, reflecting the amount of variability that is shared between them and what they have in common. In this context, a value of r equal to 0.905 corresponds to a very strong relationship between the numerical and field daily lateral earth pressures (Salkind, 2017). It is possible to observe that, in general, predictions with the numerical model produced a good match with field data. Therefore, the numerical model validation can be considered satisfactory, given the many variables and inherent imprecision involved in the whole process.

B.5.5: Analysis of the Daily Cyclic Response

Analysis of the response of the backfill-abutment system upon daily cyclic lateral displacements of the abutment was carried out after validation of the numerical model. Figures B.48 and B.49 show, respectively, the maximum and minimum lateral earth pressures as a function of the abutment height ratio (z/h), where z is the depth measured from the top of the abutment, and h is the abutment height, for selected daily cycles.

Analysis of the response of the backfill-abutment system upon daily cyclic lateral displacements of the abutment was carried out after validation of the numerical model. Figures B.48 and B.49 show, respectively, the maximum and minimum lateral earth pressures as a function of the abutment height ratio (z/h), where z is the depth measured from the top of the abutment, and h is the abutment height, for selected daily cycles.

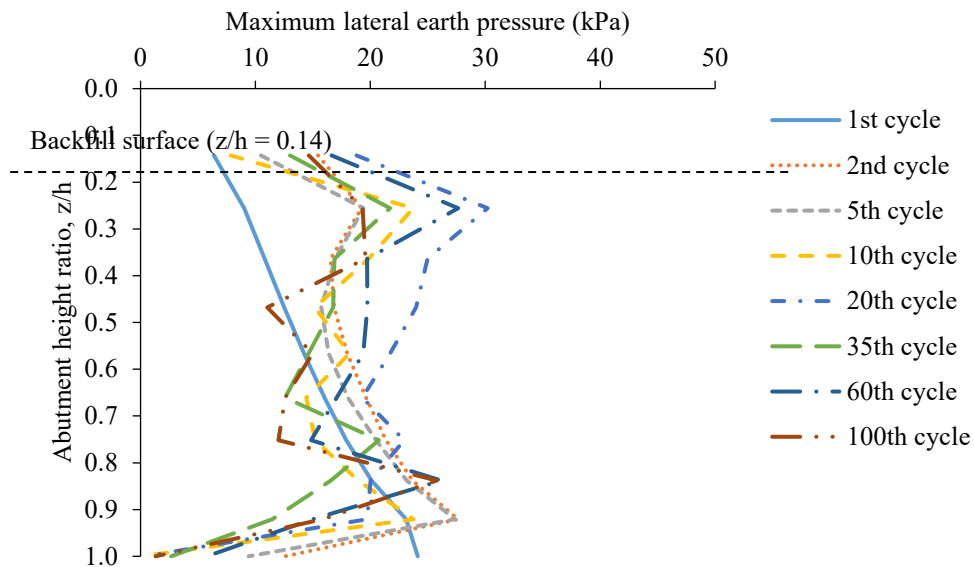


Figure B.48: Distributions of maximum lateral earth pressures along the abutment height for selected daily cycles

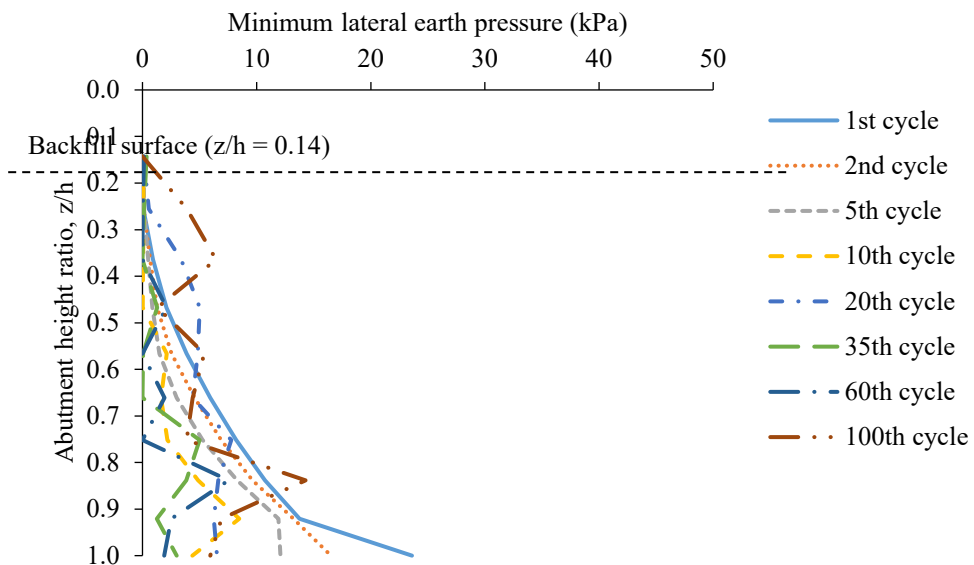


Figure B.49: Distributions of minimum lateral earth pressures along the abutment height for selected daily cycles

The lateral earth pressures presented a nonlinear distribution along the abutment height. In general, larger values of maximum lateral earth pressures occurred within the upper and bottom thirds of the abutment while larger values of minimum lateral earth pressures occurred within the bottom third of the abutment. Particularly, the minimum lateral earth pressures were nearly zero within the upper third of the abutment. No simplified shape for the distributions of maximum and minimum lateral earth pressures could expressly be identified. Similar profiles have been obtained elsewhere by physical measurements and numerical simulations (ABDEL-FATTAH; ABDEL-FATTAH, 2019; ABDEL-FATTAH; ABDEL-FATTAH; HEMADA, 2018; PAIK; SALGADO, 2003; XU; LIU, 2019).

Diagrams with a linear shape or with a regular geometric shape have been proposed by most conventional methods for predicting lateral earth pressures (CLOUGH; DUNCAN, 1991). For example, AASHTO (2012) suggests that lateral earth pressures should be assumed linearly proportional to soil depth considering lateral earth pressure coefficients calculated from Coulomb or Rankine's Theories. However, physical measurements and numerical simulations have revealed nonlinear lateral earth pressure distributions on abutments undergoing cyclic lateral displacements (ABDEL-FATTAH, M.; ABDEL-FATTAH, T., 2019; ABDEL-FATTAH, M.; ABDEL-FATTAH, T.; HEMADA, 2018; BANKS; BLOODWORTH, 2018; CARISTO; BARNES; MITOULIS, 2018; CIVJAN et al., 2013; HUNTLEY; VALSANGKAR, 2013; KIM et al., 2014; LEHANE, 2011; MITOULIS et al., 2016; XU; LIU, 2019). The nonlinear distributions observed for the lateral earth pressures can be related to the transfer of stresses between the backfill and the abutment due to soil-structure interface friction. This transfer of stresses is commonly known as arching in soils and results in nonlinear distributions of lateral earth pressures on the abutment (COSTA; ZORNBERG, 2020; HANDY, 1985; PAIK; SALGADO, 2003; TERZAGHI, 1943).

The obtained lateral earth pressure profiles can be related to the lateral displacement amplitude of the abutment. The imposed displacement amplitude was not enough to overcome the shear strength of the backfill and slip upward a soil portion toward the backfill surface during the passive direction. Therefore, since the largest lateral displacements were imposed at the top of the abutment, the maximum lateral earth pressures within the upper third of the abutment were more affected by the cyclic lateral displacements, which can justify the obtained profiles for maximum lateral earth pressures. On the other hand, the imposed displacement amplitude was enough to overcome the shear strength of the backfill and slip downward a soil portion toward the gap developed between the abutment and the backfill during the active direction. Therefore, the soil near the upper third of the abutment was displaced toward the bottom third of the abutment, which can explain the obtained profiles for minimum lateral earth pressures.

The previously mentioned behavior can be observed from shadings of relative shear stress (τ_{rel}), as shown in Figure B.50, arrows of resultant displacement (u_{res}), as presented in Figure B.51, and shadings of deviatoric strain (γ_s), as shown in Figure B.52. τ_{rel} gives an indication of the

proximity of the stress point to the failure envelope and is defined as the ratio between the maximum value of mobilized shear stress (τ_{mob}) and the maximum value of shear stress for the case where the Mohr's circle is expanded to touch the Coulomb's failure envelope with the center of Mohr's circle constant (τ_{max}). u_{res} indicates the direction of movement of the soil

elements. γ_s is defined as $\sqrt{\frac{2}{3} \left[\left(\varepsilon_x - \frac{\varepsilon_v}{3} \right)^2 + \left(\varepsilon_y - \frac{\varepsilon_v}{3} \right)^2 + \left(\varepsilon_z - \frac{\varepsilon_v}{3} \right)^2 + \frac{1}{2} (\gamma_{xy}^2 + \gamma_{yz}^2 + \gamma_{zx}^2) \right]}$, where ε_x is the axial strain in x-direction, ε_y is the axial strain in y-direction, ε_z is the axial strain in z-direction, ε_v is the volumetric strain, γ_{xy} is the shear strain in xy-plane, γ_{yz} is the shear strain in yz-plane, and γ_{zx} is the shear strain in zx-plane.

The shadings show that τ_{rel} was less than one ($\tau_{\text{mob}} < \tau_{\text{max}}$) in the whole backfill for the passive direction, which indicates the absence of soil failure. On the other hand, for active direction, τ_{rel} was equal to one ($\tau_{\text{mob}} = \tau_{\text{max}}$) in a zone of the backfill near the upper third of the abutment while τ_{rel} was less than one ($\tau_{\text{mob}} < \tau_{\text{max}}$) in the other zones of the backfill, which indicates a potential zone of soil failure near the upper third of the abutment. The arrows demonstrate that, during the passive direction, the soil was not displaced toward the backfill surface. During the active direction, the soil was displaced toward the bottom third of the abutment. The shadings also show that, with the cycles, a shear band was formed at a certain distance from the abutment, indicating a sliding surface.

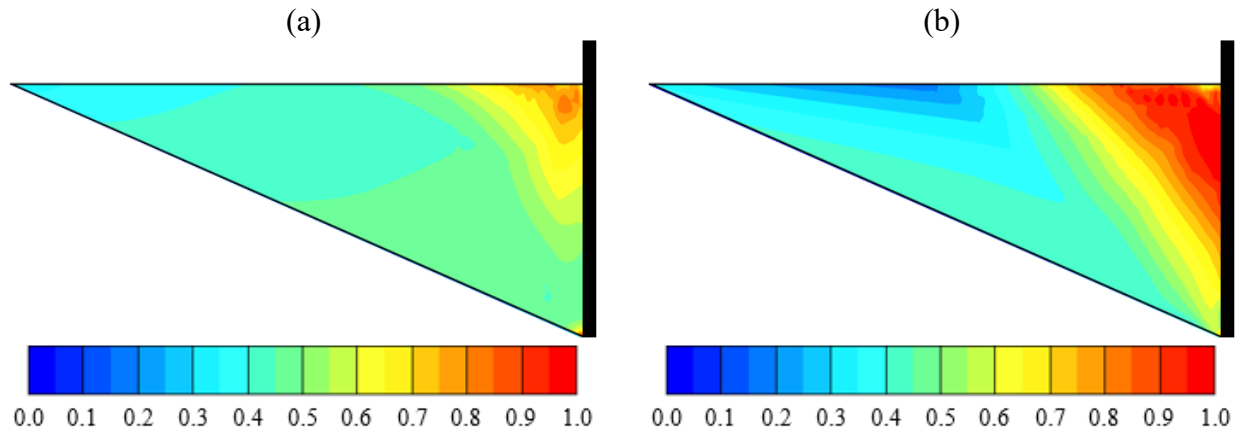
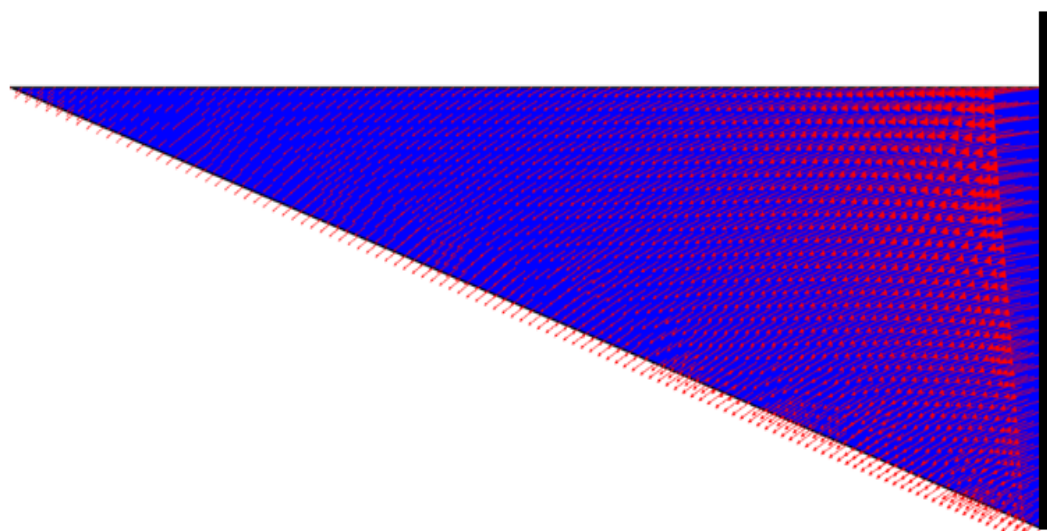


Figure B.50: Shadings of relative shear stress in the backfill for a typical daily cycle: (a) passive direction; and (b) active direction

(a)



(b)

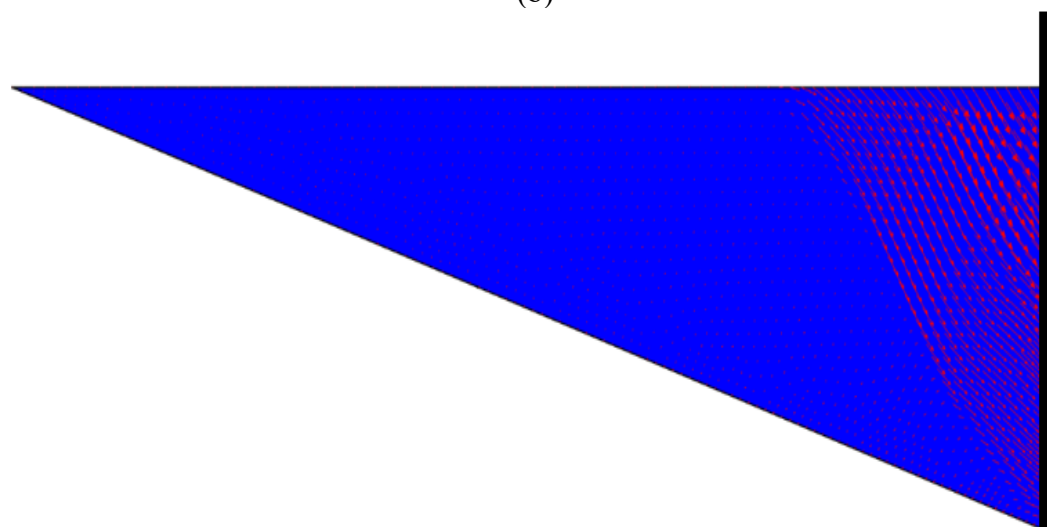
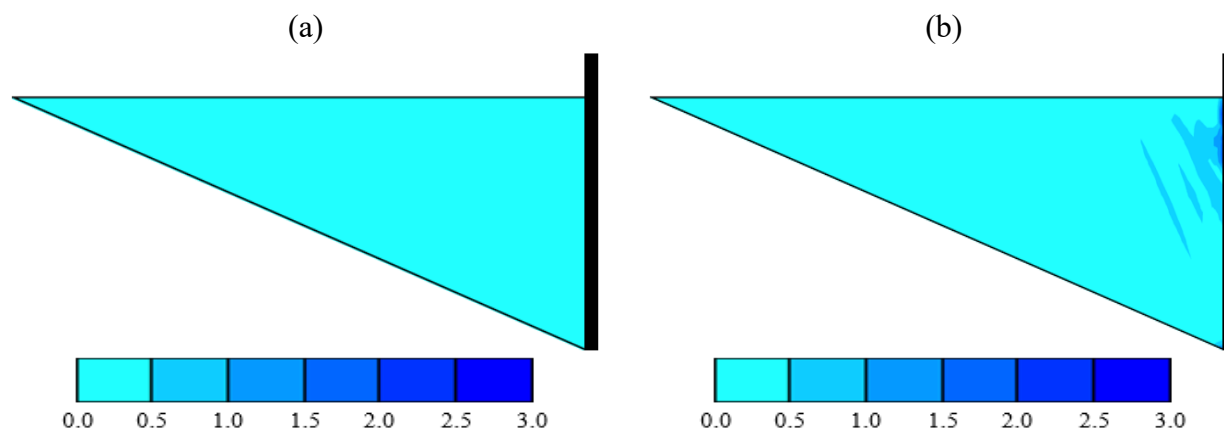


Figure B.51: Arrows of resultant displacement in the backfill for a typical daily cycle: (a) passive direction; and (b) active direction



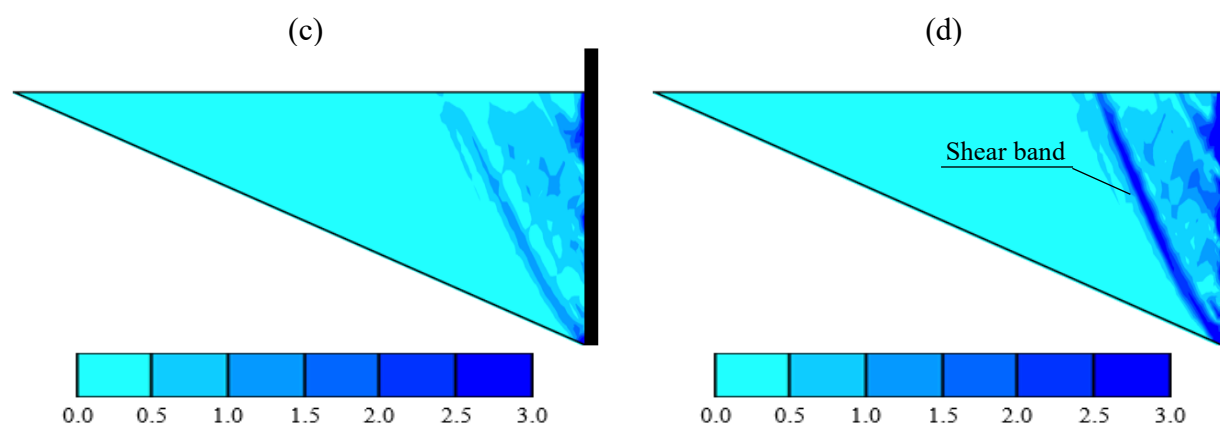


Figure B.52: Shadings of accumulated deviatoric strain (in %) in the backfill at the end of selected daily cycles: (a) 1st cycle; (b) 33rd cycle; (c) 66th cycle; and (d) 100th cycle

The lateral earth pressure coefficient (K) was calculated to assess the behavior of the lateral earth pressures with the daily cycles. K values were calculated by dividing the total lateral soil force acting on the abutment by the total lateral soil force of a triangular hydrostatic stress distribution acting over the height of the abutment (ENGLAND; TSANG; BUSH, 2000). Figure B.53 shows K values calculated for daily cycles.

The maximum lateral earth pressure coefficient (K_{\max}) remained below Rankine's passive lateral earth pressure coefficient ($K_{p,\text{Rankine}}$) throughout the entire analyzed cycles, while the minimum lateral earth pressure coefficient (K_{\min}) remained close to Rankine's active lateral earth pressure coefficient ($K_{a,\text{Rankine}}$) for almost the entire analyzed cycles. Trends for the K_{\max} and K_{\min} behavior could be identified as the cycles went by. K_{\max} firstly presented a slight downward trend within the first 46 cycles. Then, K_{\max} increased until the 62nd cycle and reduced until the 71st cycle. Lastly, K_{\max} showed a slight upward trend from the 72nd cycle. The tendencies identified for K_{\min} were firstly characterized by a decrease within the first 10 cycles. Finally, K_{\min} became virtually constant from the 11th cycle, with some minor scattering. Variation of K_{\max} and K_{\min} can be associated with the changes of δ_h due to temperature fluctuations since the daily temperature variations are not constant. Furthermore, K_{\min} was less affected by the cyclic lateral displacements of the abutment than K_{\max} .

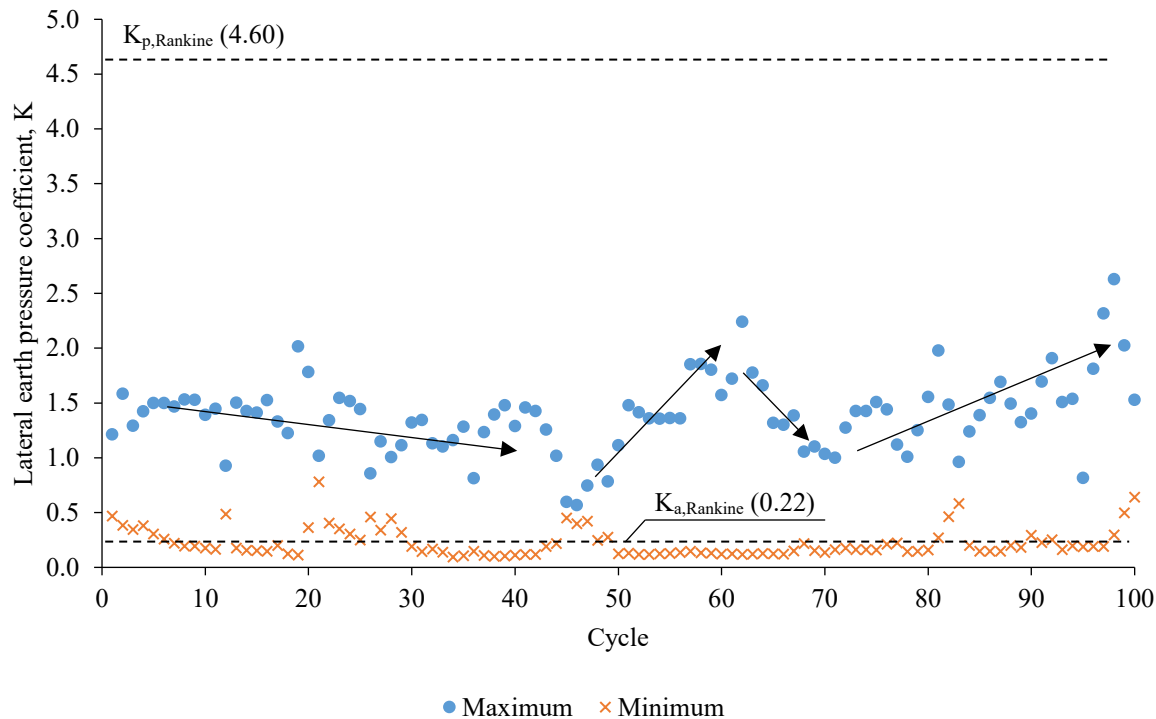


Figure B.53: Lateral earth pressure coefficients for daily cycles

Physical measurements and numerical simulations have shown that maximum lateral earth pressures are more affected by cyclic lateral displacements of the abutment than minimum lateral earth pressures (AL-QARAWI; LEO; LIYANAPATHIRANA, 2020; BANKS; BLOODWORTH, 2018; CLAYTON; XU; BLOODWORTH, 2006; ENGLAND; TSANG; BUSH, 2000; HUNTLEY; VALSANGKAR, 2013; KIM; LAMAN, 2012; LEHANE, 2011; TATSUOKA et al., 2009; XU; CLAYTON; BLOODWORTH, 2007; ZADEHMOHAMAD; BAZAZ, 2019). This probably happens due to the magnitude of lateral displacement required to reach the passive and active failure states. According to Clough and Duncan (1991) and Hambly and Burland (1979), the active failure state takes place for a magnitude of lateral displacement equal to approximately 10% of the magnitude required for mobilizing the passive failure state. This difference is mainly associated with the different confining pressures in the two failure states (ENGLAND; TSANG; BUSH, 2000), which allows that the active failure state takes place long before the passive failure state in granular backfills upon cyclic loading (TATSUOKA et al., 2009).

Vertical displacement profiles of the backfill surface along the distance from the abutment for selected daily cycles were also analyzed (Figure B.54). Displacements were obtained at the end of each cycle. In the figure, the downward vertical displacement (settlement) is taken as positive. The largest settlement occurred near the backfill-abutment interface and decreased with increasing distance from the abutment. According to the profiles, settlements were more influenced by the cyclic lateral displacements within a zone with dimension equal to abutment

height measured from the abutment. The settlement within this zone increased with the cycles, what indicates the presence of ratcheting. Moreover, no tendency of upward vertical displacement (heave) was observed on the backfill surface, what indicates the absence of the soil granular flow as defined by England, Tsang and Bush (2000).

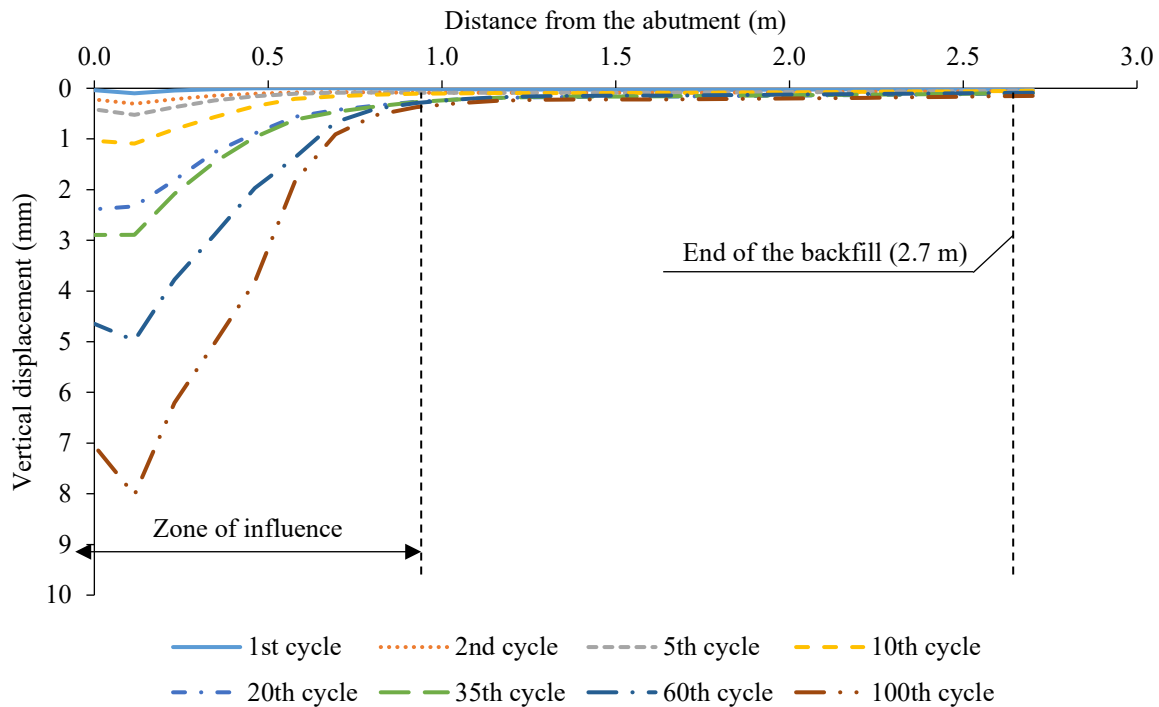


Figure B.54: Vertical displacement profiles of the backfill surface along the distance from the abutment for selected daily cycles

Figure B.55 shows the vertical displacements at the top of the backfill-abutment interface for daily cycles. The settlement increased with the cycles according to a nonlinear fashion with a slight decreasing rate. No tendency of stabilization (steady state) could expressly be identified with increasing cycles. Results of laboratory experiments and numerical simulations have shown a similar behavior for the vertical displacement of the backfill surface (AL-QARAWI; LEO; LIYANAPATHIRANA, 2020; ARGYROUDIS et al., 2016; CARISTO; BARNES; MITOULIS, 2018; DAVID; FORTH; YE, 2014; ENGLAND; TSANG; BUSH, 2000; MITOULIS et al., 2016; MUNOZ et al., 2012; TATSUOKA et al., 2009; ZADEHMOHAMAD; BAZAZ, 2019).

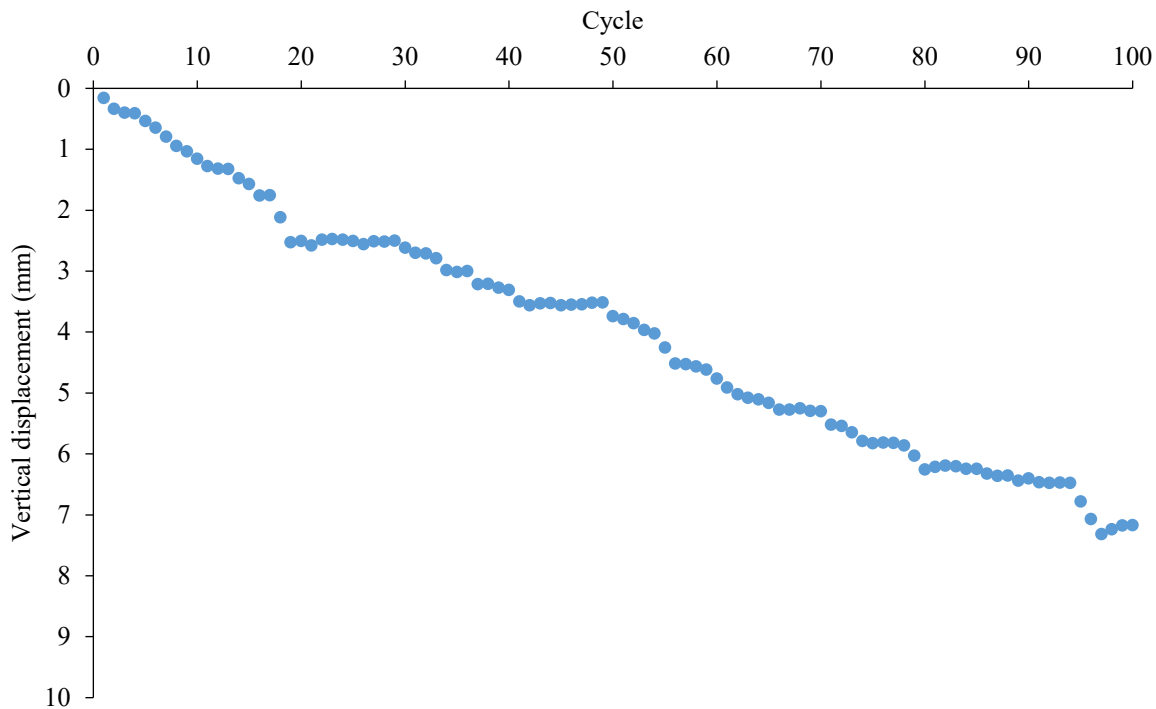


Figure B.55: Vertical displacements at the top of the backfill-abutment interface for daily cycles

As discussed earlier, the backfill surface is expected to present settlement and heave due to cyclic lateral loading. However, no heave was observed in the vertical displacement profiles of the backfill surface, as shown in Figure 6.55. The obtained profiles can be explained by the influence of the lateral displacement amplitude of the abutment. In this case, the displacement amplitude was sufficient to densify the soil near the backfill-abutment interface, but not enough to produce a soil granular flow that could raise the backfill surface. This characteristic can be noted in Figure B.56, which shows arrows of accumulated resultant displacement after the daily cyclic lateral loading. The arrows show that the whole backfill displaced downward, which indicates the absence of the soil granular flow defined by England, Tsang and Bush (2000).

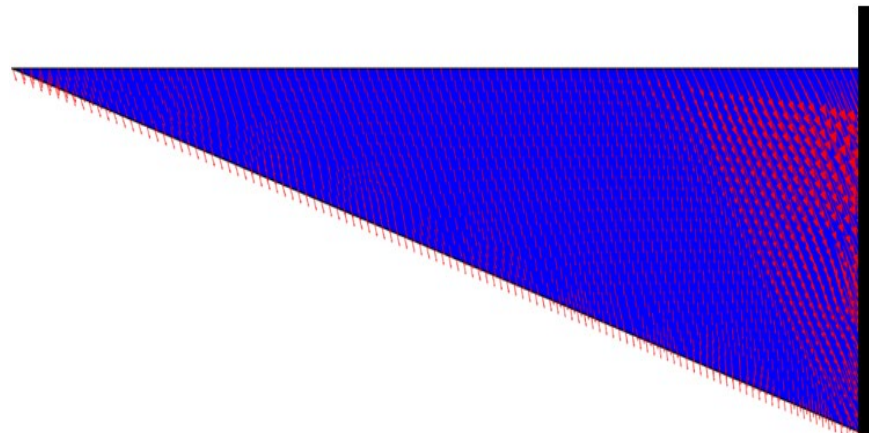


Figure B.56: Arrows of accumulated resultant displacement in the backfill after daily cyclic lateral loading

However, the displacement amplitude was not sufficient to cause the maximum densification of the backfill, what can explain the continuous settlement increase shown in Figure 6.56. On the other hand, the decreasing rate of the settlement with the cycles can be related to soil densification. Densification of the soil gradually increased the backfill stiffness with the cycles, reducing the settlement increment at each cycle. The densification of the backfill is shown in Figure B.57, which presents shadings of accumulated compressive volumetric strain in the backfill at the end of selected daily cycles. The shadings show that larger compressive volumetric strains occurred near the backfill-abutment interface and decreased with distance from the abutment, which can justify the profiles presented in Figure B.54. Moreover, the increase of the compressive volumetric strains with the cycles indicates the presence of ratcheting and can explain the continuous increase in the vertical displacement of the backfill surface (Figure B.55).

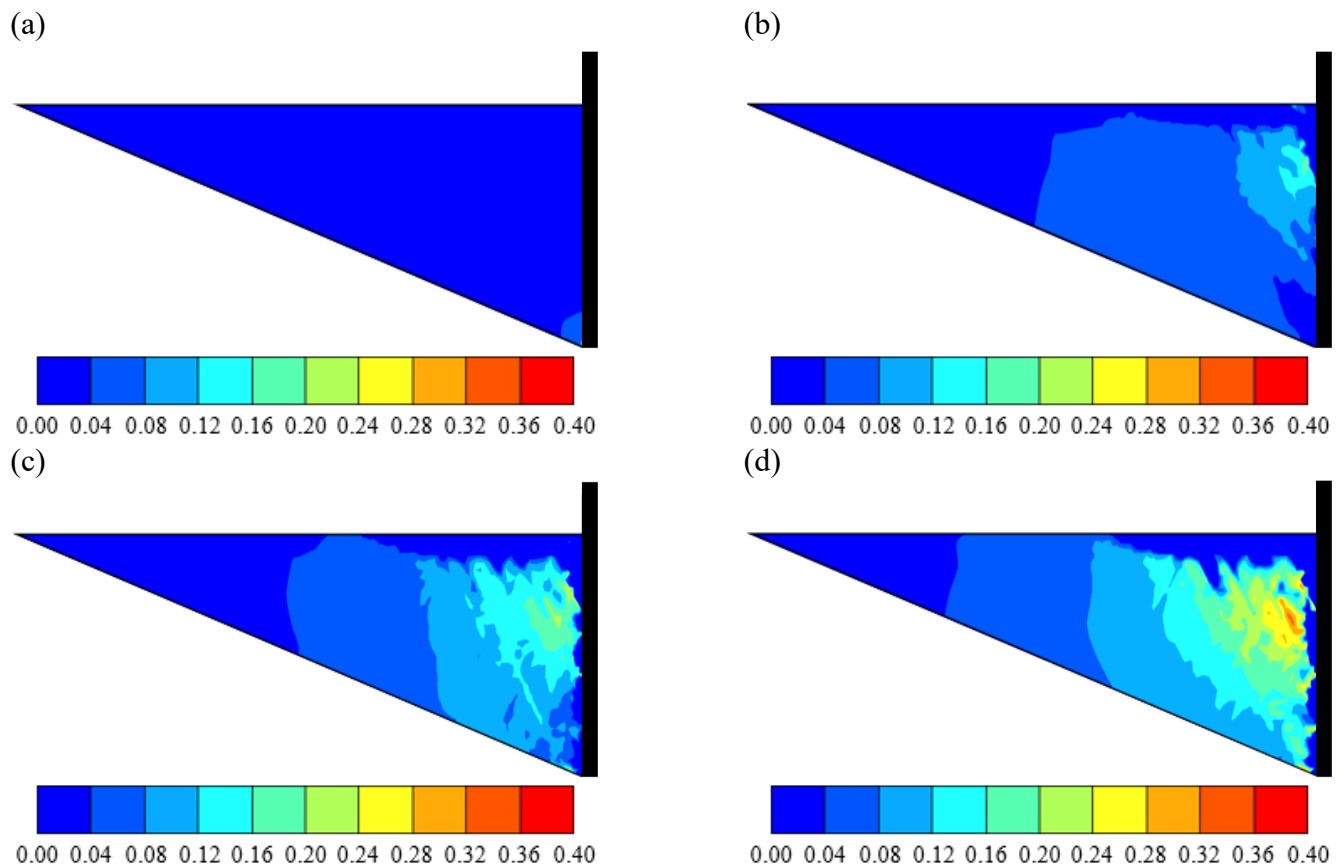


Figure B.57: Shadings of accumulated compressive volumetric strain (in %) in the backfill at the end of selected daily cycles: (a) 1st cycle; (b) 33rd cycle; (c) 66th cycle; and (d) 100th cycle

Figures C. 48 and C. 49 show the calculated lateral earth thrusts on the abutment at the end of the expansion (passive lateral earth thrust) and contraction (active lateral earth thrust) movements of the bridge superstructure, respectively. The passive lateral earth thrust remained below Rankine's passive (44.15 kN/m) throughout the entire considered period while the active lateral

earth thrust remained on Rankine's active (2.09 kN/m) for almost the entire considered period. Trends for the passive and active lateral earth thrusts can be identified as the days go by. Variations of the lateral earth thrust are associated with the changes of prescribed horizontal displacements due to temperature fluctuations.

B.5.5.1: New Geometry Sensitivity Analyses

A parametric analysis with parameters of interest was performed after predicting the response of the backfill-abutment system upon daily and annual cyclic lateral displacements. Numerical simulations were carried out by considering 50 cycles of lateral displacements of the abutment (except for the service life analysis of 100 annual cycles). This number of cycles was chosen based on the results of physical measurements and numerical simulations presented in the technical literature (AL-QARAWI; LEO; LIYANAPATHIRANA, 2020; BANKS; BLOODWORTH, 2018; CARISTO; BARNES; MITOULIS, 2018; ENGLAND; TSANG; BUSH, 2000; KIM; LAMAN, 2012; RAVJEE et al., 2018; TATSUOKA et al., 2009). Results presented in the previous section are confirmed by the findings reported in the technical literature. It has been found that stabilization (steady state) of the lateral earth pressures on the abutment, and the variation rate of the vertical displacement of the backfill surface is usually reached within 50 cycles. Limiting the number of cycles can save time and unnecessary computational efforts. The previous analyses revealed that maximum lateral earth pressures are more affected by cyclic lateral displacements of the abutment than minimum lateral earth pressures. For this reason, the parametric analysis presented in this section included results of maximum lateral earth pressures only.

B.5.5.1.1: Analysis of the Annual Cyclic Response

Analysis of the response of the backfill-abutment system upon annual cyclic lateral displacements of the abutment is presented in this subsection. AASHTO (2012) recommends designing permanent retaining walls for a minimum service life of 75 years for most applications and 100 years for a greater level of safety and/or longer service life for retaining walls supporting bridge abutments. This means that the bridge would be subjected to a minimum of 75 or 100 cycles of annual thermal variation, depending on the considered design condition. The present analysis included 100 annual cycles of lateral displacement of the abutment.

Since the bridge was completed in the summer season, it initially contracted until the winter season, when it reached its minimum longitudinal length. Then, the bridge expanded until the summer season of the next year, completing the annual cycle. Following this rationale, at new each annual cycle, the abutment was firstly displaced away from the backfill, and then it was displaced toward the backfill. This scenario was modeled by applying cycles of δ_h equal to 0.2 in to represent the cyclic lateral displacements of the abutment due to annual maximum expansions and contractions of the bridge. The value of 0.2 in was calculated considering an annual

temperature variation of 113°F, as recommended by AASHTO (2012) for the location where the bridge was built.

Figures B.58 and B.59 show the maximum and minimum lateral earth pressures as a function of the abutment height ratio for selected annual cycles, respectively. In general, the largest values of maximum lateral earth pressures occurred within the middle third of the abutment, while the largest values of minimum lateral earth pressures occurred within the bottom third of the abutment. Particularly, the lateral earth pressures for the active condition were nearly zero within the upper third of the abutment. The distributions of maximum lateral earth pressures can be approximated by a bi-linear shape with the largest pressures occurring within the middle third of the abutment. The distributions of minimum lateral earth pressures can be described by a triangular shape with the largest pressures occurring within the bottom third of the abutment. Similar profiles have been obtained by physical measurements and numerical simulations (ABDEL-FATTAH; ABDEL-FATTAH, 2019; ABDEL-FATTAH; ABDEL-FATTAH; HEMADA, 2018; BANKS; BLOODWORTH, 2018; CARISTO; BARNES; MITOULIS, 2018; CIVJAN et al., 2013; KIM et al., 2014; LEHANE, 2011; MITOULIS et al., 2016; PAIK; SALGADO, 2003).

The lateral earth pressures presented a nonlinear distribution along the abutment height due to arching in soils, as shown in the previous section. The obtained lateral earth pressure profiles can be related to the lateral displacement amplitude imposed at the abutment, which was sufficient to overcome the shear strength of the backfill in both passive and active directions. During the passive direction, the abutment forced a soil portion to slip upward toward the backfill surface, inducing a concentration of lateral earth pressures at the middle third of the abutment, which can explain the obtained maximum lateral earth pressure profiles. During the active direction, a soil portion was slipped downward toward the gap developed between the abutment and the backfill. This slip displaced the soil toward the bottom third of the abutment, which can justify the obtained minimum lateral earth pressure profiles. The previously mentioned behavior can be observed from shadings of relative shear stress (τ_{rel}), as shown in Figure B.60, arrows of resultant displacement (u_{res}), as shown in Figure B.61, and shadings of deviatoric strain (γ_s), as shown in Figure B.62.

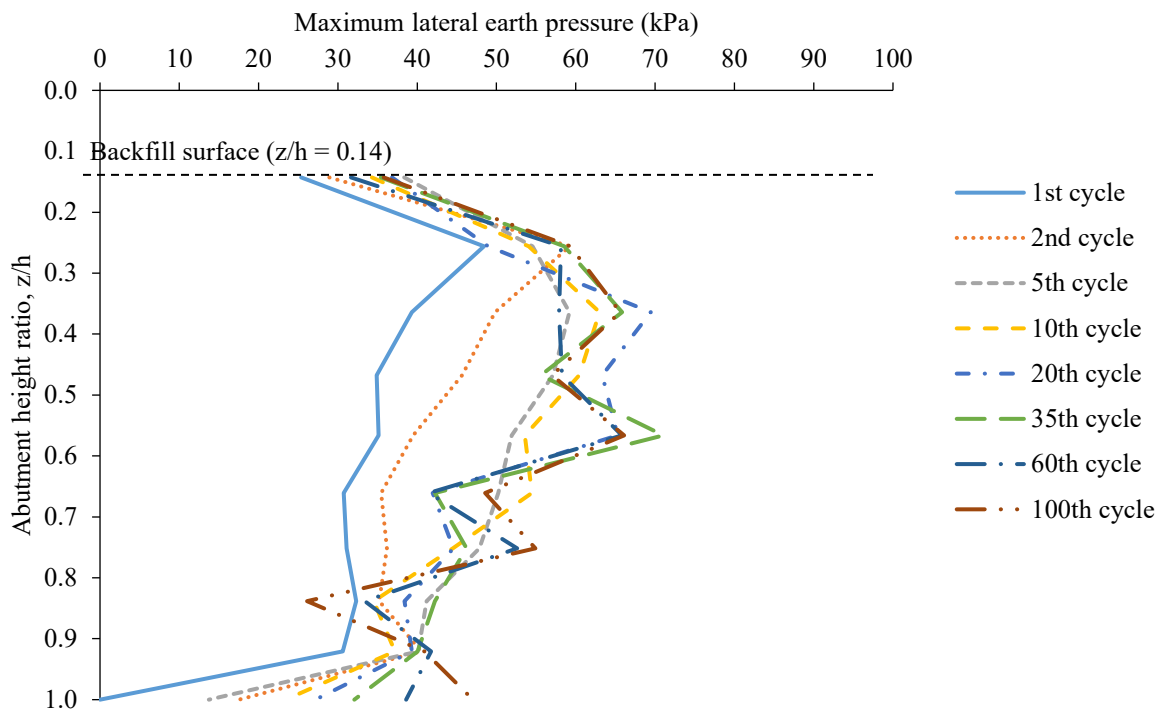


Figure B.58: Distributions of maximum lateral earth pressures along the abutment height for selected annual cycles

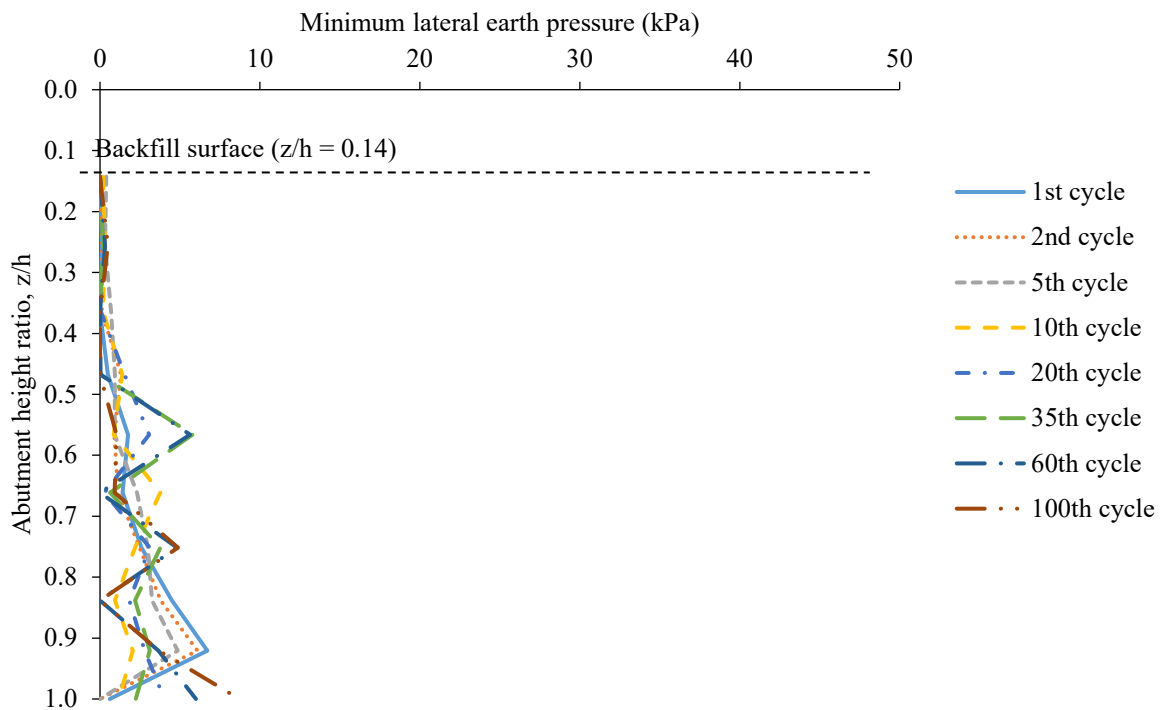


Figure B.59: Distributions of minimum lateral earth pressures along the abutment height for selected annual cycles

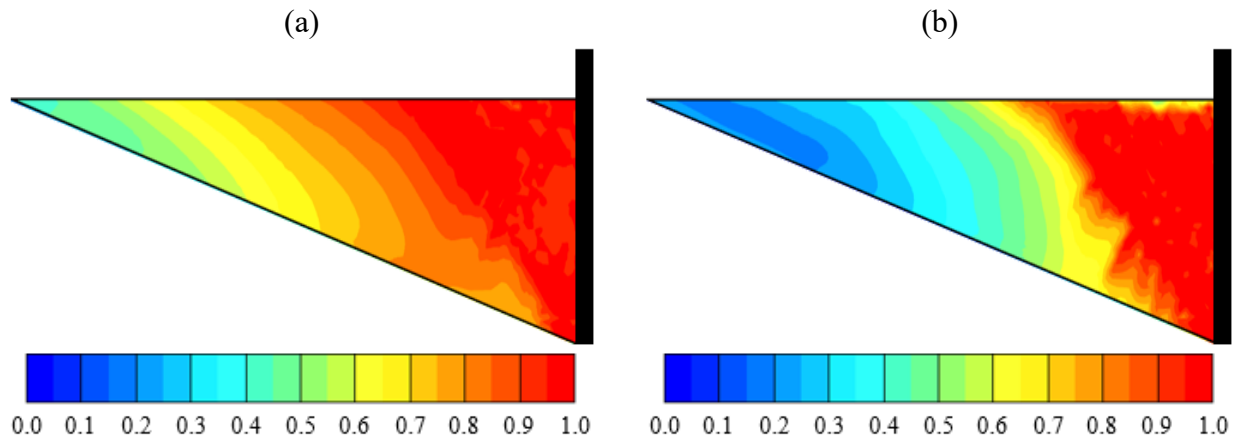


Figure B.60: Distributions of minimum lateral earth pressures along the abutment height for selected annual cycles

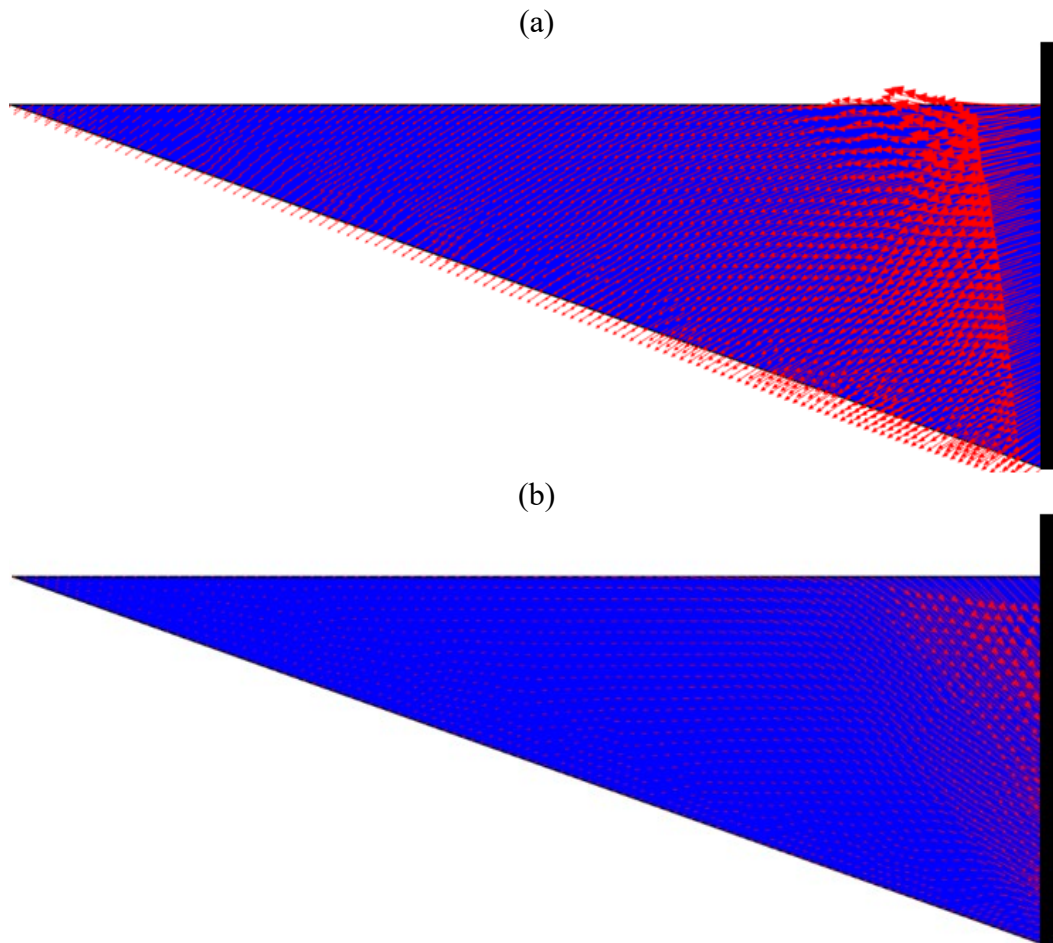


Figure B.61: Arrows of resultant displacement in the backfill for a typical annual cycle: (a) passive direction; and (b) active direction

(a)

(b)

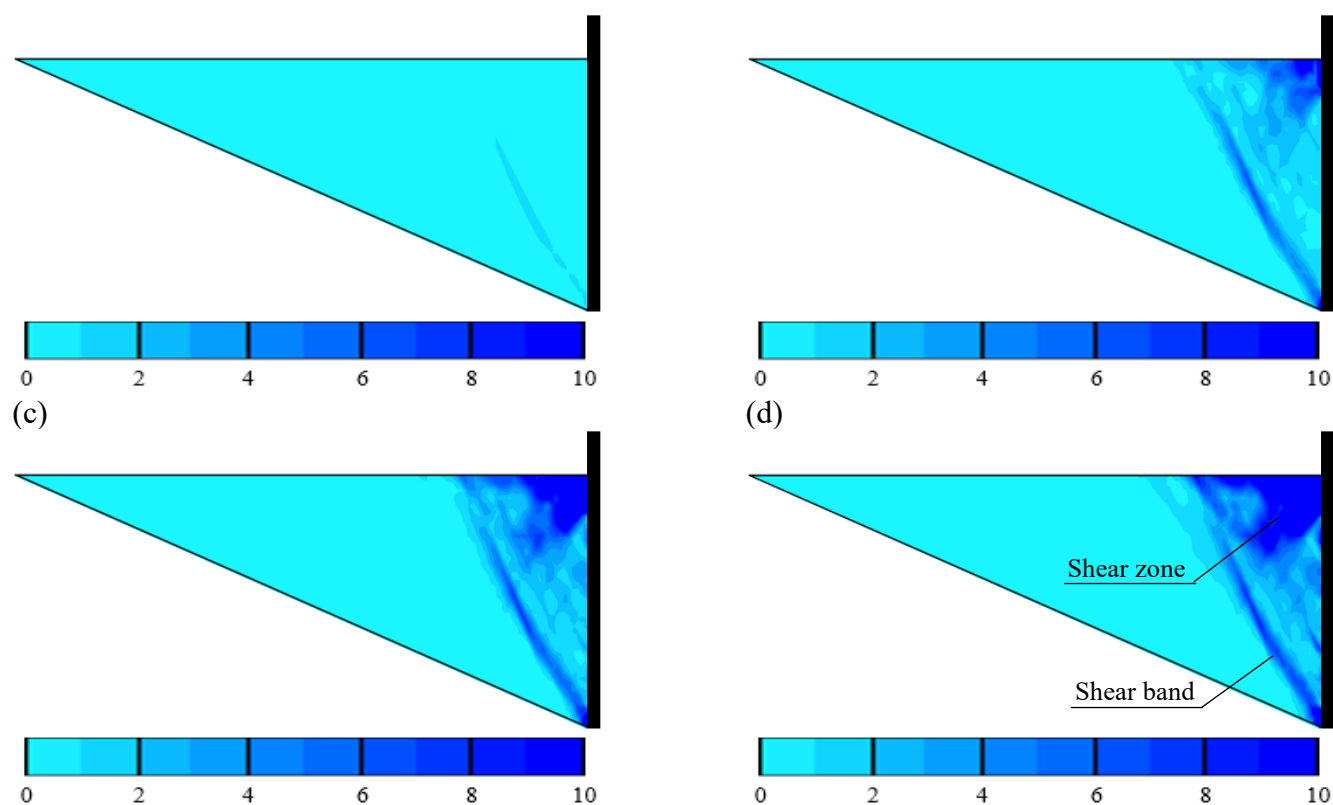


Figure B.62: Shadings of accumulated deviatoric strain (in %) in the backfill at the end of selected annual cycles: (a) 1st cycle; (b) 33rd cycle; (c) 66th cycle; and (d) 100th cycle

The shadings show potential zones of soil failure ($\tau_{rel} = 1$) near the abutment in both passive and active directions. The arrows demonstrate that, during the passive direction, the soil near the upper third of the abutment was displaced toward the backfill surface. During the active direction, the soil was displaced toward the bottom third of the abutment. The shadings also show that, with the cycles, a shear band was formed at a certain distance from the abutment, and a shear zone was formed near the upper third of the abutment, indicating sliding surfaces.

Figure B.63 presents the evolution of the lateral earth pressure coefficient (K) with the annual cycles. The maximum lateral earth pressure coefficient (K_{max}) presented a nonlinear increase with a decreasing rate within the first cycles and then reached the steady state slightly below $K_{p,Rankine}$ in the fifth cycle. The K_{max} value at the steady state can be assumed as 4.1. On the other hand, the minimum lateral earth pressure coefficient (K_{min}) remained at the steady state close to $K_{a,Rankine}$ throughout the entire analyzed cycles. Moreover, K_{min} was less affected by the annual cycles of lateral displacements of the abutment than K_{max} , probably due to the difference in magnitude of soil lateral displacement required to reach the passive and active failure states. Results of field monitoring, laboratory experiments, and numerical simulations have shown a similar behavior (AL-QARAWI; LEO; LIYANAPATHIRANA, 2020; BANKS; BLOODWORTH, 2018; CARISTO; BARNES; MITOULIS, 2018; FROSCHE; LOVELL, 2011;

GABRIELI; ZORZI; WAN, 2015; KIM; LAMAN, 2012; LEHANE, 2011; RAVJEE et al., 2018; TATSUOKA et al., 2009; ZADEHMOHAMAD; BAZAZ, 2019).

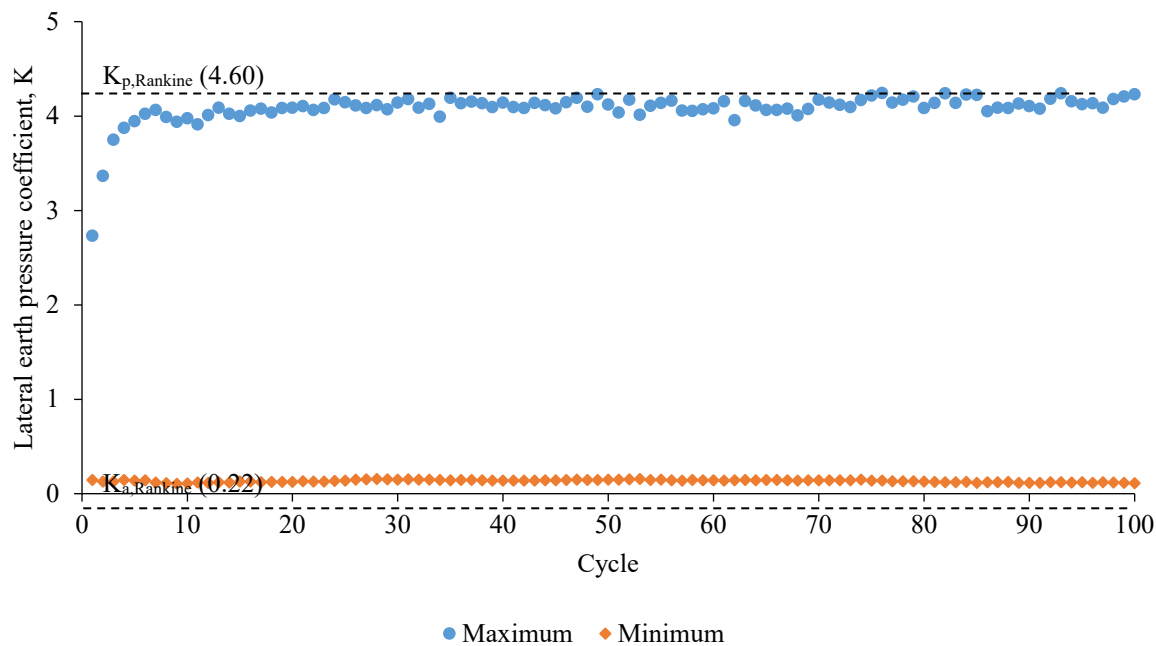


Figure B.63: Lateral earth pressure coefficients for annual cycles

The behavior observed for the variation of K_{max} with the cyclic lateral displacements of the abutment (Figure B.63) depends on the effects of soil densification and granular flow promoted by cycling. As previously mentioned, densification and granular flow have opposite effects on the backfill. While densification increases the stiffness of the soil, granular flow contributes to reducing it. The influence of the effect of soil densification appeared to be preponderant on the initial cycles, which led to increased maximum lateral pressure coefficients. However, a balance between both effects appeared to have been reached in the following cycles, resulting in constant maximum lateral earth pressure coefficients. At this moment, the soil reached the shakedown state. Figure B.64 shows the lateral earth pressure coefficient as a function of the lateral displacement of the abutment for selected annual cycles. It is possible to observe that the cyclic lateral displacements resulted in closed hysteresis loops after some cycles, which indicates that the elastic shakedown has been reached with increasing cycles.

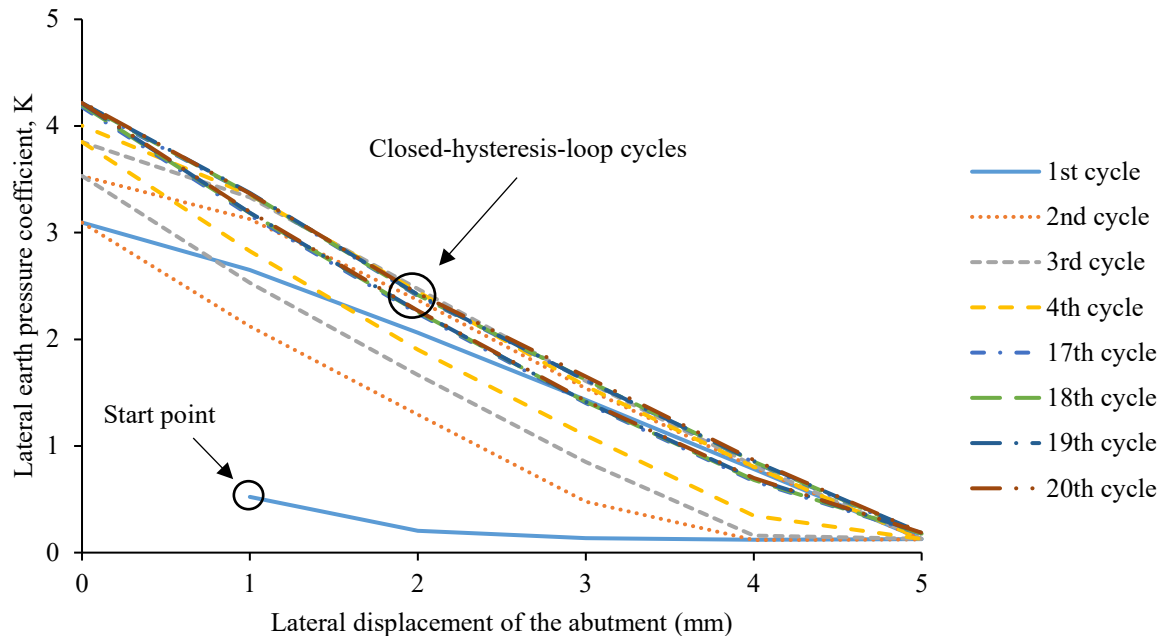


Figure B.64: Lateral earth pressure coefficients during cyclic process for selected annual cycles

Profiles of vertical displacement of the backfill surface for selected annual cycles were also presented in Figure B.65. Displacements were obtained at the end of each cycle. Positive values were assigned for the settlements in the figure. The largest settlement occurred near the backfill-abutment interface and decreased with the distance from the abutment. As the cycles increased, a heave zone was formed at a certain distance from the abutment, which suggests the presence of the soil granular flow defined by England, Tsang and Bush (2000). The peak heave was approximately 25% of the peak settlement. The influence zone of the displacements can be assumed to cover a distance equal to abutment height measured from the abutment. Within this zone, settlements and heave increased with the cycles, which indicates the presence of ratcheting.

Figure B.66 shows the evolution of the vertical displacements at the top of the backfill-abutment interface. It is noted a sharp increase in the settlement in the first five cycles, followed by a nearly linear increase in the next cycles. A tendency of reaching a steady state was not observed. The results agree with the experimental and numerical findings reported in the technical literature (AL-QARAWI; LEO; LIYANAPATHIRANA, 2020; ARGYROUDIS et al., 2016; CARISTO; BARNES; MITOULIS, 2018; DAVID; FORTH; YE, 2014; ENGLAND; TSANG; BUSH, 2000; MITOULIS et al., 2016; MUNOZ et al., 2012; TATSUOKA et al., 2009; ZADEHMOHAMAD; BAZAZ, 2019).

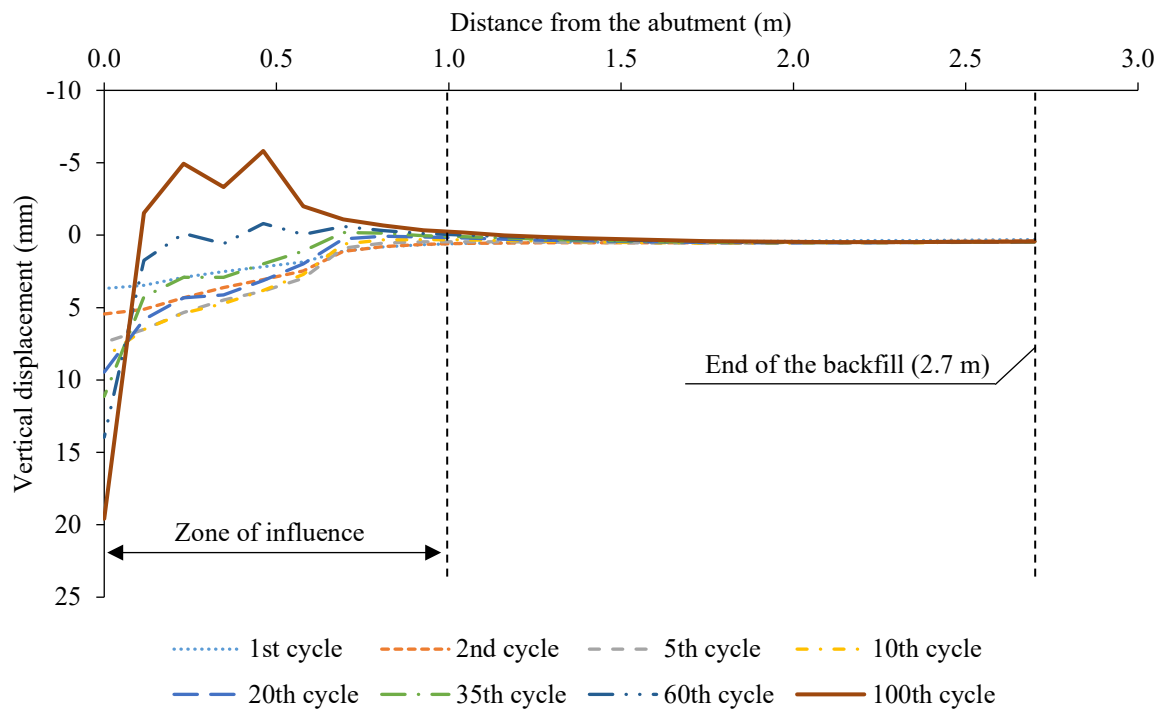


Figure B.65: Vertical displacement profiles of the backfill surface along the distance from the abutment for selected annual cycles

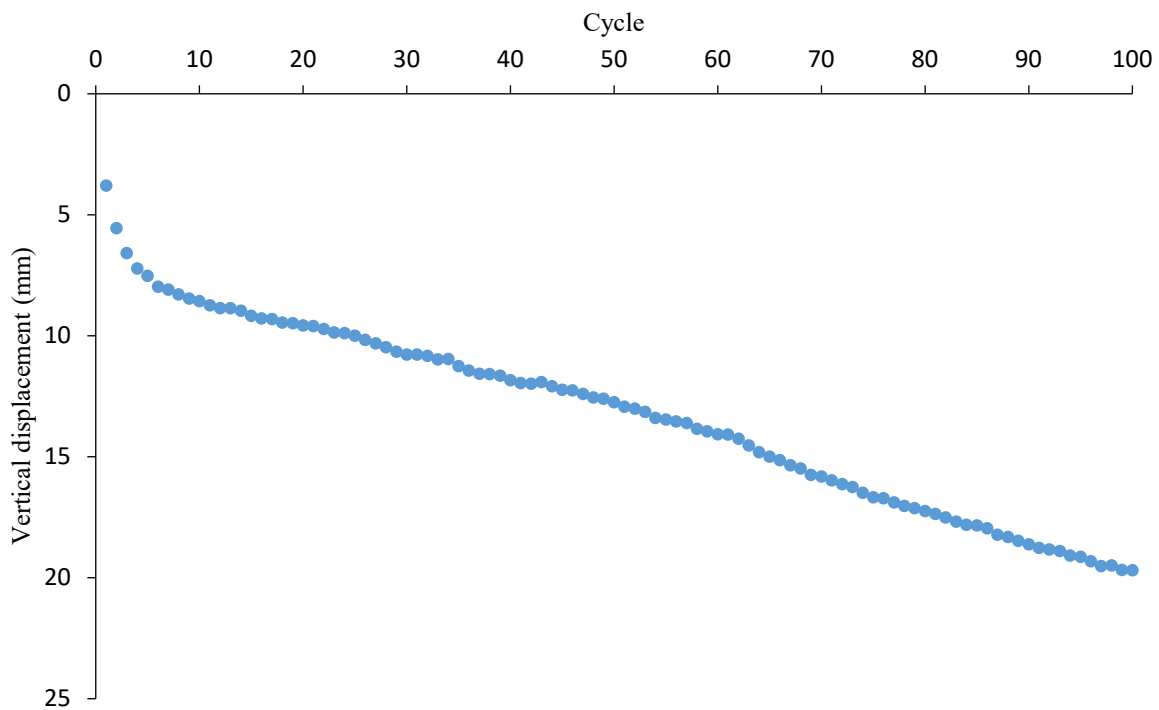


Figure B.66: Vertical displacements at the top of the backfill-abutment interface for annual cycles

Vertical displacements on the backfill surface are associated with the effects of soil densification and granular flow. While densification reduces the settlement increment, granular flow plays an opposite effect. The influence of the effect of densification appeared to be more significant for the first five cycles, while a balance between both effects appeared to have been reached in the subsequent cycles. The densification of the backfill is shown in Figure B.67, which presents shadings of accumulated compressive volumetric strain in the backfill at the end of selected annual cycles, while the vectors of accumulated resultant displacement shown in Figure B.68 suggest the occurrence of the granular flow defined by England, Tsang and Bush (2000). The shadings show that larger compressive volumetric strains occurred near the backfill-abutment interface and decreased with distance from the abutment, which agrees with the profiles of Figure B.62. Moreover, the increase in the compressive volumetric strains with the cycles shows the occurrence of ratcheting in the soil and explains the continuous increase in the vertical displacement of the backfill surface (Figure B.63). The arrows show that a soil portion is displaced toward the backfill surface, which indicates the occurrence of the soil granular flow defined by England, Tsang and Bush (2000).

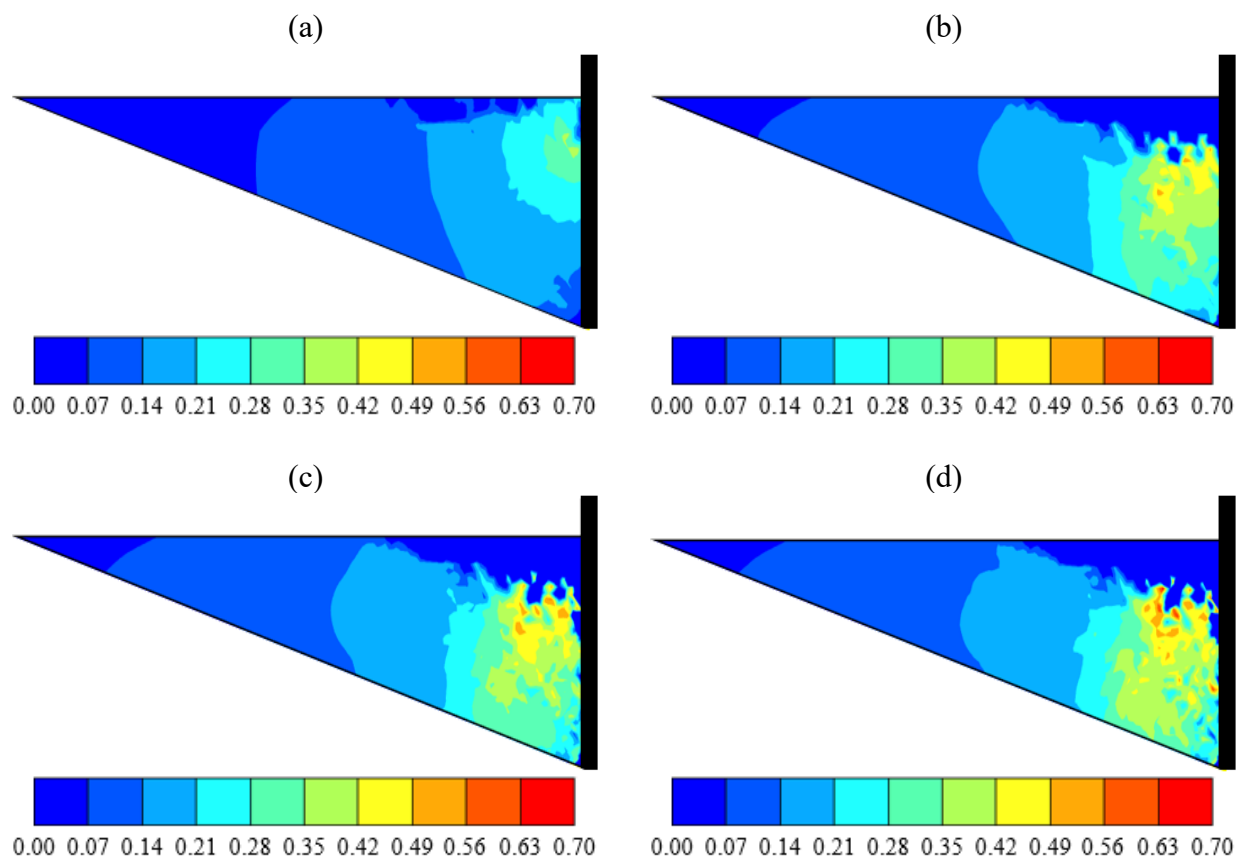


Figure B.67: Shadings of accumulated compressive volumetric strain (in %) in the backfill at the end of selected annual cycles: (a) 1st cycle; (b) 33rd cycle; (c) 66th cycle; and (d) 100th cycle

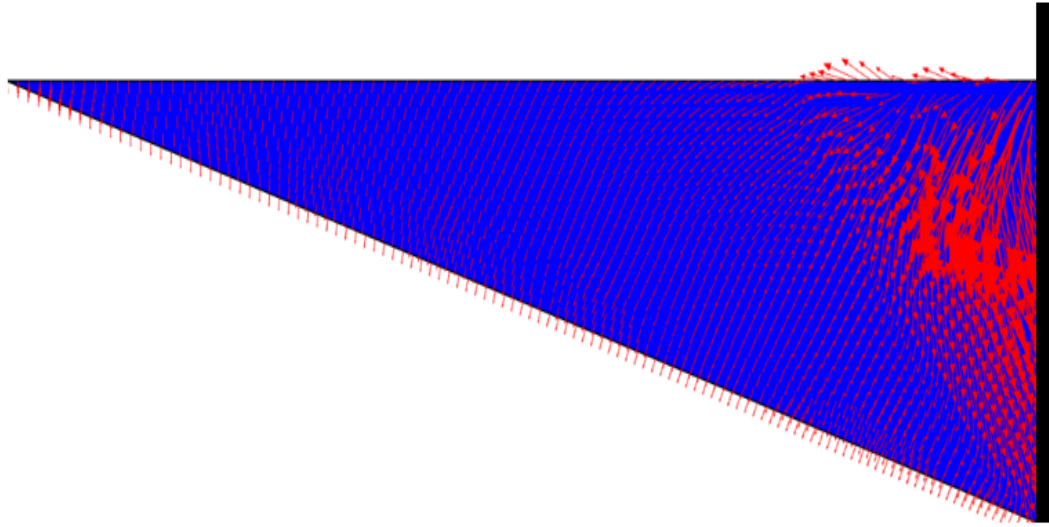


Figure B.68: Arrows of accumulated resultant displacement in the backfill after annual cyclic lateral loading

B.5.5.1.2: Bridge Completion Season

The first parameter of investigation was the influence of the completion season of bridge construction. Simulations were performed for an amplitude of prescribed horizontal displacements (δ_h) equal to 0.2 in, which represents the cyclic lateral displacements of the abutment due to annual maximum longitudinal expansions and contractions of the bridge. Four scenarios represented the lateral displacements of the abutment for bridge construction completed in spring, summer, autumn, and winter. When the bridge is completed in spring, the abutment initially displaces $\delta_h/2$ toward the backfill from spring to summer. Then, the abutment displaces δ_h away from the backfill from summer to winter. Finally, the abutment displaces $\delta_h/2$ toward the backfill from winter to spring, completing the annual cycle. When the bridge is finished in summer, the abutment firstly displaces δ_h away from the backfill from summer to winter. Then, the abutment displaces δ_h toward the backfill from winter to summer, completing the annual cycle. When the bridge is completed in autumn and winter, the abutment displaces in the opposite way as for the bridge finished in spring and summer, respectively. Figure B.69 schematically illustrates the lateral displacements of the abutment during an annual cycle for all analyzed scenarios.

(a)

(b)

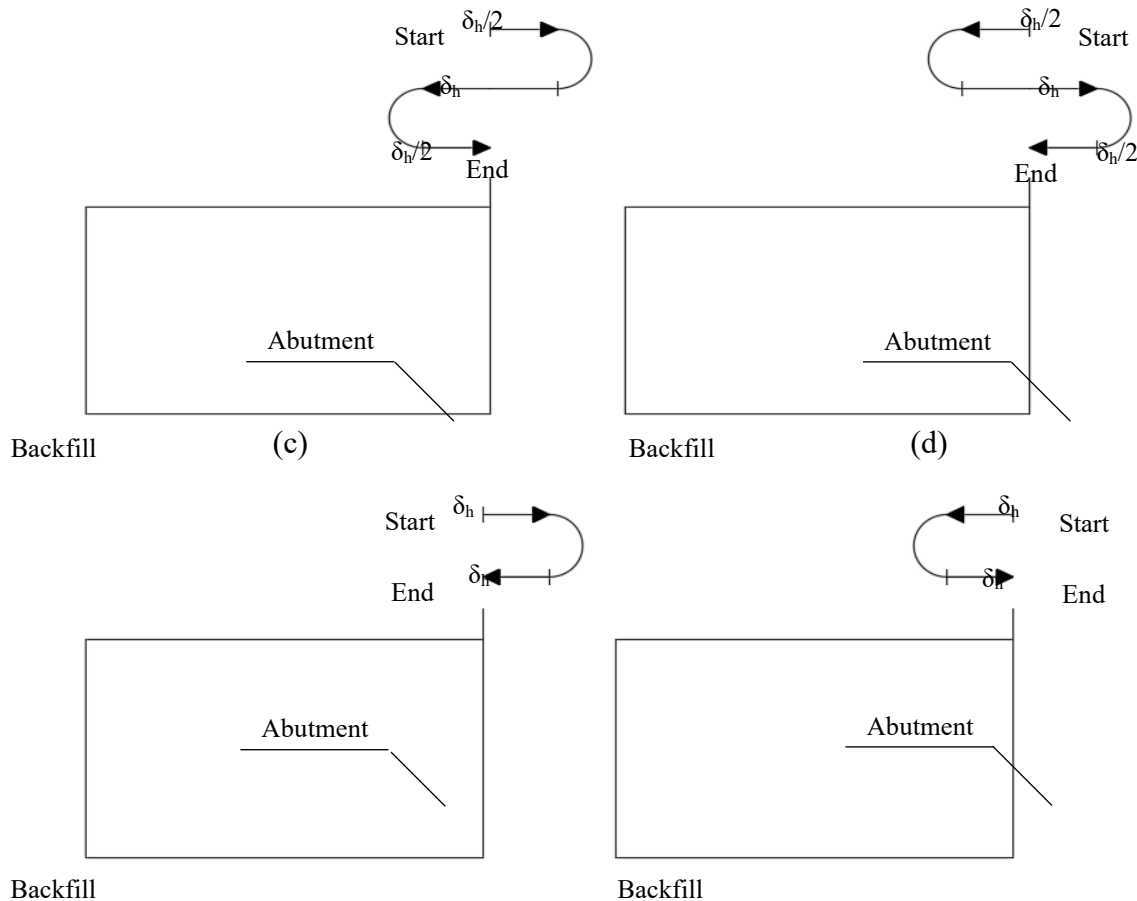


Figure B.69: Schemes of annual cycles of lateral displacements of the abutment for all analyzed scenarios: (a) autumn; (b) spring; (c) summer; and (d) winter

Figure B.70 shows the maximum lateral earth pressures along the abutment for the four scenarios after 50 annual cycles of lateral displacements. In the four scenarios, the maximum lateral earth pressures presented a nonlinear distribution along the abutment height with the largest values of maximum lateral earth pressures occurring within the middle third of the abutment. The distributions of maximum lateral earth pressures can be approximated by a bi-linear shape with the largest pressures occurring within the middle third of the abutment. Figure B.71 presents the evolution of K_{\max} with the annual cycles for the four seasons. For all analyzed scenarios, K_{\max} presented a nonlinear increase with a decreasing rate in the initial cycles and then reached the steady state slightly below $K_{p, \text{Rankine}}$ from the fifth cycle.

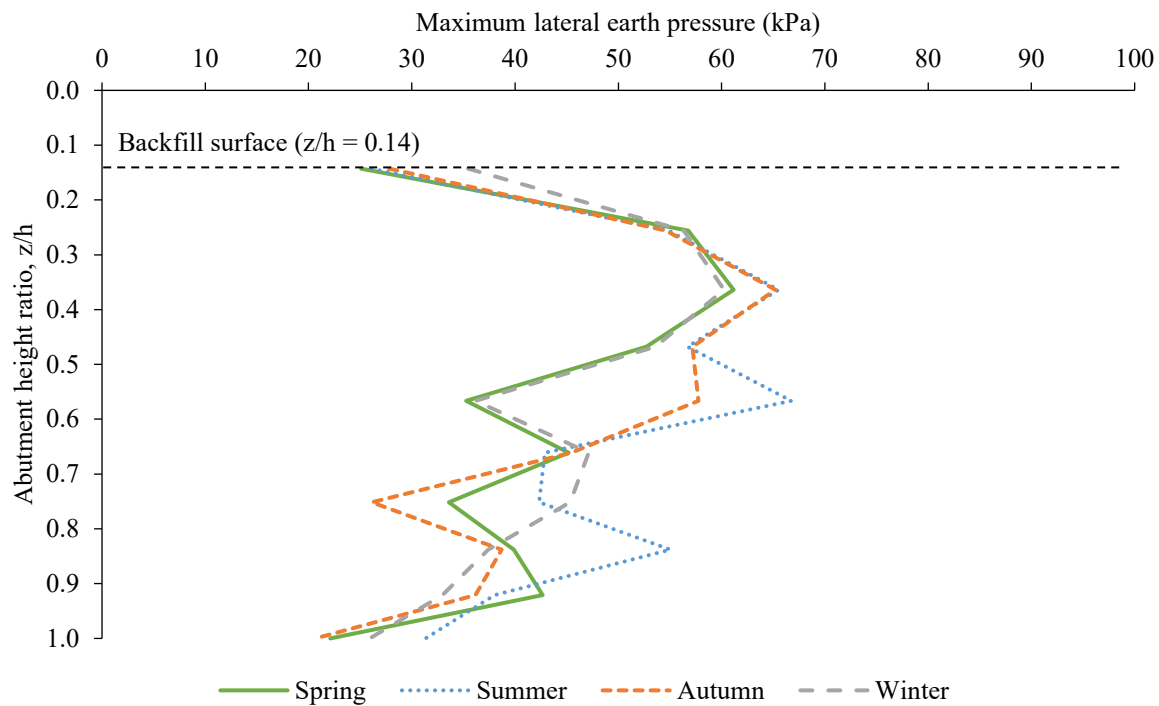


Figure B.70: Distributions of maximum lateral earth pressures along the abutment height for analyzed scenarios after 50 annual cycles

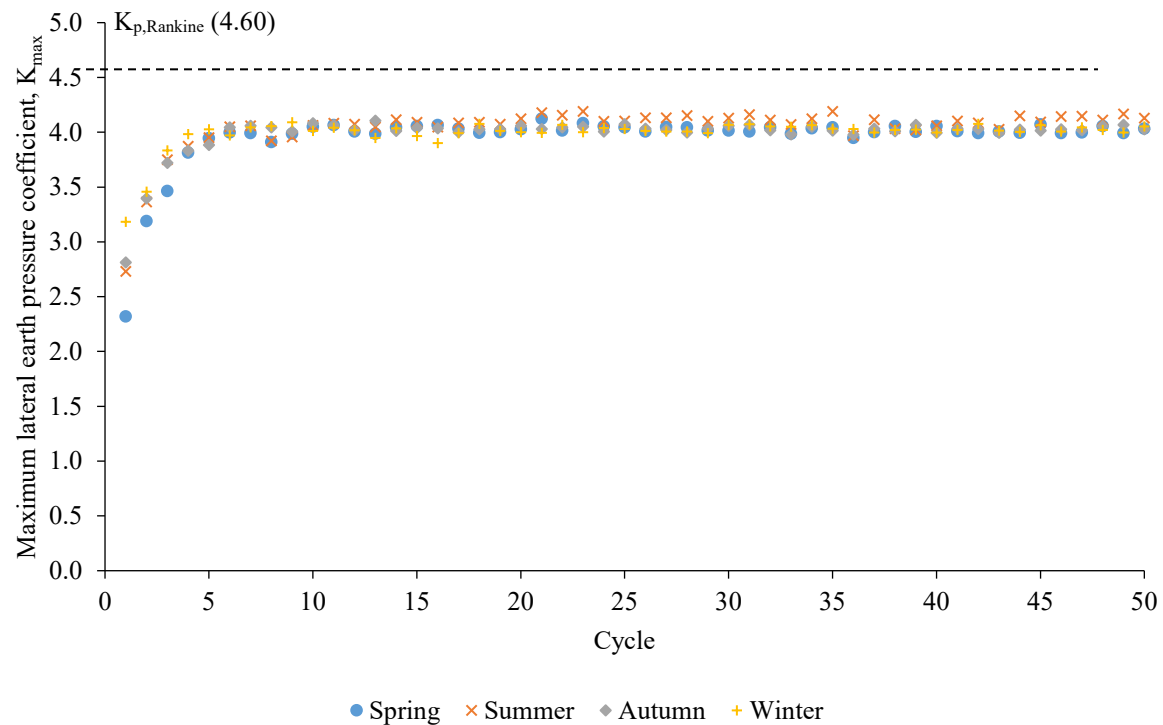


Figure B.71: Maximum lateral earth pressure coefficients for annual cycles considering analyzed scenarios

The maximum lateral earth pressure profiles (Figure B.70) and the K_{\max} values (Figure B.71) were not significantly affected by the completion season of bridge construction. Although the analyzed scenarios simulated different initial movements of the abutment, the fact that the amplitude of the displacements was the same in all scenarios can explain the observed characteristic. Similar results were observed in numerical simulations carried out by Caristo, Barnes and Mitoulis (2018), and England, Tsang and Bush (2000).

Vertical displacement profiles of the backfill surface along the distance from the abutment after 50 annual cycles were also assessed (Figure B.72). Displacements correspond to the end of each cycle. Downward vertical displacements (settlement) were considered positive in the figure. For all seasons, the largest settlement took place near the backfill-abutment interface. Settlements decreased with increasing distance from the abutment. A heave zone was formed at a certain distance from the abutment for a bridge completed in spring, autumn, and winter while no heave was observed for a bridge finished in summer. Vertical displacements took place within an influence zone equal to the abutment height measured from the abutment.

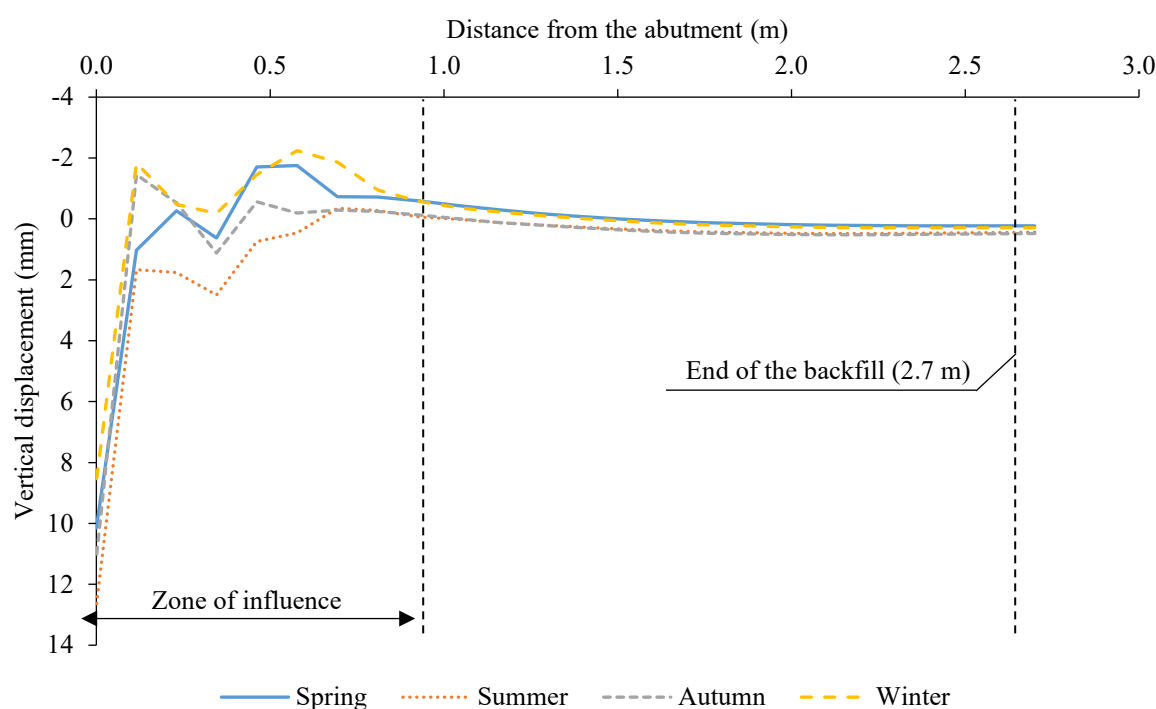


Figure B.72: Vertical displacement profiles of the backfill surface along the distance from the abutment for analyzed scenarios after 50 annual cycles

Figure B.73 shows the vertical displacements at the top of the backfill-abutment interface for varying annual cycles. For all analyzed season scenarios, settlements increased nonlinearly with a decreasing rate in the first cycles and then increased linearly. No tendency of reaching a steady state could be observed with increasing cycles. The largest settlements occurred for a bridge finished in summer, while the smallest settlements took place for a bridge finished in winter.

Intermediate settlements were obtained for spring and autumn seasons, with slightly higher values for the former.

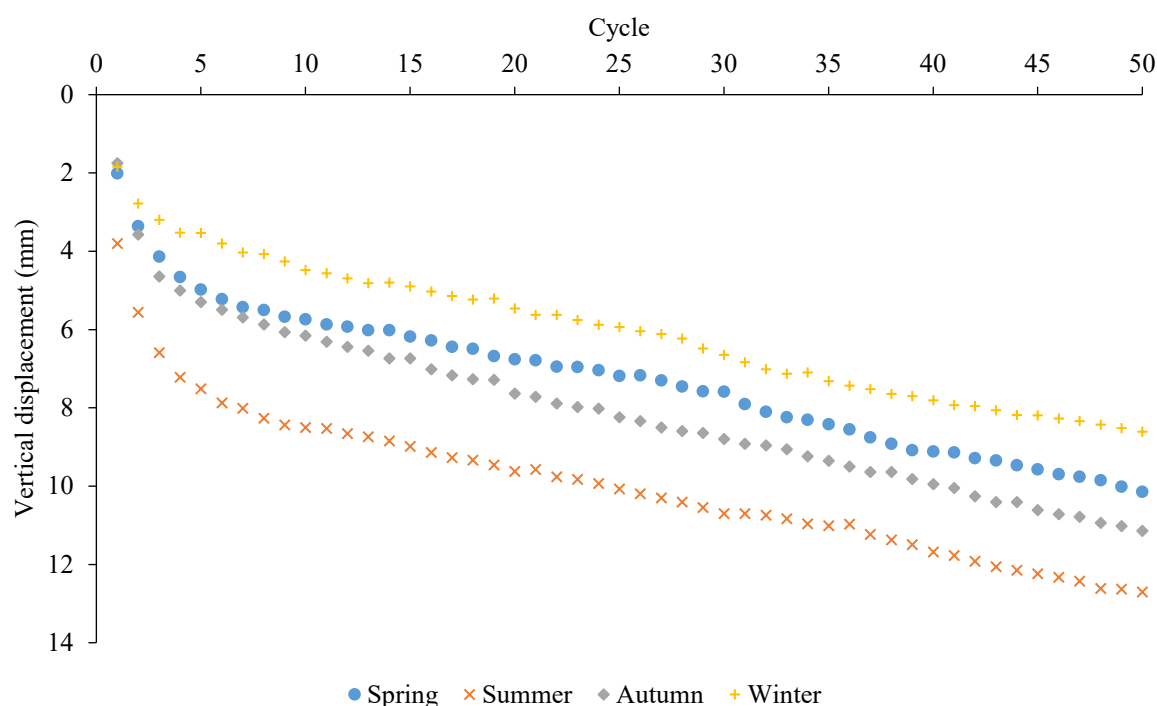


Figure B.73: Vertical displacements on the top of the backfill-abutment interface for annual cycles considering analyzed scenarios

As observed in Figures B.72 and B.73, the vertical displacements on the backfill surface were influenced by the completion season of the bridge construction. The differences in the displacements between seasons can be associated with the initial movement of the abutment (Figure B.69). When a bridge is completed in summer, the abutment firstly displaces away from the backfill, and, consequently, the soil initially tends to flow downward toward the gap developed between the abutment and the backfill, resulting in larger settlements. On the other hand, a bridge finished in winter will have the abutment firstly displacing to the backfill. Therefore, the soil initially tends to flow upward toward the backfill surface, resulting in smaller settlements. Settlements with intermediate amplitudes in spring and autumn are explained by the fact that the initial lateral abutment displacement in both seasons is half that at the beginning of summer and winter. The absence of heave for the bridge construction completed in summer may be explained by an insufficient number of cycles. In this case, more than 50 cycles are needed to develop a heave on the backfill surface, as observed in the previous subsection after 60 annual cycles.

Numerical simulations carried out by England, Tsang and Bush (2000) showed that the completion season of the bridge construction influenced the vertical displacements on the backfill surface. The authors reported that the largest settlements occurred for a bridge completed

in winter. On the other hand, numerical simulations performed by Caristo, Barnes and Mitoulis (2018) demonstrated that the vertical displacements on the backfill surface were not influenced by the completion season of the bridge construction. The differences between the results obtained by England, Tsang and Bush (2000), Caristo, Barnes and Mitoulis (2018), and the present investigation can be attributed to differences in the proposed models. England, Tsang and Bush (2000) modeled a part of an integral abutment considering only rotation movements of the abutment. Caristo, Barnes and Mitoulis (2018) completely simulated an integral abutment considering combined movements of rotation and translation of the abutment. The present investigation fully modeled a semi-integral abutment considering combined movements of rotation and translation of the abutment. Furthermore, the effects of the superstructure on the abutment and the approach slab/road on the backfill were not considered by those authors, unlike this investigation.

Finally, although the completion season of the bridge construction has not influenced the maximum lateral earth pressures on the abutment, the results showed that completing the construction of the bridge in summer represents the most unfavorable situation because of excessive settlements. For this reason, the following investigations were simulated for the summer scenario since it represented the most unfavorable situation. Another argument for simulating the summer scenario is that it represents the start condition of movement of the bridge abutment in the field.

B.5.5.1.3: Sheet Pile Stiffness

The influence of the foundation stiffness on the backfill-abutment system performance was investigated by varying the sheet pile profile. Three profiles were selected for this analysis: PZC-12, PZC-18, and PZC-28 (GERDAU, 2019). Table 6.5 shows the structural parameters of the selected profiles.

Table B.5 – Structural parameters of sheet pile profiles

Parameter	Unit	PZC-12	PZC-18	PZC-28
Normal stiffness (EA)	kN/m	2.61×10^6	3.16×10^6	4.44×10^6
Flexural rigidity (EI)	kNm ² /m	4.01×10^4	7.33×10^4	1.30×10^5
Weight (w)	kN/m/m	0.98	1.18	1.66

Source: Elaborated by the author (2020)

Figure B.74 shows the maximum lateral earth pressures along the abutment height for the three profiles after 50 annual cycles of lateral displacements. For all profiles, the maximum lateral earth pressures presented a nonlinear distribution along the abutment height. The largest values of maximum lateral earth pressures occurred within the middle third of the abutment. The distributions of maximum lateral earth pressures can be approximated by a bi-linear shape with the largest pressures occurring within the middle third of the abutment. Figure B.75 shows the

maximum lateral earth pressure coefficient (K_{\max}) values calculated for annual cycles. Similar trends were obtained for all investigated profiles. K_{\max} presented a nonlinear increase with a decreasing rate in the first cycles and then reached the steady state slightly below $K_{p, \text{Rankine}}$.

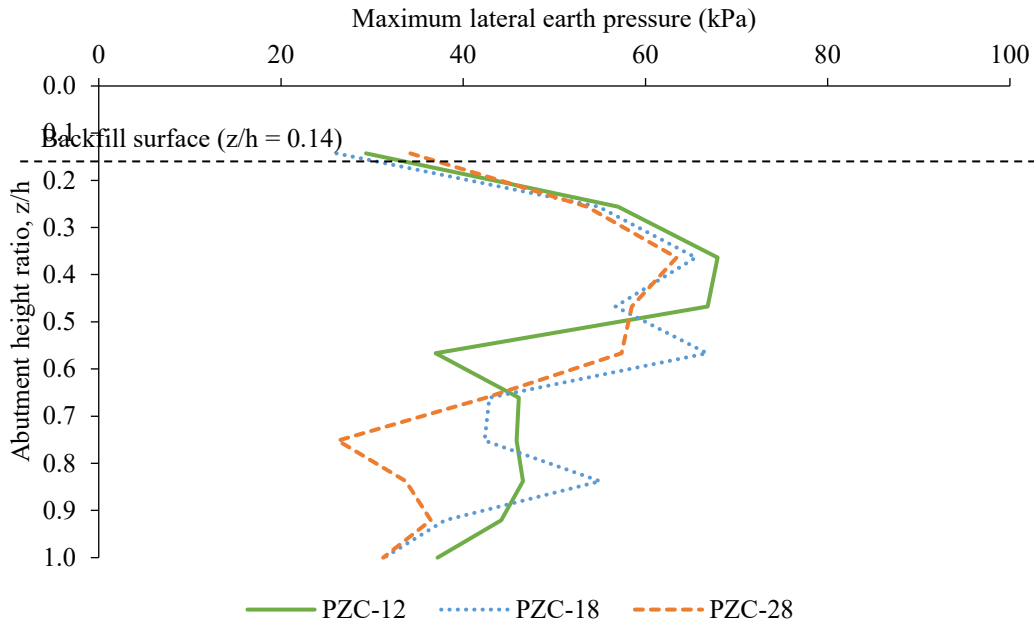


Figure B.74: Distributions of maximum lateral earth pressures along the abutment height after 50 annual cycles considering selected foundation stiffness values

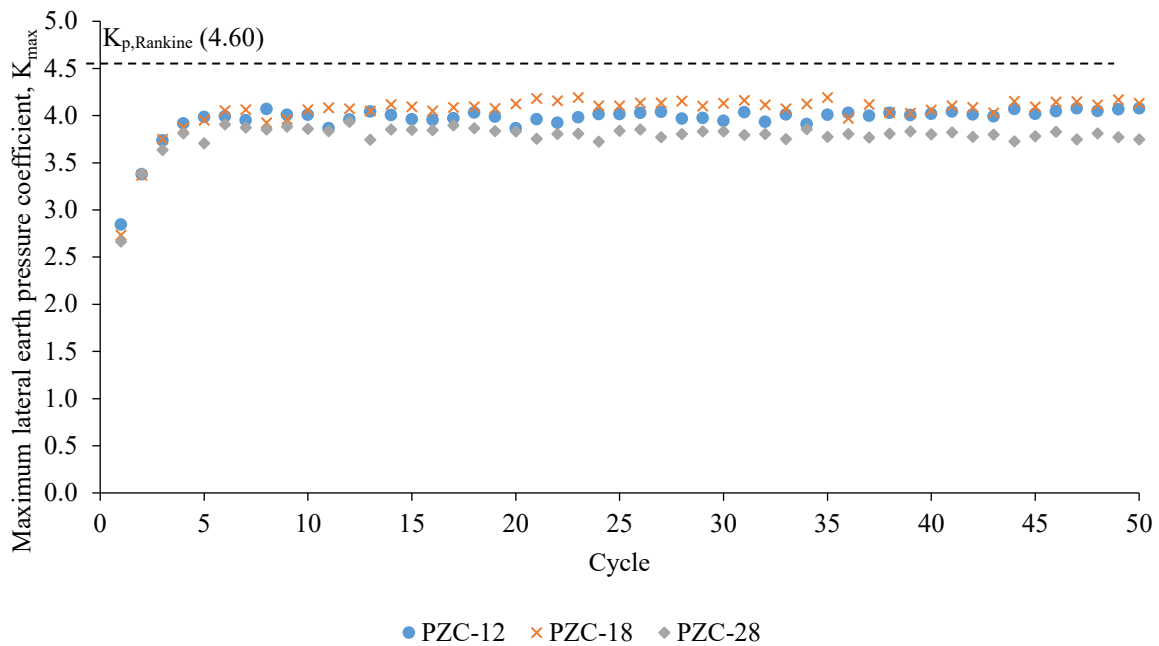


Figure B.75: Maximum lateral earth pressure coefficients for annual cycles considering selected foundation stiffness values

Vertical displacement profiles of the backfill surface along the distance from the abutment for the three profiles after 50 annual cycles are shown in Figure B.76. The displacements were obtained at the end of each cycle. Settlements are considered positive in the figure. For all profiles, the largest settlement occurred near the backfill-abutment interface and decreased with increasing distance from the abutment. A heave zone was formed at a certain distance from the abutment. The influence zone of displacements can be assumed to occur within a distance equal to the abutment height measured from the abutment. Figure B.77 shows the vertical displacements at the top of the backfill-abutment interface for annual cycles. For all investigated profiles, settlements presented a nonlinear increase with a decreasing rate in the initial cycles and then increased according to a nearly linear trend. A tendency of reaching a steady state could not be observed with increasing cycles.

As observed in Figures B.74 – B.77, the response of the backfill-abutment system upon imposed cyclic lateral displacements at the abutment was not significantly influenced by the variation of the stiffness of the sheet piles used in the foundation of the SIAB. This can be associated with the fact that the abutment is not integrated to the foundation system.

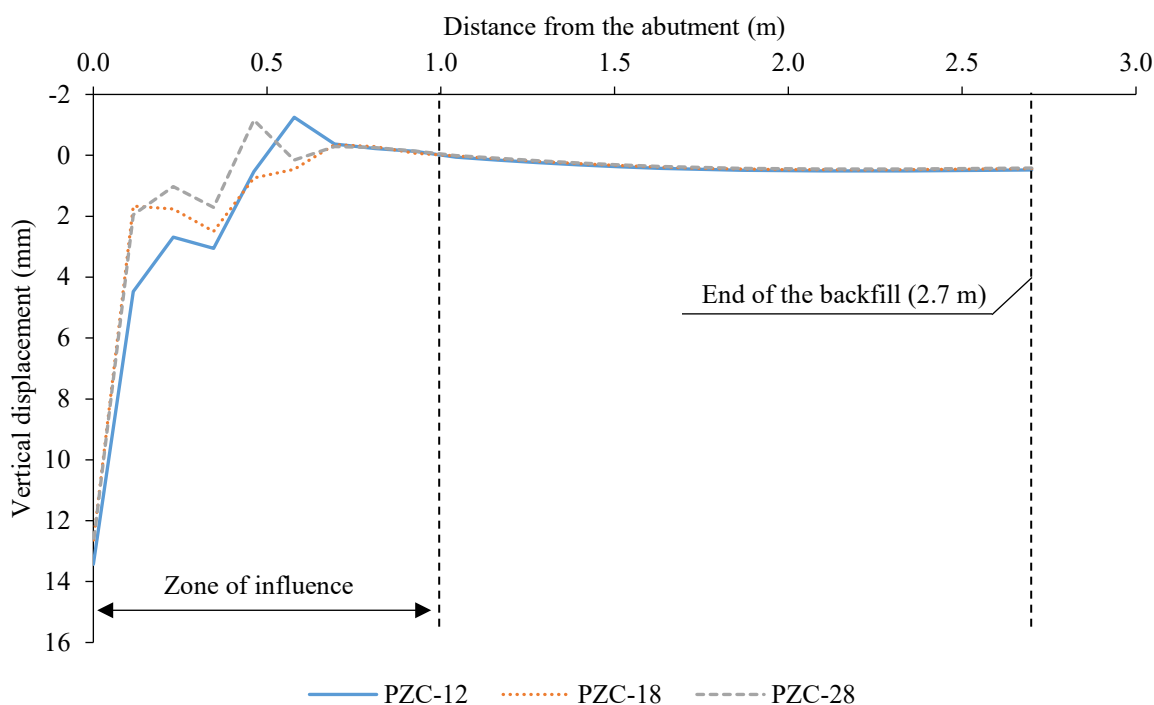


Figure B.76: Vertical displacement profiles of the backfill surface along the distance from the abutment for different foundation stiffness values after 50 annual cycles

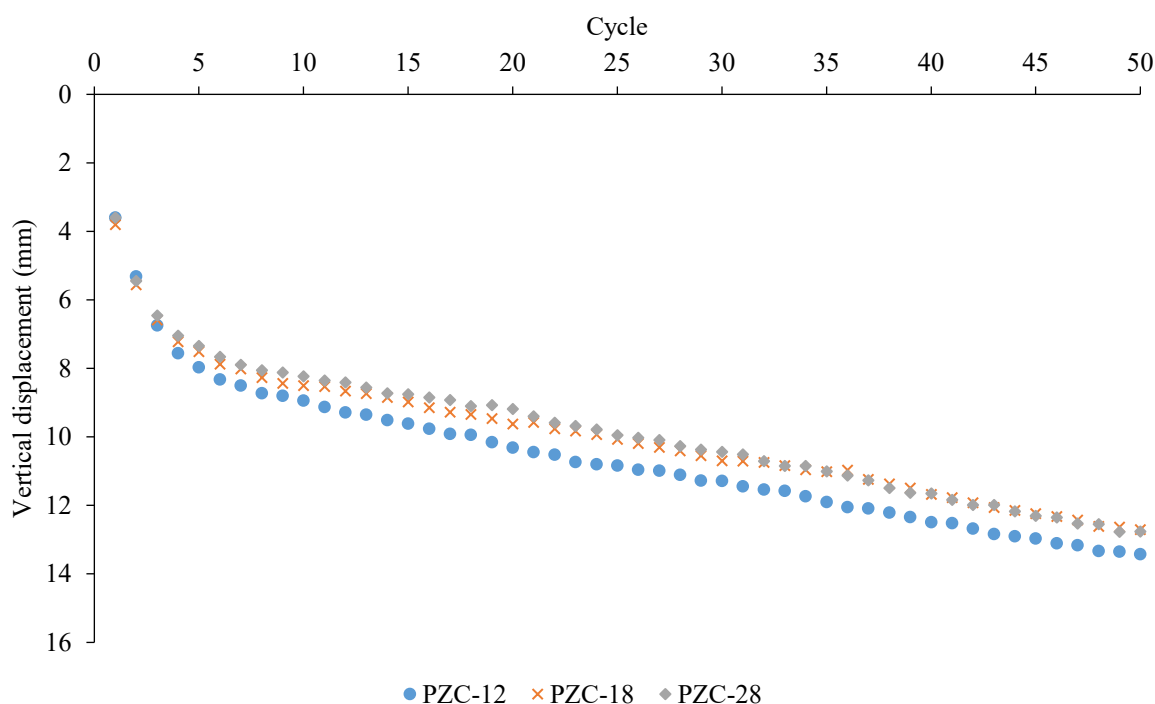


Figure B.77: Vertical displacements on the top of the backfill-abutment interface for annual cycles considering different foundation stiffness values

B.5.5.1.4: Lateral Displacement Amplitude

The last parameter of investigation was the influence of the lateral displacement amplitude of the abutment. Table B.6 presents a compilation of lateral displacements of the abutment measured or assumed in various numerical and experimental investigations. It is observed that the values of δ_h/h situate within the range between 0.1% and 0.5%. Five different values of relative lateral displacement (δ_h/h) were chosen based on information from the sources cited in Table B.6: 0.1%, 0.2%, 0.3%, 0.4% and 0.5%.

Table B.6 – Lateral displacement of the abutment from several sources in the technical literature

Reference	Amplitude (mm)	Abutment height (m)	δ_h/h (%)
Ng, Springman and Norrish (1998)	6	6.4	0.1
	12		0.2
Bloodworth et al. (2012)	16	4	0.4
Civjan et al. (2013)	12	4	0.3
	20		0.5
Huntley and Valsangkar (2013)	15	4	0.4
Mitoulis et al. (2016)	30	7	0.4
Caristo, Barnes and Mitoulis (2018)	27	7	0.4

Figure B.78 shows maximum lateral earth pressures along the abutment height for the selected amplitudes after 50 cycles. For all selected values of δ_h/h , the maximum lateral earth pressures presented a nonlinear distribution along the abutment height. The lowest amplitude presented the largest values of maximum lateral earth pressure situating within the upper and bottom thirds of the abutment. Intermediate amplitudes concentrated the largest values of maximum lateral earth pressure in the upper third of the abutment. The highest amplitude presented the largest values of maximum lateral earth pressure occurring within the middle third of the abutment.

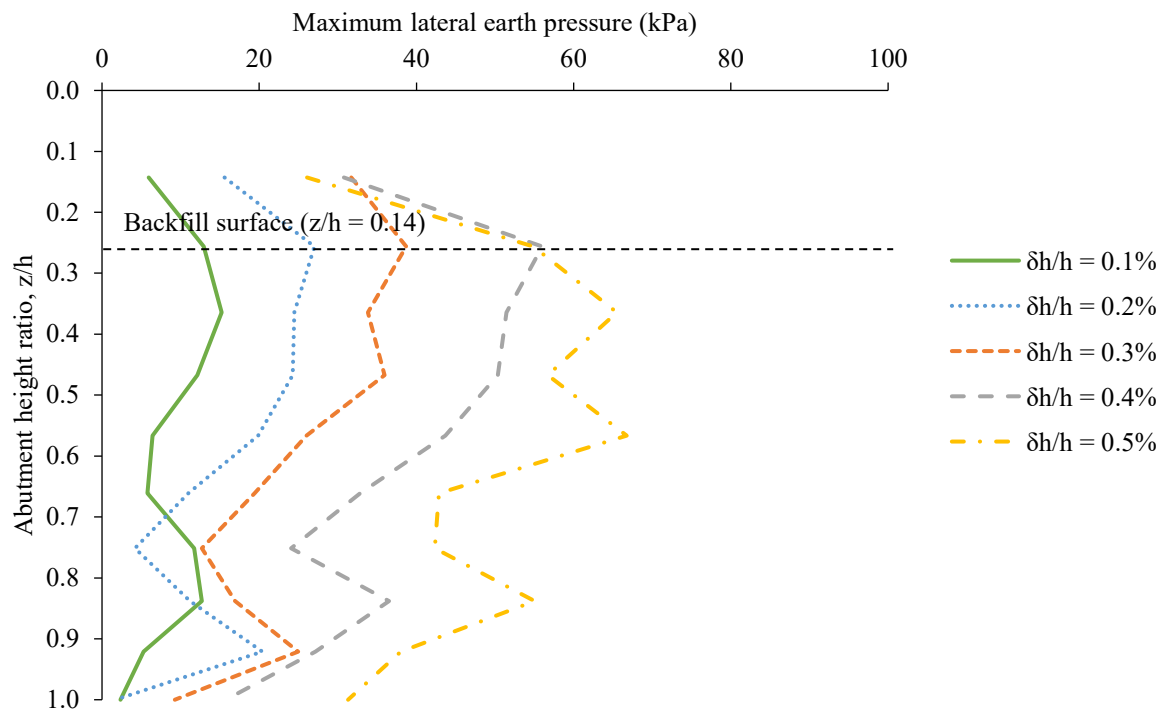


Figure B.78: Distributions of maximum lateral earth pressures along the abutment height for selected δ_h/h values after 50 cycles of lateral displacement of the abutment

As shown earlier, the behavior observed in Figure B.78 is explained by the development of shear zones in the backfill due to cyclic lateral displacements of the abutment. Figure B.79 presents shadings of deviatoric strain in the backfill for all analyzed amplitudes. The shadings show the formation of a particularly intense shear zone developing in the upper third of the abutment. The intensity of shearing increased with increasing amplitude.

(a)

(b)

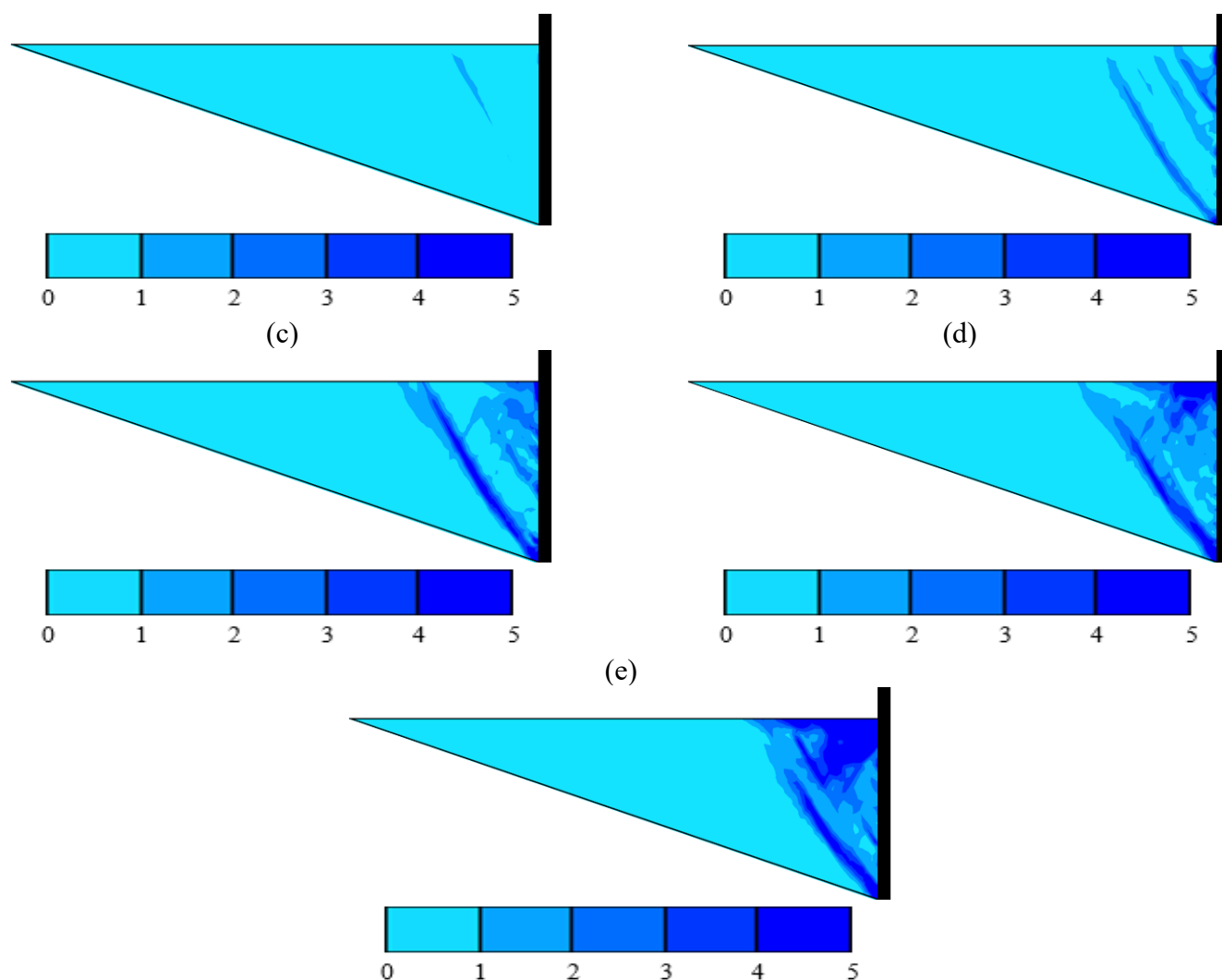


Figure B.79: Shadings of deviatoric strains (in %) in the backfill accumulated after 50 cycles of δ_h/h equal to: (a) 1 mm; (b) 2 mm; (c) 3 mm; (d) 4 mm; and (e) 5 mm

Figure B.80 shows the evolution of K_{\max} with the cycles. K_{\max} remained below $K_{p,\text{Rankine}}$ with all selected displacement amplitudes. For $\delta_h/h = 0.1\%$, K_{\max} presented a slight decrease within the first 40 cycles and then reached the steady state around 0.75. For $\delta_h/h = 0.2\%$, K_{\max} remained virtually constant around 1.5. For $\delta_h/h = 0.3\%$, 0.4% and 0.5% , K_{\max} increased within the initial cycles and then reached the steady state around 2.25, 3.2 and 4.1, respectively. As discussed earlier, the behavior shown in Figure B.80 can be explained by the effects of densification and granular flow of the soil produced by cycling. In the case of $\delta_h/h = 0.1\%$, the effect of soil granular flow prevailed over the effect of soil densification within the first 40 cycles, what reduced the maximum lateral earth pressure coefficient. A balance between both effects was reached afterward, and K_{\max} became constant. The amplitude of $\delta_h/h = 0.2\%$ resulted in a constant maximum lateral earth pressure coefficient, which revealed a balance between densification and granular flow effects. On the other hand, for δ_h/h equal to 0.3% , 0.4% and 0.5% , the effect of soil densification prevailed over the effect of soil granular flow within the

initial cycles. Eventually, a balance between both effects was reached with increasing cycles, and K_{\max} remained unchanged.

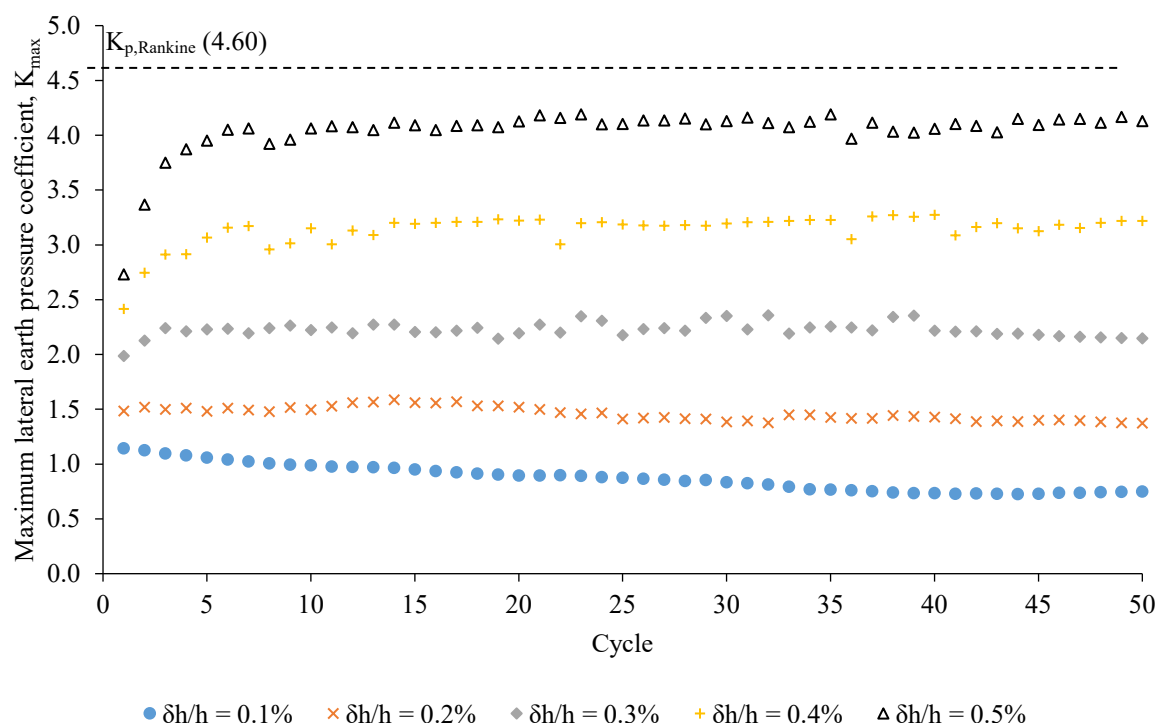


Figure B.80: Maximum lateral earth pressure coefficients with cycles considering selected δ_h/h values

For a better understanding of the influence of the lateral displacement amplitude on the maximum lateral earth pressures, the maximum lateral earth pressure coefficient at the steady state ($K_{\max,ss}$) was plotted against δ_h/h , as shown in Figure B.81. It is possible to observe that $K_{\max,ss}$ increased with δ_h/h according to an approximately linear fashion. Moreover, the results showed that maximum lateral earth pressure predictions with $K_{p,Rankine}$ proved to be on the safe side until $\delta_h/h = 0.55$. Similar results to those presented in Figures B.79, B.80 and B.81 were obtained in experimental tests and numerical simulations performed by Abdel-Fattah and Abdel-Fattah (2019), Abdel-Fattah, Abdel-Fattah and Hemada (2018), England, Tsang and Bush (2000), Gabrieli, Zorzi and Wan (2015), Ng, Springman and Norrish (1998), and Zorzi, Artoni and Gabrieli (2017).

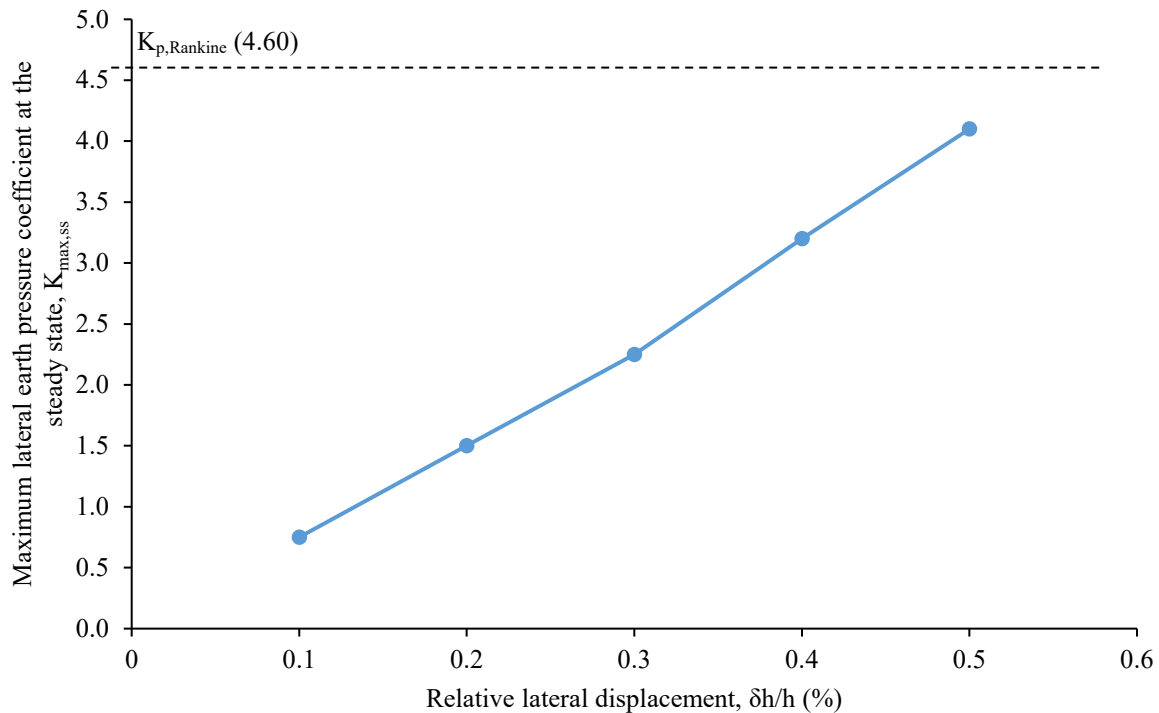


Figure B.81: Variation of maximum lateral earth pressure coefficients at steady state with relative lateral displacements

Vertical displacement profiles of the backfill surface along the distance from the abutment for the different values of δ_h/h after 50 cycles were also analyzed (Figure B.82). The displacement was obtained at the end of each cycle. Settlements were considered positive and heave values negative. All lateral displacement amplitudes yielded maximum settlements near the backfill-abutment interface. A heave zone was not identified on the backfill surface for δ_h/h equal to 0.1% to 0.4%. On the other hand, the cyclic lateral displacement of $\delta_h/h = 0.5\%$ caused a heave in the soil mass. The zone where displacements are significant can be assumed to occur within a distance equal to the abutment height measured from the abutment. Figure B.83 shows the variation of the vertical displacements at the top of the backfill-abutment interface with cycles. For all values of δ_h/h , settlements increased with cycles. For δ_h/h equal to 0.1% and 0.2%, settlements increased according to a virtually linear fashion from the beginning of cycling. On the other hand, for δ_h/h equal to 0.3%, 0.4%, and 0.5%, settlements firstly presented a nonlinear increase with a decreasing rate in the initial cycles, followed by a nearly linear increase. No tendency of reaching a steady state was noted.

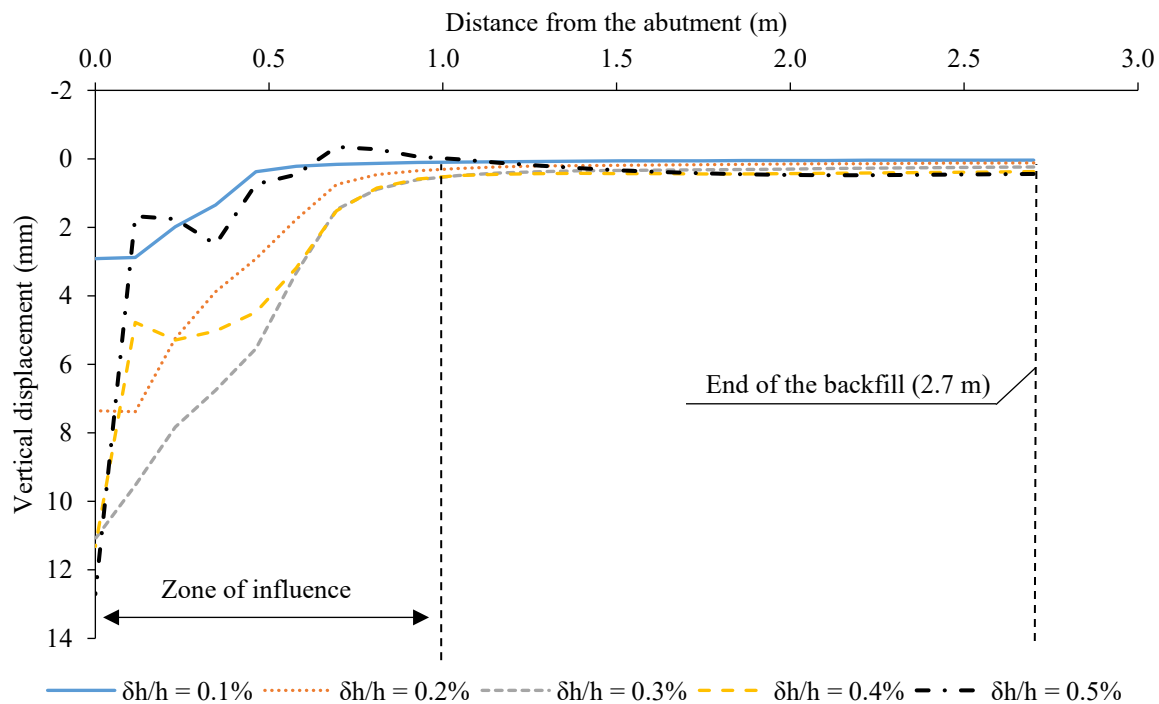


Figure B.82: Vertical displacement profiles of the backfill surface along the distance from the abutment for different $\delta h/h$ values after 50 cycles

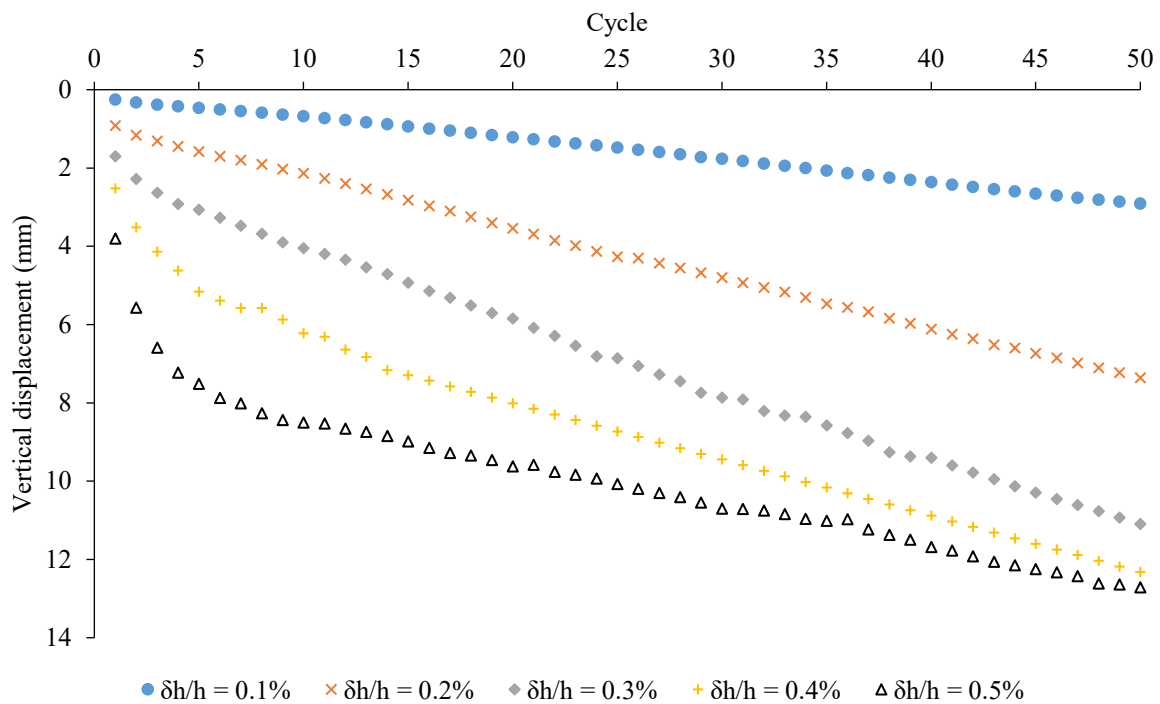


Figure B.83: Vertical displacements on the top of the backfill-abutment interface with cycles considering different $\delta h/h$ values

As discussed earlier, the behavior observed for the vertical displacement of the backfill surface can be related to the effects of soil densification and granular flow. Displacement amplitudes of 0.1%, 0.2%, 0.3%, and 0.4% were sufficient to cause densification of the soil near the backfill-abutment interface, but not to produce a soil granular flow that could raise the backfill surface. On the other hand, the displacement amplitude of 0.5% was sufficient to densify the soil near the backfill-abutment interface and produce a soil granular flow that raised the backfill surface. In the case of δ_h/h equal to 0.1%, despite having prevailed over the effect of soil densification, the magnitude of the effect of soil granular flow was not enough to affect the behavior of the settlement with the cycles. For δ_h/h equal to 0.2%, a balance between both effects occurred from the beginning of the cyclic lateral displacements of the abutment. On the other hand, for δ_h/h equal to 0.3%, 0.4% and 0.5%, the effect of soil densification prevailed over the effect of soil granular flow within the first cycles. Then, a balance between both effects was reached.

For a better understanding of the influence of the lateral displacement amplitude on the vertical displacement on the backfill surface, the maximum settlement obtained after 50 cycles of lateral displacement of the abutment was plotted against δ_h/h , as shown in Figure B.84. It is possible to observe that the settlement tended to stabilize after undergoing an initial increase. Similar results to those presented in Figures B.82, B.83 and B.84 were obtained in numerical simulations performed by England, Tsang and Bush (2000), and Ng, Springman and Norrish (1998).

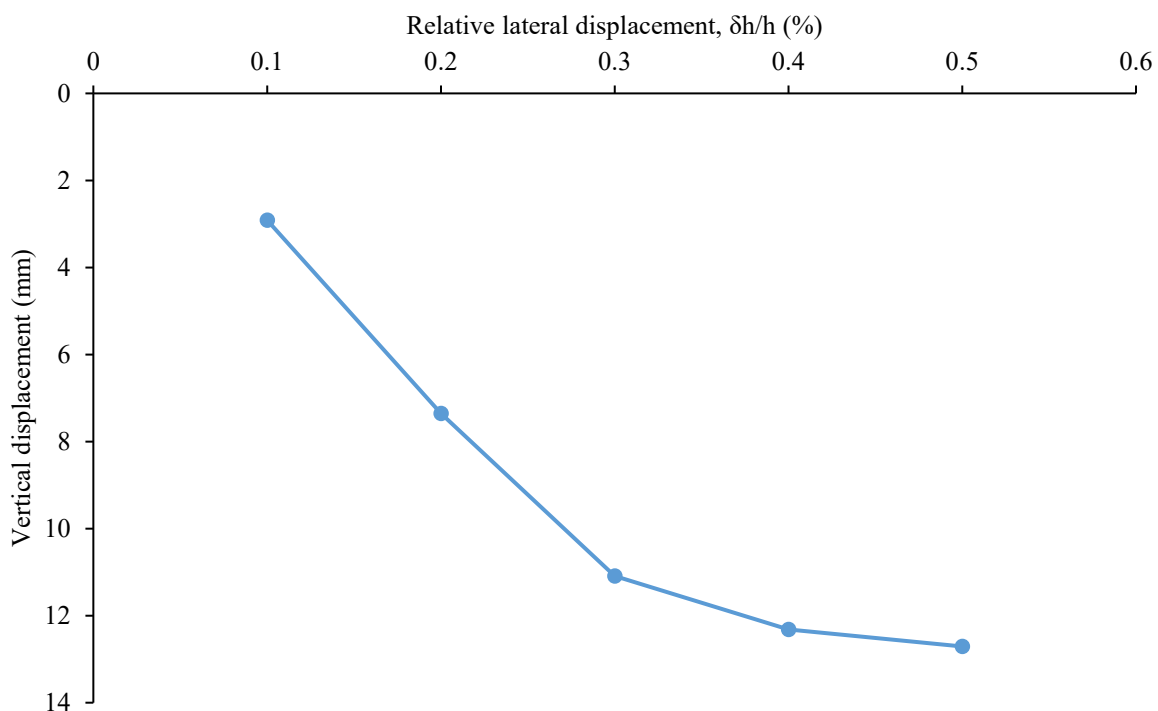


Figure B.84: Variation in vertical displacement on the top of the backfill-abutment interface with relative lateral displacements after 50 cycles

The behavior of the maximum settlement with the lateral displacement amplitude can be related to the backfill densification. Backfill soil densification can be checked in Figure B.85, which shows compressive volumetric strains in the backfill accumulated after 50 cycles of lateral displacement of the abutment for the selected values of δ_h/h . The shadings show that the compressive volumetric strains increased with increasing δ_h/h . With the lowest values of δ_h/h , compressive volumetric strains were significantly affected by the variation of the amplitude of lateral displacement of the abutment. However, it became less significant with the largest values of δ_h/h .

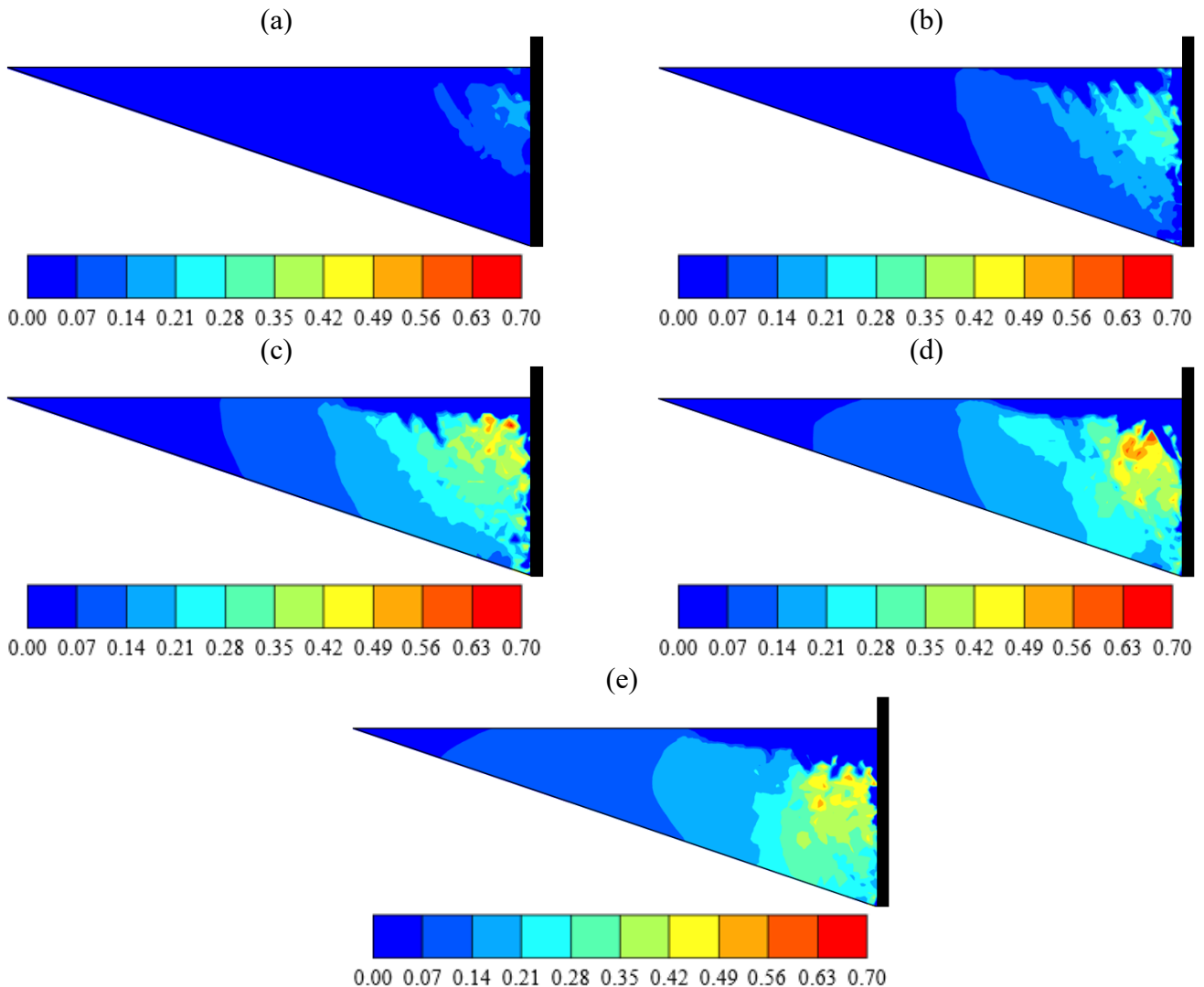


Figure B.85: Shadings of compression volumetric strains (in %) in the backfill accumulated after 50 cycles of δ_h/h equal to: (a) 1 mm; (b) 2 mm; (c) 3 mm; (d) 4 mm; and (e) 5 mm

With the presentation of the results from the sensitivity analysis performed on the Mack Creek Bridge numerical model, the following conclusions can be made:

- Predictions with the finite element numerical model produced good matches with the field data.
- The lateral earth pressure presented a nonlinear distribution along the abutment height in all numerical simulations.
- Cyclic lateral displacements of the abutment resulted in a zone of vertical displacements on the backfill surface with dimension equal to abutment height measured from the abutment in all numerical simulations.
- Vertical displacements on the backfill surface increased with cycles in all investigated conditions, which indicates the occurrence of ratcheting in the backfill.
- The largest downward vertical displacement (settlement) of the backfill surface occurred near the backfill-abutment interface and decreased with the distance from the abutment in all investigated conditions.
- Maximum lateral earth pressures were more affected by the cyclic lateral displacements of the abutment than minimum lateral earth pressures.
- The largest daily maximum lateral earth pressures occurred within the upper and bottom thirds of the abutment while the largest annual maximum lateral earth pressures occurred within the middle third of the abutment.
- The largest daily and annual minimum lateral earth pressures were developed within the bottom third of the abutment.
- Daily and annual maximum lateral earth pressure coefficients were lower than Rankine's passive lateral earth pressure coefficient while daily and annual minimum lateral earth pressure coefficients were close to Rankine's active lateral earth pressure coefficient.
- The daily maximum lateral earth pressure coefficient presented a variable behavior with cycles, which included alternating reduction and escalation, while the annual maximum lateral earth pressure coefficient firstly increased with cycles and then reached stabilization (steady state).
- The daily minimum lateral earth pressure coefficient firstly decreased with cycles and then reached a steady state while the annual minimum lateral earth pressure coefficient remained virtually constant.
- While a tendency of upward vertical displacement (heave) on the backfill surface was not observed with the daily cycle analysis, a heave zone was formed at a certain distance from the abutment with the annual cycle analysis.

- The settlement at the top of the backfill-abutment interface increased according to a nonlinear fashion with a decreasing rate for daily cycles while, for annual cycles, the settlement at the top of the backfill-abutment interface firstly presented a nonlinear increase with a decreasing rate within the first cycles and then increased according to a linear fashion.
- The maximum lateral earth pressure was not influenced by the completion season of the bridge construction.
- The vertical displacement of the backfill surface was influenced by the completion season of the bridge construction since the different initial movements of the abutment resulted in different initial responses to the backfill.
- The largest settlements occurred for the bridge construction completed in the summer season while the smallest settlements occurred for the bridge construction completed in the winter season. Therefore, completing the construction of the bridge in the summer season represented the most unfavorable situation.
- The absence of integration between the abutment and the foundation minimized the influence of foundation stiffness on the response of the backfill-abutment system.
- The maximum lateral earth pressures on the abutment and the vertical displacements of the backfill surface increased with increasing amplitude of lateral displacement.
- The largest values of maximum lateral earth pressure occurred within the upper and bottom thirds of the abutment, for the lowest value of lateral displacement, while, for the largest value of lateral displacement, the maximum lateral earth pressure concentrated at the middle third of the abutment.
- Comparatively smaller amplitudes caused a reduction of the maximum lateral earth pressure coefficient with cycles, while comparatively higher amplitudes caused an increase of the maximum lateral earth pressure coefficient with cycles. In both situations, a steady state was reached.
- The maximum lateral earth pressure coefficient in a steady state increased with the relative lateral displacement according to an approximately linear fashion, and no tendency of reaching a stabilization was observed.
- Maximum lateral earth pressure predictions with Rankine's passive lateral earth pressure coefficient proved to be on the safe side until a relative lateral displacement equal to 0.55% of the abutment height.

- No tendency of heave was observed on the backfill surface for comparatively smaller amplitudes, while a heave zone was formed at a certain distance from the abutment for comparatively higher amplitudes.
- For comparatively smaller amplitudes, the settlement at the top of the backfill-abutment interface increased according to a linear fashion, while for comparatively higher amplitudes, it firstly presented a nonlinear increase with a decreasing rate within the first cycles and then increased according to a linear fashion, for comparatively higher amplitudes.
- The settlement at the top of the backfill-abutment interface tended to stabilization after undergoing an initial increase.

B.6: Temperature Distribution Within the Deck Section

The successful installation of new equipment on Mack Creek Bridge in January 2020 allowed for hourly tracking of displacements of the bridge, as well as the status of thermal boundaries at the top and bottom of the deck. Simplified calculations done in Chapter 7 show that the full extent of displacements of the bridge cannot be fully explained with the documented procedure in the AASHTO LRFD Bridge Design Manual (2018). This can be explained by the fact that the equations and parameters provided are experimental and therefore come with errors. The AASHTO LRFD Bridge Design Manual (2018) also recommends obtaining these parameters in the lab instead of using the approximate value provided in the manual.

In this section, a procedure to calculate the temperature gradient within the deck is outlined. Once the temperature gradient is obtained, we can calculate the true coefficient of thermal expansion and possibly back-calculate the amount of shrinkage the bridge must have undergone to date.

B.6.1: General Formulation of Heat Flow in Concrete

There are many numerical packages developed for analysis of heat flow through various media. While they may use finite difference method (FDM), finite element method (FEM) or any other numerical method to analyze the flow of heat, the underlying equation governing the flow is generally the same, the heat flow equation formulated by Joseph Fourier in 1822:

$$\rho c \frac{\partial T}{\partial t} = K \left(\frac{\partial^2 T}{\partial x^2} + \frac{\partial^2 T}{\partial y^2} + \frac{\partial^2 T}{\partial z^2} \right) + q_v$$

In this equation, ‘t’ denotes time, ‘x’, ‘y’ and ‘z’ denote cartesian coordinates, ‘T’ denotes temperature at (x,y,z) at time ‘t’, ‘ρ’ is the density of the material, ‘c’ is specific heat of the material, ‘K’ is thermal conductivity of the material, and ‘q_v’ is the heat generated (e.g. hydration heat).

As can be seen, this is a 2nd order Partial Differential Equation (PDE), which can be solved using a variety of implicit and explicit approaches once the correct boundary conditions are applied.

As there is expected to be negligible variations across the length of the bridge, the heat flow equation can be reduced to a 2D problem:

$$\rho c \frac{\partial T}{\partial t} = K \left(\frac{\partial^2 T}{\partial x^2} + \frac{\partial^2 T}{\partial y^2} \right) + q_v$$

Next, to define the boundary conditions, the procedure outlined in Branco and Mendes (1993) is followed. The boundary condition associated with this problem is:

$$K \left(\frac{\partial T}{\partial x} n_x + \frac{\partial T}{\partial y} n_y \right) + q = 0$$

Where ‘ n_x ’ and ‘ n_y ’ are direction cosines of the unit outward vector normal to the boundary surfaces and ‘ q ’ is the time rate of heat transferred between the surface and the environment. The energy transferred between the surface and the environment can be due to convection (q_c), thermal irradiation (q_r), and solar radiation (q_s):

$$q = q_c + q_r + q_s$$

In this equation, q_c is dependent on the convection heat transfer coefficient (h_c) of the surface and the difference between ambient air temperature (T_{air}) and surface temperature (T_s). q_r is a measure of long wave thermal irradiation between the surface and atmosphere and is also a function of the difference between ambient air temperature and surface temperature and irradiation heat transfer coefficient (h_r). At last, heat absorbed from the solar radiation is a function of absorptivity of the surface (α), incidence angle of radiation (θ), their inclination (μ) and intensity of solar rays (I). Therefore, we have:

$$\begin{aligned} q_c &= h_c(T_s - T_{air}) \\ q_r &= h_r(T_s + T_{air}) \\ q_s &= \alpha \left(I_d \sin \theta + I_i \frac{1 + \cos \mu}{2} \right) \end{aligned}$$

A visualization of how different factors affect the flow of heat in the deck is depicted in Figure B.86. As described in Section 7.2.2, the newly installed sensors provide the necessary information (air temperature, solar radiation, wind speed, deck surface temperature, etc.) to form these boundary conditions.

Once the boundary conditions are defined, appropriate mesh size and time steps must be chosen to solve the Fourier equation.

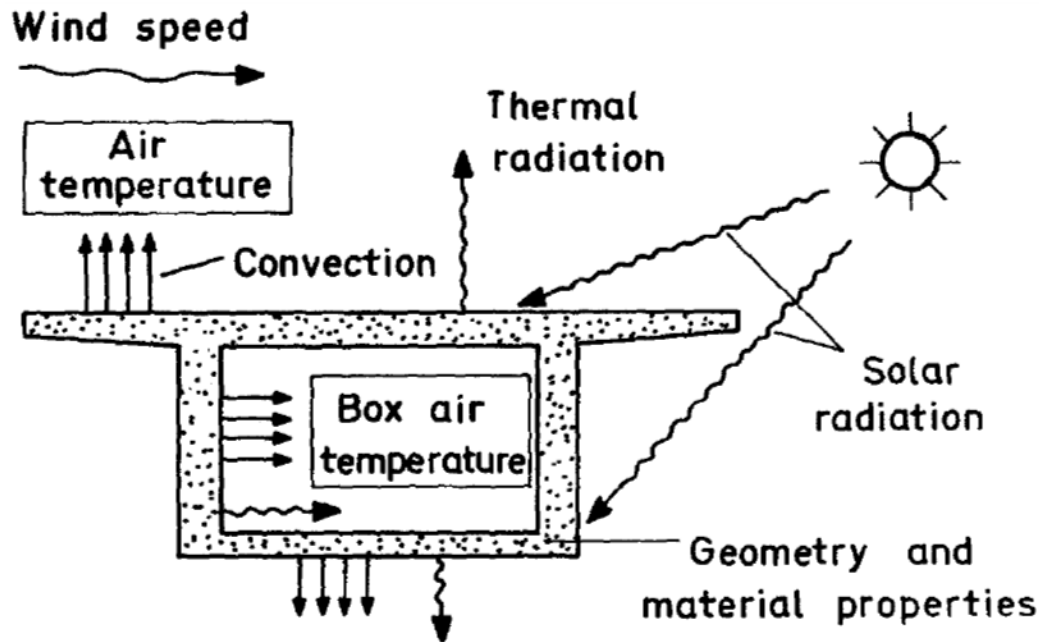


Figure B.86: Factors affecting heat flow across the bridge deck cross-section (Image from Branco and Mendes, 1993)

Once the model is verified, the results can be used to back-calculate important parameters such as coefficient of thermal expansion and shrinkage. Moreover, a sensitivity analysis can be performed to evaluate the effect of cross-section geometry, span length, material properties and environmental variables on the behavior of SIAB/IAB structures.

B.6.1.1: Preliminary FEM Heat Flow Model of Mack Creek

After collecting several weeks of data from the new sensors installed on Mack Creek Bridge, the research team began developing a finite element model of the bridge cross section in Abaqus FEA software for the heat flow analysis. The geometry of the model developed can be seen in Figure B.87. To reduce the computational effort required, several assumptions regarding symmetry and plane strain conditions were made. The model seen in Figure B.87 only includes half a box beam and deck section, assuming heat flows vertically from top to bottom and not from one side of the beam to the other; this condition can be true for middle beams but not for the beams placed on the sides of the bridge with the outer side exposed to wind and potential solar radiation. Moreover, reflective boundaries are assigned on the sides of the model developed to better simulate the thermal radiation effects between adjacent beams. These reflective boundaries can be thought of as mirror-like objects that reflect thermal radiation, emanating from the box beam edges and this mirroring action is similar to what would have occurred, had the adjacent beam been simulated.

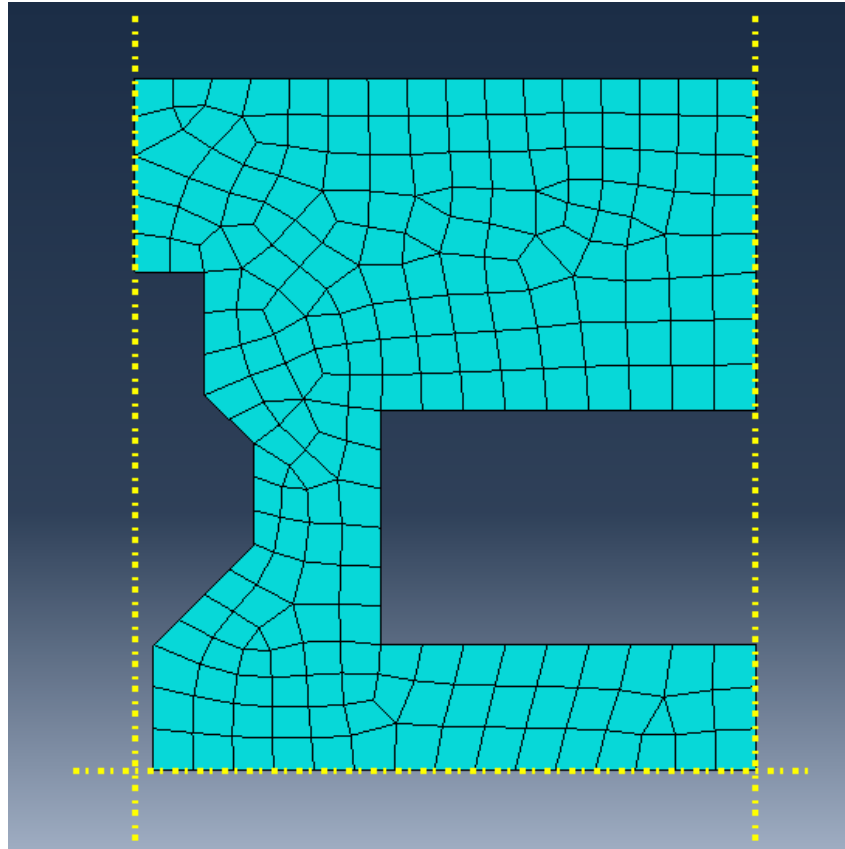


Figure B.87: Finite element model developed based on Mack Creek Bridge drawings considering symmetry in the structure

After the model was developed and meshed, boundary conditions are applied according to sensor recordings from the sensors in the field. These boundary conditions include temperature at the top surface boundary as measured by SI-111SS, wind speed, ambient temperature, and solar radiation intensity. All of these items are measured directly in the field and are fed into the model as a time series according to the frequency they were measured. An example result of the analysis is shown in Figure B.88. As can be seen, there is a nearly linear variation of temperature with depth as expected. The slight lateral variation in temperature in the cross-section can be attributed to the existence of voids in the cross-section. In this particular case, it can be seen that the temperature within the deck varies from 77 to 89.6°F, with the coldest region being the web and hottest region being the top surface, which is directly exposed to solar radiation. The temperature variation in the cross-section means that there can be different levels of thermal strains at different depths, which could lead to changes in the curvature of the bridge as well as its overall length. The temperature near the boundaries changes more rapidly compared to the inner sections due to exposure to wind, solar radiation and ambient air. Therefore, the boundary regions undergo larger amounts of thermal strains than inner sections.

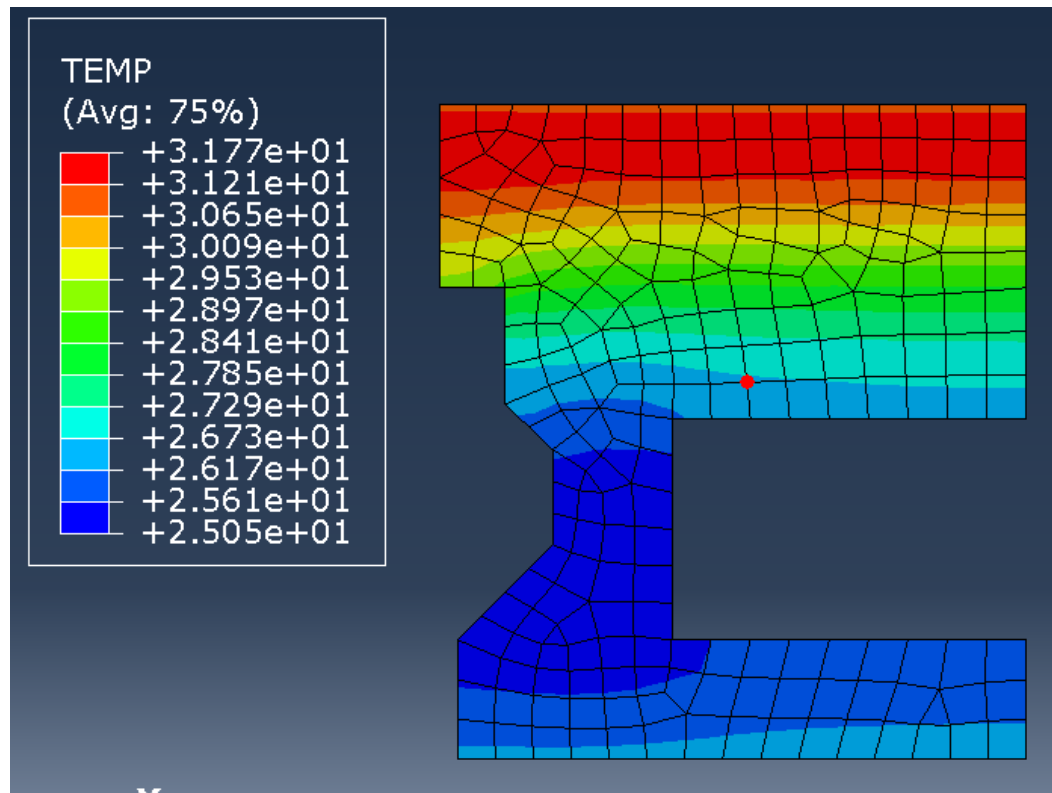


Figure B.88: Example results of FE simulation of heat flow in Mack Creek Bridge

Because the thermal conductivity of the concrete used in Mack Creek Bridge is not exactly known, this model can be used to predict this value by comparing the output of ABAQUS with field measurements. This would be the next step in this study. Once these parameters are defined with certainty, it is possible to use this model to predict thermal action for different bridge cross-section geometries and for bridges built in different regions of the state.

B.7: Conclusion to the Numerical Simulations

A preliminary numerical analysis of an ongoing investigation on a semi-integral bridge abutment undergoing cycles of induced lateral displacements was presented. The numerical simulations were validated against field data of horizontal stresses behind the abutment backwall and ambient air temperature collected from an instrumented SIAB located in Palestine, TX. The main findings of this phase of the research are as follows:

- The maximum thrust presented a variable behavior with time, which included alternating reduction and escalation. The maximum thrust remained below Rankine's passive thrust. The minimum thrust, on the other hand, showed an initial reduction followed by stabilization with time (steady-state). The minimum thrust after stabilization remained around the Rankine's active thrust.

- Settlements progressed with bridge cyclic movements, showing the occurrence of strain ratcheting. The settlement trough reached a distance of about 3.28 ft behind the abutment backwall. The numerical analysis gave underestimated settlements, as compared to settlements measured at the field.
- Smaller amplitudes of lateral displacement caused a reduction of the lateral thrust behind the backwall with the cycles, while higher amplitudes of lateral displacements caused an increase of the lateral thrust with cycles. This means that stress ratcheting behind the bridge abutment is more likely to occur with larger bridges, while stress alleviation is more likely to occur with smaller bridges.
- Settlements and the disturbance zone within the backfill soil behind the abutment increased with the lateral displacement amplitude.
- The use of alternative approach for modeling the abutment-cap system did not result in significant improvement in providing a good match with field data compared with the previous more simplified approach. The passive and active thrusts presented a variable behavior with time similar to what was calculated using the preliminary model.
- Simulation of the remainder of the 1st year shows settlement continuing to occur at the same rate with bridge cyclic movements with no observable tendency of stabilization.
- The 1st year data shows that the extent of the settlement trough reaches a distance of about 2.6 ft behind the abutment backwall by the end of the first year.
- The use of new geometry improved the match between field data and numerical results compared to the preliminary geometry. The passive and active lateral thrust, and the settlement presented a similar behavior to what was calculated using the preliminary geometry.
- When the bridge was completed in the spring, summer and autumn, the passive lateral thrust increased in the first 10 cycles before reaching a steady state. When the bridge was completed in the winter, the passive lateral thrust presented no significative variation, being virtually constant since the beginning of the cycles. The active lateral thrust presented no variation since the beginning of the cycles and was not affected by the bridge completion seasons. When the bridge was completed in the spring, autumn and winter, no variation was observed in the settlements. However, the settlements were higher when the bridge was completed in the summer. Settlement of the surface of the soil behind the bridge abutment in the four bridge completion seasons presented no significative variations, reaching a distance of about 3.28 ft behind the abutment.

In addition to the FEM model developed based on Mack Creek Bridge, it was also decided to create a separate numerical model to examine the effect of heat flow across the deck cross

section. For this model, the Fourier heat flow equation is used, where the boundary conditions are formed using the data acquired through the equipment installed on Mack Creek Bridge in January 2020. Once the numerical model is validated, it is expected to use it to better understand the effects of temperature and shrinkage on changes in deck length and the interaction with other bridge components. Finally, this model will be used to conduct a sensitivity analysis considering the effect of climate variation, material properties, deck geometry, span length, etc. to make design recommendation for SIAB/IAB structures.

References

- AASHTO. (2017). "*AASHTO LRFD bridge design specifications*", American Association of State Highway and Transportation Officials
- Abendroth, R. E., Greimann, L. F., Lim, K.-H., Sayers, B. H., Kirkpatrick, C. L. and Ng, W. C. (2005). "*Field Testing of Integral Abutments*." Iowa State University Center for Transportation Research and Education, Ames, IA.
- Abu-Hejleh, N., Zornberg, J.G., Wang, T., and Watcharamonthein, J. (2002). "Monitored Displacements of Unique Geosynthetic-Reinforced Soil Bridge Abutment." *Geosynthetics International*, Vol. 9, No. 1, pp. 71-95.
- Adams, M., Nicks, J., Stabile, T., Wu, J., Schlatter, W., Hartmann, J. (2011). "Geosynthetic Reinforced Soil Integrated Bridge System Interim Implementation Guide." Federal Highway Administration No. HRT-11-026
- Ahn, J-H., Yoon, J-H., Kim, J-H., Kim, S-H. (2011). "Evaluation on the behavior of abutment-pile connection in integral abutment bridge." *Journal of Constructional Steel Research*, Vol.67, pp. 1134-1148
- Arockiasamy, M., Butrieng, N., Sivakumar, M. (2004). "State-of-the-Art of Integral Abutment Bridges: Design and Practice." *ASCE Journal of Bridge Engineering*, Vol. 9, No. 5, pp. 497-506
- Arsoy, S., Barker, R.M., Duncan, J.M. (1999). "The Behavior of Integral Abutment Bridges." Federal Highway Administration, Rep. No. A/VTRC 00-CR3
- Branco, F. A., and Mendes, P. A. (1993). "*Thermal Actions for Concrete Bridge Design*." *Journal of Structural Engineering*, 119 (8): 2313–2331.
[https://doi.org/10.1061/\(ASCE\)0733-9445\(1993\)119:8\(2313\)](https://doi.org/10.1061/(ASCE)0733-9445(1993)119:8(2313)).
- Broms, B. B. (1964). "Lateral Resistance of Piles in Cohesive Soils." *Journal of the Soil Mechanics and Foundations Division*, 90 (2), 27–63.
<https://doi.org/10.1061/JSFEAQ.0000611>.
- Burdet, O., Einpaul, J., Muttoni, A. (2015). "Experimental investigation of soil-structure interaction for the transition slabs of integral bridges." *Structural Concrete*, Vol. 16, No. 4, pp. 470-479
- Burke, M.P. Jr. (2009). *Integral and Semi-Integral Bridges*. John Wiley & Sons
- Chen, Q., Helwig, T., Herman, R., Grisham, G., Arikan, Y. (2009). "Effects of Thermal Loads on Texas Steel Bridges." TxDOT Research Project Report 5040-1
- Civjan, S. A., Brena, S. F., Butler, D. A., and Crovo, D. S. (2004). "Field Monitoring of Integral Abutment Bridge in Massachusetts." *Transportation Research Record*, 1892 (1): 160–169. SAGE Publications Inc. <https://doi.org/10.3141/1892-17>.
- Civjan, S.A., Kalayci, E., Quinn, B.H., Breña, S.F., Allen, C.A. (2013). "Observed integral abutment bridge substructure response." *Engineering Structures*, Ed. 56, pp. 1177-1191

- Clayton, C. R. I., Xu, M., and Bloodworth, A. (2006). "A laboratory study of the development of earth pressure behind integral bridge abutments." *Géotechnique*, 56 (8): 561–571. <https://doi.org/10.1680/geot.2006.56.8.561>.
- Clough, G.W., Duncan, J.M. (1991). "Earth Pressures." *Foundation Engineering Handbook*, Second Edition, Edited by H.Y. Fung, Van Nostrand Reinhold, New York, NY, pp. 223-235
- Commonwealth of Pennsylvania - Department of Transportation (2007). "Standard Integral Abutment." BD-667M
- Coulomb, C. A. (1776). "Essai sur une application des règles de maximis & minimis à quelques problèmes de statique, relatifs à l'architecture." Paris: De l'Imprimerie Royale.
- England, G. L., Tsang, N. C. M., and Bush, D. I. (2000). "Integral bridges: a fundamental approach to the time-temperature loading problem". Thomas Telford Ltd, London.
- Fartaria, C. (2010). "Soil-Structure Interaction in Integral Abutment Bridges." Department of Civil Engineering, Architecture and GeoResources
- Fawaz, G., and Murcia-Delso, J. (2021). "Three-Dimensional Finite Element Modeling of RC Columns Subjected to Cyclic Lateral Loading." *Engineering Structures*, 239: 112291. <https://doi.org/10.1016/j.engstruct.2021.112291>.
- Frosch, R., and Lovell, M. (2011). "Long-Term Behavior of Integral Abutment Bridges." *JTRP Technical Reports*. <https://doi.org/10.5703/1288284314640>.
- Han, L., Belivanis, K. V., Helwig, T. A., Tassoulas, J. L., Engelhardt, M. D., and Williamson, E. B. (2019). "Field And Computational Investigation of Elastomeric Bearings in High-Demand Steel Girder Application." *Journal of Constructional Steel Research*, 162: 105758. <https://doi.org/10.1016/j.jcsr.2019.105758>.
- Hassiotis, S., Khodair, Y., Roman, E., Dehne, Y. (2006). "Evaluation of Integral Bridge Abutments." Federal Highway Administration, Rep. No. NJ-2005-025
- Horvath, J.S. (2005). "Integral-Abutment Bridges: A Complex Soil-Structure Interaction Challenge." Federal Highway Administration - 2005 Conference on Integral Abutments and Jointless Bridges, Baltimore, Maryland, pp. 281-291
- Huffaker, C.D. (2013). "Behavior and Analysis of an Integral Abutment Bridge." Utah State University - UMI No. 1541716
- Huntley, S. A., and Valsangkar, A. J. (2013). "Field monitoring of earth pressures on integral bridge abutments." *Can. Geotech. J.*, 50 (8): 841–857. <https://doi.org/10.1139/cgj-2012-0440>.
- Husain, I., Bagnariol, D. (1999). "Semi-Integral Abutment Bridges Manual." Ontario Ministry of Transportation, Rep. No. BO-99-03
- Iwasaki, N., Tenma, S., Kurita, A. (2011). "Portal Frame Bridges in Japan: State of the Art Report." *Structural Engineering International*, Vol. 21, No. 3, pp. 290-296

- Karalar, M., and Dicleli, M. (2016). "Effect of Thermal Induced Flexural Strain Cycles on The Low Cycle Fatigue Performance of Integral Bridge Steel H-Piles." *Engineering Structures*, 124, 388–404. <https://doi.org/10.1016/j.engstruct.2016.06.031>.
- Kim, W.S., Laman, J.A. (2010). "Integral abutment bridge response under thermal loading." *Engineering Structures*, Ed. 32, pp. 1495-1508
- Kirupakaran, K., Hanlon, B., Muraleetharan, K.K., Miller, G.A. (2012). "Field-Measured Response of an Integral Abutment Bridge." *Proceedings of the ASCE GeoCongress*, pp. 2157-2166
- Kunin, J., Alampalli, S. (2000). "Integral Abutment Bridges: Current Practice in United States and Canada." *Journal of Performance of Constructed Facilities*, Vol. 13, Ed. 3, pp. 104-111
- Laman, J.A., Kim, W.S. (2009). "Monitoring of Integral Abutment Bridges and Design Criteria Development." Federal Highway Administration, Rep. No. PA-2009-005-PSU 002
- Lawver, A., French, C., and Shield, C. K. (2000). "Field Performance of Integral Abutment Bridge." *Transportation Research Record*, 1740 (1): 108–117. SAGE Publications Inc. <https://doi.org/10.3141/1740-14>.
- Maruri, R.F., Petro, S.H. (2005). "Integral Abutments and Jointless Bridges (IAJB) 2004 Survey Summary." Federal Highway Administration - 2005 Conference on Integral Abutments and Jointless Bridges, pp. 12-29
- Matlock, H., 1970. "Correlations for Design of Laterally Loaded Piles in Soft Clay," *Proceedings*, 2nd Offshore Technology Conference, Vol. I, pp. 577-594.
- Mistry, V.C. (2005). "Integral Abutment and Jointless Bridges." *Proceedings of the FHWA Conference on Integral Abutments and Jointless Bridges 2005*, Baltimore, MD, pp. 3-11
- Mofarraj, B., and Zornberg, J. G. (2022). "Field Monitoring of Soil-Structure Interaction in Semi-Integral Bridges." *Geo-Congress 2022*, ASCE, Charlotte, NC, 33–42. <https://doi.org/10.1061/9780784484067.004>.
- Oesterle, R.G., Tabatabai, H. (2014). "Design Considerations for Integral Abutment/Jointless Bridges in the USA." *Proceedings of the 1st International Workshop on Integral Abutment/Jointless Bridges*, pp. 71-101. https://dc.uwm.edu/cee_facart/1
- Olson, S.M., Holloway, K.P., Buenker, J.M., Long, J.H., LaFave, J.M. (2013). "Thermal Behavior of IDOT Integral Abutment Bridges and Proposed Design Modifications." Federal Highway Administration, Rep. No. ICT-12-022
- ODOT. (2022). "*Bridge Design Manual 2020 Edition*." Ohio Department of Transportation, Ohio.
- O'Neill, M. W., and Dunnavant, T. W., 1984. "A Study of the Effects of Scale, Velocity, and Cyclic Degradability on Laterally Loaded Single Piles in Overconsolidated Clay," Report No. UHCE 84-7, Department of Civil Engineering, University of Houston-University Park, Houston, 368 p.

- Ooi, P.S.K., Lin, X., Hamada, H.S. (2010). "Field Behavior of an Integral Abutment Bridge Supported on Drilled Shafts." *ASCE Journal of Bridge Engineering*, Vol. 15, No. 1, pp. 4-18. [https://doi.org/10.1061/\(ASCE\)BE.1943-5592.0000036](https://doi.org/10.1061/(ASCE)BE.1943-5592.0000036).
- Pak, D., Bigelow, H., Feldmann, M. (2017). "Design of composite bridges with integral abutments." *Steel Construction*, Vol. 10, No. 1, pp. 23-30
- Peng-fei, J., Ling-wei, K. (2015). "Modeling of ratcheting accumulation of secondary deformation due to stress-controlled high-cyclic loading in granular soils." *Journal of Central South University*, Vol. 22, pp. 2306-2315
- Petzek, E., Metes, E., Toma, L., Bancila, R. (2015). "Integral bridge using the VFT-WIB technology for a three-spanned structure." *Economical Bridge Solutions based on innovative composite dowels and integrated abutments*, pp. 143-154. Springer Vieweg, Wiesbaden
- Purvis, R. L., and Berger, R. H. (1983). "Bridge Joint Maintenance." *Transportation Research Record*, 899, 1-10.
- Rankine, W. J. M. (1857). "On the stability of loose earth." *Philosophical transactions of the Royal Society of London*, 147: 9-27.
- Reese, L. C., and Welch, R. C., 1975. "Lateral Loading of Deep Foundations in Stiff Clay," *Journal of the Geotechnical Engineering Division*, ASCE, Vol. 101, No. GT7, pp. 633-649.
- Reid, R.A., Soupir, S.P., Schaefer, V.R. (1998). "Mitigation of Void Development under Bridge Approach Slabs Using Rubber Tire Chips." *Recycled Materials in Geotechnical Applications*, ASCE, pp. 37-50
- Rhodes, S., Cakebread, T. (2014). "Integral Bridges and the Modelling of Soil-Structure Interaction." International Bridge Conference, Pittsburgh, PA, pp. 41-50
- Shreedhar, R., Hosur, V.I. (2014). "Behavior of Integral Abutment Bridge Superstructure Including Soil Structure Interaction under Thermal Loading." *Journal of Structural Engineering*, Vol. 3, No. 3, pp. 19-24
- Starossek, U. (2009). "Shin Chon Bridge, Korea." *Structural Engineering International*, Vol. 19, No. 1, pp. 79-84
- Tatsuoka, F., Hirakawa, D., Nojiri, M., Aizawa, H., Nishikiori, H., Soma, R., Tateyama, M., and Watanabe, K. (2009). "A new type of integral bridge comprising geosynthetic-reinforced soil walls." *Geosynthetics International*, Vol. 16, No. 4, pp. 301-326
- Tatsuoka, F., Muñoz, H., Kuroda, T., Nishikiori, H., Soma, R., Kiyota, T., Tateyama, M., Watanabe, K. (2012). "Stability of existing bridges improved by structural integration and nailing." Japanese Geotechnical Society. *Soils and Foundations*, Vol. 52, No. 3, pp. 430-448
- Texas Department of Transportation. (1993). "Item 423: Retaining Walls" Texas Department of Transportation.
- Texas Department of Transportation. (1999). "Tex-132-E: Test Procedure for Texas Cone Penetration." Texas Department of Transportation.
-

- Texas Department of Transportation. (2015). "TxDOT Bridge Design Manual – LRFD." Texas Department of Transportation.
- Touma, F. T., and Reese, L. C. (1972). "The Behavior of Axially Loaded Drilled Shafts in Sand." Center for Highway Research, The University of Texas at Austin.
- Walter, J. R. (2018). "Experimental and numerical investigation of integral/semi-integral bridge abutments for Texas conditions." Master's Thesis, University of Texas at Austin.
- Watanabe, K. (2011). "Application of GRS integral bridge technology to Hokkaido High-Speed Train Line (Shinkansen). *Journal of Japan Railway Civil Engineering Association*, Vol. 49, No. 10, pp. 83-86
- White, H. 2nd (2007). "Integral Abutment Bridges: Comparison of Current Practice between European Countries and the United States of America." Federal Highway Administration, Rep. No. NY/SR-07/152
- White, H. 2nd, Petursson, H., Collin, P. (2010). "Integral Abutment Bridges: The European Way." *Practice Periodical on Structural Design and Construction*, Vol. 13, Ed. 3, pp. 201-208
- Zornberg, J.G., Abu-Hejleh, N., and Wang, T. (2001). "Geosynthetic-Reinforced Soil Bridge Abutments." *Geotechnical Fabrics Report*, Vol. 19, No. 2, March, pp. 52-55.